3-D Biogeochemical and hydrodynamic models in the Azores – A tool to understand marine ecosystems

Tese de Doutoramento

Cláudia Neto Viegas

Doutoramento em

CIÊNCIAS DO MAR

SICUT AURORA SCIENTIA LUCET
UNIVERSIDADE DOS AÇORES

Horta

2022

3-D Bio-geochemical and hydrodynamic models in the Azores – A tool to understand marine ecosystems

Tese de Doutoramento

Cláudia Neto Viegas

Orientadores

Prof. Doutora Maria Manuela Fraga Juliano

Doutora Maria Ana Colaço

Tese especialmente elaborada para obtenção do grau de Doutor em Ciências do Mar

Esta bolsa de doutoramento com a referência refª SFRH/BD/129683/2017
foi financiada pela Fundação para a Ciência e Tecnologia .

Host Institutions:

Marine and Environmental Sciences Centre (MARE)
OKEANOS Instituto de Investigação em Ciências do Mar da Universidade dos Açores
IMAR- Instituto do Mar

Resumo

O oceano representa cerca de dois terços da superfície do planeta Terra, e alberga o seu maior bioma, o mar profundo. Da superfície ao mar profundo, o oceano desempenha um papel fundamental como regulador de toda a biosfera, na regulação do clima, na circulação biogeoquímica, na regeneração de nutrientes, e como habitat de importantes ecossistemas marinhos. O mar profundo dos Açores apresenta uma grande variedade de comunidades marinhas, com uma grande diversidade de "hotspots", tais como montes submarinos, que albergam habitats importantes para a conservação, como jardins de corais ou agregações de esponjas, mas também espécies demersais com elevado valor comercial. O mar profundo é, ainda hoje, um grande desafio para a comunidade científica sobretudo pela sua inacessibilidade. A aplicação de modelos matemáticos torna-se vantajosa no estudo destes ecossistemas tão heterogéneos e inacessíveis. Permitem simular e estudar os processos físicos e biológicos do ambiente marinho, no espaço e no tempo, desde a interface com a atmosfera até ao fundo do mar.

O trabalho desenvolvido nesta tese de doutoramento contemplou a implementação de um modelo hidrodinâmico e de qualidade da água para simular os processos físicos e biogeoquímicos na região dos Açores, e ainda a aplicação de um modelo biofísico para estudar a dispersão larvar e a conectividade entre populações de organismos bentónicos no mar profundo. Para simular os processos físicos foi implementado e validado um modelo hidrodinâmico (MOHID Water). Para a sua validação foram utilizados dados provenientes de várias fontes, como marégrafos, detecção remota e perfis de temperatura e salinidade provenientes das bóias ARGO. Os resultados mostraram que o modelo consegue simular com precisão as propriedades hidrodinâmicas e hidrológicas da região dos Açores.

Com a componente hidrodinâmica validada, foi implementado um modelo de qualidade da água (MOHID WaterQuality), para reproduzir os principais processos bióticos e abióticos na coluna de água. O modelo foi parametrizado e calibrado para a região dos Açores. A comparação com dados de detecção remota validou a sua capacidade em simular os padrões sazonais e espaciais de fitoplâncton na região: como o típico bloom de fitoplâncton que acontece no início da Primavera, e um menor no Outono. O máximo de clorofila em profundidade *(deep chlorophyll maximum*–DCM), que ocorre em zonas

oligotróficas, como é o caso dos Açores, foi bem representado pelo modelo, entre os 50 e os 100 metros de profundidade. A validação com a climatologia (World Ocean Atlas-WOA), e com o modelo CMEMS mostrou que o modelo tem capacidade de simular as dinâmicas de nutrientes (nitrato, fósforo e sílica) e oxigénio ao longo da coluna de água. Esta dinâmica biogeoquímica, para além da componente biológica, é sobretudo forçada por fenómenos físicos, que se reflectem na profundidade da camada de mistura. O modelo consegue representar as variações sazonais e espaciais da camada de mistura superficial, cuja profundidade varia entre 20 metros no Verão, aumentando durante o Inverno, podendo chegar aos 250 metros no norte dos Açores. Os resultados obtidos mostraram que o modelo consegue representar as componentes biológicas e físicas do ecossistema marinho nos Açores.

Para estudar a conectividade entre populações bentónicas no mar profundo foi utilizado um modelo lagrangiano (CMS-Connectivity Modeling System) para simular a dispersão larvar. Foram seleccionadas duas espécies distintas: *Pheronema carpenteri*, uma esponja característica do mar profundo dos Açores, e que se pode encontrar de forma dispersa ou em densas agregações; e uma espécie não séssil, *Chaceon affinis,* um caranguejo de profundidade. Foi utilizado o Connectivity Modeling System (CMS), acoplado ao modelo hidrodinâmico MOHID Water. Foram estudados diferentes parâmetros biológicos: a duração do período larvar (Pelagic Larval Duration- PLD) e sua sazonalidade, e vários comportamentos larvares (larvas passivas, e larvas com diferentes capacidades de natação (variando na velocidade e direcção).

Os resultados mostram que existe conectividade entre as agregações de esponjas no Grupo Central (GC) do arquipélago. Os montes submarinos Condor, Princesa Alice e Banco Açores representam importantes locais de retenção de larvas. As populações estudadas da Crista Média Atlântica (CMA) (montes submarinos Gigante e Cavala) têm conectividade com o GC. Ao contrário das agregações de esponjas do Grupo Oriental (Mar da Prata e Formigas), que não apresentam conectividade com as restantes agregações em estudo, e têm menores níveis de auto-recrutamento, apresentando assim uma maior vulnerabilidade. No caso de estudo do caranguejo de profundidade, *Chaceon Affinis*, foi atribuido comportamento às larvas, com diferentes velocidades de natação, incluindo natação vertical, simulando o comportamento que estas larvas têm de nadar até à superfície. Ao contrário das larvas passivas (hipótese mais consensual para as esponjas em estudo), que permanecem

demersais, e são arrastadas pelas correntes do mar profundo caracterizadas por velocidades mais baixas, as larvas que nadam na coluna de água (caso do *Chaceon affinis*), podem deslocar-se até centenas de quilómetros, transportadas pelas correntes superficiais. Este comportamento, juntamente com o maior PLD (PLD 23, 81 e 125 dias) resulta numa conectividade mais dispersa entre as diferentes populações nos Açores. Existe conectividade entre populações de todos os quadrantes do arquipélago (entre a CMA, os Grupos Ocidental, Central e Oriental). As populações da CMA, como o Monte submarino Voador ou Gigante, são importantes zonas de recrutamento de larvas desta espécie, e estabelecem conectividade com populações o Grupo Ocidental, Central ou Oriental. No entanto, apesar de haver maior potencial de conectividade, a percentagem de larvas trocadas entre as várias populações é muito baixa, evidenciando o risco de falta de recrutamento.

Os padrões de conectividade e dispersão larvar mostram que as actuais Áreas Marinhas Protegidas (AMP) do Parque Marinho dos Açores são essenciais para manter a conectividade destas populações. E que áreas como o Mar da Prata, o complexo Gigante, e os montes submarinos Cavala, Ferradura e Voador são também, importantes para manter a conectividade ao longo do arquipélago mas também com a zonas limítrofes.

No último capítulo, os resultados dos modelos hidrodinâmico e biogeoquímico foram utilizados para estudar a ecologia das agregações de esponjas em estudo. Localizadas entre os 600 e os 1000 metros de profundidades, habitam locais caracterizados por baixos gradientes de nutrientes (0.214-0.262 mgN/l, 0.19-0.32 mgSi/l, 0.027-0.037 mgP/l), de temperatura (9.22°C-11.84°C) e oxigénio dissolvido (6.24-6.84 mgO$_2$/l) e baixas velocidades de corrente (entre 0 e 0.06m/s). Os resultados obtidos evidenciam a vantagem da aplicação de modelos para estudar os ecossistemas marinhos, e em particular, conectividade e dispersão larval no mar profundo. A metodologia implementada pode ser aplicada noutros trabalhos e aplicações, podendo servir de apoio para estudo do ecossistema marinho dos Açores, e entre outros, no suporte à gestão dos recursos de pesca e seus ecossistemas, ou no ordenamento do espaço marinho.

Palavras chave: modelação; hidrodinâmica; biogeoquímica; mar profundo; dispersão larvar; conectividade

Abstract

The ocean covers two-thirds of the planet’s surface, and it hosts the largest biome on Earth, the deep-sea. The ocean plays a key role as the regulatory body of the entire biosphere, regulating the weather, buffering biogeochemical circulation, regenerating nutrients and as food supply for marine life. It is by far the largest habitat on Earth, hosting infinitely rich biodiversity. The Azores region presents a great variety of marine communities, with a great diversity of "hotspots", such as seamounts, which host important habitats like coral gardens or sponge aggregations, but also demersal species with high commercial value. However, the deep sea is, still today, a great challenge for the scientific community due to its inaccessibility. The application of modelling tools becomes advantageous in the study of such heterogeneous and inaccessible ecosystems. They allow the simulation and study of physical and biological processes of the marine environment, in space and time, from the surface to the seabed. The principal objective of this thesis was to implement biological and biophysical 3-D models to simulate the most significant physical and biological processes which affect the Azores archipelago and assess larval dispersal and connectivity among deep-sea populations.

Marine systems are driven primarily by physical processes. As such, the validation of the hydrodynamic model is of paramount importance. Furthermore, the biogeochemical and biophysical models used, are coupled with the results of this 3-D hydrodynamic model (MOHID Water). The implementation and validation of the hydrodynamic model were undertaken in the first stage of this thesis. For its validation data from several sources were used, such as tide gauges, remote sensing and temperature and salinity profiles from ARGO buoys. The results showed that the model can accurately simulate the hydrodynamic and hydrological properties of the region.

Secondly, a biogeochemical model (MOHID Water quality) was implemented, calibrated and validated for the Azores region. The results showed that the achieved MOHID parameterization enabled a representation of different biotic and abiotic processes. Validated against remote sensing data, the model seasonal phytoplankton patterns were well reproduced, with the typically strong spring bloom, and a smoother autumn bloom. Model results show the existence of a deep chlorophyll maximum (DCM), between 50 and 100 metres depth, with its characteristic spatial and seasonal variations.

Model assessment against World Ocean Atlas (WOA), and a global ocean circulation model revealed that MOHID is able to simulate the vertical dynamics of nutrients (nitrate, phosphate and dissolved silica) as well as oxygen concentration. The results of the Chapters 2 and 3 are of the greatest importance to the characterization of marine dynamics, from the surface up to the deep-sea.

Taking advantage of the hydrodynamic model validated in Chapter 2, a biophysical particle tracking model was implemented to study larval dispersal and population connectivity in the deep-sea. Two target species were selected: a sessile organism, *Pheronema carpenteri,* a deep-sea sponge; and a non-sessile organism, *Chaceon affinis*, a deep-sea red crab (DSRC). Different scenarios and biological characteristics were studied: the seasonality of spawning, pelagic larval duration (PLD), and larval swimming behaviour (surface-oriented and bottom-oriented swimming). Model results show how the regional circulation patterns of the currents drive larval dispersion, shaping population connectivity. Spawning time and PLD are determinant factors for larval dispersion and population connectivity. The lagrangian model results suggest the existence of connectivity between *Pheronema carpenteri* sponge aggregations in the Azores, mainly among populations in the Central Group (CG) of Azorean islands. The populations of the Condor Seamount, Princess Alice, and Azores Bank reveal high retention rates, receiving larvae from several sponge aggregations. These are also important source populations. On the other side, populations from the Oriental Group may be isolated from the others. The swimming behaviour simulated for DSRC larvae contributes to the higher larvae travel distances and dispersal patterns. Larval dispersal shows potential connectivity between populations across the Azores archipelago, with variable seasonal connectivity. Uneven connectivity can occur between the furthermost populations (e.g. between Mar da Prata on the eastern and Flores Island on the western extremities of the archipelago). However, the low percentage of larvae exchange also indicates that the populations might be isolated and that despite the connected populations, caution should be made in the management of the populations before their exploitation. The model estimates that the populations in the Mid-Atlantic Ridge (MAR), namely Voador seamount, may constitute an important sink and source of larvae for the Azores region.

Larval dispersal and connectivity patterns were used to assess the effectiveness of current Marine Protected Areas (MPA) in the Azores. The results reinforced the importance of maintaining the protection efforts in the Condor, Princesa Alice MPAs, as important recruitment areas. In Condor, also for being an important source location. João de Castro MPA reveals to be crucial to promote the connectivity between the CG and the Eastern Group (EG). Due to their location, and constrained by the hydrodynamic patterns, populations from the EG may be isolated from the remaining populations. Therefore, a MPA in Mar da Prata will contribute to preserve the connectivity in the plateau south of São Miguel island, and both Mar da Prata and Formigas populations. The vulnerability of Formigas populations, which faces several scenarios with no connectivity or the absence of self-recruitment also reinforces the need to maintain Formigas MPA. Connectivity and larval dispersal patterns show that Gigante, Cavala, Ferradura, and Voador seamounts are essential locations to guarantee connectivity across the archipelago and with the neighbouring areas (in the South, West and North of the archipelago.

The ultimate goal of this thesis was to showcase the utilization of the constructed models to better understand the ecology of the target sponge species. In Chapter 5, physical and bio-geochemical model results are analysed, revealing that the studied *P. carpenteri* aggregations are located in regions with low gradients of nutrients (0.214-0.262 mgN/l, 0.19- 0.32 mgSi/l, 0.027-0.037 mgP/l) temperature (9.22°C-11.84°C), and dissolved oxygen (6.24-6.84 mgO_2/l), and low current velocities (0 e 0.06m/s).

The thesis provides an initial description of the processes which drive deep-sea larval dispersal in the Azores. It further demonstrates the capacity of the model to facilitate the study of various biological traits, serving as a baseline for assessing deep-sea connectivity and supporting management actions and marine spatial planning studies. The main results highlight the advantages of coupled model systems for studying complex marine systems and various associated scenarios. The primary objective was to provide modelling methodologies and useful data to increase the current understanding of the marine ecosystem of the Azores, from the surface to the deep-sea. These hydrodynamic and bio-geochemical results can be used in further studies, like food-web and ecosystem studies, or fisheries management studies, among others.

Keywords: modelling; hydrodynamics; biogeochemical; deep-sea; larval dispersal; connectivity.

Acknowledgments

I would like to express my thanks to all the people who, in one way or another, contributed to the development of this thesis.

My deepest and sincere gratitude goes to Doutora Ana Colaço, who challenged me to pursue this PhD project, for her enthusiasm, trust, friendship, scientific advisory and unconditional support. For always believing in me, and for giving me so many opportunities to develop my scientific skills throughout these 4 years. Also for her contagious deep-sea enthusiasm.

I would like to extend my gratitude to Professora Doutora Manuela Juliano, for her unstoppable dedication, for all the hours and days around MOHID, for helping me with these model applications, and for her pragmatism and continuous support and friendship.

I would also like to thank IMAR-Instituto do Mar, and to Okeanos, for all the support, throughout my Phd. Including my attendance to ATT: Marine Biogeochemistry Training School on biogeochemical and ecological dimensions of a changing ocean. To the European Marine Board for the internship opportunity. I am really thankful to be given this opportunity to work in this leading European think-tank in marine science policy. Thanks to Sheila Heymans, Paula Kellet, Ángel Piniella, and Kate Larkin. To all the participants in the EXPLOSEA2 cruise, in the northern Mid-Atlantic Ridge and Azores Archipelago. To the enthusiastic PI Luiz Somosa, all the crew, the scientific team, and especially the EMEPC team (Inês Tojeira, Luísa Pinto Ribeiro, and the incredible ROV team). And to Ana Colaço for giving me this opportunity.

Moreover, I am extremely grateful to all my colleagues and staff from Okeanos, especially to my open-space colleagues and friends, for making every day a better working day. To Ricardo Medeiros for being always available for any GIS data, and with a smile. To Neus for her help in the statistical analysis.

Because life is made of moments, friends and family, I would like to thank all of you:

"Powers" gang: Cristina, Sara, Hilda e Carina, for your friendship, and all our (un)useful conversations, since the very beginning of my journey In the Azores. To the "Bics" gang: a special thanks. To Maria Rakka for all the support and for being an inspiration. Ana Alves, thanks for your friendship and positive mood (and for taking care of my cats). A special thanks to David for all the support, the hugs and the special energy. Also to my friend and neighbour Dyia, thanks for everything. Meri, thanks for your joy and motivation. Miriam, you are an example of a strong woman. For my Shrekhouse friends: Anita, Margarida, João, Noélia e Marie (Salmi and Hortaliça are also thankful). To Cineclube do Faial friends, thanks for all the moments and all the movies. To my friends Rita, Rui and Carolina for the long-lasting friendship. Eva, my first friend in primary school, thanks for all the words! Carina, is very good to have a good old friend here in the Azores, thanks for everything. And, last but not least to all the island gang, because friends are family and you make this island the better place to live!

Finally, I would like to express my deepest gratitude to my mother, my father, and my sister, who always gave me unconditional support. Especially to my mother, for all the words, unconditional love and care in all the moments.

Index

List of Acronyms

ADW- Atlantic Deep Water
AEEZ- Azores Economic Exclusive Zone
BGC- BioGeoChemical
CG- Central group
Chl- Chlorophyll
Chl_a- Chlorophyll_a
CMEMS- Copernicus Marine Environment Monitoring Service
CMS- Connectivity Modelling System
DSRC- Deep-Sea Red Crab
EEZ- Economic Exclusive Zone
EG- Eastern group
ENACW-Eastern North Atlantic Central Water
FES -Finite Element Solution
FUV- Fraction of Unexplained Variation
GFS- Global Forecast System
HAMMOC-Hamburg ocean carbon cycle model
Kd- Diffuse attenuation coefficient (of downwelling radiative flux in sea water)
MAR- Mid-Atlantic Ridge
MOHID- MOdelling HYDrodynamics (in portuguese MOdelação Hidrodinâmica)
MPA- Marine Protected Areas
MW- Mediterranean Water
N- Nitrogen
NASA'sOBPG- North American Spatial Agency -Ocean Biology Processing Group
NEMURO - North Pacific Ecosystem Model for Understanding Regional Oceanography
O- Oxygen
P- Phosphorous
PDD- Particle Density Distribution

PISCES - Pelagic Interactions Scheme for Carbon and Ecosystem Studies)

PLD- Pelagic Larval Duration

RMSE- Root Mean Squared Error

Si- Dissolved Silica

SSS- Sea Surface Salinity

SST- Sea Surface Temperature

VME- Vulnerable Marine Ecosystems

WG- Western group

WOA- World Ocean Atlas

Chapter 1

General introduction

1.1. Overview

Marine ecosystems cover over 70% of the Earth's and harbour most of the planet's biodiversity (OECD, 2016). Conservation challenges facing ocean ecosystems require a detailed understanding of the ecological and physical characteristics of ocean ecosystems. From the surface up to the bottom, marine ecosystems are governed by hydrodynamic and external drivers (like meteorology), but also by biological and ecological interactions (Vallino, 2000). Marine plankton dynamics drive this biological pump, acting on the ocean's biogeochemical cycling, and on the entire pelagic food web, from the surface to the deep-sea (Chenillat et al., 2021). Primary production in the upper layer of the ocean (in the euphotic zone) and its transportation to the deeper layers are key mechanisms responsible for the interaction between the surface and the deep-sea (De La Rocha and Passow, 2007). The need to understand, monitor, simulate and forecast these dynamics has motivated the development of coupled biogeochemical-circulation models (Berline et al., 2007).

Over the past 30 years, the use of modelling tools and remote sensing has prompted our understanding of marine ecosystems and biogeochemical processes (Bracher et al., 2017). However, hampered by the difficulty of studying and monitoring, knowledge about the deep-sea is still very scarce. In the Azores, extensive scientific research efforts are increasing the knowledge of the functioning of oceanic, deep-sea and seamount ecosystems, as well as the impacts of human activities on these ecosystems (Morato et al., 2020).

A holistic approach to the biological and physical processes that influence oceanic and deep-sea ecosystem dynamics requires the use of modelling tools (Lindemann and St. John, 2014). Numerical models are used to study several physical ocean processes like the ocean circulation (Lampitt et al., 2010; Oddo and Pinardi, 2008; Yamanaka et al., 2004), winter convection and local upwelling (Gregg et al., 2003; Kessouri et al., 2021; Koné et al., 2005; Yamanaka et al., 2004). Moreover, biogeochemical models have been developed to understand and quantify the main biogeochemical processes and complex dynamics between nutrients and plankton (Arhonditsis et al., 2006). Biogeochemical models have been proven to be useful tools for ecological research, to represent the feedback between the pelagic ecosystem and the physical processes (Aumont et al., 2015; Kane et al., 2011; Vichi et al., 2007a); to predict the response of marine ecosystems to climate changes (Fennel et al., 2019; Kishi et al., 2007; Losa et al., 2019); to feed other models namely: fisheries modelling and stock assessment (Fennel, 2009; Gutknecht et al., 2016; Mitra et al., 2014); larval dispersal models (Vic et al., 2018), and more recently for deep-sea habitat studies (Liu et al., 2021). Transport processes can be studied with particle tracking models, a popular approach among physical and biological oceanography studies unravelling the influence of transport processes on marine ecosystems (Paris et al., 2013). These biophysical models have emerged as an important tool for assessing structural connectivity in the deep-sea by studying pelagic larvae dispersal (Chaput et al., 2022; Ross et al., 2020).

The current thesis focuses on the application of several modelling tools to better understand the oceanographic and ecosystem dynamics in the Azores, from the surface to the bottom layers. It includes the implementation and validation of a hydrodynamic model, and a biogeochemical model to study and characterize the biotic and abiotic processes in the Azores region. As well as the development of a particle tracking model to study physical connectivity (larvae dispersion) in the deep-sea.

1.2. The Azores Archipelago

The Azores archipelago, Figure 1.1, is composed of nine islands, spanning along 600 km in the Northeast Atlantic, between 23ºW and 33ºW and 37ºN and 40ºN. It is located on the Mid-Atlantic Ridge (MAR), which divides the archipelago in two, leaving two islands on the American plate (Flores and Corvo islands) and the others on the Eurasian plate (Figure 1.1). The Exclusive Economic Zone (ZEE) of the Azores covers an area of more than 950 000 km^2, with more than 460 seamount-like features and several designated protected areas (Morato et al., 2008; Peran et al., 2016). With an average depth of nearly 3000 m, the Azores region mainly consists of deep-sea and is dominated by a diverse mosaic of deep-sea habitats (Peran et al., 2016; Tempera et al., 2013). The deep-sea in the Azores is characterized by the presence of numerous seamounts and hydrothermal vents, hosting high biodiversity and rich communities which constitute feeding grounds for fishes, marine mammals and seabirds (Colaço et al., 2020; Creemers et al., 2019; Giacomello and Menezes, 2012; Gomes-Pereira et al., 2017; Morato et al., 2020, 2016b, 2008). These hotspots of biodiversity, are considered extremely important to the Azores, both on ecological and socio-economic levels (Giacomello and Menezes, 2012).

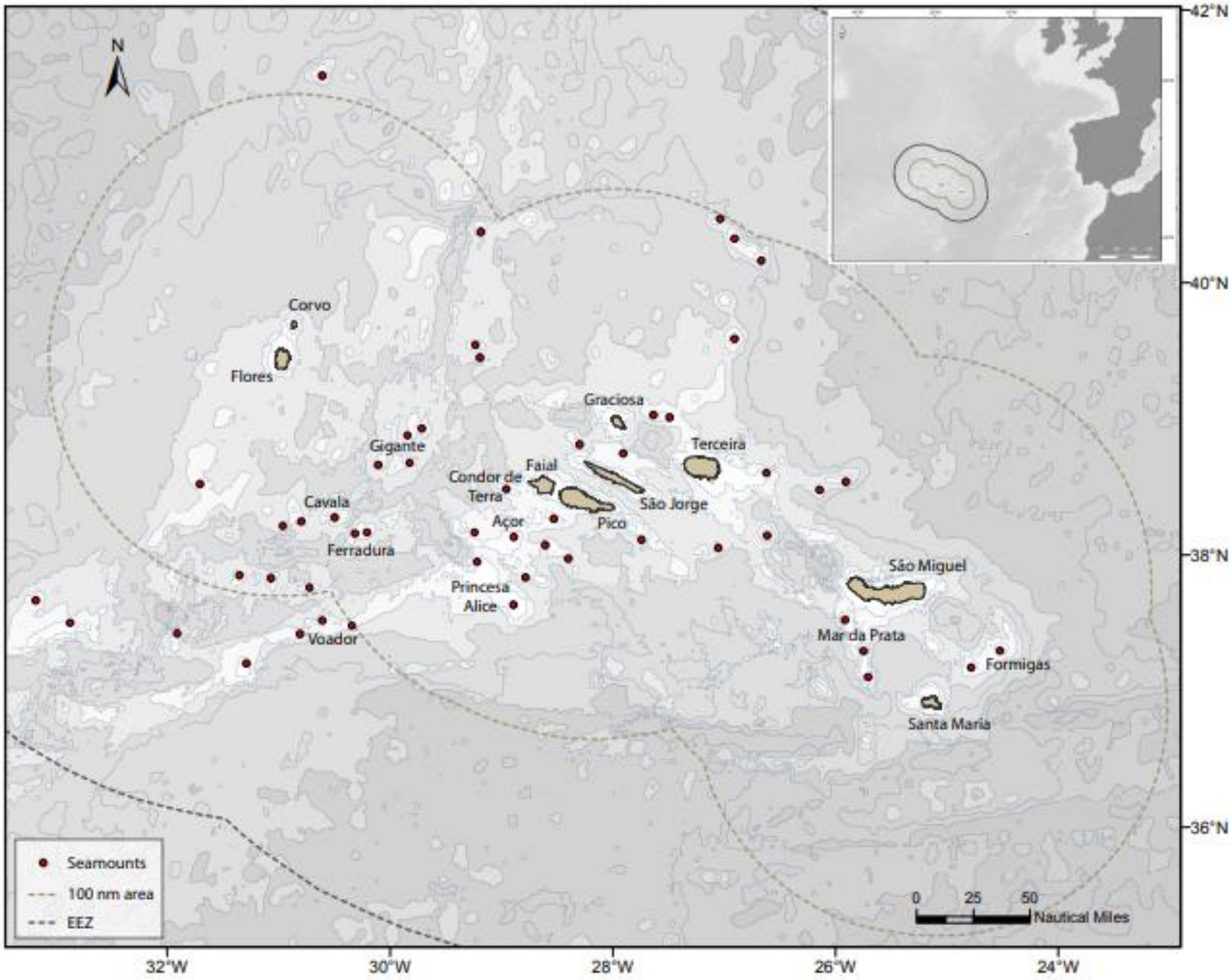

Figure 1.1- Map of the Azores archipelago, and the limits of the ZEE, the representation of the Azores islands (Flores, Corvo, Faial, Pico, São Jorge, Graciosa, Terceira, São Miguel and Santa Maria), and several seamounts, represented with a red circle. Adapted from: Braga-Henriques et al., 2013

The Azores deep-sea benthos includes a high diversity of sponges and cold-water corals which build rich communities (Colaço et al., 2020; Creemers et al., 2019; Gomes-Pereira et al., 2017; Morato et al., 2021; Pham et al., 2015). These communities have been identified as vulnerable marine ecosystems (VMEs) since they meet several of the vulnerability criteria, like fragility, slow growth rate and low recovery potential (FAO, 2008). These deep-sea organisms rely upon a planktonic larval stage for dispersal, therefore, the study of the environmental patterns responsible for their distribution is critical to inform and support the development of appropriate conservation measures (Cowen and Sponaugle, 2009; Maldonado and Young, 1999; Wang et al., 2021; Xavier et al., 2021).

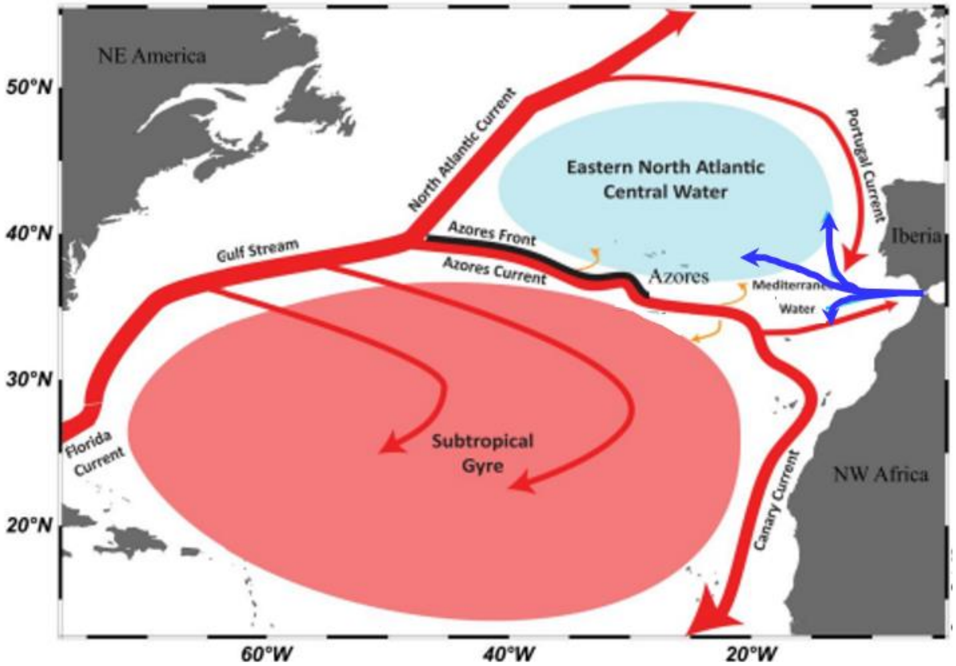

Figure 1.2- Schematic representation of the main circulation in the North Atlantic Ocean, and major water masses. Adapted from Bonfardeci et al., 2018.

The Azores region is affected by the North Atlantic ocean circulation and by the influence of several water masses (Figure 1.2). A large anticyclonic gyre is found in the subtropical region of the North Atlantic, delimited to the south by the North Equatorial Current, the subtropical gyre of the Northern Hemisphere, zonally crossed by the Azores Current (Alves and De Verdière, 1999). The East North Atlantic Central Water (ENACW) fills the depths between 100 and 600m depths, the North Atlantic Deep Water (NADW) below 1500m depth (Lázaro et al., 2013; Palma et al., 2012), and the Mediterranean Water (MW), arriving at the region at 1100m depth approximately (Juliano and Alves, 2006).

The ocean climatology in the Azores is characterized by spatial, seasonal and interannual variability typical of mid-latitudes (Amorim et al., 2017; Stramma and Siedler, 1988; Valente, 2013). The northernmost islands are under the influence of the southward branches of the North Atlantic Current (NAC), which transport colder, less saline and possibly more productive waters into the archipelago (Narciso et al., 2016). In the South, the Azores Current is a quasi-permanent feature, forming a thermohaline front, separating colder waters to the north and warmer and saltier water masses to the south (Juliano and Alves, 2007). These different physical factors that influence ocean circulations around the Azores archipelago, also influence the oceanographic biological processes controlling the distribution of nutrients and oxygen (Palma et al., 2012).

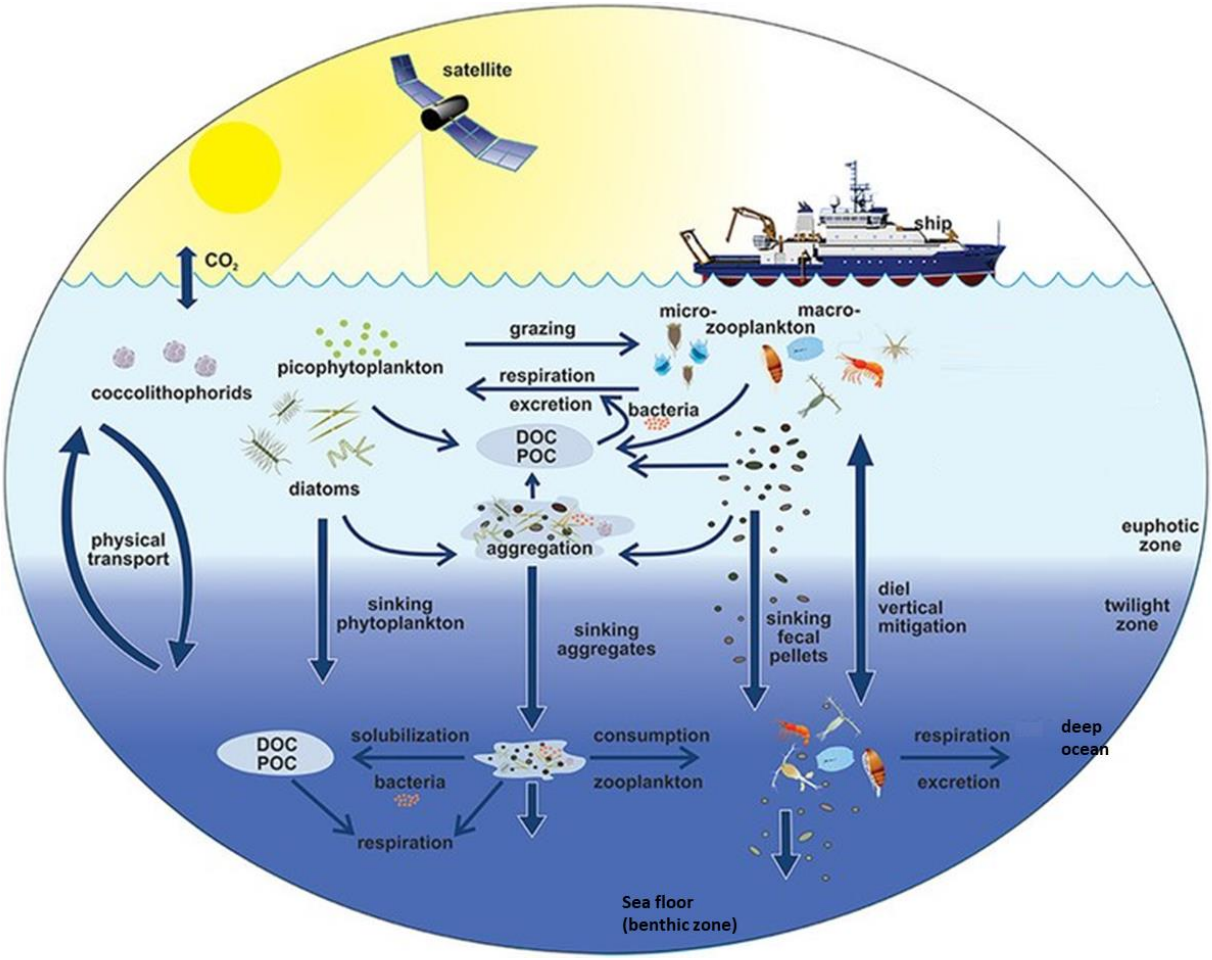

Figure 1.3- Schematic representation of the ocean's biological cycle, with the processes at the surface, in the mesopelagic zone, in the deep ocean and at the seafloor. Adapted from Siegel et al. 2016

The Azores is an oligotrophic region, characterized by a lower nutrient concentration, where light is not a limiting factor and marine phytoplankton growth is limited by nutrients

(Barcelos e Ramos et al., 2017). Phytoplankton is at the base of the marine food web and drives the biogeochemical cycles in the ocean (Lan Smith et al., 2011).

The ocean's biological pump transports organic matter, created by phytoplankton productivity in the surface ocean (euphotic zone), to the mesopelagic zone and the deep ocean where it is consumed by animals and heterotrophic microbes and remineralized back to inorganic forms (Figure 1.3). First, at the surface (in the euphotic zone) the dissolved inorganic carbon (DIC) is assimilated by the phytoplankton (picophytoplankton and diatoms) and fixed into particulate organic carbon (POC). By grazing from zooplankton this POC is assimilated and mineralized being released as DIC or dissolved organic carbon (DOC) (Siegel et al., 2016).

Because phytoplankton is on the base of most marine trophic webs, its variability affects the dynamics of the whole system (Reboreda, 2013). Phytoplankton grows and multiplies via photosynthesis, so, its productivity relies mainly on light, multiple nutrients and temperature (Behrenfeld et al., 2008; Valente, 2013). The phytoplankton also relies on i) physical drivers like temperature, hydrodynamic transport, mixing and sinking; ii) physiological factors like regulation, acclimatization, mortality, or aggregation; and iii) ecological factors like competition or grazing (Behrenfeld et al., 2008; Buitenhuis et al., 2010; Raick et al., 2005; Sunda and Hardison, 2010; Tirok and Scharler, 2013; Yool and Tyrrell, 2003). Marine phytoplankton plays an important role in the global carbon cycle via the biological carbon pump, responsible for about half of the global primary production (Siegel et al., 2016) and forming the marine food web basis.

In the ocean, light with energy for photosynthesis is only available at the surface layers, limiting the phytoplankton production to the euphotic zone. However, contrasting with light, maximum at the surface, diminishing with depth, the nutrient concentration is lower at the surface and higher in deeper layers where sinking particles decompose. The Azores, an oligotrophic region, is characterized by lower nutrient concentrations at the surface, therefore, the phytoplankton growth is dependent on physical mechanisms, that bring the nutrients from the deeper layer up to the euphotic zone (Valente, 2013). These physical, chemical and biological processes, including physiological acclimation of phytoplankton, can originate an optimal point in a certain depth along the water column, creating a deep phytoplankton maximum (also known as deep chlorophyll maximum DCM) (Fasham et al., 1985; Marañón et al., 2007). This DCM depth changes in time and space. In the Azores, the deep chlorophyll maximum (DCM) can be found below the surface at 75-150m depth, approximately (Macedo et al., 2000). Macedo et al., 2009 described a progressive descent of the DCM during spring and summer following the deepening of the nutricline, and a North-South gradient, with lower DCM in the North of the Azores than in the South. South of the Azores, at 34ºN, under the influence of the Azores Front-Current system, a high productivity region, the DCM was identified between 90 and 100 meters depth.

The phytoplankton carbon is exported from the ocean surface to deeper layers, by physical processes, down to the sea floor, either as sinking phytoplankton, faecal pellets, or aggregates. Physical processes, like winter convection, also contribute to the increase of nutrients in the surface layers (Yamanaka et al., 2004). This primary winter convection that drives nutrients from the bottom until the surface layers, is induced by seasonal climatological drivers (McKinley et al., 2018). Nutrient enrichment of the ocean surface in the Azores depends mainly on the annual changes in the mixed layer depth, and on ocean circulation causing nutrient upwelling from deeper layers (winter convection) (Valente, 2013).

Phytoplankton dynamics in the Azores, are characterized by seasonal variation at the surface, with typical spring blooms beginning in late February/March, and weaker autumn blooms in October-November (Carmo et al., 2013a; Macedo et al., 2000). The stronger spring blooms may be related to the deeper winter convection and the upper ocean layer stratification, but may also be linked to the better conditions for photosynthesis: optimal solar radiation and temperature, as well as an increase of nutrients in the surface layers caused by deep winter mixing, that induce growth of primary producers, cannot be discarded. Therefore, during summer, nutrient uptake by primary producers together with the summer stratification contributes to the decrease of nutrient concentration at the surface. During fall, the mixing of surface waters with deeper nutrient-rich waters is induced by meteorological conditions, providing the necessary nutrients for phytoplankton growth (Martinez et al., 2011).

1.3. Introduction to larval dispersal

Many marine organisms rather than dispersing as adults rely upon the larvae phase as the only means to colonize new areas, being this process crucial for individual survival, population dynamics and persistence (Ross et al., 2020). For benthic species (sessile or not sessile), the primary dispersal phase is typically associated with the earliest life history stage (spore, egg, or larva) (Cowen and Sponaugle, 2009). Larval dispersal is therefore an important ecological process able to connect populations of species that live in patches of benthic habitat separated by vast expanses of the ocean (Kough, 2014). Larval dispersal in deep-sea and seamount ecosystems depends on external factors like physical hydrodynamics or substrate conditions (Figure 1.4), but also on intrinsic factors like species-specific larval physiology and behaviours, features that influence the dispersal, settlement, colonization, and physical and genetic connectivity between different sites (connectivity), or by self-recruitment. Connectivity here is defined as the dispersal and survival of larvae from one population, that settled in another population after the pelagic larval period, and self-recruitment when after the pelagic larval period the larvae settle in the same population (Shank, 2010).

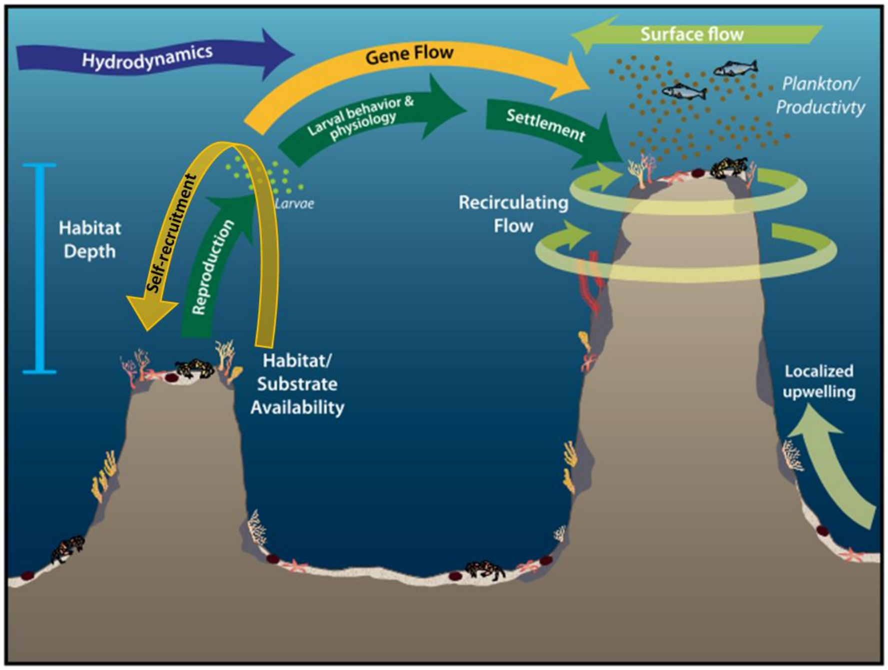

Figure 1.4- Conceptual framework of larval dispersal in the deep-sea and seamount ecosystems, considering the extrinsic (e.g., physical hydrodynamics substrate conditions) and intrinsic (e.g., species-specific larval physiology and behaviours) factors that influence the dispersal, settlement, colonization, and physical and genetic connectivity between different sites (connectivity), or by self-recruitment with larvae settling in the same population. Adapted from Shank 2010. The degree of exchange of individuals, "connectivity," among populations is critical for the stability of these populations and their capacity to exploit new areas (Cunha et al., 2020). Many subpopulations would likely go and stay extinct if they were not connected demographically to other subpopulations (Gaines et al., 2005).

The study of larvae dispersal is important for understanding a broad range of ecological and evolutionary questions, as well as for anticipating the effects of habitat fragmentation

(Connolly and Baird, 2010). Where local retention and survival of offspring are low, the sustainability of populations will depend on replenishment from elsewhere (Roberts et al., 2003). Spatially fragmented populations, or metapopulations, can be classified as “sources” or “sinks” of a particular species depending on the balance of larvae inputs and outputs (Metaxas and Saunders, 2009). The exchange of individuals between subpopulations is known as connectivity (Phelps, 2015). Larval dispersal is an important ecological process of great interest to marine ecology and conservation: in the design of effective networks of marine protected areas (MPAs) (Combes et al., 2021; Ross et al., 2017; Ross and Howell, 2013); protection of Vulnerable Marine Ecosystems (VME) (Kenchington et al., 2019), like deep-sea sponges (Howell et al., 2016; Ross et al., 2019; Samuelsen et al., 2022; Wang et al., 2021) or corals (Botsford et al., 2009; Connolly and Baird, 2010; Foster et al., 2012; Wood et al., 2014); on the spatial management of marine capture and fisheries (Fogarty and Botsford, 2007; Kough et al., 2013; Roman and Boicourt, 1999). Despite the uncertainty about larval dispersal, modelling studies have indicated how larval dispersal and the spatial configurations of MPAs interact to promote population persistence (Botsford et al., 2009).

Larvae can have direct development, and be brooded or dispersed in the water column as plankton. The planktonic larvae are transported by ocean currents (Phelps, 2015). During the pelagic larval duration (PLD), larvae can be lecithotrophic (feed upon yolk stored in egg), or planktotrophic (feed upon planktonic food) (Yearsley and Sigwart, 2011). Larvae can have swimming behaviour, and ontogenic vertical migration (Cowen and Sponaugle, 2009; Maldonado et al., 2016; Mariani et al., 2006; Treml et al., 2012). However, the behaviours governing how larvae disperse are under-described (Gary et al., 2020). After the PLD, which can vary from a few minutes to weeks or even months (Wang et al., 2021), the larvae return to the seabed and settle in a suitable substrate to develop into a juvenile. The developmental stage at which larvae are capable of transitioning and settling into a suitable benthic location is called competence (Hodin et al., 2018).

1.4. Modelling tools

The use of models is an essential tool when dealing with oceanographic studies and management questions, enabling the study of different scenarios and hypotheses. Ocean circulation is driven mainly by physical drivers like geostrophic factors (gravitational and deflective force by earth's rotation - the Coriolis force); oceanic factors (i.e. pressure gradient, water temperature and salinity variations); atmospheric factors; but also bathymetry (Hirose and Kamiya, 2003).

Local ocean conditions are often controlled by large-scale processes, leading to the need for downscaling from global and larger-scale models into local models, representing, as accurately as possible, the ocean conditions, to estimate local and regional features in a higher resolution scale (Katavouta and Thompson, 2016). Several global and regional models were developed and applied in the Atlantic Ocean, continental shelf and coastal areas, simulating physical ocean properties, namely: the Global Ocean Analysis and Forecast System, provided by E.U. Copernicus Marine Service Information (CMEMS) Marine Data Store (MDS) (https://doi.org/10.48670/moi-00016, accessed on Jully 2023); NEMO- Nucleus for European Modelling of the Ocean (Gutknecht et al., 2016;); FOAM- Forecasting Ocean Assimilation Model (Bell et al., 2004); MOHID (Campuzano et al., 2013; IST, 2003; Juliano et al., 2012), ROMS-Regional Ocean Modelling System (Costa et al., 2012).

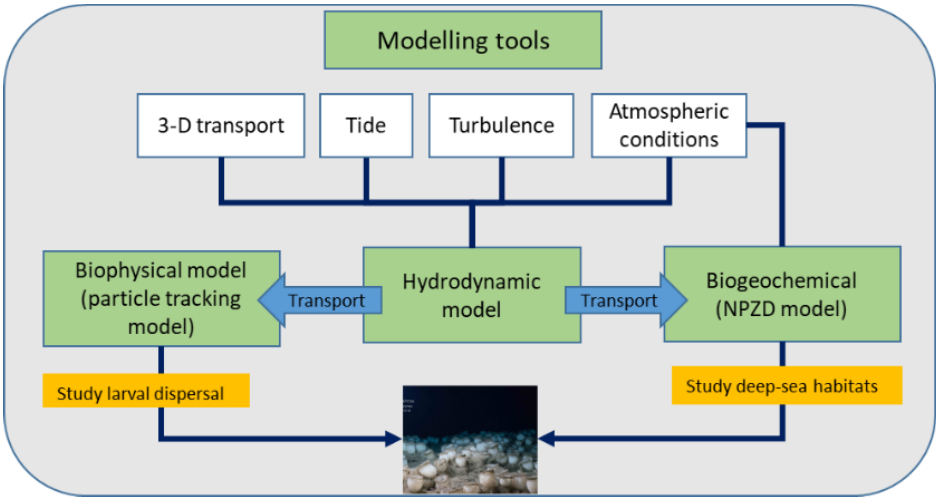

Figure 1.5- Diagram of modelling tools used in this thesis: a physical hydrodynamic model; a coupled biogeochemical (nutrient, phytoplankton, zooplankton and detritus model); a biophysical particle tracking model (bio: larval behaviour, mortality, pelagic larval duration etc.; physical: transport and particles tracking).

During the development of this thesis, different models are used (Figure 1.5), namely: a hydrodynamic model (MOHID) to simulate the physical processes in the Azores region, considering the atmospheric conditions, the physical transport in the entire water column (from the surface until the sea-floor. The tide is provided by FES 2014 model (Lyard et al., 2021), and the turbulence from GOTM- General Ocean Turbulence Model (Burchard et al., 1999); a coupled biogeochemical model (MOHID) to simulate the major biotic features, and finally a biophysical particle tracking model, CMS-Connectivity Modeling System (Paris et al., 2013), to study larval dispersal

Biogeochemical models

While hydrodynamic models are widely used and implemented, and their physical equations of state are relatively well known (Berline et al., 2007), when biogeochemical dynamics are incorporated into the models, the complexity increases, increasing concomitantly the diversity of options for model building (Robson, 2014). The number of phytoplankton functional groups (PFG) to consider in biogeochemical models is an issue under discussion in model development and depending on their level of simplicity, complexity and objectives, different models can consider different groups (Kwiatkowski et al., 2014).

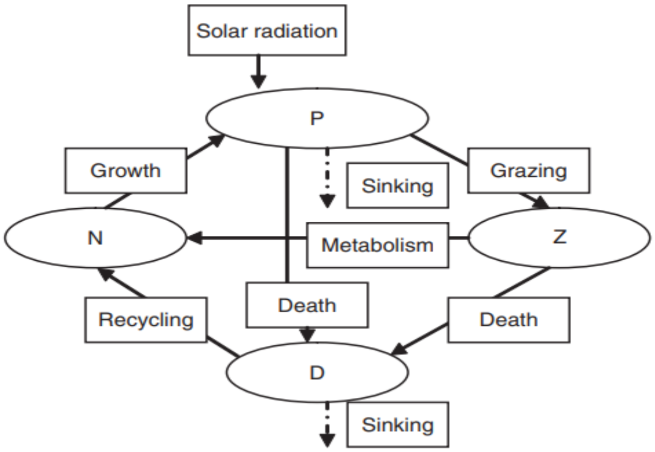

Figure 1.6- Schematic diagram of the NPZD (nutrient-phytoplankton zooplankton-detritus) model. Image from: Xu et al., 2008

Many biogeochemical models simulate the marine biological productivity following a nutrient–phytoplankton–zooplankton–detritus (NPZD) relation, where biogeochemical cycles are connected to the trophic levels through the uptake of nutrients by phytoplankton and remineralisation of organic matter (Figure 1.6) (Peña et al., 2016).

Different NPZD models are applied at a regional and global scale such as FASHAM (Haney and Jackson, 1996), PISCES (Aumont, 2005), HAMMOC (Ilyina et al., 2013). Although marine biogeochemical models have increased their complexity in the last decade, global-scale models continue to use simple phytoplankton growth models with simplification of phytoplankton physiology, namely using constant Carbon:Nitrogen ratios (C:N) assuming constant stoichiometry between carbon, nitrogen and phosphorus (Redfield ratio) (Ayata et al., 2013). Similarly, simple Chlorophyll:Carbon (Chl:C) ratios are used, based on the classical Michaelis–Menten representation of nutrient uptake (Anugerahanti et al., 2021).

Applications coupling both physical and biogeochemical models are used for different purposes: to support the European Marine Strategy Framework Directive (MSFD) requirements (Piroddi et al., 2015); to simulate the lower trophic levels of marine ecosystems (Aumont et al., 2015), study pelagic biogeochemistry (Vichi et al., 2007b), or to study the response of ocean biogeochemistry to climate changes (Buchanan et al., 2018), revealing the importance of using biological models to study space and time variations.

Biophysical models

In recent years, many studies integrated multidisciplinary approaches using biophysical modelling (Cowen and Sponaugle, 2009; Criales et al., 2019; Pata et al., 2021; Ross et al., 2020, 2016), to study planktonic larval dispersal, using 3-dimensional circulation models and particle tracking models. In these models, particles represent larvae, with passive or swimming behaviour, and different biological traits can be included: e.g. PLD, spawning seasonality, mortality, buoyancy, or diel vertical migration (Helgers et al., 2013; Leis, 2020; North et al., 2009). Ultimately, such models simulate the likely paths of larval dispersal and can be used for population connectivity studies (Metaxas and Saunders, 2009; Paris et al., 2013). and genetic markers (Bracco et al., 2019; Vic et al., 2018). Larval dispersal studies have also greatly benefited from the development and optimization of hydrodynamic models (Cowen and Sponaugle, 2009; Vasile et al., 2017; Werner et al., 2007).

Coupled with hydrodynamic models, these models allow to study dispersal scenarios, considering different organisms and larval behaviours, under different environmental conditions. Deep-sea larvae can have from a few minutes to several months of PLD (Ross et al., 2020), promoting larval dispersal over larger spatial scales, facing cross-shore transport and shelf break processes (upwelling systems, slope eddies, shelf-break jets) across offshore waters (Werner et al., 2007). Regional and ocean circulation models that capture these processes would be more appropriate than small-scale and coastal models, in modelling the larval dispersal of species with long PLD (Vasile et al., 2017). These particle tracking models have been used to study larval distribution, estimate larval transport, and study populations connectivity in VMEs (Kenchington et al., 2019; Ross et al., 2017; Wang et al., 2020), and specifically on deep-sea sponges (Busch et al., 2021; Ross et al., 2019); fisheries management (Hinrichsen et al., 2011; Mitra et al., 2014); and on the design of marine protected area (MPA) networks (Combes et al., 2021; Kenchington et al., 2019; Kough, 2014).

1.5. MOHID modelling system

In this thesis, the MOHID modelling system (Neves et al., 2003), has been used as the main modelling tool. The MOHID Water model is a 3D finite volume model developed at MARETEC (IST - University of Lisbon) which solves the 3D incompressible primitive equations (Leitão et al., 2008; Martins, 1998) built and developed using an object-oriented philosophy (Braunschweig et al., 2004). MOHID Water is an open-source model and the most relevant key strengths are its ability to deal with 2D and 3D simulations, with sigma, cartesian or lagrangian vertical coordinates; with eulerian or lagrangian transport references; and solve biogeochemical formulations.

The biogeochemical water quality MOHID module have been used in several applications in coastal areas and estuaries (Mateus 2006, Leona(de Pablo, 2022; Mateus, 2006)rdo 2022), and in the North Sea (Bernardes 2007). A deeper description of the processes and the governing equations of the transfer fluxes among the several biogeochemical water properties involved in the biogeochemical model are included in Chapter 3. Also on the MOHID water quality model website (www.mohid.com). Figure 1.7 represents schematically the different modules considered in the MOHID Water, regarding the different environmental compartments, like the atmosphere and the interface air-water, the water column with the different modules like turbulence, hydrodynamic, waterproperties, and also the interface with the sediment, between other modules.

MOHID has been applied in ocean and coastal models (de Pablo et al., 2019; Franz et al., 2017; Riflet et al., 2008; Trancoso et al., 2009), taking advantage of the downscaling approach from global circulation models to regional and local models (Campuzano et al., 2013).

MOHID has been applied also to the Azores region, coupled with a biophysical model, the Connectivity Model System (CMS), to study deep-sea mining plumes, and larval dispersion in hydrothermal vents (Purser and Marcon, 2016).

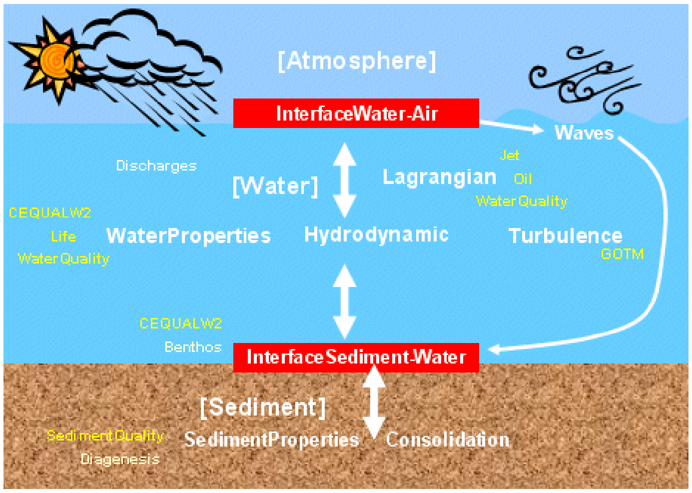

Figure 1.7. Schematic representation of MOHID Water. Adapted from IST, 2003

1.6. Thesis outline and objectives

The main aim of this dissertation is to provide modelling tools to better understand marine ecosystem processes and population connectivity in the deep-sea. The work performed in this thesis was based on the implementation of a 3-D hydrodynamic (Chapter 2) and a biogeochemical model (Chapter 3) to simulate the physical and biological processes in the Azores, as well as a biophysical model to study deep-sea larval dispersal and population connectivity (Chapter 4). The major objective of this modelling work is to provide results and information to better understand marine dynamics. In the last chapter, the constructed models are applied to a specific case, focusing on deep-sea sponge grounds in the Azores (Chapter 5).

The current Chapter 1 presents a general introduction to the Azores study region, with a characterization of the major hydrodynamic and biological patterns of the region. It also includes a brief review of the modelling approaches in use.

Chapter 2 focuses on the implementation and validation of a hydrodynamic model. Model results were used to describe the major currents and water masses influencing the Azores region. All other modelling tools used in this thesis are coupled to this hydrodynamic model, thus specific importance has been given to model validation.

Chapter 3 consists of the development and implementation of a biogeochemical model. The building process included a calibration performed by testing different parameterizations for the Azores region to find the optimal. Model results were validated against remote sensing data, climatology and global models, and were used to describe the major seasonal and spatial biotic and abiotic processes that control phytoplankton abundance in the Azores.

In Chapter 4, a biophysical model is implemented to study the larval dispersal and population connectivity for two case studies: Case study 1 focuses on the deep-sea sponge *Pheronema carpenteri*; case study 2 focuses on *Chaceon affinis*, a deep-sea red crab. Different scenarios were studied considering different biological traits: spawning seasonality, larval pelagic duration (PLD), and larval behaviour, including surface-oriented swimming. Results revealed seasonal patterns of connectivity and the importance of hydrodynamics on larval dispersal.

Chapter 5 focused on studying the spatial and temporal biogeochemical properties at specific sponge grounds of the species *Pheronema carpenteri*, taking advantage of the 3-D biogeochemical model built in Chapter 3. The ultimate goal of the chapter was to showcase the utilization of the constructed models to better understand the ecology of the target sponge species. Chapter 6 presents the final remarks of this thesis and suggestions for further research.

Chapter 2

Azores hydrodynamic model

2.1. Introduction

The use of models is an essential tool, when dealing with oceanographic studies and management questions, enabling the study of different scenarios and hypotheses. Local ocean conditions are often controlled by large-scale processes, leading to the need for downscaling from global and larger-scale models into local models (Katavouta and Thompson, 2016), representing, as accurately as possible, the ocean conditions, to estimate local and regional features in a higher resolution scale. The present generation of ocean models is capable of providing relatively high-resolution results using data assimilation, downscaling technics, and nested grids (Gutknecht et al., 2016; Lellouche et al., 2018; Neves et al., 2003; Salon et al., 2019).

Ocean ecosystems have nonlinear dynamics, and their modelling requires an adequate representation of both physical and biological processes (Siddorn et al., 2007). Ocean circulation is driven mainly by physical factors (like pressure gradient, water temperature and salinity variations); geostrophic factors (gravitational and deflective force by Earth's rotation - the Coriolis force); atmospheric factors; but also by the bathymetry (Hirose and Kamiya, 2003). Several global and regional models were developed and applied for the Atlantic Ocean, continental shelf and coastal areas, simulating physical ocean properties, namely: the Global Ocean Analysis and Forecast System, provided by E.U. Copernicus Marine Service Information (CMEMS) Marine Data Store (MDS) (https://doi.org/10.48670/moi-00016); NEMO- Nucleus for European Modelling of the Ocean (Gutknecht et al., 2016); FOAM- Forecasting Ocean Assimilation Model (Bell et al., 2004); MOHID (Juliano et al., 2012), or ROMS- Regional Ocean Modelling System (Costa et al., 2012), between others.

Hydrodynamic and circulation models, coupled with biogeochemical models, provide an advantageous tool to study and monitor the general marine biogeochemical cycles, being able to simulate complex interactions between ocean physics, chemistry and biology (Berline et al., 2007; IOC-UNESCO, 2022). On the basis of any circulation, biogeochemical, or particle tracking models, it is fundamental to have a well-calibrated and validated hydrodynamic model (North et al., 2009).

2.2. Methodology

2.2.1. MOHID hydrodynamic model

This work is based on MOHID modelling tools. The MOHID modelling system is a three-dimensional numerical program used to simulate hydrodynamics, water quality, circulation and dispersion processes in water. Several MOHID applications have been developed to study and simulate hydrodynamic processes at different locations (e.g. NorthEast Atlantic (Campuzano et al., 2013; Riflet et al., 2008); SouthWest Atlantic (Juliano et al., 2012), estuaries and coastal areas (de Pablo et al., 2019; Pinto et al., 2014; Viegas et al., 2009), including oil spills dispersion in the ocean (Juliano et al., 2012; Leitão et al., 2003).

MOHID is an open-source model, available online at https://github.com/Mohid-Water-Modelling-System/Mohid. It is programmed in ANSI FORTRAN 95, following an object-oriented approach allowing the integration of different modules in implicit and explicit ways (IST, 2003). Spatial discretization uses the finite volume approach technique, where the spatial coordinates are independent, and any geometry can be chosen for every dimension. This method allows flexibility in the subdivision of vertical and horizontal domains, and the implementation of different vertical coordinate types (cartesian and sigma). Sigma coordinate system is commonly used in oceanographic, meteorological and other fluid dynamic models (Janjic, 2003). In sigma layers, the scale is divided evenly, each layer occupies a constant percentage of the water column thickness. For the ocean surface, the sigma layers have the advantage that they move up and down with the variable surface (in this case the tide level), making it possible to maintain a high vertical resolution at the surface, and, at the same time allow for the correct simulation of the tide level evolution. The Cartesian coordinate in the remaining water column layers allows the reduction of the computational cost, using a hydrostatic approach for the entire water column (Lin and Li, 2002).

In this application, MOHID model has a 3-dimensional configuration, with 50 layers along the water column, being the bottom 43 layers in Cartesian coordinates, with a constant size, and the top 7 layers defined with sigma coordinates, changing their size considering the tide level evolution. Several modules are used (Figure 2.1), computing the physical processes like water fluxes, turbulent transport of momentum, mass and heat fluxes, providing water level, and physical and hydrodynamic water properties.

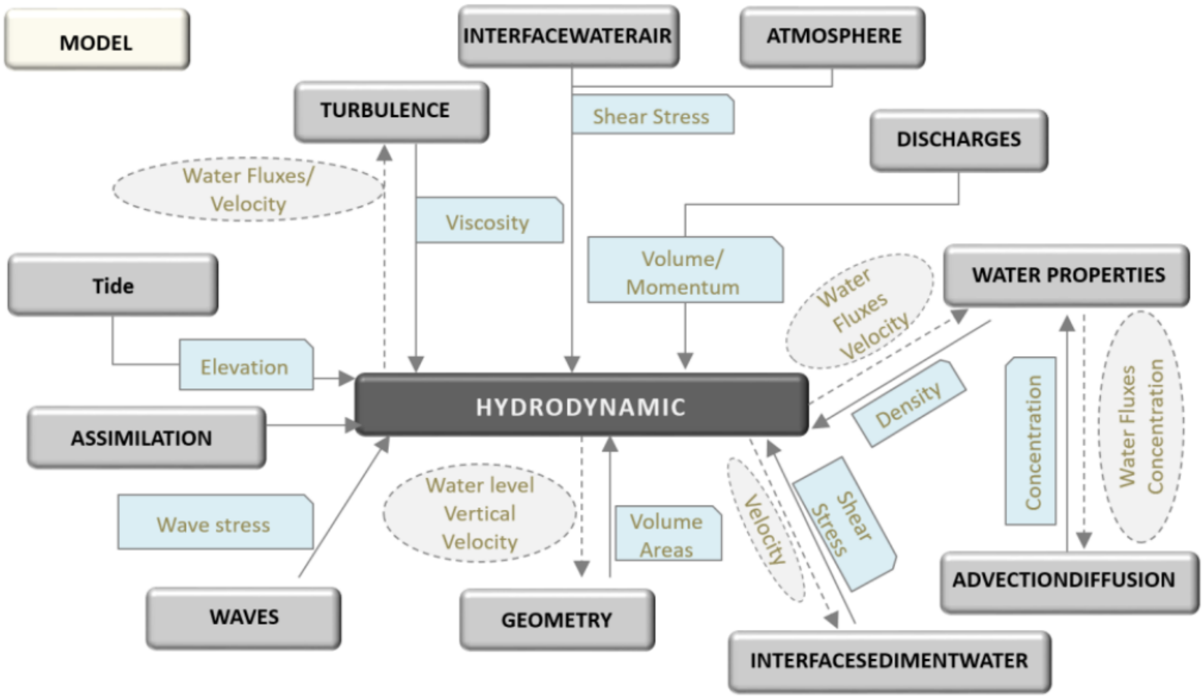

Figure 2.1- Schematic configuration of MOHID Hydrodynamic model. Modules are represented in grey rectangles. Other processes such as water quality, vertical movement of particulate properties and sediment are included as dependencies of the Waterproperties, Hydrodynamic, and InterfaceSedimentWater respectively. (Adapted from Leonardo, 2022).

MOHID uses the finite volumes approach to solve the Navier-Stokes equations, considering the Boussinesq and hydrostatic approximations.

The equations solved in the model are:

$$\frac{\partial u}{\partial x}+\frac{\partial v}{\partial y}+\frac{\partial w}{\partial z}=0 \qquad \text{eq. 2.1}$$

$$\frac{\partial u}{\partial t}+\frac{u\partial u}{\partial x}+\frac{w\partial u}{\partial z}-fv=-\frac{1}{pr}\frac{\partial p}{\partial x}+\frac{\partial}{\partial x}\left(Ah\frac{\partial u}{\partial x}\right)+\frac{\partial}{\partial y}\left(Ah\frac{\partial u}{\partial y}\right)+\frac{\partial}{\partial z}\left(Ah\frac{\partial u}{\partial z}\right) \qquad \text{eq. 2.2}$$

$$\frac{\partial v}{\partial t}+\frac{v\partial v}{\partial x}+\frac{w\partial v}{\partial z}+fu=-\frac{1}{pr}\frac{\partial p}{\partial y}+\frac{\partial}{\partial x}\left(Ah\frac{\partial v}{\partial x}\right)+\frac{\partial}{\partial y}\left(Ah\frac{\partial v}{\partial y}\right)+\frac{\partial}{\partial z}\left(Ah\frac{\partial v}{\partial z}\right) \quad \text{eq. 2.3}$$

$$\frac{\partial p}{\partial z}+pg=0 \quad \text{eq. 2.4}$$

Where *u*, *v* and z are the velocity components in the x, y and z directions respectively; *f*: the Coriolis parameter; *Av* and *Ah*: the coefficient of turbulent viscosities in the horizontal and vertical directions; *p*: the pressure; *ρr*: the reference density.

These equations are solved numerically considering the generic vertical discretization enabling the use simultaneously of both sigma and cartesian vertical coordinates. To solve the turbulence of the entire domain, MOHID has coupled the General Ocean Turbulence Model (GOTM) module. This GOTM model consists of a one-dimensional water column model that solves the most important hydrodynamic and thermodynamic processes related to vertical mixing (Burchard, H., Bolding, K., Villarreal, 1999). The inverse barometer effect is used to compute water level (Dorandeu and Le Traon, 1999). MOHID turbulence module allows parameterizing turbulence, decreasing the horizontal diffusion towards the boundary in nested models. This horizontal flow relaxation scheme can be applied for velocity U and V vectors, temperature and salinity, being advantageous when downscaling from a global circulation model solution to a local solution (IST, 2003).

MOHID Water Properties module computes the 3D eulerian transport of the water properties in the different phases (dissolved, particulate and adsorbed), in the water column that is subjected to one more transport variable: the settling velocity. Momentum, mass and heat transport are computed using a generic 3D advection-diffusion library including various advection schemes namely: first, second and third-order upwind; centred differences; and TVD (Total Variation Diminishing). Advection is solved in the three directions as a one-dimensional case and various time discretizations can be combined: explicit, semi-implicit or fully implicit. The horizontal diffusion of momentum is computed with a bi-harmonic formulation (IST, 2003). The settling velocity is computed by the Freevertical movement module.

Because the physical and ecological processes in the ocean are often non-linear and depend on several environmental forces, a data assimilation procedure is essential, allowing to combine information from global models, boundary conditions models, and monitoring data. In this model, the assimilation is performed considering the global ocean model for velocity U, velocity V, water temperature and salinity, and the meteorological model for the atmospheric forcing. The hydrodynamic model simulates the currents and density fields, fundamental for the Lagrangian transport (used in the particle tracking model) and for the Eulerian transport (used in the biogeochemical model), through advection and/or diffusion processes.

2.2.2. Model implementation

The model was implemented in a hindcast mode (simulating past conditions) from 2015 to 2017, to provide accurate results for the starting date of this PhD project (2017). After validation, the model was run in hindcast mode to provide results for the following years from 2017 to 2019, to feed biogeochemical and biophysical model applications during the scope of this PhD project. The hydrodynamic model simulates the currents and density fields, fundamental for the Lagrangian and Eulerian transports through advection and/or diffusion processes.

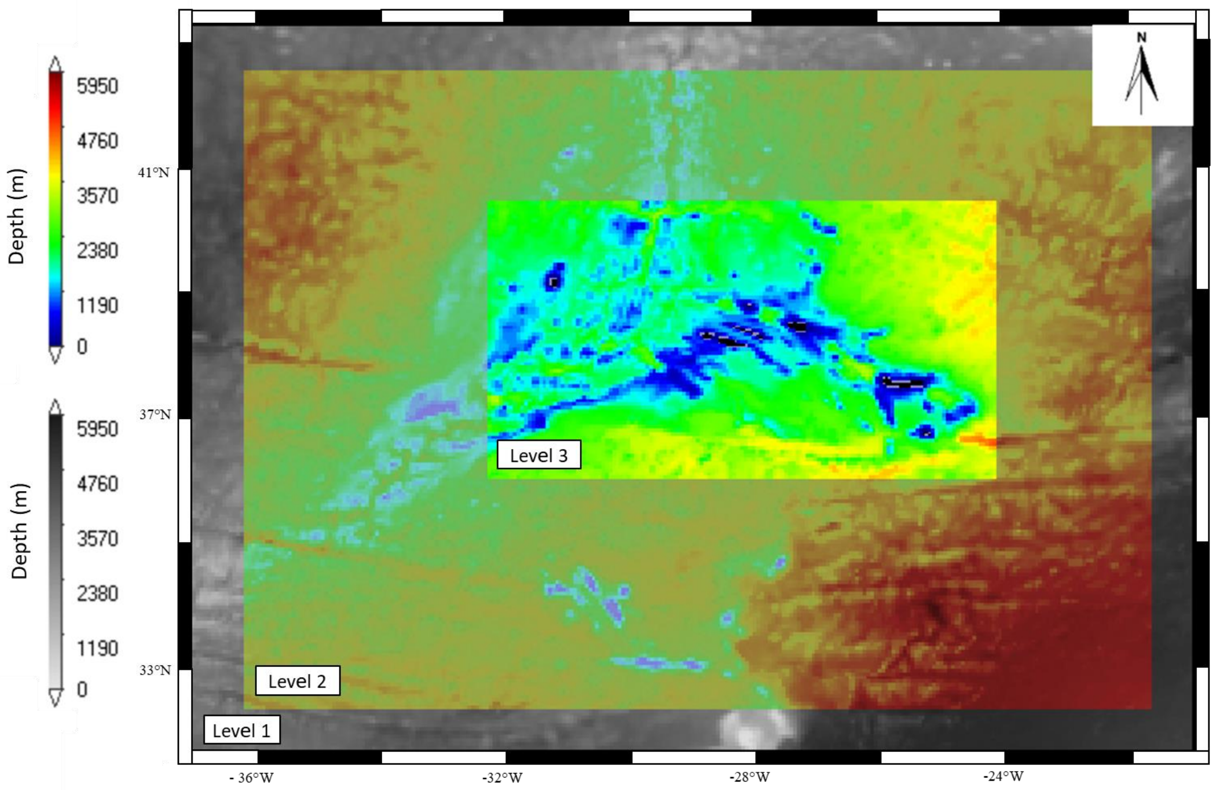

Figure 2.2 –Model domain and bathymetry (in meters): Level 1 in greyscale, level 2 and level 3 in red-blue scale.

Table 2.1- Hydrodynamic model configuration

	Parameter	**Level 1**	**Level 2**	**Level 3- Window from Level 2**
Model description	Model dimensions	2D - Barotropic	3D – Baroclinic	3D- Baroclinic
	Domain	31.812°N to 43.6321°N 20.7478°W to 37.1288°W	32.472°N to 42.9121°N 21.4078°W to 36.288°W	36.25°N to 40.74°N 23.985°Wto 32.263°W
	Bathymetry	EMODNET (1/16arc-minutes) a)	EMODNET (1/16arc-minutes) a)	Same as level 2
	Horizontal Resolution	6km	6km	
	Vertical resolution	1 layer (0-6000meters depth)	50 vertical layers: 7 sigma layers + 43 cartesian layers	
	Tide	Tide: FES2014b)	From level 1	
	Δt	180 seconds	120 seconds	
Boundary conditions	Meteorological forcing	n/a	Global Forecast System model (GFS) 0.25° resolution 1*) c)	
	Hydrodynamical forcing	n/a	CMEMS Global Ocean Circulation Model (PSY4V3R1) 1/12°resolutiond)	
	Model output	3600 seconds	3600 seconds	3600 seconds
	Simulation length	Jan/2015 – Dec/2018	Jan/2015 – Dec/2018	Jan/2017– Dec/2018

a) EMODnet Bathymetry Consortium, 2018; b) Lyard et al., 2021; c) National Centers for Environmental Prediction, National Weather Service, NOAA, 2015; d) Lellouche et al., 2018; n/a: not applicable

The model implementation consists in 3 nested levels (Figure 2.2), using a one-way downscaling strategy of nested domains. Tide is imposed at the open boundary of Level 1 using the FES2014 global tide model (Lyard et al., 2021), with a regular grid of 1/16°. It is an enhanced version of FES2012 and FES2004, used with success in different applications (Juliano et al., 2012; Leitão et al., 2008; Toublanc et al., 2018).

The model is forced by Mercator Global Ocean (PSY4V3R1) model. PSY4V3R1 is a global ocean system with 1/12° horizontal resolution, and 50 vertical levels, developed at Mercator Océan by the Copernicus Marine Environment Monitoring Service (CMEMS) (Lellouche et al., 2018). It is available online at http://marine.copernicus.eu/. This product is referred to as Mercator hereafter. This model provides 3D results for water temperature, water salinity and currents (velocity u and velocity v), and 2D sea surface level, between other parameters. Model configuration, and boundary conditions description are listed in Table 2.1.

For the atmospheric forcing, the boundary conditions are obtained from the Global Forecast System (GFSmodel), provided by NOAA- America National Ocean and Atmospheric Administration, available at https://www.ncdc.noaa.gov/. This model has hourly fields of surface wind, temperature, relative humidity, pressure, and solar radiation

The open boundary conditions are resolved by imposing a Flow Relaxation Scheme, providing a simple and stable extrapolation of the interior solution. This relaxation is applied to temperature, salinity, and velocity parameters, combined with a Flather radiation scheme (Flather, 1976). The initialization of the 3-Dimensional fields of temperature and salinity is made by a direct interpolation of Mercator fields for these two parameters, using bilinear interpolation in the horizontal and linear interpolation in the vertical fields

Nested models

The numerical model was implemented with a 0.06º (1/16) resolution using a three-level nesting model (Figure 2.2).

Level 1, represented with greyscale in Figure 2.2, is a 2D model that provides the tide solution for the 3D model, using the FES2014 model. This first level covers the geographic area from 31.8121º N to 43.63212º N, and -20.74776º W to -37.1278º W, covering the entire Azores Economic Exclusive Zone (AEEZ).

Level 2 is three-dimensional (3-D), also covering the entire AEEZ, from 32.4721ºN to 42.91211ºN, -21.40775ºW to -36.2878ºW. This second level is slightly smaller than the first one, to avoid instability problems in the boundaries. This 3-D baroclinic model with the same horizontal resolution as the first level, has 50 vertical layers. The bottom 43 layers are in cartesian coordinates, with a constant size, and the top 7 layers are sigma coordinate layers, totalizing the upper 10 meters of the water column. Below these sigma layers, the 43 cartesian layers increase in size along the water column, from top to bottom, with the top ones less than 2 meters in length. In the upper layers, the sigma coordinate layers change their size considering the tide level evolution. Model bathymetry was obtained from the EMODNET database, available online at www.emodnet, grid resolution of 1/16 * 1/16 arc-minutes (EMODnet Bathymetry Consortium, 2018).

Level 3 is a model window of Level 2, limited from 36.25ºN to 40.74ºN, and-23.9854ºW to -32.2628ºW, covering the Azores archipelago. With the same grid resolution, Level 3 was created to provide results in an area close to the archipelago. Results of level 3 are used for further model applications like the biogeochemical and biophysical models implemented in the scope of this dissertation. This nested methodology allows for saving disc space. Otherwise, when using the entire Level 2, the biogeochemical model would be computationally heavy not only in terms of computer performance but also in data storage volume.

2.2.3. Model Validation

The validation of the hydrodynamic model is crucial because hydrodynamics is at the basis of the biophysical and biogeochemical models. Model validation is performed for the Sea surface temperature (SST); the vertical profiles of sea temperature and salinity, and the water level (directly dependent on tide level).

2.2.3.1. Data used for model validation

Water level

Several gauge stations are available in the Azores region (Table 2.2), however, only the Ponta Delgada station, managed by Instituto Hidrográfico da Marinha (Portugal), has data for the required period (2014-2017). Tide gauge data was retrieved freely from the Permanent Service for Mean Sea Level website (Holgate et al., 2013; PSMSL, 2018). As there was only one station with historical data available for the validation period, it was not possible to perform any comparative study between different stations. Gauge station data was compared with model water level results for the same location, period and time step.

Sea Surface Temperature

For SST validation, model results are compared with remote sensing data, using a satellite global product: UKMO-L4HRfnd-GLOB-OSTIA (from now on referred to as OSTIA), available online[1]. OSTIA, Operational Sea Surface Temperature and Sea Ice Analysis is a high-resolution

---

[1] https://podaac.jpl.nasa.gov/dataset/UKMO-L4HRfnd-GLOB-OSTIA

product with a Level 4 processing level, providing daily sea surface temperature results on an operational basis at the UK Met Office using optimal interpolation (OI) on a global 0.054 (1/20) degree grid. Has a highly smoothed SST field and was specifically produced to support SST data assimilation into numerical weather prediction models (Stark et al., 2007). Comparisons were performed systematically using daily remote sensing data and Mohid results for the same instant.

Table 2.2- Gauge stations available in the Azores region, name, ID, location, data of available data (*https://www.psmsl.org/), and data used.

Gauge Station	**ID***	**Location**		**Data available**	**Data used**
		Lat	**Long**		
Ponta Delgada	258	37.74N	-25.67W	1978 – 2018	2014-2017
Ponta Delgada	245	37.73 N	-25.67W	1978 – 2012	-
Horta	156	38.53N	-28.63W	1905 – 1996	-
Lajes das Flores	2171	39.34N	-31.17W	2006 – 2013	-
Santa Cruz das Flores	843	39.45 N	-31.12W	1957 – 2009	-
Angra do Heroísmo	380	38.65N	-27.23W	1933 – 1996	-

Water Temperature and salinity along the water column

Model validation for salinity and temperature along the water column was performed by comparing model results with Argo floats data available online (Argo, 2020), considering all the Argo buoy profiles available for the study area, represented in Figure 2.3.

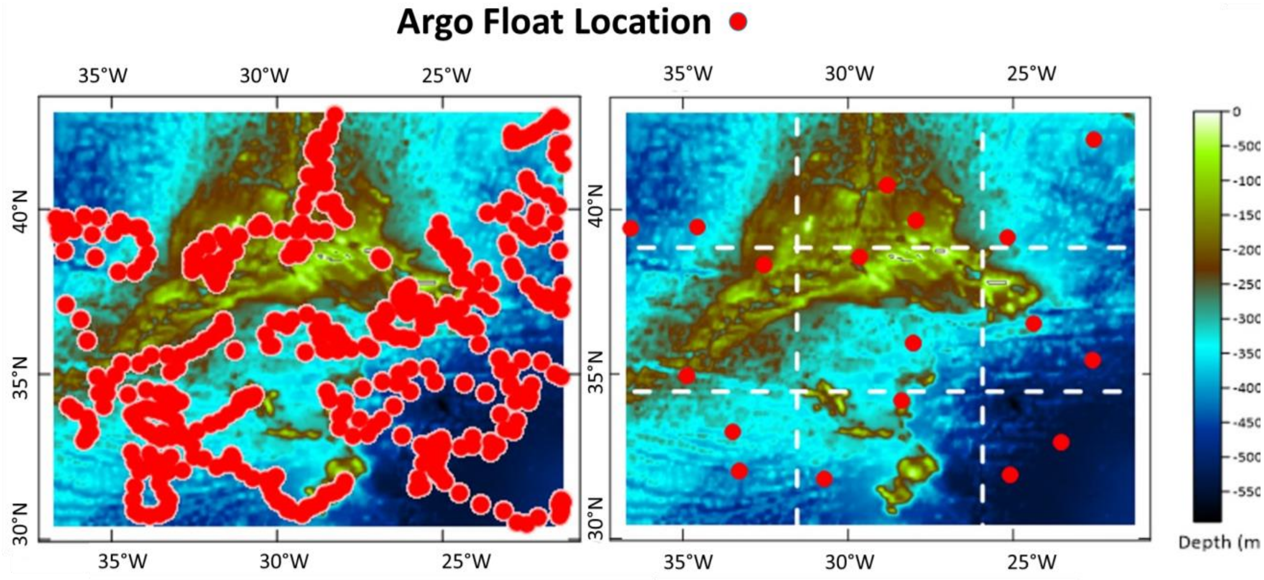

Figure 2.3- Argo buoys available in the study area, 462 buoys on the left, and on the right,18 Argo buoys used to evaluate model performance in the different 9 subareas: NorthWest (NW), NorthCenter (NC), NorthEast (NE), CenterWest (CW), 2 buoys selected in each subarea.

To have a deeper analysis of model performance along the water column, the study domain was divided into 9 subareas: NorthWest (NW), NorthCenter (NC), NorthEast (NE), CenterWest (CW), CenterCenter (CC), CenterEast (CE), SouthWest (SW), SouthCenter (SC), and SouthEast (SE), represented in Figure 2.3 (right). From each subdomain, 2 Argo buoys were selected, considering their location (selecting buoys spread out in the different subdomains), and the different bathymetric conditions, comprising different geographic and topographical situations. These Argo profiles of salinity and temperature were compared with the paired model results profiles (for the same location, depth and time).

To characterize the different water masses in the domain and along the water column, all the Argo profiles, together with respective model results, were considered, through their Temperature-salinity (T-S) curves. In these T-S curves, water temperature is plotted against the water salinity. These T-S curves make it possible to characterize the thermohaline vertical structure of the water column and can be used to define and locate water masses (Emery, 2001). In this analysis, also the MERCATOR model results are used, providing the means to do a comparative analysis of MOHID and the boundary conditions model performance.

2.2.3.2. Statistical methods

The most common statistical indexes used for model validation, as recommended by Allen et al. (2007), are the root mean square error (RMSE) (eq. 2.5), which is one of the most widely used for calibration and validation, together with bias (eq. 2.6), and Pearson correlation coefficient (R) (eq. 2.7) (Gómez-Zambrano et al., 2017), and finally Taylor diagrams, (Allen and Somerfield, 2009). The RMSE error is interpreted as a deviation of the simulated results from the measurements and it has the benefit of penalizing large errors. Small absolute values of RMSE indicate a good agreement between the model and observations (de Pablo et al., 2019).

$$RMSE = [\frac{1}{N}\sum_{i=1}^{N}(O_i - M_i)^2]^{0.5} \qquad \text{eq. 2.5}$$

Model Bias is a simple statistic parameter that measures the mean deviation between modelled (M) and observed data (O), which yields a positive bias as an indicator for the model's overestimation and, conversely, a negative bias for the model’s underestimation (eq. 2.6).

$$Bias = \sum_{i=1}^{n} \frac{1}{n}(M_i - O_i) \qquad \text{eq. 2.6}$$

The Pearson correlation coefficient (R), referred to as correlation, (eq. 2.7), measures the statistical relationship, or association, between two variables, in this case, the observed data (*O*), and the modelled data (*M*).

$$R = \frac{\sum_{i=1}^{n}(M_i - \bar{M}_i) - (O_i - \bar{O}_i)}{\sqrt{\sum_{i=1}^{n}(M_i - \bar{M}_i)^2}\sqrt{\sum_{i=1}^{n}(O_i - \bar{O}_i)^2}} \qquad \text{eq. 2.7}$$

Taylor diagrams are an advantageous tool to evaluate model performance, aggregating in the same diagram correlation, standard deviation, the centred RMSE (eq. 2.9) and bias between model and reference data. Standard deviation (SD), defined by eq. 2.8, is used to measure the spread of data around the mean.

$$SD = \sqrt{\frac{\sum_{i=1}^{n}(M_i - \bar{M}_i)^2}{n-1}} \qquad \text{eq. 2.8}$$

The centred RMSE error (CRMSE) is the mean-removed RMSE, thus calculated as follows:

$$CRMSE = [\tfrac{1}{N}\sum_{i=1}^{N}(M_i - \bar{M})_i - (O_i - \bar{O}_i)^2]^{0.5} \qquad \text{eq. 2.9}$$

Taylor diagrams use the Law of Cosines (Taylor, 2001), where the radial coordinate is r = σ_m and the angle is θ = arccos(R). Centred RMSE then appears as the radial distance from the position of a perfect model (r = σ_0, θ = 0), (eq. 2.9). These diagrams can be normalized, comparing different variables, or variables with different variances, by normalizing (i.e., making dimensionless) their standard deviations (Elvidge et al., 2014).

2.3. Model validation results

Water Level

Model water level results were compared against tide gauge measurements. Comparison results, represented in Figure 2.4 show how the model is able to simulate the diurnal tide variations, including maximum and minimum water levels for low and high tides. A correlation higher than 0.97 was obtained (Table 2.3), evidencing a good model performance for simulating water level. Nevertheless, an overestimation of the water level can be identified over time, resulting in a bias of 0.045 for the entire year of 2015. Statistical results for water level validation, including correlation, RMSE and the average, are summarized in Table 2.3.

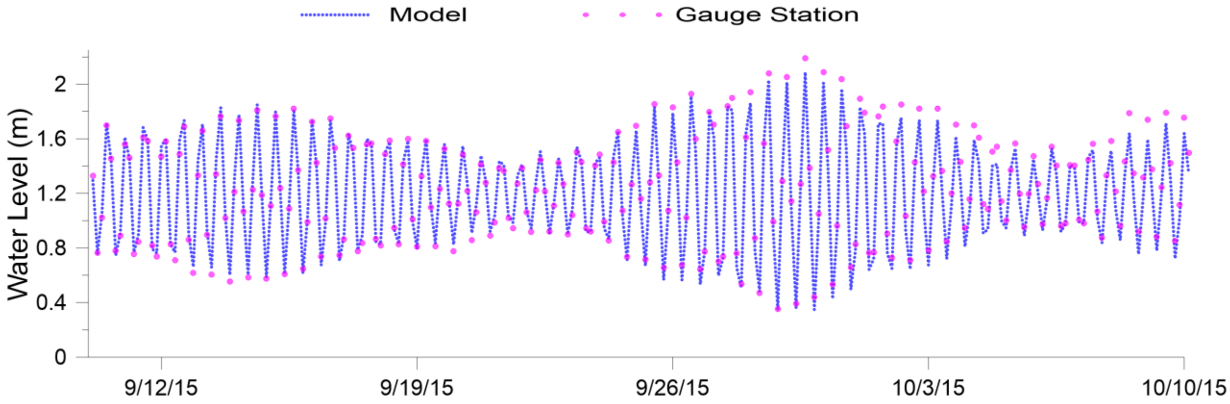

Figure 2.4- Water level model results (in blue) and observed tide gauge station data (pink), for a period of one month covering the period of the September high tides (between 10 September to 10 October 2015).

Table 2.3- Statistical results (Pearson correlation coefficient (R), Bias, Root Mean Square Erros (RMSE) and averages) for water level validation comparing Mohid water level results and measured data from Ponta Delgada Gauge Station for 2014, 2015, and 2016.

Year	R	Bias	RMSE	average gauge station (m)	average model (m)
2014	0.973	0,001	0.089	1.17	1.17
2015	0.978	0.045	0.094	1.16	1.20
2016	0.973	-0.140	0.002	1.14	1.00

The good correlation with tide results together with a constant difference in average values, indicate that mismatches between model results and gauge data are not related to tide amplitude, neither irregular along the year, nor related to spring or neap tides. A bias of 0.045 meters is verified for 2015, and -0.14 meters for 2016 (Table 2.3).

Sea Surface Temperature

Sea surface temperature validation was performed comparing model results with satellite data. Comparisons were performed systematically, using a product for the Operational Sea Surface Temperature and Sea Ice Analysis (OSTIA) system, provided by the UK's Met Office, and available at the Copernicus Marine Service website (https://data.marine.copernicus.eu/).

Statistical results of this validation are summarized in Table 2.4, for the reference year of 2015. The temporal evolution of SST simulated by MOHID, and measured by satellite, for the entire domain, are depicted in the graph of Figure 2.5 and the BIAS, and RMSE of this validation, along with the reference year, in Figure 2.6. Results of the correlation coefficient (R), BIAS and RMSE are also represented as maps, in Figure 2.7.

Table 2.4- Statistical analysis (correlation (R), Bias, RMSE and averages) for sea surface temperature validation comparing model SST with remote sensing data.

R	Bias (^{o}C)	RMSE (^{o}C)	Model average (^{o}C)	Satellite average (^{o}C)
0.992	0.042	0.367	20.267	20.225

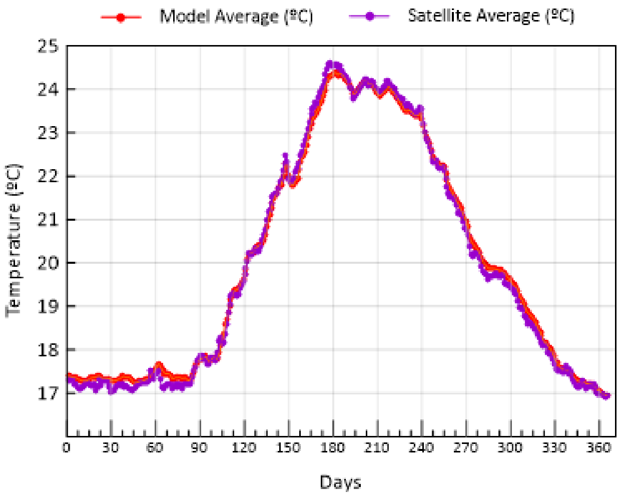

Figure 2.5- Temporal evolution of SST average from MOHID (red) and satellite (purple) along the reference year.

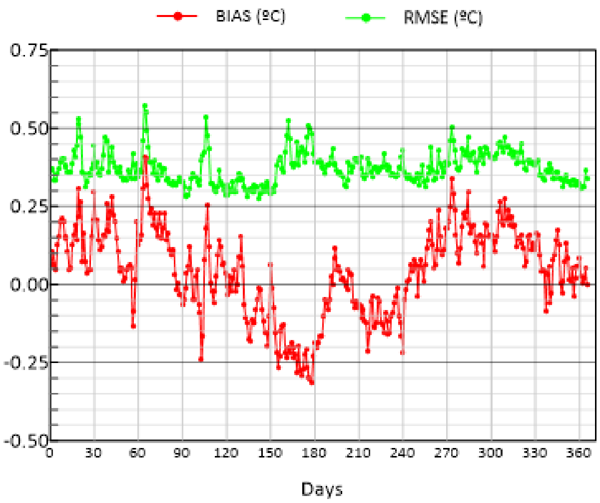

Figure 2.6- Temporal evolution of the statistical analysis for SST validation considering Bias (red) and RMSE (green) along the reference year.

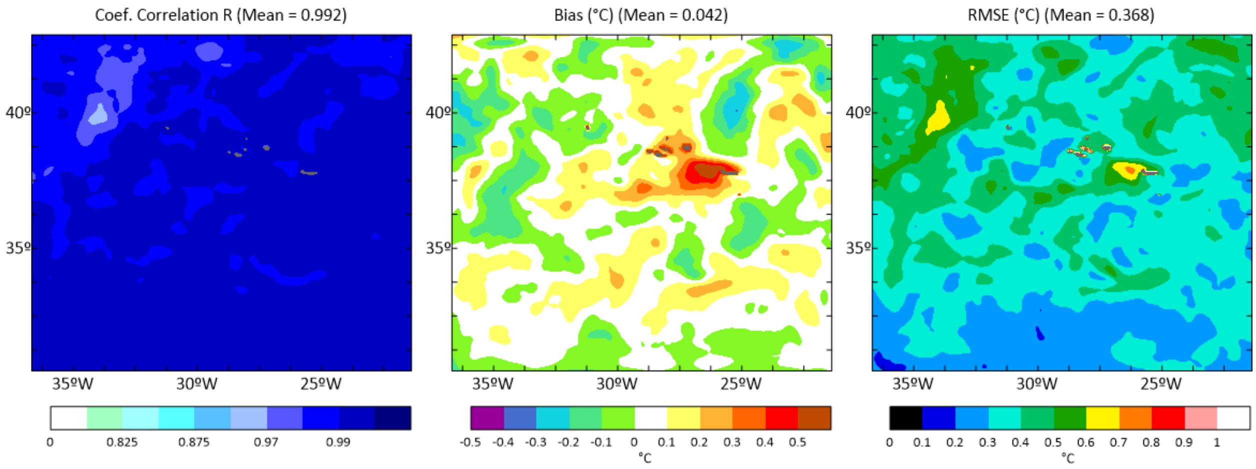

Figure 2.7- Maps of statistic analysis results along the domain for coefficient correlation R (left), Bias (centre) and RMSE (right) for the comparison between sea surface temperature from MOHID and satellite data.

Validation results show that MOHID simulates the seasonal variations of SST values in the domain. Results show a strong correlation, higher than 0.99, indicating that Mohid can simulate with accuracy the yearly variation of SST, and along the domain. MOHID has on average a positive bias of 0.042ºC. However, during spring and summer the bias is negative (Figure 2.6). This bias can be a consequence of different MOHID and satellite vertical resolutions. While the satellite measures are related to the first layer of the water column, model results refer to the first model cartesian layer (located at 3 meters depth). This limitation was also identified in CMEMS models (Legaloudec et al., 2015). Model bias ranged from 0.25ºC to 0.5ºC, with positive and higher bias and RMSE near the islands (Figure 2.7). This uncertainty around the islands can be a consequence of remote sensing quality data, once they are influenced by cloud covering. This is a known limitation, identified in the Azores region (Lafon et al., 2004). This bigger bias around the archipelago can also be a result of the local and punctual phenomena that occur near the islands (islands' effects), not solved by the model. These limitations can be easily surpassed using a higher resolution model in the coastal areas. However, considering the objectives of this study, the resolution used was the best commitment resolution/computational demand.

Water Temperature and salinity along the water column

Vertical profiles of temperature and salinity from Argo buoys are matched up with model results for the same position, depth and instant, producing time series of paired model and observation profiles. Statistical analysis is performed, integrating each vertical profile, and comparing model results with Argo data. The general statistical analysis results are resumed in Table 2.5, and on Taylor diagrams,Figure 2.8, with the representation of all the paired buoys/model statistical results (correlation, normalized standard deviation, normalized centred RMSE, and normalized bias). These Taylor diagrams are normalized by the standard deviation of each paired Argo buoy/model comparison.

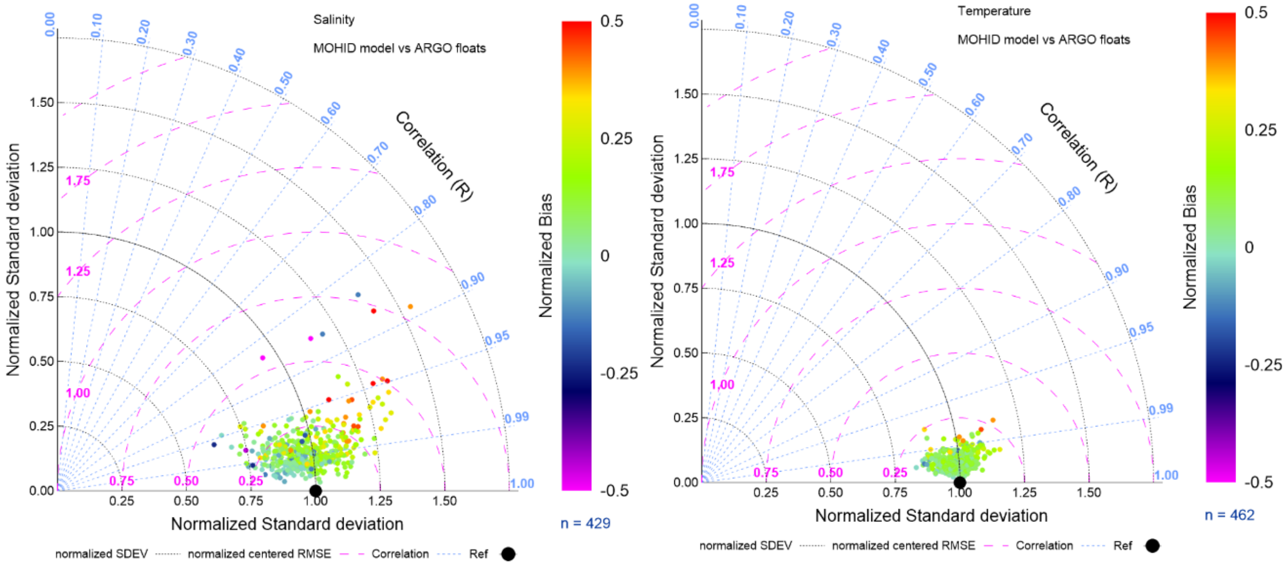

Figure 2.8- Taylor diagram of statistical comparison between modelled and Argo buoys' vertical profiles for temperature (left), and salinity (right). The black dot is the reference (Ref), representing the perfect adjustment between model results and Argo buoy data. Coloured dots represent each comparison Argo/model: the colour represents the normalized bias; the azimuthal angle represents the Pearson correlation coefficient (R); the normalized standard deviation is the radial distance to the reference point (Ref); the pink semicircles centred at the Ref are the normalized centred RMSE scale. Bias, SD and RMSE are normalized by the standard deviation of each buoy.

Table 2.5- Statistical results for model validation of sea temperature and salinity along the water column comparing Mohid results with Argo buoys data for 2015.

	n	**R**	**Bias**	**RMSE**	**SD**		**average**	
					Model	Argo	Model	Argo
Temperature (^{o}C)	462	0.996	0.440	0.646	4.72	4.77	11.63	11.19
Sanity (PSU)	429	0.983	0.042	0.098	0.406	0.414	35.70	35.66

Taylor diagram analysis indicates that for temperature, paired model/Argo results are highly correlated, with a normalized RMSE lower than 0.25, for all the comparisons except one. For salinity, results are more heterogeneous, nevertheless with a correlation higher than 0.95. Some outliers can be identified by their extreme bias and a normalized RMSE higher than 0.5.

These outliers can be associated with salinity sensor limitations. The calibration drift of salinity sensors over time is a common problem in oceanography, as well as in the Argo buoys (Wong et al., 2020). Even with all the research, technology developments, and data quality procedures from the Argo program, this is still a limitation of Argo buoys. This limitation on salinity sensor calibration justifies the number of Argo buoy profiles with salinity (n=429) lower than the temperature profiles (n=462). Vertical profiles of temperature (Figure 2.9), and salinity (Figure 2.10), point out that MOHID can reproduce the vertical variability, in the different parts of the domain, however, with a positive bias.

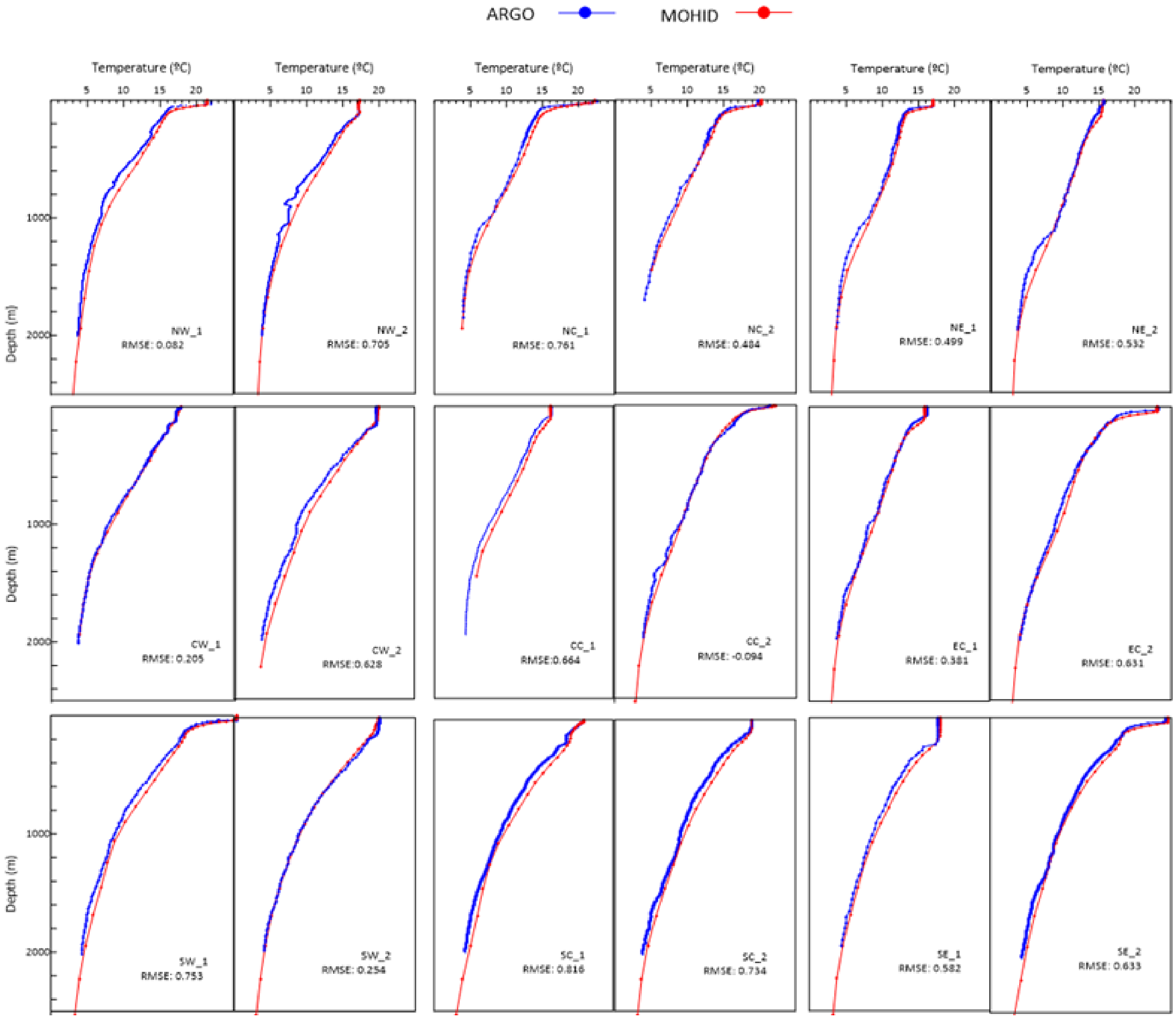

Figure 2.9- Depth profiles of temperature measured by Argo buoys (blue) and predicted by Mohid (red), and RMSE values.

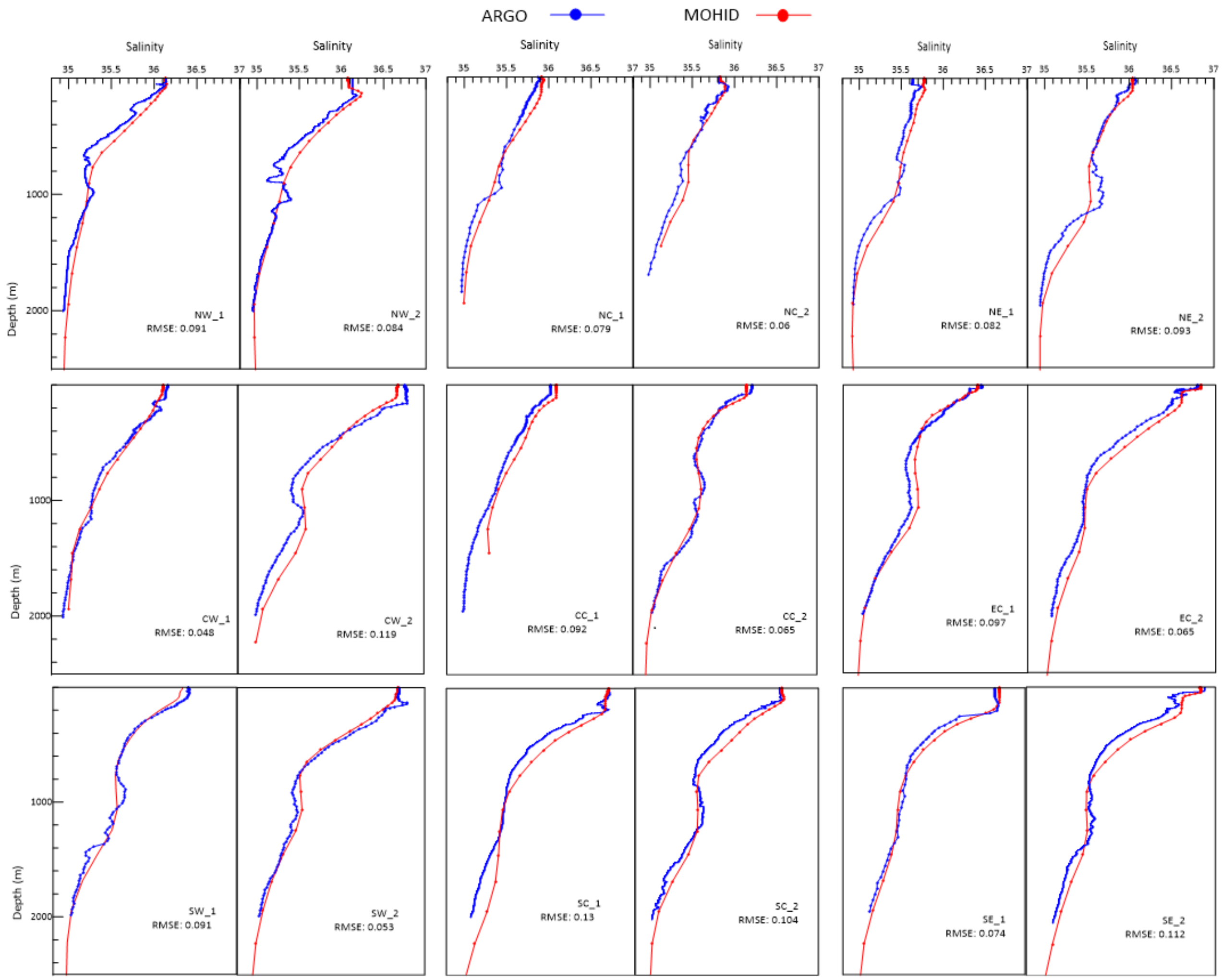

Figure 2.10- Depth profiles of salinity measured by Argo buoys (blue) and predicted by Mohid (red), and RMSE values.

To better analyse the model's performance along the water column, 18 Argo buoys were selected along the domain, as represented in Figure 2.3.(subdomains: NW; NC; NE; CW; CC; CE; SW; SC; SE). Each Argo profile was compared with the equivalent model depth profile (same location, depth, and time), for temperature (Figure 2.9), and salinity (Figure 2.10).

Validation results evidence MOHID capability to simulate vertical variability of temperature and salinity, with a correlation of 0.99 for temperature, and 0.98 for salinity; and RMSE of 0.65$^{\mathrm{o}}$C, and 0.042 PSU respectively. An overestimation of MOHID temperature and salinity results occurs along the water column. This overestimation was identified in other model applications for the Azores and North-East Atlantic, using ROMS (Sala et al., 2013), and HYCOM (Sala et al., 2016). A bigger variability for salinity than for temperature values is notorious along the water column. Vertical profiles show that Argo buoys can detect small local phenomena, not represented by the model. This is a consequence of the bigger data frequency of Argo floats, which provides dozens of values along the water column, (up to 150), while MOHID, only provides 23. One for each vertical layer from the surface up to the 2000 meters depth. These results highlight the importance of gathering both methodologies, with monitoring data detecting local phenomena and raising essential questions, and model tools helping to understand them, and to study hypotheses around different phenomena.

2.4. Model Results and Discussion

Water masses in the Azores region

In the T-S diagrams, the temperature on the vertical axis is plotted against the salinity on the horizontal axis. All the T-S diagrams obtained from the Argo buoys and respective MOHID results are plotted and compared in Figure 2.11. T-S diagrams, together with the horizontal distribution of annual temperature and salinity averages, at different depths, allow for the identification of different water masses in the study area.

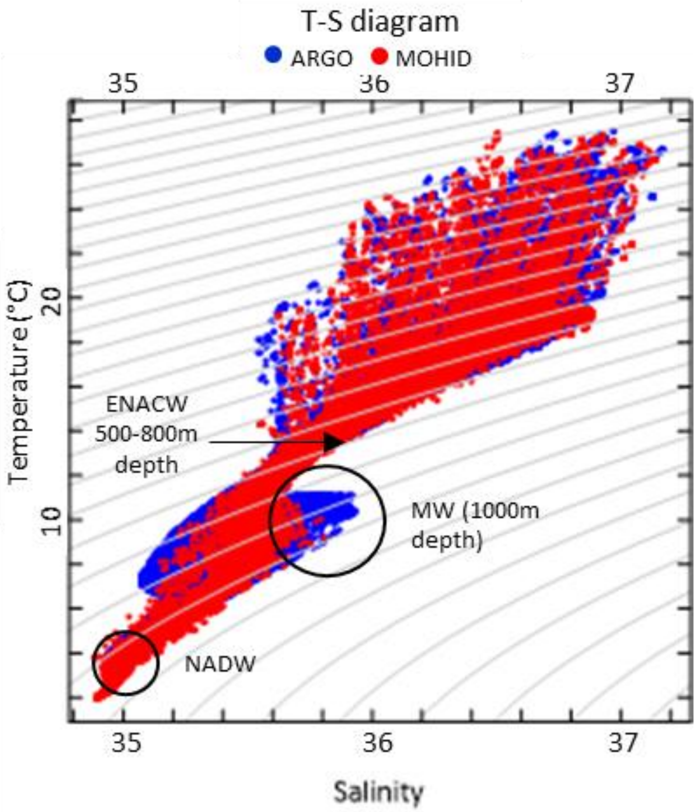

Figure 2.11 - Temperature-Salinity diagram for all the Argo buoy profiles (blue) and respective model results (red) in the study area during 2015. The signs of the MW and NADW are marked with a circle, and the ENACW with an arrow.

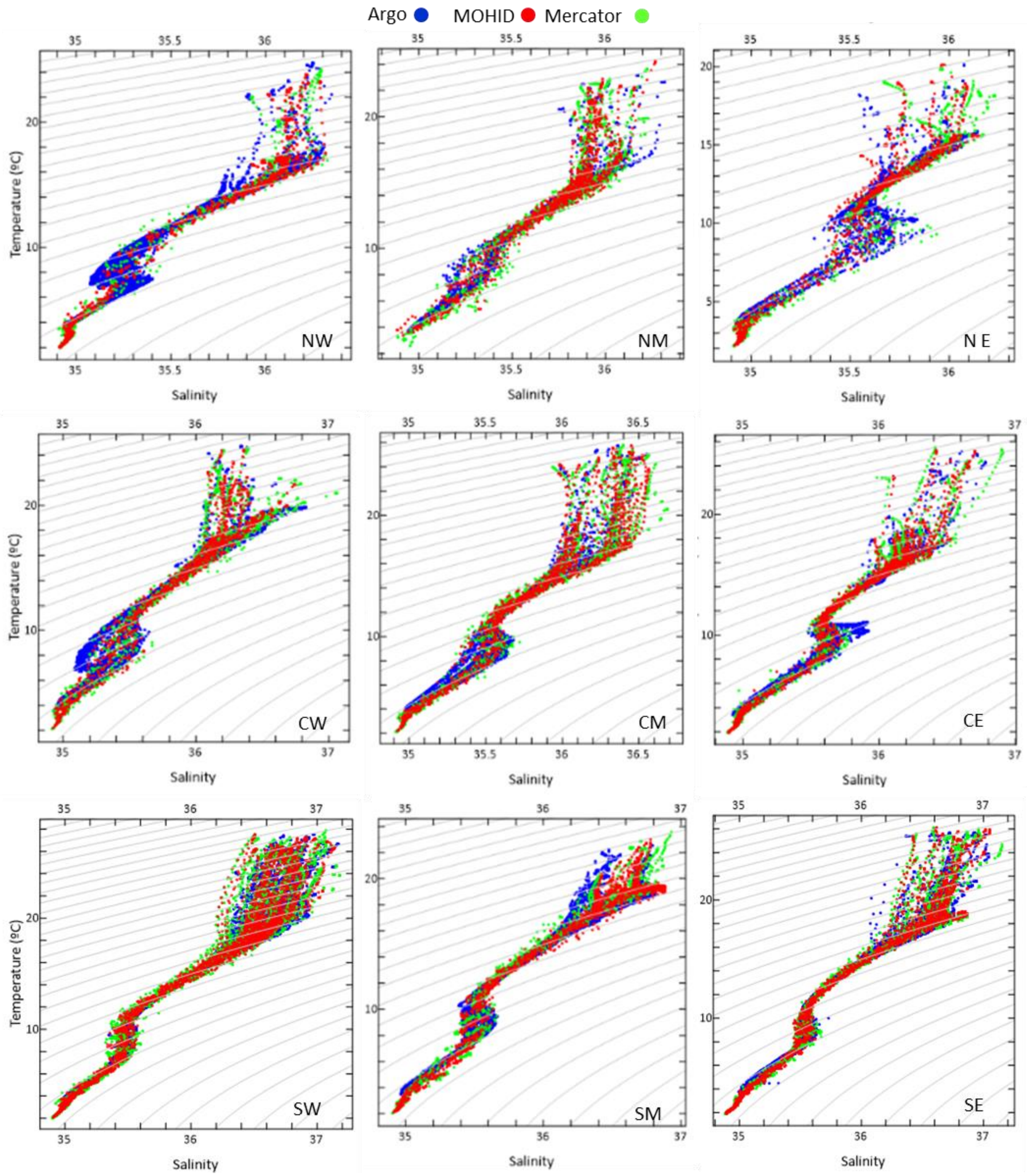

Figure 2.12- Temperature-Salinity diagram for all the Argo buoy profiles (blue), MOHID model results (red), and MERCATOR (green), in each study domain sub-area

To study the distribution of the water masses along the study area, the T-S diagrams were analysed in the 9 domain subdivisions, as shown in. These T-S diagrams also include the MERCATOR model results providing additional information about the models' performance. T-S diagrams for the entire domain, show that like Argo buoy profiles, model results can be used to identify different water masses. T-S diagrams (Figure 2.11) evidence the existence of a mixed layer, until the 200 meters depth, characterized by the temperature and salinity variability. This mixed-layer heterogeneity is a result of the seasonal variations in the ocean-atmosphere exchange (Marrero-Díaz et al., 2006), affecting the water properties until the 150-200 meters depth.

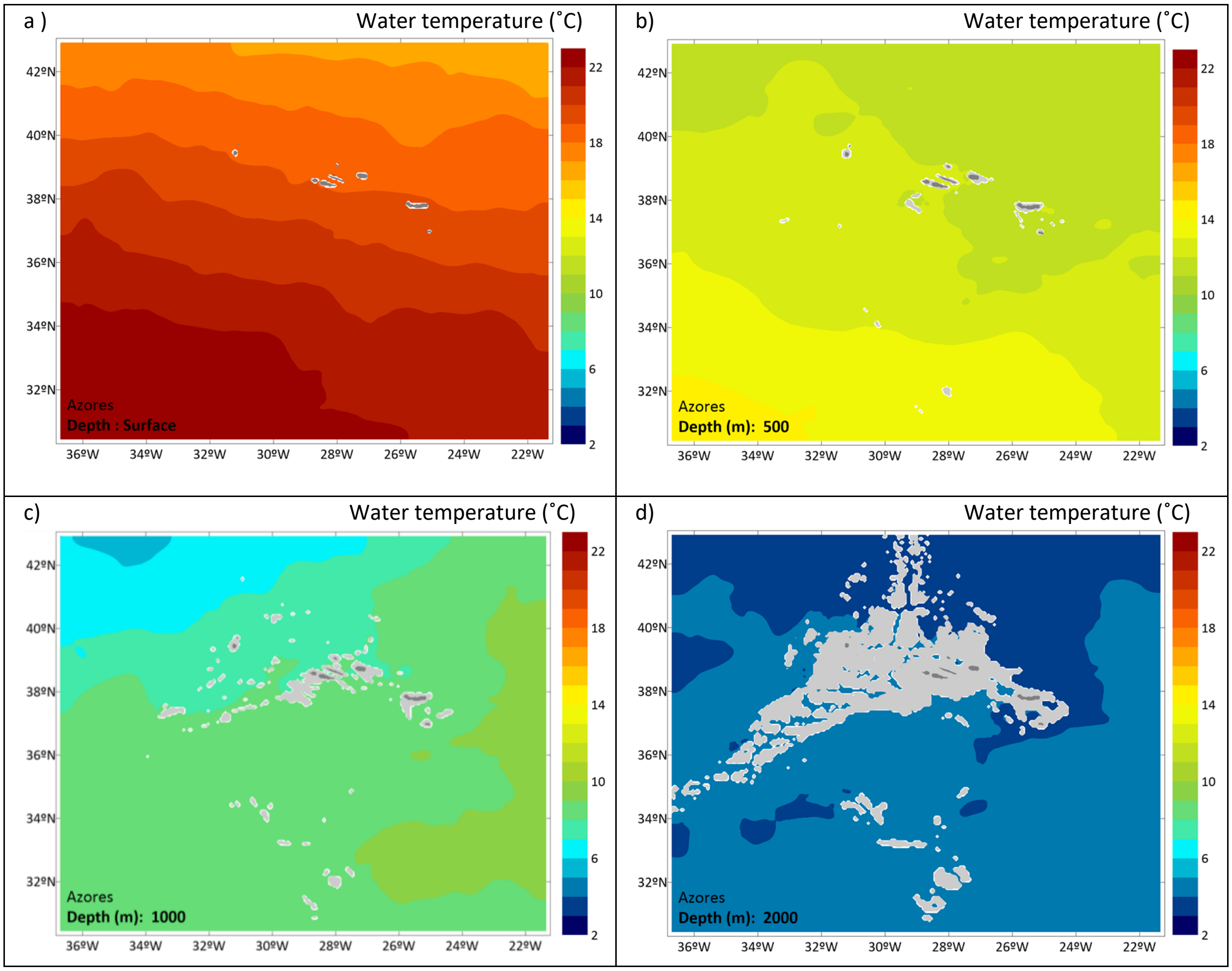

Figure 2.13 Average model results for the reference year of 2015, along the entire domain for water temperature at different depths: at the surface a), 500 meters depth b); 1000 m depth c) and 2000m depth d).

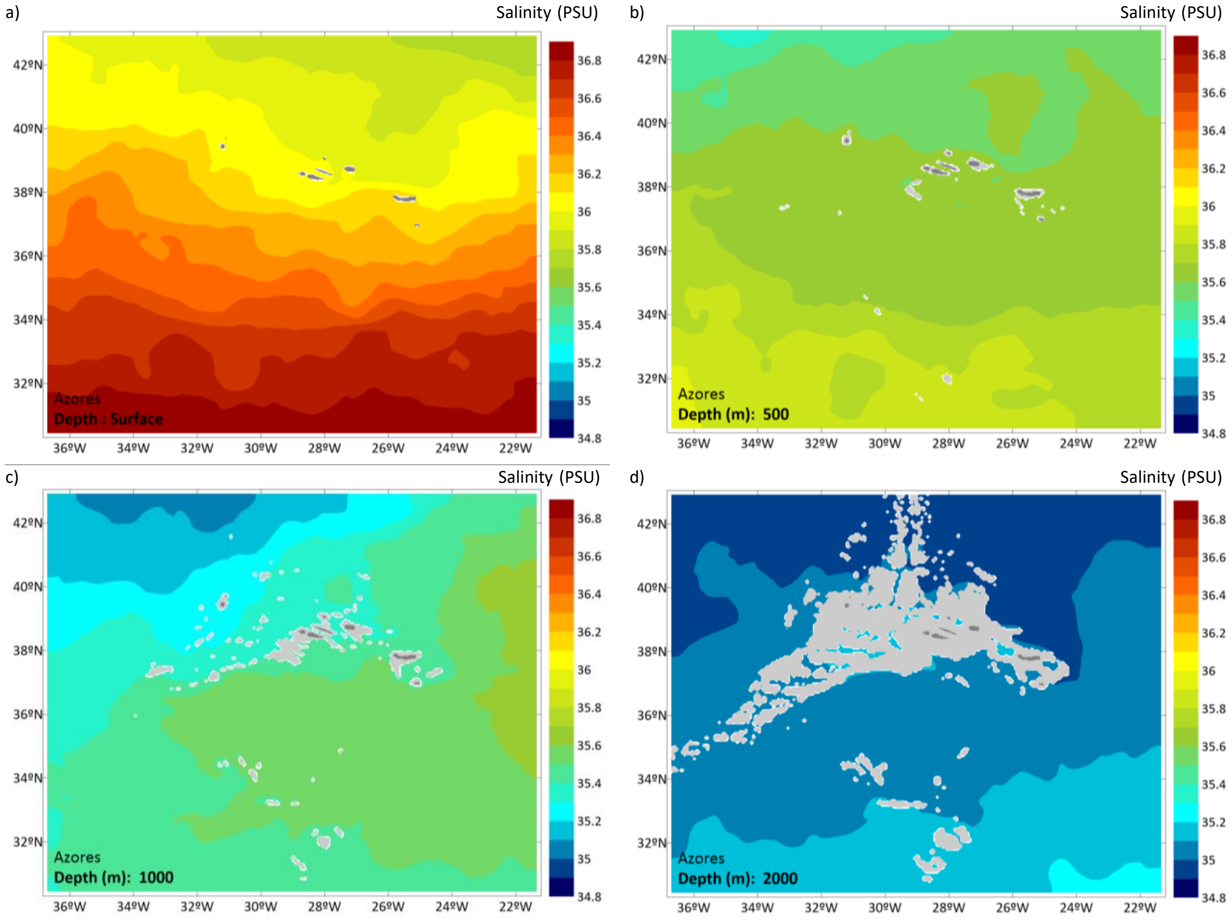

Figure 2.14 Annual average of sea salinity model results at different depths: a)surface, b)500m, c) 1000m, and d) 2000m depth.

The Mediterranean Water mass (MW) is characterised by temperature and salinity ranges of 2–11 °C and 35.0–36.2 (Palma et al., 2012), in the intermediate depths, around 1000 to 1500 meters depth (Juliano and Alves, 2007; Palma et al., 2012). In the study area, the Mediterranean water MW) mass signal can be identified in the T-S diagrams by the higher salinity values for water temperature values of around 10 degrees (Figure 2.11). The MW signal is stronger in all the Eastern quadrants (NE, CE and SE), where the T-S diagrams show higher salinity values for water temperature values of around 10 degrees (Figure 2.12). The average model results show the variability along the Azores region, in the surface layer, for SST and salinity, with a strong positive gradient of SST and salinity from North to South (Figure 2.13). This temperature spatial variability is enhanced by two eastward flows (Lafon et al., 2004): in the North, by the influence of the cold southern branch of the North Atlantic Current (NAC), that crosses the Mid-Atlantic

Ridge (MAR) at 45-48˚ N (Bower et al., 2002) and the warm Azores Current (AzC), that crosses MAR at 34-36 ˚ N (Klein and Siedler, 1989). The signal of the MW is visible at model results for 1000 meters depth for salinity results, with a demarked higher salinity in the Eastern part of the domain (Figure 2.14), not denoted in the other depths. Furthermore, the temperature values at 1000m depth reveal the signal of the MW (Figure 2.13).

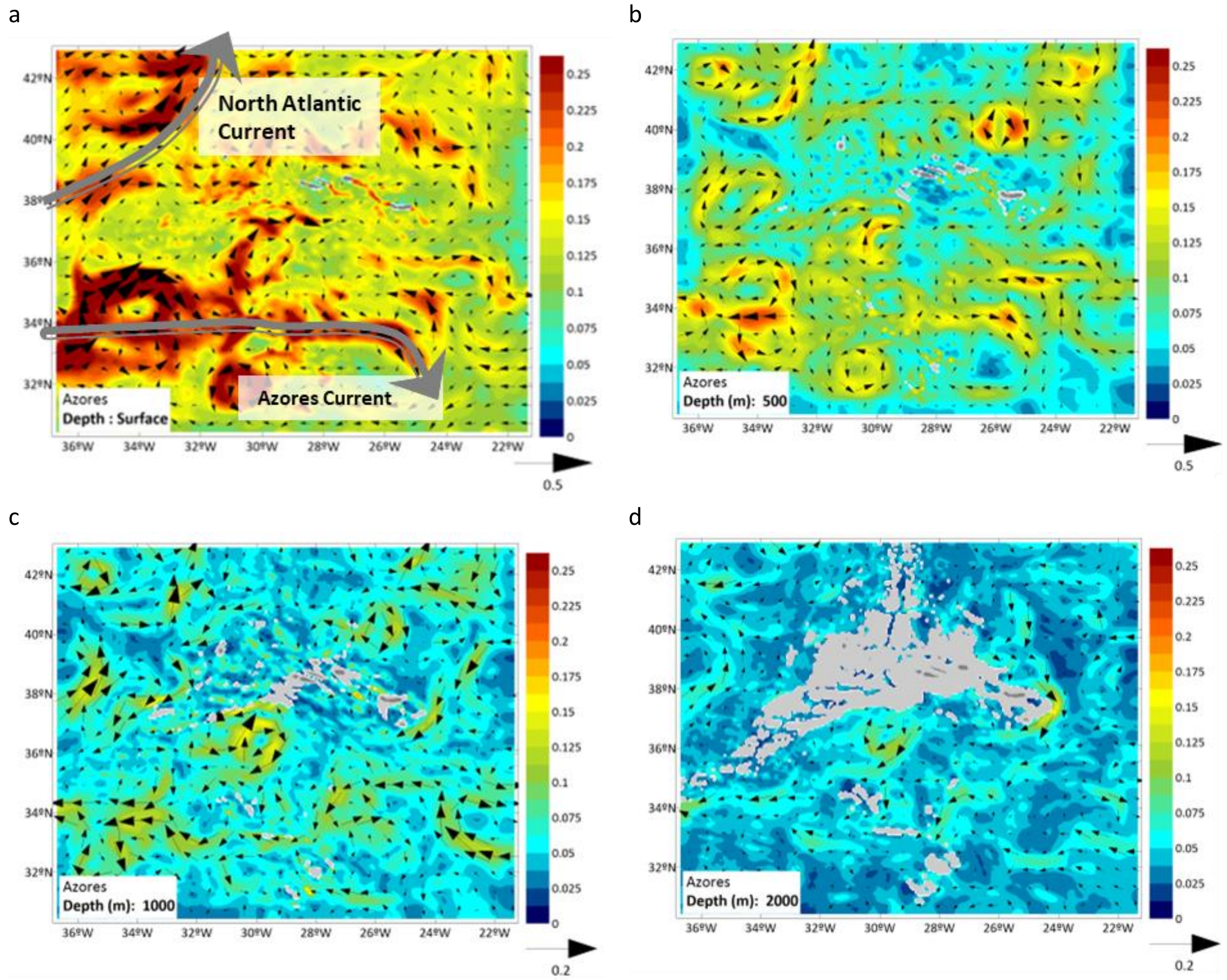

Figure 2.15- Annual average of model results for velocity modulus (colour scale) and direction (vector scale), from MOHID results, at different depths: a)surface, b)500m, c) 1000m, and d) 2000m depth.

Surface average results of velocity modulus and direction (Figure 2.15 a) represent the general sea-surface ocean circulation for the study area. Two main currents are visible around the Azores region. The Azores Current (AC), is located in the south of the archipelago, moving eastward, and the North Atlantic Current (NAC) moving northward, West and North of the archipelago. The AC has its origin as a branch of the Gulf Stream, heading south-eastward and crossing the Mid-Atlantic Ridge south of the Azores (Comas-Rodríguez et al., 2011). The signal of the AC is visible in the Azores region (Figure 2.15 a), with higher velocities up to 100 meters depth (Figure 2.15 b). Below the 500m depth, the velocities are lower, and the major currents are located near the island's platform, following mainly the Southwest direction, (Figure 2.15 c) and d)). In the superficial layers, the NAC moves northward and is visible West and North of the archipelago.

2.5. Conclusions

In the present work, a 3D-MOHID Water model application was implemented for the Azores region. Validation against the tidal gauge located at Ponta Delgada showed that MOHID simulate the observed water levels with accuracy, reproducing the amplitude and tidal phases with a correlation higher than 0.97. Although the Azores has been an object of study for hydrodynamic model applications and validation, few model applications for this area consider tide~~.~~ It would have been desirable to have more gauge stations to conduct this validation at a wider range of locations, namely on other islands. However, by this period and domain, only data from one gauge station was available.

Results show that MOHID adequately represents physical oceanographic properties: water level, SST, water temperature and salinity along the water column.

For SST, a good agreement between MOHID and the satellite-derived observations has been proved, with a correlation higher than 0.95 for the entire domain, emphasizing the strength of MOHID results. Some differences were detected around the archipelago. In further applications, this limitation can be surpassed through downscaling with a higher resolution model to local regions.

For the entire water column, MOHID evidences the ability to simulate the general patterns of temperature and salinity, with a correlation higher than 0.95 with Argo buoys data. The deeper analysis of these results shows the importance of a 3D high-resolution model, to better understand and describe the heterogeneity of water properties in the different water depths. Results revealed that the accuracy of MOHID to reproduce the physical properties of the study area was adequate. When using modelling tools, errors can increase over time and create instabilities (Guillou et al., 2018; Ménesguen et al., 2007) which was not the case in this study, since no instabilities were identified.

Validation results evidence the importance of monitoring data programs. Even with the higher vertical model resolution (50 vertical layers), small-scale variations identified in the Argo data are not represented with this model resolution. Also, model tools can help to have a holistic approach to the entire study area, and to study different hypotheses, enhancing the importance of the monitoring work for model validation, raising questions and answering several study hypotheses, or providing more detailed and in-situ data.

This implementation and validation work for the main physical parameters shows that this regional model can represent the patterns observed by monitoring data. The general currents and water masses are well simulated by MOHID. Thus, this regional model is capable of providing adequate boundary conditions for higher-resolution local and biogeochemical and biophysical models, to study biological patterns.

Chapter 3

Biogeochemical model in the Azores

3.1. Introduction

Biogeochemical dynamics in an ocean region are complex, and their study will benefit from a modelling approach. A biogeochemical model helps to study the transfer functions linking biological and chemical standing stocks. Different models follow several parameterizations, with prioritization of the different processes (Kwiatkowski et al., 2014). While the hydrodynamic models are widely used and implemented, and their physical equations of state are relatively well known, when considering biogeochemical dynamics, the complexity increases, and consequently the diversity of options (Ménesguen et al., 2007). The hydrodynamic model, by solving the advection-diffusion equations, provides the physical variables to the biogeochemical model (water temperature, salinity, velocity and density).

Many biogeochemical models simulate marine biological productivity and describe the biogeochemical cycles following a nutrient–phytoplankton–zooplankton–detritus (NPZD) approach. These models connect biogeochemical cycles and trophic levels through the uptake of nutrients by phytoplankton and the remineralisation of organic matter. In this work, the MOHID water quality model, an NPZD model (Mateus, 2006), is used. Other examples of NPZD models are PISCES (Pelagic Interactions Scheme for Carbon and Ecosystem Studies) (Aumont, 2005) or HAMMOC (Hamburg ocean carbon cycle model) (Ilyina et al., 2013), among others (Berline et al., 2007; Fasham et al., 1990; Fennel, 2009; Xu et al., 2008) applied in regional and global domains.

MOHID Water Quality simulates the marine biological productivity and the major biogeochemical cycles. It is a nutrient–phytoplankton–zooplankton–detritus (NPZD) model (Vallino, 2000). Nutrients are incorporated into phytoplankton biomass through phytoplankton growth, and then by grazing are transferred into zooplankton biomass. Hereafter, by phytoplankton and zooplankton's mortality, the nutrients are incorporated into the detritus pool, and by nitrification and mineralization, nutrients will be available again in the water column, closing this cycle. The main processes simulated in the MOHID water quality module are depicted in Figure 3.1.

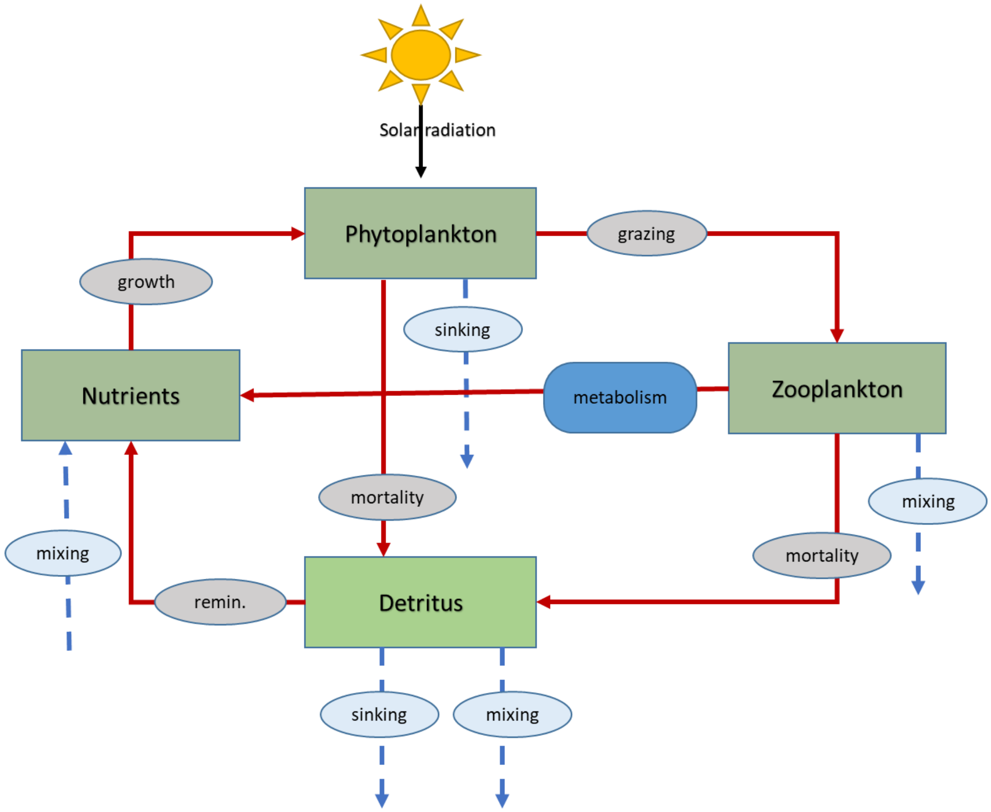

Figure 3.1- Schematic representation of the MOHID Water quality module, with the major fluxes in the (NPZD model N-Nutrients; P-Phytoplankton; Z-zooplankton; D-detritus).

The number of phytoplankton groups to consider in biogeochemical models is under discussion in model developments, and it is a relevant factor considering their objectives, computational requirements and limitations. Different models can consider different Phytoplankton Functional Groups (PFG), different dynamics and parameterizations. Namely, to control the phytoplankton dynamics: in the North Atlantic, in the CCSM-BEC model, the light dependency of growth plays an important role, while in the PlankTOM5 ocean biogeochemistry model, and the NEMURO (North Pacific Ecosystem Model for Understanding Regional Oceanography), the difference in the maximum growth rates is the major factor for this calibration (Hashioka et al., 2013). Also, different top-down or bottom-up controls can have different effects on phytoplankton growth. While in PISCES, CCSM-BEC, and PlankTOM5 models the top-down control, by zooplankton grazing, helps to control phytoplankton and diatoms dynamics. In other models, this control is more effective by bottom-up processes, by nutrient half-saturation constants (bottom-up control) (Gnanadesikan et al., 2011). Also regarding their complexity, global-scale models continue to use simple phytoplankton growth models, with simplification of phytoplankton physiology, namely using constant Chl:C ratio using the classical Michaelis–Menten representation of nutrient (Anugerahanti et al., 2021) and assume constant C:N:P stoichiometry, based on the carbon, nitrogen and phosphorous Redfield ratio (Ayata et al., 2013). MOHID also use these constant rates.

3.2. Methodology

A 3-D biogeochemical model is implemented in the Azores region to simulate the major biogeochemical processes in the region. A general description of the major processes simulated by the biogeochemical model is presented. Thereafter, the model was applied to the Azores region, it was parameterized and calibrated, and finally, was validated against available data. In this case, when applying the model for the Azores region, the calibration process was performed by tunning the different parameterizations, to adjust the physical-biological model formulations, to better represent the highly dynamic marine environment observed in the Azores

Associated with the parametrization process a successive calibration analysis was performed by comparing model results and analyzing its temporal, seasonal and spatial dynamics, comparing it with the available in-situ data, climatology for the region or any other registered information. Model assessment and validation were performed using several statistical methods and comparisons with other model results.

3.2.1. MOHID Water Quality module

The MOHID Water Quality module is integrated into MOHID solution (www.mohid.com) (Instituto Superior Técnico, 2003). This biogeochemical module, like all the MOHID solutions, is *open source* and available online (https://github.com/Mohid-Water-Modelling-System/Mohid).

The model was initially based on the EPA biogeochemical model (Bowie et al., 1985) considering general state variables including phytoplankton, zooplankton, oxygen, dissolved silica, nitrogen and phosphorous cycles. The Water Quality module is coupled in a physical model, using an offline approach, where the numerical scheme of the biogeochemical processes is solved offline, over the physical solution. Biogeochemical processes are solved using the advection-diffusion equations with biogeochemical source and sink terms. The process is 0-D, grid-independent, the processes take place inside the control volume, which undertakes local production and destruction terms, and the time step is independent and lower than the hydrodynamic time step (Trancoso et al., 2009).

State variables include the main inorganic nutrients (nitrate, phosphate and dissolved silica), dissolved oxygen, two phytoplankton groups (small phytoplankton and diatoms), and zooplankton (Tabel 3.1)). The carbon cycle is estimated explicitly, like in other biogeochemical models (e.g. MEDUSA-Yool et al., 2013), from other elemental cycles (N, P, Si), using a fixed stoichiometry for Carbon (C), Nitrogen (N), and Phosphorous (P), following the Redfield ratio (C:N:P ~106:16:1). This Relfied ratio, created by Redfield in 1958, is based on the proportions of the life's essential elements (C/N/P), which are essential to the metabolic requirements of phytoplankton (Hirose and Kamiya, 2003; Weber and Deutsch, 2010). Redfield ratio was extended to include dissolved silica (C:Si:N:P = 106:15:16:1-Brzezinski, 1985).

Three living compartments are represented: zooplankton, and two Phytoplankton Functional Types (PFTs): small phytoplankton, and diatoms. Diatoms differ from the other groups because their growth is limited by dissolved silica. Diatoms are the main source of biogenic silica in the model. These PFTs differ in how the environment influences their growth (influenced by light and nutrient concentration), their respiration, excretion and metabolic rates, and, therefore, their effects on biogeochemistry (Litchman et al., 2015). Similarly to other model applications for the Atlantic Ocean (Ward et al., 2013), MOHID does not consider large dinoflagellates because they are assumed to be of limited importance in open ocean waters (Vichi et al., 2007a). MOHID follows the Monod approach for phytoplankton growth (Monod, 1942), where growth is limited by the availability of external nutrients.

Table 3.1- State variables considered in the Water Quality module

Variable	Description		Units
ϕPhy	Phytoplankton concentration (mainly flagellates)	Organism	mgC/l
ϕDia	Diatoms concentration		mgC/l
ϕZoo	Zooplankton concentration		mgC/l
ϕNH4	Ammonia concentration	Nitrogen	mgN/l
ϕNO2	Nitrite concentration		mgN/l
ϕNO3	Nitrate concentration		mgN/l
ϕPON	Particulate Organic Nitrogen Concentration		mgN/l
ϕDONnr	Dissolved organic nitrogen non-refractory concentration		mgN/l
ϕDONre	Dissolved organic nitrogen refractory concentration		mgN/l
ϕIP	Inorganic phosphorous concentration	Phosphorous	mgP/l
ϕPOP	Particulate Organic Phosphorous concentration		mgP/l
ϕDOPnr	Dissolved organic Phosphorous non-refractory concentration		mgP/l
ϕDOPne	Dissolved organic Phosphorous refractory concentration		mgP/l
ϕDissSi	Dissolved silica concentration	Silica	mgSi/l
ϕBioSi	Biogenic Silica concentration		mgSi/l
ϕOxy	Dissolved Oxygen concentration	Oxygen	mgO$_2$/l

Phytoplankton and zooplankton groups are quantified in mgC/l. Phytoplankton carbon biomass is often inferred from chlorophyll measurements (Chl) using a constant carbon-to-chlorophyll ratio (Arteaga et al., 2016). *In situ* measurements of phytoplankton Chl:C are scarce, and this carbon-to-chlorophyll ratio is a major unknown variable in marine ecosystems understanding (Taylorl et al., 1997). Environmental factors like nutrient concentration and light availability can induce physiological changes in phytoplankton, and consequently this Chl:C ratio (Arteaga et al., 2016). However, the use of a constant Chl:C ratio, is a common approach in biogeochemical models.

Table 3.2 summarises the different Chl:C ratios used in different models (Arteaga et al., 2016; Aumont et al., 2015; Fasham et al., 1985; Fennel et al., 2006; Itoh et al., 2015; Macedo et al., 2000). This carbon-to-chlorophyll conversion allows comparing model results with remote sensing data, and other data sources, for model calibration and validation. Non-biological state variables used in the model are inorganic nutrients (nitrogen, phosphorus and dissolved silica), and oxygen.

Table 3.2- Chlorophyll to carbon ratio used in several models or obtained in several studies

Parameter	Model/*In-situ* location	Source	Value	units
minimum chl/C	PISCES (global model)	Aumont et al, 2015	0.0033	mgChl/mgC
maximum chl/C	PISCES (global model)	Aumont et al, 2015	0.05	mgChl/mgC
Chl/C	Azores front	Macedo et al, 2000; Irwin et al. 1983	0.03125	mgChl/mgC
Chlorophyll/C	Model / Local study	Itoh et al., 2015	0.036	mgChl/mgC
Chlorophyll/C	MEDUSA (coastal zones)	Yool et al., 2013	0.05	mgChl/mgC
Chlorophyll/C	Global study	Arteaga et al. 2016	< 0.01 to 0.05	mgChl/mgC
maximum Chlorophyll/C	ROMS-Bio Fennel (global model)	Fennel et al, 2006	0.053	mgChl/mgC
Chlorophyll/C	Azores Front EAW	Fasham et al., 1985	0.031	mgChl/mgC
Chlorophyll/C	Azores Front WAW	Fasham et al., 1985	0.0115	mgChl/mgC
Chlorophyll/C	Azores Front combined	Fasham et al., 1985	0.0185	mgChl/mgC
Chlorophyll/C	MOHID	*this application	0.0185	mgChl/mgC

3.2.1.1. State Variables

Organisms

Three living compartments are represented in this application: zooplankton, and two Phytoplankton Functional Types (PFTs): small Phytoplankton (Phy) and Diatoms (Diat). Diatoms are unicellular photosynthetic algae, part of phytoplankton. This group is estimated to contribute for 20 to 40% of the primary production in the ocean, and an even greater percentage of the export production for the euphotic zone (DeMaster, 2001), making them major players in the cycling of all biological elements (Yool and Tyrrell, 2003).

One of the distinctive features of diatoms is that they form a major portion of their cell walls out of silica, and they develop a strategy to take up dissolved silica from the environment, mineralizing it and forming biogenic silica (DeMaster, 2001). On the other side, typically its larger size implies higher maximum growth rates (Marañón, 2005), and higher half-saturation constants for nutrient-limited growth or nutrient uptake, contrasting with smaller phytoplankton (Litchman et al., 2015). When considering biogeochemical models different combinations of these mechanisms can result in different rates. Therefore, in the different model applications and study areas, different rates can be used. Models should be calibrated for the different parameterizations for each case study.

Phytoplankton

Phytoplankton simulation in MOHID follows several statements (Figure 3.2). The organisms consume inorganic nutrients (ammonia and nitrate from the nitrogen cycle, and inorganic phosphorus from the phosphorus cycle). During the photosynthetic process, dissolved oxygen is produced. Phytoplankton growth is limited by nutrient availability, temperature, and light availability as a source of energy for photosynthesis. Oxygen is consumed during the respiration process, accompanied by the production of ammonia. Phytoplankton concentration reduces by excretion, mortality, grazing and settling. By excretion, produces dissolved organic material (Refractory Dissolved Organic Nitrogen, Non-Refractory Dissolved Organic Nitrogen, Refractory Dissolved Organic Phosphorus and Non-Refractory Dissolved Organic Phosphorus). By mortality, phytoplankton increases the dissolved organic material and the particulate organic material (Particulate Organic Nitrogen and Particulate Organic).

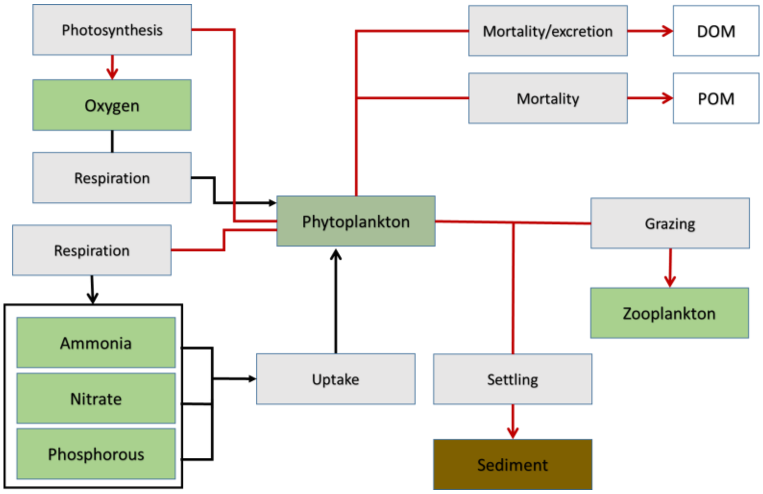

Figure 3.2- Internal flux of Phytoplankton (small phytoplankton) in the Water Quality module.

The settling process is modelled in the water properties module. The simulation of the diatoms cycle in MOHID follows similar internal fluxes to small phytoplankton, nonetheless including dissolved silica, which is an essential chemical requirement for diatoms (Figure 3.3). By mineralization, diatoms produce biogenic silica.

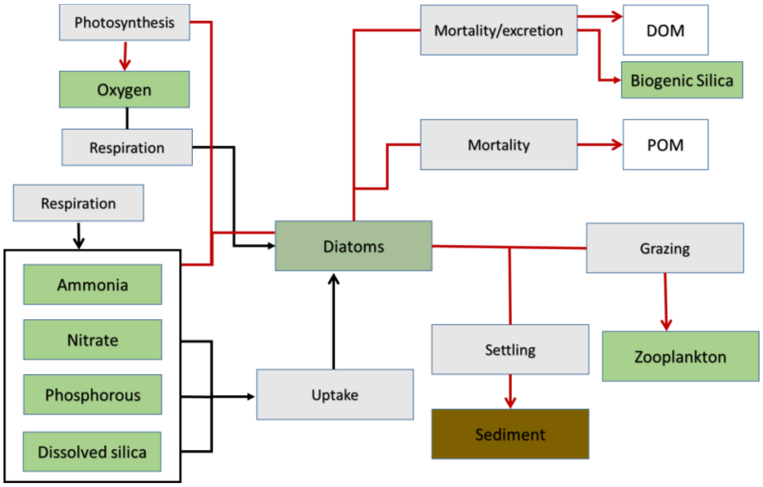

Figure 3.3- Internal flux of Diatoms in the WQ module

Zooplankton

Zooplankton is essential in biogeochemical cycles because it controls the phytoplankton abundance by grazing. Zooplankton consumes oxygen by respiration (Figure 3.4), by mortality and excretion contribute to the detrital pool, returning particulate and dissolved organic matter into the water column. Large and small detritus, as well as phytoplankton, have an associated vertical sinking rate.

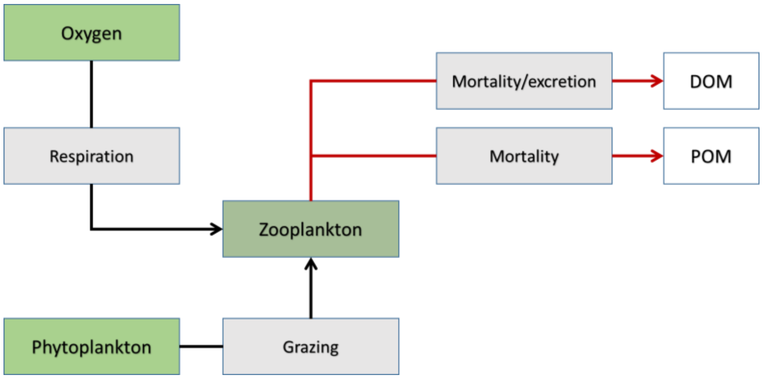

Figure 3.4- Internal flux of zooplankton in the WQ module

Zooplankton’s pool is induced by gross growth rate and by phytoplankton grazing (Gz), losses are due to respiration (r_z) and non-predatory mortality of the zooplankton (m_z), and predatory mortality (g_z) and dependent on the zooplankton concentration (ϕ_z) (eq. 3.1). Zooplankton's gross growth rate depends on a minimum concentration of phytoplankton for grazing and is limited also by temperature and light (however with different constants than phytoplankton).

Zooplankton gross growth rate is given by:

$$\frac{\partial \phi_z}{\partial t} = (G_z - r_z - m_z) * \phi_z * g_z \qquad \text{eq. 3.1}$$

Zooplankton concentration is given by eq. 3.2, where Z_1 is the zooplankton concentration in (mgC/l), μ_{z1} is the zooplankton gross growth rate, e_{z1} the excretion rate and m_{z1} the mortality, all in day $^{-1}$:

$$\frac{\partial Z_1}{\partial t} = (\mu_{z1} - e_{z1} - m_{z1}) * Z_1 \qquad \text{eq. 3.2}$$

Finally, *G*, the rate of mortality due to grazing, is given by:

$$G = \frac{G_z}{E} \times Z \qquad \text{eq. 3.3}$$

where g_z is the net growth rate of zooplankton, *E* is the assimilation efficiency, and Z is the zooplankton concentration.

By grazing, zooplankton consumes phytoplankton and diatoms, with different preferences and assimilation coefficients. This grazing is dependent on the ingestion rate and limited by the concentration of phytoplankton and diatoms, from the capture efficiency, from the half-saturation constant for ingestion, and from a minimum threshold standing stock of phytoplankton and diatoms below which predation ceases. It is assumed that zooplankton mortality is related to starvation, being directly related to the concentration of prey, where below a threshold of prey, the mortality is maximum.

Nutrients

Nitrogen

The Water Quality module includes nitrogen as organic and inorganic nitrogen. The inorganic nitrogen is divided into ammonia (NH4), nitrite (NO2) and nitrate (NO3). The organic nitrogen is divided into particulate organic nitrogen (PON), dissolved organic nitrogen non-refractory (DONnr) and dissolved organic nitrogen refractory (DONre). DONnr includes small molecular substrates, assumed to be degraded in the way of production and DONre includes substrates with a longer turnover. The sources of ammonia are the inorganic matter from the excretion and respiration of phytoplankton and zooplankton, and the mineralization of the refractory and non-refractory dissolved nitrogen (Figure 3.5). The sinks of ammonia are the uptake by phytoplankton and the nitrification of ammonia (producing nitrite).

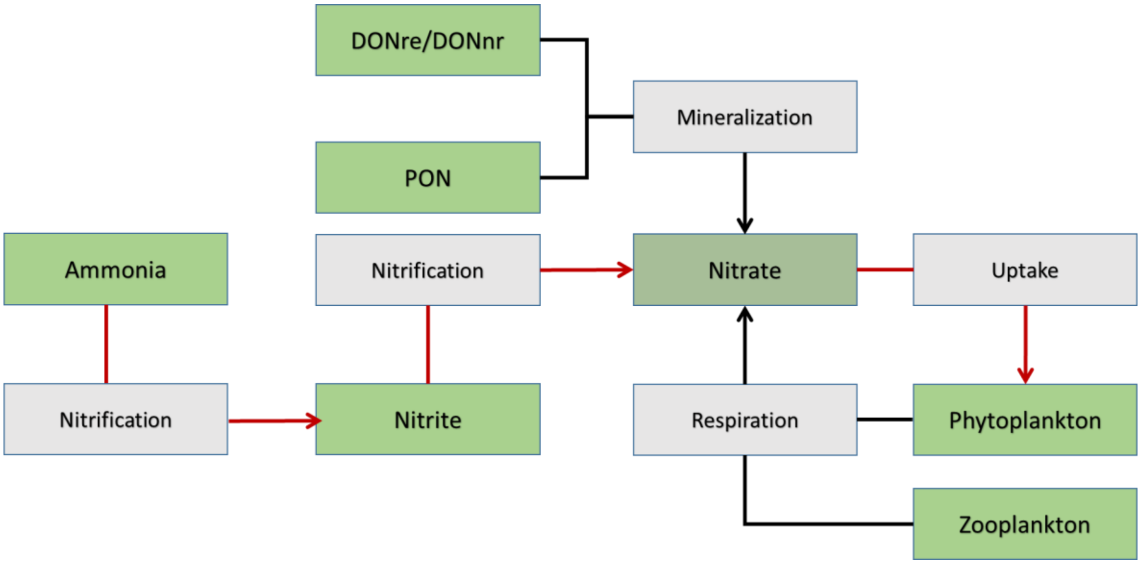

Figure 3.5- Internal fluxes of ammonia in the WQ module

The nitrification process considers two-stage processes, the oxidation of ammonia to nitrite (NO_2^-), and then to nitrate (NO3). Nitrification rate, PON decomposition rate, and DON mineralization rates, at a reference temperature, can be parametrized in MOHID. They are temperature-dependent with a specific temperature coefficient for each case. Nitrification and denitrification rates are calculated as a semi-saturation function, with specific, and also parameterized half-saturation constants.

Inorganic phosphorous

Like nitrogen, phosphorous also is simulated in the organic and inorganic forms (Figure 3.6). The inorganic phosphorus is assumed to be available as orthophosphate (PO4) for uptake by phytoplankton. The organic phosphorus is divided into particulate organic phosphorus (POP), dissolved organic phosphorus non-refractory (DOPnr) and dissolved organic phosphorus refractory (DOPre). The rate equations of phosphorus are implemented in the same way as the nitrogen cycle, except that there is just one compartment of inorganic phosphorus. The inorganic phosphorous sources are respiration and excretion from phytoplankton and zooplankton, and the mineralization of the DOP and the POP. The sink of Inorganic phosphorous is the phytoplankton uptake. The respective POP, DOPre, and DOPnre, mineralization rates at a reference temperature, and respective temperature coefficients are parameterizable in MOHID.

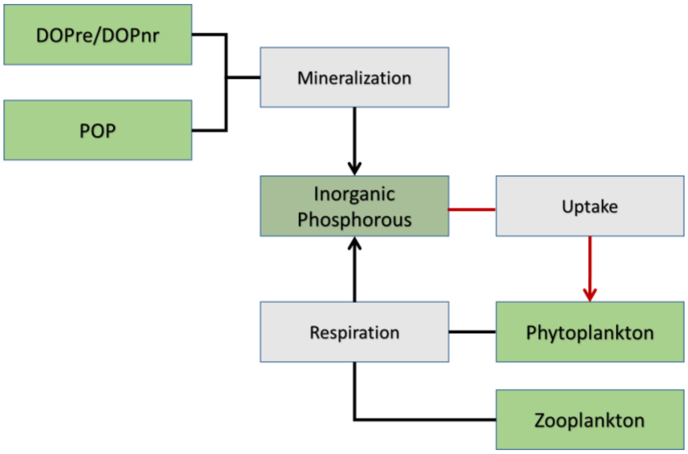

Figure 3.6- Internal fluxes for the inorganic phosphorous cycle in the WQ module

Dissolved silica

Unlike the other major nutrients such as nitrate and phosphate, which are needed by almost all marine planktonic organisms, dissolved silica is an essential chemical requirement only for some, such as diatoms or siliceous sponges (DeMaster, 2001).

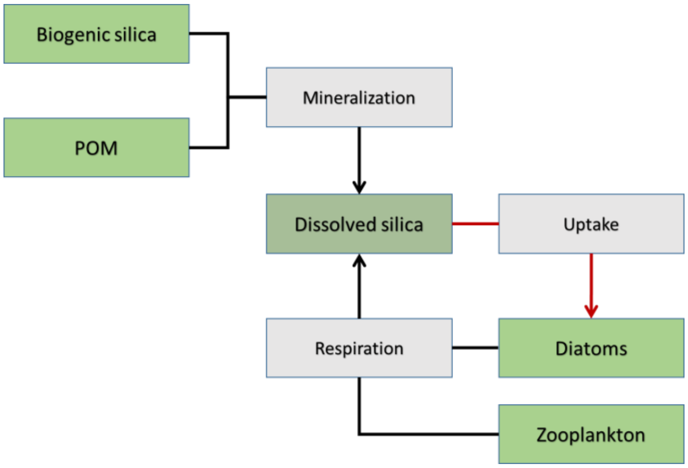

Figure 3.7- Internal fluxes for dissolved silica cycle in MOHID WQ module

The recirculation of Si in the ocean is essentially through its utilization by planktonic diatoms, which consume dissolved silica to elaborate a skeleton of biogenic silica (BSi) but other siliceous consuming organisms like sponges can have a negligible contribution in the silica cycle (Maldonado et al., 2019). In MOHID silica's cycle, Figure 3.7, Diatoms are the sinks of dissolved silica, and this process is controlled by the biogenic dissolution rate in the water column. A source of silica is the silica that has been recycled by upwelling from the deep ocean and seafloor (Yool and Tyrrell, 2003).

Dissolved oxygen

Oxygen is an essential component of animal life, playing an important role throughout the nutrient cycles. In the WQ module, the sources of oxygen are photosynthesis, denitrification and nitrate uptake by phytoplankton (Figure 3.8). The sinks of oxygen are the nitrification, the mineralization of the inorganic nitrogen forms into DOM and POM, and the phytoplankton and zooplankton respiration.

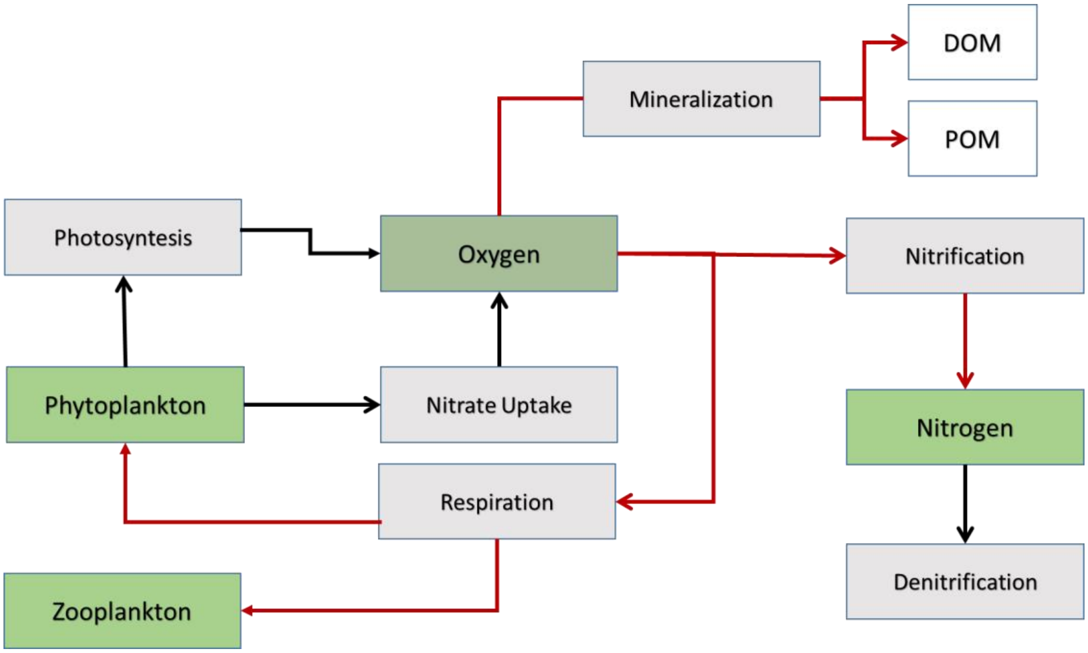

Figure 3.8- Internal fluxes for oxygen cycle in MOHID

3.2.1.2. MOHID parameterization

Limitation growth factors (Phytoplankton and zooplankton growth)

From now on, in this document, the Phytoplankton term, (Phy), will be used to refer to the total phytoplankton, considering both groups: small phytoplankton (Phy_s) and diatoms, (Diat). The phytoplankton growth rate is limited by temperature, light intensity and nutrient availability: nutrient limitation Ψ(Nut), considering Nitrogen and Phosphorous (N and P), and dissolved silica (Si) only for diatoms; temperature limitation $\Psi(T)$, and light limitation $\Psi(L)$ (eq. 3.4).

Each growth limitation factor can range from a value of 0 to 1. A value of 1 means the factor does not limit the growth (i.e., is at optimum intensity, nutrients are available in excess, etc.) and a value of 0 means the factor is so severely limiting that growth is inhibited entirely.

$$\mu Phy = \boldsymbol{\mu}_{Phy}^{max}.\ \Psi\ (T)_{Phy}.\Psi\ (L)_{Phy}.\Psi\ (N)_{Phy} \qquad \text{eq. 3.4}$$

Mohid uses a multiplicative formulation in which all factors are multiplied together. The major criticism of this approach is that the computed growth rates may be excessively low when several limitation factors are considered (Baird et al., 2001), mainly for nutrient limitation.

Phytoplankton growth

Phytoplankton groups are described in terms of carbon concentration (mgC/l). The phytoplankton net growth is dependent on different processes, where μ_{Phy} is the growth rate (d^{-1}), r the respiration, ex the excretion, and *m* the non-predatory mortality of phytoplankton, and *G* the grazing by zooplankton.

$$\frac{\partial \Phi_{Phy}}{\partial t} = (\mu_{Phy} - r_{Phy} - ex_{Phy} - m_{Phy})\Phi_{Phy} - G \qquad \text{eq. 3.5}$$

The respiration is divided into dark respiration and photorespiration, being *re* the dark respiration and rp the photorespiration (eq. 3.6).

$$r = re + rp \qquad \text{eq. 3.6}$$

Following Park et al. (1980) considerations, dark respiration is defined by eq. 3.7, where k_{er} is the Phytoplankton endogenous respiration constant (FENDREPC) (Bowie et al., 1985).

$$r_e = K_{er}e^{0.069T} \qquad \text{eq. 3.7}$$

Photorespiration (r_p) is proportional to the gross photosynthetic rate being k_p the proportionality factor (designated as PHOTORES in the MOHID parameters) (eq. 3.98).

$$r_p = k_p\mu \qquad \text{eq. 3.8}$$

By excretion (ep. 3.9) phytoplankton produces dissolved organic material. Light may influence the excretion of a substance by causing a change in the permeability of the cell membrane or, if an active transport system is involved, by regulating the supply of energy-rich compounds, therefore the excretion rate is formulated similarly to photorespiration, being higher at both low light levels and inhibitory at high light levels (Collins, 1980).

In MOHID the excretion rate is expressed as (eq. 3.9):

$$ex_{Phy} = \varepsilon_{Phy} * \mu_{Phy} * (1 - \Psi\,(L)_{Phy}) \qquad \text{eq. 3.9}$$

where ε_{Phy} is the phytoplankton excretion constant, and $\Psi\,(L)_{Phy}$ the Light limitation factor.

Phytoplankton mortality

The natural mortality, also called non-grazing mortality, m_{phy}(day^{-1}), follows the Michaelis-Menten formulation and is given by:

$$m_{Phy} = m_{max} * \frac{\frac{\Phi_{Phy}}{\mu_{Phy}}}{Km + \frac{\Phi_{Phy}}{\mu_{Phy}}} \qquad \text{eq. 3.10}$$

Natural mortality, m_{phy}, is proportional to the biomass of phytoplankton and inversely proportional to the gross growing rate μ, where Km is the half-saturation constant for mortality, and m_{max}, *the* maximum rate of natural mortality. Finally, G, the rate of mortality due to grazing, is given by eq. 3.11.

$$G = \frac{G_z}{E} \times Z \qquad \text{eq. 3.11}$$

where G_z is the net growth rate of zooplankton, and Z is the zooplankton concentration.

Nutrients limitation

For nutrient limitations, $\Psi(\mathrm{Nut})_{Phy}$ Mohid uses the minimum formulation, where the most severely limiting factor alone is assumed to limit growth, between N or P for small phytoplankton (eq. 3.12) and between N, P and Si for diatoms (eq. 3.13).

$$\Psi(Nut)_{Phys} = min(\, L_N^{pn}, L_P^{pn}) \qquad \text{eq. 3.12}$$

$$\Psi(Nut)_{Dia} = min(\, L_N^{pd}, L_P^{pd}, L_{Si}^{pd}) \qquad \text{eq. 3.13}$$

Nutrient limitation in MOHID follows the Michaelis-Menten function, considering the half-saturation constant concept, K, corresponding to the nutrient concentration for which the uptake is 50% of the maximum. In the case of Nitrogen limitation for Phytoplankton, the model considers (eq. 3.14):

$$\Psi\ (N)_{PhyS} = \frac{N}{K_N + N} \qquad \text{eq. 3.14}$$

Where K_N is the half-saturation constant for Nitrate, in mgN/l. N is the useful concentration of inorganic nitrogen (ammonia + nitrate), in mgN/l. The same formalism is used for the other nutrients (Inorganic phosphorous, and dissolved silica (for diatoms)). Using this formulation, the half-saturation constant takes more importance for lower concentrations of each nutrient.

For phosphorous, the above equation takes the form (eq. 3.15):

$$\Psi\ (P)_{PhyS} = \frac{PO4}{K_{PO4} + PO4} \qquad \text{eq. 3.15}$$

And for dissolved silica (eq. 3.16):

$$\Psi\ (Si)_{Diat} = \frac{Si}{K_{Si} + Si} \qquad \text{eq. 3.16}$$

where Ψ(P) represents the nutrient uptake due to phosphorus presence, PO4 the phosphorus concentration (assumed to be completely available as orthophosphate) (mg P/l) and Kp the half-saturation constant for phosphorus limitation (mg P/l).

The Nitrate half-saturation constant for Phytoplankton is set to relatively low values, giving to phytoplankton a reasonably strong preference for Nitrate.

Temperature limitation

The concept of Thornton and Lessen, (1978), is adopted to compute the temperature limitation factor (Ψ(T)) on autotrophic and heterotrophic organisms. This function uses optimum temperature curves for which the growth rate increases up to an optimum and then decreases at higher temperatures.

$$\Psi(T) = K_A^{(T)} * K_B^{(T)} \qquad \text{eq. 3.17}$$

$$K_A^{(T)} = \frac{K_1 . e^{\gamma_1 (T - T_{min})}}{1 + K_1 . (e^{\gamma_1 (T - T_{min})} - 1)} \qquad \text{eq. 3.18}$$

$$K_B^{(T)} = \frac{K_4 . e^{\gamma_2 (T_{max} - T)}}{1 + K_4 . (e^{\gamma_2 (T_{max} - T)} - 1)} \qquad \text{eq. 3.19}$$

With:

$$\gamma_2 = \frac{ln \frac{k_3(1 - k_4)}{k_4(1 - k_3)}}{T_{max} - T_{max}^{opt}} \qquad \text{eq. 3.20}$$

$$\gamma_1 = \frac{ln \frac{k_2(1 - k_1)}{k_1(1 - k_2)}}{T_{min}^{opt} - T_{min}} \qquad \text{eq. 3.21}$$

Where Toptmin (°C) and Toptmax (°C) represent the temperature interval for an optimal process, and Tmax (°C) and Tmin (°C) are the maximum and minimum tolerable temperatures where processes are completely inhibited. The remaining constants (K1, K2, K3 and K4) control the shape of the response curve of the temperature effect; these values are assumed equal for all organisms in this model.

Different organisms have different light affinities. Using this different coefficients model, we can limit the growth differentially for the different organisms. Figure 3.9 shows the result of different MOHID parametrizations for diatoms and for small phytoplankton temperature limitation factors, where the temperature interval for an optimal process is different. For small phytoplankton (PhyS) TopTmin is 16,5^{o}C, TopTmax is 26,5^{o}C, and for diatoms are 15^{o}C and 26.5^{o}C respectively. With these different optimal temperature intervals, the growth of the diatom is more limited at lower temperatures than phytoplankton growth.

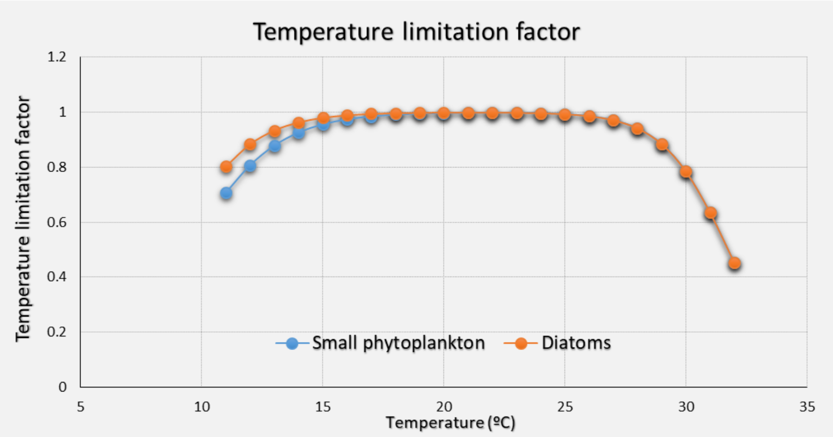

Figure 3.9- Temperature limitation factor for small phytoplankton and diatoms

Light limitation

Primary producers' photosynthetic rate is dependent on the light intensity. The light limitation factor defines the relationship between the ambient light levels and, phytoplankton and diatoms growth (Haney and Jackson, 1996). Phytoplankton is limited to the uppermost layers of the water column where light intensity is sufficient because photosynthesis is possible only when light reaching the algae cell is above a certain intensity. The depth to which light will penetrate in water, and hence the depth at which production can occur, is dependent on several factors, including absorption of light by water, the wavelength of light, transparency of water, reflection from the surface of the water, reflection from suspended particles, latitude, and season of the year.

Like in other models (e.g. ERSEM (Vichi et al., 2007b), MOHID assumes that light extinction in-depth follows the decay given by Lambert-Beer's law, which considers that shortwave radiation decays exponentially with depth according to the attenuation coefficient, eq.3.22, (Zhang et al., 2018).

$$I(z) = I_0 . e^{-k_d . z} \qquad \text{eq. 3.22}$$

where:

I(z)- is the available radiation at depth (z);

I_0- is the incident radiation at the sea surface (Wm^{-2});

k_d- the light extinction coefficient (m^{-1});

z- the depth.

The photosynthetic rate ($\Psi\ (L)_P$) increases with the light intensity until a maximum photosynthetic rate (in d^1) is reached (at optimal shortwave radiation S_{opt}). For values higher than S_{opt}, the photosynthetic rate decreases. The photosynthetic response to the light is given by Steele's formula:

$$\Psi\ (L)_P\ = \frac{I(z)}{I_{opt}}.e^{\left[1-\frac{I(z)}{I_{opt}}\right]} \qquad \text{eq. 3.23}$$

where:

I_z- the shortwave radiation (Wm^{-2}) at depth z (m);

I_{opt}- optimum shortwave radiation (Wm^{-2});

z – vertical position (depth) (m).

Light extinction coefficient, can be calculated using different methods (e.g. Parsons ocean formulation (Leitão et al., 2008)), however, satellite-based remote sensing is a more effective and rapid method for acquiring Kd over large areas than conventional measurement methods (Shen et al., 2017). The Kd value at the wavelength of 490 nm (Kd_490)) is one of the most commonly used standard water colour remote sensing products (Mouw et al., 2016; Sathyendranath et al., 2019; Tomlinson et al., 2019). For this application, Kd is obtained from an Ocean Color product, Aqua/MODIS Level-3 Binned Downwelling Diffuse Attenuation Coefficient Data Version 2018, available online at https://oceancolor.gsfc.nasa.gov/.[2] This product computes an algorithm using the empirical relationship derived from *in situ* measurements of Kd_490 and blue-to-green band ratios of remote sensing reflectances (Rrs), to calculate the light extinction coefficient (Kd) for downwelling irradiance at 490 nm (Kd_490) in m^{-1}, using the product provided by NASA (Losa et al., 2017). It is a daily product with 4km resolution.

Different PFTs have different responses to light. MOHID computes the different light limitation factors for the different PFT optimum light intensity (Figure 3.10) and shows the light limitation factor for small phytoplankton and diatoms' optimal light intensity used in MOHID (80W/m2 and 110W/m2 respectively).

---

[2] https://oceancolor.gsfc.nasa.gov/data/10.5067/AQUA/MODIS/L3B/KD/2018/.

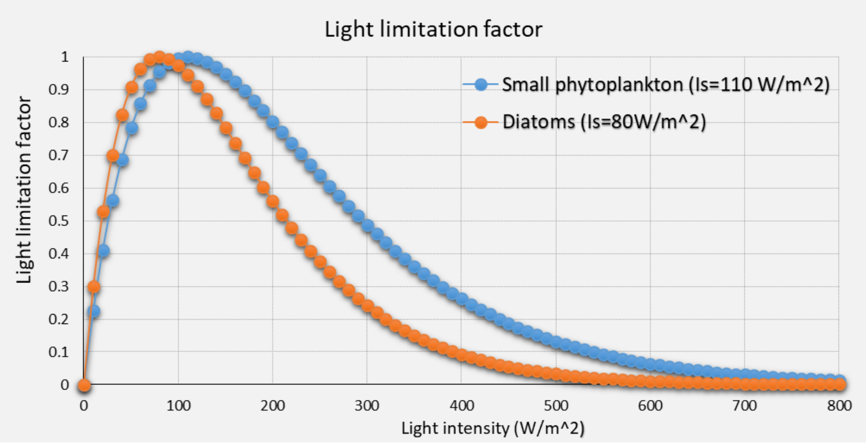

Figure 3.10- MOHID's Light limitation factor considering different optimum light intensities for photosynthesis (in blue for small phytoplankton and orange for diatoms (80 and 110 Wm^2 respectively)

Zooplankton top-down control

Zooplankton plays an important role in biological cycles and in the food web establishing a link between primary production and higher trophic levels (Lenz et al., 2000), and an essential role in recycling and exporting nutrients through the water column (Mitra et al., 2014). Zooplankton's grazing pressure over the phytoplankton is named top-down control. Where total phytoplankton biomass is controlled by the zooplankton grazing pressure (Hashioka et al., 2013).

In MOHID, zooplankton can feed differentially on several organisms (prey), having a preference for small phytoplankton or diatoms. The limitation factor for zooplankton *Grossgrowth rate* depends on its efficiency in the capture of small phytoplankton and diatoms, and the zooplankton's *Assimilation Coefficient* of Phyto and diatoms.

Zooplankton growth is limited by the total biomass of prey, the maximum ingestion rate ($Zoo_{IngestionMax}$), and by water temperature.

In this formulation, it is assumed that zooplankton will try to feed up to the maximum ingestion capacity, although it will give preference to each type of food (small phytoplankton, or diatoms), being both preference rates parameterized in the model. The capacity to graze is quantified using a Monod equation with a half-saturation constant (ZooHalfSat).

The zooplankton ingestion rate is given by:

$$Zoo_{Ingestion} = Zoo_{IngestionMax} * \frac{\sum_{i=1}^{NPreys} Food_i}{ZooHalfSat + \sum_{i=1}^{NPreys} Food_i} \qquad \text{eq. 3.24}$$

$Food_i$ is computed based on the preference of zooplankton for $Prey_i$ on the hunting efficiency of that prey and also on the minimum value of that prey (*ZooPreyMin*). This value is imposed in the model to guarantee that the prey is not extinguished.

$$Food_i = ZooPreferencePrey_i * ZooHuntingEfficiency_i (Prey_i - ZooPreyMin_i) \qquad \text{eq. } 3.25$$

Grazing is distributed among preys according to their contribution for $Zoo_{Ingestion}$. This contribution is accounted for by the contribution of $Food_i$for total ingestion:

$$PreyConsumption_i = Zoo_{Ingestion} * \frac{Food_i}{\sum_{i=1}^{NPreys} Food_i} \qquad \text{eq. } 3.26$$

Summing up all prey consumption gets:

$$\sum_{i=1}^{NPreys} PreyConsumption_i = Zoo_{Ingestion} \qquad \text{eq. } 3.27$$

Zooplankton can feed differently on several organisms (preys) (in this case by small phytoplankton and diatoms differently).

3.2.2. Model implementation

The biogeochemical model is coupled to the 3-D hydrodynamic model over the domain from 25-32 ^{0}W to 36-41^{0}N, with 6 km resolution (1/18^{0}). The physical model is a MOHID hydrodynamic model previously implemented and validated for this domain. The configurations, as well as the model validation, are described in detail in Chapter 2 of this dissertation. The model implementation is represented in Figure 3.11, and detailed in

Table 3.3. Model bathymetry was obtained from the EMODNET database, available online at www.emodnet, with a grid resolution of 1/16*1/16 arc-minutes (EMODnet Bathymetry Consortium, 2018).

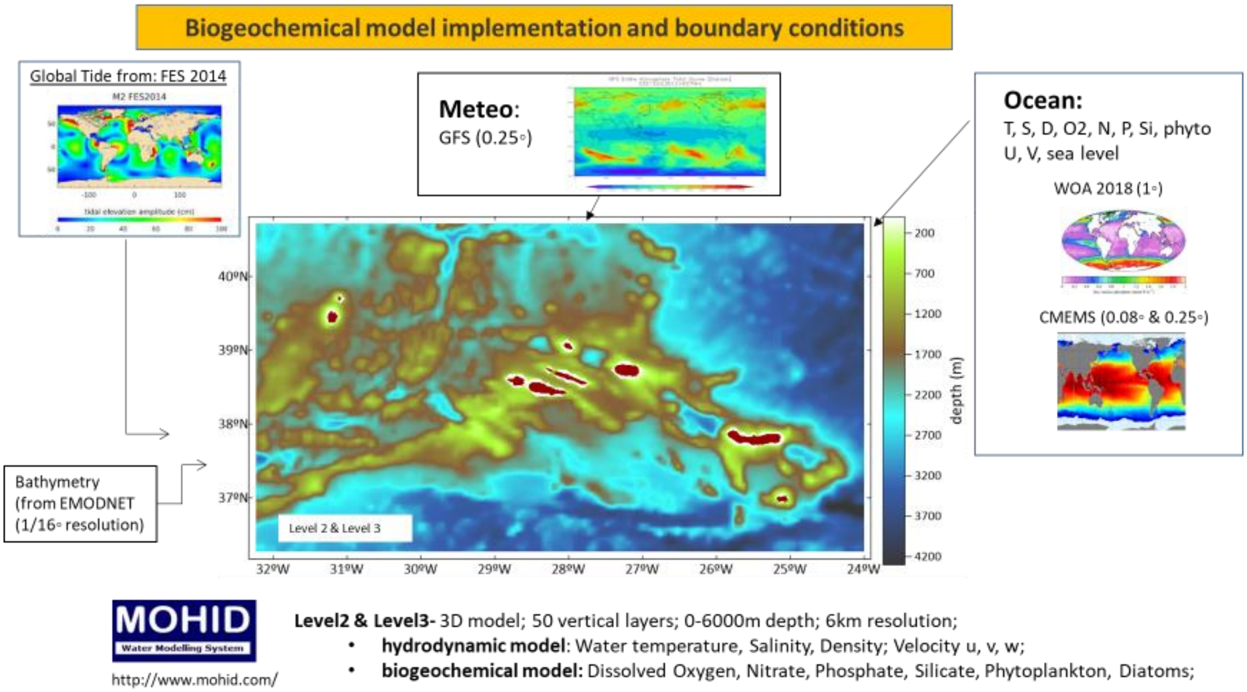

Figure 3.11- Schematic configuration and boundary conditions for the MOHID Water Quality model

3.2.2.1. Initial conditions and open boundary conditions

The biogeochemical model runs over a 3D hydrodynamic model solution described in Chapter 2. The tide is imposed using the FES2014 model (Lyard et al., 2021), and the biogeochemical properties are imposed at the open boundary using Mercator Global Ocean (PSY4V3R1) model results, with a 1/12^{0} resolution. Atmospheric boundary conditions are provided by the Global Forecast System model (GFS), with a 0.25^{0} resolution, provided by NOAA-

America National Ocean and Atmospheric Administration, available at https://www.ncdc.noaa.gov/.

Biogeochemical parameters were initialized using Operational Mercator Ocean Biogeochemical global ocean analysis and forecast systems with 0.25^{o} resolution model, a product provided by CMEMS, with 1/4 degree resolution (Julien, 2019). From now on referred to as CMEMS-Bio.

Table 3.3- Biogeochemical model configuration, major characteristics, boundary and initial conditions, model variables and output interval, simulation length

	Description
Model characterization	3D – Baroclinic
Domain	36.25^{o}N to 40.74^{o}N, and-23.9854^{o}W to -32.2628^{o}W
Bathymetry	EMODNET 1/16 arc-minuts [1]
Horizontal Resolution	6km
Vertical resolution	50 vertical layers: 7 sigma layers + 43 cartesian layers
Tide	From level 1(FES2014)[2]
Δt	120 seconds
Boundary conditions:	
Meteorological forcing	Global Forecast System model (GFS) 0.25^{o} resolution) [3]
Hydrodynamic conditions	MOHID solution
Initial conditions	N; P; Si; O2 from Operational Mercator Ocean biogeochemical global product with 0.25^{o}resolution[4]
	Phytoplankton and zooplankton constants along the domain;
Assimilation	No
Biogeochemical variables	N; P; Si; O2; Phytoplankton (small phytoplankton + diatoms); Zooplankton (see Table 3.1)
Physical variables	Velocity u, v, z; Salinity; temperature; Water level: from MOHID hydrodynamic model
Model output interval	3600 seconds
Simulation length	Jan/2017– Dec/2018

1) EMODnet Bathymetry Consortium, 2018; 2) Lyard et al., 2021; 3) National Centers for Environmental Prediction, National Weather Service, NOAA, 2015; 4) Julien, 2019;

For the biogeochemical parameters, initialization using World Ocean Atlas (WOA) climatology is frequently used in ocean model applications (e.g. PISCES (Kane et al., 2011); METB (Aumont et al., 2015); MEDUSA (Yool et al., 2013); FASHAM (Haney and Jackson, 1996)). WOA climatology is based on a collection of scientifically quality-controlled oceanographic *in situ* data (Garcia et al., 2018). Iit is a monthly climatology with 1 degree of horizontal resolution (Garcia et al., 2018), available online at https://www.ncei.noaa.gov/access/world-ocean-atlas-2018/. Another approach is to use model data instead of climatology data for model initialization

(Deutsch et al., 2021; IOC-UNESCO, 2022). In this case, is used a global model, provided by Copernicus Marine Service: Global Ocean Biogeochemistry Analysis and Forecast model (product ID- GLOBAL_ANALYSIS_FORECAST_BIO_001_028). This is a daily product, regularly calibrated and validated (Perruche C et al., 2016). Nutrients (N, P, Si) and oxygen are initialized using this product from now on named as CMEMS_Bio, in this thesis. Both data sources have a variable vertical resolution: until 150 meters' depth resolution goes up to 25 meters; from 150m until 1000m, up to 100 meters per depth layer; above 1000 meters depth until the bottom layers, resolution decreases, with each layer with more than 300 meters in length. Table 3.4 summarises the different initialization data sources used in this work, with examples of other models or applications using the same methodology.

Table 3.4- Initial conditions used in MOHID, and other models applications, for the biogeochemical parameters.

Parameter	Initial conditions in MOHID	Initial conditions in other model applications
Oxygen	Operational Mercator Ocean Biogeochemical global ocean analysis and forecast systems (0.25°resolution) [1]	WOA (1°resolution)[2] (used in: a), b), c), d), f)
Dissolved silica		
Inorganic phosphorus		
Nitrate		
Phytoplankton	Fixed value [3]	SeaWiFS monthly climatology[8] (used in f); *In situ* data; analytical results
Diatoms	Fixed value from ocean colour data from Copernicus [4]	n/d
Zooplankton	Fixed value [5]	n/d

1 - CMEMS model results (Julien, 2019); 2- WOA2018 monthly climatology (Garcia et al., 2018); 3- Botelho, 2014; 4-Xi et al., 2020a; 5- Carmo et al., 2013b; (a)- PISCES(Kane et al., 2011); (a)-METB(Aumont et al., 2015); (c)-MEDUSA(Yool et al., 2013); (d)-FASHAM(Haney and Jackson, 1996); (e)- FENNEL(Rocha et al., 2019); *n/d - not used in the model, or not defined)

After initialization, the model runs in continuous mode, assuming a null gradient boundary condition, where the value of a variable is equal to the value at an adjacent interior point, using the results of the previous run as the boundary condition for the next run.

Simulation length and frequency

The simulation starts in January 2017, and the model was run for two years. The calibration and validation process was performed only after February 2017 (giving 4 weeks of initialization period). After the initialization, the model was run in a continuous mode, without assimilation, with a time step of 120 seconds, and hourly model outputs.

3.2.2.2. Model parameterization

The parameterization process is always necessary when applying a model to a new domain, and is commonly performed by tuning the model within the range of literature parameter values, and by comparing the model results with *in situ* data, or other data sources available, until finding the best fit between computed results and observed data (Arhonditsis et al., 2006). MOHID Water Quality parameterization was based on MOHID default values and adapted considering other biogeochemical model applications and different case studies. Different model applications used on global and regional scales were considered: PISCES (Aumont, 2005), ERSEM (Edwards et al., 2012), Biofenel (Rocha et al., 2019), NEMURO (Mattern et al., 2017; Yamanaka et al., 2004), PlankTOM5 (Buitenhuis et al., 2010) and CCSM-BEC (Moore et al., 2001). Also, other multidisciplinary and inter-comparison studies were used in this parametrization (Gnanadesikan et al., 2011; Hashioka et al., 2013; Litchman et al., 2007), as well as different studies in the Azores region (Barcelos e Ramos et al., 2017; Macedo et al., 2000; Valente, 2013). Some of the main characteristics of these models are summarized in Table 3.5.

Because different biogeochemical models consider different methodologies and limitation factors, different importances to top-down or bottom-up processes, and different PFT, the parametrization is not a linear process. Also, for the same model different parametrizations can be found considering different case studies, domains, or environmental conditions (Aumont et al., 2015; Hashioka et al., 2013). The big aim of this parametrization process was to achieve satisfactory results, able to simulate the known typical dynamics in the Azores.

Table 3.5- General characteristics of MOHID and other biogeochemical models, considering the biogeochemical cycles, NPZD components, phytoplankton functional types (PFT), and nutrient ratios.

Model	Biogeochemical cycles	Autotrophic PFT	Heterotrophic PFT	Detritus	C:N ratio	C : N : P	Chl:C
MOHID 1)	N, P, Si, O_2	Phytoplankton (small phytoplankton); Diatoms	Zooplankton (with different PFT preferences)	Yes	Fixed	106:16:1	Fixed
PISCES 2)	N, Si, PO_2, Fe, Ca	Nanophytoplankton, Diatoms	Micro & mesozooplankton	Yes	Fixed	172:122:16:1	Fixed/variable
NPZDmodel 3)	N, P	Nanophytoplankton	Zooplankton	Yes	variable	106:16	Variable
MEDUSA 4)	N, P, Si, Fe, $CaCO_3$, C	Phytoplankton (all excluding diatoms); Diatoms	Micro & mesozooplankton	Yes	Fixed	106:16:1	variable
HAMOOC 5)	N, P, Fe	Phytoplankton	Zooplankton	Yes	Fixed	122:16:1	Fixed
HadOCC 6)	N, P, Si, O_2, C	Phytoplankton	Zooplankton	Yes	Fixed	106:16:1	Fixed

1)-(Instituto Superior Técnico, 2003); 2)- (Aumont, 2005); 3)(Peña et al., 2016); 4)(Yool et al., 2013); 5) (Ilyina et al., 2013); 6)-(Palmer and Totterdell, 2001)

3.2.2.3. Model calibration and validation

In general, for biogeochemical model applications, the most common approach for model calibration and validation for phytoplankton (or chlorophyll_a) is based on contrasting model outputs with satellite-derived surface chlorophyll (Silva et al., 2013). Several model applications follow a similar approach for model assessment, using remote sensing data (Anugerahanti et al., 2021; Capotondi et al., 2019; Costa et al., 2012; Espinoza-Morriberon et al., 2016; Lacroix et al., 2007; Perruche C et al., 2016), or WOA climatology (Espinoza-Morriberon et al., 2016) for model validation.

The model was initialized in January 2017, calibration tests were performed for the years 2017 and 2018. The model calibration effectiveness is reflected in model results and evaluated by model validation.

Ideally, model results should be calibrated mostly with *in situ* data, however, regarding the water column in the ocean, these data are scarce (Table 3.6). The most frequent data available is from Argo buoys (with temperature and salinity) and remote sensing data (for sea surface temperature and chlorophyll). Biogeochemical Argo buoys are a potential source of *in situ* data, providing profiles of biogeochemical parameters along with the space, depth and time, being used for model assessment in the Atlantic (Roemmich et al., 2019), however, the absence of this type of data for the Azores study area and period does not allow this type of data for model validation. The number of profiles available for the Azores region (data accessed and updated in May 2022) was less than 20 profiles from 2011 to 2022, and only with Oxygen data, and no nutrients (more information in Table 3.6). The other *in situ* data available consist mainly of fixed points, from discrete and short-duration sampling from different projects, also intense sampling programs were developed in the Azores, but for specific locations, such as the Condor Seamount (Carmo et al., 2013b; Giacomello and Menezes, 2012), Terceira island (Barcelos e Ramos et al., 2017; Narciso et al., 2016). *In situ* data is available from ocean transects and cruises (detailed in Table 3.6), nonetheless, these data represent also discrete points, useful for an ocean scale analysis, but not representative of the Azores region.

Table 3.6- Biogeochemical *in situ* data available for the Azores region

Source Type/name	Parameter	EOV name	reference	Year	nº of datasets	Depth/ profiles/ resolution
Condor and other Seamounth projects	Phytoplankton	Phytoplankton biomass and diversity	b	2009/2010;	7 stations	5, 25, 50, 75, 100 and 150 m
	Chlorophyll	n/a	b, m	2004; 2009/2010;	>20 stations	
	Nitrate	Nutrients	b	2009/2010	7 stations	
	Phosphate	Nutrients	b	2009/2010	7 stations	
	Dissolved silica	Nutrients	b	2009/2010	7 stations	
	Dissolved Oxygen	Oxygen	b, m	2004; 2009/2010;	7 stations	profile
	Carbon	Inorganic Carbon	m	2004	7 stations	
	Conductivity (CTD)	Subsurface Salinity	b, m	2004; 2009/2010;	7 stations	
	Temperature (CTD)	Subsurface temperature	b, m	2004; 2009/2010;	7 stations	
	Chlorophyll		b	2009/2010	7 stations	
	Zooplankton	Zooplankton biomass and diversity	b	2009/2010	4 stations	-
	Primary production		m	2004; 2009/2010;	7 stations	-
Ocean Transects; Atlantic cruises; site-specific projects	Mesozooplankton biomass	Zooplankton biomass and diversity	b, c, d, e, f, g, h, i, j	1976/2011	>20 datasets	-
	Nitrate	Nutrients	k, n, q, s	1980, 1993, 1996, 1997, 2003,2011, 2012	< 20 datasets	profile
	Dissolved silica	Nutrients	p	1980,1993, 1996, 1997		profile
	Phosphate	Nutrients	o, q, s	1956, 1980,1993, 1996, 1997, 2011		profile
	Carbon	Inorganic Carbon	k, l, n	1980,1993, 1996, 1997, 2003, and 2012		profile
	phytoplankton	Phytoplankton biomass and diversity		1993, 1996, 1997		profile
	chlorophyll		k, l, n	1993, 1996, 1997, 2003, 2012		profile
	Oxygen	Oxygen	o, q, s, t	1980,1993, 1996, 1997, 2011		profile
	Conductivity (CTD)	Subsurface Salinity	o, q, s, t	1980,1993, 1996, 1997, 2011		profile
	Temperature (CTD)	Subsurface Temperature	o, q, s, t	1980,1993, 1996, 1997, 2011		profile
BiogeoArgoBuoys	Oxygen	Oxygen	u	2011;2012;2013;2014;2016; 2017;2018	<20[1]	profile
	Conductivity (CTD)	Subsurface Salinity		2012;2013;2014;2016	>20	profile
	Temperature (CTD)	Subsurface Temperature		2012;2013;2014;2016	>20	profile
Remote sense data	Temperature	Surface Temperature	v	continuous	n	4 Kilometers
	phytoplankton	Phytoplankton biomass and diversity	v	continuous	n	
EMSO Azores	Several	Nutrients, Oxygen, Salinity, Temperature	w	Continuous (2016-2021)	n	Surface, bottom
Glider	Conductivity (CTD)	Subsurface Salinity			1	profile
	Temperature (CTD)	Subsurface Temperature		2019	1	profile

a-Boyer, Tim P. et al (2018); b- Carmo et al. (2013);c-Dias et al. (1976); d-Sobral et al. (1985);e-Muzavor (1981);f-Roden, (1987); g-Silva (2000);h-Sobrinho-Gonçalves and Isidro (2001); i-Sobrinho-Gonçalves and Cardigos (2006); j-Santos (2011); k- Christiansen, Bernd, (2015); l-Head, Robert (2013); m- Irwin, Brian (2013);n- Becker, S et al. (2020); o- Vidal, Montserrat, (2016); p- Lochte, Karin; Helder, Wim (2004); q- Swift, James (2006); r- Kähler, Paul; Koeve, Wolfgang (2008); s- IFREMER (2001) ; t- Arhan, Michel (2010); u- https://biogeochemical-argo.org/ ; v- https://oceancolor.gsfc.nasa.gov/ ; w- @IFREMER; [1]- Accessed on May 2022

Besides these data, a deep-sea ocean observatory from the EMSO project (European Multidisciplinary Seafloor and water column Observatory (EMSO) provides a long-term fixed data time-series at the deep-sea floor, in the Lucky Strike hydrothermal vent, however, outside the model domain. Also, recent scientific cruises organized by the University of the Azores, and multidisciplinary campaigns, provide new and valuable data, however, these data are limited temporal and spatially. These validation limitations are common in oceanographic and regional models, and to surpass them some models use climatology data like WOA climatology (Espinoza-Morriberon et al., 2016; Gutknecht et al., 2016) for the assessment of model results along the water column (Salon et al., 2019). This is the case in the Azores region, where *in situ* biogeochemical measurements available are scarce, and not able to characterize seasonal patterns or the water column variations in the entire region of study.

3.2.3. Data available for model calibration and validation

Considering the scarcity of *in situ* data for the study area, model calibration and validation were performed using: remote sensing data (weekly based), WOA climatologic data (Garcia et al., 2018), and CMEMS model results (Perruche C et al., 2016).

Remote sensing data- For the surface layers, remote sensing data was used for phytoplankton model assessment. A Global chlorophyll-a data product, OceanColor-CCI-Merged v5.0, developed by ESA Ocean Colour Climate Change Initiative (Ocean_Colour_cci) was used (Sathyendranath et al., 2021). This product provides chlorophyll_a results, on a weekly based, and is available online at https://oceancolor.gsfc.nasa.gov/l3/. Chlorophyll (Chl), is widely taken as a proxy for phytoplankton biomass, due to its distinctive optical properties (Anugerahanti et al., 2021 Werdell and Bailey, 2005;) considering different phytoplankton functional types (including diatoms) (Xi et al., 2020b). Remote sensing data is interpolated on the model spatial resolution.

WOA2014 Climatology- WOA monthly climatology, based on a collection of scientifically quality-controlled oceanographic *in situ* data (Garcia et al., 2018), with a 1-degree resolution, and a variable resolution along the water column for the nitrate, phosphate, dissolved silica and Dissolved Oxygen.

CMEMS_Bio- Operational Mercator Ocean Biogeochemical global ocean analysis and forecast systems (DOI: 10.48670/moi-00015), with 0.25 degrees resolution, and a variable resolution along the water column for the parameters: nitrate, phosphate, dissolved silica, dissolved oxygen, phytoplankton and chlorophyll.

3.2.4. Model parameterization

MOHID general parameterization is based mainly on an EPA Surface Water Quality model review (Bowie et al., 1985). A good performance of biogeochemical models, for specific case studies and simulation times implies reasonable parameterizations of the different processes (including top-down, and bottom-up effects) (Fennel et al., 2011). General parameters used in MOHID and other biogeochemical models are resumed in the following tables. Tables also include values used in other works and *in situ* studies.

Phytoplankton growth parameterization

Phytoplankton growth is limited by nutrient availability, light and temperature (Eq.2.12). There is a wide range of estimated phytoplankton growth rates in oligotrophic regions, from 0.1 to more than 1d-1 (Marañón et al., 2003; Ward et al., 2013) (see Table 3.11). This variability can arise from the spatiotemporal heterogeneity of phytoplankton dynamics in oligotrophic regions, but also from the lack of agreement between measurement methods (Cáceres et al., 2013).

To parameterize the phytoplankton growth, besides the growth rates, also the limitation factors, and the top-down control (zooplankton grazing) are calibrated. Besides the uncertainty around phytoplankton growth rate, the parametrization of the half-saturation constants is rather difficult as observations show that they can vary by several orders of magnitudes, and the different models' parameterizations and studies in the literature reveal different values, as listed in Table 3.10 and Table 3.11 These dissimilarities result from the intrinsic characteristics of each case study, regarding case-study locations, model resolution, time scales, and specific phytoplankton dynamics (e.g. oligotrophic or high productivity regions), but can be related to different model configurations (Hashioka et al., 2013). In the model parametrization process, the first step was to balance the phytoplankton and nutrient concentrations, through the growth rate and limitation factors.

Table 3.7- Model parameters for small phytoplankton with their default values in MOHID

Parameter	Description	Units	MOHID
PHYGROWMAXF	Phytoplankton Maximum gross growth rate	d^{-1}	1.2 (1-2)
PHYNSATCONS	Nitrogen half-saturation constant for phytoplankton	mgN/L	0.014(0.07-0.014)
PHYSATCONS	Phosphorus half-saturation constant for phytoplankton	mgP/l	0.001
PHYPHOTOIN	Optimum light intensity for phytoplankton photosynthesis	W m-2	80 (120)
PHYFENDREPC	Endogenous respiration constant for phytoplankton	d^{-1}	0.0175
PHOTORES	Fraction of actual photosynthesis oxidized by photorespiration for phytoplankton	n/a	0.125
EXCRCONS	Excretion Constant for phytoplankton	n/a	0.07
FMORTMAX	Maximum Mortality Rate for phytoplankton	d^{-1}	0.02
FMORTCON	Mortality half-saturation rate for phytoplankton	mgC/d	0.3
ASS_EFIC	Assimilation efficiency of the phytoplankton by zooplankton	n/a	0.8
PHOTOIN	Optimum light intensity for phytoplankton photosynthesis	W m-2	110 (120)
TOPTFMIN	Minimum temperature of the optimal interval for phytoplankton photosynthesis	ºC	16.5
TOPTFMAX	Maximum temperature of the optimal interval for phytoplankton photosynthesis	ºC	26.5
TFMIN	Minimum tolerable temperature for phytoplankton photosynthesis	ºC	4
TFMAX	Maximum tolerable temperature for phytoplankton photosynthesis	ºC	37
FRATIONC	Phytoplankton Nitrogen/Carbon Ratio	mgN/mgC	0.18
FRATIOPC	Phytoplankton Phosphorus/Carbon Ratio	mgP/mgC	0.024
FSOLEXCR	Fraction of soluble inorganic material excreted by phytoplankton	n/a	0.4
FDISSDON	Fraction of dissolved organic material excreted by phytoplankton	n/a	0.5

Table 3.8- Model parameters for diatoms with their default values MOHID

Parameter	Description	Units	MOHID
DIGROWMAXF	Diatoms Maximum gross growth rate	d^{-1}	1.2 (2)
DINSATCONS	Nitrogen half-saturation constant for diatoms	mgN/L	0.042
DIPSATCONS	Phosphorus half-saturation constant for diatoms	mgP/l	0.002
DISISATCONS	Silica half-saturation constant for diatoms	mgSi/l	0.028
DIFENDREPC	Endogenous respiration constant for diatoms	n/a	0.0175
DIPHOTORES	Fraction of actual photosynthesis which is oxidized by photorespiration for diatoms	n/a	0.0125
DIEXCRCONS	Excretion constant for diatoms	n/a	0.018
DIFMORTMAX	Maximum mortality Rate for diatoms	d^{-1}	0.08
DIFMORTCON	Mortality half-saturation rate for diatoms	mgC/d	0.3
DIASS_EFIC	Assimilation efficiency of the diatoms by zooplankton	n/a	0.8
DIPHOTOIN	Optimum light intensity for diatoms photosynthesis	W/m2	110
DITOPTFMIN	Minimum temperature of the optimal interval for diatoms photosynthesis	ºC	15
DITOPTFMAX	Maximum temperature of the optimal interval for diatoms photosynthesis	ºC	26.5
DITFMIN	Minimum tolerable temperature for diatoms photosynthesis	ºC	4
DITFMAX	Maximum tolerable temperature for diatoms photosynthesis	ºC	37

Table 3.9- Main biogeochemical model parameters for zooplankton with default values used in MOHID, calibrated values (), and values from other models and bibliography

Parameter	Description	Units	MOHID	Pisces$_a$ *	ROMS$_b$ *
INGCONSZ	Half-Saturation Constant for Grazing	mgC/l	0.2	0.24	nd
ZOOEFFCAPHY	Capture Efficiency of phytoplankton by zooplankton	n/a	0.8	nd	nd
DIZOOEFFCAP	Capture efficiency of diatoms by zooplankton	n/a	0.8	nd	0.5-23
ZINGMAX	Zooplankton maximum ingestion rate	d^{-1}	2	nd	n/a
ZOPHYASS	Assimilation Coefficient of Phyto by Zooplankton	n/a	0.8	0.7	0.75
DIZOASS	Assimilation Coefficient of Diatoms by zooplankton	n/a	0.8	0.7	0.75
PHYRATING	Proportion of phytoplankton in zooplankton ingestion	n/a	0.5	1	nd
DIRATINGZOO	Proportion of Diatoms in mesozooplankton ingestion	n/a	0.5	0.5 (1)	nd
TOPTZMIN	Minimum temperature of the optimal interval for zooplankton growth	ºC	15	nd	nd
TOPTZMAX	Maximum temperature of the optimal interval for zooplankton growth	ºC	26.5	nd	nd
TZMIN	Minimum tolerable temperature for zooplankton growth	ºC	4	nd	nd
TZMAX	Maximum tolerable temperature for zooplankton growth	ºC	37	nd	nd

*- PISCES and ROMS consider Phytoplankton and Diatoms together; a)PISCES (Aumont et al., 2015); b)ROMS (Rocha et al., 2019); *n/a not applied; *nd - not used int he model, or no information available)

Table 3.10- Main biogeochemical model parameters for small phytoplankton (Phy) growth and nutrient limitation constants used in MOHID, and other models and case studies

Model or case study, domain and range in the literature												
Model/case study	MOHID	Pisces ^{a,b}	ROMS ^{c}	FENNEL^{d}	Plank-TOM ^{e}	Medusa ^{f}	Ward, et al ^{g}	Chai et al., ^{h}	Nemuro ^{i}	Macedo et al^{j}	Maranon et al ^{k}	HAMOCC 5 ^{l}
Domain/location	Azores	Global	global	North Atlantic	global	global	North Atlantic	Equatorial Pacific	North Pacific	Azores front Spring bloom	North Atlantic	global
Phytoplankton Maximum gross growth rate (d^{-1})	1.2	0.66 (0.6)*	0.69	0.69 (0.65-3)	0.4 (0.6)	0.53	0.1-1	2	0.8	0.1-0.85	0.1-1.3	0.6
Nitrogen half-saturation constant (mgN/l)	0.014	3.6E^{-3} 3.6E^{-3}- 0.024)*	0.014 (0-0.021)	0.014	nd	0.015	0.028-0.042	0.007	0.014	0-0.028	nd	0.002
Phosphorus half-saturation constant (mgP/l)	0.001	0.012 (0.012-0.074)*	nd	nd	2.4	nd	nd	nd	nd	nd	nd	0.0003

*- PISCES and ROMS consider Phytoplankton and Diatoms together; a)PISCES (Aumont et al., 2015); b)PISCES (Hashioka et al., 2013); c)ROMS (Rocha et al., 2019); d)(Fennel, 2009); e)-PLANKTOM(Hashioka et al., 2013);f)-MEDUSA model (Yool et al., 2013); g)- (Ward et al., 2010); h) (Chai et al., 2002); i)-NEMURO (Yamanaka et al., 2004); j)- (Macedo et al., 2000); k)- (Marañón, 2005); l)-HAMMOCC5- (Ilyina et al., 2013); *nd - not used in the model, or no information available)

Table 3.11- Main biogeochemical model parameters for diatoms growth and nutrient limitation constants used in MOHID, and other models and case studies

Model or Case Study, domain and range in the literature									
Model/case study	MOHID	Pisces [a,b]	ROMS [c]	Plank-TOM [e]	Medusa [f]	Ward, et al [g]	Chai et al., [h]	Nemuro [i]	HAMOCC5 [l]
Domain/location	Azores	global	global	global	global	North Atlantic	Equatorial Pacific	North Pacific	global
Diatoms Maximum gross growth rate (d-^{1})	1.2	0.66	nd	0.6	0.5	1-2	3	0.4	0.851
Nitrogen half-saturation constant for diatoms (mgN/l)	0.015	3.6E-3 (3.6E-3- 0.024)	0.5	nd	0.01	0-0.028	0.014	0.042	nd
Phosphorus half-saturation constant for diatoms (mgP/l)	0.002	0.012 (0.012-0.074)	0.01	nd	0.084	nd	nd	nd	0.003
Silica half-saturation constant for diatoms (mgSi/l)	0.084	nd	nd	0.1	0.084	nd	0.084	0.17	0.225

*- PISCES and ROMS consider Phytoplankton and Diatoms together; a)PISCES (Aumont et al., 2015); b)PISCES (Hashioka et al., 2013); c)ROMS (Rocha et al., 2019); d)(Fennel, 2009); e)-PLANKTOM(Hashioka et al., 2013);f)-MEDUSA model (Yool et al., 2013); g)- (Ward et al., 2010); h) (Chai et al., 2002); i)-NEMURO (Yamanaka et al., 2004); j)- (Macedo et al., 2000); k)- (Marañón, 2005); l)-HAMMOCC5- (Ilyina et al., 2013); *nd - not used in the model, or no information available

Nutrient limitations parameterization

Phytoplankton nutrient uptake rate follows the Monod approach, using a hyperbolic relationship of the form N/(K_S + N), where K is the half-saturation constant. During the model calibration process, while calibrating the phytoplankton growth, when the concentration of the nutrient was too low, it was necessary to increase the half-saturation constant to have the minimum phytoplankton growth rate to maintain the population. However, this Ks increase diminishes the nutrient limitation, inducing a higher phytoplankton growth rate that could achieve overstated nutrient assimilation rates, resulting in a too-fast (and possibly not real) nutrient assimilation. A modified Monod's formulation (Eq.3.28) was considered, using a modified half-saturation constant, dependent on nutrient concentration (Eq.3.29) (Sharada et al., 2005).

$$modifiedgrowth = \frac{[NO3]}{[NO3] + Ksmodified} \qquad \text{Eq. 3.28}$$

$$Ksmodifeid = \sqrt{\frac{[NO3]}{KsRef}} * KsRef \qquad \text{Eq. 3.29}$$

With this modified nutrient uptake, the phytoplankton was able to increase the uptake rate with lower nutrient concentrations but reduce it with high concentrations. In this way, the nutrient uptake is not so efficient with higher nutrient concentrations (Figure 3.12).

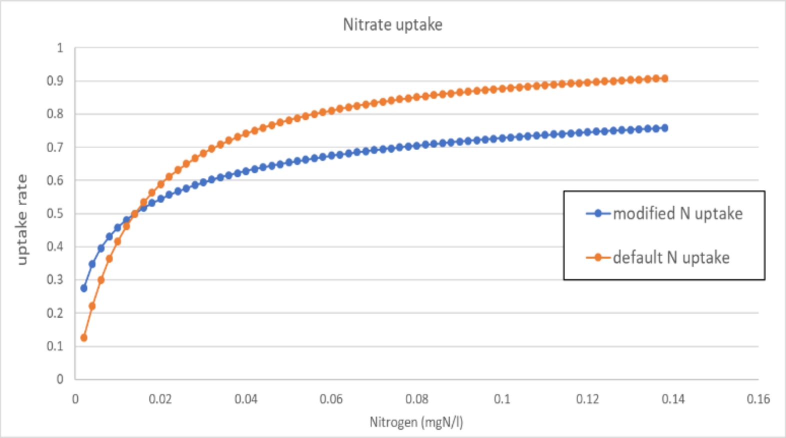

Figure 3.12- Modified and Default nutrients uptake considering the reference Monod formulation (in orange), and the modified formulation (in blue).

This modified nutrient limitation factor, induces a decrease in nutrient uptake, diminishing the extreme nutrient uptake, producing a balanced solution between phytoplankton growth rate and nutrient availability, avoiding unreal nutrient depletion.

Zooplankton top-down control calibration

Zooplankton, by grazing, can control the phytoplankton concentration. This top-down control can control the size of the phytoplankton blooms that occur in oligotrophic regions (Cáceres et al., 2013). Moreover, the parameterization of zooplankton can also help to control the small phytoplankton *versus* diatoms dynamics. In MOHID, these parameterizations are performed by balancing the zooplankton maximum ingestion rate (*Zingmax*), and by changing the zooplankton preference for small phytoplankton (*Phyrating)* or diatoms (*Dirating*) (Table 3.12).

Table 3.12- Zooplankton parametrization differences between simulation *MOHID* and *MOHID _zoo*

Parameter	Parameter description	units	MOHID	MOHID _zoo
Zingmax	Zooplankton maximum ingestion rate	d^{-1}	2	2.5
Phyrating	Proportion of Phytoplankton in zooplankton ingestion	--	0.5	0.7
Dirating	Proportion Diatoms in zooplankton ingestion	--	0.5	0.3

Results of this parametrization tests, represented on the graph in Figure 3.13, show the effect of different parameterization of zooplankton grazing rates on phytoplankton dynamics, revealing how it can control the phytoplankton concentration, limiting the phytoplankton bloom.

With parametrization “*MOHID_zoo*”, in pink, zooplankton has a higher grazing rate, (2,5d^{-1}, contrasting with 2d^{-1} from “*MOHID*”) controlling the phytoplankton concentration by the higher ingestion rate, resulting in a lower small phytoplankton concentration during the entire simulation, comparing with “*MOHID*”. Furthermore, “*MOHID _zoo*” has a preference for small Phytoplankton rather than Diatoms, which, in this case, allows diatoms to grow. As can be seen in Figure 3.13, diatoms concentration is higher in simulation “*MOHID _zoo*” than in the other one. These results show how zooplankton grazing can control the phytoplankton bloom (top-down control (Hashioka et al., 2013)).

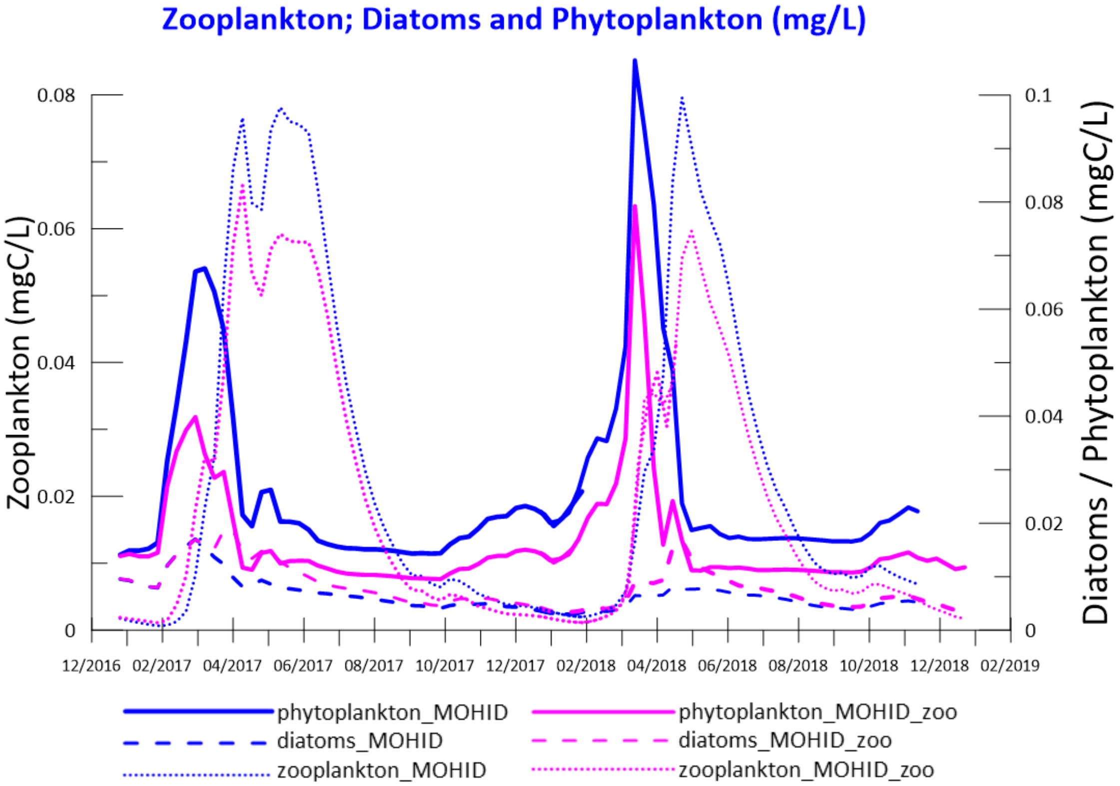

Figure 3.13-Surface weekly average results phytoplankton, diatoms and zooplankton concentration (in mgC/l), from Mohid model simulation “Mohid_v3” in blue; “Mohid_v3_zoo” in pink; All results are weekly averaged, for the entire domain at the surface, represented in mgC/l for 2017 and 2018.

Phytoplankton and zooplankton concentrations along the year reveal the importance of the *Zoopreymin* parameter, which establishes a minimum prey concentration (small phytoplankton + diatoms) for zooplankton grazing, to guarantee that prey is not extinguished.

3.2.5. Model validation and assessment

Model validation was performed at the surface and along the water column, comparing MOHID results against the CMEMS-bio model and WOA climatology, for nitrate, phosphate, dissolved silica and dissolved oxygen. At surface model was also validated for phytoplankton, comparing model results against remote sensing data. Along the water column, fixed points distributed along with the model domain were selected for model validation (Figure 3.13). These points are distributed evenly along the domain, along the longitude: 3 points in the North of the domain, 3 in the centre and 3 in the South. Also a point in a seamount, namely Condor seamount. Also, a meridional and zonal section was created for model results analysis. In these sections, 3-D results are reduced into the x and y dimensions' map by taking a section in a zonal dimensional, and meridional dimension, representing on the YY axis the depth, and along with the XX axis the Longitude, or the Latitude. The selected sections cross the domain at the Pico island in the Central Group (CG) (Figure 3.14- Schematic representation of validation points and domain sections.): Meridional section at: -28.5 ° W; and Zonal section at: 38.5°N.

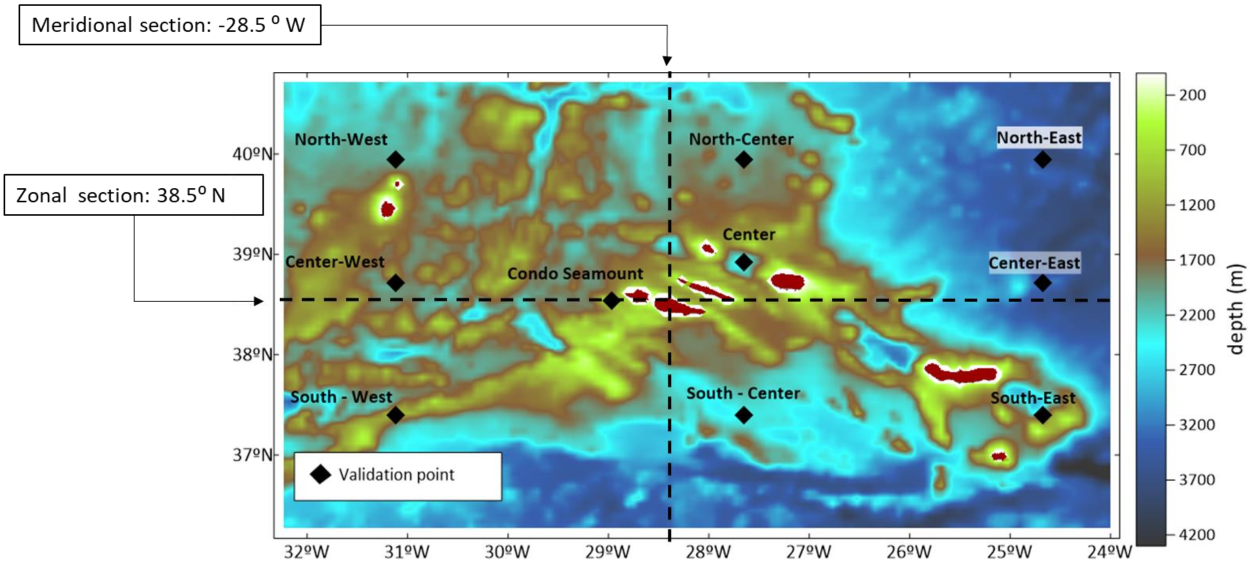

Figure 3.14- Schematic representation of validation points and domain sections.

Phytoplankton validation

Model validation was performed using the product OceanColor-CCI-Merged v5.0, L3, Global product (Sathyendranath et al., 2021). This remote sensing product provides a mass concentration of chlorophyll_a for the surface layer, considering a daily attenuation coefficient of downwelling radiative flux in seawater (kd_{490}). The same *kd* product, developed by NASA's

Ocean Biology Processing Group (OBPG), and available at the SeaWiFS Bio-optical Archive and Storage System (SeaBASS)[3] is used by MOHID. A constant carbon to chlorophyll_a conversion ratio of 0.0125 mgC/l is used (based on other applications for the study area (Fasham et al., 1985; Macedo et al., 2000) as well as global applications (Arteaga et al., 2016; Taylorl et al., 1997) summarized in Table 3.2.

Model skill evaluation was performed by comparing model results with remote sensing data in two ways: First, by comparing the entire model domain average, to evaluate the temporal evolution of model performance; Secondly, by comparing each grid data point to evaluate the model performance spatially. The validation was done on a weekly basis, as this is the frequency of satellite data.

Nutrients and dissolved oxygen validation

Model results of nitrate, inorganic phosphorous, dissolved silica, and dissolved oxygen, were compared with WOA climatology and CMEMS-bio model, for 2017 and 2018. At the surface, the model was validated considering averages of the entire domain. While along the water column time series of fixed locations were used (Figure 3.13). Validation was performed by comparing model results at each layer depth, using the vertical resolution of WOA and CMEMS respectively.

3.2.6. Statistical methods and skill assessment

Different methodologies and statistical indexes are used in 3-D oceanographic models (Stow et al., 2009). The conventional model assessment can be higher subjective (with a side-by-side approach), or can rely on statistical methods. In the present study model assessment was performed using: the root mean square error (RMSE), bias, and Pearson correlation coefficient (r) (Gómez-Zambrano et al., 2017), and Taylor diagrams, (Allen and Somerfield, 2009).

In the “side by side” approach, spatial maps for several parameters are compared with data spatial maps. This approach is frequently used in 3D oceanographic models, enabling assessing model capability to represent the major seasonal and geographical features, based on visually-oriented qualitative statements (Stow et al., 2009).

---

[3] - https://oceancolor.gsfc.nasa.gov/atbd/kd_490/

3.3. Model validation results

3.3.1. Model validation at the surface

Phytoplankton

To estimate the reliability of the model, surface phytoplankton results were compared against remote sensing data. Model results simulate a realistic temporal evolution of phytoplankton concentration in the entire domain along the year, reproducing the seasonal phytoplankton dynamics (Figure 3.15). The model represents the typical spring bloom and the weak autumn phytoplankton bloom. The model overestimates the phytoplankton concentration, with a positive bias of 0.076 mgC/l for the entire validation period. Only during the winter, the model bias is negative or close to zero (Figure 3.16). Model overestimation is higher during the intense spring bloom, resulting in higher RMSE and bias values during March 2017 and March 2018.

The difference between model results and remote sensing data is lower near the islands and higher in the borders of the domain, with higher values in the northeast of the domain. In the vicinity of the islands, estimated phytoplankton results are lower than remote sensing data (negative bias in Figure 3.19).

The higher values of RMSE occur during the spring blooms, when the bias is higher, in March 2017 and March 2018 (Figure 3.16). The average correlation between the model and remote sensing data is 0.535 (Figure 3.20), with the lowest values occurring in the region away from the island and near the domain borders.

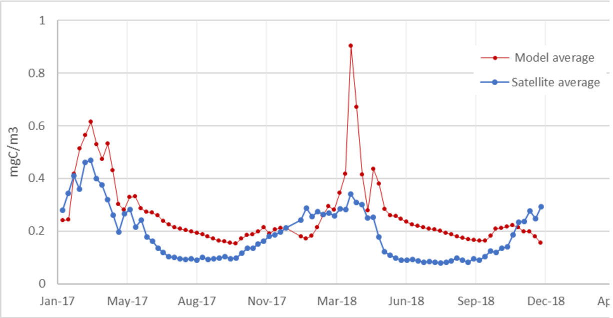

Figure 3.15- Weekly average for phytoplankton concentration at surface, for MOHID in red, and satellite (Chl_a converted to Phytoplankton) in blue, in mgC/l for the year 2017 and 2018

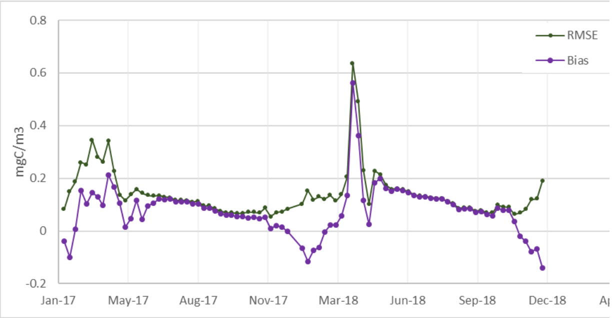

Figure 3.16-Temporal evolution of statistical results for bias and RMSE resulting from the statistical comparison between MOHID and Remote sense data in mgC/l for the year 2017 and 2018, on a weekly basis.

Table 3.13- Statistic results for the comparison between MOHID and remote sense data for phytoplankton in (mgC/l) considering model and data average, correlation coefficient (R), BIAS, and root mean square error (RMSE)

	Model Average (mgC/l)	**Data average (mgC/l)**	**Bias (mgC/l)**	**R**	**RMSE (mgC/l)**
2017	0.276	0.207	0.069	0.643	0.150
2018	0.258	0.175	0.083	0.43	0.173
2017-2018	0.267	0.191	0.076	0.535	0.163

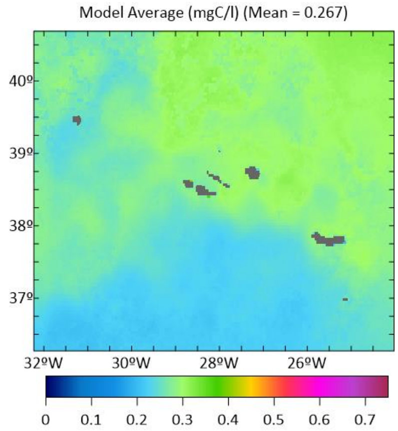

Figure 3.17- MOHID phytoplankton average for 2017-2018 (in mgC/l)

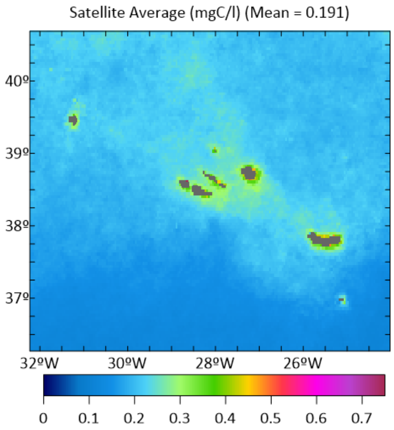

Figure 3.18- Satellite phytoplankton average concentration for 2017-2018 (in mgC/l) (converted from chl_a to C)

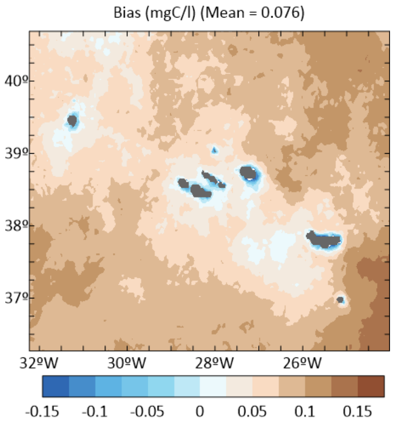

Figure 3.19- BIAS between remote sensing data and MOHID results for 2017-2018 (in mgC/l)

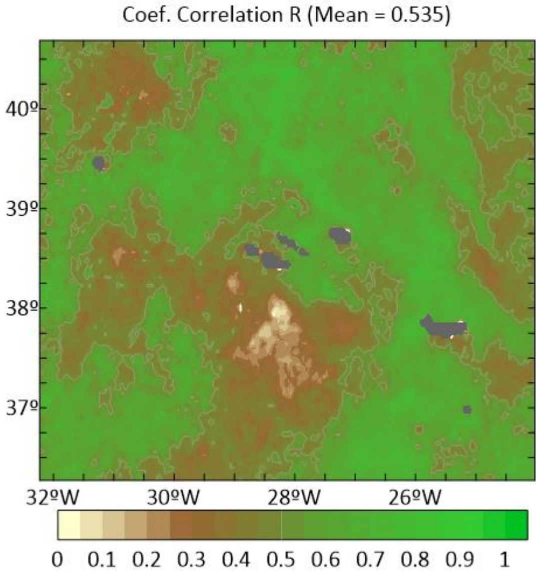

Figure 3.20- Map of the correlation coefficient between remote sensing data and model results, for 2017-2018

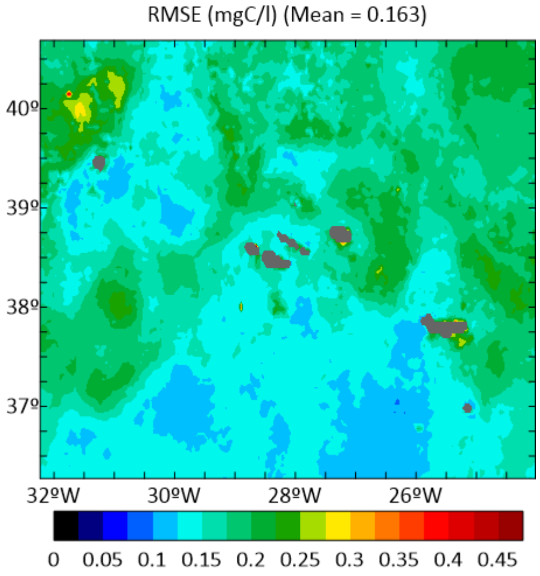

Figure 3.21- Map of RMSE obtained from the statistical analysis for 2017-2018

Phytoplankton results show a north-south gradient, with a lower concentration in the south part of the domain. Like the remote sensing data, MOHID estimates higher phytoplankton concentrations near the islands. Also, the highest BIAS and RMSE are located in the borders of the domain, except for a higher RMSE value south of São Miguel island.

Nutrients (N, P, Si) and Dissolved oxygen

The model was validated at the surface for 2017 and 2018, for nutrients (N, P, Si) and dissolved oxygen, comparing model results with the CMEMS-Bio model and WOA monthly climatology.

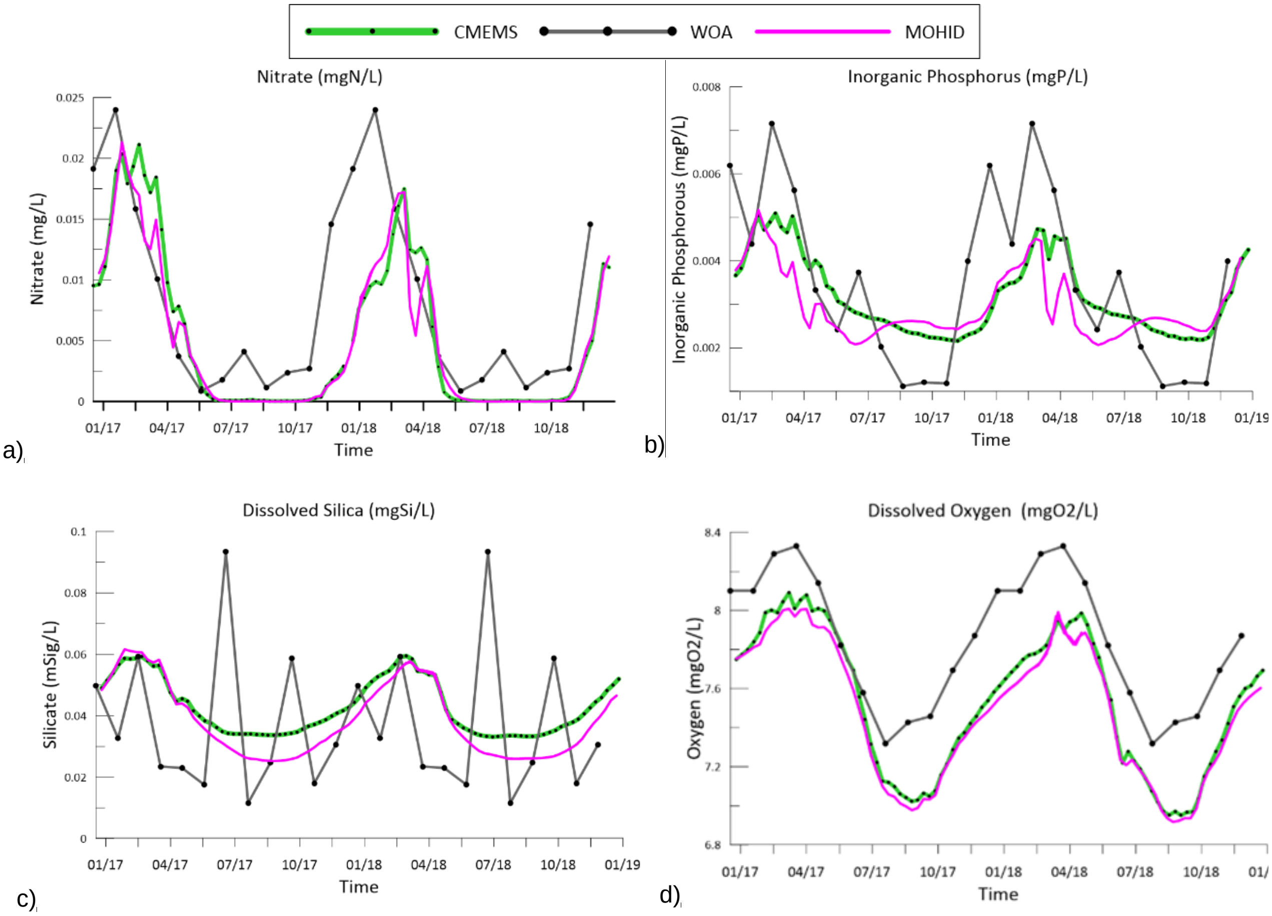

Figure 3.22-Surface average results from MOHID model (in blue); CMEMS-Bio model (in green), both weekly averaged; and monthly climatology from WOA is represented in yellow, for 2017 and 2018., for Nitrate, a); Inorganic phosphorus b); Dissolved Silica c); and dissolved oxygen d).

Table 3.14- Statistic results for the comparison between MOHID with CMEMS-Bio model, considering correlation coefficient (R), BIAS, Root mean square error (RMSE), for the surface average (weekly based) for Nitrate, Dissolved silica, Inorganic Phosphorus, dissolved oxygen

	MOHID Average (mg/l)	CMEMS-Bio average (mg/l)	Bias (mg/l)	R	RMSE (mg/l)
Nitrate (mgN/l)	0.0037	0.0048	0.0011	0.9276	0.00280
Dissolved silica (mgSi/L)	0.0409	0.0411	0.0002	0.9038	0.00502
Inorganic phosphorus (mgP/l)	0.0028	0.0032	-0.0004	0.7561	0.00091
Dissolved oxygen (mgO/L)	7.4651	7.4268	-0.0480	0.9970	0.05500

Table 3.15- Statistic results for the comparison between MOHID with WOA climatology, considering correlation (R), BIAS, Root mean square error (RMSE), for the surface average (monthly based) for Nitrate, Dissolved silica, Inorganic Phosphorus and Dissolved oxygen

	MOHID Average (mg/l)	WOA average (mg/l)	Bias (mg/l)	R	RMSE (mg/l)
Nitrate (mgN/l)	0.004	0.008	-0.004	0.896	0.005
Dissolved silica (mgSi/L)	0.038	0.080	-0.042	0.015	0.071
Inorganic phosphorus (mgP/l)	0.003	0.006	-0.003	0.558	0.004
Dissolved oxygen (mgO/L)	7.465	7.427	-0.048	0.997	0.055

Statistical results are summarised in Table 3.14 and Table 3.15. Results show that the annual cycle of nutrients at the surface is well reproduced by the model. A correlation of 0.92 and 0.9 was obtained for nitrate and dissolved silica, respectively. The lowest values of correlation were obtained for inorganic phosphorous and oxygen. MOHID can mimic the seasonal variations, and also the minimum and maximum values when compared with the CMEMS-Bio model (Figure 3.22).

MOHID simulates seasonal oxygen dynamics similar to the CMEMS-Bio model. However, both CMEMS-Bio and MOHID results are lower than WOA climatology data. This difference can be a consequence of the local interface water-air processes, which are solved by the models and not considered in the WOA climatology. At the surface, the dissolved oxygen concentration is continuously replenished by physical processes in the atmosphere (like ventilation) with the oxygen solubility varying inversely with temperature, and by photosynthetic production (Dolan, 2018). These processes can be represented with a high resolution by the models, contrasting with the coarser WOA resolution, both spatial and timely. Nevertheless, the model represents the same seasonal variation as WOA.

3.3.2. Model validation along the water column (in fixed points)- Nutrients (N, P, Si) and Dissolved oxygen

Model validation for nitrate, phosphate, dissolved silica and dissolved oxygen was performed by comparing the monthly averages, at fixed points, along the entire water column. Model validation was performed in the entire water column by comparing MOHID, CMEMS-bio and WOA, for the same instant at all the depth layers of CMEMS-bio and WOA. Validation was performed using 9 locations distributed along the study domain and an additional point in the

Condor Seamount (Figure 3.14). Figure 3.23 to Figure 3.26 show one example of a monthly average, for MOHID, CMEMS-Bio and WOA time series, along the water column for the different parameters (nitrate, inorganic phosphorous, dissolved oxygen and dissolved silica, in the validations points.

MOHID simulates adequately the vertical nutrients and oxygen variability, in the different comparison points along the domain (Figure 3.23 to Figure 3.26). Comparison along the water column denotes the higher vertical resolution of WOA climatology than MOHID and CMEMS models, with WOA climatology allowing the description of vertical variances not represented by MOHID and CMEMS-Bio. WOA has 77 vertical layers up to 3000 meters depth, while MOHID and CMEMS have 44 layers.

MOHID results for nutrients and dissolved oxygen have the same variation along the water column as CMES-Bio and WOA data, with the correlation varying between 0.84 for dissolved oxygen, and 0.99 for nutrients (Table 3.17). Similarly to WOA and CMEMS-Bio results, MOHID Water column profiles show an increase of nitrate and phosphate concentrations along the water column, until the 1000 meters depth followed by a constant maximum value up to the sea bottom. Also for dissolved silica, MOHID can simulate the WOA climatology vertical profiles. In all the cases, MOHID underestimates the *in situ* data (with a bias of -0.007 mgN/l for nitrate and -0.001 mgP/l for inorganic phosphorous). Although the final statistic outcomes a bias value of 0 mgSi/l against WOA, the vertical profiles show that the model is either over or underestimating the WOA climatology data. Taylor diagrams illustrating the MOHID-WOA comparisons for all the vertical profiles, (Figure 3.28) show that the normalized bias ranges from -0.5 to 0.5. The MOHID-WOA comparisons with higher bias have also higher RMSE and lower correlation.

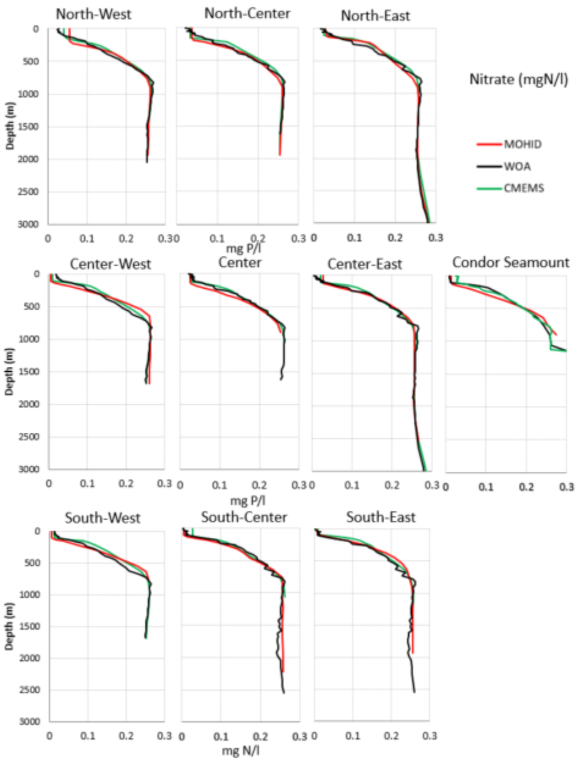

Figure 3.23- CMEMS-Bio, MOHID and WOA results of Nitrate (mgN/l), along the water column, for 10 locations along the domain for 15 March 2018

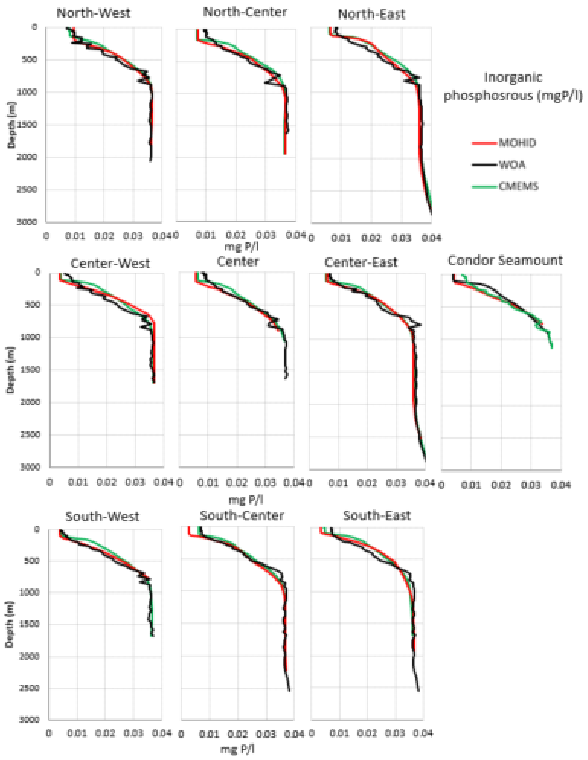

Figure 3.24- CMEMS-Bio, MOHID and WOA results of Inorganic phosphorus (mgP/l), along the water column, for 10 locations along the domain for 15 March 2018

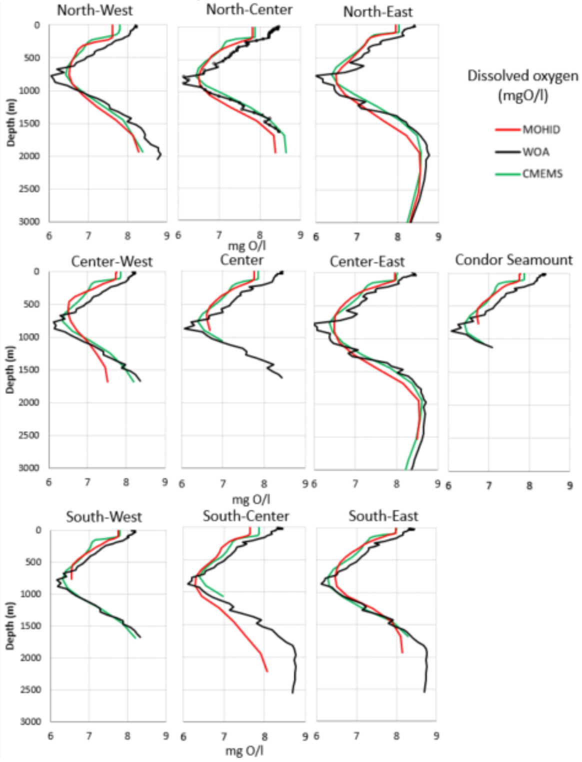

Figure 3.25- CMEMS-Bio, MOHID and WOA results for dissolved oxygen (mgO2/l), along the water column, for 10 locations along the domain for 15 March 2018

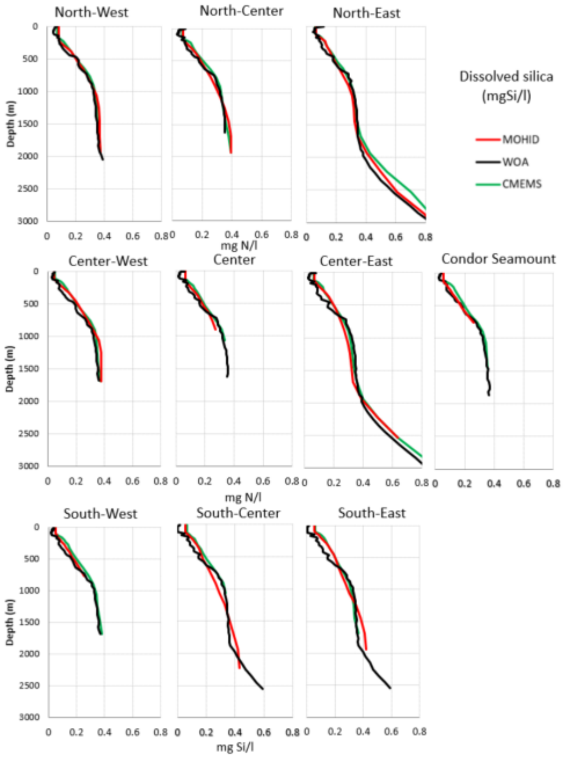

Figure 3.26- CMEMS-Bio, MOHID and WOA results for Dissolved silica (mgSi/l) along the water column, for 10 locations along the domain for 15 March 2018

Table 3.16- Statistic results for the comparison between MOHID and WOA climatology data and CMEMS-Bio model, considering the correlation coefficient (R), BIAS, Root mean square error (RMSE), considering 10 points, along the water column, for Nitrate, Dissolved silica, Inorganic Phosphorus, dissolved oxygen and phytoplankton.

	Nitrate (mgN/l)		Dissolved Silica (mgSi/l)		Inorganic phosphorus (mgP/l)		Oxygen (mgO/l)		Phytoplankton (mgC/l)
	Mohid vs WOA	Mohid vs CMEMS	Mohid vs WOA	Mohid vs	Mohid vs WOA	Mohid vs CMEMS	Mohid vs WOA	Mohid vs CMEMS	Mohid vs CMEMS
R	0.983	0.981	0.971	0.992	0.983	0.983	0.865	0.887	0.941
Bias	-0.007	-0.006	0.0	-0.01	-0.001	-0.001	-0.215	-0.035	0.001
RMSE	0.016	0.014	0.031	0.017	0.002	0.002	0.334	0.166	0.005

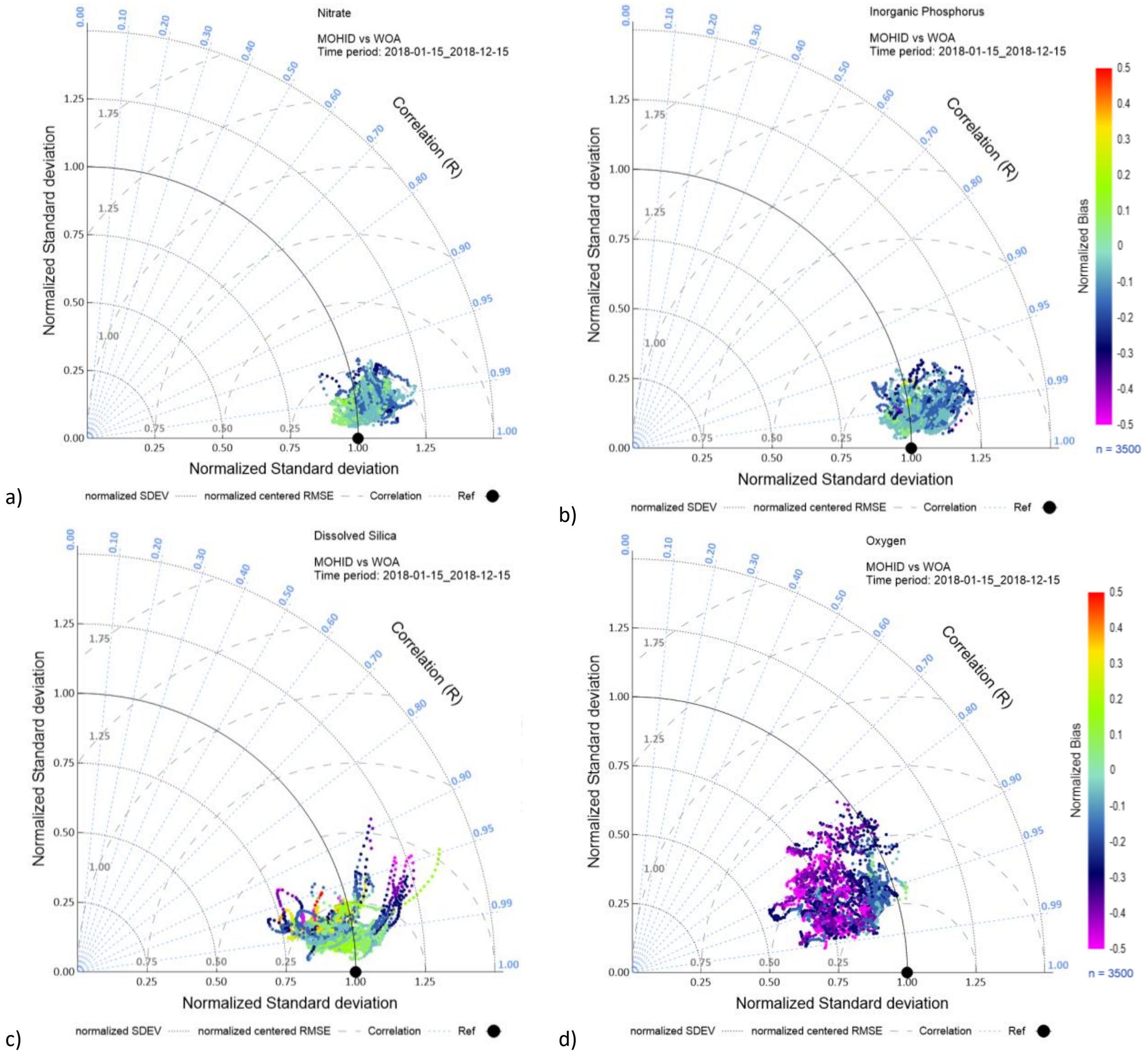

Figure 3.27- Taylor diagrams summarizing statistical results for MOHID validation against WOA climatology for a) Nitrate (top left); b)Inorganic phosphorus (top right); c) Dissolved silica (bottom left); and d) Dissolved oxygen (bottom right). The black dot is the reference (Ref), representing the perfect adjustment between model results and WOA climatology. Coloured dots represent each vertical profile comparison MOHID/WOA; the colour represents the normalized bias; the azimuthal angle represents the Pearson correlation coefficient (R), the normalized standard deviation is the radial distance to the reference point (Ref); the dotted semicircles centred at the Ref are the normalized centred RMSE scale. Bias, SD and RMSE are normalized by the standard deviation of each vertical profile.

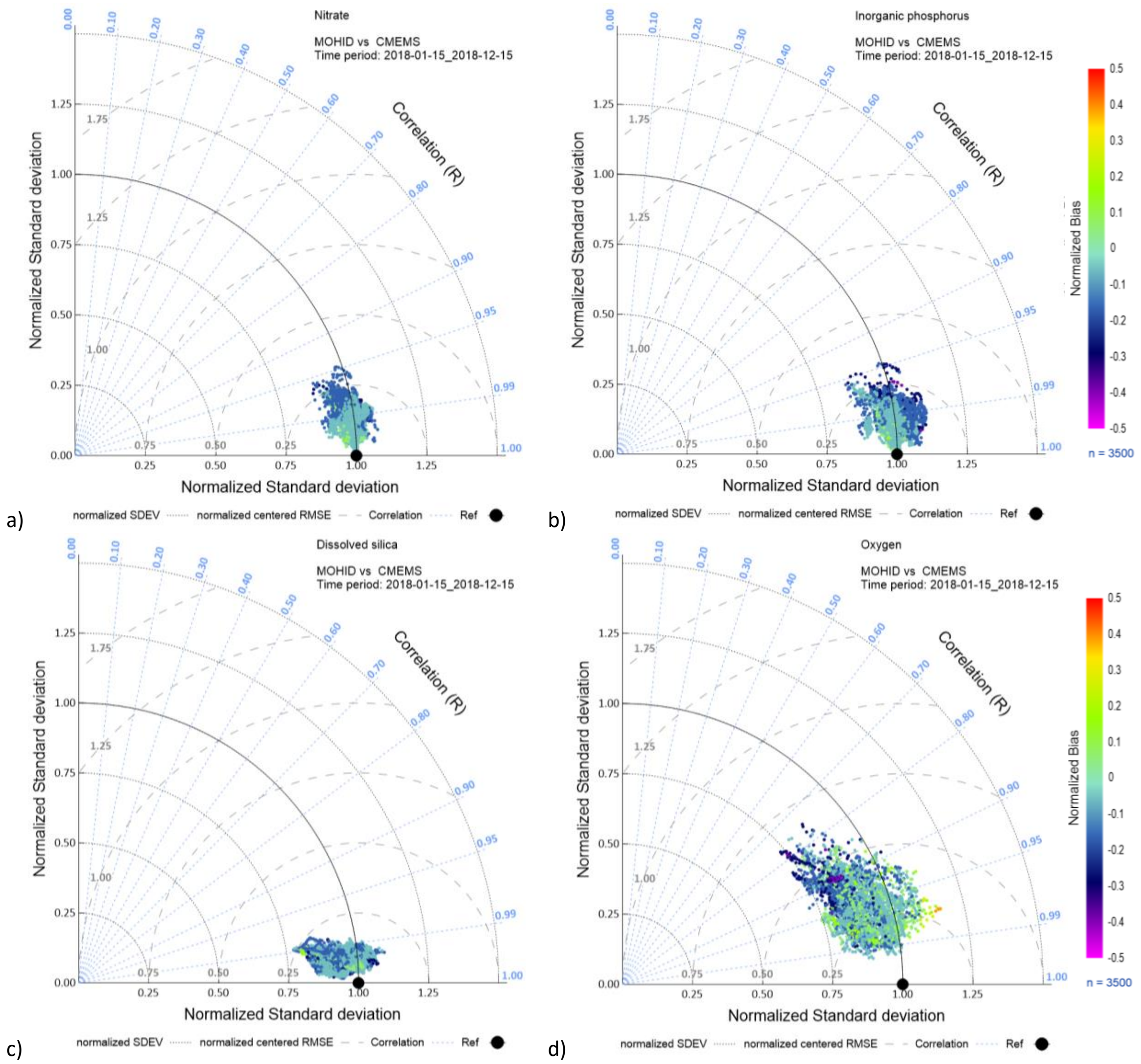

Figure 3.28- Taylor diagrams summarizing statistical results for MOHID validation against CMEMS-Bio for a) Nitrate (top left); b)Inorganic phosphorus (top right); c) Dissolved silica (bottom left); and d) Dissolved oxygen (bottom right). The black dot is the reference (Ref), representing the perfect adjustment between model results and CMEMS-Bio data. Coloured dots represent each vertical profile comparison MOHID/CMEMS-Bio; the colour represents the normalized bias; the azimuthal angle represents the Pearson correlation coefficient (R); the normalized standard deviation is the radial distance to the reference point (Ref); the dotted semicircles centred at the Ref are the normalized centred RMSE scale. Bias, SD and RMSE are normalized by the standard deviation of each vertical profile.

For oxygen validation, Taylor diagrams highlight the underestimation of MOHID results. Nevertheless, this underestimation, vertical profiles represented in Figure 3.25, shows that MOHID can simulate oxygen concentration along the water column, representing the vertical profiles along the water column, with a decrease of oxygen concentration along the depth, with a demarked minimum oxygen zone, between 750 and 1000meters depth, followed by an increase of oxygen concentration until the deepest layers (Figure 3.25). The minimum oxygen concentration simulated by MOHID is at the same depth as WOA and CMEMS-Bio. There is a visible distinction between model results (both MOHID and CMEMS-Bio), and WOA climatology data, for all the parameters, however, the seasonal variations follow the same variations.

Taylor diagrams of model validation against WOA and CMEMS-Bio data, in Figure 3.27 and Figure 3.28, depict this good model performance. Dissolved oxygen is the parameter that reflects a higher standard deviation and lower correlation with the observed data. When compared with WOA, dissolved silica reveals higher bias (ranging from -0.5 to 0.5), RMSE and standard deviation (and Figure 3.28 c).

3.4. Model results

3.4.1. Spatial variability at the surface

Model validation at the surface and along the water column shows that MOHID can simulate spatial and seasonal variability of the biotic and abiotic parameters. MOHID simulates the seasonal winter increase of nutrient concentrations at the surface, with maximum values in February and March, followed by a decrease during the spring with the lowest values in summer, for nitrate, inorganic phosphorus and dissolved silica (Figure 3.22).

Table 3.17- Maximum and minimum weekly average concentrations for the entire domain, and maximum and minimum absolute values of weekly average concentrations at the surface, for 2017 and 2018, for nitrate, dissolved silica, inorganic phosphorus, and dissolved oxygen.

	Maximum domain average concentration	Maximum value	Minimum domain average concentration	Minimum value
Nitrate (mgN/l)	0.021	0.064	1.41E-05	1.00E-05
Dissolved silica (mgSi/L)	0.062	0.086	0.025	0.015
Inorganic phosphorus (mgP/l)	0.005	0.011	0.002	0.001
Dissolved oxygen (mgO/L)	8.010	8.440	6.980	6.800

Model results reveal spatial variability along the model domain, with phytoplankton and nutrient concentrations varying up to one order of magnitude along the domain (Table 3.17). A latitudinal gradient is denoted, with Nutrient and phytoplankton concentrations higher in the north part of the domain (Figure 3.29 to Figure 3.32). Nitrate concentration at the surface achieves the maximum value of 0.06 mgN/l, while the maximum domain average is about 0.02 mgN/l, these maximum values occur in February and March (Figure 3.22). The dissolved silica and inorganic phosphorus maximum average concentrations are observed in March, with maximum values of 0.062 mgSi/l, 0.0025 mgP/l, and maximum weekly values in descript point of 0.086 mgSi/l and 0.011 mgP/l (Table 3.17).

The maximum nutrient concentration during February and March is followed by nutrient depletion, induced by phytoplankton growth. Nitrate concentration at the surface can achieve null values during the summer months (Jully, August and September) (Figure 3.29). Inorganic phosphorous and dissolved silica average concentrations also have a seasonal depletion, however, less pronounced during spring without a total depletion (Figure 3.22). The domain average concentration of inorganic phosphorous reaches its lowest value in June with 0.0022 mgP/l (average values for the entire study domain), while for dissolved silica, the minimum of 0.025 mgSi/l is at the end of the summer. This seasonal variation is representative of the oligotrophic regions, where the low nutrient concentration limits phytoplankton growth. In this case, nitrate concentration can be more restrictive than phosphorous, achieving values close to zero in the summer months, while inorganic phosphorous is not depleted. After the summer months, induced by the winter convection, the nutrient concentrations at the surface start to increase, reaching their maximum at the end of the Winter (February/March) (Figure 3.29).

The phytoplankton model results at the surface (Figure 3.32), show that MOHID spatial resolution allows the simulation of local and regional phytoplankton patterns, with high variability along space and time. Phytoplankton concentration along the domain shows spatial and seasonal synchrony with nutrient concentrations (Figure 3.29, Figure 3.30 and Figure 3.31 for nitrate, dissolved silica and inorganic phosphorous respectively). This relation is highly visible in the northern part of the domain, where higher nutrient concentrations follow the same patterns as phytoplankton concentrations. Surface results show how the increase of nutrients is related to the phytoplankton concentration, though, with one month delay. Surface concentrations of phytoplankton (Figure 3.32) and zooplankton (Figure 3.33) show a similar seasonal variation, with zooplankton maximum concentrations occurring one month after the phytoplankton maximum. Zooplankton concentration starts to increase in March, after the phytoplankton bloom, with higher values in April, May and June. During June, the phytoplankton concentration at the surface is close to zero in the entire domain except in the top north, justifying the concentration of zooplankton that persist in this area during June, July and August. In October, it occurs an increase in phytoplankton concentration again (autumn bloom), mainly in the northern part of the domain, with higher values during December in the Eastern part of the domain. The same patterns were verified for 2017 (results are present in Annexe II).

Nitrate and phosphate seasonal patterns follow the typical patterns of oligotrophic regions, with values close to zero at the surface. Nutrient concentrations are generally higher in the northern part of the domain. The similarities in spatial and temporal dynamics of the nitrate and inorganic phosphorous are observable. For dissolved silica, in the winter months, the concentration is also higher in the Northern part of the domain, however, from July to November the concentrations are lower in the southern part of the domain

At the surface, the oxygen concentration has the lowest values during the summer months. Latitudinal and longitudinal gradients are denoted, with higher oxygen concentration in the North and in the East (Figure 3.34). These spatial gradients follow the sea surface temperature distribution (Figure 3.35), with richer oxygen areas in the colder regions, and lower oxygen concentration in the southwest of the domain, where sea surface temperature is higher.

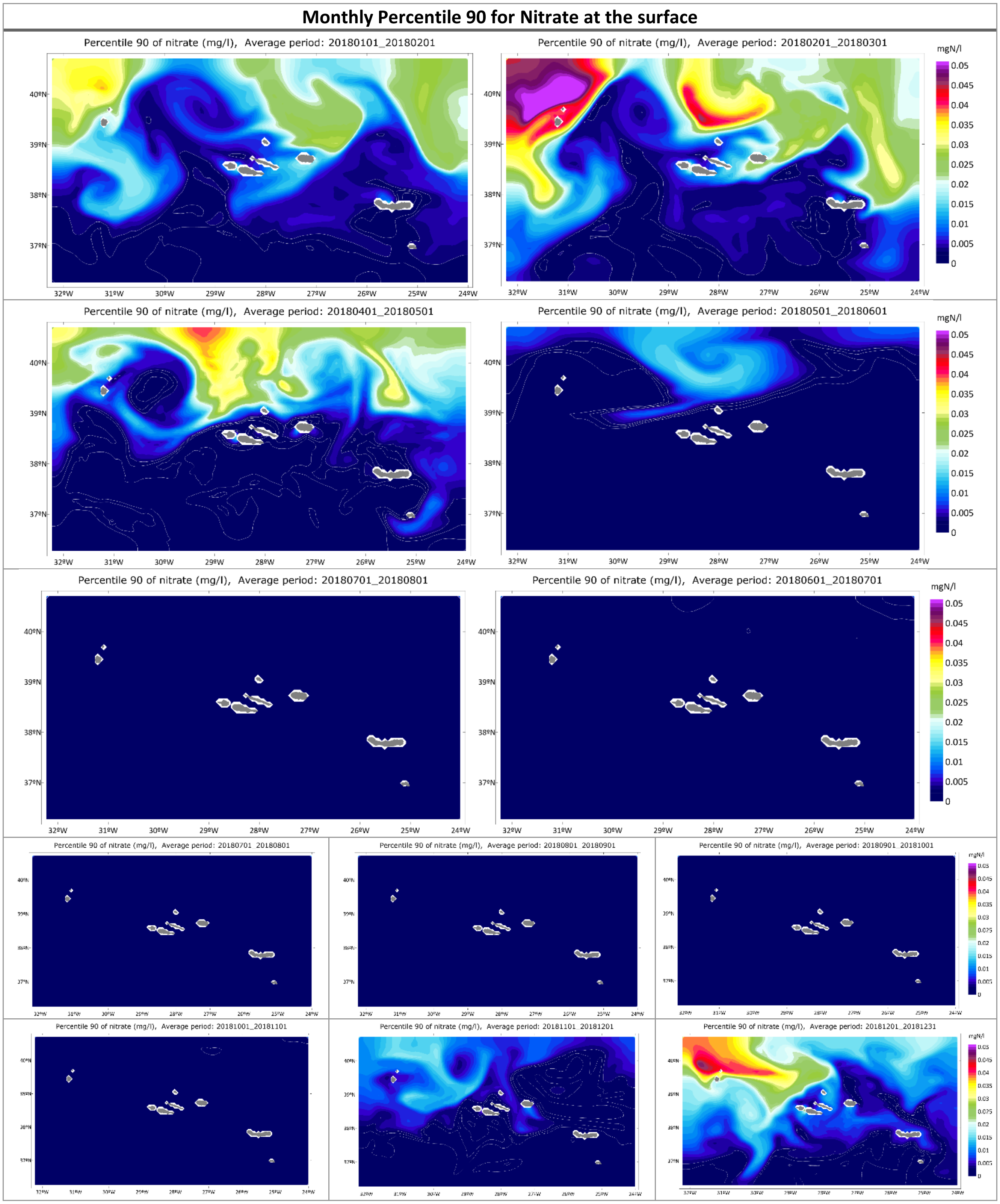

Figure 3.29- Monthly Percentile 90 for nitrate model results at the surface from January 2018 to December 2018

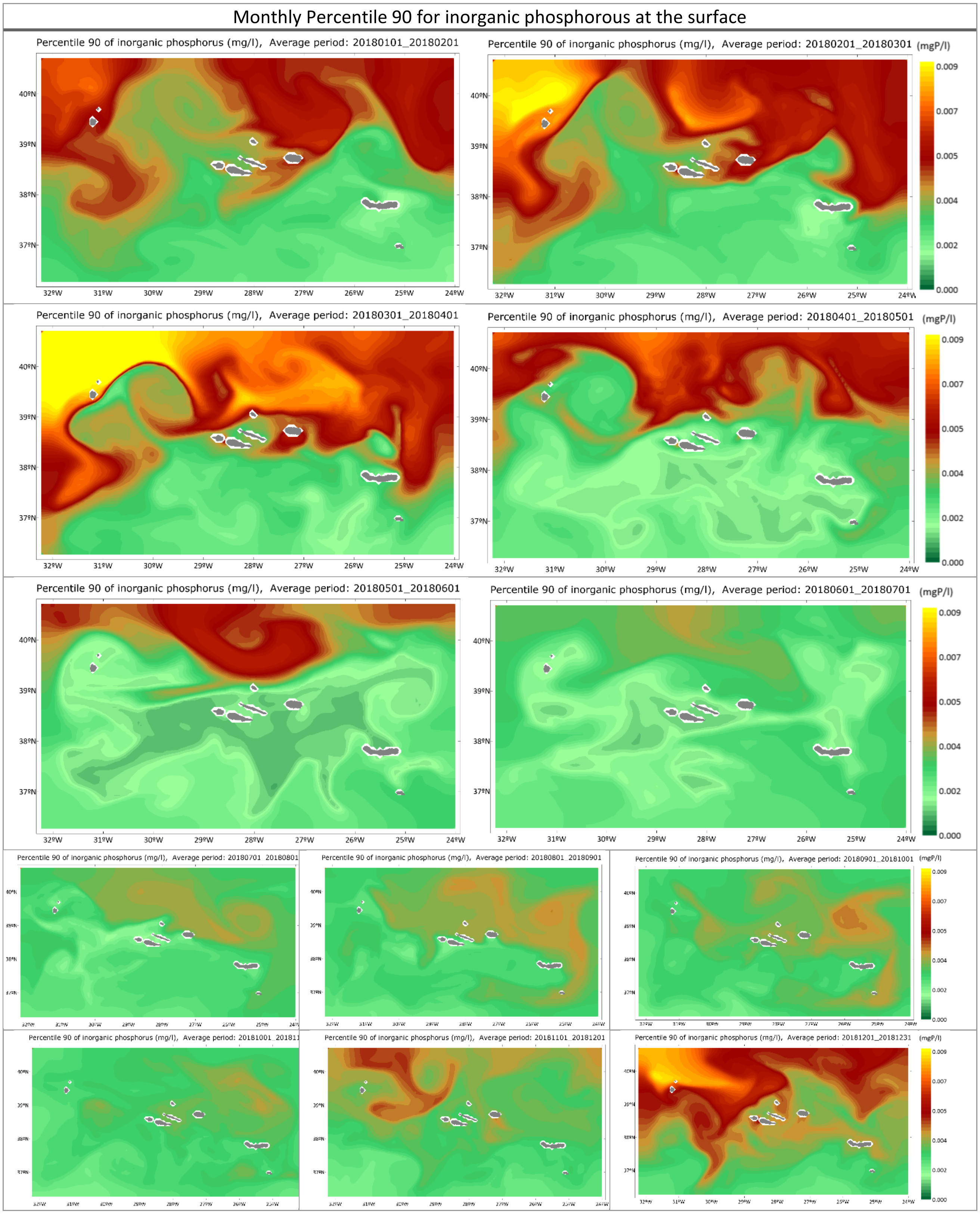

Figure 3.30- Monthly Percentile 90 for inorganic phosphorous model results at the surface from January 2018 to December 2018

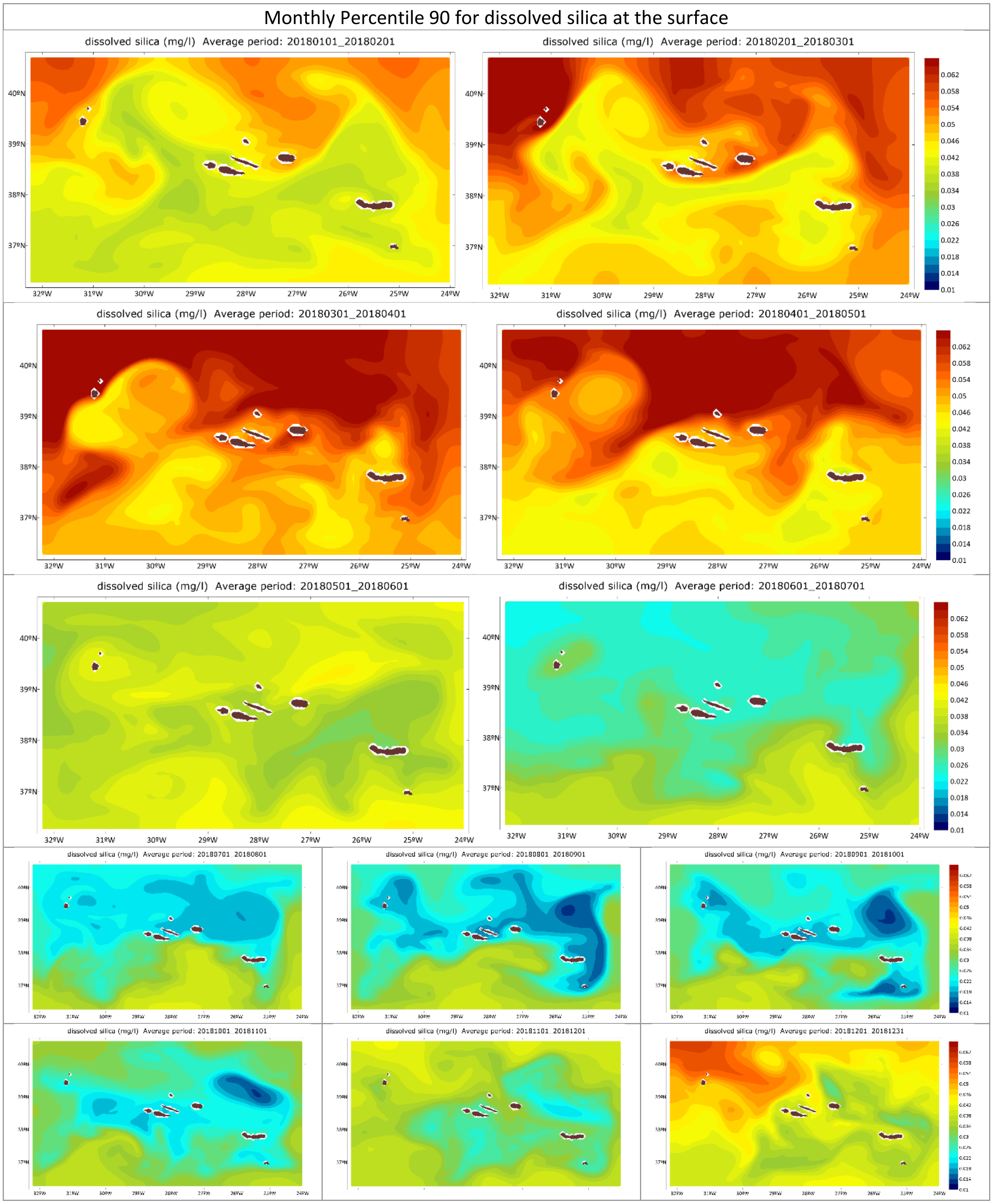

Figure 3.31- Monthly Percentile 90 for dissolved silica model results at the surface from January 2018 to December 2018

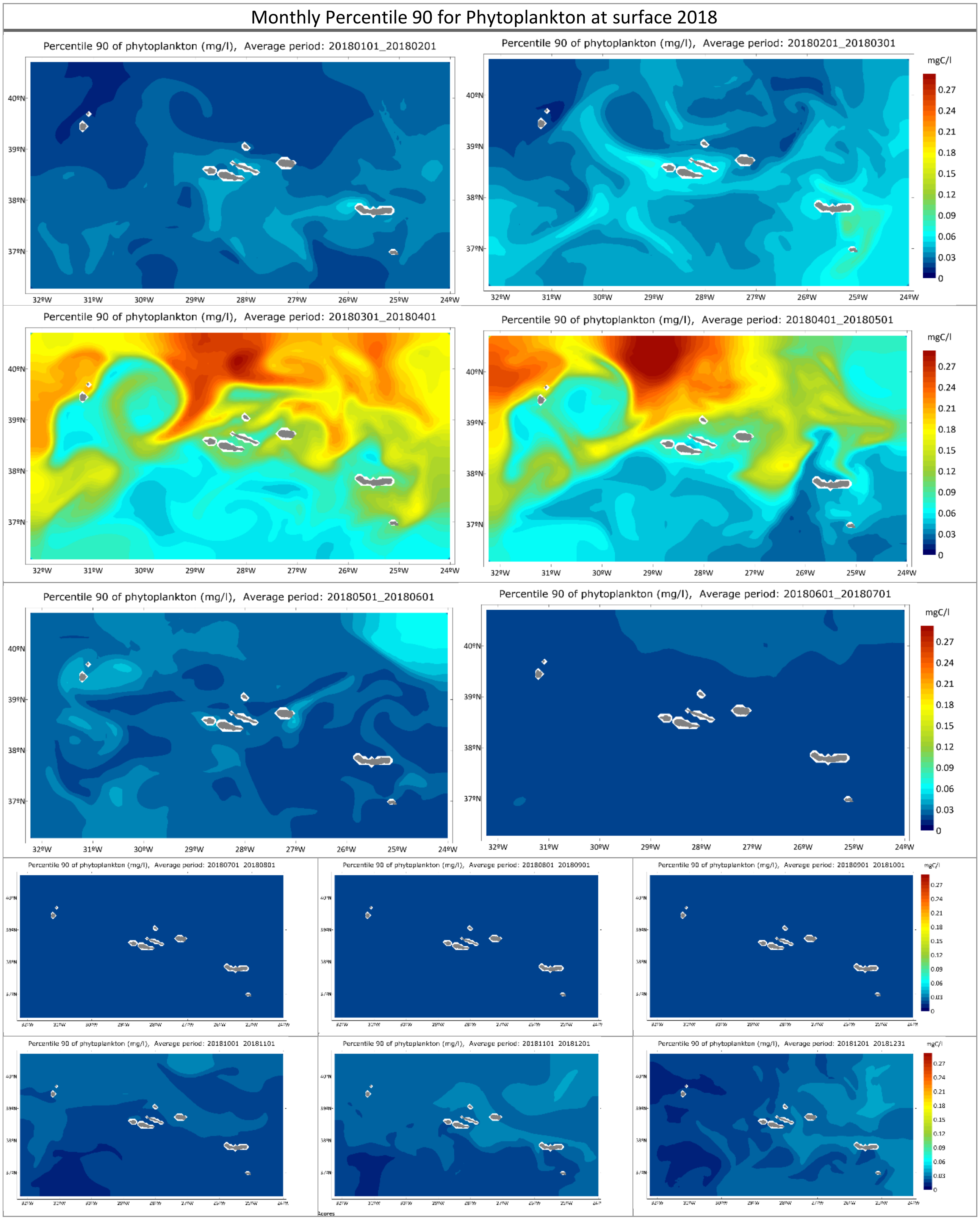

Monthly Percentile 90 for Phytoplankton at surface 2018

Percentile 90 of phytoplankton (mg/l), Average period: 20180101_20180201

Percentile 90 of phytoplankton (mg/l), Average period: 20180201_20180301

Percentile 90 of phytoplankton (mg/l), Average period: 20180301_20180401

Percentile 90 of phytoplankton (mg/l), Average period: 20180401_20180501

Percentile 90 of phytoplankton (mg/l), Average period: 20180501_20180601

Percentile 90 of phytoplankton (mg/l), Average period: 20180601_20180701

Percentile 90 of phytoplankton (mg/l), Average period: 20180701 20180801

Percentile 90 of phytoplankton (mg/l), Average period: 20180801 20180901

Percentile 90 of phytoplankton (mg/l), Average period: 20180901 20181001

Percentile 90 of phytoplankton (mg/l), Average period: 20181001 20181101

Percentile 90 of phytoplankton (mg/l), Average period: 20181101 20181201

Percentile 90 of phytoplankton (mg/l), Average period: 20181201 20181231

Figure 3.32- Monthly Percentile 90 for phytoplankton model results at the surface from January 2018 to December 2018

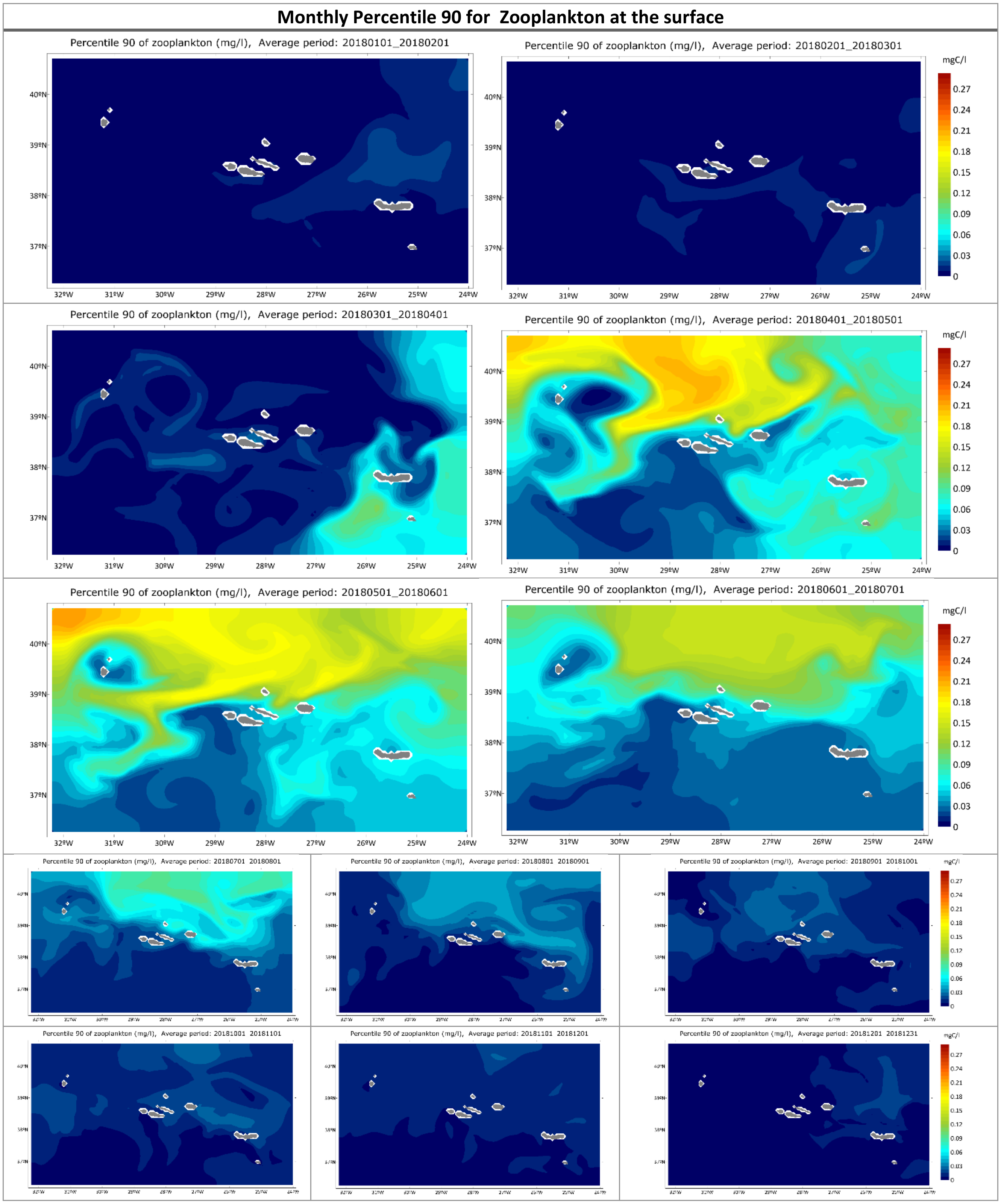

Figure 3.33- Monthly Percentile 90 for zooplankton model results at the surface from January to December 2018

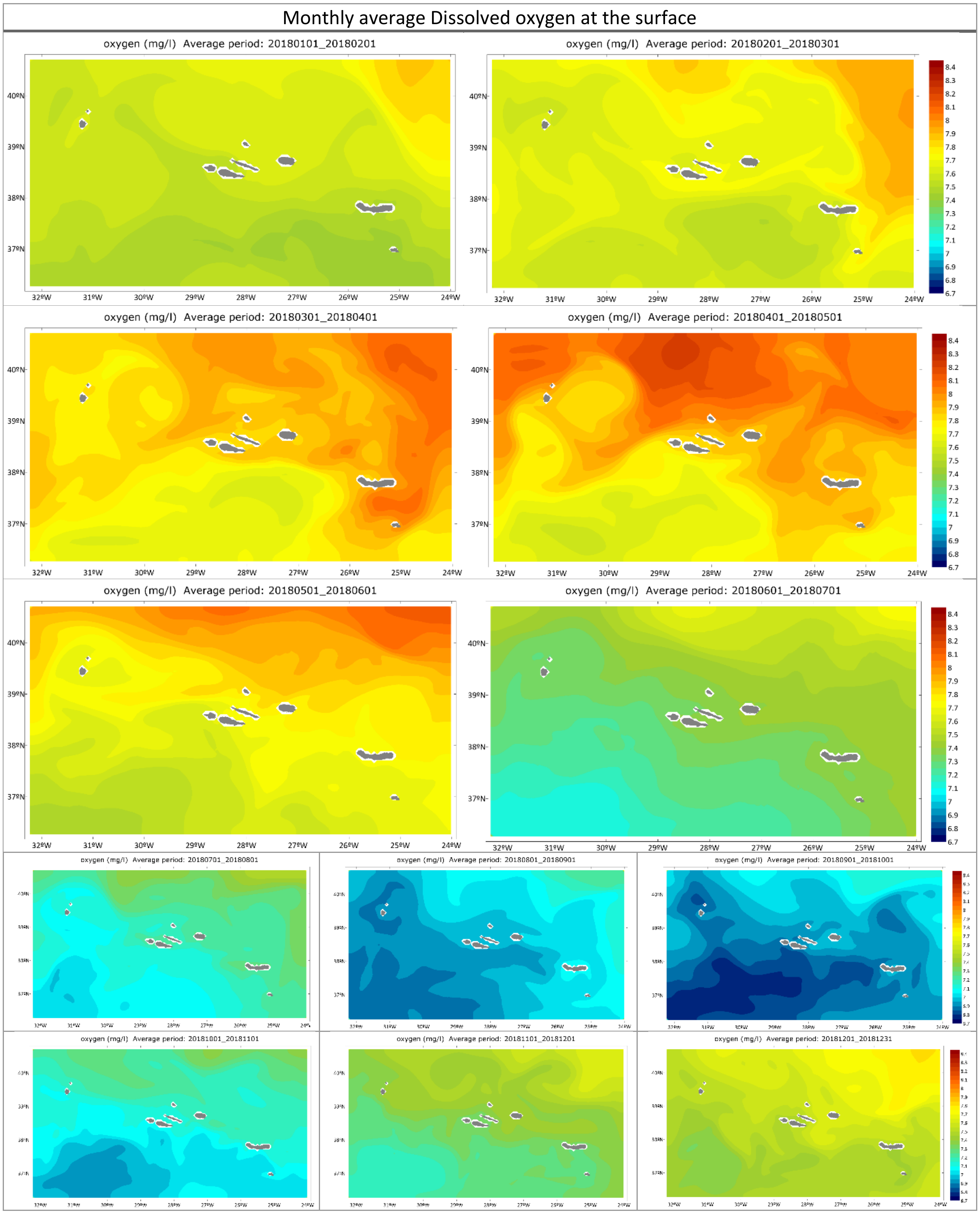
Monthly average Dissolved oxygen at the surface

oxygen (mg/l) Average period: 20180101_20180201

oxygen (mg/l) Average period: 20180201_20180301

oxygen (mg/l) Average period: 20180301_20180401

oxygen (mg/l) Average period: 20180401_20180501

oxygen (mg/l) Average period: 20180501_20180601

oxygen (mg/l) Average period: 20180601_20180701

oxygen (mg/l) Average period: 20180701_20180801

oxygen (mg/l) Average period: 20180801_20180901

oxygen (mg/l) Average period: 20180901_20181001

oxygen (mg/l) Average period: 20181001_20181101

oxygen (mg/l) Average period: 20181101_20181201

oxygen (mg/l) Average period: 20181201_20181231

Figure 3.34- Monthly average for dissolved oxygen model results at the surface from January 2018 to December 2018

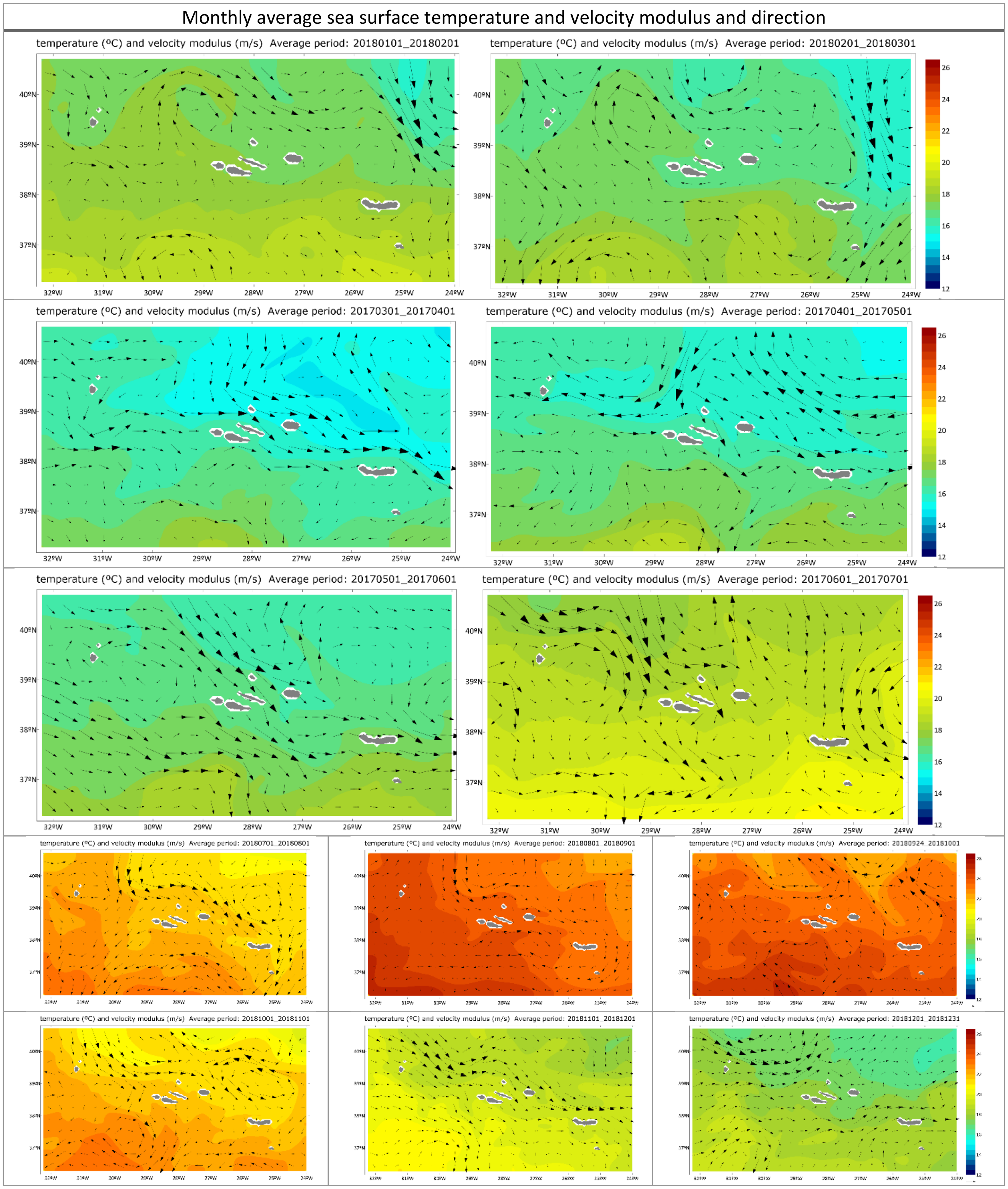

Monthly average sea surface temperature and velocity modulus and direction

temperature (ºC) and velocity modulus (m/s) Average period: 20180101_20180201

temperature (ºC) and velocity modulus (m/s) Average period: 20180201_20180301

temperature (ºC) and velocity modulus (m/s) Average period: 20170301_20170401

temperature (ºC) and velocity modulus (m/s) Average period: 20170401_20170501

temperature (ºC) and velocity modulus (m/s) Average period: 20170501_20170601

temperature (ºC) and velocity modulus (m/s) Average period: 20170601_20170701

temperature (ºC) and velocity modulus (m/s) Average period: 20180701_20180801

temperature (ºC) and velocity modulus (m/s) Average period: 20180801_20180901

temperature (ºC) and velocity modulus (m/s) Average period: 20180924_20181001

temperature (ºC) and velocity modulus (m/s) Average period: 20181001_20181101

temperature (ºC) and velocity modulus (m/s) Average period: 20181101_20181201

temperature (ºC) and velocity modulus (m/s) Average period: 20181201_20181231

Figure 3.35- Monthly average of sea surface temperature and hydrodynamic vectors for 2018 at the surface

3.4.2. Vertical distribution: Nutrients, phytoplankton, dissolved oxygen and temperature

To study the biogeochemical properties along the water column in the Azores region, vertical profiles along the meridional and zonal sections crossing the domain at 28.5ºW and 38.5ºN respectively were considered. Water properties were studied considering monthly averages and the entire simulation period averages (February 2017 to December 2018).

At the surface, the dissolved oxygen ranges from 7.4 mgO2/l to 7.6 mgO2/l (Figure 3.36) with the lower concentrations in the South and West of the domain transects. Oxygen concentrations increase from the surface until 50 meters to 100 meters depth. This higher concentration is not constant along the domain. In the selected transects, this maximum occurs in the northern part of the 28.5˚W meridional section, and in the Eastern part of the zonal section, between 28˚W and 24˚W. Below the 100 meters depth, the dissolved oxygen concentration decreases achieving the minimum concentration between 500m and 1000 meters depth. Below this minimum dissolved oxygen increases again reaching its maximum at the sea bottom.

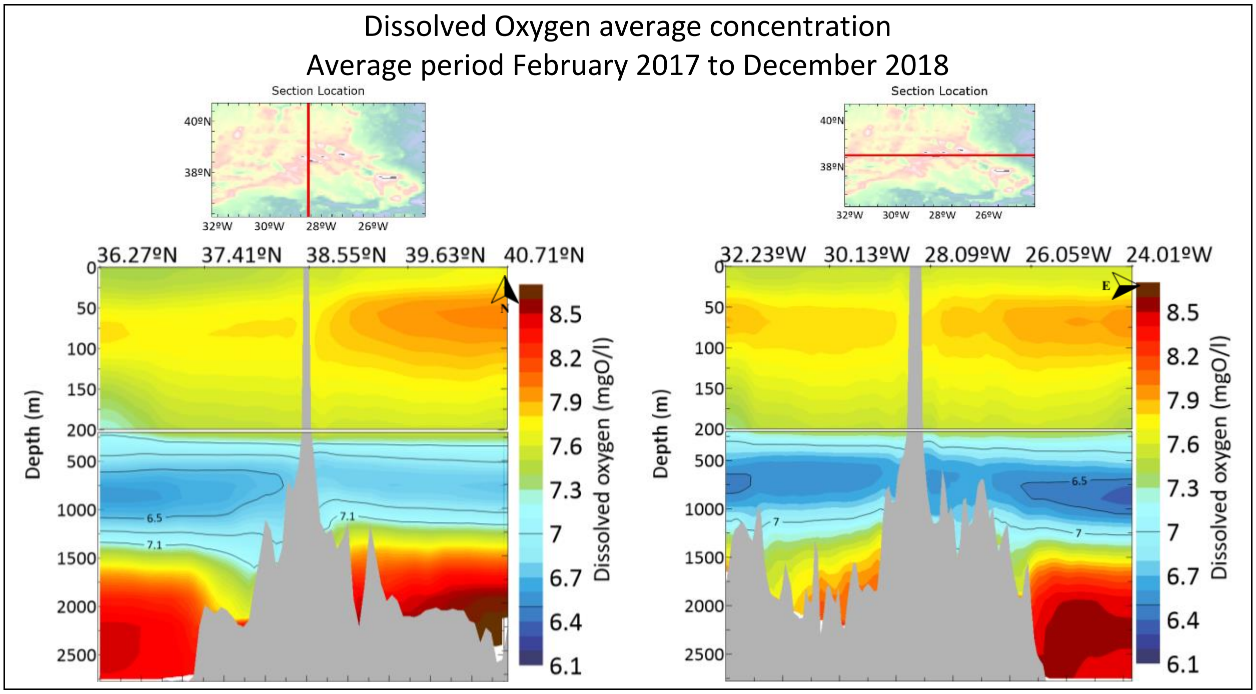
Dissolved Oxygen average concentration
Average period February 2017 to December 2018

Figure 3.36- Dissolved oxygen average concentration along the meridional section at 28.5ºW (on the left), and the zonal section at 38.5ºN (on the right), for the period between February 2017 and December 2018, from 0 to 3000 m depth. Depth profiles present a higher resolution until 250 meters depth and less resolution from 250 meters to 3000 meters depth.

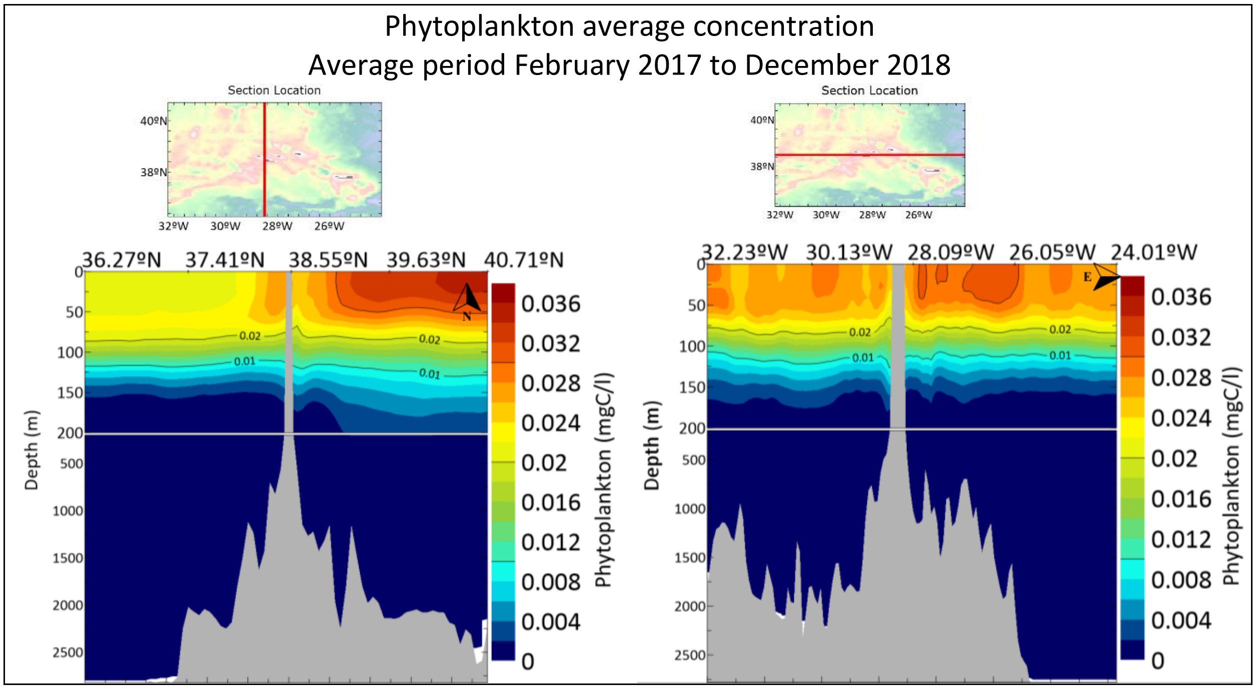

Figure 3.37- Phytoplankton average concentration along the meridional section at 28.5ºW (on the left), and the zonal section at 38.5ºN (on the right), for the period between February 2017 and December 2018, from 0 to 3000 m depth. Depth profiles present a higher resolution until 250 meters depth and less resolution from 250 meters to 3000 meters depth

Phytoplankton average concentrations for the entire simulation period range from 0.036 mgC/l to 0.02 mgC/l at the surface, in the selected sections (Figure 3.37). Phytoplankton biomass is higher at the surface, with a decay along the water column, achieving a minimal concentration between 150 and 200 meters depth. In the selected transects, the higher average phytoplankton concentrations are located in the northern part of the meridional section, with concentrations ranging from 0.034 to 0.024mgC/l, between 40.71˚N and 38.5˚N. In the southern part of the transect, is 0.026mgC in the vicinity of the Pico island, and 0.02 from 38˚ to 36.27˚N. The spatial phytoplankton distribution is more heterogenic in the longitudinal transect, with concentrations ranging from 0.028 to 0.02 mgC/l in the first 75 meters of the water column.

Nutrient vertical profiles show similarities between nitrate, phosphate and dissolved silica concentrations along the water column (Figure 3.38), with lower concentrations at the surface, increasing up to the sea bottom.

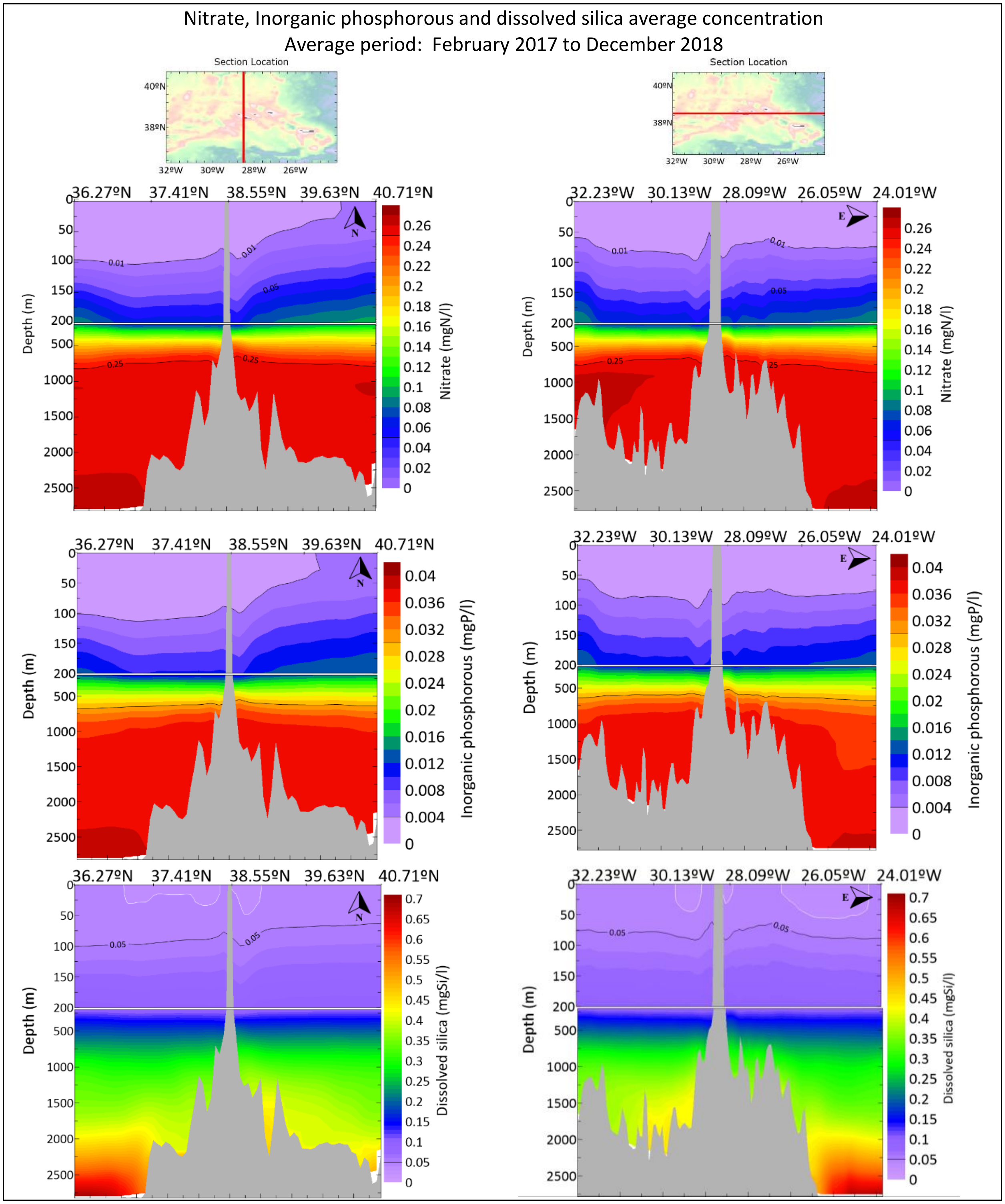

Figure 3.38- Average nutrient concentration for nitrate (top), inorganic phosphorous (middle), and dissolved silica (bottom), along the meridional section at 28.5ºW (on the left), and the zonal section at 38.5ºN (on the right), for the period between February 2017 and December 2018, from 0 to 3000 m depth. Depth profiles present a higher resolution until 250 meters depth and less resolution from 250 meters to 3000 meters depth.

Average nutrient concentrations for the simulation period, at the first 100 meters depth, ranges from 0.01 to 0.02mg/l for Nitrate, from 0.004 to 0.006 mgP/l for phosphate, and from

0.025 to 0.075mgSi/l for silicate. These concentrations increase along the water column, achieving the maximum at the sea bottom, with average values of 0.26 mgN/l for nitrate, 0.04 mgP/l for phosphate, and 0.7 mgSi for silicate.

Meridional and zonal sections at 28.5˚W and 38.5˚N respectively, show that, at the surface, higher nutrient concentrations (nitrate, inorganic phosphorous and dissolved silica) are found in the northern part of the domain (Figure 3.37). This North-south gradient is very tenue for the dissolved silica concentrations. Conversely, a longitudinal gradient is not observed.

3.4.3. Deep chlorophyll maximum (DCM)

The deep chlorophyll maximum (DCM), is characterised by a maximum chlorophyll concentration in depth (equivalent to a maximum phytoplankton concentration in depth). It is typical of oligotrophic regions (Cornec et al., 2021), and is also documented for the Azores region, it occurs after the spring bloom and is established below the mixed layer (Macedo et al., 2000).

Vertical profiles of phytoplankton biomass along the study area (Figure 3.39) illustrate this DCM establishment and its seasonal and spatial variability. Phytoplankton concentrations along the water column show a vertical gradient with seasonal variations (Figure 3.39). The phytoplankton monthly average concentration for these study points varies between 0 to 0.025 mgC/l, however, in March, due to the spring phytoplankton bloom, the concentrations achieve values higher than 0.04 mgC/l.

The DCM becomes established at different depths in the Azores, from 50 meters to 100 meters depth, mostly in the summer months, July, August, September, and also in October. In the locations Eastwards of the study area (North-East, Center-East and South-East points), the DCM occurs in shallow depths, around 50 meters depth, while in the other points between 50 and 75 meters. In the North-West and North-Center points, the phytoplankton concentration achieves the highest values of 0.02 mgC/l, at 75 meters, and 90 meters depth, the deepest in this analysis.

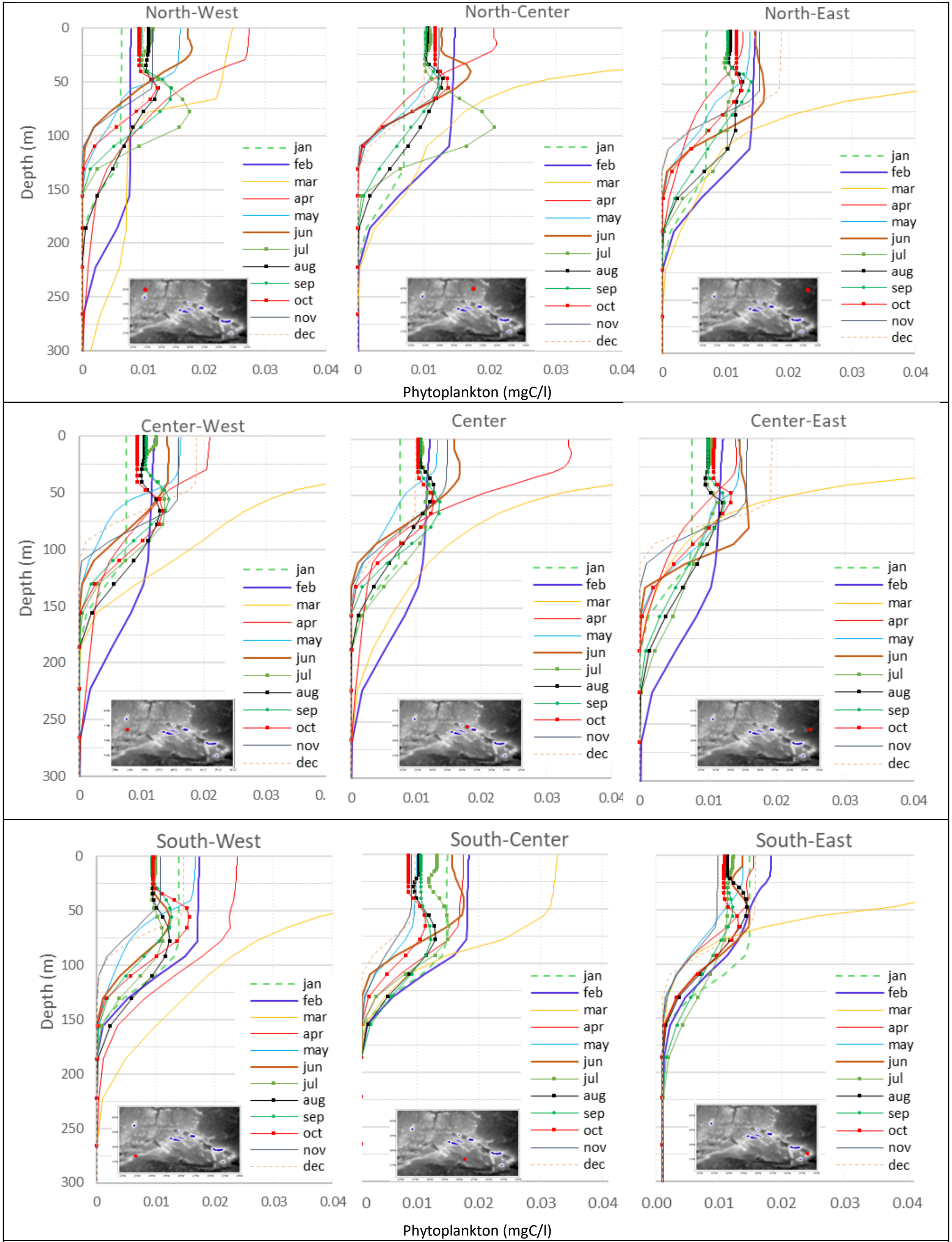

Figure 3.39- Monthly averages for phytoplankton modelled results, along the water column, from the surface until 300meters depth, for three fixed points (North-West, North-Center, North-East, Center-West, Center and Center-East) at the different quadrants, from February 2017 to January 2018

3.4.4. Seasonal and spatial variability

To study the biogeochemical seasonal patterns in the Azores, model results are analysed on a monthly basis along vertical profiles at the meridional and zonal sections, crossing the domain at 28.5˚W and 38.5˚N respectively (Figure 3.40 to Figure 3.43), and also the fixed depths along the domain.

Phytoplankton and diatoms biomass concentration along the year at the surface layers reveal a highly dynamic variation, with the demarked spring bloom, and the deep phytoplankton maximum at deeper layers after the spring bloom (Figure 3.42 to Figure 3.45). The spring phytoplankton bloom is visible at the surface layers, during February, March and April, with higher concentrations at the surface, than the diatoms. Diatoms concentration ranges from 0 to 0.015 mgC/l, with the maximum concentrations occurring from June to September, and not during February, March and April months with the maximum phytoplankton concentration. Also, the vertical diatom distribution is different than for the phytoplankton case. The maximum diatoms concentration does not occur in the surface layer, but in the sub-superficial depth, between 50 and 100 meters depth.

Phytoplankton higher concentrations occur at the surface layer, with a spring bloom during February, March and April. During this spring bloom, the concentration achieves values higher than 0.3mgC/l at the surface (Figure 3.32). Along the water column, phytoplankton concentration achieved values of 0.03mgC/l at 200 meters depth during April 2018, in the North of the domain. This higher phytoplankton concentration at deeper layers is more intense in the North of the domain than in the South. In the North, phytoplankton concentration can go up to 250 meters depth, while in the South, it goes to 150 or 200 meters depth in the selected meridional section.

After April, the phytoplankton bloom dissipates at the surface, however, maximum phytoplankton remains at deeper depths, between 50 and 100 meters depth. This maximum deep phytoplankton concentration (corresponding to the DCM) persists from June to September, with concentrations ranging from 0.02 to 0.03mgC/l, while at the surface the concentrations range from 0.02 and 0.015mgC/l. After September, this DCM concentration dissipates, and the phytoplankton biomass becomes more homogenous along the water column. During November and December the phytoplankton concentration increases, with higher concentration at the surface up to 0.03mgC/l, but the higher phytoplankton bloom only occurs in March, with a clear concentration increase.

Oxygen concentration in the euphotic zone is highly dynamic. The monthly average oxygen concentration represented in the vertical section along the meridional and zonal sections to (Figure 3.42 to Figure 3.45) shows that the oxygen concentration is associated with the phytoplankton concentration. In the depths and locations where the DCM is achieved, the maximum phytoplankton concentrations match the high oxygen concentration.

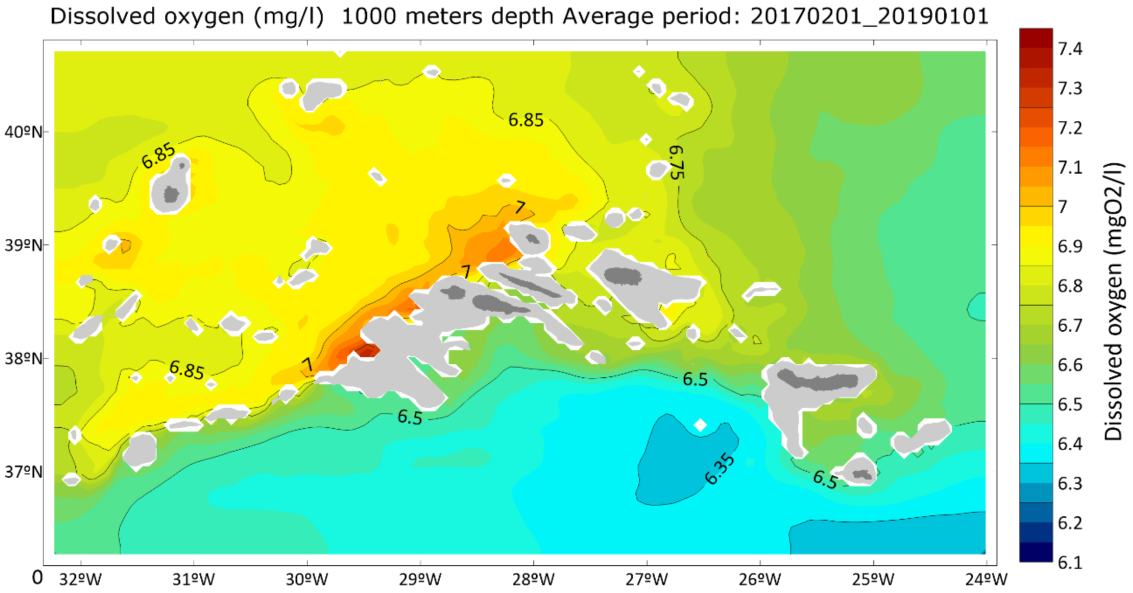

Figure 3.40- Average dissolved oxygen concentration, for the simulation period (February 2017 to December 2018), at 1000 meters depth. Azores islands are represented in dark grey, and the bathymetry up to 1000 meters depth in light grey.

At 1000 meters depth is visible a North-South oxygen gradient, with higher concentrations in the northern part of the domain, with the archipelago and the MAR forming a visible barrier distinguishing the northern and southern parts of the domain. The maximum oxygen concentration occurs on the northern slope of the 1000 meters bathymetric around the Central Group of the Azores archipelago (Figure 3.40). The north slope of the 1000 meters depth bathymetric has an average concentration ranging from 6.75 to 7.4mgO2/l, while in the southern from 6.75 to 6.5 mgO2/l. Also, a longitudinal negative gradient is denoted, with higher oxygen concentration on the West, and lower on the East, ranging from 6.85 mgO2/l on the West to 6.35mg O2/l in the southEast. The seasonal analysis shows a decrease in oxygen concentrations, at 1000meters depth during the summer months (from June to September) in the southern part of the archipelago (Figure 3.40), accentuating the MAR and the archipelago barrier effect between the northern and the southern parts of the domain. By contrast, on the northern side of the 1000 meters bathymetric slope, the oxygen concentrations achieve the maximum values from February to June.

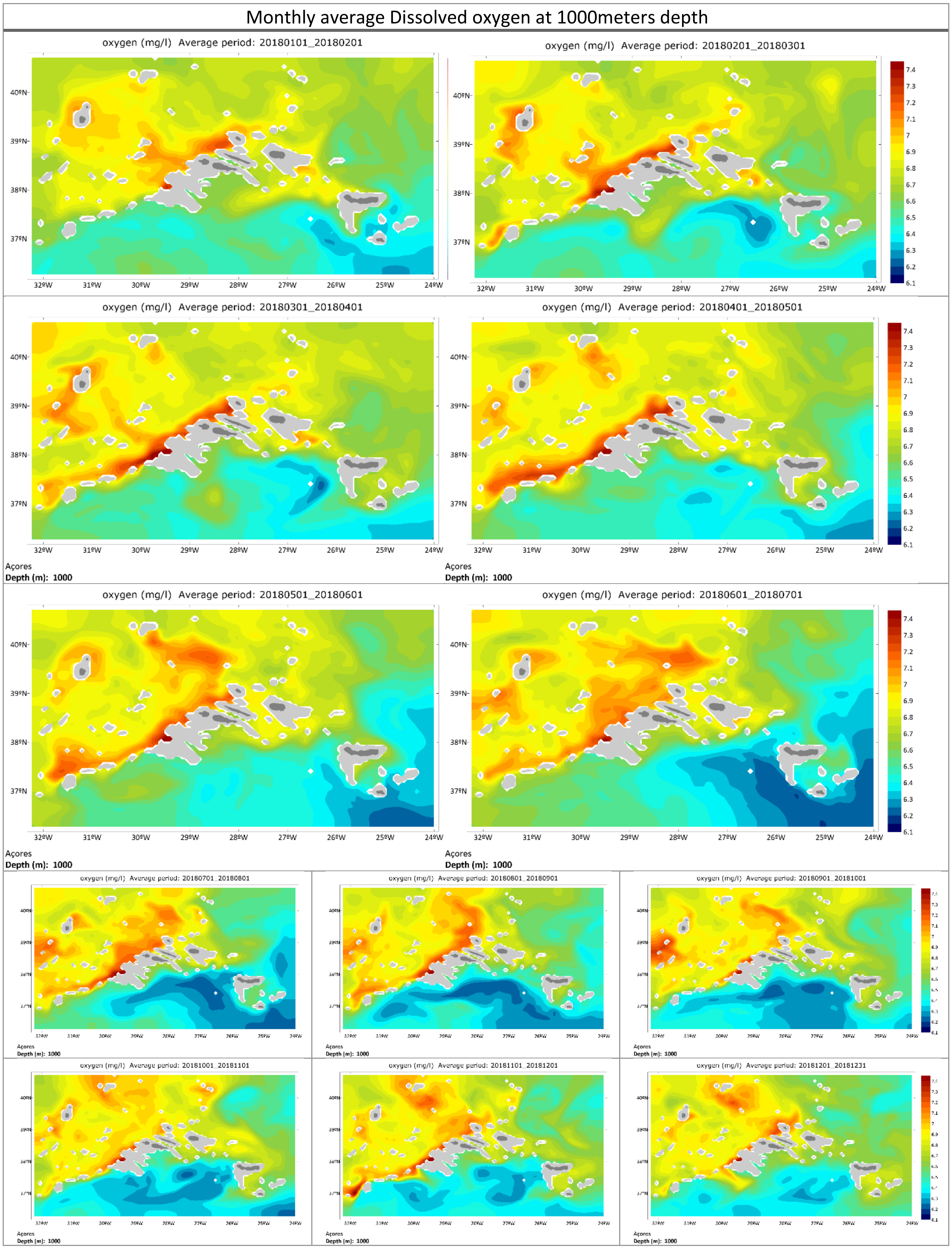
Monthly average Dissolved oxygen at 1000meters depth

oxygen (mg/l) Average period: 20180101_20180201

oxygen (mg/l) Average period: 20180201_20180301

oxygen (mg/l) Average period: 20180301_20180401

oxygen (mg/l) Average period: 20180401_20180501

oxygen (mg/l) Average period: 20180501_20180601

oxygen (mg/l) Average period: 20180601_20180701

oxygen (mg/l) Average period: 20180701_20180801

oxygen (mg/l) Average period: 20180801_20180901

oxygen (mg/l) Average period: 20180901_20181001

oxygen (mg/l) Average period: 20181001_20181101

oxygen (mg/l) Average period: 20181101_20181201

oxygen (mg/l) Average period: 20181201_20181231

Figure 3.41- Monthly average for dissolved oxygen model results at 1000meters depth from January 2018 to December 2018

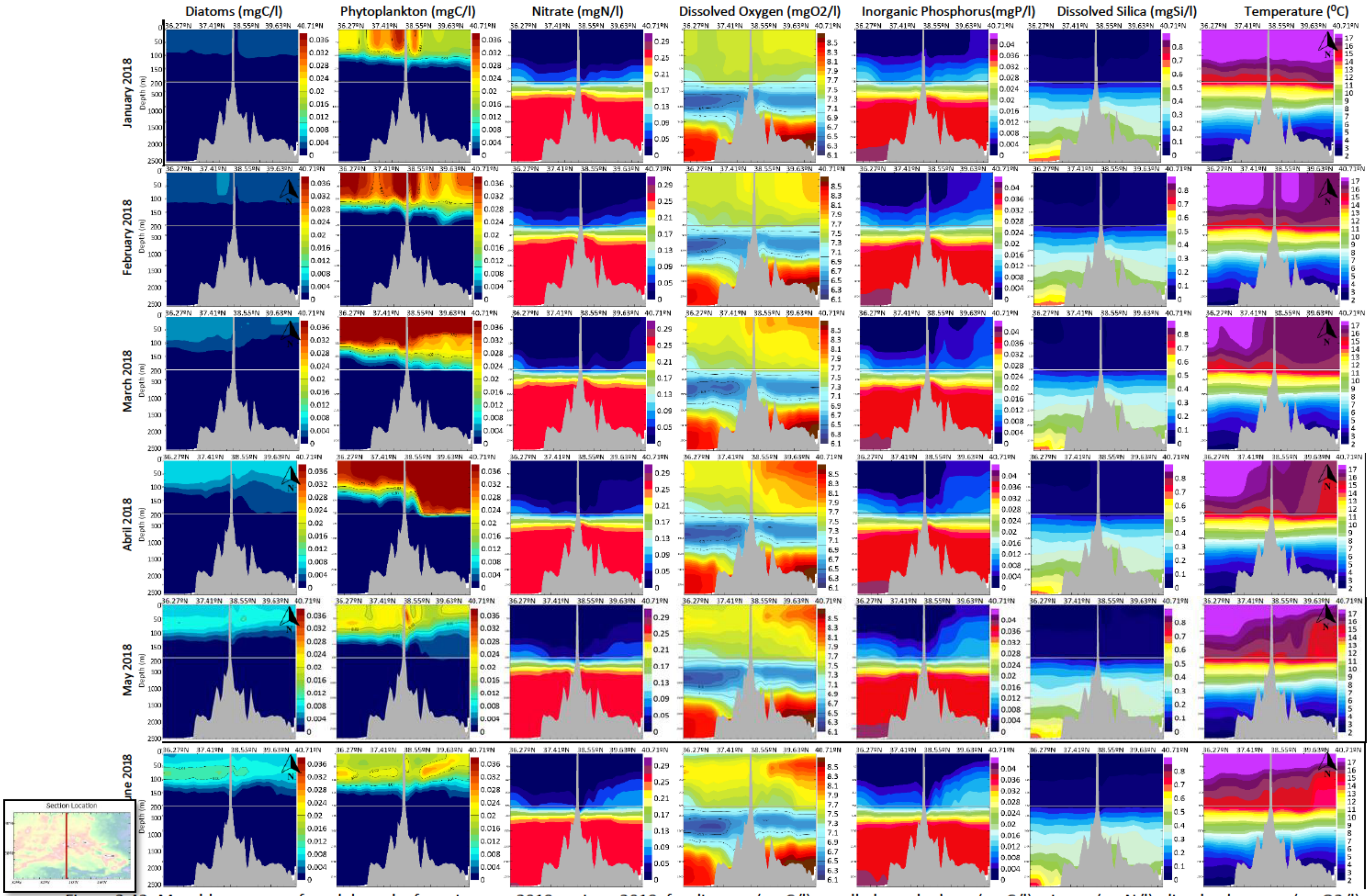

Figure 3.42- Monthly average of model results from January 2018 to June 2018, for diatoms (mgC/l), small phytoplankton (mgC/l), nitrate (mgN/l), dissolved oxygen (mgO2/l), inorganic phosphorus (mgP/l), dissolved Silica (mgSi/l), and temperature (ºC) along water column (from surface 3000meters depth), along the meridional section at -28.5ºW, from 36.27ºN to 40.71Nº. Depth profiles present a higher resolution until 250 meters depth, and less resolution from 250 meters until 3000 meters depth

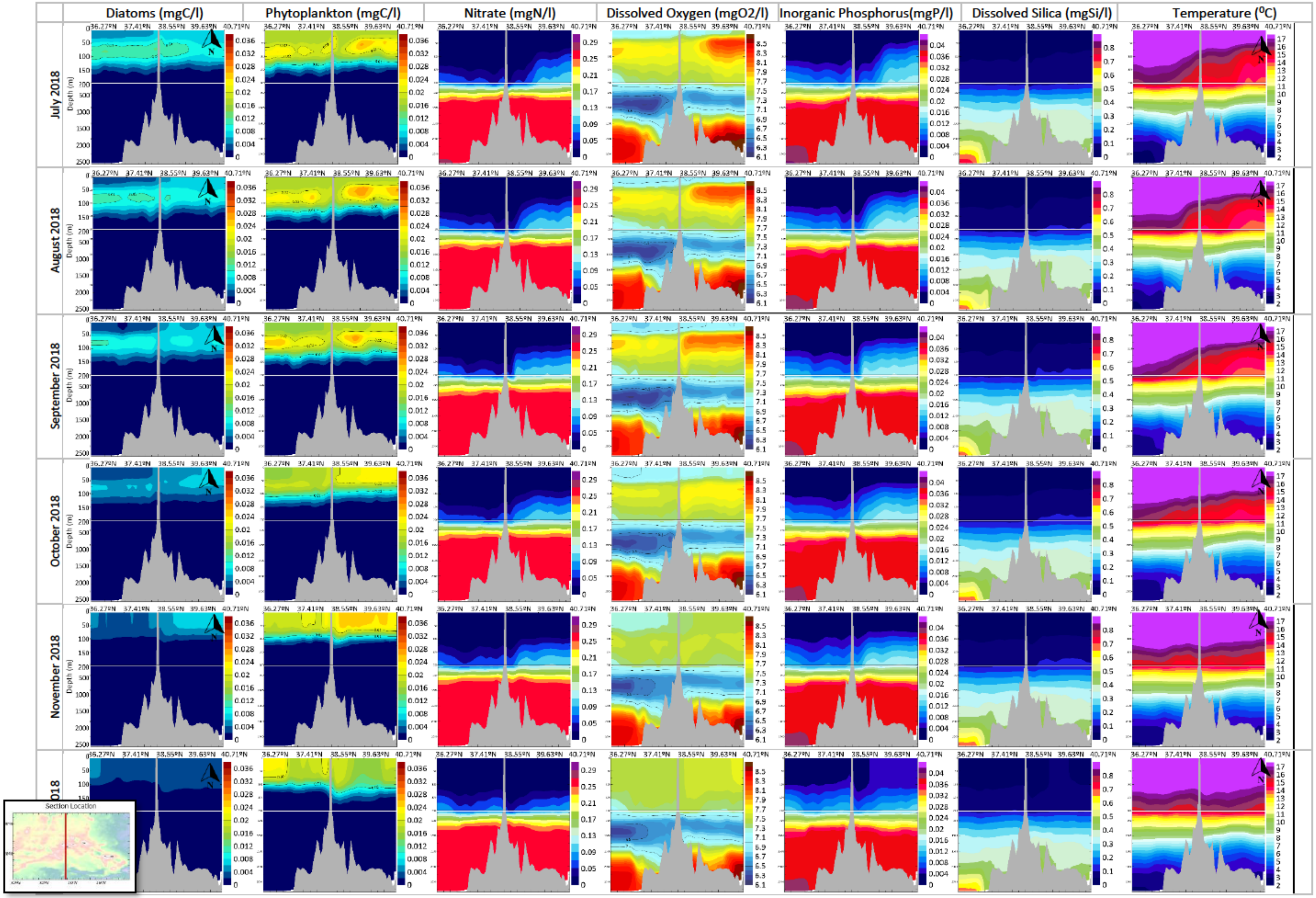

Figure3.43- Monthly average of model results from July 2018 to December 2018, for diatoms (mgC/l), small phytoplankton (mgC/l), nitrate (mgN/l), dissolved oxygen (mgO2/l), inorganic phosphorus (mgP/l), dissolved Silica (mgSi/l), and temperature (⁰C) along water column (from surface 3000meters depth), along the meridional section at -28.5W Depth profiles present a higher resolution until 250 meters depth, and less resolution from 250 meters until 3000 meters depth.

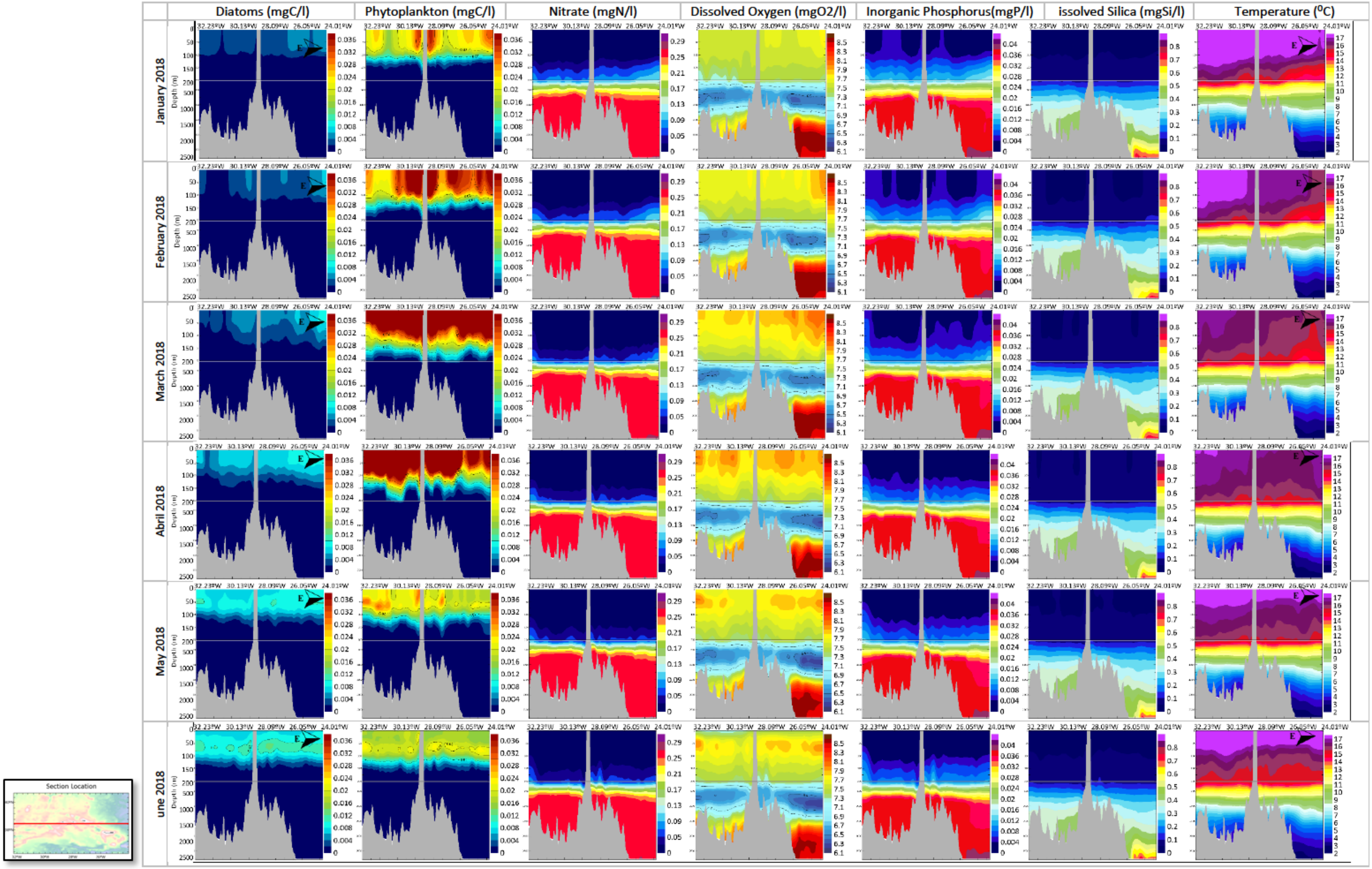

Figure 3.44- Monthly average of model results from January 2018 to June 2018, for diatoms (mgC/l), small phytoplankton (mgC/l), nitrate (mgN/l), dissolved oxygen (mgO2/l), inorganic phosphorus (mgP/l), dissolved Silica (mgSi/l), and temperature (ºC) along water column (from surface 3000meters depth), along the zonal section at 38ºN. Depth profiles present a higher resolution until 250 meters depth, and less resolution from 250 meters until 3000 meters depth

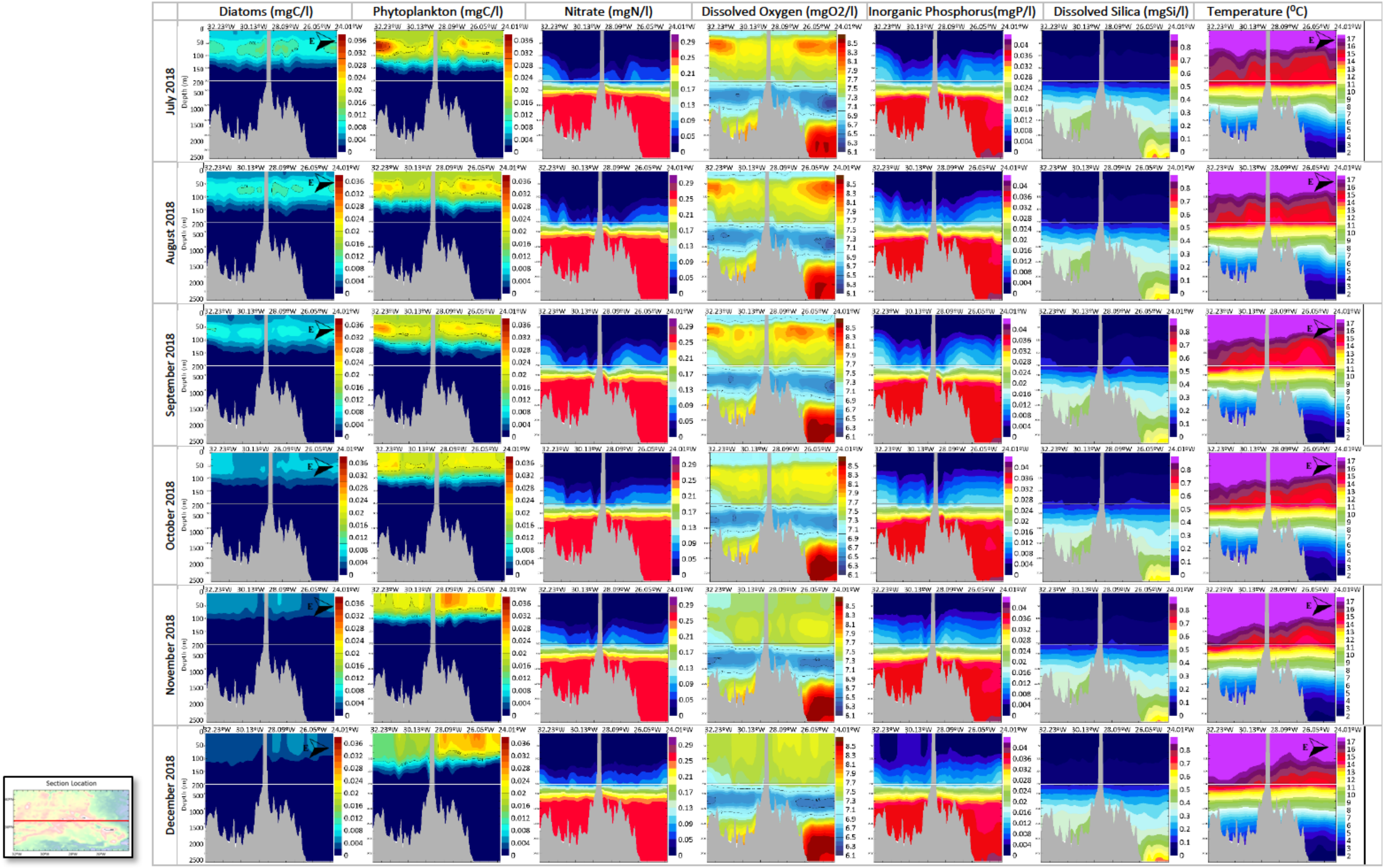

Figure 3.45-Monthly average of model results from July 2018 to December 2018, for diatoms (mgC/l), small phytoplankton (mgC/l), nitrate (mgN/l), dissolved oxygen (mgO2/l), inorganic phosphorus (mgP/l), dissolved Silica (mgSi/l), and temperature (ºC) along water column (from surface 3000meters depth), along the zonal section at 38ºN. Depth profiles present a higher resolution until 250 meters depth, and less resolution from 250 meters until 3000 meters depth

3.4.5. Mixed layer depth and nutrient dynamics

The mixed layer depth (MLD) is defined as the uppermost layer of uniform density (constant temperature and salinity) (Thomson and Fine, 2003). Mixed layer dynamics act directly, on the nutrient supply, on the availability of light, and consequently, on phytoplankton dynamics (Doney et al., 2001).

The average MLD for the study area reveals a highly seasonal pattern, Figure 3.46, with a larger MLD during winter, achieving 160 meters depth during late February and March. In spring and summer, the seasonal stratification begins and the mixed layer shallows to its minimum, 20 meters depth, during the summer (late June, July and August). The larger MLD matches with the highest nitrate concentration at the surface, with a maximum value of 0.02 mgN/l in February. The nutrient increase at the surface is followed by a phytoplankton maximum concentration (a strong spring bloom for small phytoplankton, and a lighter increase for diatoms biomass), during March and April. After this spring bloom, the nitrate concentration at the surface is depleted, and the phytoplankton concentration remains on the minimal values (0.004 mgC/l for small phytoplankton and 0.001 mgC/l for diatoms).

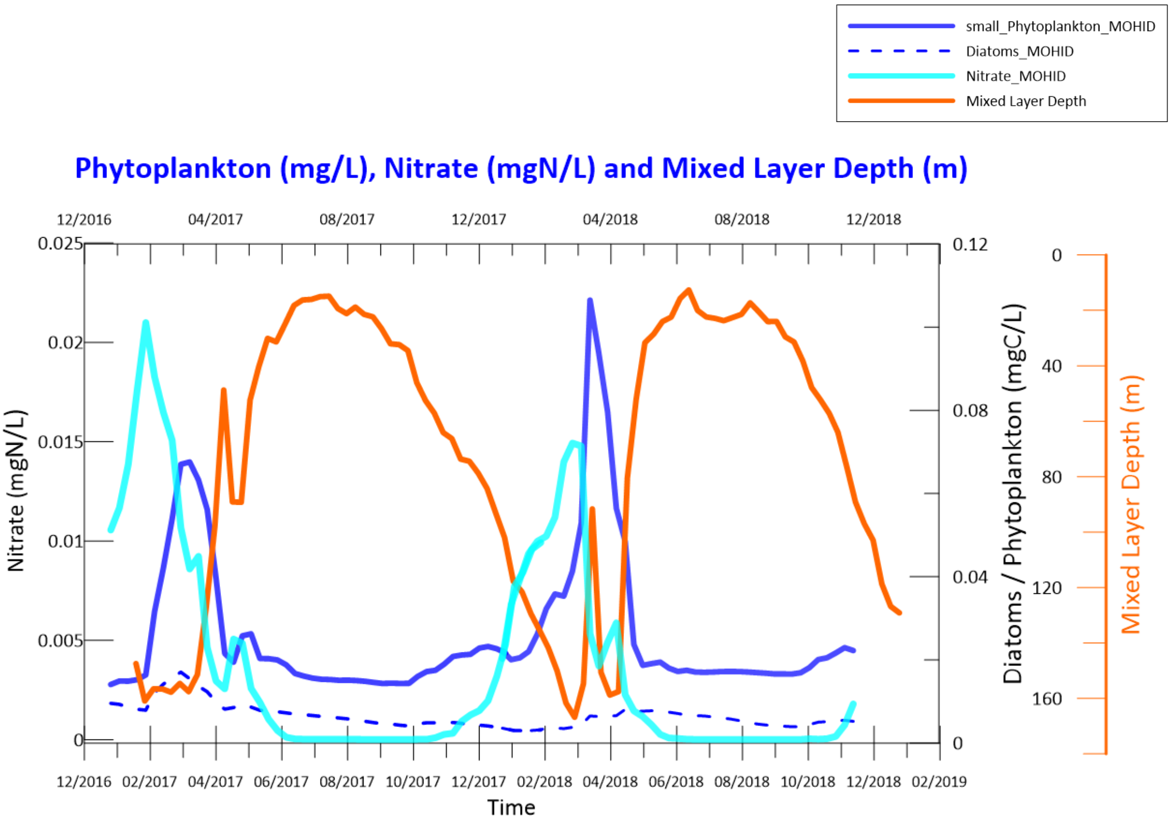

Figure 3.46- Surface average results for phytoplankton and diatoms concentration (in mgC/l), in dark blue; for Nitrate in light blue, and mixed layer depth (meters) in orange. All results are weekly averaged, for 2017 and 2018.

The MLD, nitrate and phytoplankton concentrations have similar seasonal patterns. The shallowing of the MLD is proceeded by nitrate concentration decrease at the surface. During April 2017 and 2018, an episodic MLD deepening (from 50 meters to 80 meters in April 2017 and from 100 meters to 160 meters depth in April 2018) proceeded by an increase of nitrate concentration in both situations. Phytoplankton concentration is in phase with the nutrient dynamics, the increase of phytoplankton biomass occurs after the increase of nutrient concentrations at the surface. The MLD deepens from September and reaches its maximum (>160m) in March. After the beginning of the deepening, in October, the phytoplankton concentration at the surface started to increase (from 0.0125 to 0.025 mgC/l from October to December 2018). This increase corresponds to the autumn phytoplankton bloom, with a smoother increase than the spring phytoplankton bloom.

3.4.6. Spatial distribution of the Mixed Layer Depth

The spatial variability of the MLD is highly dynamic in the Azores region. The North of the Azores region is characterized by stronger winter vertical mixing and the MLD can go up to 250 meters depth (Figure 3.47), while in the south of the domain, it goes only until 100 meters depth. Contrasting with the winter months, during summer the MLD is shallower.

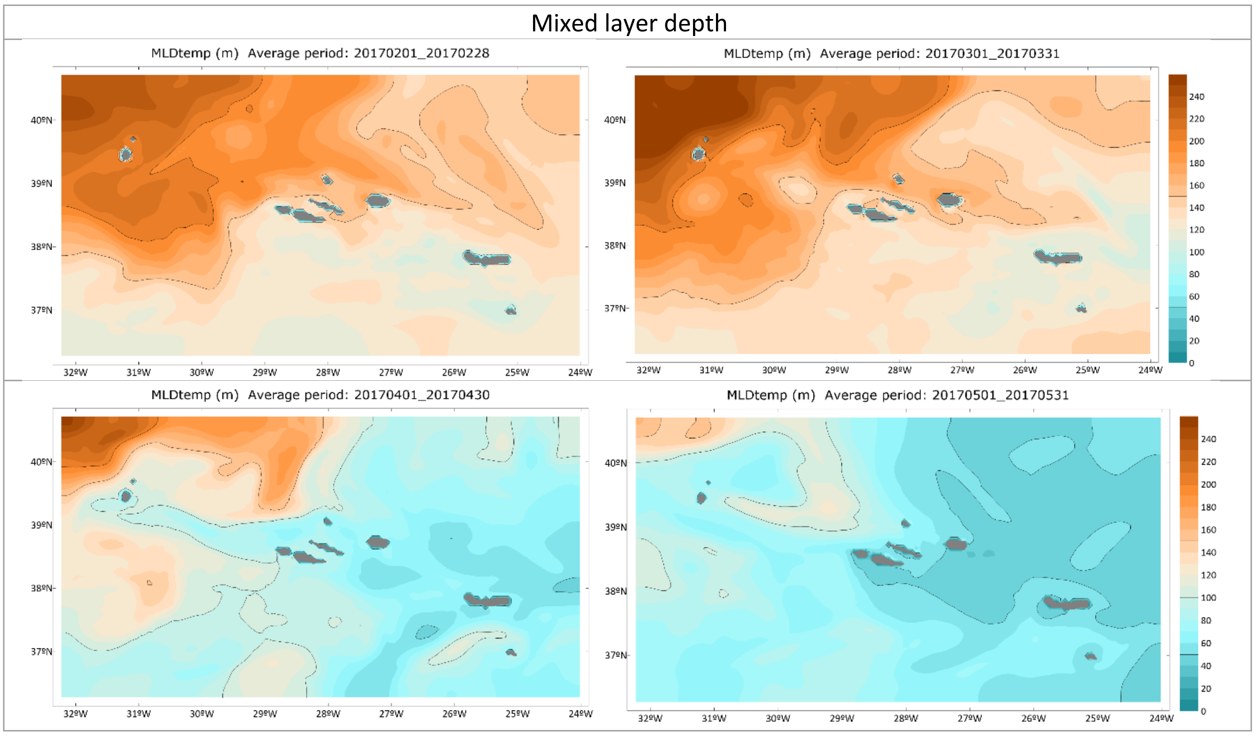

Figure 3.47- Monthly average for mixed layer depth, in meters, from February 2017 to May 2017, using a colour scale between 0 and 250 meters

Around the islands, the MLD is generally above the 25 meters depth. In the Central and Eastern quadrants of the domain, the MLD can achieve a depth between 15 and 35 meters depth, while on the Western there is more variability, with higher MLD in June (Figure 3.48). Spatial variation also reveals a longitudinal gradient. During winter (), around the islands from the Western Group (WG), the MLD can go up to 250 meters in depth, in the central part of the domain up to 150m and in the eastern part around 75 meters. The same regional gradient was verified by Valente, 2003.

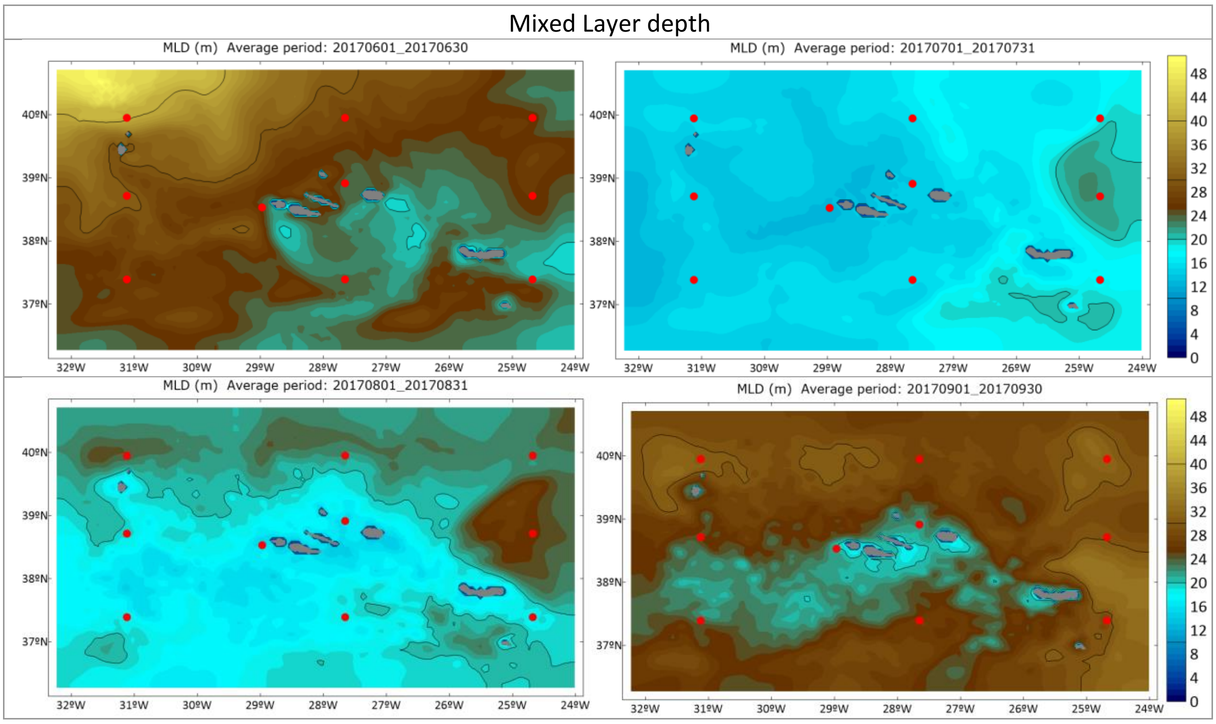

Figure 3.48- Monthly average for mixed layer depth, in meters, from June 2017 to September 2017, using a colour scale between 0 and 50 meters. Red points represent the locations used for model validation.

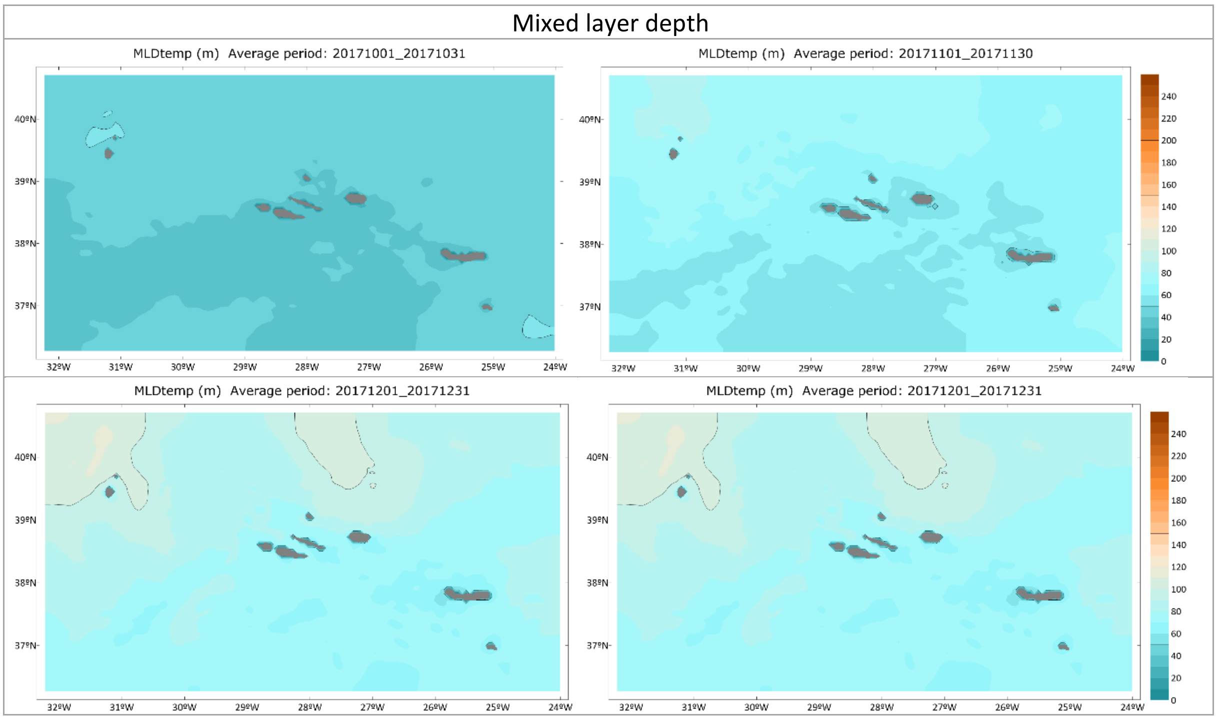

Figure 3.49-- Monthly average for mixed layer depth, in meters, from October 2017 to January 2018, using a colour scale between 0 and 50 meters. Red points represent the locations used for model validation.

3.4.7. Hydrodynamic spatial and seasonal patterns

The hydrodynamic patterns in the Azores from 2017 to 2018 present a higher spatial and seasonal variability. At the surface, the northern part of the study area is characterized by a strong current from the West, moving Southeastward, surrounding the islands on their northern side (Figure 3.50). These strong currents, for the year 2018, achieved velocities higher than 0.3m/s from September to December. The velocities are lower near the islands (0.1m/s) and in the southern part of the domain. Spatial hydrodynamic patterns are associated with the topography of the Azores region. At 500 meters depth, (Figure 3.53 to Figure 3.56), the direction and velocity of the major hydrodynamic patterns are shaped by the archipelago bathymetry. From July to September, two major hydrodynamic patterns stand out, one in the north of the islands, and a different one in the south, with velocities up to 0.15m/s. From January to April, a mesoscale vortex is formed between the islands of the Central Group and the Western Group. This vórtex moves westwards surrounding the Western Group during May, June and July 2018. At 1000 meters depth, the current velocities are weak, ranging mainly from 0 to 0.06m/s. The higher velocities occur from July to September 2018, moving Westwards, in the south of the archipelago, surrounding the archipelago and the MAR on their southern side. During the winter months (November, December and January, February), a strong current, moving from the northeast, forms intense hydrodynamic patterns in the North of the Eastern Group, with velocities up to 0.14m/s. However, these currents contrast with the lower velocities (0 to 0.02m/s) in the East and the North limits of the domain. At 2000 meters depth, the lower velocities are dominant (<0.05 m/s). The higher velocities occur in the vicinity of the Eastern Group from November to March, where the and southeast of the MAR from August to October, with velocities of 0.12 to 0.14m/s.

Vertical meridional and zonal sections, along the domain (Figure 3.53 to Figure 3.56) clearly show the vertical gradient of the velocity modulus. At the surface layers, the velocity modulus can be higher than 0.25m/s, decreasing along the water column up to velocities close to zero near the bottom. The stronger velocities can achieve depths up to 500 meters in the northern part of the domain, during most of the year, between 39.6ºN and 40ºN.

During the summer months of July and August 2018, in the southern part of the domain, a strong velocity modulus can be identified at the South of the Central Group, Figure 3.35, with velocities ranging from 0.15 to 0.18m/s from 500 meters depth up to 1500 meters depth, moving westwards, as can be seen by the negative value of the velocity u component (represented on the first column of Figure 3.54), and, as was visible on Figure 3.52.

The analysis of the different velocity components helps to better study the hydrodynamic patterns along the water column. The velocity vector $\vec{u}$ describes the longitudinal transport, the velocity vector $\vec{v}$ the latitudinal.

The meridional section at -28.5ºW, crossing the Central Group, (Figure 3.53 and Figure3.54), shows that the dominant current in the north of the central group is moving North-South from January to June (negative values in the velocity $\vec{v}$ component), and from South to North from July to December (positive values in the velocity $\vec{v}$ component). However, in the vicinity of the central group, close to the island slope, the current is mostly moving north-south, on the northern slope, and south-north on the southern slope. At this location the vertical velocity (velocity component $\overrightarrow{w}$), is mostly negative. The analysis of the component $\overrightarrow{w}$ must be taken with caution due to its lower amplitude. The magnitude of the vector $\overrightarrow{w}$ ranges from -0.0002 to 0.0002m/s, three orders of magnitude lower than the vector $\vec{u}$ and $\vec{v}$, which makes this analysis more sensitive than quantitative.

Along the meridional section of 38.5ºN, between the MAR and the Central Group, current velocities can have different directions at the surface layers than below 500 meters depth. Moving westward in the upper layers, and eastward below 500 meters depth, from June to November (Figure 3.55 and Figure 3.56).

The vertical component (velocity component $\overrightarrow{w}$), is very variable along the archipelago slope. However, reveals the predominance of upward velocity at depths between 1000m to 2000 meters depth. Above 1000 meters depth, the meridional transect at -28.51ºN reveals a mostly downward velocity, along the north and south slope of the Central Group (Figure 3.55 and Figure 3.56).

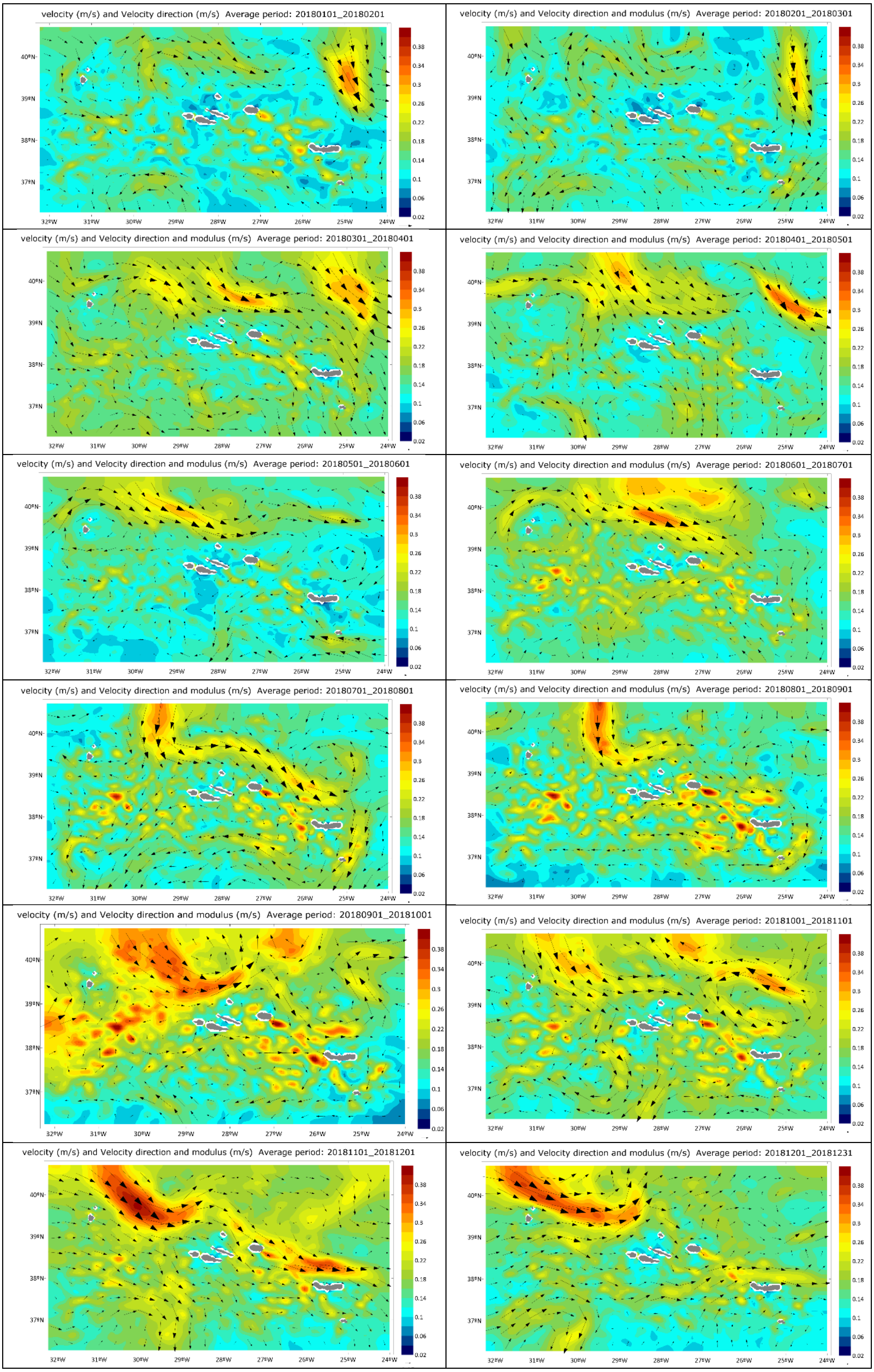

Figure 3.50- Monthly average, from January to December 2018 of velocity modulus and direction at the surface

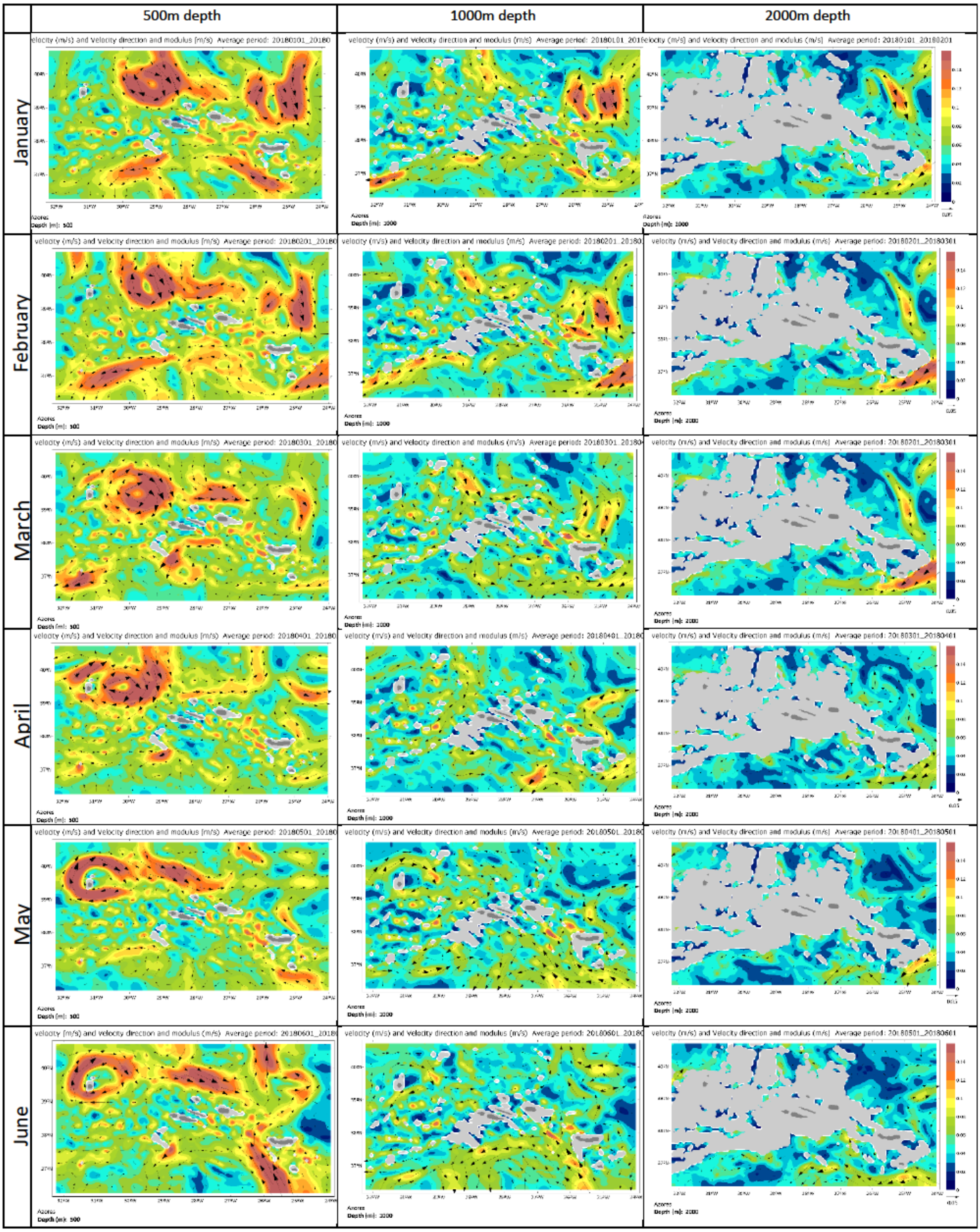

Figure 3.51- Monthly average, from January to June 2018 of velocity modulus and direction at surface, 500m 1000m and 2000m depth. All images are plotted with the same colour scale.

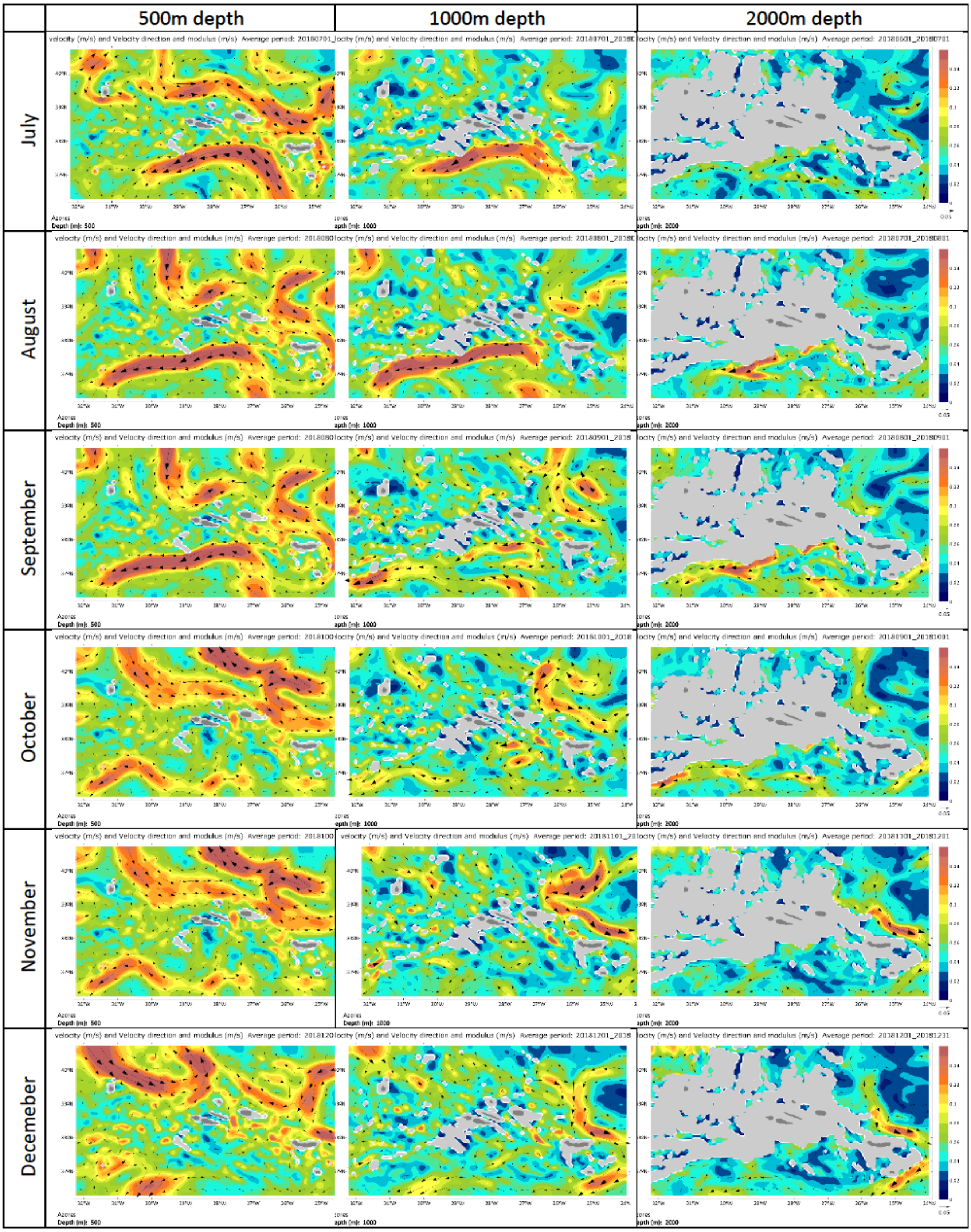

Figure 3.52- Monthly average of velocity modulus and direction, 500m 1000m and 2000m depth. All images are plotted with the same colour scale

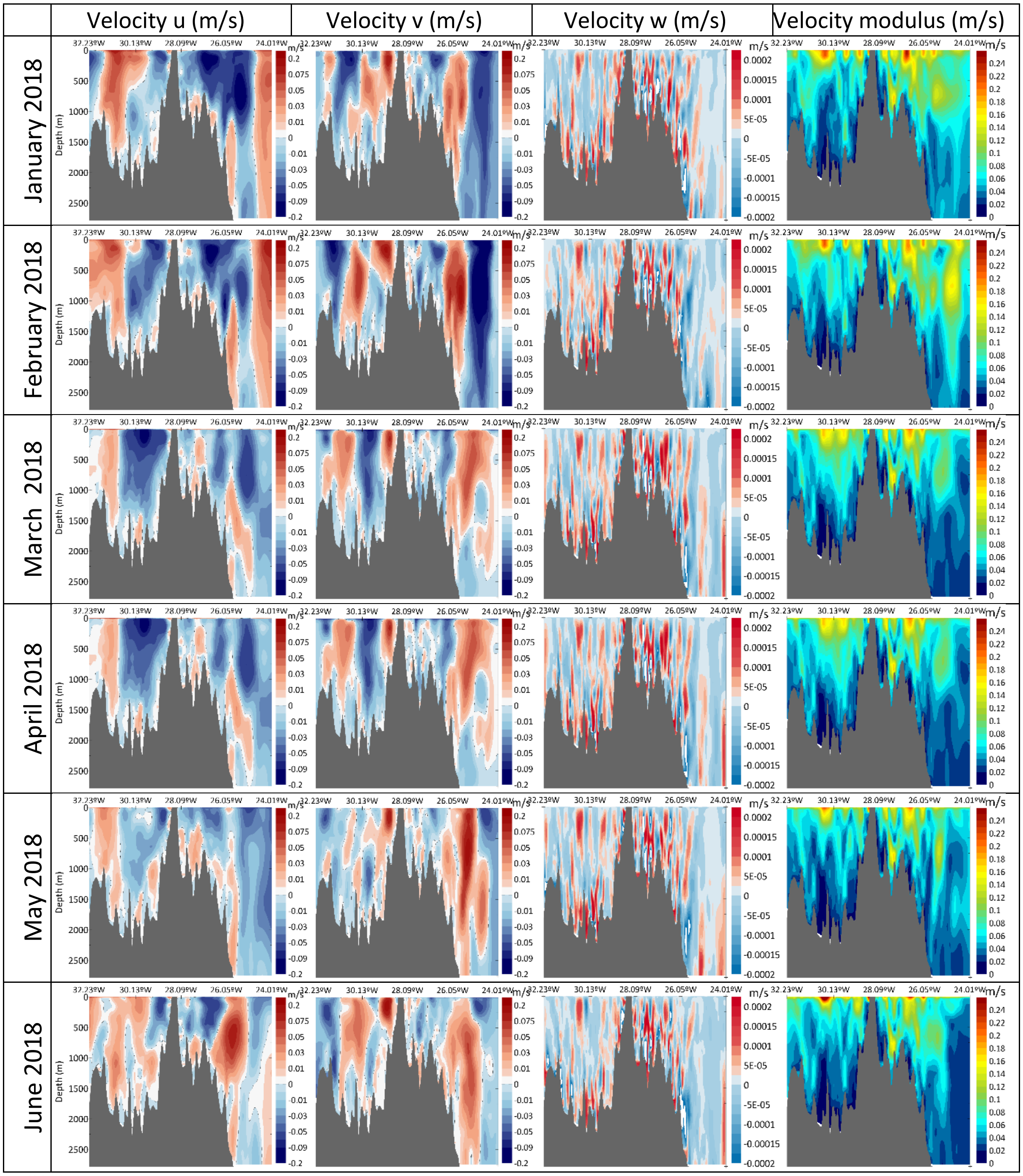

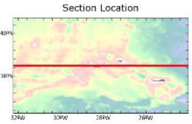

Figure 3.53 - Monthly average of velocity u, v, w and velocity modulus in m/s along the water column in the zonal section of 38.5ºN for January to June 2018

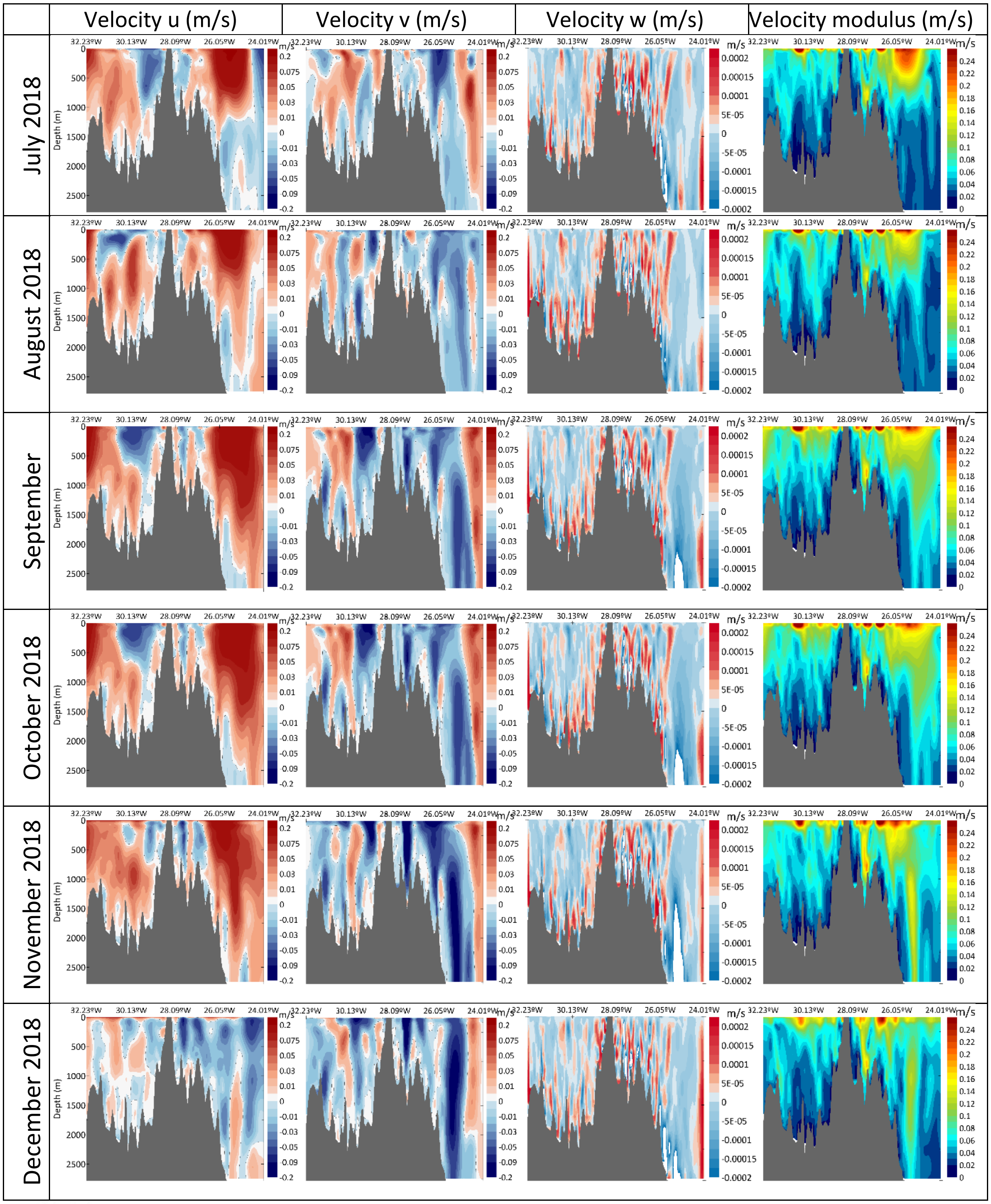

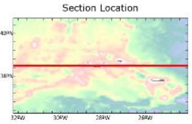

Figure 3.54 - Monthly average of velocity u, v, w and velocity modulus in m/s along the water column in the zonal section of 38.5ºN for June to December 2018

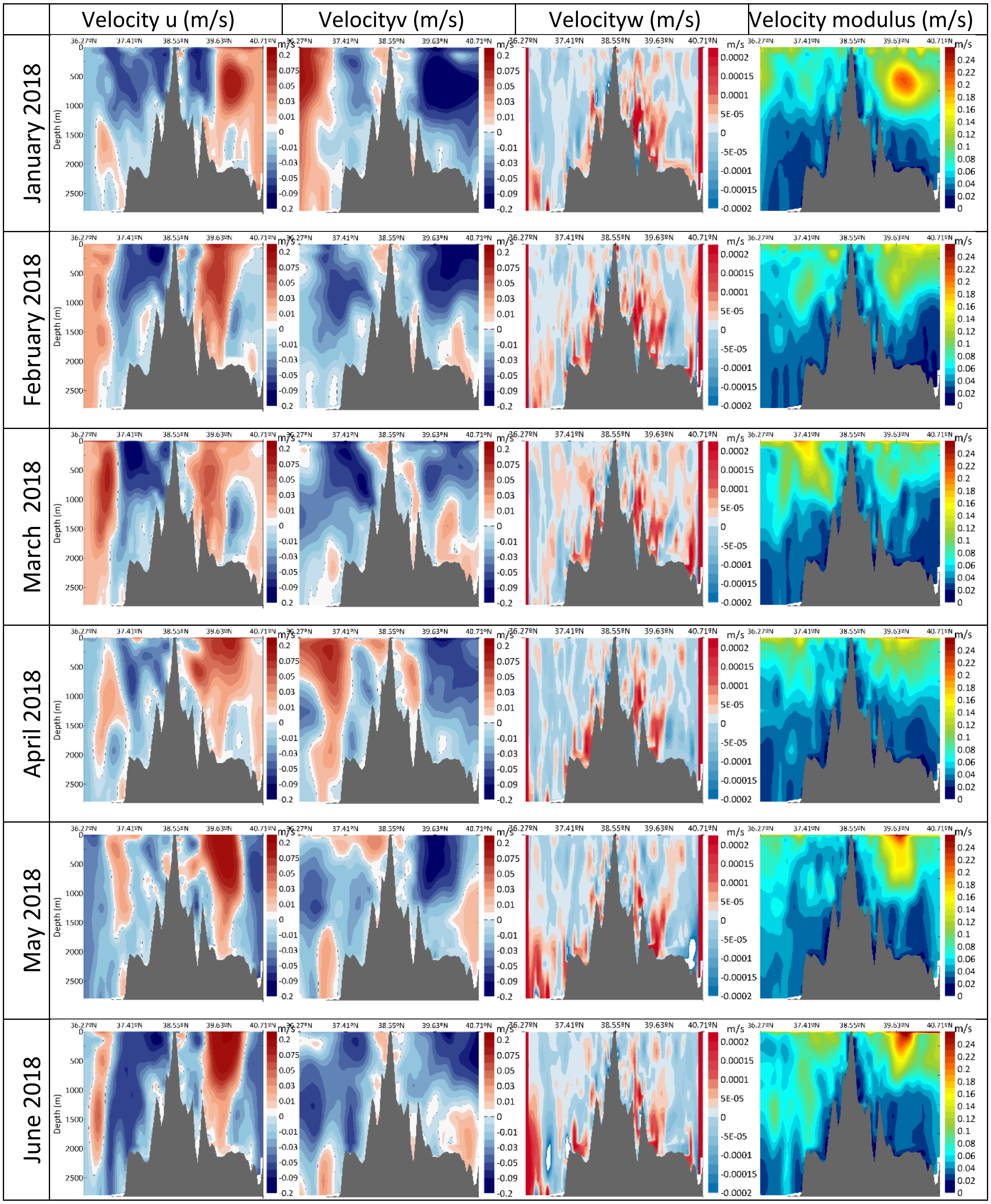

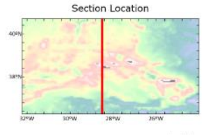

Figure 3.55- Monthly average of velocity u, v, w and velocity modulus in m/s along the water column in the meridional section at -28.5ºW, for January to June 2018

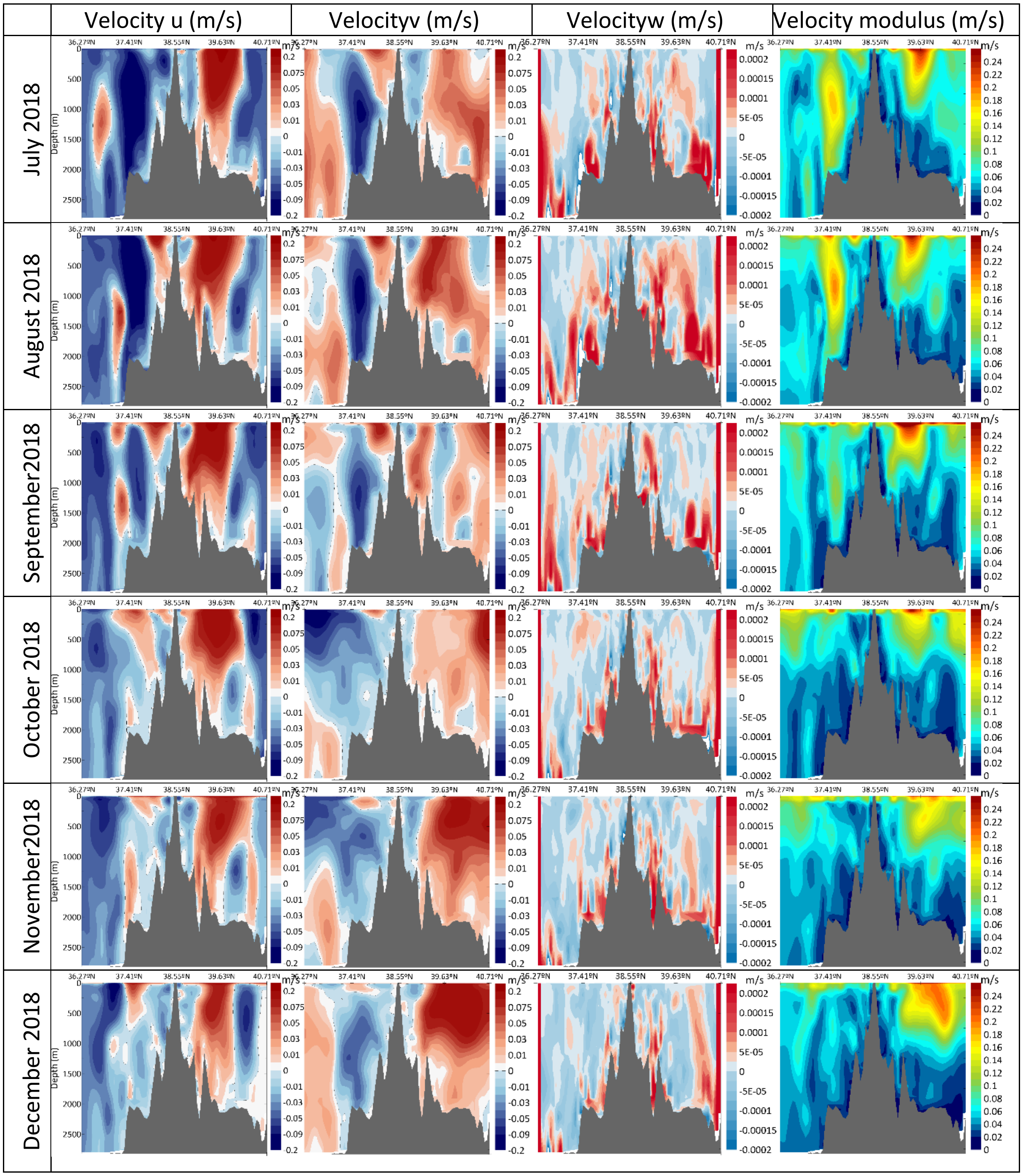

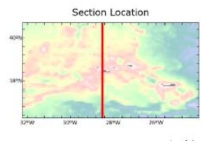

Figure 3.56- Monthly average of velocity u, v, w and velocity modulus in m/s along the water column in the meridional section at -28.5^{o}W, for June to September 2018

3.5. Discussion

The leading objective of this chapter was to implement a biogeochemical model able to simulate the general biotic and abiotic characteristics in the Azores region to better understand and study their dynamics. The present configuration of the MOHID biogeochemical model reproduced adequately the dynamics of different biogeochemical variables (phytoplankton, nutrients and dissolved oxygen) in the Azores.

3.5.1. Model parameterization assessment

The calibration work was processed in a step-by-step approach, with successive model runs, starting with the standard model parametrization values, testing values from other biogeochemical models and case studies, and considering values within the range of literature, until a satisfactory fit was obtained for the Azores region, with model results able to simulate the general spatial and seasonal dynamics.

The MOHID biogeochemical model runs over a hydrodynamic solution previously validated for the Azores region (Chapter 2). In MOHID the biogeochemical processes are solved by the "Water quality module", inside each control volume (domain grid cell). This "offline" coupling of transport processes and biogeochemical processes is a common approach used on local, regional and global models (e.g. Aumont et al., 2015; Fennel et al., 2006; Hashioka et al., 2013). The biogeochemical model time step can be, and often is, different from the transport model time step. The latter needs, due to numerical reasons, smaller time steps than the biochemical models. In this application, the hydrodynamic model has a timestep of 120 seconds, while for water quality the timestep is 3600 seconds, increasing computational efficiency.

Since biogeochemical models are more detailed and complex, it is important to define modelling objectives, to calibrate the model to pursue those objectives. In this case, the major objective was to simulate biotic dynamics in the Azores region, to provide 3-dimensional results to proceed to further studies, and to support the current scientific needs in the Azores. This application was applied to study biogeochemical processes at a regional scale, to support other studies, and to provide biogeochemical data for the entire Azores region. The model was applied, calibrated and validated for the years 2017 and 2018.

Phytoplankton growth is driven both by the physical and environmental conditions in the ocean and in the interface with the atmosphere(Fasham et al., 1985). Being the Azores region characterized by a high spatial, and seasonal variability of the marine environment (Amorim et al., 2017; Valente, 2013), and a highly dynamic region, influenced by different ocean currents and water masses (Palma et al., 2012; Sala et al., 2016), this calibration process is very particular for this region.

Because phytoplankton rules the major biotic processes in the epipelagic zone, the model was calibrated firstly by tuning phytoplankton growth and the different limitation growth factors. Different model parameterization tests were performed based on other models and case studies, as compiled in Table 3.7 to Table 3.11. Besides the growth rates, also "bottom-up", and "top-down" processes were studied. The bottom-up control refers to the different limitation factors such as nutrient limitation, light limitation and temperature control, and "top-down" control is performed by grazing pressure by zooplankton (Chen et al., 2014; Daewel et al., 2019; Hashioka et al., 2013).

Different growth rates and limitation factors were used for small phytoplankton and diatoms, to find the best fit for the Azores region. Conceptually, smaller phytoplankton have advantages for light and nutrient harvesting by their relatively high surface/volume ratio, which allows more efficient exploitation at low nutrient concentrations, and consequently a higher growth rate. Larger phytoplankton, namely diatoms, have an advantage in utilizing nutrient pulses and exploiting vertical gradients (Sommer et al., 2017). For these reasons, in the Azores, an oligotrophic region (due to the low nutrient concentrations), it could be expected small phytoplankton have higher growth rates. However, several studies show that this statement cannot be considered in all situations (Barcelos e Ramos et al., 2017; Karpowicz et al., 2020; Teira et al., 2005). Hashioki et al., 2013, performed an inter-comparison study with different biogeochemical models (PISCES, NEMURO, PlankTOM5 and CCSM-BEC), and showed how different models need different parametrizations to regulate phytoplankton growth, due to the different governing processes and model configurations. Also, phytoplankton growth is driven by physical and environmental conditions (e.g. currents, wind, upwelling, vertical mixing, solar radiation, temperature, and nutrient availability) (Fasham et al., 1985) making this calibration and parameterization processes unique for each location. The same is valid for the half-saturation constants that, in general, increase with the size of the phytoplankton cell as a consequence of a smaller surface-to-volume ratio (Eppley and

Thomas, 1969). Diatoms should have larger half-saturation constants than small phytoplankton, however, these constants are very difficult to quantity (Mulder and Hendriks, 2014) and can change orders of magnitude between different models (Table 3.10 and Table 3.11)). Several tests were performed until achieve a parameterization able to mimic the general phytoplankton dynamics for this case study.

The use of the modified *Ks* (Nitrate half-saturation factor) allows having better results regarding phytoplankton growth, considering that phytoplankton can adapt nutrient uptake considering environmental concentrations, reducing efficiency under high nutrient conditions, and increasing efficiency under oligotrophic and lower nutrient concentrations (Buchanan et al., 2018).

Finally, to fine-tune the solution, the parameterization process focuses on the “top-down” process. In MOHID this top-down control allows parameterizing the zooplankton grazing and its preference for small phytoplankton or diatoms. The effect that the top-down processes have on phytoplankton and diatoms concentration controls the general concentration maintaining the same seasonal patterns (Figure 3.13). The limitation of phytoplankton concentration resulting from zooplankton grazing plays an important role in controlling the phytoplankton bloom. The model considers a minimum threshold for phytoplankton concentration below which grazing ceases, to avoid total phytoplankton depletion.

These calibration and parametrization processes were performed and assessed by comparing model results for the different parameterizations with available data (remote sensing data, WOA and CMEMS-Bio model), until achieving a parameterization able to simulate the general seasonal and spatial biotic patterns in the Azores region.

3.5.2. Model validation and results

All the model parameterization and calibration processes are reflected in the model performance. Model validation for phytoplankton at the surface reveals that seasonal and spatial phytoplankton concentrations are well reproduced (Figure 3.15). The seasonal cycle of surface phytoplankton is in phase with satellite estimations (for chlorophyll_a) (Figure 3.15). The model can simulate the prevalent strong spring bloom and a smoother Autumn bloom. However, the solution is overestimating the phytoplankton concentration at the surface

(Figure 3.15). Nevertheless, the higher positive bias occurs when the error of the solution (RMSE) is higher, during the spring phytoplankton bloom. This overestimation of phytoplankton concentration during the bloom was also detected in other model applications in oligotrophic regions (Gutknecht et al., 2016). This difficulty in simulating with precision the phytoplankton bloom is transversal to the general biogeochemical models and is one of the major challenges of biogeochemical modellers (Hashioka et al., 2013). The constant Chl:C ratio used in MOHID, to compare phytoplankton concentration with satellite chlorophyll_a concentrations, can also contribute to this bias. MOHID uses the simplistic fixed C:Chl ratio, likewise in other biogeochemical models (Aumont, 2005; Ilyina et al., 2013; Palmer and Totterdell, 2001) (see Table 3.5). However, it is known that this relationship is highly variable and can change with temperature, daily irradiance and nutrient concentration (Cloern et al., 1995; Geider et al., 1997) since phytoplankton tends to adapt their C:Chl ratio to the prevailing environmental conditions. However, even complex biogeochemical models generally use a constant C:Chl ratio on phytoplankton estimations. This is a typical approach for global and regional models where this empirical Chl:C reveals adequate to simulate oceanographic modelling scenarios, despite the associated error (Ayata et al., 2013).

Analyzing these results on a spatial scale, this positive bias does not occur near the islands, but near the borders, concurrently with higher error values (RMSE) and lower correlation values (Figure 3.20 and Figure 3.21). These statistical results highlight the importance of choosing a model domain bigger than the area of interest, to dissipate the boundary conditions limitations. Results indicate that MOHID can improve the solution from the borders of the domain to the centre. Around the islands is clear an underestimation of phytoplankton values, negative BIAS, that can be a consequence of local islands inputs, that are not considered by the model once that on this model configuration, the nutrients inputs are only from the oceanography general conditions.

Model validation was performed with WOA climatology and CMEMS-bio model results, and remote sensing data. WOA climatology is based on a collection of scientifically quality-controlled oceanographic in-situ data (Garcia et al., 2018). It is a widely used product for ocean model initialization and validation, climate studies, and operational forecasting, with the advantages of being based on thousands of in-situ measurements (with no satellite or model data) providing a climatological mean with global coverage. However, while it is useful as a climatology database, it does not represent small-scale (temporal and spatial) variations, which can be limiting for small-scale models (spatially and temporally).

Model (MOHID and CMEMS-Bio) results and WOA exhibit a difference, which may be due to the different timescale. While WOA has a climatological monthly means scale, models have an hourly scale. However, it is visible that both models, MOHID and CMEMS-Bio, follow the same general behaviour as WOA climatology, showing that despite local and seasonal behaviour the ocean biogeochemical dynamics tend to follow a tendency. However, models and high-resolution models have the advantage of identifying and allowing to study of local and temporal behaviour that climatology cannot represent.

Validation results, for nutrient concentration at the surface and along the water column, are shown in Table 3.14 to Table 3.17, where can be seen that the seasonality of nutrient concentrations (nitrate, inorganic phosphorous and dissolved silica) is well computed by MOHID. The model simulates the expected behaviour for the study area, with an increasing concentration of nutrients in the winter, during December, January, and February, followed by a depletion during spring and summer when the lower values are achieved, typical of this oligotrophic region, to what follows an increase during fall and winter (Amorim et al., 2017; Valente, 2013). These results show that meteorological and ocean physical processes that drive the interannual variability of biogeochemical properties in the Azores region are well reproduced by the model.

MOHID validation against CMEMS-Bio and WOA, for Nitrate concentration at the surface, has correlation values of 0.928 and 0.896 respectively, evidencing the good MOHID performance. On the other side, the validation for inorganic phosphorous presents a lower correlation, with values of 0.5 against CMEMS-Bio and 0.558 against WOA. In both cases, MOHID is underestimating the nutrient concentrations at the surface. However, similarly to these nutrient underestimations, MOHID is overestimating the phytoplankton concentrations (Figure 3.15). So, this higher phytoplankton concentration induces higher nutrient assimilation, originating these lower nutrient concentrations at the surface. However, besides this mismatch, it is important to denote that the model can simulate the yearly seasonal variations.

Surface dissolved silica concentration reveals some mismatch compared with WOA climatology, with higher differences for July. For July, WOA climatology has a concentration value much higher than in the other months that does not follow the seasonal tendency of the following and previous months, nor even the typical silicate patterns in the North Atlantic region (Amorim et al., 2017; Garcia et al., 2013). Analysing the seasonal WOA nutrients average results (averaged for the entire domain), it is visible a higher variability in dissolved silica values, than for nitrate or phosphate. This mismatch also occurs when comparing WOA against the CMEMS-Bio results. Another in-situ data source could provide additional data to better understand this mismatch. Also, a longer simulation run could help to understand these results. This simulation was only performed for 2 years, not enough to infer if it is a spatial or temporal limitation that is causing this difference between MOHID results and WOA data. Nonetheless, a comparison between MOHID and the CMEMS-Bio model reveals a good correlation (0.983) for dissolved silica values.

Monthly average results along the water column at fixed points show that MOHID can simulate correctly the nutrients and oxygen concentrations along the water in the different regions of the domain. The lowest correlation is observed in the dissolved oxygen concentrations (R=0.868). With MOHID reproducing lower concentrations than WOA. Similarly, CMEMS-Bio model results are also lower than the climatology. This underestimation is also reported in other model applications (Espinoza-Morriberon et al., 2016), which reports that it might be related to various factors such as: positive biases in old measurements, interpolation limitations, and the effects of variability in ocean circulation (Bianchi et al., 2012). Sensitivity studies of the oxygen simulation need to be explored to understand these differences. Also, for the surface, validation results have a negative bias, with MOHID higher than WOA climatology data. At the surface, oxygen concentration at the surface is highly related to the interface of water-air processes, influenced by temperature, pressure and wind can cause local and temporal oxygen dynamics (Buchanan et al., 2018), not characterized by the climatology of WOA.

Despite the negative bias, the model reproduced the vertical structure of the dissolved oxygen profile compared with WOA data (correlation of 0.865), with the minimum oxygen zone at the same depth (between 700/1000m depth).

Validation results show that this model application is capable of simulating the general biogeochemical patterns in the Azores region, at the surface, and along the water column. In the euphotic zone, the model can simulate phytoplankton growth, with nutrient assimilation (dissolved phosphorous, nitrogen, dissolved silica) and oxygen production. MOHID simulate the subsurface remineralization that conversely releases/consumes these elements (Matear and Hirst, 2003). MOHID can also reproduce the observed nutrient increase at the surface in the Winter resulting from the winter convection induced by the physical factors.

This model is a simplistic approximation of the complex lower trophic levels, considering only 2 Phytoplankton Functional Types, and 1 zooplankton group. This configuration is shared by many other biogeochemical model applications (Jung et al., 2020; Peña et al., 2016; Yool et al., 2013). Nevertheless, models are always a simplification of the ecosystem chains, and increasing the number of compartments will not necessarily improve the performance of the model given the difficulty of obtaining the necessary observations to guide and validate models (Peña et al., 2016).

The major limitation of this model assessment is the lack of in-situ data. The model is only being compared with a climatology (monthly based) and against another model. CMEMS-Bio model is frequently validated (Perruche C et al., 2016) and widely used, however, like any other model, has its constraints. This limitation of in-situ data scarcity is shared with other biogeochemical ocean model applications, that also use other ocean models for validation (Hjelmervik, 2012). In situ measurements collected during cruises can provide a high-quality but very sparse in time and space for validation of biogeochemical results (Lancelot et al., 2005).

New and more *insitu* data and biogeochemical and ecological observation systems will allow for significant advances in model calibration and development. The existence of long time-series data from insitu observatories and fixed stations could be advantageous.

3.5.3. Biogeochemical characteristics in the Azores

Model validation shows that MOHID simulates the general spatial and temporal biogeochemical patterns in the Azores region.

At the surface, is denoted a strong North-South gradient, with lower sea temperature in the North, and warmer in the South. The lower temperatures in the North of the domain are influenced by the atmospheric conditions but also by the cooler North Atlantic Water masses influence (Barton, 2001; Palma et al., 2012). For nutrients, phytoplankton and dissolved oxygen, a positive North-South gradient is notable. This gradient is denoted for nutrient concentration at the surface, but in the deeper layers is not so marked. These modelled nutrient gradients are in accordance with the typical patterns of the North Atlantic region (Garcia et al., 2018).

At the surface, the oxygen concentration has the lowest values during the summer months, and latitudinal and longitudinal gradients are denoted, with higher oxygen concentration in the North and the East (Figure 3.34). These spatial gradients follow the sea surface temperature distribution, with richer oxygen areas in the colder regions, and lower oxygen concentration in the southwest of the domain, where sea surface temperature is higher. This is can be related to the sea surface temperature that decreases the oxygen solubility hence decreasing oxygen concentration at the surface (Matear and Hirst, 2003). These gradients can be enhanced by the meanders of the major currents that influence the Azores region (Lafon et al., 2004): the cold southern branch of the North Atlantic Current, that crosses the Mid-Atlantic Ridge (MAR) at 45-48º N (Bower et al., 2002), and the warmer Azores Current (Figure 2.15), that crosses MAR south of the Azores at 34-36º N (Klein and Siedler, 1989).

The model can simulate the typical oxygen patterns along the water column, characterized by an increase in the euphotic zone, followed by a decrease until achieving a minimum oxygen concentration between 500m and 1000 meters depth. Below this minimum dissolved oxygen increases again reaching its maximum at the sea bottom. The typical ocean profile (Garcia et al., 2018). This increase is related to pressure rise and water temperature drop, inducing oxygen solubility. Furthermore, this increase in oxygen concentration can also be related to the physical processes of the deep ocean circulation, namely by the influence of the North Atlantic Deep Water, characterised by its lower temperature and higher oxygen concentrations, and observed about 2500 to 3000m and below, in the Azores region (Bashmachnikov et al., 2015; Palma et al., 2012). These factors contribute to the higher oxygen concentration in the northern part of the domain, rather than in the southern part (Figure 3.34).

In the euphotic zone, modelled oxygen concentration oxygen increases from the surface until 50 meters to 100 meters depth. This increase can be related to the oxygen produced by phytoplankton photosynthesis. Average oxygen patterns along the domain longitudinal and latitudinal transects show these relations. The higher oxygen average concentration (7.9mgO2/l) in the Western part of the domain matches with a higher phytoplankton average concentration. The monthly oxygen and phytoplankton concentrations along the water column (Figure 3.47 to Figure 3.50) show that maximum dissolved oxygen concentrations match the higher concentration of phytoplankton. This result shows that the model can simulate the production of oxygen by the photosynthesis process.

3.5.4. Biotic and abiotic processes in the Azores

Physical processes have a strong influence on biogeochemical patterns (Moll and Radach, 2003). The tendency of ocean circulation and mixing is to drive nutrients from areas of high to low concentration, to continually force surface nutrient concentrations toward deep concentrations and vice-versa (Sarmiento et al., 1993). Biogeochemical model results make evident how the ocean's physical processes are closely related to the biogeochemical processes, shaping the seasonal biotic and abiotic processes in the Azores region. Vertical mixing is one of those factors shaping the mixed layer depth. As was explored and validated in Chapter 2 of this thesis, the hydrodynamic model can simulate the major currents and water masses in the Azores region.

The seasonal and spatial dynamics of the MLD are characterized by a typical larger MLD during winter (Figure 3.47), followed by a decrease from spring to summer (Figure 3.48 and Figure 3.49). These results are in accordance with the typical patterns reported for the Azores (Valente, 2013). In this case, the temperature-based MLD is used instead of density-based, because it is the most reliable estimate method for regions with higher gradients like the subtropical gyre and in the North Atlantic high latitudes (de Boyer Monté Gut et al., 2004).

This strong latitudinal gradient (maximum of 250m depth in the North of the Azores, contrasting with the maximum of 160m depth in the south), is also a consequence of the North Atlantic Deep water influence on the North of the domain (de Boyer Monté Gut et al., 2004).

In the winter due to the strong winter mixing, nutrients are transported to the euphotic zone. As can be seen in the dynamics between the MLD and the nitrate concentration at the surface along the simulation period (Figure 3.46). At the surface, nutrient concentrations increase, with a maximum value of 0.02 mgN/l in February. These higher nutrient concentrations are favourable for phytoplankton growth. Surface analysis along the study area shows how the phytoplankton patterns are related to the nutrient concentrations, mainly the maximum values. The maximum phytoplankton concentrations (Figure 3.32) occur in the locations with maximum nutrient concentrations (Figure 3.29). This is more denoted during the spring bloom, with the maximum values occurring in the upper part of the domain.

This association is also notorious for the sea surface temperature (Figure 3.35), with lower temperatures in the upper part of the domain. A major factor inducing these patterns is the mixed layer depth (MLD). The spatial variability of the nutrient concentrations is highly related to the MLD, even so, the biotic factors, like the primary production, also contribute to these dynamics (the biological pump).

The winter vertical mixing and vertical advection induce the nutrient supply for the surface layers (McKinley et al., 2018). These processes are well represented by MOHID. The model can simulate the increase of nutrient concentration at the upper layers during winter, by simulating the winter convection, causing the nutrient upwelling from deeper layers up to the surface layers. This (relative) high nutrient concentration induces phytoplankton growth, which will consequently consume these nutrients, causing, therefore, their depletion after the phytoplankton bloom, processes also represented by the model. This decrease is very intense in the spring months, starting in March, and achieves values close to zero in June. This nutrient depletion is stronger for nitrate than for inorganic phosphorous in MOHID. This goes in line with the major statement that nitrate should be the most limiting nutrient for phytoplankton growth in the Azores region (Fasham et al., 1990).

Phytoplankton and nutrients dynamics in the Azores

Regarding the euphotic zone, the model simulates the general patterns in the Azores region, including the deep phytoplankton maximum, typical of oligotrophic regions, and descript for the Azores region (Carmo et al., 2013a; Macedo et al., 2000; Santos et al., 2013), induced from both physical and biologic processes.

Along the domain, at the surface, results reveal that the spring blooms are evident during March and April, with higher values in the north part of the domain. These modelled nutrient gradients are in accordance with the typical patterns of the North Atlantic region (Garcia et al., 2018). During the smoothest autumn bloom, phytoplankton concentration is higher near the islands than in the upper part of the domain.

The summer thermocline induced by the weather conditions tends to confine the phytoplankton in the euphotic zone, as a consequence of inducing the vertical stratification with the consecutive diminution of the MLD, strengthening the seasonal thermocline (Sverdrup, 1953). This thermocline will make the nutrient enrichment from deeper layers more difficult, resulting in a lower nutrient concentration at the surface. Therefore limiting phytoplankton growth. By August all nutrients are depleted in the mixed layer (Figure 3.46). This nutrient depletion is a consequence of the phytoplankton nutrient consumption, demonstrating the bottom-up control that phytoplankton takes over the nutrients cycle in the ocean (Hashioka et al., 2013). This relation between nutrients concentration and phytoplankton growth is a characteristic of oligotrophic waters, like the North Atlantic, and specifically, the Azores region (Barcelos e Ramos et al., 2017; Giacomello and Menezes, 2012) where the concentration of the nutrient is one of the bigger limitations for phytoplankton growth (Calbet et al., 2009). At the beginning of autumn, the weather conditions induce the vertical mixing and the MLD deepening, and therefore nutrient entrainment into the MLD.

These results corroborate the seasonality reported for the Azores region, showing that nutrient concentrations vary with mixed layer depth (Valente, 2013). During the winter, the strong mixing transports nutrients into the euphotic zone, inducing phytoplankton growth. After the spring, the nutrients are depleted in the mixed layer (Figure 3.34) and the deep-chlorophyll maximum establishes below the mixed layer, as expected for the North Atlantic region (Hahn-Woernle et al., 2016). The model simulates the seasonal evolution of the total phytoplankton concentration reflecting the seasonal variations reported for the Azores region, and its oligotrophic characteristics.

3.6. Conclusions

The main objectives of this chapter were the implementation, calibration and validation of the MOHID biogeochemical model in the Azores region. Model validation results show that the biogeochemical model was able to reasonably reproduce the seasonal patterns of phytoplankton biomass, nutrients and oxygen in the Azores. The MOHID biogeochemical model was able to simulate the major biotic and abiotic processes. It allowed to make a general characterization of the spatiotemporal patterns of phytoplankton biomass, at the surface and along the euphotic zone. As well as a general characterization of the phytoplankton and zooplankton dynamics, and nutrients and oxygen at the surface and along the water column.

Different parameterizations as the phytoplankton growth rate, half-saturation constants for nutrients uptake, mortality, and zooplankton grazing, were tested, considering the high seasonal variability of the environmental conditions in the Azores (like solar radiation, nutrients availability, etc.), until achieving a good model performance.

Despite a general phytoplankton overestimation, the model can simulate the general seasonal and spatial phytoplankton patterns, with the intense spring phytoplankton bloom, the autumn bloom, the general patterns at the surface, along with the depth, with a detectable deep maximum of phytoplankton concentration between 50 and 100 meters depth during the summer months.

Model results suggest that meteorological, physical, and biological processes that drive the interannual variability in the Azores region are correctly reproduced by MOHID. Comparison between MOHID, CMEMS-Bio model results, and WOA climatology, at the surface and along the water column, reveals a similar seasonality in nutrients and dissolved oxygen concentration, revealing that MOHID can simulate the biogeochemical dynamics in the study area. The model can simulate the increase of nutrient concentration at the upper layers during winter, by simulating the winter convection, causing the nutrient upwelling from deeper layers up to the surface layers. Also, the winter vertical mixing and vertical advection, inducing nutrient supply for the surface layers are well represented by MOHID. This (relative) high nutrient concentration induces phytoplankton growth, which will consequently consume these nutrients, causing, therefore, their depletion after the phytoplankton bloom, processes also represented by the model. This decrease is very intense in the spring months, starting in March, and achieves values close to zero in June. This nutrient depletion is stronger for nitrate than for inorganic phosphorous in MOHID. This goes in line with the major statement that nitrate should be the most limiting nutrient for phytoplankton growth in the Azores region (Fasham et al., 1990).

Model parametrization and calibration processes revealed that MOHID responds to the different bottom-up and top-down controls, being able to adapt to other case studies with other phytoplankton or nutrient dynamics. Therefore MOHID Water Quality model can be applied to other case studies, with other domains and/ or resolutions. A nesting modelling strategy can be applied to study these processes at a local scale, on an island scale or a seamount scale. It would be useful to study the biotic processes, and the physical processes at a higher resolution, allowing the study at a seamount scale, like population connectivity studies. A longer run would help to better understand and calibrate the biotic patterns, these 2 years' runs are the first approach for this model application.

Chapter 4

Particle tracking model- Larval dispersal and connectivity

4.1. Introduction

Connectivity between marine populations is a fundamental process driving its persistence and influencing ecosystems' structure, biodiversity, productivity, dynamics and resilience (Busch et al., 2021; Kenchington et al., 2019). Connectivity in deep-sea habitats is a key element for spatial management and conservation plans including Marine Protected Areas (MPA) (Combes et al., 2021; Lima et al., 2020). Benthic species rely on their larval phase for individual species survival, increasing population dynamics and persistence (Hilário et al., 2015). Larval dispersal contributes to i) individuals exchange, necessary to maintain populations and genetic connectivity over space and time; ii) the colonization of new habitats or immigration into existing communities that can influence community structure and species diversity, promoting population connectivity and maintenance (Adams et al., 2012). Some species present a pelagic larval phase, during that period, larvae are advected by ocean currents, being able to "migrate" between geographically separated populations (Paris et al., 2013). Though planktonic larval stage and larval dispersal are crucial to understanding population connectivity in the deep-sea (Ross et al., 2020), little is still known about deep-sea larval behaviours and dispersal. Difficulties in collecting in-situ data have delayed the progress in deep-sea biology and larval behaviour studies (Kenchington et al., 2019).

Recently, the use of biophysical and particle tracking models has become advantageous to study larval retention and dispersal patterns in the deep-sea and in the entire water column considering different oceanographic and topographic features like seamounts, deep-sea banks or island slopes (Combes et al., 2021; Cowen and Sponaugle, 2009; Werner et al., 2007). These biophysical particle tracking models allow the study of particle dispersal (larvae dispersal) and populations connectivity by using the physical component (hydrodynamic model), integrating the biological component (e.g. larvae behaviour passive, swimming, bottom oriented, etc.); pelagic larvae duration, mortality, response to temperature, etc.); and including the definition of recruitment areas and settlement depths (Busch et al., 2021).

Several model applications have been applied to simulate larval dispersal, allowing the study of populations connectivity in vulnerable marine ecosystems (Kenchington et al., 2019; Ross et al., 2017; Wang et al., 2020), including deep-sea sponges aggregations (Busch et al., 2021; Ross et al., 2019). These models also allow for assessing the role of larval dispersal in the maintenance of population dynamics and supporting management plans for fisheries and vulnerable marine ecosystems (VME) (Combes et al., 2021; Kenchington et al., 2019; Kough, 2014). Several studies highlight the importance of oceanographic features, like seamounts, or hydrodynamic patterns, for larval retention or dispersal (Combes et al., 2021; Cowen and Sponaugle, 2009; Werner et al., 2007). The Azores region is characterized by its complexity of bathymetric features, including 9 islands, more than 460 seamount-like features, and hosting a high diversity of sponge grounds, that may be classified as VME (Morato et al., 2016a; Pham et al., 2015; Somoza et al., 2020). Recently, several areas of the Azores were included in the Azores Marine Park (AMP) due to its vulnerability and ecological relevance. The AMP was implemented in 2011 by a regional law decree (DLR 28/2011/A) and was extended in 2016 to include Condor and Princesa Alice seamounts, and D. João de Castro bank as Marine Protected Areas (MPAs) (DLR 13/2016/A). More recently, in 2019, after the discovery of the Luso hydrothermal vent field on the slopes of Gigante seamount, an important fishing ground, a new MPA was declared around this vent field, the Luso MPA (DR 68/2019).

The establishment of these MPAs, increases the protection of these regions, but also creates the need for generating and implementing management plans and measures with well-defined objectives and regulations (Abecasis et al., 2013; Combes et al., 2021). In the design and establishment of effective and resilient MPAs and coherent networks of MPAs, it is necessary to take into account population connectivity, which allows populations to thrive and biodiversity and ecosystem services to be maintained (Lausche et al., 2021). This is especially the case of deep-sea habitats due to their vulnerability, where systematic conservation planning approaches have rarely been applied (Combes et al., 2021; Lima et al., 2020).

The objective of this chapter is to apply a biophysical particle tracking model to study larval dispersal and populations connectivity for two different case studies, considering different organisms: a deep-sea sponge- *Pheronema carpenteri*, a sessile organism; and a deep-sea crab- *Chaceon affinis*- a non-sessile organism; and assess the effectiveness of the current MPA in the maintenance of the different populations' connectivity.

4.2. Methodology

4.2.1. Particle tracking model

To study larval dispersal and connectivity, a coupled biophysical particle tracking model was applied to the Azores region. The particle tracking model was adapted from the CMS- Connectivity Modelling System (CMS v2.0; Paris et al. 2013) and coupled with the 3-D MOHID hydrodynamic and biogeochemical models.

The CMS-Connectivity Modelling System is an open-source model, freely available online[4]. It was created at the University of Miami, for the multi-scale tracking of biotic and abiotic particles in the ocean, like complex larval migrations providing probability estimates of populations connectivity (Paris et al., 2013). This particle tracking model has been used extensively to study the dispersal of larvae in the deep-sea, and the connectivity between different organism populations (Antonio Baeza et al., 2019; Criales et al., 2019; Gary et al., 2020; Longmore et al., 2014; Metaxas and Saunders, 2009; Ross et al., 2020), also for physical oceanography applications (Sala et al., 2016; van Sebille et al., 2018). This model runs offline, over a 3D hydrodynamic model, applying its velocity fields (u, v, w) to each particle, using a 4th-order Runge–Kutta numerical discretization method to differentiate particle positions through space and time. Thus, the model can run with a time step lower than the hydrodynamic solution, ensuring that particles cannot cross a model grid cell in a single time step and allowing for more accurate estimates of particles dispersal (Paris et al., 2013; van Sebille et al., 2018). It is a modular and probabilistic model, allowing the inclusion of additional 'behaviours' to the particles. Modules distributed with the code include mortality, vertical migration, and a connectivity module designed to generate a connectivity matrix output from the source to the final destination of the particles. CMS allows tracking all the particles (larvae), along with the entire study calculating its travel distance, depth, and settlement positions. The model computes the probability of larval exchange (connectivity) between several spawning locations and recruitment areas; mortality, and behaviour; providing results over time including particles' location (x, y and depth), water properties, and particle status.

MOHID hydrodynamic model results were used to provide the hydrodynamic conditions for the dispersal simulations. MOHID provides a 1/16º horizontal resolution (6km),

---

[4] https://github.com/beatrixparis/connectivity-modeling-system

and 50 vertical layers, with hourly outputs, in a 3-D resolution. Besides the velocity vectors, MOHID also provides, among other parameters, temperature, salinity and biogeochemical water properties for further analysis. As described in *Chapter 2* and *Chapter 3* of this dissertation, this model application was validated for the study area (both hydrodynamic and biochemical parameters).

4.2.2. Model implementation

This particle tracking model was used to study larval dispersal and connectivity between different populations. Each population is one release, and larvae are represented by lagrangian tracers. In this implementation, each population is defined as a release location, characterized by a position (longitude, latitude and depth). For connectivity studies, recruitment areas and settlement areas are defined. Each population is defined by a polygon, which is a recruitment area. Due to the many uncertainties about deep-sea larvae biology, different decisions were taken in the modelling hypothesis, considering several pelagic larval duration (PLD), and seasonal scenarios to encompass different potential situations. This is one advantage of using modelling tools, allowing to study of different hypotheses and scenarios (Swearer et al., 2019; Wang et al., 2020).

Different scenarios were computed considering different spawning seasonality and pelagic larval duration (PLD). Larvae can be passive or assume behaviour. Passive larvae are advected by the hydrodynamic fields, without any behaviour or swimming velocities. The larvae assumed different behaviours: like swimming velocity, buoyancy, swimming surface-oriented or bottom-oriented. The model can assume different larvae stages, with different durations and behaviours. Swimming velocities can be temperature-dependent. Larvae that died or strayed outside the model domain are removed from the remainder of the simulation. CMS particle tracking model allows the tracking of all the larvae advected by the hydrodynamics, calculating their travel distance, depth, and settlement positions.

The model also considers mortality and different settlement strata. Each release is defined by the following parameters: location, depth, number of particles released, frequency of the release and release date. The implemented lagrangian model uses the 3D hydrodynamic model to simulate the larval dispersal, and the different scenario hypotheses to study larval dispersal and population connectivity (Figure 4.1).

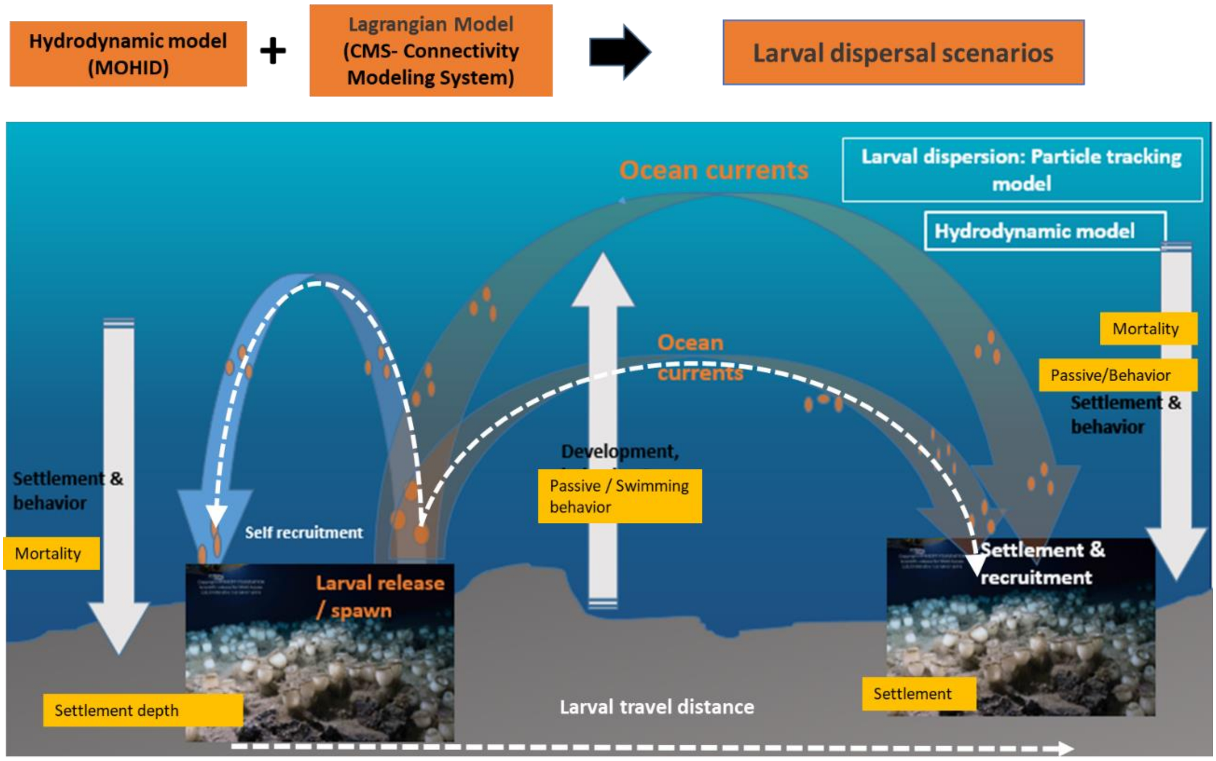

Figure 4.1- Diagram representing larval release and dispersal and model tools to simulate larvae dispersal

Release locations- Each release location represents a population in the study. Their position should be defined considering the location in the study area, and the model domain and resolution (North et al., 2009). The locations should be sufficiently far from the domain limits to avoid boundary effects like massive loss of particles out, which would bring uncertainties on model results; and regarding model resolution, separated by several domain cells, or by bathymetric barriers (e.g. island, seamount). Each release location is therefore defined by a point (longitude, latitude and depth).

Settlement locations- In this study, for the connectivity assessment, each population is a recruitment area. Each population is therefore defined by a polygon of 6*6km (model resolution). Each population Is a release location and a settlement location.

Spawning- Since there is no information about the frequency and seasonality of larvae emissions, a hypothetical number must be defined (Cowen and Sponaugle, 2009). To standardize this approach the same number of particles for all the locations was considered, assigning the same hypothetical relevance to all the release points, considering the same release size and frequency. Regarding frequency, particles are released with a time step of 1,5 hours, for all the scenarios. Moreover, for the correct and most efficient model implementation, the number of particles to release was calibrated to provide accurate larvae dispersion results, considering the computational efficiency.

4.2.3. Model parameterization and calibration

Lagrangian models have the advantage of being less computationally heavy than eulerian models, enabling the use of thousands of particles for dispersal studies. Nonetheless, the number of particles to use is an important statement, that needs to be calibrated for each model application. The hydrodynamic model has a turbulence factor, and the lagrangian model has a diffusivity factor to simulate processes smaller than the model resolution. Without diffusivity, all lagrangian tracers released at a specific location in space and time would follow identical tracks (Ross et al., 2016). Though, in reality, this does not happen and the lagrangian models consider the diffusivity parameter to get a more realistic solution.

The number of particles to release in each simulation should be enough to surpass this diffusivity and to provide confident results, and robust larval transport predictions, bearing in mind the random factor that all the dispersal models have. If too few particles are released, trajectories can have statistical outliers and do not satisfactorily represent the desired ensemble average, with a risk of inducing erroneous conclusions (North et al., 2009).

Because the number of particles can increase the computational demand, a trade-off between computational time and result accuracy should be established. Sensibility testing should be done to calibrate the correct number of particles, considering different scenarios of hydrodynamic situations, at different release locations (considering longitude, latitude and different depths). The correct number of particles should avoid two typical errors: the number of particles is insufficient to capture the model diffusivity, and the particle release distribution does not adequately sample a subarea of particular importance (Jones et al., 2016).

To estimate the best number of particles, and avoid these accuracy errors, different methodologies can be used by analysing:

- Dispersal pathlength distances saturation;
- Particle density distribution, and the evaluation of the fraction of unexplained variation (Simons et al., 2013).

Dispersal pathlength saturation

One method of defining the correct number of particles is by analysing the dispersal pathlength saturation. Following this method, a correct number of particles must create a saturated dispersal path without abrupt variation along with travel distance. An adequate number of particles is achieved when these variations are smoother. The pathlength is calculated by summing the travel distances during each time step, for all the particles, during the entire particles' lifetime. Dispersal pathlength saturation is analysed by graphing the probability of dispersal pathlength distances binned into small increments (e.g. 2km) (Kough et al., 2013).

Particle density distribution, and the fraction of unexplained variation analysis

Simons et al. (2013), propose a method for testing the best number of particles using the Fraction of Unexplained Variation (FUV) analysis. This method ensures that a simulation closely approximates a reference solution. As particles are released and tracked in three dimensions within the model domain, the vertically integrated particle distribution at a particular point in time is quantified with a two-dimensional Particle Density Distribution (PDD) (Simons et al., 2013).

The PDD is calculated in two steps:

i) Firstly by vertically integrating the number of particles within a grid cell to create a two-dimensional (2-D) distribution;
ii) And secondly dividing the distribution by the total number of particles released.

To calculate the fraction of unexplained variation, firstly, a simulation is computed with a larger number of particles (the reference simulation), and its PDD is calculated. Because this solution is computed for the largest number of particles available, it is considered to provide the best representation of the particle distribution along the study area. Afterwards, different subsets are tested, calculating the PDD for the different number of particles (n) extracted randomly from the reference simulation. This second step is repeated several times, 100 times, in this case, to have a representative subset sampling. Finally, each tested subset is compared with the reference solution by computing the FUV between them.

The FUV is calculated by:

$$\mathrm{FUV} = 1 - r^2 \qquad \text{Eq. 4.1}$$

where r is the linear correlation coefficient between two different PDDs.

The third step is to calculate the FUV upper bound for each subset and tracking time. The FUV upper bound was identified where 95% of the FUV distribution lies below the bound.

FUV methodology presents several advantages: i) FUV result is a value between 0 and 1, providing a consistent scale for comparing PDDs which may contain very different numbers; ii) FUV is a conservative measure of difference where the grid cells are independently evaluated. Therefore, it may detect differences in the PDDs even if the particles have the same patterns but slightly shifted in space (something that would be masked when using the typical correlation analysis between patterns of distribution); iii) FUV provides a single number that can quantify the difference between two PDDs.; iv) The use of a squared correlation coefficient naturally induces a description of the difference magnitude in terms of the residual variance. In the end, PDDs with a very high FUV are virtually uncorrelated and represent two very different spatial distributions of particles. With this methodology, it is assumed that the number of particles in use is enough to describe the distribution when the FUV is lower than 0.05, considering the 95% confidence level. This cut-off represents the maximum amount of dissimilarity that will be tolerated between the reference and sub-sampled PDDs. For each number of particles to test (from 5,000, 50,000, 100,000, 125,000, 150,000, 190,000), 100 different subsets were tested, and respective FUVs were estimated.

Time length

Larvae particle dispersal and connectivity studies were performed for the year 2017. Several scenarios were also tested for 2018 to compare dispersal patterns.

4.2.4. Model application and analysis techniques

In this work, the results of simulated larval dispersal scenarios were analysed in four different ways: i) by analysing the Particle Density Distribution (PDD); ii) by larvae dispersal maps; iii) by studying the particles' depth and travel distance along with the simulation; and, iv) by using connectivity matrices.

Particle density distribution - As previously described, PDD represents the particle density distribution in 2-D vertically integrated maps. In the 2-D map used in this study, all particles are represented and each domain grid cell (6km x 6km) represents the integrated number of tracers in the entire water column.

Larvae dispersal maps- Particle dispersal maps represent particle distribution. In these maps, particles are not integrated into the water column, and all the particles in each cell are graphed. Some particles can “mask” others, by overlapping. In these maps, each particle colour represents only one category: release’s id, depth, particle’s relative time, or any other property considered by the model. Also, water properties provided by the hydrodynamic model can be plotted (like temperature, salinity, dissolved oxygen, etc.).

Travel distance and depth -Histograms were used to analyse potential travel distances from all the different release points for the different scenarios. These distances were calculated from individual particle trajectories as the sum of straight-line distances between each time step. Also, histograms of particle depths were used to analyse how particles are distributed along the water column.

Connectivity Matrices- Connectivity between 2 locations was assumed when, at least, one modelled particle released from one location (source node) settled in another location (receiving node), after the PLD. When settling on the same location, this is considered self-recruitment. Connectivity is quantified by the percentage of particles that settle upon each location. These matrices represent the percentage of self-recruitment and connectivity between different populations. Source populations are represented as rows (j), and recruitment areas (receive node) as columns (i), self-recruitment in each population is represented in the matrix diagonal. Colours represent the percentage of settled particles in both situations: self-recruitment and connectivity.

4.3. Case Study 1- *Pheronema Carpenteri*

4.3.1. Introduction

Deep-sea sponges are characteristic organisms of the deep-sea (Pham et al., 2015). Dense sponge aggregations, known as “sponge grounds”, are a key component of marine benthic ecosystems, promoting, along with corals, the enhancement of local biodiversity, and are believed to act as feeding, reproductive, nursery and refuge areas for a high number of invertebrates and fish (Beazley et al., 2021; Pham et al., 2015). Due to their vulnerability, and their need for protection, deep-sea sponge grounds can be classified as vulnerable marine ecosystems (VMEs) (FAO, 2009).

Deep-sea sponges are thought to play an important role in the deep-sea nutrient cycle, recycling the nutrients, through their capacity of filtering large quantities of water properties (Leis, 2020). Also, they contribute to the biogeochemical cycling of dissolved nutrients, namely carbon and nitrogen, but also for silicate in the case of siliceous sponges (like the sponges of the class Hexactinellida) (Howell et al., 2016; Maldonado et al., 2016; Ross et al., 2019).

4.3.1.1. *Pheronema carpenteri*

Pheronema carpenteri (Thomson, 1869*)* is a hexactinellida sponge from the genus *Pheronema* (de Voogd et al., 2022). It is a nest-shaped sponge, up to 25 cm high and 30 cm across, and can be more than 200 g in wet weight. These sponges are anchored in the bottom by rooting tufts of long spicules (Maldonado et al., 2016)*,* and can form aggregations of up to 475 individuals per 1,000 m^2, with peak abundances and wet weight biomass up to six individuals/m^2 (average 1.5 individuals m^2) and 1.1 kg/m^2 (average 372 g/ m^2), respectively (Rice et al., 1990).

P. carpenteri aggregations can occur from south of Iceland and west of Scotland, across the Porcupine Seabight, the Azores, northern Spain, Portugal coast, Canary Islands, and off Morocco forming the most extensive sponge aggregations at 800–1,350m depth (Barthel et al., 1996; Maldonado et al., 2016; Rice et al., 1990; Tempera et al., 2013; White, 2003). They can also be found on the margins of Greenland and Canada, on the south side of the Faroes-Iceland Ridge (Howell et al., 2016).

In the North Atlantic, dense aggregations of hexactinellida were identified in the continental slopes, and some of them are reported to have persistent spicule skeletons after death (Maldonado et al., 2005). These spicule mats created by the senescence and death of hexactinellida sponges, like *P. carpenteri,* can form biodiversity hotspots (Henry and Roberts, 2014), and may even function as reducers of sediment erosion in the deep-sea (Black et al., 2003).

Pheronema carpenteri in the Azores

In the Azores, sponge aggregations dominated by *P. carpenteri* have been recorded on the Cavala, Condor, and Mar da Prata seamounts, and in the Açores bank, in depths between 700 m and 924 m (Tempera et al., 2013 citing several sources: Pérès et al., 1972; Tempera et al., 2012; Pereira, 2013). In Condor seamount, *P. carpenteri* multispecific aggregations with higher sponge density were found at 700-825 m depth, whereas mixed substrates found approximately between 430-1100 m were the most taxonomically diverse. More recently, a dense aggregation in the South of Pico was identified (Colaço et al., 2020; Creemers et al., 2019). Additionally, data from exploration missions, collected from observers and bycatch, allow the identification of several sponge aggregations namely in the South of Faial, North of Pico island, in Formigas, Açores bank and more recently in Gigante seamount ((Colaço et al., 2020). Moreover, during the development of this work, but not included, more sponge observations were reported in the Azores, by multidisciplinary scientific cruises and exploration missions, performed among others, by researchers at the University of the Azores (Friedlander et al., 2019; IMAR, 2018; Somoza et al., 2020).

4.3.1.2. Deep-sea sponges' biological traits

The current understanding of deep-sea larval behaviour for deep-sea sponges is extremely limited (Busch et al., 2021), mainly due to the inherent difficulty to assess deep-water habitats (Lopes, 2005). During their life cycle, after hatching, sponge larvae are pelagic, drifting in the water column for a limited period (Pelagic Larval Duration, PLD), before settling on the seafloor, in a recruitment area, to become sessile juvenile sponges (Maldonado, 2006).

Hexactinellids are currently assumed to be viviparous with lecithotrophic larvae (Maldonado and Young, 1999). Available data about hexactinellida sponges biology results mainly from studies with shallow-water sponges (Barthel et al., 1996; Boury-Esnault et al., 1999), artic populations (Leys and Lauzon, 1998), and other cases (Bett and Rice, 1992; Boury-Esnault et al., 1999; Guillas et al., 2019). The available data from these studies indicate that most sponge larvae are anchiplanic, with a short planktonic larval duration of minutes to a few days (usually< 2 weeks) (Maldonado et al., 2016; Ross et al., 2019). However, this short PLD is only reported for shallow-water species and is believed to not be representative of deep-sea water taxa such as *P.carpenteri*. Deep-sea species are thought to have longer PLDs than their shallow-water counterparts (Hilário et al., 2015). Furthermore, Vacelet et al, 1999, suggest that unciliated hoptimella larvae sponge may remain in the plankton for longer periods, perhaps months (Maldonado, 2006). Environmental factors like seawater temperature can influence the duration of the reproductive period (Maldonado, 2006).

Information about sponges' spawning periodicity is limited. Previous studies often assume that deep-sea sponges do not experience seasonality, unlike their littoral relatives, because they are too deep to be influenced by light (Barthel et al., 1996). However, further studies pointed out that despite their deep-sea habitat, sponges experience seasonality which influences their growth rates and perhaps reproductive period, which, in turn, may be regulated by patterns of primary production in the photic zone of the ocean and subsequent sinking of the generated production (Leys and Lauzon, 1998). Information about deep-sea sponges' biological traits found in the literature review is summarized in Table 4.1.

Spetland et al (2007), collected information about *Geodia barretti* sponge biology, (located at 60–250 meters' depth, in Norwegian fjords), identifying one (Spring) or two (Spring and October) discrete peaks of gamete release over the year cycle. Maldonado et al., 2017, also suggest a synchronization between sinking primary production and deep-sea sponge reproduction (Kenchington et al., 2019).

For applying particle tracking models to study larvae dispersal, it is essential to include information about their biological traits like spawning seasonality, larvae behaviour, and pelagic larval duration (Busch et al., 2021). When and how often marine species release larvae (i.e., spawning window and periodicity) can be determinants for connectivity among sites (Treml et al., 2012). Therefore, this information, together with other important life history parameters like PLD and larval mortality, is essential to developing dispersal phenotypes to model connectivity (Treml et al., 2012). Larvae mortality can be caused by predation, by advection away from suitable settlement habitats, or it can occur by “physiological stress” caused by an overextended planktonic phase (Maldonado, 2006).

Table 4.1- Pelagic larval duration, spawning seasonality, of deep-sea sponges, from different locations and depths, used/obtained in other studies

Organism/Taxa	PLD	Spawning season	Organism location	Reference
sponges (generic)	<14days	n/a	n/a	1)
sponges (generic)	n/a	phytoplankton blooms (March/autumn)	Several; Northwest Atlantic	2)
Demosponge	14	After spring bloom	Cantabrian sea	3)
Demosponge *(Geodia barretti)*	n/a	Spring & Autumn/ phytoplankton blooms	Norwegian fjords, deep continental shelf	4);5)
Hexactinellida	> 24h (<24h (shallow sponge)/)	--	North Atlantic	6)
Alectonid sponges (Demospongiae)	>30 days/ months	n/a	n/a	7)
Hexactinellida	n/a	All year round / phytoplankton blooms	Fiords, British Columbia	2)
Oopsacas minuta (**Hexactinellida**)	n/a	All year round	submarine cave, France	2)

1) Maldonado, 2006; 2) Kenchington et al., 2019; 3) Busch et al., 2021; 4) Spetland et al. 2007; 5) Leys and Lauzon et al., 1998; 6) Ross et al., 2019; 7) Vacelet 1999. n/a- no information available or not applicable

In the absence of data and information about *P. carpenteri*, the information about the class hexactinellida, other classes of deep-sea sponges or even another phylum of deep-sea organisms, can be useful to study different scenarios (Busch et al., 2021; Maldonado, 2006; Ross et al., 2019).

4.3.2. Model Setup

4.3.2.1. Sponge locations

The *P.carpenteri* sponge aggregations in the study are located along the Archipelago (Figure 4.2), in a bathymetric range from 630 to 1000 meters depth (Table 4.2). Location 1 (L#1) and 2 (L#2) are located over the Mid-Atlantic Ridge (MAR), in the Cavala (L#1) and Gigante (L#2) Seamounts, locations 3 to 8 in the central group (CG), and L#9 (Mar da Prata) and L#10 (Formigas), in the Eastern Group (EG).

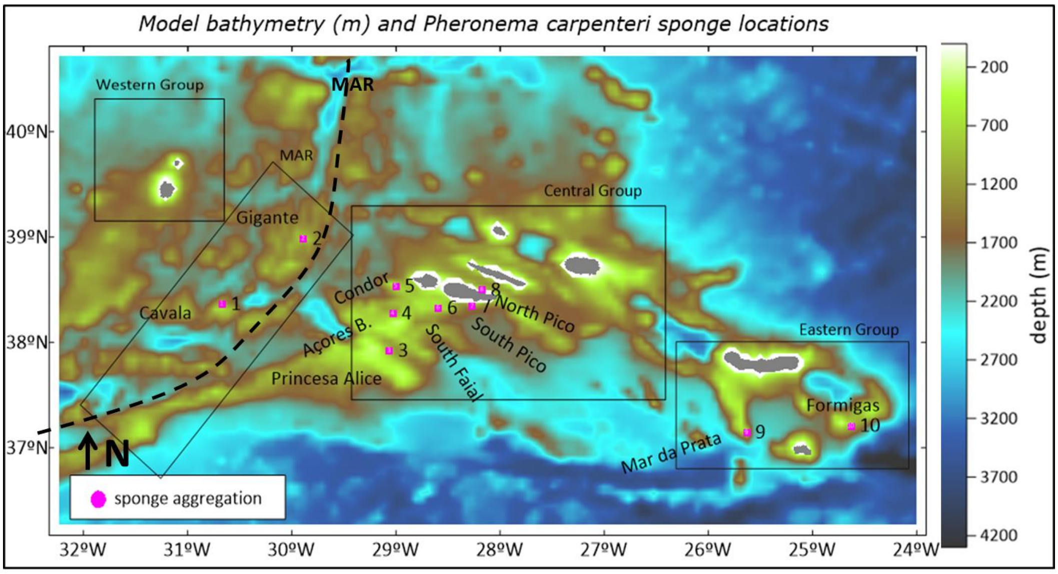

Figure 4.2-Bathymetry of the study area, with the representation of the Mid-Atlantic Ridge (MAR) with a dashed line, the 9 islands of the Azores archipelago in brown, the location of the *Pheronema carpenteri* sponge aggregations in the study with pink circles; black polygons depicts the groups in analysis: MAR Group (L#1 Cavala, L#2-Gigante); CG-Central Group(L#3-Princesa Alice, L#4-Açores Bank, L#5-Condor Seamount, L#6-South of Faial, L#7-South of Pico, L#8); EG- Eastern Group (L#9-Mar da Prata, and L#10-Formigas).

Table 4.2- *Pheronema carpenteri* sponge aggregations in the study, their location, depth, source and name/location

Location	**Longitude (ºW)**	**Latitude (ºN)**	**Depth (m)**	**Nome/localização**	**Group**	**Source**
L#1	-30.6701	38.3632	900	Cavala	MAR	emodnet[1]
L#2	-29.88809	38.98353	766	Gigante	MAR	Exp-Fund.Azul [2]
L#3	-29.06232	37.9183	900	Princess Alice	CG1	Biodiaz [3]
L#4	-29.02941	38.273	825	Açores Bank	CG2	Sponges-Observer_2017[4]
L#5	-28.99877	38.53281	775	Condor Seamount South	CG3	IMAR-DOP/UAz (CoralFish, Corazon, Condor) [5]
L#6	-28.59288	38.32531	630	South of Faial	CG4	Sponges-observer_2017[2]
L#7	-28.26657	38.33921	1000	South of Pico	CG5	Sponges-Lula[2]
L#8	-28.1735	38.49624	822	North of Pico	CG	Exp-Fund.Azul[2]
L#9	-25.63083	37.14111	780	Oeste West of São Miguel (Mar da Prata)	EG	IMAR-DOP/UAz (CoralFish, Corazon, Condor) [5]
L#10	-24.63	37.205	904	Formigas	EG	Colecta[6]

1-http://ipt.vliz.be/eurobis/resource?r=imagedop_video_annotations; 2-Colaço et al., 2020; 3-Institute of Marine Research (IMAR-Azores), Portugal; 4-Department of Oceanography and Fisheries (DOP)-UAC, Portugal (2016). 5-ImageDOP Bentic Video http://www.vliz.be/en/imis?dasid=4492&doiid=304; 6-DOP/internal unpublished data

4.3.2.2. Model configuration

In this implementation, each sponge aggregation is defined as a release location, characterized by a position (longitude, latitude and depth), and as a recruitment area, defined by a polygon. Different scenarios were computed considering different spawning seasonality and PLD. Following the most used approach when modelling sponge larvae dispersal in the deep-sea, larvae behaviour was considered passive (Kenchington et al., 2019; Swearer et al., 2019).

Larvae mortality is computed following the half-life concept (the time it takes to half the population to die) likewise in other deep-sea larval dispersal studies (North et al., 2009; Paris et al., 2013). The model configuration is summarized in Table 4.3.

Theoretical “larvae” (passive tracers) were released from the 10 locations in the study, considering the same number of larvae per release. The number of particles released was defined by calibration methods (), and it was established to use a total of 150000 particles per release per month.

Larvae dispersal was studied for different season scenarios: i) an early release; and ii) seasonal releases. The yearly release allows the study of a higher range of potential dispersal and connectivity patterns throughout the year. Seasonal releases for March and October are used to analyse several aspects of the larval dispersal patterns, namely: particles depth, total travel distances, different PLD, and to compare larvae dispersal and connectivity between different scenarios. Particle simulations were performed for the years 2017 and 2018, considering monthly releases in March and October (Autumn situation), to simulate the spring and autumn spawning situations respectively (Table 4.4).

The larvae were released at a regular interval, every 90 minutes, to capture the full range of potential larval trajectories within the spawning period (Ross et al., 2016). Several PLDs were considered to cover different larval reproductive behaviour (based on literature).

Table 4.3- Biophysical model configuration for case study 1

Model parameter	Parameter description
Hydrodynamic model resolution	6*6km
Model time step	7200 seconds
Number of release points	10
Release depth	Sea bottom
Number of larvae per release	150000/month (calibrated)
Release time step	1.5 hours
Behaviour	Passive (Ross et al., 2019)
Mortality	Half-life (North et al., 2009)
Strata	600 to 1000m (*P.Carpenter*i bathymetric range)
Scenarios	Several considering PLD and seasonality

Scenarios

Different scenarios were studied to cover different spawning seasonality and larvae behaviour, considering the PLD, seasonal spawning and release length. The scenarios studied are summarized in Table 4.4.

Table 4.4- Scenarios considered in this study, with spawning date and pelagic larval duration

Scenario	PLD (days)	Release date	Release length (days)
PLD15_March_2017	15	March 2017	31
PLD15_October_2017	15	March 2017	31
PLD30_March_2017	30	October 2017	31
PLD30_October_2017	30	October 2017	31
PLD15_year_2017	15	January-December 2017	365
PLD30_year_2017	30	January-December 2017	365
PLD15_March_2018	15	March 2018	31
PLD15_October_2018	15	March 2018	31
PLD30_March_2018	30	October 2018	31
PLD30_October_2018	30	October 2018	31

4.3.3. Model calibration

The number of particles to use in the model was calibrated for this specific case study, considering the 10 release locations, and the scenarios in the study. Two methods were used to calibrate the number of particles: i) the dispersal pathlength saturation; and ii) the fraction of unexplained variation (FUV) analysis. Two different scenarios were analysed: *PLD30_March_2017*, and *PLD30_October_2017*. The longest scenarios were considered to contemplate the worst conditions with the higher dispersal situations, that, in this case, correspond to PLD30. The analysis is performed considering a monthly release, with particles released every 900 seconds during the 30 days. Therefore, by day 30, the last particles are being released, and they will be moving up to 30 days more (PLD30).

Particle density distribution, and the fraction of unexplained variation analysis

In this calibration step, the number of particles tested goes from 5000 up to the reference value of 200 000 particles released per month at each location. Results show that by day 45 the FUV is above 0.05 for the majority of the releases with 100 000 released particles (Figure 4.3). However, by day 60, FUV results show that the number of particles required to achieve a robust PDD (FUV below 0.05 (Simons et al., 2013)) should be 150 000 particles per release per month, for both tested scenarios.

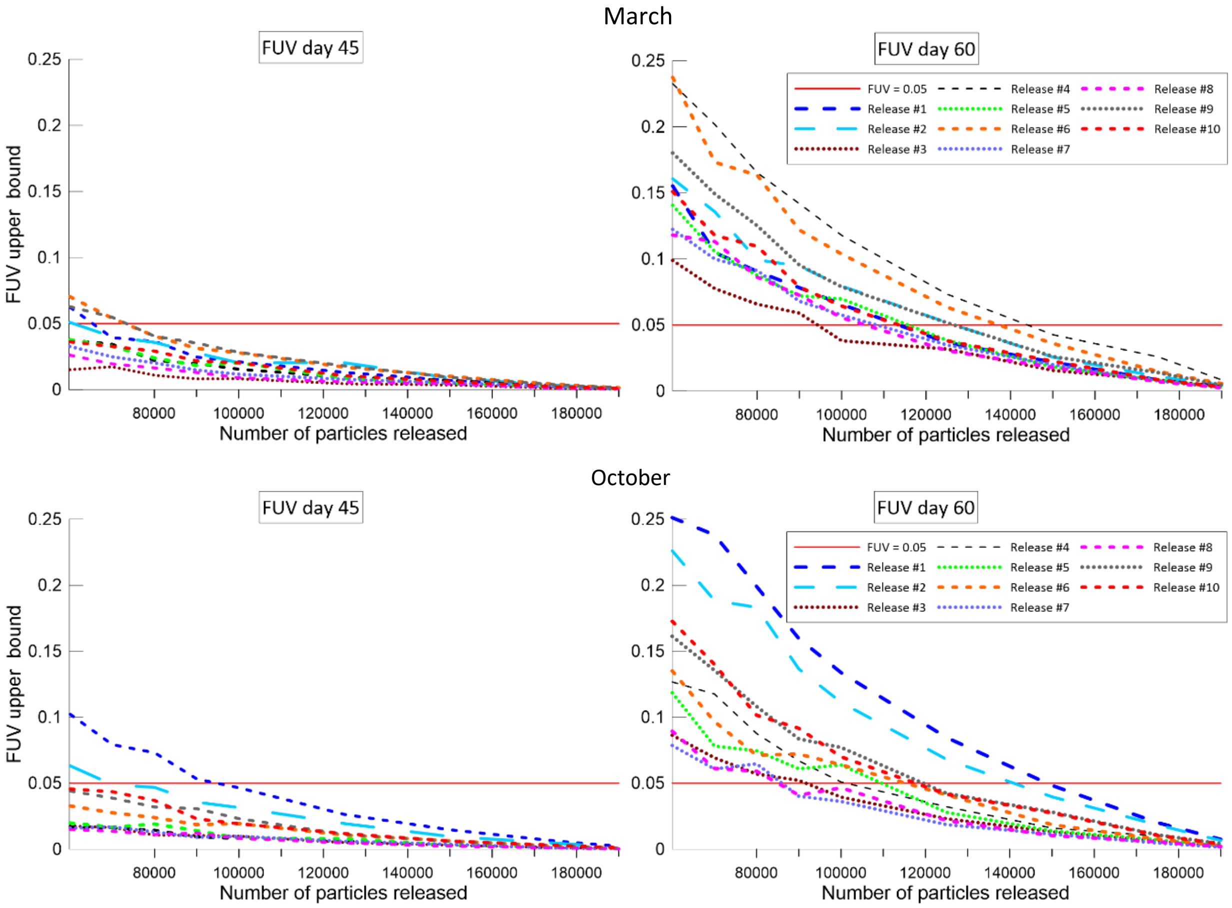

Figure 4.3- Fraction of unexplained variation (FUV) upper bound for the 10 releases, considering different numbers of particles released, for March scenario (top), and October (down) with a PLD30 and tracking time of 45 days (left) and 60 days (right) for the different 10 release locations. The horizontal red line is drawn at an FUV upper bound of 0.05. For the reference simulation, (for each situation) it was considered a release of 200000 particles per month, per release. For each number of particles to test (from 5000, 50000, 100000, 125000, 150000, 190000), were tested 100 different subsets, and the FUV upper bound of each test was estimated (Simons et al., 2013).

Dispersal pathlength saturation

Dispersal pathlength saturation (Figure 4.4 and Figure 4.5) shows that a total of 100 000 particles per release per month, provide a saturate movement for all the release locations. Results show that a release of 1000 particles provides a discontinuous result with abrupt changes in the travel distances, with 10000 particles per month, the fluctuations get smoother, but only with 100 000 particles, the dispersal pathlength distance doesn't reveal abrupt changes along with travel distance.

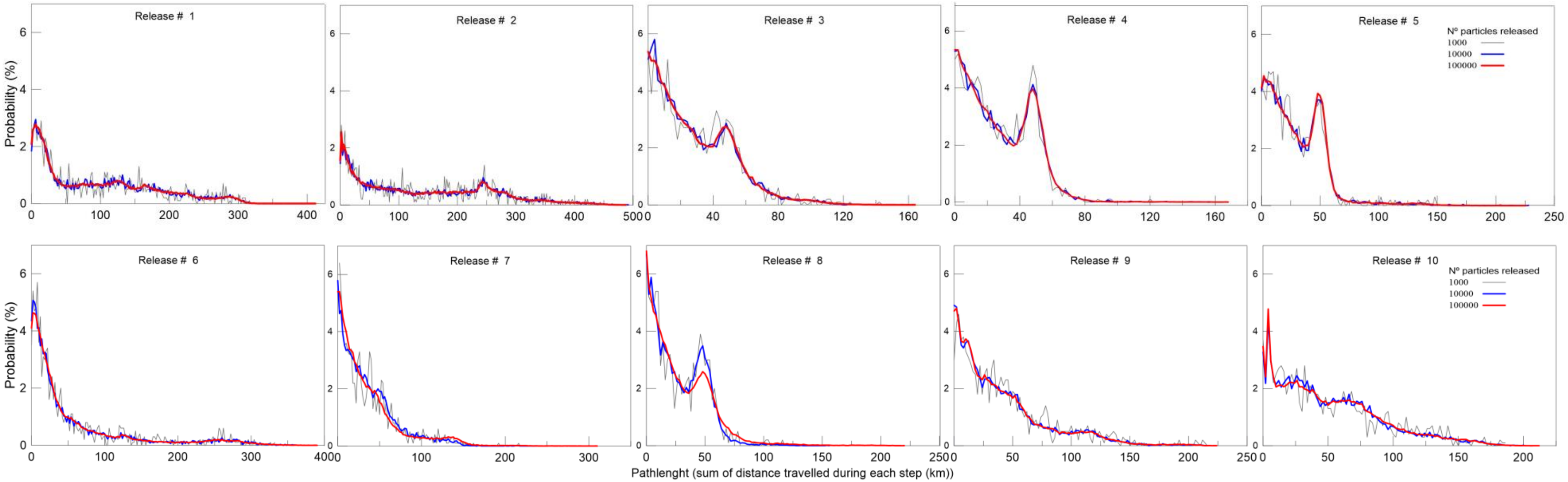

Figure 4.4- Probability of dispersal pathlength distances, for scenario *PLD30_March_2017* (considering a PLD30), with different numbers of particles (1000; 10000; 100000). The X-axis is the pathlength travelled by each particle (sum of distances moved during each time-step) binned into 2km increments, and the Y-axis is the probability.

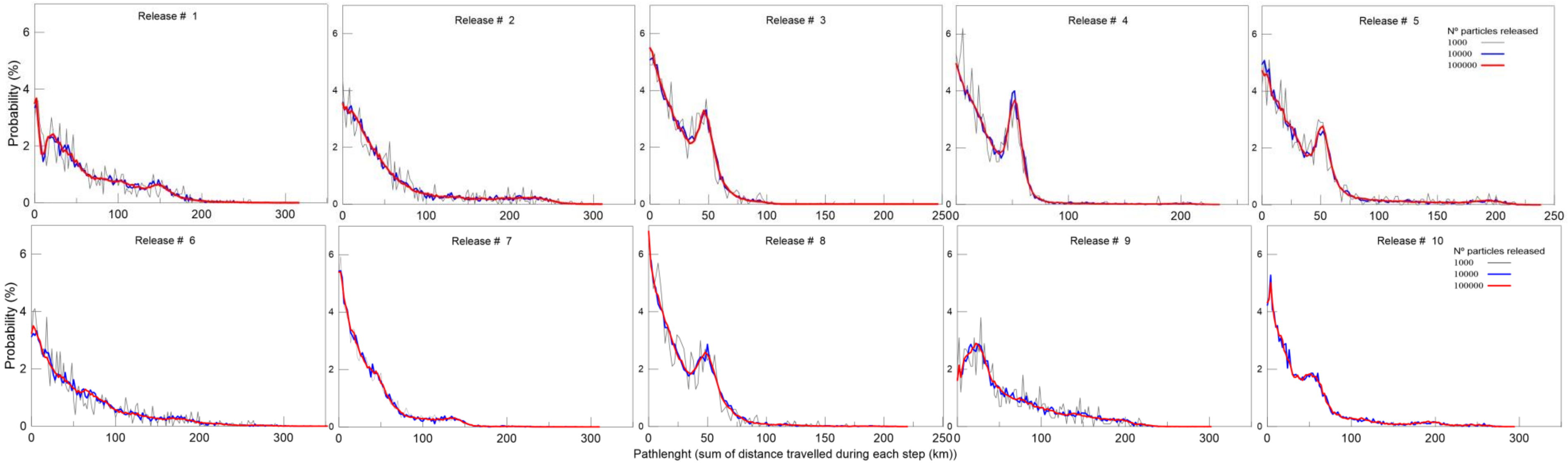

Figure 4.5- Probability of dispersal path length distances, for scenario *PLD30_October_2017* (considering a PLD30), with different numbers of particles (1000; 10000; 100000). The X-axis is the travelled path length of each particle (sum of distances moved during each time-step) binned into 2km increments, and the Y-axis is the probability.

4.3.4. Results

4.3.4.1. Particle density distribution

Larval dispersion has heterogenic distribution patterns considering the spawning seasonality, as can be seen in the particle density distribution (PDD) results (Figure 4.6 and Figure 4.7). PDD illustrates the larval dispersal plume distribution along the study area but also indicates the potential particle exchange between different locations. Particle plumes from the MAR group can achieve the Central Group (CG) only during the Winter and Autumn months (January, February, September, October, November and December months). Larvae dispersal plumes from the MAR can also achieve the Western Group surrounding Flores and Corvo islands during March, April, May and June months. Between CG and WG larvae exchange only occurs during July, November and December, however with lower PDD, revealing a lower probability of particle exchange. Larvae from the Eastern Group don't achieve the sponge locations from the CG and vice-versa. Only a residual exchange of particles occurs between these two groups.

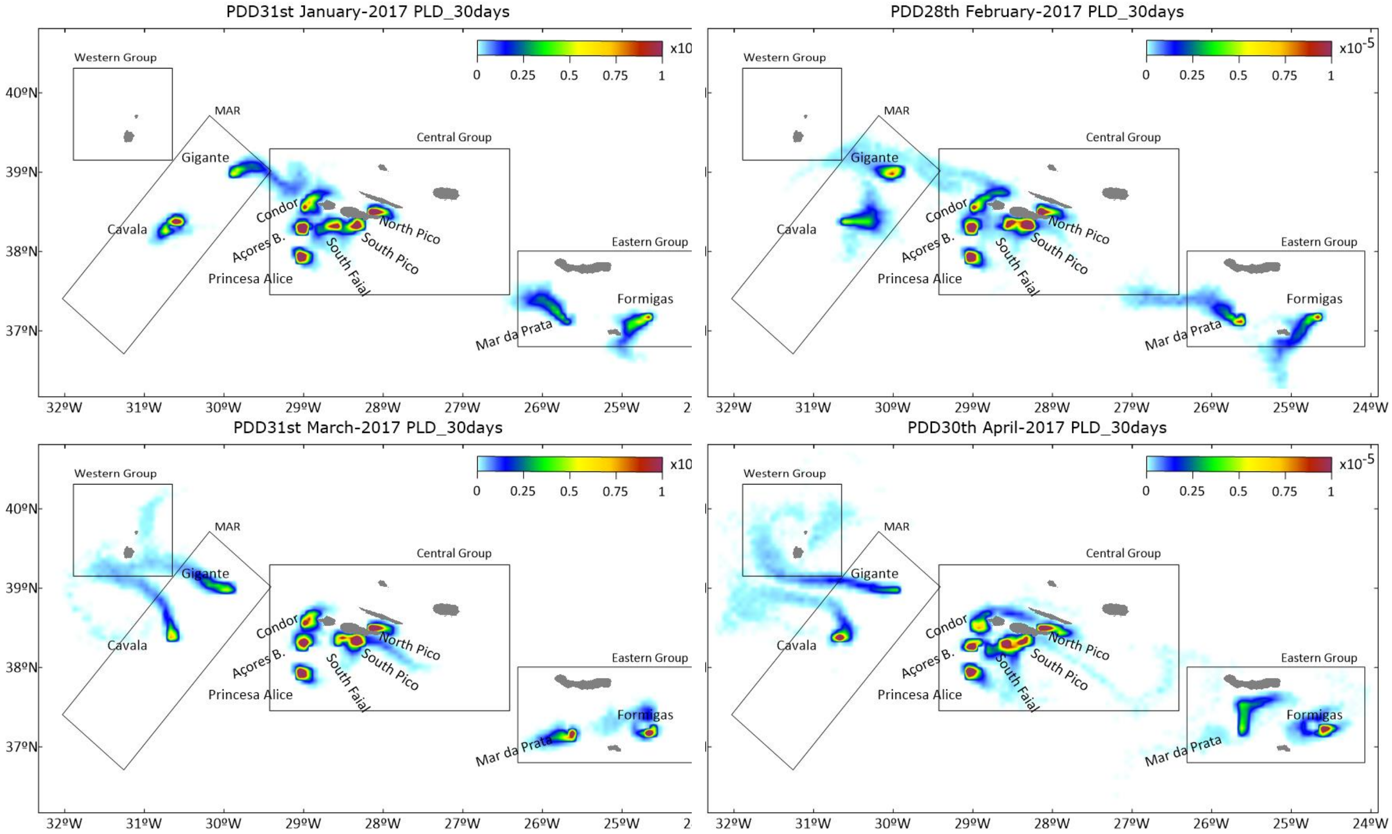
PDD31st January-2017 PLD_30days

PDD28th February-2017 PLD_30days

PDD31st March-2017 PLD_30days

PDD30th April-2017 PLD_30days

Figure 4.6- Particle density distribution for the annual release with a PLD of 30 days, for 31st January (top left): 28th February (top right); 31st March (bottom left); 30th April (bottom right); Black polygons represent the different release groups: MAR Group (L#1-Cavala, L#2-Gigante); Central Group (L#3-Princesa Alice, L#4-Açores Bank, L#5-Condor Seamount, L#6-South of Faial, L#7-South of Pico, L#8); Eastern Group (L#9-Mar da Prata, and L#10-Formigas).

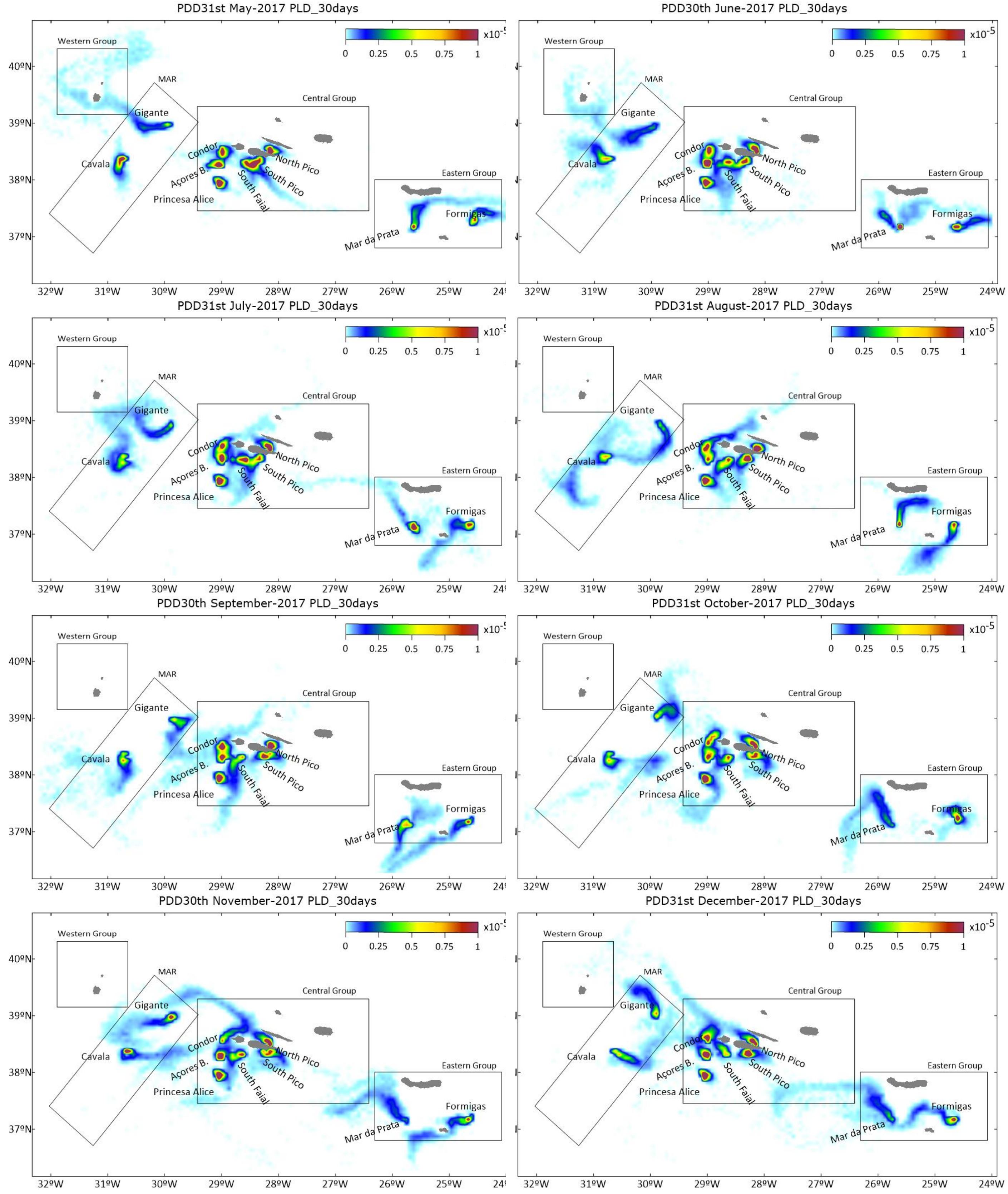

PDD31st May-2017 PLD_30days

PDD30th June-2017 PLD_30days

PDD31st July-2017 PLD_30days

PDD31st August-2017 PLD_30days

PDD30th September-2017 PLD_30days

PDD31st October-2017 PLD_30days

PDD30th November-2017 PLD_30days

PDD31st December-2017 PLD_30days

Figure 4.7- Particle density distribution for the annual release with a PLD of 30 days, 31st May; 30th June; 31st July; 31st August; 30th September, 31st October; 30th November, 31st December. Black polygons represent the different release groups: MAR Group (L#1-Cavala, L#2-Gigante); Central Group (L#3-Princesa Alice, L#4-Açores Bank, L#5-Condor Seamount, L#6-South of Faial, L#7-South of Pico, L#8); Eastern Group (L#9-Mar da Prata, and L#10-Formigas).

4.3.4.2. Particle distribution and hydrodynamic patterns

Larvae are advected by ocean currents, seasonal hydrodynamic patterns contribute to different particle dispersal plumes. The hydrodynamic patterns and the PDD (monthly average) for March and October, are represented in Figure 4.8 and Figure 4.9, respectively, at 750 meters depth.

During March an eddy is formed between the Western Group and the MAR, contributing to particle retention in this area. Apart from this eddy, it is denoted an absence of particles over the most intense currents. During October, the hydrodynamic patterns are different and, without this eddy, particles are advected along the MAR and towards the Central Group. In the Central Group dispersal plumes to the CG. In the Central Group, in both situations, the larvae plumes achieve different sponge aggregations.

Between the Central and Eastern Groups, the hydrodynamic patterns go mainly in the Eastwards direction during March, while in October it is clear a strong current coming from the East going Westwards. In the North-West part of the domain, currents are stronger during October than during March. For the October case, the major hydrodynamic fields present another pattern, and the higher velocity matches the absence or reduced particle density, and the higher density of particles occurs in locations with lower currents magnitude.

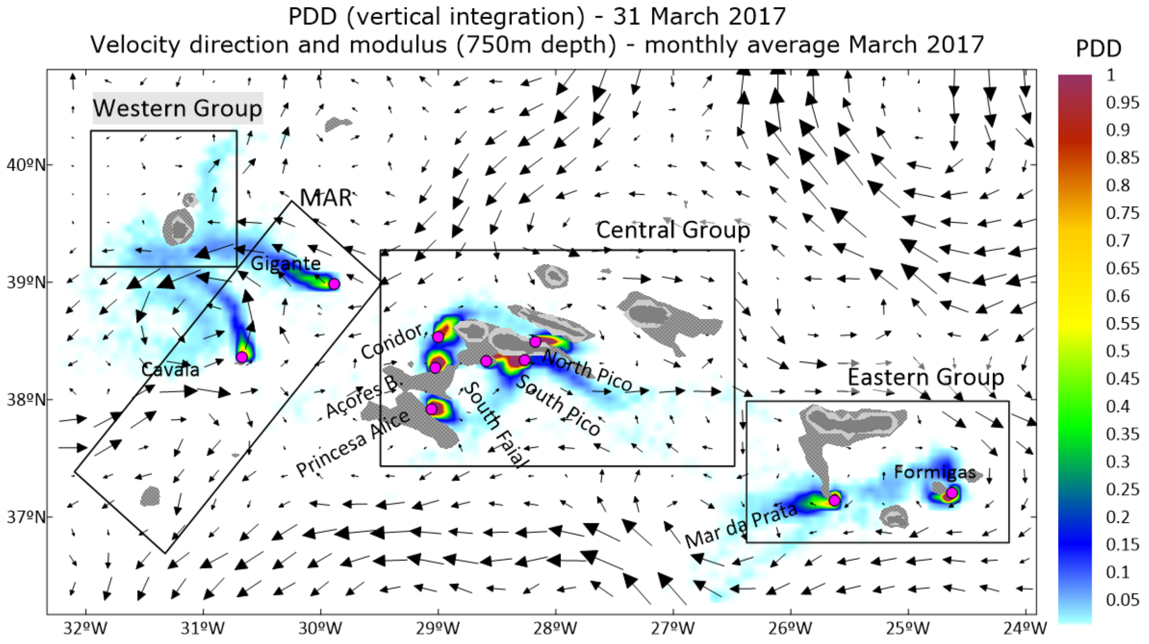

Figure 4.8- Particles density distribution integrated into the entire water column, represented by a gradient colour scale from blue to red, where 0 is white), vectors represent the monthly average of velocity modulus and direction at 750 meters depth. For 31 March 2017.

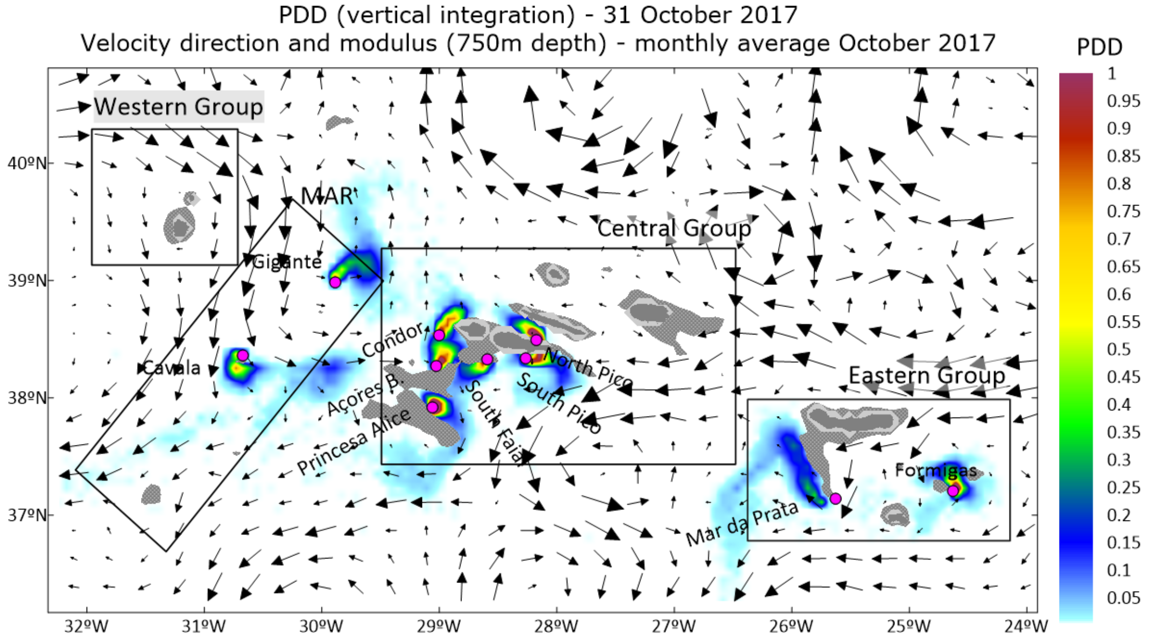

Figure 4.9- Particles density distribution integrated into the entire water column, represented by a gradient colour scale from blue to red, where 0 is white), vectors represent the monthly average of velocity modulus and direction at 750 meters depth. For 31 October

4.3.4.3. Particles travel distance

Larvae can travel from a few kilometres to more than 400km (Table 4.5). Travel distances are highly non-normal, and the Shapiro-Wilk Normality Test was performed to confirm it. Therefore, histograms of dispersal distances and median and the 95th percentile are used for this analysis, rather than mean values. Particle travel distances can range from a few meters to hundreds of kilometres. Maximum total travel distances are one order of magnitude larger than median distances. Across all March and October scenarios, the longer PLD gives rise to higher travel distances. Larvae travel distances change both seasonality and spatially. During the March release larvae from the MAR locations (L#1) and (L#2) have higher travel distances than the remaining locations (p95th of 207 and 220 km respectively).

The overall median particle distance In the CG, in all the tested scenarios, is lower than in the other groups (from 8 to 20km), which can contribute to higher self-recruitment levels. The October release contributes to higher travel distances. Besides the maximum travel distances registered, most larvae (more than 50%) travel up to 25km with a PLD of 15 days, as represented in histograms in Figure 4.10 and Figure 4.11. Only larvae from the Mar da Prata release (L#9), show different behaviour. With a PLD of 30 days, 50% of the larvae travel up to 50 km (28% are reported in the first bin of 25 km, and 22% in the second bin (25-50 km)).

Table 4.5- Particle travel distances for the different scenarios. Maximum distance (max); median distance (med) and percentile 95th

	Travel distance (kilometres)											
	PLD_15_March			PLD_30_March			PLD_15_October			PLD_30_October		
	max	med	P95	max	med	P95	max	med	P95	max	med	P95
Cavala L#1	221	14	126	375	43	207	152	16	73	325	33	138
Gigante L#2	285	18	107	462	44	220	179	15	77	334	32	195
Princesa Alice L#3	75	8	36	146	16	58	97	7	34	192	15	51
Açores B. L#4	83	8	39	186	15	53	132	10	43	314	18	71
Condor S. L#5	128	10	55	326	19	80	158	10	61	359	26	168
South Faial L#6	205	10	50	436	21	132	196	14	61	385	26	128
South Pico L#7	127	9	40	254	20	87	108	9	42	341	20	98
North Pico L#8	69	8	38	270	15	55	85	7	39	286	16	63
Mar da Prata L#9	118	10	47	264	22	97	176	27	86	406	50	148
FormigasL#10	113	11	59	218	24	96	168	11	55	345	23	162

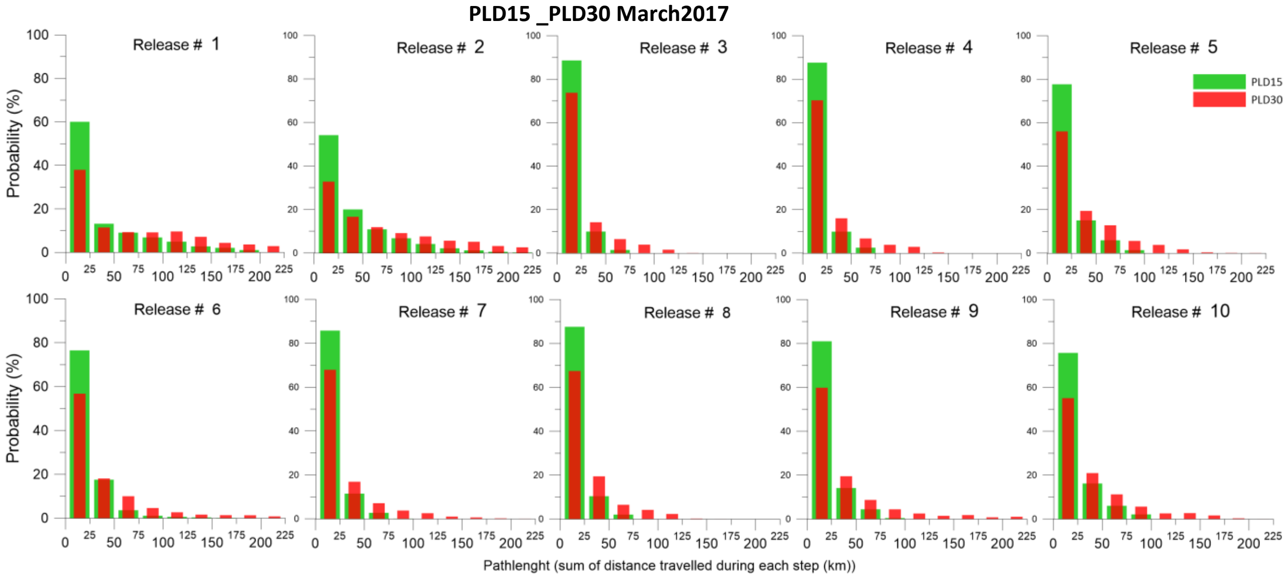

Figure 4.10- Histogram (in %) of the total travelled distance from each particle to the release point, in km, considering a PLD of 15 days in green, and a PLD of 30 days in red for March release. Distances greater than 225 km were extremely rare and were not shown.

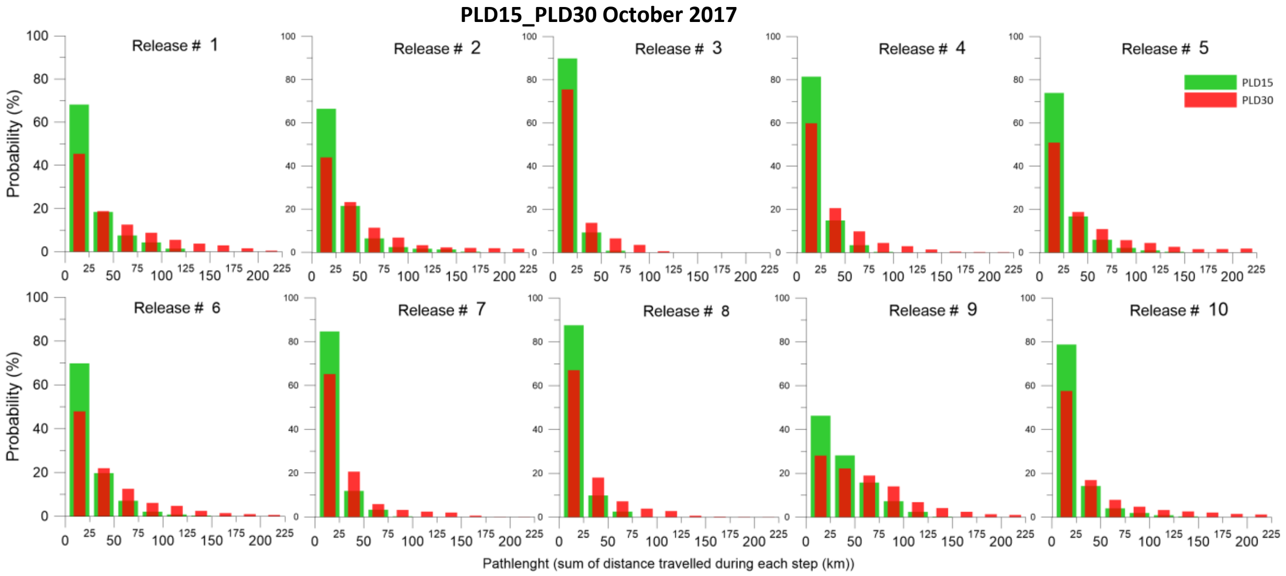

Figure 4.11- Histogram (in %) of the total travelled distance from each particle in km, considering a PLD of 15 days in green, and a PLD of 30 days in red for the October 2017 release. Distances greater than 225 km are rare and not shown.

4.3.4.4. Particles depth

Model results show that despite travelling in different bathymetric ranges, larvae mostly remain in a bathymetric range of the spawning location. Histograms of particles' depth along their trajectory are represented in Figure 4.12 for the March release, and in Figure 4.13 for the October release. In all the locations, except for Location L#1, larvae remain mostly in the bathymetric range of the release (>40%) (Figure 4.12, Figure 4.13). In all the situations a longer PLD contributes to a wider distribution of particle depth along the water column. Results show no significant difference between the particle depth during March and October releases.

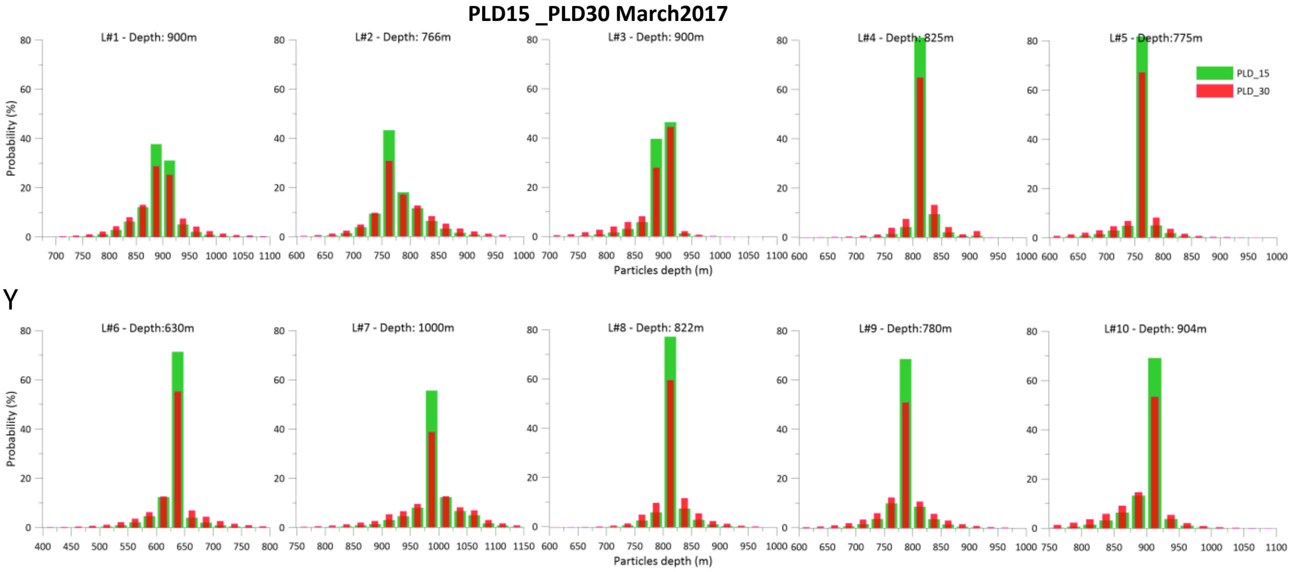

Figure 4.12- Histogram of particles' depth along their trajectory, for each location, for PLD15 and a PLD30 days for March 2017 release. The depth of the respective release is detailed in the top of each graph

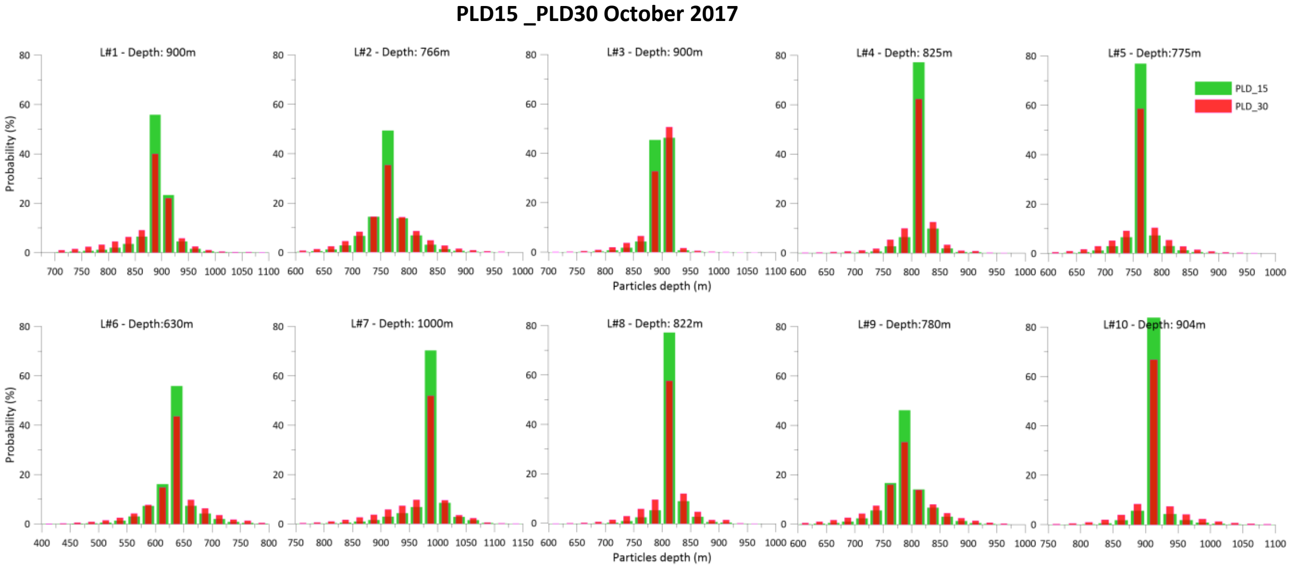

Figure 4.13- Histogram of the particles' depth along their trajectory, for each location, for PLD15 days and a PLD30 for the October 2017 release. The depth of each respective release is detailed at the top of each graph.

4.3.4.5. Connectivity between sponge aggregations

Larvae dispersal originates different connectivity relations considering the different pelagic larval durations (PLD). Connectivity is illustrated by connectivity matrices, and also by connectivity arrows represented on the maps. Matrices depict the percentage of self-recruitment and connectivity between different sponge aggregations. A PLD of 30 days (Figure 4.15) enables more connectivity between the different sponge aggregations than a PLD of 15 days (Figure 4.14). Although, lower PLD (15 days), gives rise to higher self-recruitment levels.

The connectivity between sponge aggregations of the central group is much higher in a scenario of PLD of 30 days than with 15 days (PLD15). There is no connectivity between the EG and the CG or WG, in both scenarios. In the WG the connectivity between Formigas (L#10) and Mar da Prata Seamount (L#9), is unidirectional, with a PLD of 15 days, and bidirectional with a PLD30.

The yearly release allows for the analysis of all different spawning and hydrodynamic scenarios. However, deep-sea sponges spawning may have seasonality, related to phytoplankton blooms (Leys and Lauzon, 1998). Seasonal analysis was performed for March and October releases.

Yearly release- PLD 15

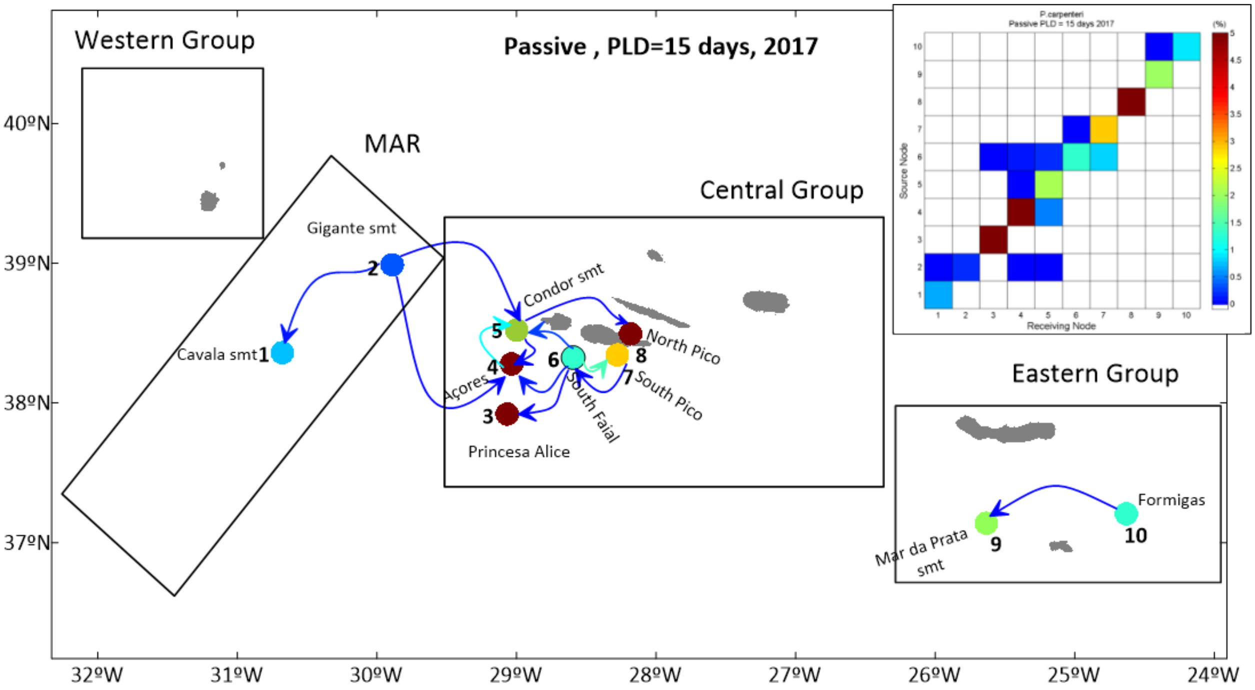

Figure 4.14-Map of connectivity relations, and respective connectivity matrix, for a yearly release (2017) with a PLD 15, connectivity arrows and auto-recruitment circle colours represent the percentage of settled particles.

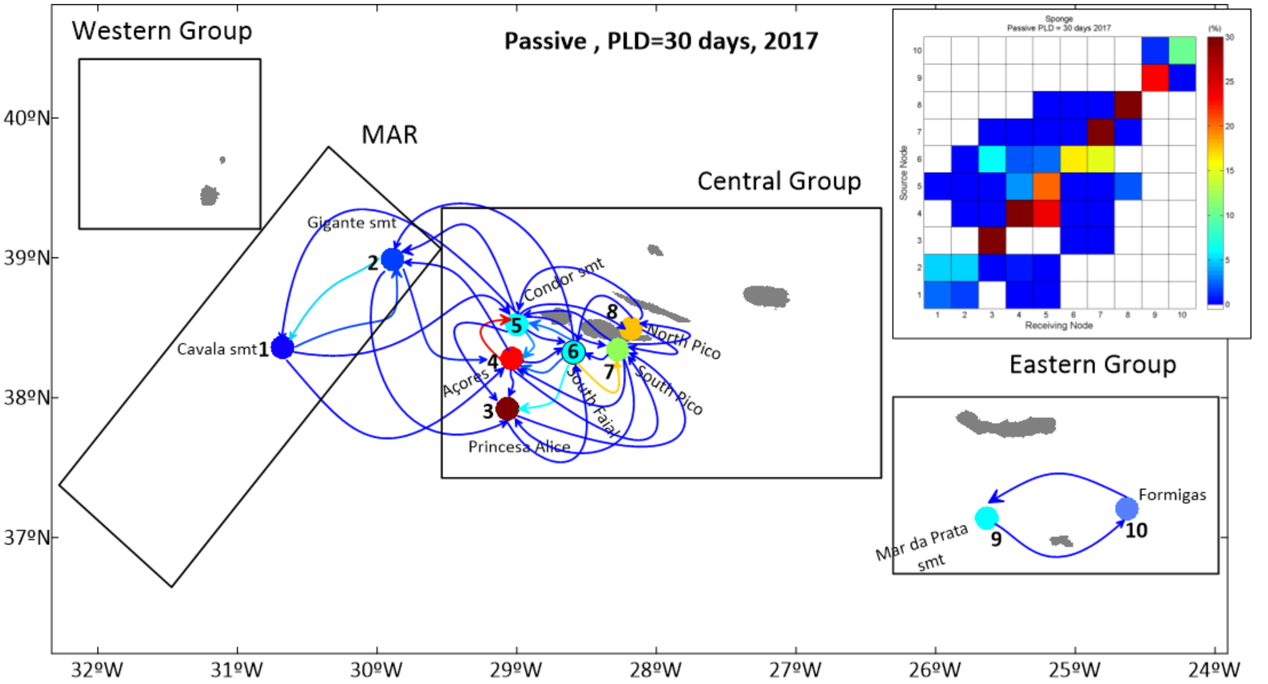

Figure 4.15- Map of connectivity relations, and respective connectivity matrix, for a yearly release (2017) with a PLD 30, connectivity arrows and auto-recruitment circle colours represent the percentage of settled particles.

Seasonal releases (March and October)

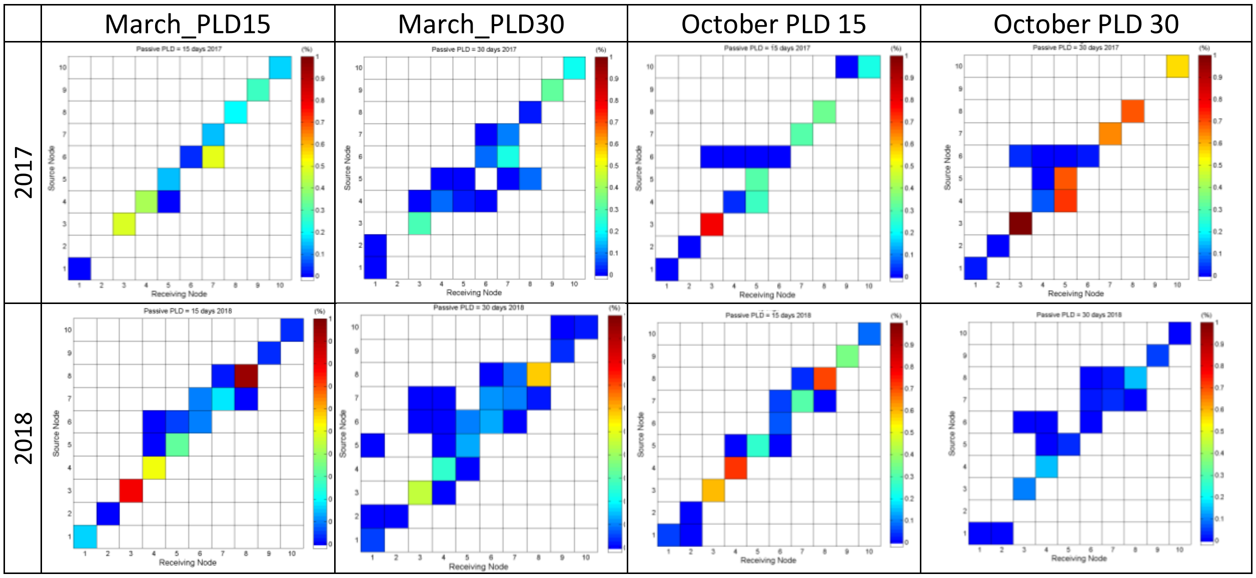

Figure 4.16- Connectivity matrices for the March_PLD15, March_PLD30, October_PLD15 and October_PLD30 for 2017 on top and 2018 on the bottom, connectivity and auto-recruitment colours represent the percentage of settled particles.

The hypothesis of a seasonal spawning release, occurring only for one month, in March and October, conducts to lower larvae exchange between the different sponge aggregations (Figure 4.16). Only in the scenario March_PLD_30_2018 occurs the connectivity between larvae from the CG and MAR, between Azores bank (L#4) and locations L#1 and L#2. In the remaining scenarios, no connectivity occurs between the different groups.

In the CG, connectivity between different sponge aggregations reveals seasonality, with a higher number of connectivity relations in March scenarios. Also, the self-recruitment percentage is different from March to October, with the releases from CG revealing the highest self-recruitment percentage in October. In different situations, Gigante seamount (L#2) doesn't have self-recruitment, nor connectivity with any other release. The same for Mar da Prata seamount (L#9), with no self-recruitment in *October_PLD30_2017*. This absence of self-recruitment indicates that these can be more vulnerable sponge aggregations, depending on larvae from other locations for reproduction.

Particles settlement location

Besides the sponge aggregation locations in the study, larvae can also settle in other regions of the domain. The study of the location of settled particles was performed within the defined bathymetric range of 600 to 1000 meters depth. Results show that seasonal dynamics can induce different settlement positions (Figure 4.17 for the March release, Figure 4.18 for October, and the yearly release). This difference is more denoted in the settlement locations in the WG, and along the MAR, where larvae from different populations settle in different locations depending on the seasonality.

During the March release (Figure 4.17) larvae from Cavala (L#1) and Gigante (L#2) seamounts settled around Flores and Corvo Islands, while during October did not. Moreover, larvae from Cavala can settle in seamounts West of the MAR, like the Buchanon seamounts' complex after the March release. While, after October, larvae from Cavala settle along the MAR and along the western slope of the central group of the Azores archipelago, including the Voador seamount.

In the Central Group, despite the proximity of the different locations, seasonal differences are denoted. During March, larvae from North of Pico (L#8) settle in the Eastern part of the channel between Pico and São Jorge islands, while in October in the Western part. During March, larvae from Condor Seamount settle in the West and North of São Jorge island, while in March don’t. Between the CG and the EG, only larvae from the South of Faial (L#6) and Mar da Prata (L#9) settle, in João de Castro bank, specifically South of Faial during March, and Mar da Prata during October. During March, larvae from the South of Faial can also settle on the West and

North of São Miguel island in the EG. These results confirm the prominent West-East dispersion during March, and East-West during October.

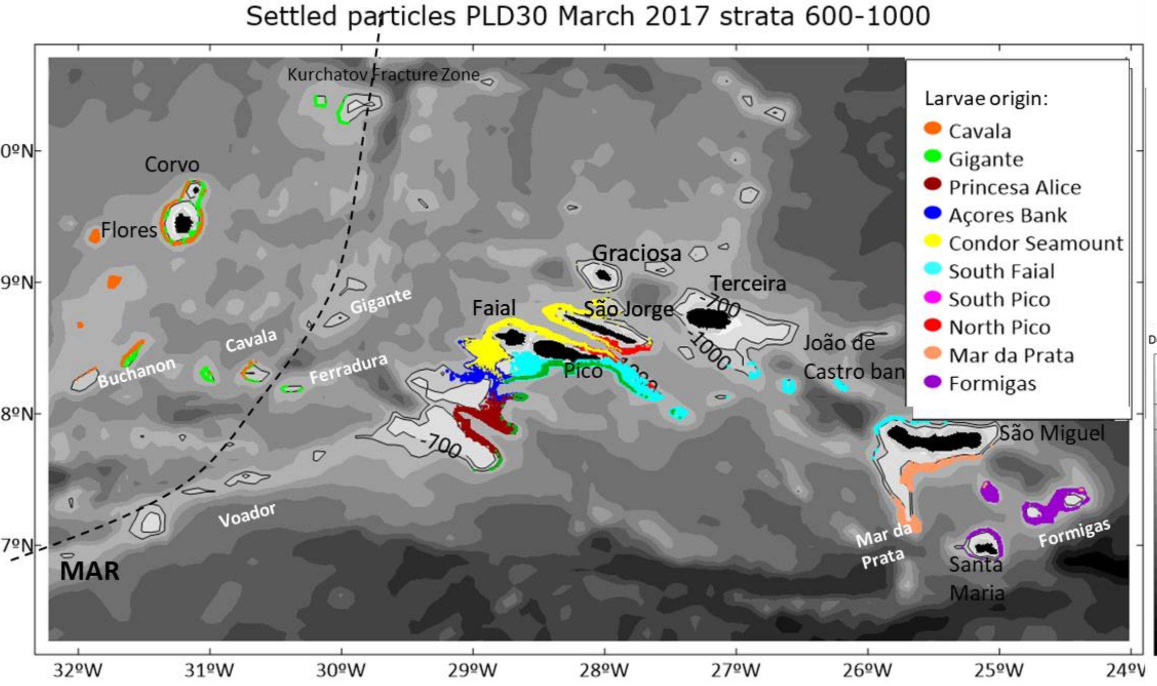

Figure 4.17- Location of settled particles along the domain, in the bathymetric range from 600 to 1000m depth, for March release. Different colours represent different releases. Bathymetry is represented in a grey colour scale.

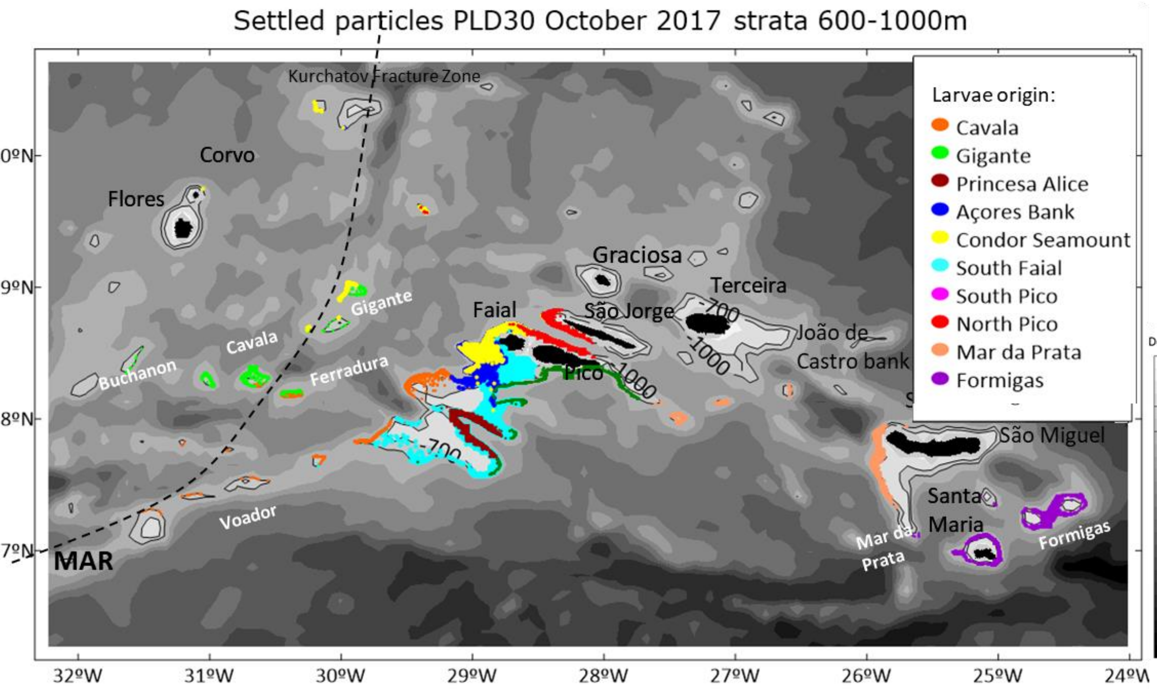

Figure 4.18- Location of settled particles, in the entire domain, in between the bathymetric range of 600 to 1000m depth, for October. Different colours represent different releases. Bathymetry is represented in a grey colour scale.

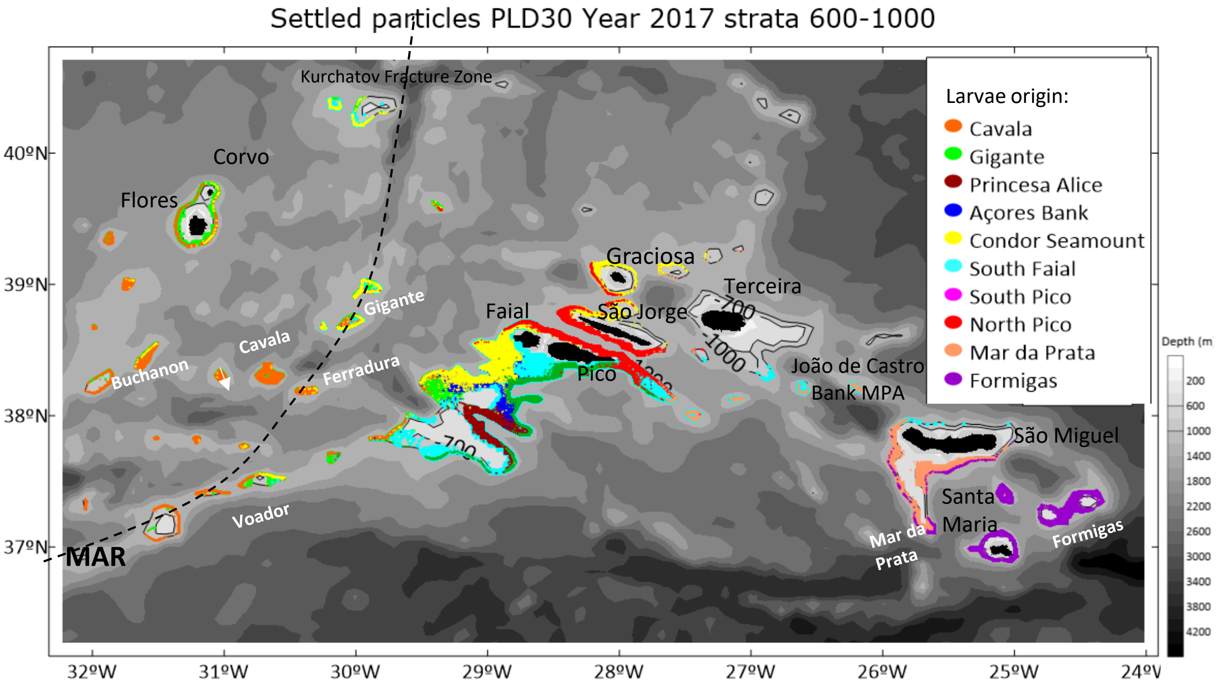

Figure 4.19- Location of settled particles, in the entire domain, in the bathymetric range from 600 to 1000m depth, for the yearly release of 2017, for each origin; Different colours represent larvae origins: a) Cavala; b)Gigante; c) Princesa Alice; d) Açores bank; e)Condor Seamount; f) South Faial; g) South Pico; h) North Pico, i) Mar da Prata, j) Formigas. Due to the higher number of particles represented an overlapping may occur in the different settled locations. Bathymetry is represented in a grey colour scale.

The yearly release considers all the monthly scenarios, and consequently more settled larvae along the Azores region. As a consequence of the multiple populations in the study, overlapping of the represented particle occurs, in the map of Figure 4.19. Thus, representations of the settled larvae from each larvae origin are represented in Figure 4.20.

Considering the bathymetric range from 600m to 1000m, larvae can settle around all the islands except Terceira island (Figure 4.19). The larvae settle along the MAR and different seamounts West and East of the MAR, and in different locations in the Central Group. The Central Group is an important recruitment area. This result highlights the potential connectivity between the populations in the Central Group.

Major results show that during the yearly release, larvae from Cavala and Gigante seamounts mostly settle along the MAR, around Flores and Corvo islands, and along the west slope of the Central Group, but they hardly achieve the East part of the Central Group (Figure 4.20 a) and b)). Gigante Seamount can receive larvae from different locations (Cavala (L1), Gigante(L#2), Açores bank (L#4), Condor (L#5), and South of Faial (L#6) Figure 4.15), contrasting with the seasonal releases where larvae exchange occurs only during the October scenario, between Gigante (L#2) and Cavala (L#1) seamounts. The larvae from South of Faial (L#6) are the ones with a wider range of settling locations, they can settle along MAR, in the WG, in the CG, in João de Castro bank, and in the EG, in the North of São Miguel (Figure 4.20 f)).

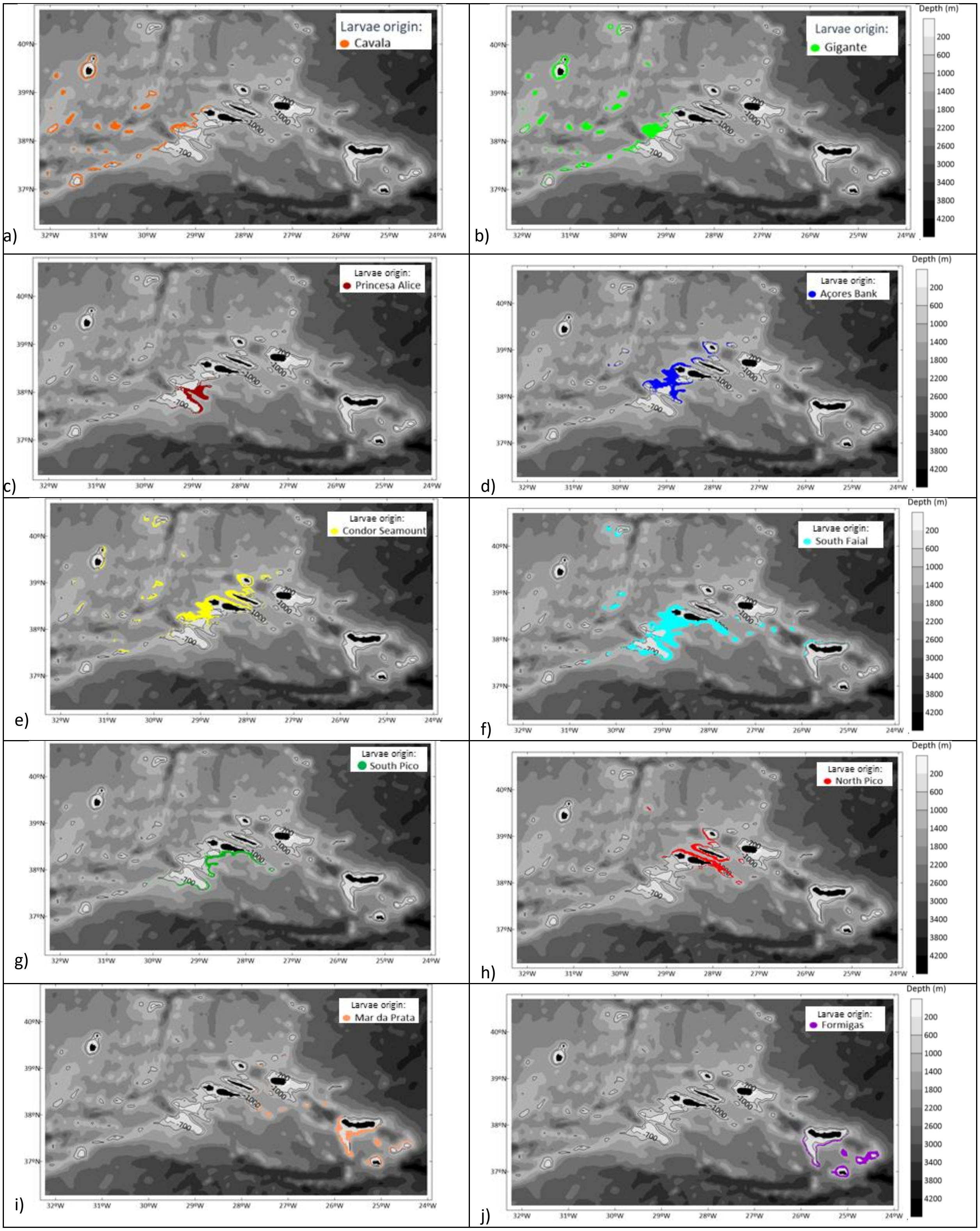

Figure 4.20- Location of settled particles, in the entire domain, in the bathymetric range from 600 to 1000m depth, for the yearly release of 2017 with a PLD of 30 days, for each origin. Different colours represent different releases: a) Cavala; b)Gigante; c) Princesa Alice; d) Açores Bank; e)Condor Seamount; f) South Faial; g) South Pico; h) North Pico, i) Mar da Prata, j) Formigas. Bathymetry is represented in a grey colour scale.

Among the populations in the study, the ones from the Eastern Group are the most isolated, with no larvae exchange with the remaining populations. Mainly due to their distance from the remaining populations, but also as a consequence of the hydrodynamic patterns between the CG and the EG, hampering their advection in the Westwards direction Figure 4.7. This lack of connectivity with the remaining populations in the study indicates that these populations are susceptible to being isolated from the remaining populations in the study. Formigas population only exchanges larvae with the Mar da Prata population and faces several scenarios with no self-recruitment (Figure 4.16), revealing its vulnerability. Moreover, Larvae from Formigas only settle in the EG locations, not being able to achieve any region in the CG (Figure 4.20j)). Despite not settling in the other sponge locations in the study, larvae from Mar da Prata can settle in different locations along the Central Group: in Dr João de Castro bank, on the East of Pico and São Jorge islands, North of Graciosa and Terceira islands (Figure 4.20i)). This potential connectivity with locations of the Central Group shows the relevance that this population can have in the connectivity along the archipelago, not only from being able to establish connectivity between the EG and different locations in the CG but also bridging the gap of connectivity that Formigas population faces.

Model results suggest that larvae from Princesa Alice have low dispersal potential (Figure 4.20 f)). But it is an important sink location, receiving larvae from Gigante, and all the locations from the Central Group except North of Pico.

The release point considered in this case study for the Princesa Alice seamount is located in the southern slope of the seamount, outside the MPA delimitation. Larvae from Mar da Prata em South of Faial can settle in the João de Castro MPA (Figure 4.19). Larvae from none of the other aggregations under study settle at this location.

Larvae from Formigas only settled in the Mar da Prata seamount and along the plateau of São Miguel and Santa Maria islands, with no connectivity with the remaining populations in the study. This low number and variability of larvae exchange highlight the susceptibility of this population, which may be isolated from the other populations. The studied sponge aggregations from Formigas and Condor are located inside the MPAs.

4.3.5. Discussion

Larval dispersal is an important ecological process (Ross et al., 2020). This is of particular importance for deep-sea sponges, as they are sessile organisms throughout their adult life (Cowen and Sponaugle, 2009), therefore, relying upon larval dispersion for colonizing new areas, and for population dynamics and persistence (Ross et al., 2020).

Pheronema carpenteri larvae were modelled as passive tracers, similarly to other modelling studies on deep-sea sponge larvae dispersal (Kenchington et al., 2019; Swearer et al., 2019). Because particles are advected by the hydrodynamic conditions, it is required an accurate high-resolution hydrodynamic solution (Ross et al., 2020) and a calibrated lagrangian model, to ensure that particle dispersal can provide reliable dispersal patterns (North et al., 2009). Regarding this, calibration tests were performed to determine the correct number of particles to use for this case study.

The FUV method (Fraction of Unexplained Variation) (Simons et al., 2013), indicates that the most efficient number of particles was 150000 particles per month, per release. Sponge locations at the MAR (L#1 and L#2,) reveal a higher FUV, requiring a higher number of particles to produce a valuable result. This can be a consequence of their higher dispersal travel distance (Table 4.5), but also their proximity to the model limits that can originate the escape of particles out of the domain. Moreover, the dispersal pathlength saturation method indicates 100000 as an efficient number of particles to produce an accurate result. In this situation, the higher number of particles (150000) was chosen. Nevertheless, this decision is always a compromise between computational time and result accuracy (Jones et al., 2016), and in this case, it was possible to choose the higher number of particles: 150000 per month per release.

The pelagic larval duration (PLD) is one of the most relevant parameters when applying the larvae dispersal model (Henriksen et al., 2003; Howell et al., 2016; Wang et al., 2021). The results of this study corroborate the common assertion regarding the positive relationship between PLD and dispersive capabilities in marine larvae (Holstein et al., 2014). Results show that longer PLDs generate higher dispersal patterns, higher travelled distances and consequently higher particle exchange between different sponge aggregations.

All the hypotheses in the study, regarding different PLDs and different seasonal releases, allow the study of a wider range of scenarios and biological hypotheses.

Connectivity and self-recruitment

Model results for seasonal releases (March and October) show that apart from Gigante Seamount (L#2) and Mar da Prata (L#9), all the other locations have self-recruitment, locally retaining a proportion of their larvae. Gigante seamount and Mar da Prata can have no self-recruitment in different scenarios. Therefore, these populations can be more vulnerable, because of the absence of self-recruitment. Gigante seamount is located in a highly hydrodynamic region, over MAR, under the influence of strong hydrodynamic patterns that contribute to a higher particle dispersal away from the recruitment area (Figure 4.8 and Figure 4.9). In Mar da Prata, for the scenarios revealing no self-recruitment (October 2017 PLD15 and PLD30) the travel distances are maximal. The median travel distances are the greatest in both scenarios: 27km for PLD_15_october and 50km for scenario PLD_30 _October, with a maximum travel distance of 406km in the last case. These long distances are a consequence of the strong currents occurring during October between the CG and EG.

Even with their long larvae travel distances, sponge aggregations at the Eastern Group (EG) are isolated from the others in the study, revealing no particle exchange among other sponge aggregations in the study (no connectivity). Mainly due to their distance, but also constrained by the stronger currents between CG and EG.

All the scenarios in the study show that sponge locations in the CG are well connected, with the exchange of larvae between different populations. This connectivity can result from the proximity of these sponge aggregations, but also from the local hydrodynamic patterns characterized by lower velocities, contrasting with the strong hydrodynamic patterns that occur at the WG and MAR during March and between CG and EG during October.

The yearly release was performed to analyse the potential connectivity between all the sponge aggregations, considering more scenarios than the March and October spawning scenarios. The connectivity matrices for this yearly release (Figure 4.15), reveal higher particle exchange between the sponge aggregations. In the CG, with PLD30, most of the locations are connected. However, most of these connectivity levels are lower, with less than 0.75% of larvae supply (Table A1 in ANNEX 2), and the self-recruitment range from 0 to 4%. When considering PLD15, which is the most consensual PLD for deep-sea sponges larvae (Maldonado, 2006; Wang et al., 2020), the yearly scenario shows higher self-recruitment percentages, from 0 to 5.4% (maximum in Açores Bank (L#4)) however with fewer particles exchanged between different releases. This self-recruitment is beneficial to maintain the population, but the lack of connectivity and particle exchanges between different populations is disadvantageous for these populations.

Sponge aggregations from CG can also be connected with the MAR. This connectivity is bidirectional, between Cavala Seamount, Açores Bank, and Condor Seamount. Particles from the Gigante seamount can settle in Princesa Alice, Açores Bank, and in the Condor seamount. These results point out that these 3 locations: Princesa Alice, Açores Bank, and Condor Seamount are important sinks of larvae in the Azores region.

Scenarios with 15 days of PLD show no connectivity between sponge locations North and South of Pico in 2017, but the existence of connectivity in 2018. This shows how the system is dynamic, and how the hydrodynamic patterns can have different patterns from one year to another. Maps of particle distribution (Figure 4.8 and Figure 4.9) show how dynamic is this region, and how the hydrodynamic patterns can influence larvae dispersal. Larval dispersal plumes from, North of Pico sponge aggregation (L#7), located in the channel between Pico and São Jorge islands, reveal high dynamic dispersal patterns, being advected in towards East on March (Figure 4.8), and towards West on October (and Figure 4.9). Only a higher model resolution or a multiyear analysis would provide more information to better study the connectivity between these two locations.

Particles vertical migration

Model results show that larvae remain mostly at the same bathymetric range of the spawning location. This can be a consequence of the passive behaviour of these larvae, without swimming activity, depending mainly on the hydrodynamic patterns for their dispersion. Therefore, due to the lower vertical currents, and lower velocity, typical from the deep-sea, and bottom layers (as shown in Chapter 3), maintaining the larvae dispersal in the deeper layers. This demersal larvae behaviour was reported in other deep-sea dispersal studies and might be related to larval behaviour in searching for potential recruitment areas in their suitable bathymetric range (Young et al., 2012).

Temporal and spatial variability

Particle dispersal patterns reveal high variation along space and time, as a consequence of high dynamic oceanographic conditions in the region. During March, the domain is under the influence of a strong current, over MAR, with strong velocities at 750 meters creating a strong hydrophysical barrier, preventing particles from crossing between MAR and CG. By the influence of the meanders of this current, particles from Gigante Seamount (L#2) are advected away from this recruitment area, avoiding any self-recruitment in this sponge ground during Spring scenarios. Conversely, these hydrodynamic patterns form an eddy, originating particle exchange between the Gigante and Cavala seamounts.

In October, hydrodynamic patterns are different, inducing particle exchange between MAR and CG. Between CG and EG the high-velocity currents, and consequent formation of an eddy, create a hydrodynamic barrier between these two groups blocking particle exchange. Contrasting with the eddy identified in March over MAR, the October eddy does not contribute to particle retention, but the opposite, avoiding particles from crossing that area. This eddy creates (Figure 4.10), creating a strong hydrodynamic and physical barrier.

Contrasting with strong currents that can transport particles out of the domain, or for regions without suitable recruitment areas, near the islands and seamounts, the lower velocities induce higher particle retention and, consequently, higher connectivity between different release locations.

Results show that larvae can travel up to 225km, with 30 days of pelagic duration. However, particles from Princesa Alice seamount don’t travel more than 100km. This lower travel distance can be a consequence of the lower velocities in this region, which also induce a higher percentage of self-recruitment.

All these results highlight the seasonal and spatial variability of the hydrodynamic patterns around the archipelago, responsible for the generation of highly spatiotemporally variable submesoscale patterns that influence larval dispersal, revealing the importance of studying different spawning scenarios.

The model resolution, 6km*6km, does not allow the dispersal analysis at a seamount scale resolution, nor how connectivity can change along the island's slope. This type of analysis would require a downscaling or a hydrodynamic model with higher resolution (North et al., 2009). Nonetheless, the model reflects the seamounts and islands' effects on a regional scale, simulating the typical lower velocities in the seamounts (Giacomello and Menezes, 2012; Lima et al., 2020). These lower velocities induce connectivity in these areas, as it is visible in larval dispersal within the region, enhancing particles' retainment, higher levels of connectivity between different sponge aggregations, also higher levels of self-recruitment. The connectivity depicted on the connectivity matrices (Figure 4.16) reflects these dynamic oceanographic patterns in the regions. Connectivity results show that sponge locations from the central groups are highly connected. This high exchange and retention of larvae is a particularly important process for ecosystem resilience, also indicating the retention of other deep-sea species like cold-water corals (CWC) that inhabit these deep-sea regions in the Azores (Bode et al., 2019; Swearer et al., 2019).

The different larvae exchange between different groups (MAR and CG), contributes to the persistence of these populations, mitigating the risk of recruitment failure in case of the absence of self-recruitment (Cowen and Sponaugle, 2009; Wang et al., 2021). Furthermore, this higher exchange of larvae would enhance genetic diversity conferring greater resilience to the population (Holstein et al., 2014).

Results point out a higher vulnerability of Mar da Prata aggregation, due to the absence of a permanent self-recruitment, and low connectivity patterns between the populations in the study.

4.3.6. Partial conclusions Case Study 1

The larval dispersion and connectivity between 10 selected *Pheronema carpenteri* sponge aggregations in the Azores were estimated using a biophysical particle model application. The model was able to simulate larval dispersal in the Azores region and to study different seasonal and biological trait scenarios. Model results show that sponge aggregations from the Azores Central Group are well connected, revealing particles exchange between the different deep-sea sponge populations in the study. However, there is some degree of isolation among the larvae of the Eastern Group and the other populations in the study.

Major results indicate that sponge aggregations from the Central Group can represent a significant source and sink of larvae. The CG receive larvae from different sponge aggregations, acting as a nursery for *P. carpenteri* sponges in the Azores. During October, there is connectivity between MAR and CG, while in March there is not. Condor Seamount can exchange larvae with Cavala seamount, in MAR Group. Princesa Alice has high particle retention, receiving larvae from several sponge aggregations, serving as a sink aggregation in the Azores. These results reinforce the importance of maintaining the protection efforts in the MPA Condor and Princesa Alice, once they are important recruitment areas.

Sponge aggregation from the EG are not connected with the remaining populations. And Mar da Prata sponge aggregation faces scenarios without any connectivity or self-recruitment, being, consequently, more vulnerable. Therefore, the Formigas MPA, is of great importance to guarantee the maintenance of these sponge aggregations, due to their lack of particle exchange with the remaining populations in the study, and the weak recruitment taxes.

Nevertheless, larvae from Mar da Prata, present long travel distances, being able to settle in different locations in the CG, serving as a potential connectivity link between CG and the EG.

Açores Bank, South of Faial, and South of Pico also exchange particles among different aggregations, potentially inducing higher resilience through the exchange of larvae from multiple populations.

Results show that larvae from the CG and EG can settle in João de Castro bank. These settled particles indicate potential connectivity from both groups with João de Castro Bank pointing out a possible interconnection between these groups.

The pelagic larval duration is crucial for population connectivity. A PLD of 15 days can contribute to a higher fragmentation of the *P. carpenteri* populations in the study area, while the connectivity resulting from a PLD of 30 days would ultimately regulate populations' persistence and recovery after disturbance (Cowen and Sponaugle, 2009). More information regarding deep-sea sponges' biology or larval behaviour would provide essential data for more detailed studies.

Furthermore, this modelling approach can provide valuable information for the implementation of protection plans and the establishment and prioritization of future management plans.

4.4. Case Study 2- *Chaceon affinis*

4.4.1. Introduction

Chaceon affinis is a deep-sea red crab (DSRC) that inhabits various substrata on continental slopes, seamounts and deep-water banks in the northeast Atlantic (Castro et al., 2010; Gonzalez et al., 1998). Widespread throughout the world, several DSRC species are of interest to fisheries such as *Chaceon quinquedens* Smith, 1879 and *Chaceon fenneri* (Manning and Holthuis, 1984) (Tuset et al., 2011). In European waters, *C. affinis* has been considered a candidate for further exploitation (Pinho et al., 2001; Santos et al., 2019). However, despite the growing interest in the exploitation of crab resources, in the Azores fishery exploitation of *C. affinis* is discouraged (Santos et al., 2019). Further scientific studies to guide management and define sustainable levels for the exploitation of these resources are necessary. The use of modelling tools to study the larval dispersal of this species in the Azores region provides additional information about recruitment mechanisms, and population connectivity, supporting further scientific studies.

Several studies regarding *C. affinis* were developed in the Macaronesia and other Atlantic areas (Guerao et al., 1996; Weinberg et al., 2003), particularly in Gorringe Bank (Hilário and Cunha, 2013) and in the Azores region (Pinho M. et al., 2020; Santos et al., 2020), focused on ecological characteristics, describing the biology and population dynamics and also fishing dynamics. Different reproductive parameters have been studied previously for *C. affinis*, including size at the first maturity stage, sex ratio and fecundity (Fernandez-Vergaz et al., 2000; López Abellán et al., 2002; Tuset et al., 2011), however important questions related to mating behaviour, larvae behaviour, synchrony and seasonality remain unanswered.

4.4.1.1. *Chaceon affinis*

C. affinis inhabits continental and island slopes, seamounts, and deep-water banks, at a depth of 400–1500 meters in the northeastern Atlantic, from Iceland to Senegal (López Abellán et al., 2002), including Macaronesia and other Atlantic areas (Guerao et al., 1996; Hilário and Cunha, 2013; Landeria and Tamura, 2018; Pinho et al., 2001; Weinberg et al., 2003).

In the Azores, higher abundances of *C. affinis* were reported between 700 and 900 m depth (Pinho et al., 2001). Segregation by sex, related to depth, was reported, with the dominance of males occurring at depths up to 800 meters, while females between 800 and 1000 meters depth (Biscoito et al., 2015; Pinho et al., 2001). The presence of females in deeper areas may be related to seasonal downward movements of ovigerous females (López Abellán et al., 2002; Santos et al., 2019). The upper bathymetric distributions of C*. affinis* might also be related to the presence of *Cancer bellianus*, a predator, that inhabits shallower depths, creating a border of competition at around 500–600 m depth, where larger males of *C. affinis* exist maintaining the area of distribution and isolating reproduction and recruitment zones (López Abellán et al., 2002). In the Azores, *C. affinis* presents a patchy distribution, with non uniform distribution and abundances in different specific habitats (Pinho et al, 2020).

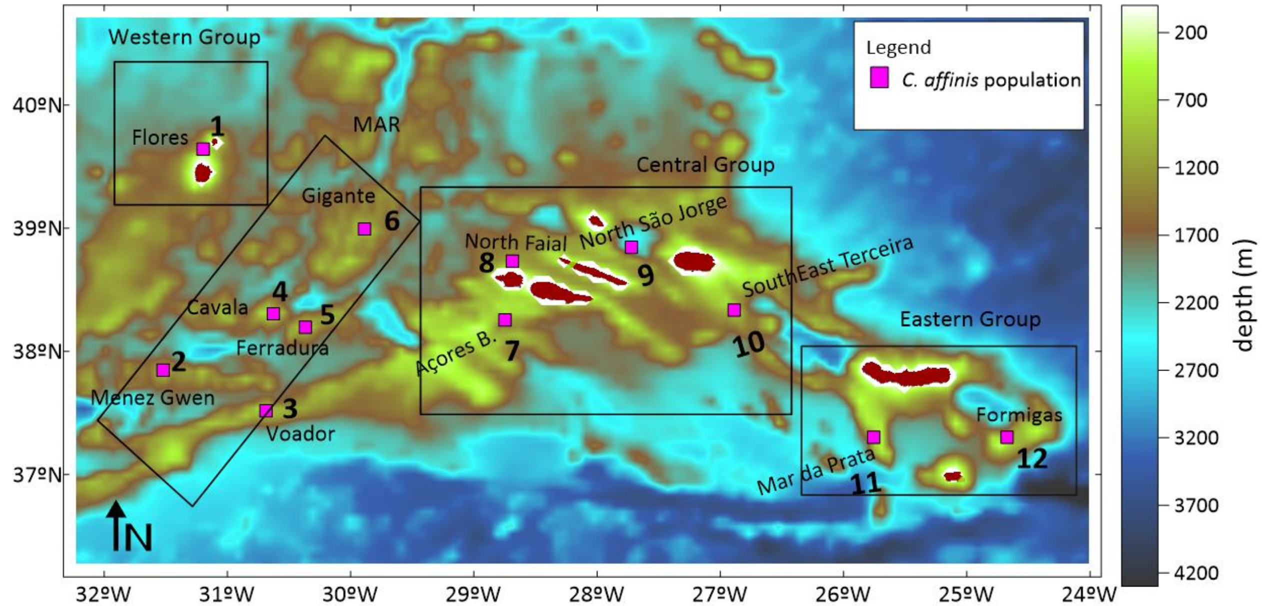
Model bathymetry (m) and *Chaceon affinis* populations

Figure 4.21- *Chaceon affinis l*ocation considered in this case study, locations are based in the bibliography (Santos et al., 2019 and Kaschner et al. 2019), and grouped in different clusters (Western Group, MAR, Central Group and Eastern group) for better results discussion.

Like most deep-water species, deep-sea crabs present k-strategist life traits, characterized by exhibiting slow growth, long life cycle, late maturity (5–15 years), low fecundity, irregular recruitment and often very low resilience which makes them highly vulnerable to overfishing (Da Silva Cortinhas et al., 2022; Guerao et al., 1996). Therefore, a good knowledge of their early life-history dynamic and reproductive strategies is crucial to better understanding the vulnerability of DSRC stocks, and to define strategies for species protection and implementing guidelines for sustainable fishery management (Santos et al., 2019).

Regarding the spawn frequency, studies suggest that females spawn probably every two years (Stevens and Guida, 2016). In the Azores, *C. affinis* ovigerous females were found between October to March, with the peak of spawning activity occurring during the autumn and winter (Pinho et al., 2001). Ovigerous females were found from October to April, in Madeira islands, and all year round in the Canarias (Biscoito et al., 2015). Tuset et al. (2011) observed ovigerous females in the last developmental stage during all quarters of the year. These studies suggest that gonad maturation and release of larvae are asynchronous throughout the spawning season (Biscoito et al., 2015; Tuset et al., 2011). The number of eggs in *C. affinis* can range from 200 000 to 600 000 eggs, with six development stages (Tuset et al., 2011).

4.4.1.2. Larvae biology

C. affinis larvae are released in the water column (Landeria and Tamura, 2018). The larvae phase is pelagic and consists of four zoeal stages and a final megalopa (Tuset et al., 2011). Larvae are planktotrophic (Sulkin and van Heukelem, 1980), and can achieve the surface layers (Landeria and Tamura, 2018). Recruitment takes place in deep waters, nevertheless, individuals migrate to the upper slope as they grow (López Abellán et al., 2002).

Guerao et al. (1996) described the morphology of the first zoa stage of *C. affinis,* evidencing no differences in larval morphology between different species of *Chaceon*. So, in the absence of more information considering this species, information about other species from the same family can be valuable. Other species from the same family, namely *C. quinquedens*, which is widely distributed throughout the western Atlantic, from Nova Scotia to South Carolina, have been the object of several studies considering larval behaviour (Kelly et al., 1982; Martínez-Rivera and Stevens, 2020). The PLD varies considerably, being as short as 23 days or as long as 125 days (Kelly et al., 1982).

Despite not inhabiting the Azores region, *C. quinquedens* is a deep-sea crab distributed from 200m to 1500m depth, larvae are hatched in water temperatures from 6 to 10ºC and can cross thermocline while swimming up to the surface, where they survive in temperatures up to 24ºC (Kelly et al., 1982). *In-situ* experiments on *C. quinquedens* larval behaviour, performed by Kelly et al., 1982, confirm that in the first development stage larvae show a strong negative response to gravity, with a swimming behaviour able to cross thermoclines (Table 1.8) (Kelly et al., 1982).

Table 4.6- Location, depth, and biology characteristics (pelagic larvae duration, spawning seasonality, larval development and number of larvae stages)

Species	Location	Depth range (m)			PLD (days)	Seasonality Ovigerous females	Spawning seasonality	Larval development	Nº larvae stages
		all	Female	Male					
Chaceon affinis	North/ Northeast Atlantic	140-2000 a)	n/a	n/a	n/a	-Spring g); -October to May e); -All year a); -March-April e);	-all year round a); -peak in winter and autumn c); -peak in March and Summer i)	Planktotrophic a)	4 Zoeal + megalopa a)
	Azores	-400-1500 b), d), e); -higher density: 700-900 c)	800-1000 c);h)	<800 c), h)					
	Canaries & Madeira	600-1000 j)	n/a	n/a					
Chaceon quinquedens	Western Atlantic	200 – 1000 h); f)	n/a	n/a	23-125 h)	n/a	Seasonal	Planktotrophic f)	4 Zoeal + megalopa h)
Chaceon bicolour	Western Pacific	200 – 1620 f)	n/a	n/a	n/a	n/a	Continuous		n/a
Chaceon fenneri	Western Atlantic	200 – 1500 f)	n/a	n/a	n/a	n/a	Seasonal		n/a
Chaceon maritae	Eastern Atlantic	200 – 950 f)	n/a	n/a	n/a	n/a	Continuous		n/a

a) Tuset et al., 2011; b) Biscoito et al., 2015; c) Pinho et al., 2001; d) Biscoito et al., 2015; e) López Abellán et al., 2002; f) Guerao et al., 1996; g) Hilário and Cunha, 2013; h)Kelly et al., 1982; i)Landeria and Tamura, 2018; j) Castro et al., 2010. *n/a not applied or no information available.

Table 4.7-Mean number of days for Chaceon *quinquedens* larvae from hatching to successive moults during larval development at 10º, 15º and 25ºC, values obtained from a study performed by Kelly et al 1982

Stage	Number of days from hatching up to the successive zoe at different temperatures		
	10ºC	15º	25ºC
Zoe I	30	17.2	7.2
Zoe II	60	33.8	11.5
Zoe III	99	52.5	18
Zoe IV	125.4	81	23.3

Table 4.8-Mean swimming rate estimated by Kelly et al 1982, for Chaceon *quinquedens* larvae, during larval stage I zoe, at different temperatures. Kelly et al., 1982

Water temperature (ºC)	Mean swimming rate (cm/s)
11	1.4
11-15	1.7
15	1.7

4.4.2. Model setup

4.4.2.1. *Chaceon affinis* locations

The study area covers the Azores archipelago. The *C. affinis* populations considered in this study, based on different data sources and studies (Santos et al., 2019 and Kaschner et al. 2019), are located in different seamounts, banks, and around the islands (Figure 4.21 and Table 4.9).

Table 4.9- Populations considered in this study, Release number, name, group name, location and depth.

Release number	Population name/location	Group	Longitude ºW	Latitude ºN	Depth (m)
L#1	Flores	Western Group	-31.2	39.64	800
L#2	Menez Gwen	MAR	-31.525	37.8417	950
L#3	Voador Seamount	MAR	-30.69	37.51	820
L#4	Cavala	MAR	-30.63	38.3	800
L#5	Ferradura	MAR	-30.37	38.19	910
L#6	Gigante Seamount	MAR	-29.89	38.99	900
L#7	Açores bank	Central group	-28.75	38.25	900
L#8	North of Faial	Central Group	-28.69	38.728	1060
L#9	North of São Jorge	Central Group	-27.7738	28.73075	1050
L#10	South-East of Terceira	Central Group	-26.89	38.33	828
L#11	Mar da Prata	Eastern Group	-25.7575	37.295	950
L#12	Formigas	Eastern Group	-24.675	37.295	1000

4.4.2.2. Model configuration

In this model implementation, each *C. affinis* population is defined as a release location, characterized by a position (longitude, latitude and depth), being also a recruitment area, defined by a polygon. Particle dispersal is computed with different behaviours, considering the swimming behaviour surface-oriented, and bottom-oriented, with a variable swimming velocity depending on water temperature, the passive behaviour and larval development stages.

Larval Behaviour

Chaceon larvae have different behaviours during the 5 larval stages (Tuset et al., 2011), with swimming capability achieving the ocean surface (Landeria and Tamura, 2018; Tuset et al., 2011). The biophysical model will simulate this swimming behaviour.

In the absence of detailed information about *C. affinis* larvae behaviours, modelled behaviours were based on, *Chaceon quinquedens*, another deep-sea red crab species from the same subfamily (Kelly et al., 1982). Larval PLD and swimming behaviour are detailed in Table 4.11.

Lagrangian particles simulate these behaviours at the different development stages, with a swimming behaviour surface-oriented during the first development stage (with a swimming velocity water temperature related), and bottom-oriented in the last development stage and megalopa. In the absence of more detailed data available about larval behaviour, passive behaviour was assumed during development stages II, III and IV, similar to other model approaches of deep-sea larvae (Ross et al., 2017).

Number of larvae

The number of larvae released by the model was tested in the model calibration step, and based on the number of eggs of this species (200000–600000 eggs) (Tuset et al. 2011). A total of 396,800 particles (larvae) were released, per month for each location, with 800 particles released every 90 minutes for 30 days (1 month). This is a representative number of larvae for one unique female specimen, so, substantially lower than the real larvae number. However, in the modelling language, this number represents a proportional rather than complete representation of potential larval dispersal and fate (Ross et al., 2017).

Larvae mortality is computed following the half-life concept (the time it takes half the population to die) likewise other deep-sea larval dispersal studies (North et al., 2009; Paris et al., 2013).

Simulations were set for two different seasonal scenarios in 2017, with one monthly release during March, and another during October, to cover different spawning seasons reported for this species (Hilário and Cunha, 2013; López Abellán et al., 2002; Pinho et al., 2001). The larvae were released at a regular interval, every 90 minutes, to capture the full range of potential larval trajectories within this period (Ross et al., 2016). Several PLDs were considered to cover different larval reproductive behaviours based on the literature. To study the connectivity between populations, each population is defined by a polygon, where larvae can settle. The 12 release locations in this study are also recruitment locations, and the settlement depth was defined as between 800m to 1200meters depth (Pinho et al., 2001; Santos et al., 2019). The general model configuration of this case study is summarized in Table 4.10

Table 4.10- Biophysical model configuration for case study 2

Model parameter	Parameter description
Hydrodynamic model resolution	6*6km
Model time step	7200 seconds
Number of release points	12
Release depth	Sea bottom
Number of larvae per release	396800/month (Tuset et al., 2011)
Release time step	7200 seconds
Behaviour	Several behaviours(Table 4.11)
Mortality	Half-life (North et al., 2009; Paris et al., 2013
Strata	800 to 1200m
Scenarios	Several considering PLD and seasonality and behaviours (Table 4.12)

4.4.2.3. Scenarios

Different scenarios were studied considering the PLD, spawning seasonality, different larval behaviours and swimming velocities reported for this species (Table 4.12) (based on Guerao et al., 1996; Kelly et al., 1982, Landeria and Tamura, 2018). Was considered a surface-oriented swimming behaviour in the first development stage, and a bottom-oriented swimming behaviour for the last development stage and megalopa (Kelly et al., 1982). Bearing in mind the gradual reduction of larval activity during the late stages reported for deep-sea larvae (Kelly et al., 1982; Leis, 2020), it was considered for the last stage a velocity 10 times lower than the velocity in the first stage.

The different behaviours in the study are:

i) **Behaviour_1**- mimics the behaviour reported for *G. quinquedens*, with a swimming behaviour surface-oriented during the first larval stage and a swimming behaviour bottom-oriented in the last stage, with lower activity than during the first stage (Kelly et al., 1982), and a passive behaviour during stages 2, 3, and 4;

ii) **Passive behaviour-** larvae are passive during the entire PLD, following the most common approach to deep-sea larvae modelling (Ross et al., 2019).

Table 4.11- Swimming velocity and direction surface-oriented, bottom-oriented or passive) and swimming velocity in the different larval stages and megalopa (* refers to data based on Kelly et al., 1982)

	Behaviour _1			**Passive_behaviour**		
Larvae development stage	zoe1	zoe2 + zoe 3	zoe 4 + megalopa	zoe1	zoe2 + zoe 3	zoe 4 + megalopa
PLD- cumulative days	15	90	125	15	90	125
	7	53	81	7	53	81
	7	18	23	7	18	23
Behaviour	surface oriented	passive	bottom oriented	passive		
velocity (m/s) (15ºC)	0.014	---	0.0014	---		
velocity (m/s) (11ºC)	0.017	---	0.0017	---		

Table 4.12- Scenarios considered in this study, for March 2017 (on left), and October 2017 (right).

Release date: March 2017		**Release date: October 2017**	
Scenario	PLD (days)	Scenario	PLD (days)
March_PLD_23_Behaviour 1	23	October_PLD_23_Behaviour 1	23
March_PLD_81_Behaviour 1	81	October_PLD_81_Behaviour 1	81
March_PLD_125_Behaviour 1	125	October_PLD_125_Behaviour 1	125
March_PLD_23_Passive	23	October_PLD_23_Passive	23
March_PLD_81_Passive	81	October_PLD_81_Passive	81
March_PLD_125_Passive	125	October_PLD_125_Passive	125

4.4.2.4. Model calibration

The number of particles to use in the model was calibrated using the dispersal pathlength saturation method. Calibration results show that in a release of 360 000 particles, the percentage of particles in each 2km bin doesn't reveal any abrupt fluctuation, resulting in a smoother line, representative of a dispersal pathlength saturation for all the release locations (Figure 4.22). Therefore it was considered a total number of 360000 particles per location per month.

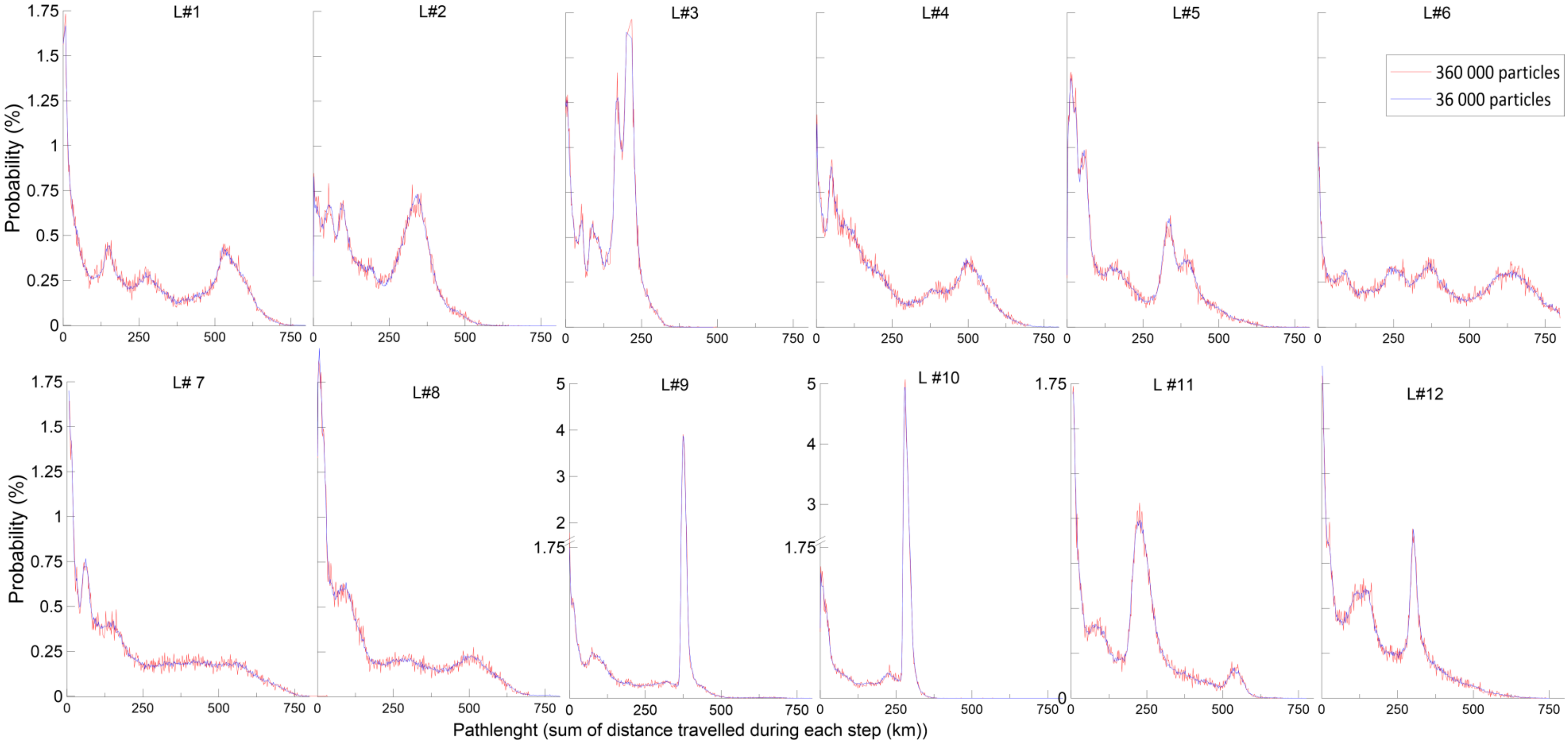

Figure 4.22- Probability of dispersal pathlength distances, for scenario *PLD_81_March_Behaviour_1_2017*, with different numbers of particles (360000 and 36000). The X-axis is the pathlength travelled by each particle (sum of distances moved during each time-step) binned into 2km increments, and the Y-axis is the probability.

4.4.3. Results

4.4.3.1. Larval dispersal

To study *Chaceon affinis* larval dispersal different scenarios were tested, considering a swimming behaviour surface-oriented (Behabiour_1), and passive behaviour. Results for the different scenarios show that larvae can be advected in the entire study area, mostly in the western, central and southern parts of the domain, and rarely in the north-northeast part of the domain (Figure 4.23 and Figure 4.24). Larvae with swimming behaviour have a more dispersive path than passive larvae (Figure 4.23 and Figure 4.24 with the passive behaviour depicted in the right column). Different patterns along time and space can be identified in the different scenarios. On the last month of simulation (day 123), it is clear a higher particle density for the passive behaviour than for the scenario with swimming behaviour. For the March release, the higher particle density occurs mainly near the release points of the CG and WG (Figure 4.23) contrasting with the absence of particles between MAR and the CG. In the Passive scenario (on the right in Figure 4.23), different patterns can be distinguished: i) a North-South larvae pathway along the WG and MAR locations; ii) the absence of particles between MAR and the CG; iii) higher larvae density in the CG and the WG. With the larvae swimming behaviour, a higher dispersal occurs longitudinally over the southern part of the domain. On the contrary, in the October release, particle density is higher between the MAR and the CG. A north-south larvae pathway in between MAR and the CG is formed (Figure 4.24). In the 3rd month of simulation, the higher particle density occurs away from the release points. Dispersal patterns reveal higher particle distribution between the CG and the WG, in March than in October

The higher dispersal in the Behaviour_1 scenario is a consequence of the tracers' swimming behaviour. With the surface-oriented swimming behaviour when achieving the surface layers tracers are advected by the surface currents, characterized by higher velocities, than the deeper currents.

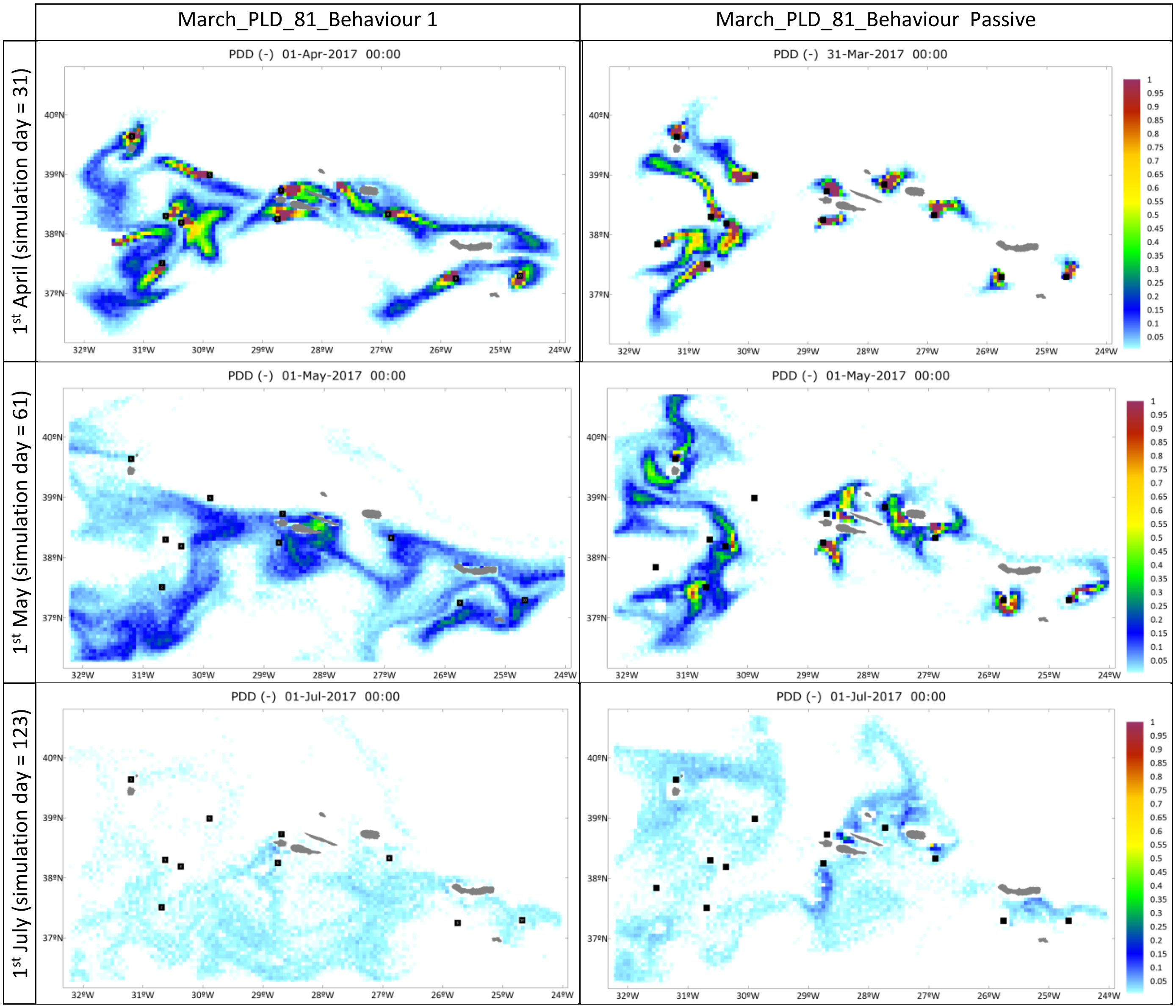

Figure 4.23- Particles density distribution for March release, with PLD of 81 days, for behaviour 1 on the left "March_PLD_81_Behaviour_1", and passive behaviour "March_PLD_81_Behaviour_Passive" on the right, for day 1st April (30 days after the first released particle, and 1 day after the last released particle (simulation day = 31) (top), 1st May (second row) (simulation day = 61)) and 1st July 2017 (bottom row) (simulation day = 123). The coloured legend (from blue to red) represents the particle density distribution integrated with the water column, from 0 to 1, for each domain cell

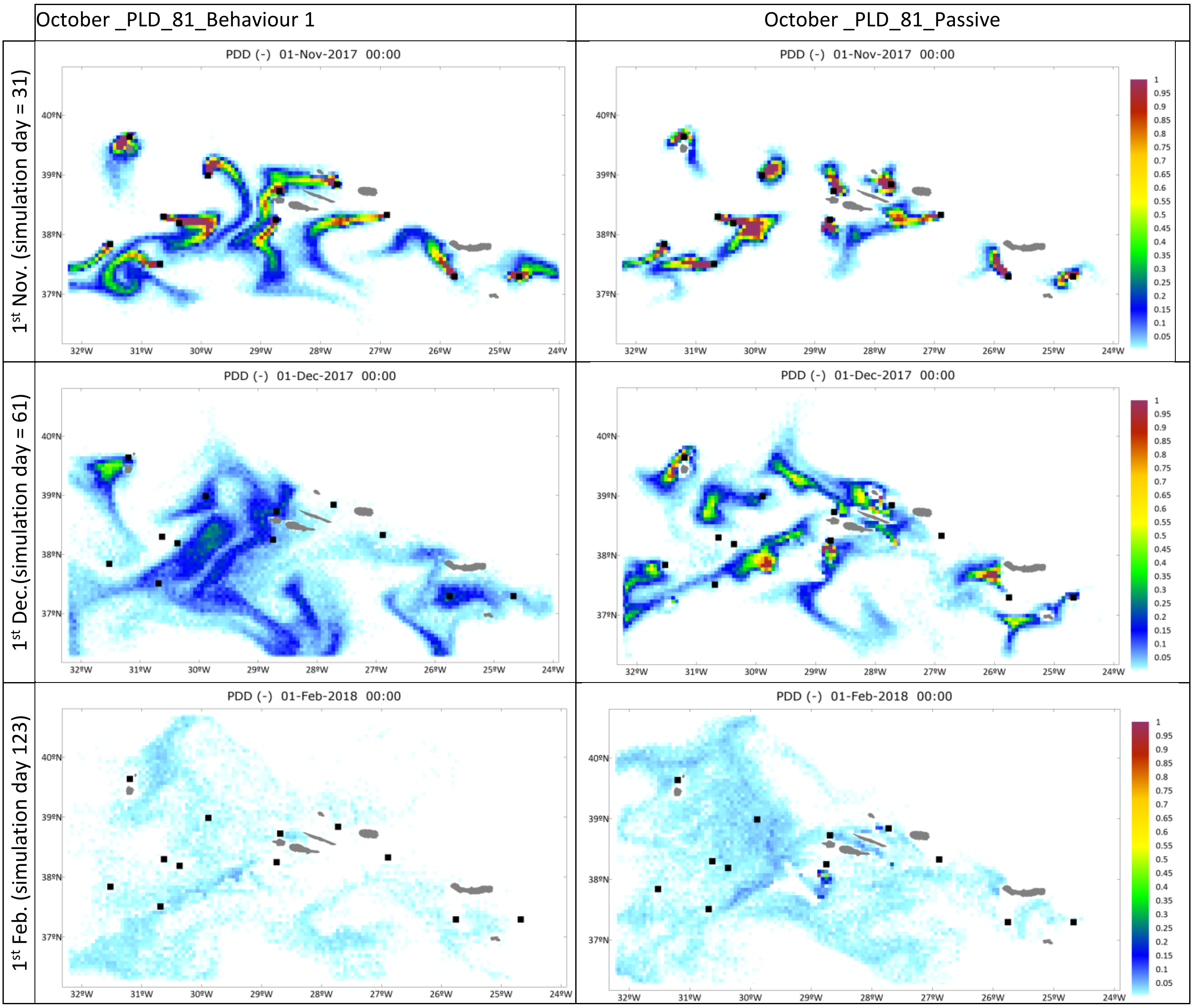

Figure 4.24- Particles density distribution (PDD) for October release, with PLD of 81 days, for behaviour 1 on the left "October_PLD_81_Behaviour_1", and passive behaviour "March_PLD_81_Behaviour_Passive" in the right, for the days: 1st November 2017 (30 days after the first released particle, and 1 day after the last released particle (simulation day = 31)) (on top), 1st December (second row) (simulation day = 61)) and 1st February 2018 (bottom row) (simulation day = 123). The coloured legend (from blue to red) represents the particle density distribution integrated with the water column, from 0 to 1, for each domain cell

4.4.3.2. Particles vertical migration

According to different studies DSRC larvae have swimming behaviour and can swim from the sea bottom up to the surface (Kelly et al., 1982; Landeria and Tamura, 2018). Model simulations were able to simulate this larvae swimming behaviour, with particles achieving the most surface layers, as can be seen in histograms in Figure 4.26, Figure 4.27, and Figure 4.28. In contrast, particles with passive behaviour stay mostly in the deeper layers. Particle's vertical migration is similar for March and October scenarios, not demonstrating any seasonal patterns.

In all scenarios, the larvae can move to depths of more than 1000 or 1200 meters depth, mainly for particles with passive behaviour. Only releases L#1, L#2 and L#12 show a distinct distribution of particle depths. These differences are a consequence of the percentage of particles that are advected out of the domain. As particles achieve the most surface layers, are consequently exposed to stronger currents (Figure 4.25), which induce a higher dispersion. The surface layers have stronger velocities, with the velocity modulus average reaching 0.25 m/s, while the deeper layers have lower velocities, less than 0.04 m/s. The vertical decrease of velocity modulus occurs in the entire domain.

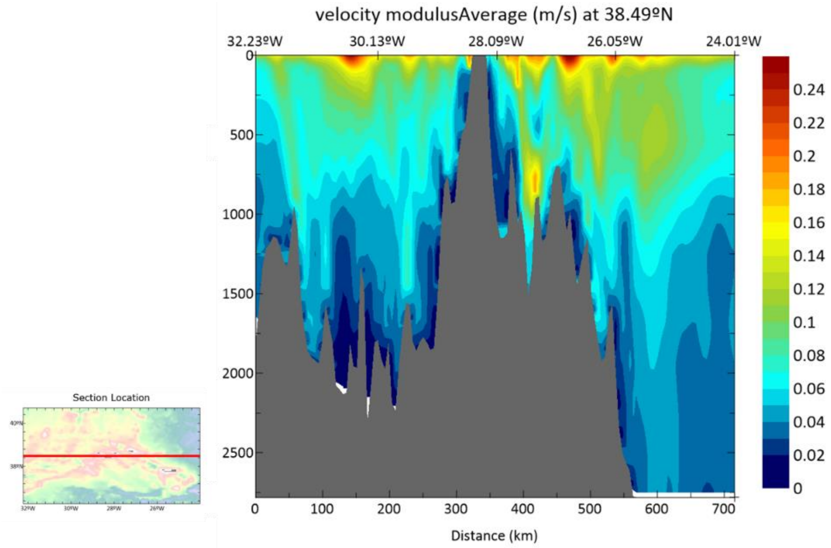

Figure 4.25- Annual average (2017) average of the velocity modulus along the water column for a longitudinal section of the study domain. The map on the left shows a representation of the section.

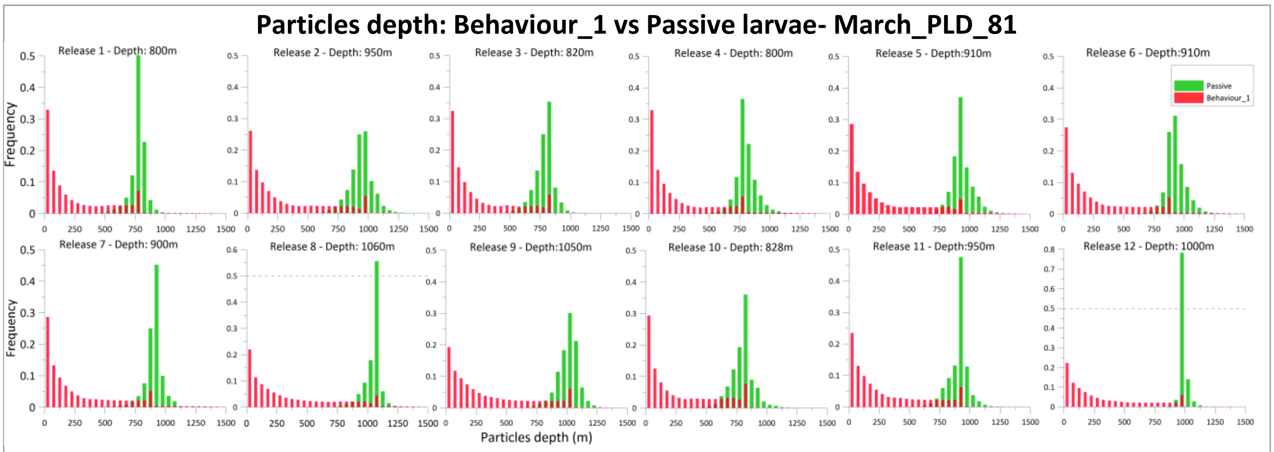

Figure 4.26- Histogram of the particles' depth along their trajectory, for each release point, considering the passive behaviour (green), and Behaviour_1 (red). The depth of the respective release is detailed at the top of each graph

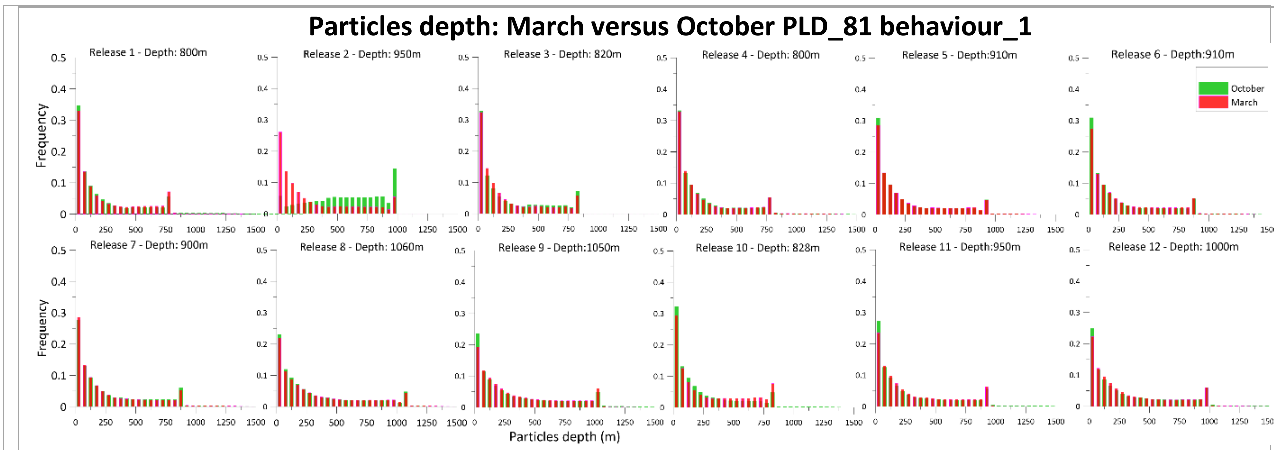

Figure 4.27- Histogram of the particles' depth along their trajectory for each release, for Behaviour_1 PLD_81 for March (red), and October release (in green). The depth of the respective release is detailed at the top of each graph

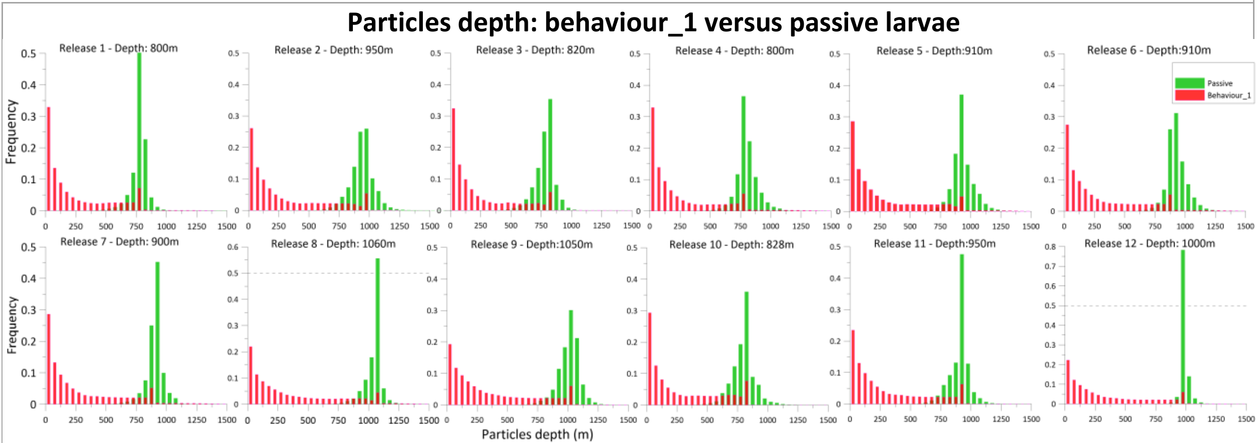

Figure 4.28- Histogram of the particles' depth along their trajectory for each release point, considering the passive behaviour (green), and Behaviour_1 (red). The depth of the respective release is detailed at the top of each graph

4.4.3.3. Particles travel distance

As a consequence of the swimming behaviour and longer PLDs, larval dispersal has various dispersive patterns. Median travel distances can range from a few kilometres (<15 km for release L#1), to more than 250km (276km for L#6) (Table 4.13). The total travel distance can be more than 1000 km, for L#10. However, considering the highly non-normal particle dispersal, median and percentile 95th dispersal distances are used, rather than maximum travel distances (Phelps, 2015). The percentile 95th and the maximum travel distances are generally one order of magnitude higher than the median distances in all the releases (Figure 4.30, Figure 4.31 and Table 4.13), mainly for higher PLDs. The lower median and percentile 95th travel distances are associated, generally, with higher percentages of tracers advected away from the domain (Table 4.13). On average, 30 to 40% of particles from releases L#1 (Flores island), L#2 (MenezGwen), and L#3 (Voador Seamounth), are advected out of the domain (Figure 4.29). Furthermore, the maximum values can achieve 90% for L#2, and 57% for L#3 during scenario

October_PLD125 with Behaviour_1. These higher percentages of particles advected out of the domain are reflected in the travel distances, which achieve anomalous lower values (Figure 4.30 and Figure 4.31). These locations are sited in the WG and the MAR, closer to the domain borders than the others.

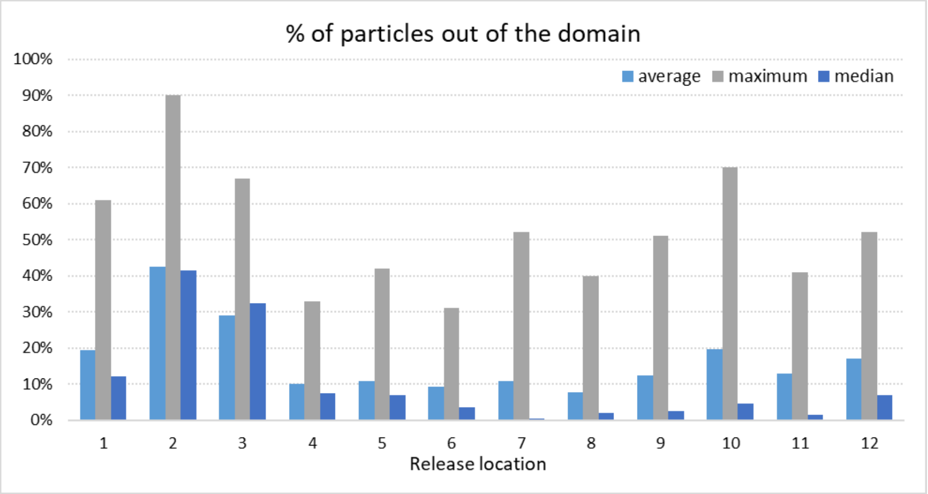

Figure 4.29- Average, maximum and median values of the percentage of particles that went out from the domain over all the scenarios in the study for each location.

The percentage of particles that are advected out of the domain is higher for the simulations with swimming behaviour and longer PLD (Figure 4.29). Particles from the WG, MAR, and EG can leave the domain in different scenarios. In the October scenarios with PLD125, 90% of L#2 particles’, are advected out of the domain, while in March about 47% (Table 4.13). This percentage of particles leaving the domain underestimates particles' travel distances, as can be seen in the histograms of Figure 4.32, Figure 4.33, and Figure 4.34. Histograms show that L#2 particles only travel up to 150km during the October release, contrasting with the March release. During the March release, 89% of the particles left the domain and the median travel distance was 29km, while the maximum was 135km. The simulated swimming behaviour induces higher travel distances (median from 17 to 259km) than the passive behaviour (median from 12 to 75 km). This difference increases with the longer PLD. The major differences occur in the release points near the domain limits, L#1, L#2, and L#3, on the West, and releases L#9, L#10, L#11 and L#12 with their particles leaving the domain by the southern boundary (Figure 4.23 and Figure 4.24).

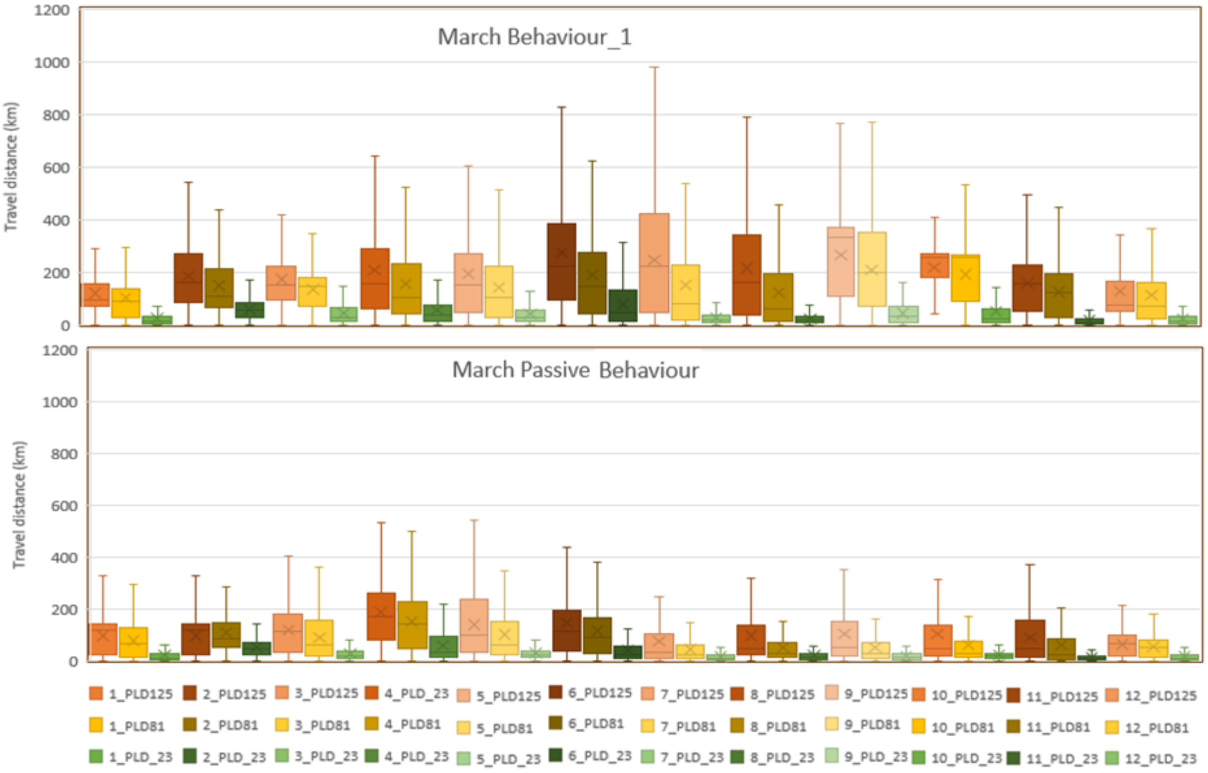

Figure 4.30- Boxplot of particles travelling distances for March release for behaviour_1 (top) and passive behaviour (bottom), with PLD of 23 (in green), 81 (in yellow/army green), and 125 days (in orange/brown). Boxplot represents the first and third quartiles and the median values, and the whiskers represent the minimum and the maximum travel distances. Outliers are not represented.

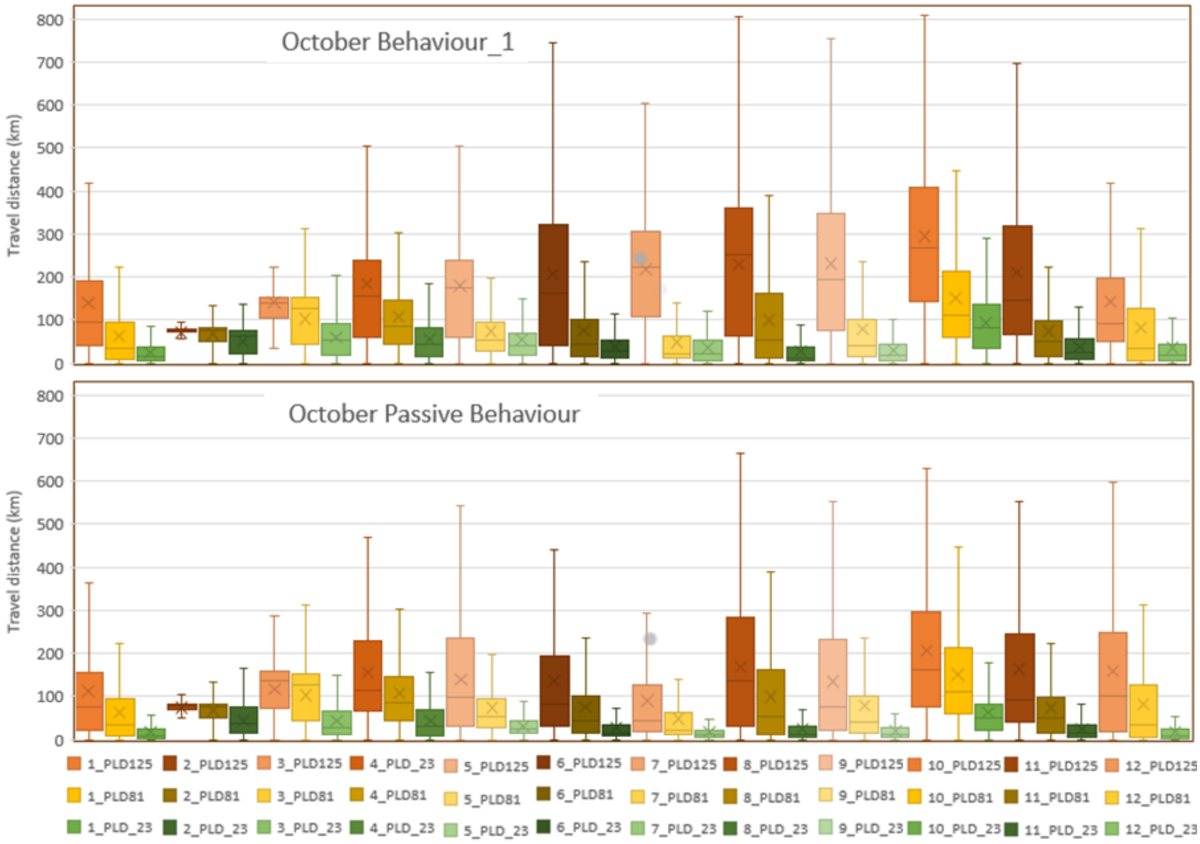

Figure 4.31- Boxplot of particles travelling distances for October release for behaviour_1 (top) and passive behaviour (bottom), with PLD of 23 days (in green), 81 days (in yellow/army green), and 125 days (in orange/brown). Boxplot represents the first and third quartiles and the median values, and the whiskers represent the minimum and the maximum travel distances. Outliers are not represented.

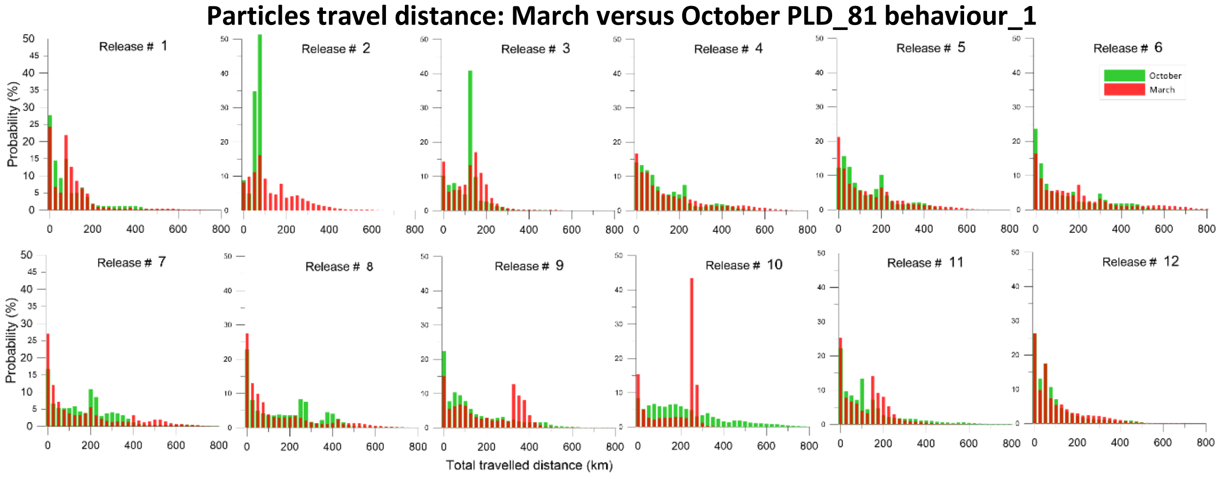

Figure 4.32 Histogram (in %) of the total travel distance from particles from each release, in km, considering a PLD of 81 days, for the October release in green, and the March release in red.

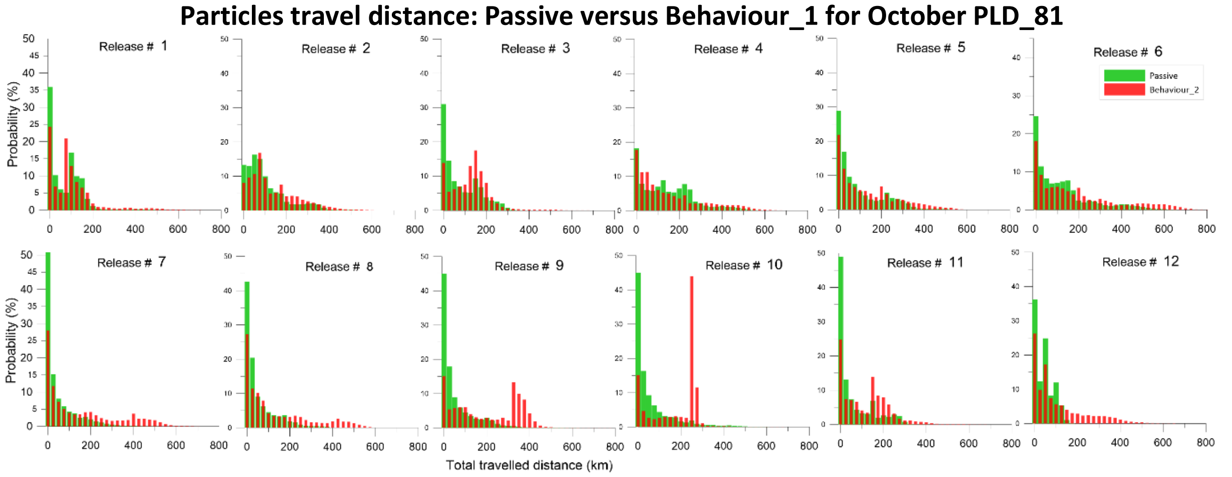

Figure 4.33- Histogram (in %) of the total travel distance from particles from each release, in km, for the October 2017 release, considering a PLD of 81 days, for the Passive behaviour in green, and Behaviour_2 in red.

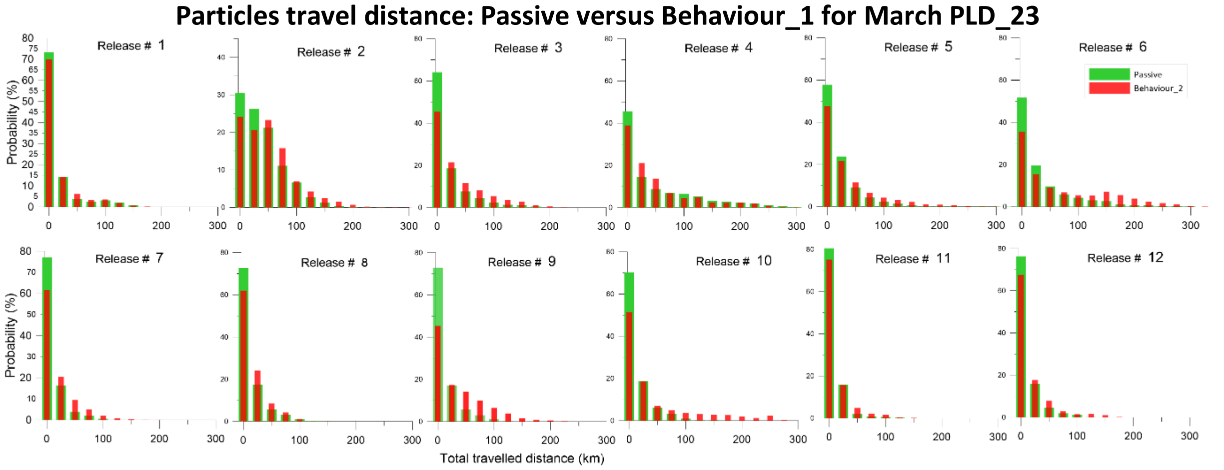

Figure 4.34- Histogram (in %) of the total travel distance from particles from each release, in km, considering a PLD of 23 days, for the Passive behaviour in green, and Behaviour_2 in red, for the March 2017 release

Table 4.13- Median (Med), 95th percentile (P95), and maximum(max) travel distance (km), and the % of particles from each release that went out of the domain (Out), for simulations with Behaviour_1, and Passive behaviour, for March and October with PLD125, 81 and 23 days. Minimum and maximum values for each scenario are underlined. Maximum travel distance includes the outliers.

		Travel distance (km)																							
Behaviour 1		March_PLD 125				March PLD_81				March PLD 23				October PLD_125				October PLD_81				October PLD_23			
		Med	P95	Max	Out (%)	Med	P95	Max	Out (%)	Med	P95	Max	Out (%)	Med	P95	Max	Out (%)	Med	P95	Max	Out (%)	Med	P95	Max	Out (%)
WE	Location_1	63	465	1186	61	53	434	841	46	16	100	292	2	94	420	847	39	38	220	549	20	16	81	209	0
MAR	Location_2	165	472	1149	47	120	378	938	37	55	155	342	0	30	80	153	90	29	79	133	84	23	79	158	45
	Location_3	149	477	1115	46	103	280	830	42	27	135	255	2	89	347	985	67	80	268	846	56	43	142	292	7
	Location_4	194	618	1238	23	130	497	946	12	34	207	338	1	134	426	1217	33	103	370	820	20	41	167	376	0
	Location_5	171	566	1270	24	109	436	927	16	27	150	331	0	126	381	1095	42	102	346	810	24	40	181	351	1
	Location_6	259	719	1319	31	194	612	991	14	40	239	410	2	153	490	1230	24	105	431	918	15	29	158	272	0
CG	Location_7	169	573	1111	29	99	493	912	11	20	90	313	0	129	442	1078	52	115	479	901	31	23	124	368	0
	Location_8	152	573	1119	21	91	469	870	5	19	78	241	0	137	444	1084	40	106	446	885	25	18	107	261	0
	Location_9	136	528	1433	51	108	376	1090	35	29	136	303	0	149	504	1325	22	108	419	975	6	21	96	299	0
	Location_10	79	303	1432	70	64	271	1207	58	24	189	297	2	212	569	1146	38	183	544	943	16	75	253	441	0
EG	Location_11	126	430	1044	41	62	284	737	38	14	74	384	0	130	530	1133	33	93	461	936	20	24	124	252	0
	Location_12	81	423	995	52	71	353	780	31	18	95	256	1	93	415	894	41	68	341	695	26	20	161	380	0

Behaviour Passive		March_PLD 125				March PLD_81				March PLD 23				October PLD_125				October PLD_81				October PLD_23			
		Med	P95	Max	Out (%)	Med	P95	Max	Out (%)	Med	P95	Max	Out (%)	Med	P95	Max	Out (%)	Med	P95	Max	Out (%)	Med	P95	Max	Out (%)
WE	Location_1	48	270	913	41	38	145	638	33	13	94	194	3	77	340	725	8	55	249	569	5	13	75	274	0
MAR	Location_2	117	356	1013	25	97	242	763	14	42	121	311	1	49	160	427	69	43	138	360	67	22	80	178	31
	Location_3	71	249	699	35	58	181	450	23	19	96	218	1	67	168	416	57	59	164	380	48	25	136	218	7
	Location_4	178	465	1080	33	136	323	760	24	27	208	358	2	126	349	790	17	100	288	670	7	30	133	362	0
	Location_5	92	355	1001	20	69	235	790	11	24	98	375	0	94	306	596	9	72	235	525	3	27	94	280	0
	Location_6	149	542	976	7	98	326	717	5	24	148	357	0	122	389	701	1	77	301	587	0	19	123	271	0
CG	Location_7	76	307	846	3	51	155	637	0	13	62	219	0	68	247	733	4	51	181	633	1	15	65	274	0
	Location_8	78	267	772	10	55	156	513	1	16	72	226	0	98	376	748	14	66	323	572	4	16	101	265	0
	Location_9	82	320	893	10	57	168	695	1	16	74	252	0	77	347	1022	11	56	280	751	4	17	76	300	0
	Location_10	80	361	883	8	57	171	678	2	19	75	299	0	142	443	892	15	115	405	842	7	48	183	458	0
EG	Location_11	64	266	738	16	46	173	494	10	11	50	242	0	88	420	753	5	65	305	665	1	17	84	237	0
	Location_12	35	108	338	53	31	87	247	41	12	60	164	3	74	459	876	10	49	357	757	5	12	91	307	0

4.4.3.4. Connectivity between *C. affinis* populations

C. affinis larval dispersal generates different connectivity patterns among the different study populations, revealing potential connectivity along the entire archipelago. The length of the larval period, and the spawning seasonality, give rise to different patterns of connectivity between the different study populations. Connectivity between the different populations is represented in the connectivity matrices in Figure 4.35 and Figure 4.36.

The connectivity patterns can be seen to differ significantly between the two behaviours (the swimming behaviour and the passive behaviour). The lowest PLD in the study (23 days) leads to higher levels of self-recruitment, however, less connectivity between different populations. The swimming behaviour (Behaviour_1, Figure 4.35, induces more larvae exchange between the different populations in the study (than the passive behaviour (Figure 4.36). Spawning seasonality also contributes to different connectivity relations. March spawning scenarios prompt a higher exchange of particles between different populations than the October scenarios.

With the swimming behaviour, the simulated larval dispersal for the March release prompts higher connectivity among populations over the entire archipelago than for the October release. For PLD of 125 and 81 days, the percentage of exchanged particles is mostly lower than 0.1%. With a PLD of 23 days, does the quantity of particle exchange and self-recruitment particles achieve a percentage of 0.1% in different populations in all the groups. However, several populations do not reveal self-recruitment or connectivity with other populations in the PLD 23 scenarios. Namely Menez Gwen (L#2) and Ferradura seamount (L#5), for March scenarios, and Flores (L#1), Cavala (L#4) and South of Terceira populations (L#10) for October scenarios.

For the passive behaviour, (Figure 4.36), higher levels of self-recruitment occur in the different locations with a higher percentage of settled particles, mainly with lower PLD. For the March release, with a PLD of 23 days all the locations present self-recruitment, with a percentage of settled particles higher than 0.1% in all the locations except L#2, L#4, and L#6. Contrasting with the higher levels of self-recruitment, connectivity patterns are more patchy with passive behaviour.

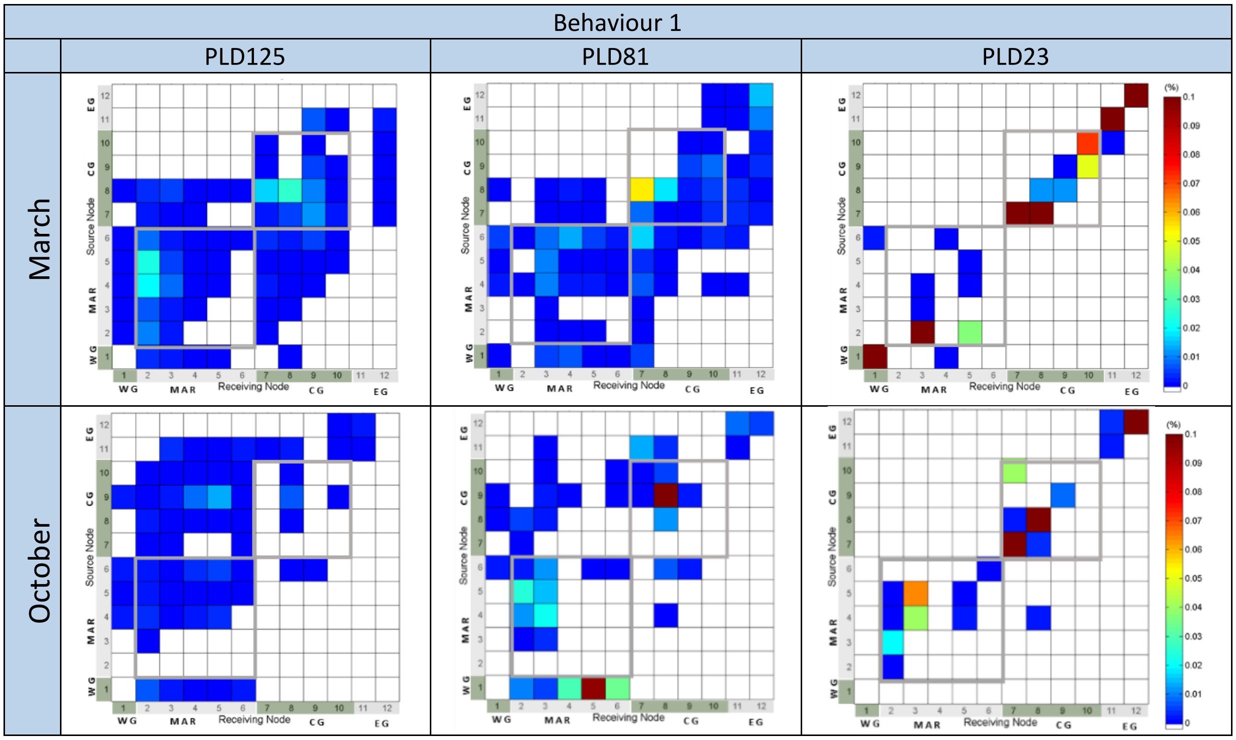

Figure 4.35- Connectivity matrices for Behaviour_1, for PLD125, PLD81 and PLD23, from left to right, for Spawning in March on top, and in October, down. Colours represent the percentage of modelled particles from each population (source node) in vertical axes, that settled in a recruitment area (receiving node) in horizontal axes. Diagonal cells represent auto-recruitment. Each release point is a recruitment area: WG:L#1; MAR: L#2 to L#6; CG: L#7 to L#10; EG:L#11 and L#12).

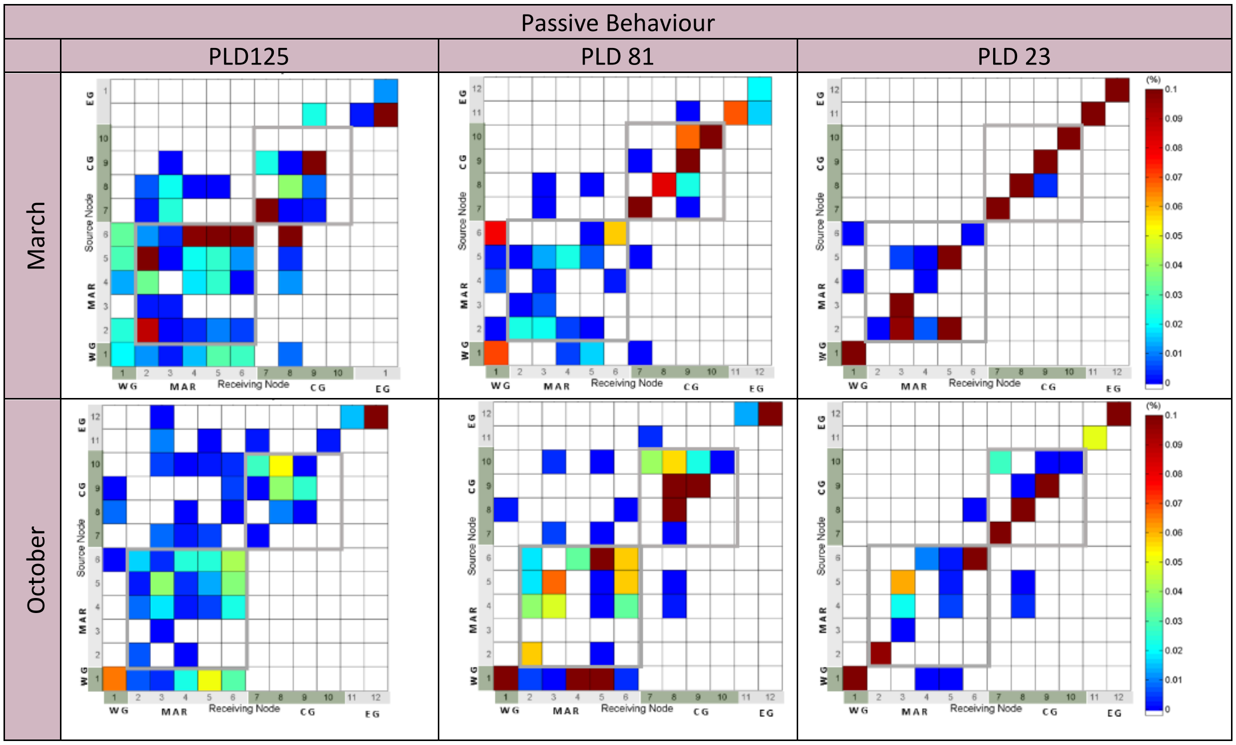

Figure 4.36- Connectivity matrices for Passive_behaviour, for PLD125, PLD81 and PLD23, from left to right, for Spawning in March on top, and in October, down. Colours represent the percentage of modelled particles from each population (source node) in vertical axes, that settled in a recruitment area (receiving node) in horizontal axes. Diagonal cells represent auto-recruitment. Each release point is a recruitment area: WG:L#1; MAR: L#2 to L#6; CG: L#7 to L#10; EG:L#11 and L#12)

Connectivity results between the different populations show that, with the March release, the exchange between the different groups is multiple, with exchanges between EG and CG, CG and MAR, and between MAR and both CG and WG. In October, the exchange is mostly unidirectional to the MAR populations, with lower connectivity with the populations located in the CG and EG.

October scenarios reveal a higher East-West larvae exchange, with larvae from the Eastern Group (in particular Mar da Prata- L#11) settling in the MAR populations, for the scenarios with PLD 125. Also, larvae from the Central Group can settle along the MAR and in the WG. However, during these October scenarios, the populations from the Central Group can face no self-recruitment. Population L#10 (Southeast Terceira) has no self-recruitment in all the October scenarios. Furthermore, for the October scenario with swimming behaviour, larvae from WG don’t achieve the most eastern locations (EG, CG), while during March they can settle in North of Faial (L#8) for a PLD of 125 days, or in Açores bank (L#7), with a PLD of 81 days.

Contrasting with this, the March scenarios with swimming behaviour, promote higher connectivity between the different groups, contrasting with October scenarios where several populations from the CG and MAR don’t receive larvae from other populations. Namely, during march scenarios with swimming behaviour: i) larvae from the CG can settle in the CG, MAR and EG; ii) larvae from all the CG populations can settle in the WG, L#7 to L#10 can settle in Formigas population in scenarios March_PLD125 and March_PLD81; iii) larvae from L#8 (North of Faial) can settle in the WG, in all the populations along the MAR and the CG, and also in the WG; iv) larvae from MAR can settle in the WG, along MAR, in the CG and the EG for a scenario with PLD of 81 days; v) larvae from the WG can settle along the MAR, and in Açores Bank (L#7) considering a PLD of 81 days, and in North of Faial (L#8) for a PLD of 125 days.

Model results show that larvae from the MAR populations have a higher probability of settling in MAR, and other populations during March release. Additionally, with the October release, for PLD125, populations with more particle exchange are also located in the MAR, receiving particles from the MAR, CG and also from EG.

Among the populations in MAR, only larvae from Cavala, Ferradura and Gigante seamount (L#4, L#5 and L#6) settle in populations from the Central Group, but with a low percentage of larvae exchange. Contrariwise, larvae from Menez Gwen (L#2) and Voador (L#3) don’t settle in the CG. For PLD81, it is clear a higher number of connectivity relations, in the entire archipelago, for March, than for the October scenarios.

4.4.4. Discussion

A biophysical particle tracking model was applied to study the connectivity between different *Chaceon affinis* populations in the Azores. This model allows studying the dispersal of these deep-sea red crab larvae and population connectivity in the Azores, simulating different spawning seasonality and larval behaviour hypotheses including swimming behaviour. This kind of model has been used to support fisheries decision-making (Swearer et al., 2019). Populations of this species in the NE Atlantic may be isolated in several coastal groups and seamounts (Santos et al., 2019). In Madeira islands, tagged specimens were found in the same location 3 years later (Biscoito et al., 2015). These facts show that besides being a benthic moving organism, *C. affinis* benefit from the larvae phase for population dispersal.

Model implementation and calibration

In this case study, 12 populations are considered, located throughout the archipelago, from the most Western island (Flores island (L#1)), through MAR and the Central Group, up to the Eastern Group (EG). Different scenarios were tested considering the available information about the DSRC larvae behaviours, including the PLD from 23 to 125 days (Kelly et al., 1982), and the swimming behaviour with larvae able to achieve the surface layers (Hilário and Cunha, 2013; Landeria and Tamura, 2018). Major model results show that simulated larvae can be advected out of the domain, induced by the longer PLD, and by their capability to achieve the surface layers being exposed to the strong surface current. This is a common limitation of larvae dispersal model applications, specifically in oceanic regions, where the influence of strong currents advect tracers out from the domain (Busch et al., 2021; Kenchington et al., 2019; Wang et al., 2021). This is the case in the Azores region, where, under the influence of the strong currents, that originate highly dynamic dispersal patterns, the particles are dragged out of the domain. A bigger model domain could minimize this particle's loss. However, due to the strong currents avoiding all the particle loss would require a very large domain, out of the scope of this study. It would also require a higher computational effort. A compromise between model domain, resolution, and computational efficiency must always be achieved. Similarly to other model applications, it was assumed this limitation of particles loss out of the domain, and it was taken into consideration when interpreting connectivity results (Swearer et al., 2019; Wang et al., 2021).

One way to surpass this domain size limitation is by increasing the number of tracers in use, ensuring that during the simulation, the tracers' trajectory is representative of the real dispersal scenarios (Simons et al., 2013). Calibration tests showed that a total number of 3.6 x 10^5 released particles at each location produce saturated dispersal pathlengths, while one order of magnitude lower doesn’t. This number of particles is in line with other model applications for ocean regions (Kenchington et al., 2019; Ross et al., 2017). A review about the state of the art of biophysical models of marine larval dispersal reports that in applications with multiple locations, the number of particles released from each location ranged from 1 to 4.2 × 10^7, with a median of 178 (Swearer et al., 2019).

In this model calibration, the FUV method (Simons et al., 2013), was not performed because it requires the first simulation with a higher number of particles, and subsequent subsample pools of trials to estimate the variability (and the fraction of unexplained variability), which was very computationally demanding. The number of particles used in the pathlength calibration tests totals more than 4 million particles per simulation.

Therefore, for this case study, a total of 3.9 x 10^5 particles per month, per release was used: through the release of 900 particles every 90 minutes during 30 days, for each location, totalizing more than 4.7 million particle trajectories being simulated in each scenario. Furthermore, this number of particles is one order of magnitude bigger than other applications as the one explained in Case Study 1 for *P. carpenteri*.

Scenarios and behaviours in the study

The different tested scenarios consider different PLDs, spawning seasonality, and larval behaviours, based on the information available (Table 4.4). In the absence of detailed information about *C. affinis* larvae, it was used the available information about other deep-sea red crabs from the same subfamily. In terms of modelling, is a common and acceptable approach to use data from other congener or confamilial species, although it should always bear in mind that behaviours can differ among close relatives (Leis, 2020). When using these scenarios several assumptions have been made, which should be taken into consideration when interpreting connectivity results (Swearer et al., 2019; Wang et al., 2021; Young et al., 2012).

Besides the swimming behaviour surface-oriented in the first larvae development stage, also swimming behaviour bottom-oriented in the last development stage is also considered. For the DSRC larvae, the swimming velocity depends on the water temperature (Kelly et al., 1982). This model application is capable of adapting the swimming behaviour considering the environmental conditions, simulating the larvae dispersal that is affected not only by the currents but also by temperature (Werner et al., 2007).

In this case, the simulated swimming velocity ranges from 1.4 cm/s at 11ºC, to 1.7 cm/s at 15ºC depending on the water temperature. This increase in the swimming velocity allows the simulation of these larvae's behaviour, which can cross strong thermoclines and swim from the deep-sea up to the surface (Kelly et al., 1982).

Model results showed that in this model configuration, using the swimming behaviours, larvae were able to achieve the surface layers, simulating the behaviour observed in the different in-situ studies, where *C. affinis* larvae were collected at the surface (Guerao et al., 1996; Landeria and Tamura, 2018). Contrarily, with the passive behaviour where deep-sea, the larvae never achieve the surface layers, not even with the larger pelagic durations.

Particles dispersal

Estimates of particle trajectories reveal that particles can travel up to 1400km in the study area (Table 4.13), demonstrating the potential for *C. affinis* larvae to travel across the entire archipelago during their PLD. However, the maximum travel distances are one order of magnitude higher than the median values, revealing a higher dispersive system. This distance magnitude is in line with other DSRC dispersal estimates (Kelly et al., 1982), and deep-sea larvae with long PLD (Wang et al., 2021). It is a consequence of vertical swimming behaviour, but mainly due to the residence time near the surface, where the average velocity modulus is higher (Figure 4.25) which has a large impact on theoretical travel distances (Gary et al., 2020). These higher dynamic currents at the surface layers justify the differences among the travel distances from the passive particles and the particles with a swimming behaviour. This swimming behaviour is imposed by the model only during the first development stage.

Particles simulated with a passive behaviour don’t achieve the most surface layers and are advected mainly in the deeper layers. They can be advected in both surface or deeper directions, in a bathymetric range of approximately 500-meter depth (as is depicted in the histograms of particle depth (Figure 4.26). Given the weaker currents in the deeper water layers (Figure 4.25), the passive behaviour results in lower total travel distances Figure 4.30 and Figure 4.31). Similar results have been obtained in deep-sea larvae dispersal studies revealing the impact of vertical migration on larvae dispersal and travel distances away from the release location (Kool et al., 2013; Young et al., 2012). Moreover, model results show that this passive behaviour with lower vertical movement and travel distances induces higher self-recruitment levels, and lower connectivity between different populations, as is depicted in the connectivity matrices of Figure 4.36.

Even with the general lower travel distances, the passive behaviour reflects the different hydrodynamic patterns in the deeper layers, resulting in different connectivity patterns between populations along the year. With passive behaviour, connectivity occurs mostly between populations from the same group, or with neighbouring groups. But, also between populations from the EG and the MAR group. Namely, larvae from Formigas (L#12), can settle in Voador seamount (L#3), and larvae from Mar da Prata (L#11) in Voador seamount, but also Ferradura seamount (L#5), with a PLD of 125 days for the October release. This connectivity relation is not present in any other tested scenario.

The highly dispersive scenarios contribute to a large percentage of “lost” particles, particles advected out of the domain. The population with a higher percentage of “lost” particles, L#2, Menez Gwen, is the most western population in the study, located in the MAR, (Figure 4.29). This higher percentage of lost particles from Menez Gwen justifies the results of lower particle exchange with other populations, mainly in the October scenarios. For this population, connectivity matrices only reveal self-recruitment and connectivity in the Passive behaviour scenarios and for the scenario *October_PLD_23_Behaviour_1*. This result is, therefore, an underestimation of the potential particles exchanged from Menez Gwen populations with other recruitment locations. Once out of the domain, particles are “lost” for the model. However, because currents are very dynamic in the Azores, these larvae in a real situation can be advected again for the Azores region. Also, these larvae that drift to other regions can settle in other recruitment zones (not considered in this study nor this domain), additionally, this region can receive particles from remote regions.

Larvae dispersal, even with swimming behaviour, is mainly induced by hydrodynamic patterns (Wang et al. 2021). The model reveals different seasonal dispersal results, reflected in particle density distribution and in the connectivity between populations. Particle density distribution (PDD) results (Figure 4.23 and Figure 4.24) show a density decrease over time but also depict the establishment of “larval corridors”, that might induce particle exchanges between different populations.

For the March release with PLD81, a “larvae corridor” is formed between CG and MAR, and also between WG and CG, likely forming a longitudinal larval corridor. In October, larvae distribution is more concentrated mostly between CG and MAR, with a North-South larvae corridor more evident than the longitudinal one. This dispersal is reflected in the connectivity matrices. After the March release, the exchange between the different groups is multiple, with exchanges between EG and CG, CG and MAR, and between MAR and both CG and WG, while in October, the exchange is mostly unidirectional to the MAR populations, with lower connectivity with the populations located in the CG and EG. Particles released from WG during October don’t achieve the most eastern locations (EG, CG), For MAR only particles from locations L#4, L#5 and L#6 settled in populations from the Central Group but with a low percentage of larvae exchange.

Passive behaviour is the most unlike, with larvae travelling in the deeper water layers without achieving the surface layers. Behaviour_1 scenario is the one that best simulates the realistic behaviour for this species, simulating the presence of larvae at the surface and patchy connectivity between different populations. These seasonal dispersal patterns can be useful to support studies of fisheries planning and management, by providing information on seasonal and spatial dispersal behaviours.

Connectivity between different populations

Major results show multiple connectivity relations between the different populations. For the October releases, self-recruitment does not occur in most of the western locations (WF, MAR and CG). Self-recruitment is even lower for particles with swimming behaviour than for the passive behaviour scenarios. The absence of self-recruitment is more evident in the most dispersive scenarios with higher PLD. Despite the low self-recruitment in these scenarios, the multiple connectivity relations between the different populations is a positive feature and can be indicative of higher resilience of these populations mitigating the absence of self-recruitment that occurs in the most dispersive scenarios, and the risk of recruitment failure (Holstein et al., 2014; Pata et al., 2021). This result can indicate high levels of potential connectivity between the different populations of *C. affinis* in the Azores, however with low larvae exchange, mostly less than 0.1%.

Results show that Voador Seamount (L#3), located in MAR, is a major sink area, receiving larvae from all the groups, including from the Formigas (L#12) population from the EG. Also Gigante Seamount, in the MAR group, exchanges particles with populations from all the groups, in the majority of the scenarios in the study, including the passive behaviour, being one important source population. North of Faial population, (L#8), reveals higher connectivity relations with all the other groups, with larvae settling in all the other populations (in different scenarios), however, receiving fewer larvae from other populations. These results can support the higher abundance of *C. affinis* reported in these two seamounts when compared with the coastal zones of the Azores (Santos et al. 2021).

Menez Gwen (L#2) also has a higher abundance of this species in the Azores. Recent studies, after the identification of a new hydrothermal vent in Gigante Seamount, suggest the hypothesis of a higher abundance of this species near hydrothermal vents (Santos et al. 2021). Model results show connectivity with different locations, including Açores bank in the CG, but mainly serving as a potential nursery area, receiving larvae from different releases in MAR, WG and CG. However, model domain limitations constrain the analysis of this location. L#2 is located near the domain borders, and a higher percentage of larvae are advected out of the domain, so these results may be underestimated. However, when analyzing the results of the passive larvae behaviour, this population reveals higher levels of connectivity, being the one with more connectivity relations for a PLD of 23 days. The model domain limitation restricts the correct analysis of this population's larval dispersal, however, it confirms that this location can receive larvae from different populations in the MAR group (L#3, L#4, L#5). Even with the underestimation caused by the domain limitation, it reveals the potential of Menez Gwen as a sink area.

Results show that seasonality is determinant for population connectivity, March and October scenarios give rise to different connectivity relations. The October spawning scenarios reveal fewer connectivity relations than the March scenarios. This is a consequence of the hydrodynamic patterns, characterized by strong currents during October, inducing particle dispersion instead of retaining. It is clear a higher particle exchange from East to West in the October release, with larvae from the Eastern Group settling in the MAR populations; and from West to East in the spawning release in March.

The scenarios tested in this study indicate that the March spawning season and longer PLD results in higher connectivity relations than the October scenario. However, the shorter PLD induces higher self-recruitment levels in all situations.

Model results show how larvae biological characteristics like the PLD and larvae swimming behaviour, including vertical up and bottom-oriented swimming activity, can have a large impact on larval dispersal patterns, similar to other studies (Metaxas & Saunders 2009, Ross et al. 2020).

The modelled larvae dispersal results for *Chaceon affinis* show high dynamic connectivity among different locations. However, with a low percentage of larvae exchange (when comparing with case-study 1, using the same methodology but with different biological traits, the percentage of larvae exchange is one order of magnitude lower). Although an adequate flow of larvae among sub-populations is crucial for the sustainability of marine resources (Phelps 2015), larvae reaching a site does not necessarily equate to successful recruitment (Kough, 2014). Furthermore, the transition from pelagic larva to benthic juvenile and on to adulthood is dependent on a variety of post-settlement processes, not considered in this study (Cowen & Sponaugle 2009, Kough 2014).

All these scenarios' results must be taken as a hypothesis and must be taken into consideration bearing in mind the inherent model limitations and all the theoretical assumptions taken in the absence of detailed biological traits and larval behaviours (Bode et al. 2019). Nevertheless, this methodology shows capabilities to assess larval dispersal of *Chaceon affinis* species in the Azores region.

4.4.5. Conclusions – Case Study 2

The modelling methodology taken in this study was able to simulate the larvae dispersal, and the larvae swimming behaviour, surface-oriented, enabling tracers to achieve the surface layers, and mimic the behaviour observed for these deep-sea larvae, that were collected at the surface in different studies (Tuset et al. 2011, Landeria & Tamura 2018). This approach represents an initial step to understanding the factors determining larval dispersal patterns of this species in the Azores.

Model results show how the hydrodynamic patterns in the region have a strong influence on particle dispersal, producing different connectivity results for the different seasonal scenarios (March versus October), PLDs, and larvae behaviours. Moreover, the uncertainties about larvae swimming behaviours can generate different connectivity relations.

The general results of this biophysical model application suggest that populations of *Chaceon affinis* in the Azores may be connected and patchily distributed. Populations in MAR, namely Voador Seamount are important sinks and sources of larvae for the Azores region. Simulated larvae from the WG (Flores island), and larvae from the EG settle in the CG and at the MAR populations.

The low percentage of larvae exchange between populations also indicates that despite existing connectivity between populations, they might be isolated, and caution should be made in the management of the populations and their reserves' before any exploitation.

This particle tracking model approach can be valuable for further studies in distribution and population dynamics, supporting decision-making regarding fisheries assessment studies for this DSRC species in the Azores, the establishment of protected areas and guaranteeing the protection of this species before the development of any fishery activity (Santos et al. 2019).

Nevertheless, a multidisciplinary approach must always be used together with ecological and biological studies, and if possible including population genetics (Swearer et al. 2019, Busch et al. 2021). Different habitats can have different species-specific effects on movement (Kool et al. 2013), further study should also consider the deep-seabed and neighbourhood characteristics, as well as local landscape aspects, providing a better understanding of larval dispersal (Combes et al. 2021).

The biophysical model provides predictions of the settlement distribution of larvae, but it does not account for post-settlement processes such as predation and competition, which will reduce recruitment success. A comprehensive study of hydrologic data, particle motions, genetic data sets (Feng et al. 2017), and correction for natural mortality and habitat suitability would also aid the understanding of the dynamics involved.

4.5. Final Chapter 4 discussion

Larval dispersion is fundamental to population dynamics, and an important topic regarding deep-sea management and conservation plans (Cowen & Sponaugle 2009, Gary et al. 2020, Combes et al. 2021). Many benthic organisms, not only sessile organisms like deep-sea sponges but also moving organisms like DSRC, rely on the larval stage as the only opportunity for any significant migration between different populations (Wang et al. 2021). Therefore, understanding the drivers of larval dispersal, and their spatial and temporal constraints is of the utmost importance to marine managers and ecologists (Ross et al. 2020).

This study used a 3-D biophysical particle tracking model to simulate the larval dispersal of two different organisms to assess population connectivity. The findings of this work show how the regional patterns of the currents drive the larval dispersion. Due to the dynamic temporal and spacial hydrodynamic patterns in the region, the spawning time and the PLD are determinant factors for larval dispersion and population connectivity.

Model results indicate the existence of connectivity between *Pheronema carpenteri* sponge aggregations in the Azores. Central Group seems to have well-connected populations, being also connected with the MAR populations. Sponge aggregations from the CG serve as source populations for several locations. Regarding *Chaceon sp.*, despite the multiple larvae exchange between different populations, the most plausible scenarios reveal a low percentage of successfully settled larvae.

Larvae behaviour

Deep-sea sponge larvae are lecithotrophic (non-feeding) (Maldonado and Young, 1999), a characteristic typically associated with shorter planktonic larval duration (PLD) (Yearsley and Sigwart, 2011). In contrast with the planktotrophic larvae from the DSRC (Tuset et al., 2011), which are believed to have longer PLD from 23 to 125 days (Kelly et al., 1982). Simulated scenarios reveal the importance of the PLD on larval dispersion and population connectivity. For both case studies, model results reveal higher dispersal potential for longer PLDs, therefore more connectivity among different populations, however with lower self-recruitment in the different populations.

The longer PLD considered in the *C. affinis* case study conducts to higher travel distances and dispersion patterns, however, with less percentage of particles exchange. The results of these two case studies show how larval behaviour influences dispersal and travel distances (Cowen and Sponaugle, 2009; Kough et al., 2013).

Considering passive behaviour, travel distances can vary in one order of magnitude when considering a PLD of 23 or 125 days. When adding swimming behaviour, this difference in the travel distances is even higher. The swimming behaviour estimated for *C. affinis* larvae increases travel distances up to hundreds of kilometres allowing the potential connectivity between populations from Flores Island, in the Western Group, and Mar da Prata, in the Eastern Group.

Different studies show the relevance of investigating a range of possible behaviours to assess different dispersal and connectivity patterns between different populations (Gary et al., 2020; Holstein et al., 2014; Kough et al., 2013; Paris et al., 2013). In this work, different behaviours are tested (PLD, spawning seasonality, swimming behaviour). The swimming behaviour is revealed to have a large impact on larvae travel distance.

Model constraints and limitations

In this study, all the populations for the same species are simulated with the same number of particles, not reflecting population abundances, size or reproduction rate. The quantitative approach, considering population size, was not used, only a qualitative approach.

The number of particles was calibrated for each case study, and once calibrated all the particles simulated are valid, therefore all connections that occur are considered valid. Even if the model estimates that only one particle has settled, this is a valid and potential connection. In nature these unlikely events can happen, long-lived species colonies that live for hundreds of years need a single larva to become established (Botsford et al., 2009).

Although, concerning mortality, this model uses the simplistic concept of the fixed half-life concept (Connolly and Baird, 2010; Leis, 2020). Behaviours in this study are not constrained by the limits of larvae energy stores, and no time-varying mortality, contrasting with the characteristics that are believed to occur in the sea. However, longer PLD increases the probability of planktonic mortality, reducing post-settlement growth or survival (Metaxas and Saunders, 2009).

Model connectivity results may indicate potential qualitative, but not quantitative connectivity. So, when extrapolated for a more complex study, including population abundancies or other fisheries-relevant features, these findings might be even more relevant. Despite all the model limitations, these applications provide a useful tool for decision-making and are a powerful tool for testing hypotheses about marine dispersal.

The major limitation of larval dispersal models is the lack of validation and the difficulty of doing it in the deep-sea (Leis, 2020; Swearer et al., 2019). This enforces the necessity of using an accurate and validated hydrodynamic model. In this study, the hydrodynamic model was previously validated for the entire water column (see Chapter 2). However, this model, like many other oceanographic models was not validated at the bottom layer, for the bottom currents. The complex topography of the Azores (Morato et al., 2008; Peran et al., 2016) can induce local mesoscale activity (Holliday et al., 2000) which likely promotes greater local retention and therefore differences in modelled predictions (Ross et al., 2020). The calibration of the model at the deep-sea bottom layers, and also the better bottom resolution would minimize these limitations.

Furthermore, deep-sea particle tracking models are neither validated nor their predictions (larvae trajectories) can be tested or proved (Leis, 2020). Empirical data required for model assessment is costly to obtain, these costs increase for the deep-sea, and over broad scales (Bode et al., 2019; Kough et al., 2013). However, different studies using coupled biophysical particle tracking models, for assessing marine dispersal reveal confident results on these modelling tools, mainly verifying model dispersal and connectivity results comparing results against genetic studies (Selkoe and Toonen, 2011), and specifically deep-sea sessile organisms (e.g. for corals (Wood et al., 2014) (Ross et al., 2017)). Biophysical model sensitivity analysis for parameters like mortality, swimming velocity, and age of competency, among others for which empirical data are scarce could improve model accuracy (Paris et al., 2013).

Assessment of the Azores Marine Park regarding larval dispersal patterns and connectivity for *P. carpenteri* and *C. affinis* case-studies

Connectivity among different benthic populations promotes the increase of their genetic diversity (Busch et al., 2021; Wang et al., 2021), and the resilience of the species (Bracco et al., 2019). It is an essential aspect of the establishment of management and protection plans for marine ecosystems (Combes et al., 2021). Detailed knowledge of the patterns of physical and biological interactions that drive the transport of the planktonic phases is crucial to improve the effectiveness of the MPAs (Stratoudakis et al., 2019). Larval dispersal and connectivity model results obtained for these two target species in the Azores were used to evaluate the effectiveness of the current MPA in the maintenance of the connectivity of these populations. If MPAs are isolated from one another they are more vulnerable to local extinction as they cannot be replenished by organisms or larvae from other locations (Stratoudakis et al., 2019).

The study of larvae dispersal and the connectivity for each one of these two deep-sea species can be seen as a pilot study for the connectivity of deep-sea organisms in the Azores. In particular for sessile organisms like deep-sea sponges, which depend on larval dispersal to colonize new habitats (Metaxas and Saunders, 2009), and support remote populations (Gary et al., 2020). Or for an organism as *C. affinis*, which besides being non-sessile, presents low mobility, benefiting from larval dispersal to colonize new habitats. Furthermore, due to its low mobility, *C. affinis* is highly vulnerable to local depletion in case of intensive fishery effort (Triay-Portella et al., 2017). The life pattern of *C. affinis* is characterised by a very low rate of growth, a biennial reproduction (Pinho et al., 2001), and a late first sexual (Biscoito et al., 2015). These biological traits originate in a low rate of resilience or recoverability, and the recolonisation of larvae from other areas and their growth will take a long time (Triay-Portella et al., 2017). Therefore, the study of potential larvae dispersal patterns, and the identification of major sources and sinks of larvae can contribute to the assessment of f management and protection plans (Combes et al., 2021).

Among the 10 deep-sea sponge aggregations in the study, two are localized in MPAs: Condor and Formigas populations, and Princesa Alice just adjacent to the limits of the Princesa Alice MPA. Connectivity results (Figure 4.14, Figure 4.15, and Figure 4.16) and the distribution of hypothetical settled larvae (Figure 4.20) show that MPA of Princesa Alice and Condor receive larvae from different populations in the study, being important sink locations. Moreover, larvae from Condor seamount (Figure 4.20e)) can settle in different locations in the Central Group, in the Western Group (around Flores and Corvo islands), but also along MAR: in the North, at the 40.3ºN (Seamounth South of Kurchatov Fracture Zone); at 39ºN in the Gigante Seamount; and also in Voador Seamounth at37.5ºN. These results show the potential connectivity that sponge populations from Condor can have with different populations in the Azores, being an important source of larvae. These results reinforce the importance of maintaining this MPA.

Princesa Alice sponge aggregation in the study, adjacent to the limits of the PMA, reveals the importance of increasing the limits of this MPA. Due to its potential to retain larvae from several locations in the study: Cavala, Gigante and Condor seamounts also from South of Faial), it is an important sink location.

Major results reveal a lack of connectivity between the EG populations and the remaining populations in the study, mainly due to their distance from the remaining populations, but also as a consequence of the hydrodynamic patterns between the CG and the EG, hampering the larvae advection in the Westwards direction Figure 4.7. For *P. carpenteri* no connectivity was identified between EG and the remaining populations, and for the *C. affinis*, the exchange of larvae with the remaining populations was scarce. For the *C. affinis* case study, even with the swimming behaviour: Formigas and Mar da Prata populations only exchange larvae with MAR populations in the October scenarios. Moreover, they only receive larvae from the remaining populations during march scenarios with swimming behaviour larvae. Notwithstanding this lack of connectivity, populations of Mar da Prata also face a lack of self-recruitment in different scenarios. These results highlight the necessity of protection measurements in Mar da Prata in this location, to minimize the impacts of its limited capacity to retain larvae.

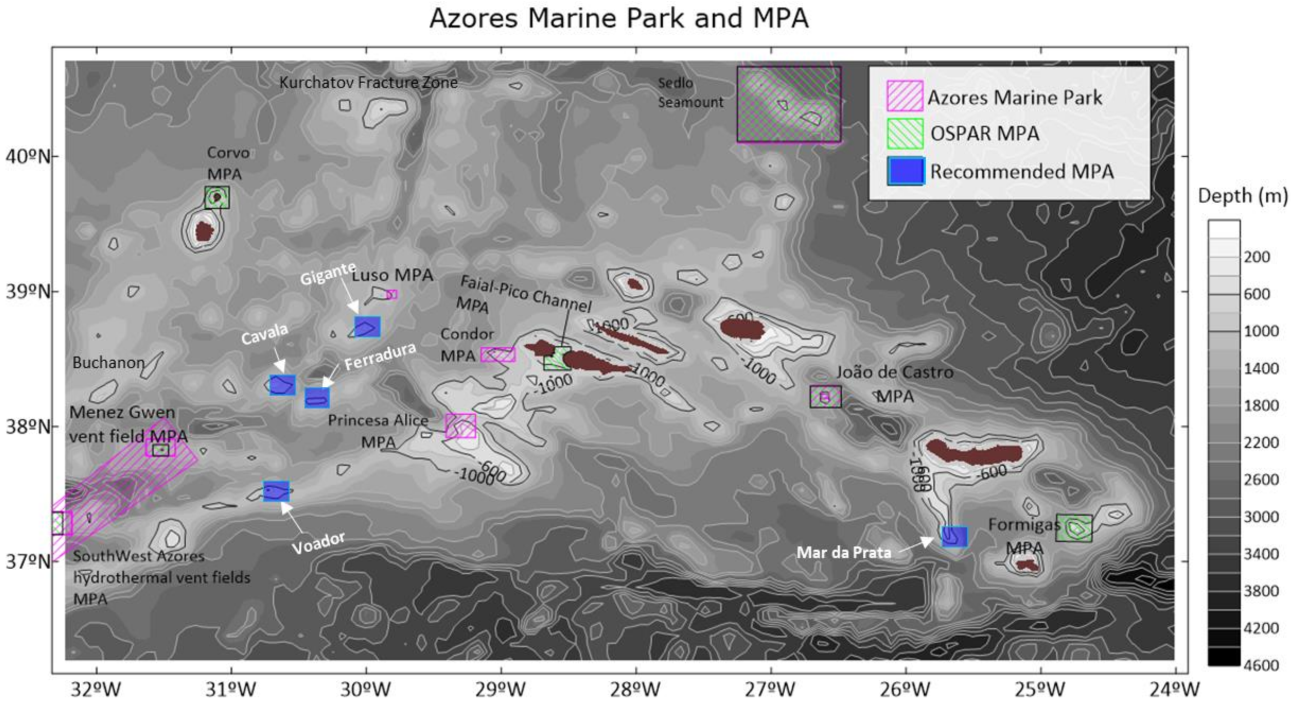

Figure 4.37- Representation of the current Azores Marine Park, OSPAR MPA, and proposed protection areas (in blue). Bathymetry is represented in a grey colour scale;

The MPA of João de Castro Bank can receive larvae from CG and Mar da Prata (in the EG) sponge aggregations (Figure 4.20i) being an important connection point between the Central and the Eastern parts of the archipelago. This potential connectivity shows the relevance that this MPA can have in the connectivity along the archipelago, mainly regarding the EG.

Gigante seamount, located in the MAR, is a potential recruitment area for deep-sea sponges, retaining larvae from different populations from the CG (Condor, Açores bank and South of Faial), and also from Cavala and Gigante Seamount. The larval dispersal results also show that larvae from the Gigante seamount can settle along the MAR, up to seamounts located South of Kurtchatof Fracture Zone (North of the domain), and in seamounts West of the MAR like the Buchanon Seamount.

For the *C. affinis* case study, larvae from the Gigante seamount were able to settle in the Mar da Prata population, in the Eastern Group. This was the population with more larvae exchanges, establishing connectivity with all the populations in the study.

Therefore, this population can be crucial to maintain populations connectivity in Azores regions: between the CG and the MAR, between the MAR and the Northwest part of the archipelago (including the islands of Flores and Corvo); with the SouthWest part of the archipelago, including the Buchanon seamount; and also with the EG, for the case of larvae with swimming behaviour and longer PLD.

Cavala Seamount can be a significant source population, its larvae can settle along the MAR, in different populations of the CG (Condor and Açores bank), and along the western slope of the CG, being an important population to guarantee the connectivity between the MAR and the CG populations. Considering its swimming behaviour and the longer PLD, *C. affinis* larvae, from the Cavala Seamount can also settle in the Mar da Prata populations. Thus the protection of this population will be beneficial for ensuring populations connectivity in the archipelago.

Ferradura seamount can be an important sink population, it can retain *C. affinis* larvae from Mar da Prata, and for the *P. carpenteri* case, it can retain larvae from Cavala and Gigante (from the MAR), and Condor population (from the CG). Therefore, Ferradura seamount is also suggested as a new recommended MPA in the Azores.

Larval dispersal patterns show that Voador seamount can retain *C. affinis* larvae from the EG populations in different October scenarios. Moreover, this seamount can retain *P. carpenteri* from MAR (Cavala and Gigante), and from CG populations (Condor, South of Faial and Condor) promoting the connectivity between the eastern and western parts of the MAR, but also the connectivity with other locations south of the Azores EEZ.

4.6. Conclusions

The applied particle tracking model provides valuable information for the connectivity and dispersal patterns of deep-sea organisms in the Azores.

Model results show how the hydrodynamic patterns in the region have a strong influence on particle dispersal, producing different connectivity patterns for the different seasonal scenarios and larvae behaviours (PLD, swimming behaviour, settlement and recruitment).

The differences obtained in the larval dispersal and connectivity responses over the years 2017 and 2018 highlight the model's capability to simulate the hydrodynamic patterns of the region, characterized by a high variability from the surface up to the deep-sea (Lima et al., 2020; Sala et al., 2013). This model application was able to simulate the major currents in the Azores, with particular eddies and temporal features that form hydrodynamic barriers or contribute to particle retention or dispersal. The hydrodynamic patterns allow for achieving the proposed objectives of studying larvae dispersal over the archipelago, at a regional scale.

Major results indicate that sponge aggregations in the Central Group of the Azores are well connected, however, populations from the Eastern Group can be isolated from the remaining populations in the study. Larval dispersal results show that sponge aggregations from the Central Group can represent a significant sink and source for *P. carpenteri* sponges in the Azores. Results reinforce the importance of maintaining the protection efforts in the MPA (Condor and Princesa Alice), once they are important recruitment areas. Despite no estimated connectivity between the sponge aggregations of EG with CG, model results show potential connectivity from both groups with João de Castro seamount pointing out a possible interconnection between these groups.

Conversely, the longer PLD considered for the *C. affinis*, as well as the swimming behaviour, conducts to higher travel distances and dispersion patterns, creating more patchy connectivity patterns all over the Archipelago. However, with less percentage of particles exchange. Populations from the Western group, in Flores island can be connected with the populations from the central group. Also, larvae from the EG can settle in the MAR locations. Model results indicate that the populations in MAR, namely Voador seamount may be an important recruitment area and nursery for the Azores region.

Population connectivity results allow to assess the rates of successful population establishment, by the levels of larvae exchange among different subpopulations but also the levels of self-recruitment and to identify populations with the risk of being geographically isolated among populations. (Antonio Baeza et al., 2019; Ross et al., 2020). Additionally, larval dispersal allows to study of the spatial distribution and identification of potential recruitment areas.

These results will therefore provide important information for marine spatial planning and the assessment of the performance of the existent marine protected areas (MPA).

Results of these implemented case studies show that the MPA of Condor and Princesa Alice are of utmost importance, being important recruitment areas. Furthermore, Condor deep-sea sponge population can exchange larvae with populations in the MAR, and along the entire CG. João de Castro MPA serves as an important linkage between the more isolated populations from the eastern group and the rest of the archipelago. This connection can be crucial for the *P. carpenteri* populations that reveal no connectivity between the selected EG populations and the remaining populations in the study. For more effective protection the extension of the Princesa Alice MPA is also suggested.

The MAR was also revealed to be an important larvae retention area. Passive sponge larvae and both passive and swimming larvae from *C. affinis* settle in different locations along the MAR. Therefore MAR can act as a linking point between the Western populations and the CG and Eastern populations which may be poorly connected due to hydrodynamic currents in the archipelago. Therefore, besides the marine protected areas of the Menezgwen, and the most recent Luso hydrothermal vent PA, the Azores archipelago would benefit from more protection regulations along the MAR. New MPAs are proposed: in Cavala and Ferradura seamounts, in Gigante, and in Mar da Prata (in the Eastern Group).

Gigante is a potential recruitment area for deep-sea sponges, A new protected area in Gigante Seamount complex ensures connectivity between sponge populations from the Western Group and MAR, and from MAR and the Central Group, and the potential connectivity with populations along the MAR towards the north until the of Kurtchatof Fracture Zone, and towards the south but also in the West of the MAR in the Buchanon seamount.

Cavala is a significant source population, and a PA in this seamount could assure connectivity with different populations of the CG (Condor and Açores bank), and along the western slope of the CG. But also with the western part of the domain, including Flores and Corvo islands and the Buchanon seamount complex.

For the *Chaceon affinis* case study, the MPA of Gigante, Cavala and Ferradura can also guarantee connectivity between the MAR and the Eastern Group. Ferradura is pointed as a new MPA, because it can retain deep-sea sponge larvae from Cavala and Gigante (from the MAR), and Condor population (from the CG), and also due to its important potential capacity of retaining swimming larvae from the Mar da Prata population.

The exchange of *Chaceon affinis* larvae between MAR and the EG can occur, but it is very rare. Also for the *Pheronema carpenteri* case study, this population faces different scenarios with the lack of self-recruitment and the lack of connectivity. These results highlight the necessity of protection measurements in Mar da Prata in this location, to minimize the impacts of its limited capacity to retain larvae.

To support the persistence and recovery of local populations from disturbance, each MPA should be adequately connected to the others (Gaines et al., 2010). Therefore, new MPA are proposed for the Azores region: in Ferradura, Cavala and Gigante Seamounts, to ensure the connectivity between the CG, the MAR and the Western part of the Archipelago. In Mar da Prata, a new MPA is proposed for further protection, to reduce its vulnerability to scenarios of lack of recruits and difficulty in exchanging larvae with the population further west. A new MPA in Mar da Prata will also contribute to preserving the connectivity in the plateau south of São Miguel island and to diminish the vulnerability of the populations from the Eastern Group of the Azores archipelago.

This study considers specific *P. carpenteri* populations, and specific *C. affinis* populations serving as pilot case studies for the entire archipelago, providing a widespread study of connectivity throughout the archipelago for these species. This is the first approach of this methodology which reveals to provide worthwhile results and information for further studies.

Further studies should include more populations of *P. carpenteri* in the Azores, including the ones identified in recent years on scientific cruises in the Azores. Also, a different approach, regarding the density of the populations, should be included. This is of greatest importance regarding the *C. affinis* case study, to provide further information for species sustainability, and define vulnerable areas for its protection responding to future fisheries exploitation interests (Santos et al., 2019). This methodology of studying larval dispersal and population connectivity can be included in ecological studies for *C. affinis*, considering any new information regarding this species' biology.

This model application allows for studying larval dispersal at a regional level. However, it is worth saying that this methodology proves to be suitable for larval dispersal assessment to other regions, and domain scales. It can also be applied in further studies at a local scale (like a restricted group of islands, or even a seamount), using nested domains and high-resolution models.

Furthermore, this modelling approach can provide valuable information not only for the assessment of current protection plans, but also in the establishment and prioritization of future management plans at a local or ocean scale (Combes et al., 2021), but also to support deep-sea conservation studies for fisheries management.

Chapter 5

Environmental characteristics at deep-sea sponge locations in the Azores

5.1. Introduction

In the North Atlantic, deep-sea sponges can be found as isolated specimens, patchily distributed, and as dense sponge aggregations (Maldonado et al., 2015; Pham et al., 2015; Wang et al., 2021). Mainly forming monospecific populations, *Pheronema carpenteri* aggregations were documented in the Porcupine Seabight (Rice et al., 1990), on the continental slope of Morroco (Barthel et al., 1996), and in the Azores, at different locations and seamounts (Colaço et al., 2020; Friedlander et al., 2019; ICES. 2019. Azores ecoregion – Ecosystem overview and ICES, 2019; Somoza et al., 2020; Xavier et al., 2015). Although they are believed to support a high biological diversity (Henry and Roberts, 2014), the ecological importance of the deep-sea sponges is greater where they form dense aggregations, known as “sponge grounds” (Wang et al., 2021).

Deep-sea sponge aggregations are believed to play an important role in the biogeochemical cycling of dissolved nutrients, particularly, the *P. carpenteri* aggregations serve as a sink in the marine silica cycle which is thought to influence primary productivity and the carbon cycle (Maldonado et al., 2005; Hendry et al., 2019), and also by acting as a silica reservoir (Maldonado et al., 2011). Sponge aggregations can also act as refuges, nurseries and foraging sites for demersal fish species (Graves et al., 2022). Specifically, hexactinellid sponges like *Pheronema carpenteri* are also characterized as biodiversity hotspots, not only by their three-dimensional structural complexity but also due to the role of the spicule mats created by their senescence and death (Henry and Roberts, 2014).

Because they are sessile organisms, the environmental conditions at these sea sponges can be crucial for their survival, once they cannot move in case of any change or variation in their environment. The understanding of the environmental factors that contribute to deep-sea benthic organisms' distribution is an issue under research. Several studies have looked at the environmental and biogeochemical deep-sea characteristics to understand *Pheronema* aggregations distribution (Barthel et al., 1996; Bett and Rice, 1992; Howell et al., 2016; Rice et al., 1990; Vieira et al., 2020; White, 2003).

Pheronema carpenteri are deep-sea sponges, mainly located from 600 up to 1200 meters depth (Maldonado et al., 2015; Rodríguez-Basalo et al., 2021), deeper than the permanent thermocline and winter mixed layer, in depths where the temperature variability due to seasonal stratification is likely to be minimal (Graves et al., 2022). Sponge grounds, (Leys and Lauzon, 1998), and specifically *Pheronema* aggregations (Rice et al., 1990) are commonly associated with low bottom currents, however, located in regions with increased near-bottom current velocities due to seafloor topography interacting with local and regional hydrodynamics. Because sponges may not be able to support strong current velocities, they would rather benefit from the resuspended or undeposited organic matter carried by these higher currents (Rice et al., 1990). Also White et al. (2003), in the Porcupine Seabight (Bathyal NE Atlantic), shows that deep-sea sponge aggregations are located in regions with low current velocities when compared with areas without sponge aggregations, where bottom velocities are higher. Roberts et al. (2021), studying deep-sea sponges' distribution across the North Atlantic, (not specifically the *P. carpenteri*), concluded that water masses and major currents constrain the distribution of deep-sea sponges on a basin scale (Roberts et al., 2021). The local currents around seamounts (Clark et al., 2010), and the circulation above their summits), can induce an accumulation of suspended matter as well as benthic biomass (Lavelle and Mohn, 2010). Howell et al. (2016), used environmental parameters, Maximum Entropy Modelling and presence/absence data, to study the drivers for *P. carpenteri* distribution. Besides being siliceous sponges, dissolved silica was not the most relevant parameter, although, water depth and bottom water temperature could be predictors of the distribution of *P. carpenteri* aggregations. Current speed is also thought to play an important role in driving the distribution of *P. carpenteri* sponge habitat (Howell et al., 2016). Reported *P.*

carpenteri aggregations were identified in a temperature range of 2.73–20.9 °C, with dissolved silica values ranging from 0.42 to a maximum of 0.62 mgSi/l (Howell et al., 2016).

5.1.1. *Pheronema carpenteri* aggregations- case study

In the Azores, several sponge aggregations have been identified. This study refers to the sponge aggregation identified in the scope of the SPONGES project, as previously referred to in Chapter 4 (Colaço et al., 2020). From these sponge aggregations, the ones in the South of Pico (Figure 5.1), Princesa Alice, and Condor Seamount were reported as dense sponge grounds (Colaço et al., 2020).

Figure 5.1- *P. carpenteri* aggregation in South of Pico and individual sponge sample (a), and individual sponge sample from Princesa Alice Bank (b). Photo credits from a) REBIKOFF FOUNDATION, and b) (Colaço et al., 2020).

The Azores region is under the influence of different oceanographic features and water masses (Caldeira and Reis, 2017), characterized by a high spatial, seasonal, and inter-annual variability of marine climatology (Amorim et al., 2017). The use of the 3-D hydrodynamic and biogeochemical models helps to consider all these variables and study the spatial and temporal variability at these specific *Pheronema carpenteri* sponge grounds.

5.2. Methodology

5.2.1. Study site

The *Pheronema carpenteri* sponge aggregations considered in Chapter 4 were used for this study (Figure 5.2 and Table 5.1). Environmental conditions were analysed at the sponge location at the bottom layer and along the water column, using vertical profiles crossing several sponge aggregations (Figure 5.2).

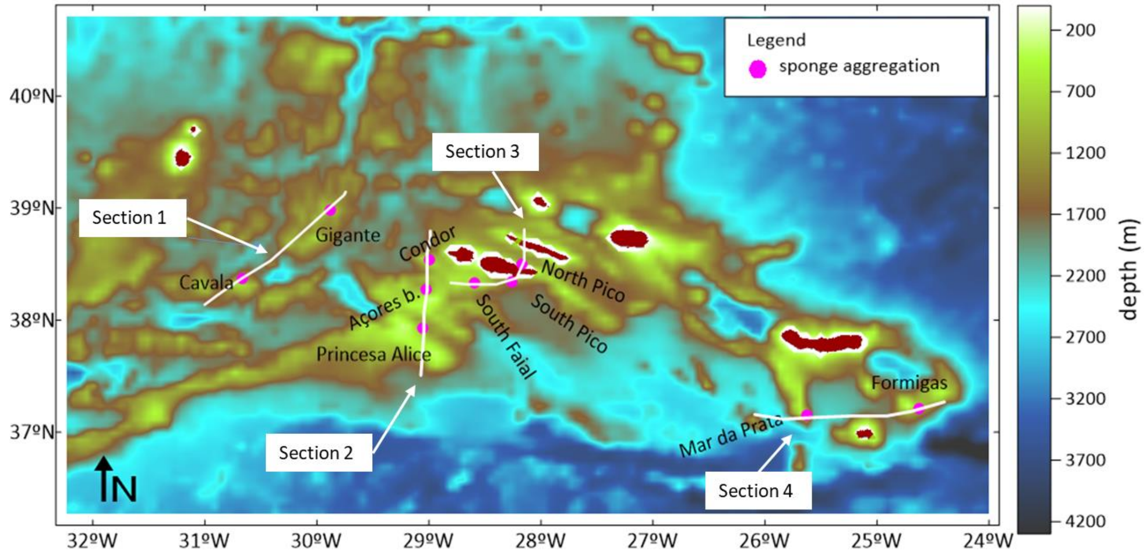

Figure 5.2 Representation of sponge aggregations with pink circles, and the different sections used to analyse model results. Sections across the sponge aggregations (sections 1 to 4) are represented with white lines.

Table 5.1- *Pheronema carpenteri* sponge aggregations in the study, their location, depth, source and name/location

Sponge aggregation	Longitude (◦W)	Latitude (◦N)	Depth (m)	Name/Location	Group
1	-30.6701	38.3632	900	Cavala	MAR_1
2	-29.88809	38.98353	766	Gigante	MAR_2
3	-29.06232	37.9183	900	Princesa Alice	CG_1
4	-29.02941	38.273	825	Açores Bank	CG_2
5	-28.99877	38.53281	775	Condor Seamount	CG_3
6	-28.59288	38.32531	630	South of Faial	CG_4
7	-28.30216	38.3579	1000	South of Pico	CG_5
8	-28.1735	38.49624	822	North of Pico	CG_6
9	-25.63083	37.14111	780	West of São Miguel (Mar da Prata)	EG_1
10	-24.63	37.205	904	Formigas	EG_2

Table 5.2. Sections used for model results analyses, type of section (meridional or zonal, location, limits and sponge locations across de section

	Details/sponge aggregations in the transect
Section 1	Across sponge aggregations Cavala (L#1) and Gigante (L#2)
Section 2	Across sponge aggregations Princesa Alice(L#3), Açores Bank (L#4) and Condor (L#5)
Section 3	Across sponge aggregations South of Faial (L#6), South of Pico/L#7) and North of Pico (L#8)
Section 4	Across sponge aggregations: Mar da Prata (L#9) and Formigas (L#10).

5.2.1.1. Biogeochemical model results

Biogeochemical data obtained from the MOHID biogeochemical model implemented in the scope of this PhD work were used in this study. The variables used are those shown in Table 5.3.

Table 5.3- Biogeochemical and physical variables used in this study

Variable	Description	Units	Dt	Details
ϕPhy	Phytoplankton concentration	mgC/l	Hourly	3D
ϕNO3	Nitrate concentration	mgN/l	Hourly	3D
ϕIP	Inorganic phosphorous concentration	mgP/l	Hourly	3D
ϕSi	Dissolved silica concentration	mgSi/l	Hourly	3D
ϕOxy	Dissolved Oxygen concentration	mgO2/l	Hourly	3D
ϕTemp	Temperature	ºC	Hourly	3D
ϕSal	Salinity	PSU	Hourly	3D
Velocity mod	Velocity modulus	m/s	Hourly	3D
Velocity w	Velocity vector w (vertical velocity)	m/s	Hourly	3D
Depth	Depth	m	--	--

Model results are provided on an hourly basis, with a 6km resolution, and a vertical variable resolution. Model results were quantified at the sponge aggregation locations, and along different sections for the years 2017 and 2018. Sections and the locations in the study are represented in Figure 5.2 and described in

Table 5.2. Phytoplankton was considered for the sponge location but at the surface.

5.2.2. Data processing and statistical analysis

Biogeochemical model results are analysed at the sponges' aggregation locations, at the bottom depth, and also along the water column, for 2 years period (2017 and 2018). Firstly, to avoid the redundancy of information in the variables, a correlation analysis was carried out using Spearman’s rank correlation coefficient to identify redundant variables. Highly correlated variables (<−0.7 or >0.7) were not used in the parameter analysis (Graves et al., 2022; Ramiro-Sánchez et al., 2019).

To analyse the environmental conditions at the sponge locations, boxplots representing the median, the upper and lower quartiles, and the minimum and maximum data values were generated. For each sponge location was used hourly data at the specific sponge location and depth. To characterize the entire domain, weekly averages for the same depth range (600 to 1000 meters depth) were considered. Model results were also analysed for the entire bottom layer, and along the water column following a profile that crosses different sponge aggregations (Figure 5.2).

5.3. Results

5.3.1. Environmental data at *Pheronema carpenteri* aggregations

At each location and time, the different variables were compared using the Spearman rank correlation coefficient (ρ), to identify highly correlated variables (Figure 5.3). A correlation coefficient (ρ), greater than 0.7 was obtained for Salinity and Temperature (ρ=0.74), and between the nutrients (Si, N and P). Phosphate is highly correlated with nitrate and dissolved silica (ρ=0.9 and ρ=0.82 respectively). This correlation analysis shows that depth is not highly correlated with any other parameter, including temperature or salinity for these locations.

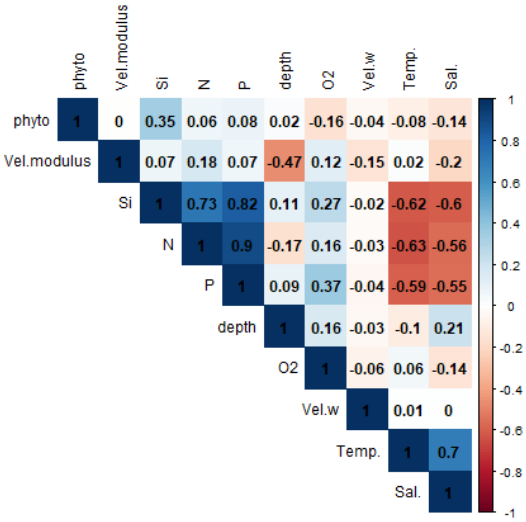

	phyto	Vel.modulus	Si	N	P	depth	O2	Vel.w	Temp.	Sal.
phyto	1	0	0.35	0.06	0.08	0.02	-0.16	-0.04	-0.08	-0.14
Vel.modulus		1	0.07	0.18	0.07	-0.47	0.12	-0.15	0.02	-0.2
Si			1	0.73	0.82	0.11	0.27	-0.02	-0.62	-0.6
N				1	0.9	-0.17	0.16	-0.03	-0.63	-0.56
P					1	0.09	0.37	-0.04	-0.59	-0.55
depth						1	0.16	-0.03	-0.1	0.21
O2							1	-0.06	0.06	-0.14
Vel.w								1	0.01	0
Temp.									1	0.7
Sal.										1

Figure 5.3- Spearman's rank correlation coefficient for the biogeochemical parameters in the study: Phytoplankton (phyto), depth, Oxygen (O2), Dissolved Silica (Si), Nitrate (N), Phosphate (P), Velocity w (Vel.W), velocity modulus

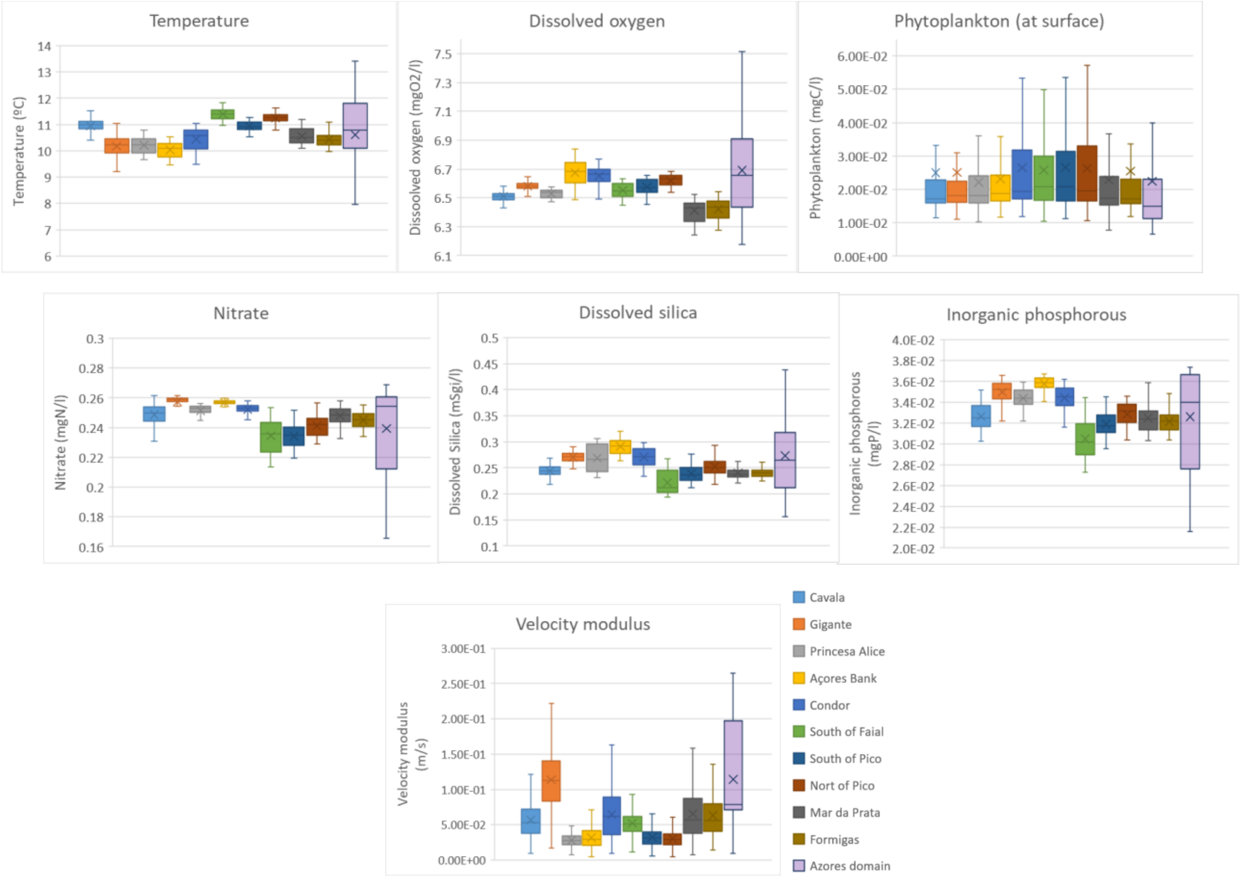

Figure 5.4- Boxplots of biogeochemical parameters (temperature, dissolved oxygen, nitrate, dissolved silica and inorganic phosphorous) and velocity modulus, for the sponge aggregation locations in the study, and for the entire domain from 600 to 1000 meters depth. Boxplots are created using the first and third quartile, whiskers represent the minimum and maximum values, and mean values are represented with a cross.

Pheronema carpenteri aggregations in the study are found in a bathymetric range from 600m to 1000m. Model results show that the range of values is relatively low compared with the range for the entire domain for the same depth range (Figure 5.4). The total range of variation for the period in analysis (2017 and 2018) at the different sponge locations, is about: 2.62 ºC for temperature, 0.048mgN/L for nitrate, 0.127mgSi/l for dissolved silica, 0.01mgP/l for inorganic phosphorous, and 0.61mgO2/l for dissolved oxygen (Table 5.4). Despite the low range of values, a longitudinal gradient is denoted for the nutrients. Higher concentrations are found at most Western locations (from Cavala to Condor Seamount), and lower in the Eastern locations.

Table 5.4 Biogeochemical model results at sponge aggregations, maximum, minimum, median, the interval range (Maximum – Minimum) and standard deviations for temperature, nitrate, dissolved silica, dissolved oxygen, and inorganic for the period 2017-2018. Minimum values are highlighted in grey and maximum values in bold.

	Temperature (◦C)				Nitrate (mgN/l)				Dissolved Silica (mgSi/l)				Dissolved Oxygen (mgO2/l)				Inorganic Phosphorous (mgP/l)			
Station	Min/max	Median	Range	StDev	Min/max	Median	Range	StDev	Min/max	Median	Range	StDev	Min/max	Median	Range	StDev	Min/max	Median	Range	StDev
Cavala	10.23-11.60	11.00	1.37	0.24	0.230-**0.262**	0.250	0.032	0.0065	0.217-0.269	0.245	0.051	0.01	6.43-6.58	6.51	0.152	0.033	0.030-0.035	0.033	0.0049	0.0012
Gigante	9.22-11.03	10.22	**1.81**	0.37	0.239-0.261	**0.259**	0.020	0.0049	0.249-0.290	0.271	0.042	0.01	6.44-6.65	6.58	0.207	0.034	0.031-**0.037**	0.035	0.0049	0.0012
Princesa Alice	9.66-10.78	10.22	1.12	0.29	0.236-0.256	0.253	0.020	0.0040	0.231-0.306	0.267	**0.075**	**0.027**	6.47-6.58	6.54	0.104	0.027	0.032-0.036	0.034	0.0037	0.0010
Açores Bank	9.46-10.54	10.10	1.08	0.29	0.248-0.260	0.257	**0.011**	0.0015	0.264-**0.320**	**0.292**	0.056	0.015	6.49-**6.85**	**6.68**	**0.355**	**0.094**	**0.033-0.037**	**0.036**	0.0037	0.0007
Condor	9.49-11.04	10.59	1.55	0.41	0.238-0.258	0.253	0.019	0.0033	0.233-0.299	0.272	0.065	0.017	6.47-6.77	6.67	0.298	0.068	0.032-0.036	0.035	0.0046	0.0011
South of Faial	10.95- **11.84**	**11.41**	0.89	0.23	0.214-0.253	0.236	**0.040**	0.0011	0.193-0.267	0.212	0.074	0.022	6.45-6.63	6.55	0.183	0.050	0.027-0.034	0.030	**0.0071**	**0.0019**
South of Pico	10.52-11.28	10.92	0.76	**0.18**	0.219-0.252	0.235	0.032	**0.0076**	0.211-0.276	0.237	0.065	0.016	6.45-6.66	6.57	0.203	0.052	0.030-0.034	0.032	0.0049	0.0011
Nort of Pico	10.70-11.63	11.26	0.94	0.19	0.229-0.257	0.242	0.028	0.0065	0.218-0.298	0.251	0.080	0.020	6.54-6.68	6.63	0.144	0.040	0.030-0.035	0.033	0.0042	0.0011
Mar da Prata	10.70-11.20	10.51	1.10	0.26	0.232-0.258	0.249	0.025	0.0064	0.220-0.279	0.237	0.059	0.012	6.24-6.53	6.43	0.284	0.072	0.030-0.036	0.032	0.0055	0.0014
Formigas	9.96-11.11	10.41	1.15	0.25	0.234-0.255	0.245	0.022	0.0054	0.224-0.267	0.240	0.043	0.01	6.28-6.54	6.43	0.267	0.069	0.030-0.035	0.032	0.0045	0.0010
Total range= Max.–Min.	2.62	1.31	n/a	n/a	0.048	0.024	n/a	n/a	0.127	0.08	n/a	n/a	0.61	0.25	n/a	n/a	0.01	0.006	n/a	n/a

Table 5.5 Biogeochemical model results at sponge aggregations, maximum, minimum, median, the interval range (Maximum – Minimum) and standard deviations for salinity, velocity modulus for each sponge location, and phytoplankton at the surface for the period 2017-2018. Minimum values are highlighted in grey and maximum values in bold.

	Salinity				Velocity modulus (m/s)				Phytoplankton at the surface (mgC/l)			
Station	Min/max	Median	Range	StDev	Min/max	Median	Range	StDev	Min/max	Median	Range	StDev
Cavala	35.31- 35.59	35.49	0.282	0.068	0.0097-0.153	0.054	0.143	0.025	0.0114 - 0.169	0.0172	0.158	**0.0212**
Gigante	35.22- 35.62	35.40	**0.398**	**0.079**	**0.0173-0.222**	**0.113**	0.207	**0.042**	0.0110 - 0.140	0.0186	0.129	0.0181
Princesa Alice	35.41- 35.56	35.51	0.157	0.043	0.0076-0.049	0.027	0.041	0.009	0.0102 - 0.064	0.0183	0.053	0.0093
Açores Bank	35.32- 35.51	35.46	0.198	0.052	0.0051-0.0714	0.030	0.066	0.013	0.0112 - 0.075	0.0191	0.064	0.0111
Condor	35.25- 35.55	35.49	0.302	0.077	0.0092-0.176	0.061	0.176	0.033	0.0117 - 0.083	0.0197	0.071	0.0141
South of Faial	35.47- 35.61	35.55	0.141	0.035	0.0095-0.113	0.051	0.103	0.017	0.0106 - 0.105	0.0222	0.094	0.0137
South of Pico	**35.48**- 35.60	35.55	0.123	0.029	0.0059-0.084	0.031	0.079	0.013	0.0113 - 0.106	**0.0236**	0.094	0.0146
Nort of Pico	35.45- 35.62	**35.56**	0.176	0.04	0.005-0.065	0.029	0.060	0.011	0.0106 - 0.095	0.0220	0.085	0.0132
Mar da Prata	35.40- **35.76**	35.54	0.352	0.055	0.0074-0.22	0.057	**0.211**	0.038	0.0078 - 0.111	0.0177	0.104	0.0154
Formigas	35.42- 35.72	35.53	0.298	0.065	0.0144-0.156	0.056	0.141	0.03	**0.0118 - 0.187**	0.0174	**0.176**	0.0209
Total range= Max.–Min.	0.54	0.16	0.275	0.05	0.217	0.086	0.17	0.033	0.1792	0.0064	0.123	0.0119

Nitrate concentrations range from 0.214 to 0.262 mgN/l (standard deviation from 0.0011 to 0.0076), with low variation at sponge locations at Gigante, Princesa Alice, Açores Bank and Condor seamounts. In opposition, the South of Faial, South of Pico and North of Pico populations have the lowest minimum nutrient values and the higher range of values. At the South of Faial sponge aggregation, nitrate values range from 0.214 to 0.253 mgN/l, South of Pico from 0.219 to 0.252, and in the North of Pico from 0.229 to 0.257 mgN/l, the median values are 0.236, 0.235 and 0.242 mgN/l respectively. This relatively higher nutrient variability at the bottom matches the higher variability of the phytoplankton concentrations at the surface, and higher maximum concentration values (for South of Faial, South of Pico and North of Pico locations) (Figure 5.4).

Dissolved silica concentrations vary from 0.19 mgSi/l in the South of Pico to 0.32 mgSi/l in Açores bank, with higher variation at the locations of Princesa Alice and South of Faial. The range observed at these sponge locations is low when compared with the total range at the Azores bottom layer (Figure 5.5), ranging from 0.05 to 1 mgSi/l (Figure 5.9), while at the sponge location from 0.19 to 0.32 mgSi/l. Inorganic phosphorous concentration ranges from 0.027 in the South of Faial to 0.037 mgP/l in Açores Bank and Gigante seamount.

Temperature ranges from 9.22ºC to 11.84ºC (total range of 2.62ºC), with median values ranging from 10.1ºC to 11.43ºC (1.31ºC difference from the low median to the higher). This range of values is relatively low considering the range at the bottom layer for the entire domain (Figure 5.7).

Dissolved oxygen values at the sponge aggregations range from 6.24 to 6.84 mgO2/l. The lower oxygen concentrations are at Mar da Prata and Formigas aggregations, ranging from 6.24 to 6.53 and 6.28 to 6.54 mgO2/l respectively, with standard deviation values of 0.072 and 0.069 mgO2/l. The highest concentration and the highest range is at the Azores bank, maximum of 6.85 mgO2/l, ranging from 6.49 to 6.8 mgO2/l, and a median value of 6.68. Compared with the entire bottom layer, these sponge aggregations are located in zones with low oxygen concentrations Figure 5.9Figure 5.10.

South of Pico is the aggregation with a lower temperature range (0.76 ºC, and standard deviations of 0.18), and lower nitrate and inorganic phosphorous minimum and median values. Conversely, South of Faial is the aggregation exposed to higher temperatures, ranging from 10.95

to 11.84°C. This is also the shallowest sponge aggregation in the study, at 630 meters depth. Princesa Alice is distinguished from the other locations by the higher variation of dissolved silica values (0.231-0.306 mgSi/l), and Açores bank, has the maximum dissolved silica concentration of 0.32 mgSi/l. South of Faial South of Pico and North of Pico, distinguish among the other locations by the lower water temperature ranges, and maximum median values

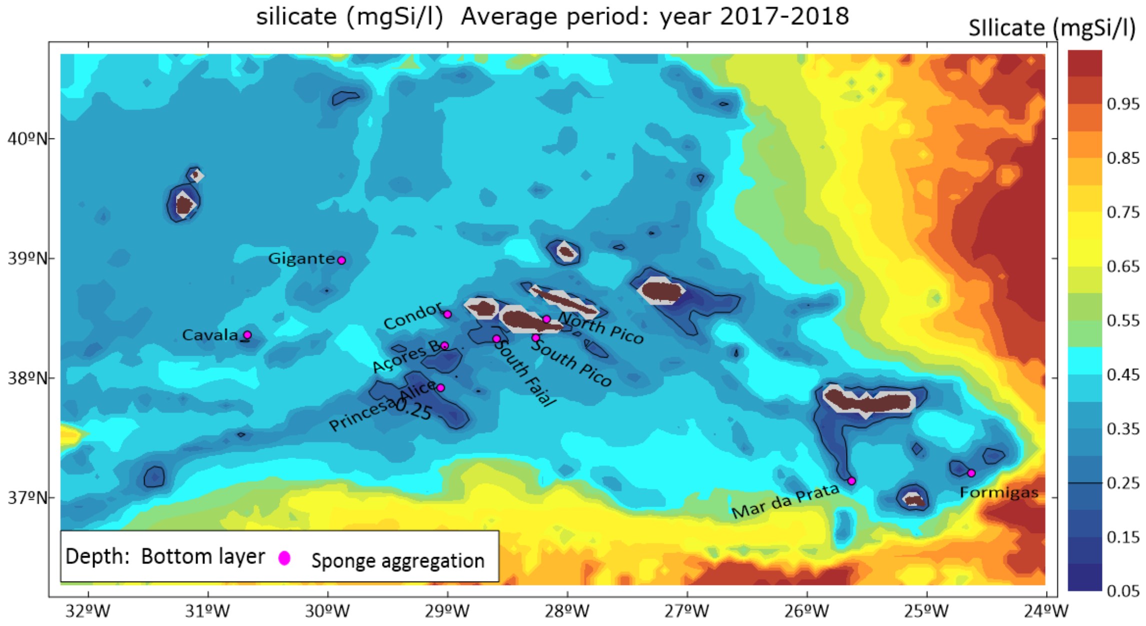

Figure 5.5- Average model results for dissolved silica at the bottom layer. Sponge locations are represented with a pink circle

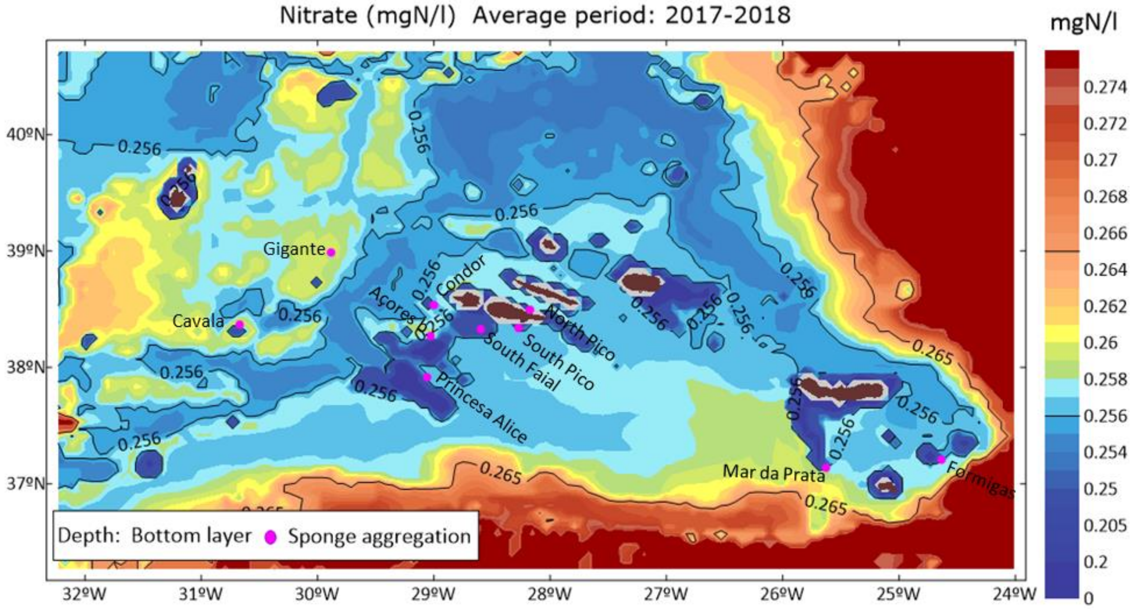

Figure 5.6- Average model results for nitrate at the bottom layer. Sponge locations are represented with a pink circle

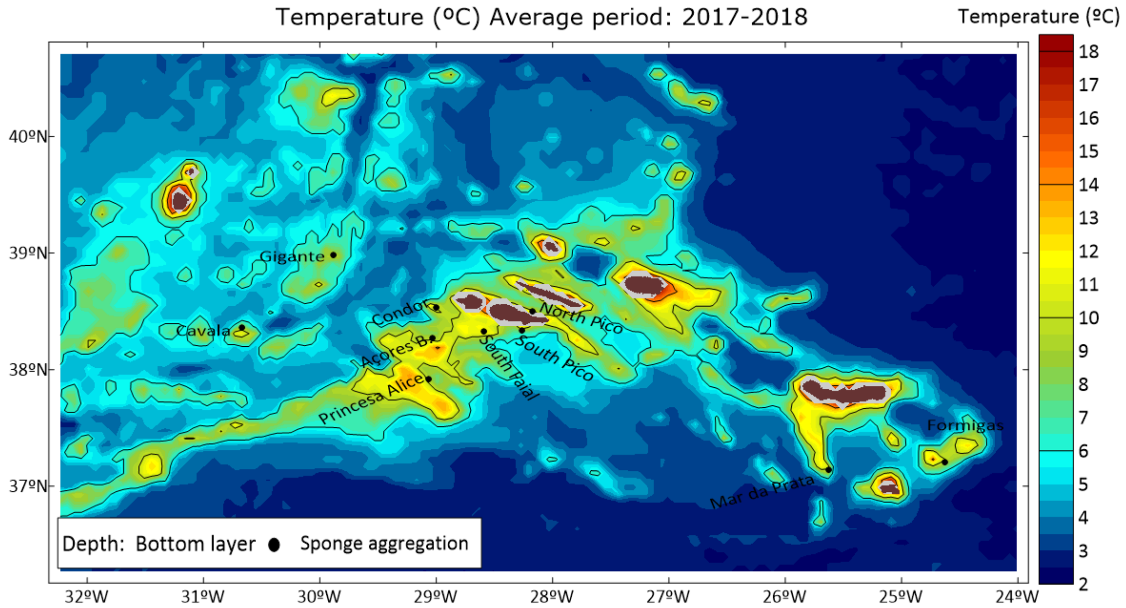

Figure 5.7- Average model results for the temperature at the bottom layer. Sponge locations are represented with a black circle

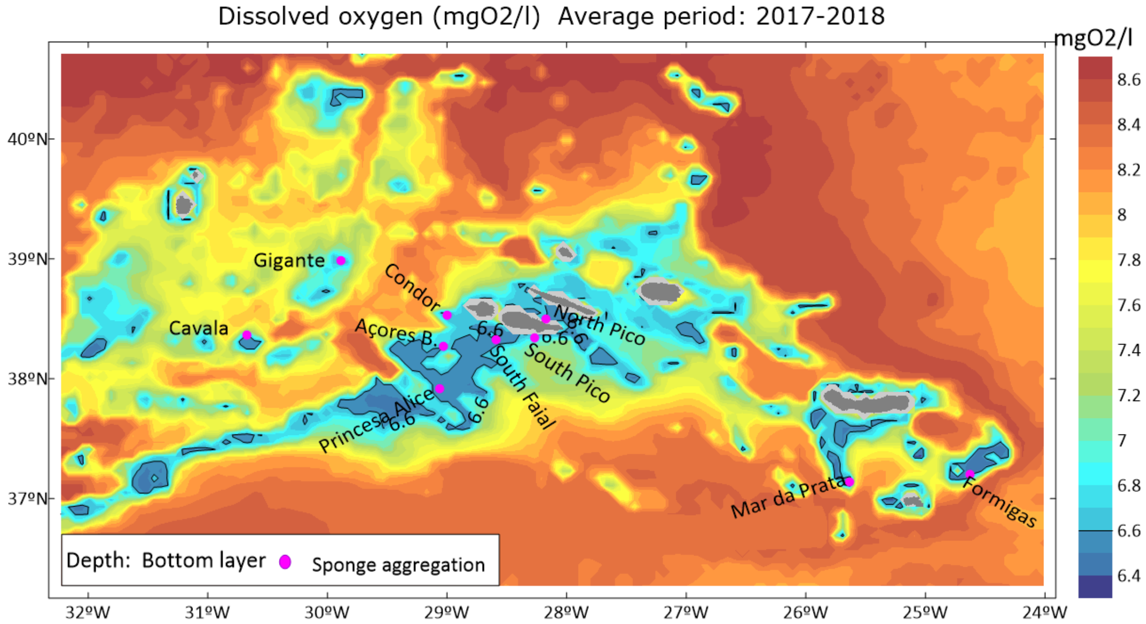

Figure 5.8- Average model results for dissolved oxygen at the bottom layer. Sponge locations are represented with a pink circle

5.3.2. Environmental conditions at sponge locations along sections and at the bottom layer

The biogeochemical water properties were analysed along different sections of the domain, crossing the different sponge aggregations in the study. Nutrient concentrations change along the water column, with the characteristic increase from the surface down to the sea bottom (Figure 5.9). Furthermore, model results along the bottom layer, show that the sponge aggregations in the study are located in regions with relatively low nutrient concentrations (Figure 5.5, Figure 5.6), and low oxygen values (Figure 5.8). For the water temperature at the sponge locations, Figure 5.7, is denoted a zonal gradient, with higher temperatures at western sponge locations. The lower oxygen concentrations are at the Mar da Prata and Formigas sponge locations (Figure 5.8).

Sections along the sponge aggregations show that sponge aggregations are located at the bathymetric range of the minimum oxygen concentration (Figure 5.9), this is more evident for sponge locations at Mar da Prata end Formigas.

Along the water column, the velocity modulus can range from 0.25m/s at the surface, until values close to zero at the bottom layer, with a denoted decrease along the water column (Figure 5.10). The average velocity at the bottom layer ranges from 0 to 0.1m/s (Figure 5.11), with the higher velocity modulus related, mainly, to depths above 600 meters (Figure 5.10). At the sponge locations, except for the Gigante aggregation, the average velocity modulus is lower than 0.05 m/s. At Gigante aggregation, the velocities can achieve values of 0.2m/s, as can be verified in the boxplot analysis (Figure 5.4). The median velocity modulus is 0.113 m/s at Gigante aggregation (Table 5.5), while in the remaining locations, median values range from 0.026 m/s at Princesa Alice to 0.06m/s at Condor Seamount. Nevertheless, the sponge aggregations in the study are located in regions with lower velocities (Figure 5.11).

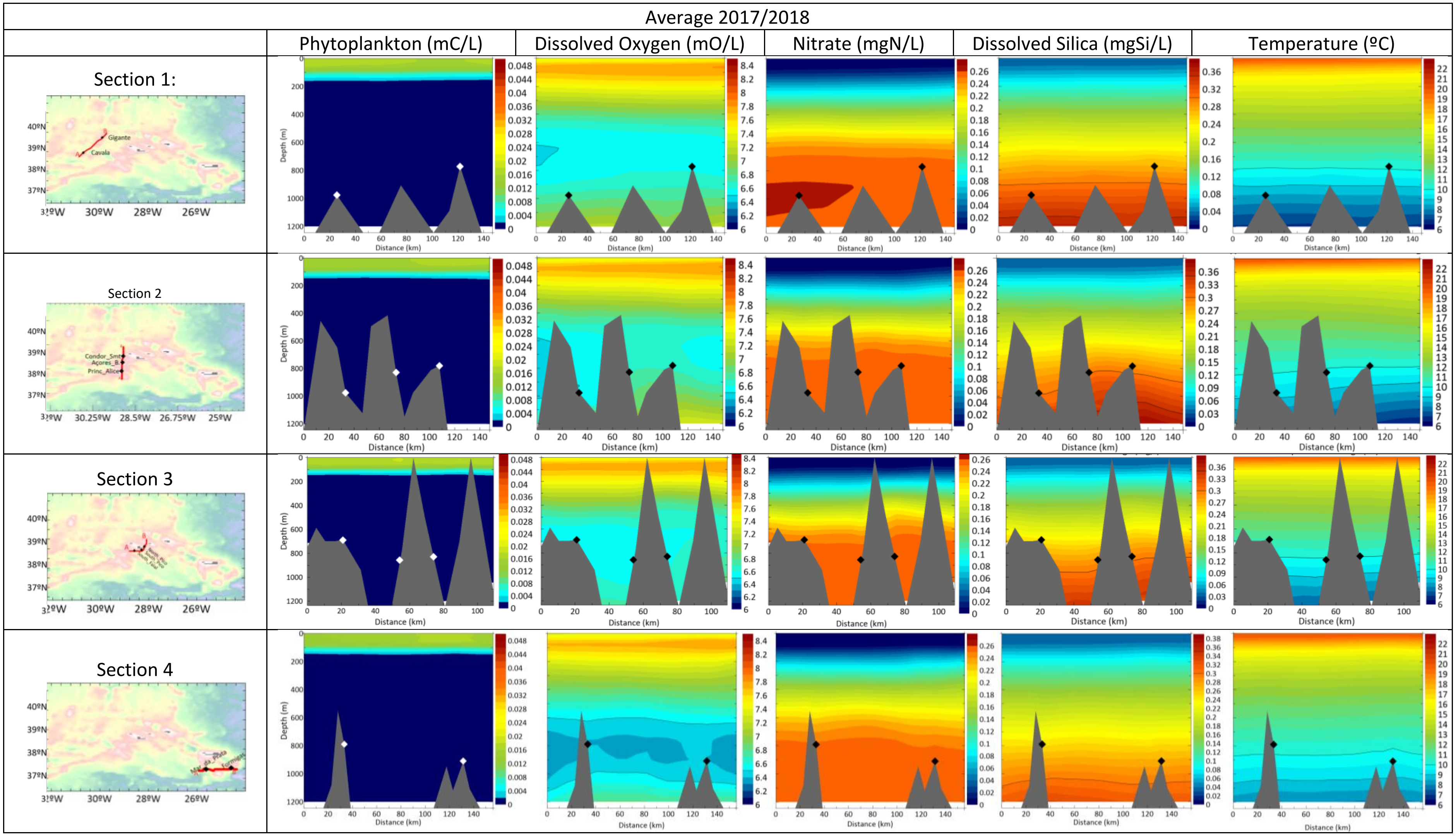

Figure 5.9- Average of model results for 2017 and 2018, from the surface up to 1200 meters depth, for dissolved oxygen, nitrate, dissolved silica and temperature, for sections 1, 2, 3 and 4 (top to down respectively). The black/white mark represents the sponge location. The bottom topography is represented in grey

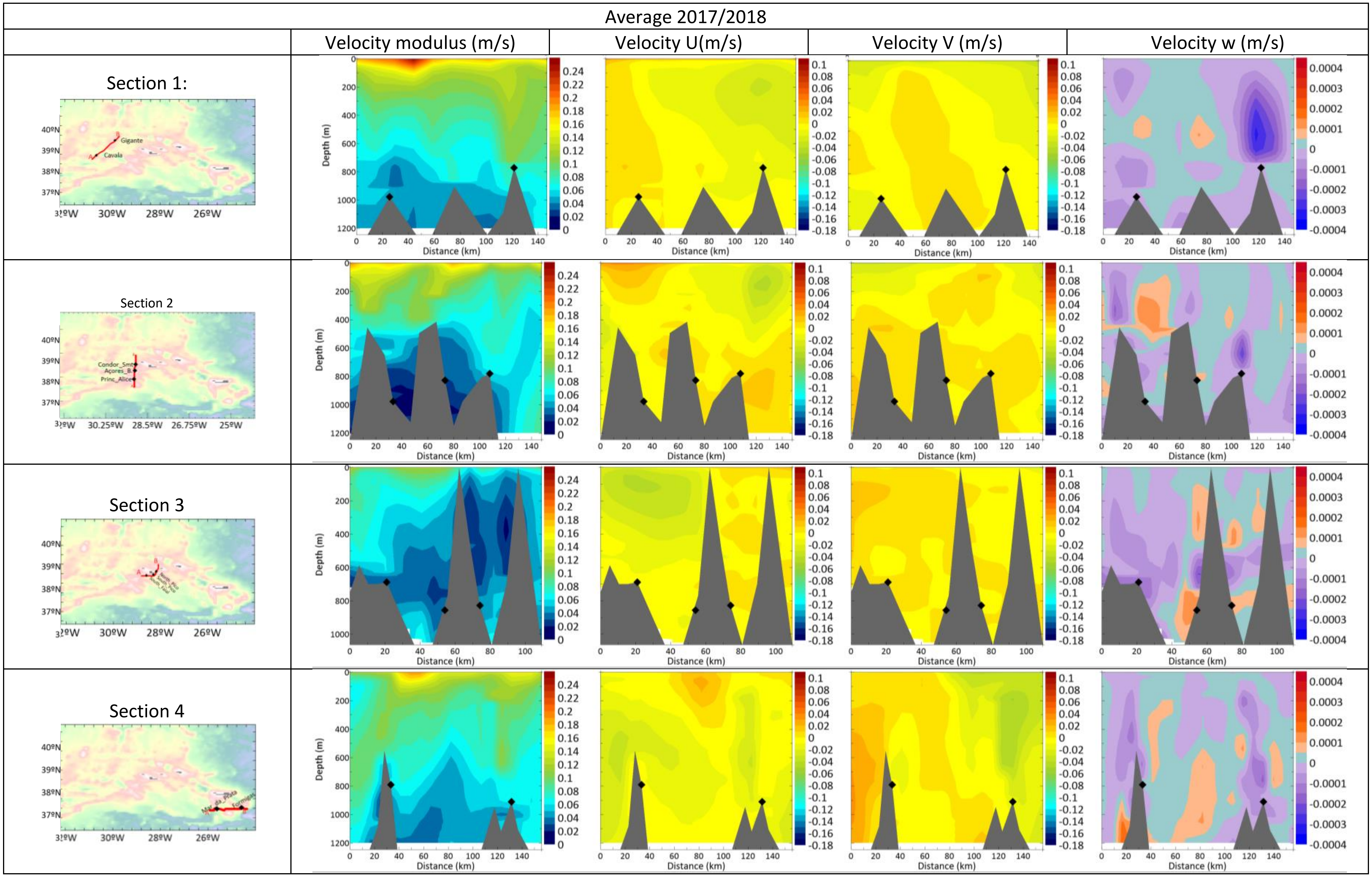

Figure 5.10- Average of model results for 2017 and 2018, from the surface up to 1200 meters depth, for dissolved oxygen, nitrate, dissolved silica and temperature for sections 1, 2, 3 and 4 (top to down respectively). The black/white mark represents sponge location. The bottom topography is represented in grey

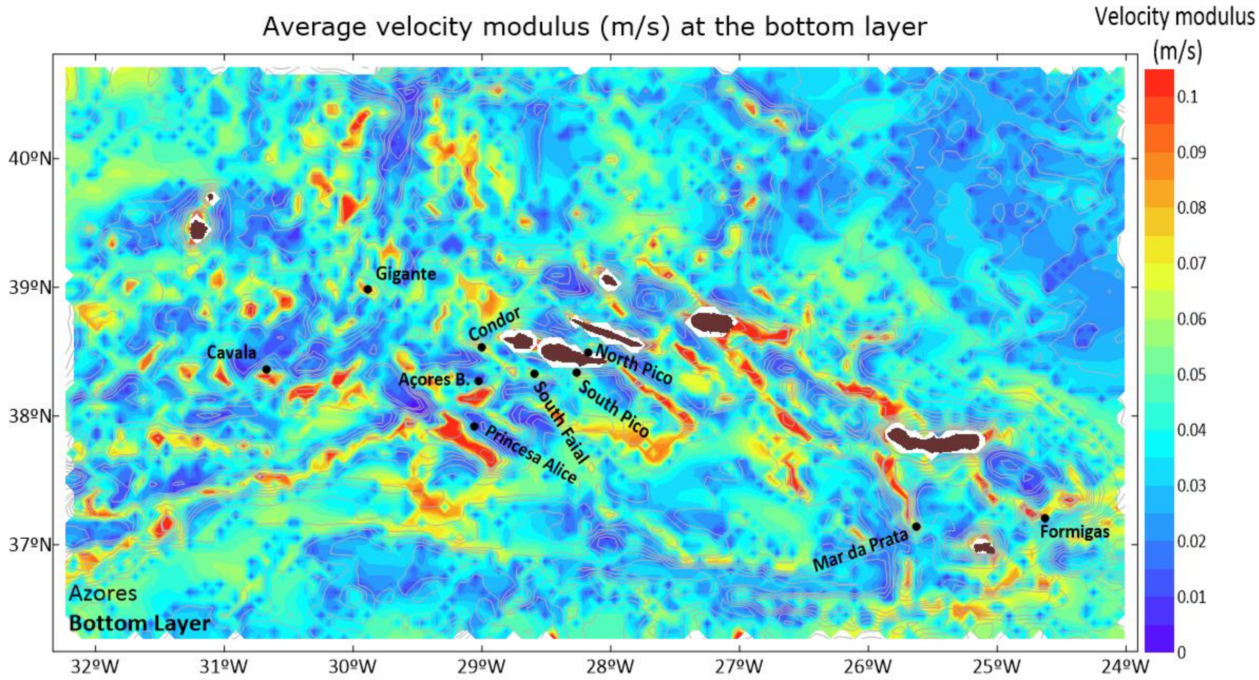

Figure 5.11- Average model results for velocity modulus at the bottom layer. Sponge aggregations are represented with a black circle.

Hydrodynamic patterns and physical water properties (water temperature and salinity) show different patterns regarding seasonality. The hydrodynamic patterns, local eddies and vortices along the study area have effects on the larval dispersal and connectivity between these sponge aggregations, as was discussed in Chapter 4 of this dissertation.

Contrasting with the nutrients, that present low seasonal and spatial variation at the bathymetric range of these sponge locations, the hydrodynamic and physical properties can have demarked seasonal patterns. Model results for velocity directions and modulus (Figure 5.13), and salinity (Figure 5.12) were studied for March and October, to capture the time of the phytoplankton blooms in this region (the spring bloom in March, and the lower autumn bloom in October). Results were analysed at 750 meters depth to consider a representative depth for the sponge aggregations in the study. During March an eddy is formed, between WG and MAR. At 750 meters depth, it is visible a major current from North to South-West, over the MAR. The highest velocities achieve the 0.175m/s in March, and 0.2 m/s in October (Figure 5.13). During October, the major hydrodynamic fields present another pattern, with lower velocities along the MAR. In the Central Group, the averaged ocean circulation consists of highly variable along-shelf currents that follow bathymetric features, with a less pronounced velocity dynamic near the central group. These hydrodynamic features are reinforced by the salinity contrasts. A salinity gradient is notable between the NorthWest part of the domain, and the Eastern part, more demarked during October (Figure 5.12).

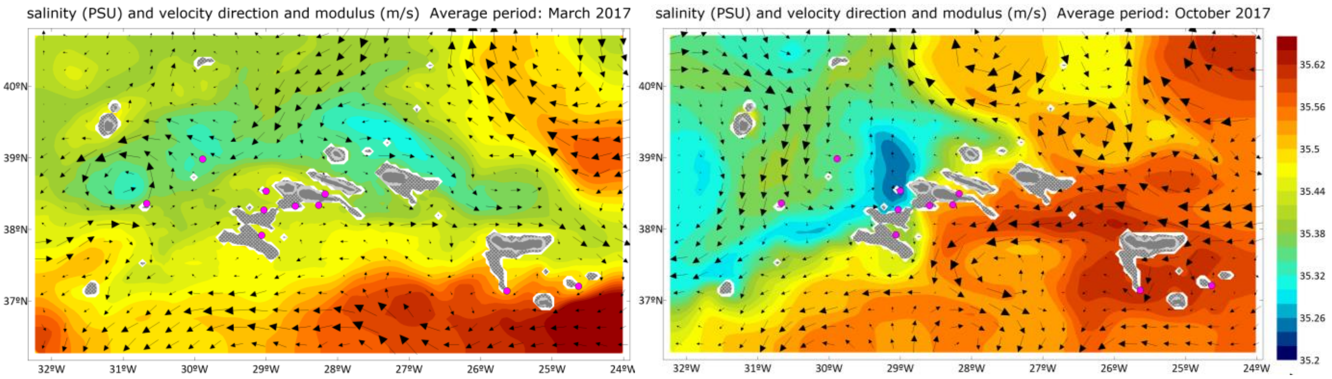
salinity (PSU) and velocity direction and modulus (m/s) Average period: March 2017

salinity (PSU) and velocity direction and modulus (m/s) Average period: October 2017

Figure 5.12- Monthly average of sea salinity and vectors representing velocity direction for March (on left) and October (on right), sponge aggregations are represented with a pink circle.

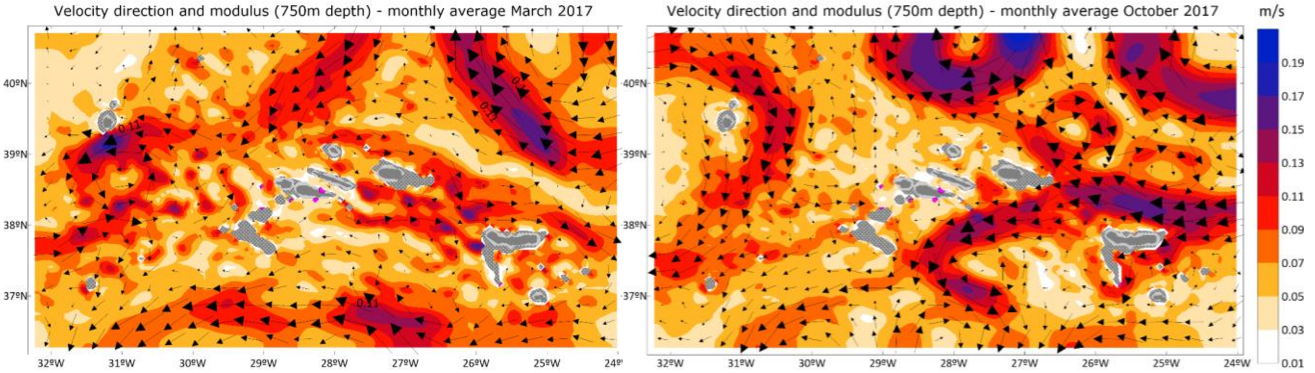
Velocity direction and modulus (750m depth) - monthly average March 2017

Velocity direction and modulus (750m depth) - monthly average October 2017

Figure 5.13- Monthly average of velocity modulus and direction at 750m depth for direction for March (on left) and October (on right), sponge aggregations are represented with a pink circle

Between the Central and Eastern Groups, the hydrodynamic patterns go mainly in the Eastwards direction during March, with velocity modulus ranging from 0.05 up to 0.15 m/s, while in October it is clear a strong current coming from the East going Westwards with a velocity modulus from 0.1 up to 0.2 m/s. Also in the North-West part of the domain, currents are stronger during October than during March.

Vertical velocity (vector w) has a high variability along the domain without a clear spatial pattern (Figure 5.10). This higher variability can be a sequence of its lower values. Only at the South of Pico, and North of Pico, do sponge locations have a similar pattern, with a positive velocity w, indicating a vertical upwards direction. For the Azores Bank, the velocity w is also positive, however not so denoted as around Pico island.

The nutrient concentrations increase along the water column (Figure 5.9), with maximum values at the bottom layer, higher during the winter months. As a sequence of the nutrients input by the winter convection (Berline et al., 2007). However, the seasonal gradient verified at the sponge locations is very low. In the zonal section, located across Mar da Prata and Formigas, the nutrient concentrations are lower, and the sponges' aggregations are located in the lower oxygen regions.

5.4. Discussion

The *P. carpenteri* aggregations in the study are located between 600 and 1000 meters depth, deeper than the permanent thermocline and winter mixed layer, in depths where variability due to seasonal stratification is likely to be minimal (Graves et al., 2022).

Model results at these sponge locations reveal low variations in the nutrient concentrations, with a low spatial and temporal variation. A total variation of 0.048mgN/L for nitrate, 0.127mgSi/l for dissolved silica, 0.01mgP/l for inorganic phosphorous was quantified. This low variation contrasts with the gradients along the water column and at the surface, as has been described in Chapter 3 of this thesis. The low variation is limited by the absence of primary production (Hirose and Kamiya, 2003), being related mostly with the winter convection (Yamanaka et al., 2004), but also due to the settling of organic matter (Hirose and Kamiya, 2003), both simulated by the biogeochemical model.

Despite the low range of values, a longitudinal gradient is denoted for these target sponge aggregations. Higher nutrient concentrations are found at most Western locations (from Cavala to Condor Seamount), and lower in the Eastern locations (Figure 5.4). The ones in the South of Faial, South of Pico and North of Pico have the lower minimum nutrient values, but the highest range of nitrate and phosphate concentrations. This relatively higher nutrient variability at the bottom matches the higher variability of the phytoplankton concentrations at the surface (Figure

5.4). This higher phytoplankton concentration at the surface may induce higher nutrient dynamics at the bottom layers by the remineralization of the organic matter (Gnanadesikan et al., 2011). These results can also indicate that the biogeochemical model is simulating correctly the phytoplankton mortality and decomposition, and secondly the mineralization of the organic matter.

Nevertheless, the phytoplankton influence is not immediate at the bottom layer and can take from days up to several months up to several months to reach these depths (Samuelsen et al., 2022). For this analysis period (years 2017 and 2018), these results were obtained, however, a deeper spatial and temporal analysis, with a longer simulation time, should be performed to study the relationship between phytoplankton concentration and sponge locations. These small differences in nutrient concentrations may be relevant, for these deep-sea ecosystems, and may provide information to better understand the different dynamics of the different sponge populations in the Azores. The benthic fauna is believed to be very responsive to the episodic deposition of fresh phytodetritus in food variation (Ragueneau et al., 2000).

Sponge aggregations in the study are located in different temperature ranges, from 9.22 to 11.84 ◦C, a total range of 2.62ºC (Table 5.4), a relatively low range compared with the temperature at the bottom layer Figure 5.7. South of Pico, is distinguished from the other aggregations in the study by the lower water temperature variance (0.18°C), ranging from 10.52 to 11.28 °C. This lower temperature range also occurs for the South of Faial and North of Pico locations, recognized as dense sponge aggregations (Colaco et al., 2020). This result may suggest that a low range of temperature can be advantageous for this species.

All the sponge grounds in the study are located at the depth of the minimum oxygen concentrations (Figure 5.9). Dissolved oxygen ranged between 6.24 and 6.54 mgO2/ at the Eastern Group and between 6.43 and 6.85 mgO2/l in the remaining sponge aggregations. The sponge aggregations in the Eastern Group are distinguished from the remaining by the lower oxygen values. This oxygen gradient can be a consequence of the water masses circulation in the region. The relatively lower oxygen concentrations at the Mar da Prata and Formigas sponge locations (Figure 5.8) may be a consequence of the Mediterranean Water Mass. The Mediterranean water mass, characterised by the lower oxygen concentration (Bashmachnikov et al., 2015), achieves the eastern Azores region between 500 and 1200 meters depth (Palma et al., 2012).

These deep-sea sponge grounds are believed to have an important role in biogeochemical cycling, by filtering large quantities of water and serving as a sink of dissolved silica (Maldonado et al., 2019). However, these processes are not considered in this MOHID biogeochemical model dynamics, nor the general global and regional biogeochemical models (Samuelsen et al., 2022).

Dissolved silica is essential for sponges that have siliceous spicules, the case of *P. carpenteri* sponges (Howell et al., 2016). At these specific aggregations dissolved silica concentrations range from 0.193 to 0.320 mgSi/l, with the lowest value in the South of Faial, and the highest in the Açores bank. Princesa Alice distinguishes from the among locations by the higher variation of dissolved silica values (0.231-0.306 mgSi/l). Despite being essential for these sponges, the dissolved silica concentration is not pointed as the most effective proxy for *P. carpenteri,* compared with depth and temperature range. Currents speed can have a significant play an important role in driving the distribution of *P. carpenteri* sponge habitat, (Howell et al., 2016)

Regarding the current speed, except for the Gigante sponge aggregations, the other aggregations in the study are located in locations with lower velocities, Figure 5.11. The relatively higher velocity modulus at the Gigante seamount can be related to model bathymetry and resolution. Gigante seamount (38°59’N, 29°53’W) is approximately 16 km long and 6–13 km wide at the 1000-m depth contour, with the summit at 300 meters depth with an area of 11,6km^2 (Cascão et al., 2017). Considering the model resolution, 4*4km, this seamount can be represented by 1 to 3 domain cells. In this specific location, the hydrodynamic patterns reveal a strong vertical gradient, from the surface until the top of this seamount, as can be verified in the vertical profiles of section_1 (Figure 5.10), where model average results show the effect of the seamount at the velocity modulus, with higher velocities on the top of this seamount, than in the remaining seamounts. Also, the vector w, has the highest magnitude in this location, with a value of -0.004m/s, while in the other locations, the magnitude of this velocity vector is lower (Figure 5.10). The remaining sponge aggregations in the study are located in regions with lower velocities and without an evident vertical gradient. The sponge aggregations at Cavala, Princesa Alice, Açores bank, Condor, Mar da Prata and Formigas are located in regions with lower velocity modulus, however adjacent to locations with higher velocities. For the sponge aggregations near the islands: South of Faial (L#6), South of Pico (L#7) and North of Pico(L#8), this pattern is not verified. However, results along the different sections and at different periods show that at these sponge aggregations, the vertical velocity vector is positive.

These results are in accordance with the hypothesis of Bett and Rice (1992), White (2013), and Howell (2016), that these sponges might inhabit areas with lower bottom velocities, but under the influence of vertical velocities that induce the resuspension of particulate matter, or in the vicinity of stronger currents (Rice et al., 1990). Current literature suggests an association between internal wave activity and *P. carpenteri* distribution (Graves et al., 2022). A further analysis should be performed for the Azores region to study this hypothesis, by using modelling tools.

5.5. Conclusions

Up to now, consistent monitoring time series of the environment at deep-sea sponges are missing not only in the Azores but across the entire North Atlantic (Samuelsen et al., 2022). In this study, modelling tools are used to study the spatial and temporal biogeochemical properties at specific sponge grounds of the species *Pheronema carpenteri*, taking advantage of the 3-D hydrodynamic and biogeochemical models implemented in Chapter 2 and Chapter 3 of this thesis. These sponge aggregations are located between 600 and 1000 meters depth, and at the depth of the minimum oxygen concentrations (Figure 5.9).

Model results show that sponges are located under steady environmental conditions, with lower nutrient gradients and low current velocities. Nutrient concentrations at these deep-sea sponges' locations vary from 0.214 to 0.262 mgN/l, 0.193 to 0.32 mgSi/l, and 0.027 to 0.037 mgP/l. Major results are in concordance with published studies which point out that these deep-sea sponges inhabit environments with low nutrient gradients and low current velocities (Howell et al., 2016; Rice et al., 1990; White, 2003). Despite the low nutrient concentration range, the higher nitrate and phosphate concentration variances at the sponge locations match with the higher phytoplankton concentration at the surface.

The temperature at sponge aggregations ranges from 9.22 to 11.84 ◦C (a total range of 2.62ºC). However, the maximum difference between sponge aggregations' median temperature values is 1.31ºC. At the South of Pico location, this fluctuation has the minimum values, with 0.77ºC variation.

These model results provide valuable information about environmental conditions at the *P. carpenteri* sponge locations. To improve this analysis, other locations must be considered, like the sponge locations identified in recent oceanographic campaigns, as well as a comparative analysis with locations without sponges. The density of each sponge aggregation and the floor characteristics at each location can also improve this analysis. The use of a higher-resolution model and the analysis of the tidal components can provide additional information for this study. Also, in-situ current measurements at one of these sponge aggregations will provide useful information for this study.

This application shows that model results can be used to better describe deep-sea sponge habitat characteristics. This study also contributed to a comprehensive knowledge of the spatial and temporal near-bottom variability of the environmental parameters characterizing the Azores.

Chapter 6

Final Remarks

A good understanding of the dynamics of the marine environment is the basis for improved knowledge of the Azores marine ecosystem. Besides the physical mixing, the marine ecosystems are also ruled by biological processes (i.e. photosynthesis and respiration) which control the distribution of nutrients and oxygen in ocean waters (Palma et al., 2012). Models provide a useful framework to simulate and study these marine ecosystems, from the surface up to the deep-sea, considering the physical and biological processes, along different space and time scales. Moreover, models allow to integration of knowledge, data and information, and to study scenarios and hypotheses, responding to research challenges and supporting the implementation and assessment of protection and management plans (Heymans et al., 2018).

The overall objective of this thesis was to study the general biotic and abiotic features that characterize the Azores' marine ecosystem, from the open ocean up to the deep-sea, and to assess larval dispersal and population connectivity in the Azores deep-sea environment through numerical modelling approaches. Different models were implemented to respond to the following research questions and hypotheses:

- *Q1- Can a regional hydrodynamic model simulate the general spatio-temporal hydrodynamic and physical features that characterize the Azores region? – The use of a hydrodynamic model*
- *Q2- Can a biogeochemical model simulate seasonal and spatial biotic and abiotic processes in the Azores region? How do these processes influence the Azores pelagic environmental characteristics? – The use of a biogeochemical model*
- *Q3- Are the deep-sea populations connected in the Azores? Case study 1- a deep-sea sponge Pheronema carpenteri; Case study 2- Chaceon affinis, a deep-sea red crab. – The use of a biophysical particle tracking model*
- *Q.4 How the MPA are effective in the protection of these selected deep-sea species, regarding their connectivity patterns?*
- *Q.5 What are the spatial and temporal biogeochemical properties at the specific sponge grounds of the species Pheronema carpenteri in the Azores?*

Q1. Can a regional hydrodynamic model simulate the general spatio-temporal hydrodynamic and physical features that characterize the Azores region? – The use of a hydrodynamic model

The marine ecosystem is first and foremost forced by physical processes (Cullen et al., 2002). Therefore, the implementation and validation of a hydrodynamic model for the Azores region is of utmost importance. As so, firstly, a hydrodynamic 3D model (MOHID) was implemented and validated for the Azores region, and secondly, a biogeochemical model, to simulate the major biotic and abiotic processes, in the Azores region, from the surface until the deep-sea. And finally, a biophysical particle tracking model was implemented to assess larval dispersal and population connectivity in the deep-sea.

A 3D hydrodynamic model-MOHID (IST, 2003), was implemented and validated for the Azores region. The validation against Argo buoys data, tide gauge stations and remote sensing data, reveals the model's capability to simulate the general hydrodynamic and physical features in the Azores. The model allows to simulate the dominant currents and the major water masses that influence the Azores marine system: namely the Azores Current, the North Atlantic Current, the Mediterranean Water Mass, the East North Atlantic Central Water, and the North Atlantic Deepwater. Furthermore, the model bathymetry and resolution (6*6km), allow to simulation of the local and seasonal eddies and recirculations relevant to the biotic and abiotic processes in the region.

Q2. Can a biogeochemical model simulate seasonal and spatial biotic and abiotic processes in the Azores region? How do these processes influence the Azores pelagic environmental characteristics? – The use of a biogeochemical model

A biogeochemical model, coupled in the hydrodynamic model was implemented for the Azores region, simulating the major biogeochemical pelagic processes representing the trophic, chemical and physical interactions in the water column. The model was calibrated and parameterized for the Azores region, allowing the simulation of the typical phytoplankton and nutrient dynamics in the region: The nutrient concentrations at the surface are low, with the maximum concentration during the winter (<0.021mgN/l; <0.005mgP/l; <0.06mgSi/l), induced by the winter convection, followed by a depletion during the spring and summer (to values close to zero), induced by the phytoplankton consumption. This seasonal variation is representative of the oligotrophic regions, where the low nutrient concentration limits phytoplankton growth (Maranõn et al., 2000), which is the case of the Azores (Teira et al., 2005; Valente, 2013). The model was validated against remote sensing data, and the seasonal and spatial phytoplankton patterns are well reproduced by the model with the typical strong spring bloom, and the lower autumn bloom (Valente, 2013), being well represented by the model. Also, the deep chlorophyll maximum (DCM), characteristic of the Azores region (Macedo et al., 2000), with a higher phytoplankton concentration between 50 and 100 meters in depth, is well represented, with spatial and temporal variations, and more denoted in the summer months, July, August, September, and also in October.

These nutrient and phytoplankton dynamics are also influenced by the Mixed Layer Depth (MLD) (Doney et al., 2001). The average MLD for the study area reveals a highly seasonal pattern, with a larger MLD during winter, achieving 160 meters depth during late February and March. In spring and summer, the seasonal stratification begins and the mixed layer shallows to its minimum, 20 meters depth, during the summer (late June, July and August). The North of the Azores region is characterized by stronger winter vertical mixing and the MLD can go up to 250 meters depth (Figure 3.47), while in the south of the domain, it goes only until 100 meters depth.

Model assessment reveals that MOHID can simulate the general biogeochemical patterns in the entire water column, reproducing the vertical and spatial variation for nutrients (Nitrate, Phosphate and Silicate), dissolved oxygen, temperature and salinity. However, the degree of approximation to the real system and the complexity of biogeochemical models is a challenge to biogeochemical modelling (Vichi et al., 2007b). Even after the calibration process, MOHID overestimates the phytoplankton concentration (a limitation also reported for other applications in oligotrophic regions (Gutknecht et al., 2016)). Models can always improve and reproduce more small-scale processes. This methodology also leaves open the possibility of future model improvements, representing other or more detailed biological and physical processes, and responding to new scientific objectives.

Nevertheless, the model implemented presented a significant advantage over available data (both from satellite images and in-situ measurements) by allowing the study of three-dimensional processes in the entire water column, from the surface up to the deep-sea. And also, allows the study of different processes, namely the larval dispersal (Chapter 4) and the study of deep-sea environments (Chapter 5).

Q.3 Are the deep-sea populations connected in the Azores? Case study 1- a deep-sea sponge *Pheronema carpenteri*; Case study 2- *Chaceon affinis*, a deep-sea red crab. – The use of a biophysical particle tracking model

Taking advantage of the hydrodynamic model validated in Chapter 2, a particle tracking model was implemented to study larval dispersal in the deep-sea. Larval dispersal is an important factor in promoting connectivity, especially for sessile benthic organisms (Ross et al., 2017) and it has been integrated into MPA planning (Botsford et al., 2009; Gaines, 2001; Ross et al., 2017), and to inform deep-sea fisheries management (Lausche et al., 2021). This study considers two deep-sea target species: i) a sessile organism, *Pheronema carpenteri* a deep-sea sponge; and ii) a non-sessile organism, *Chaceon affinis*, a deep-sea red crab (DSRC). Population self-recruitment levels and the exchange of larvae among populations were studied. These processes have consequences for a number of fundamental ecological processes that affect population regulation and persistence, and therefore the maintenance of deep-sea ecosystems (Cowen and Sponaugle, 2009). Different scenarios and biological traits are studied: spawning seasonality, larval pelagic duration (PLD), and larval behaviour (including surface-oriented swimming).

The methodology applied in this study represents an important development in the study of larval dispersal and population connectivity in the Azores deep-sea, through the use of modelling tools, allowing to study of different scenarios and hypotheses. Results show that the regional patterns of the hydrodynamic currents drive the larval dispersion, shaping population connectivity. It is also worth mentioning that the hydrodynamic model was able to simulate the highly spatiotemporally variable hydrodynamic patterns responsible for the deep-sea larvae dispersal. The model assessment shows that the larval behaviour: either passive or swimming behaviour, the Pelagic Larval Duration (PLD), and spawning seasonality are determinant factors for larval dispersal and consequently for populations connectivity in the Azores.

Pheronema carpenteri larvae were modelled as passive tracers (Kenchington et al., 2019; Swearer et al., 2019), considering PLD scenarios of 15 days and 30 days and seasonal spawning, based on other deep-sea sponges studies (Kenchington et al., 2019; Ross et al., 2020; Wang et al., 2021, 2020). Model results indicate the existence of connectivity between *Pheronema carpenteri* sponge aggregations in the Azores. Sponge aggregations from the Central Group (CG) seem to have well-connected populations, also connected with populations at the Mid-Atlantic Ridge (MAR). The Eastern Group (EG) populations are isolated from the remaining populations in the study. MAR is revealed to be an important source of sponge larvae, exchanging larvae with MAR and Central Group populations. MAR also has the capability of retaining larvae from populations from the CG. Populations along the MAR can also contribute to the connectivity between the MAR and the Western region of the archipelago. EG populations are revealed as more vulnerable, due to their lack of connectivity with the remaining populations of the archipelago, and by the absence of self-recruitment in different scenarios for the Mar da Prata population. Although there is no connectivity between these specific CG and EG populations, larvae from both groups may settle on the João de Castro Bank, a Marine Protected Area (MPA). Therefore, the MPA of João de Castro Bank can serve as a linking point between the Central Group and Eastern Group promoting the connectivity between these groups.

In what regards *Chaceon affinis.*, more scenarios were studied, considering different larval stages and swimming behaviours longer PLD (23, 81, and 125 days), based on studies with this species (Hilário and Cunha, 2013; Pinho et al., 2001; Tuset et al., 2011) and another Deep Sea Red Crab, the *Geryon quinquedens* (Guerao et al., 1996; Kelly et al., 1982). The model was able to simulate the swimming behaviour, with larvae being able to achieve the surface layers, as was reported for this species (Landeria and Tamura, 2018).

Larval dispersal shows potential connectivity between populations across the Azores archipelago, from the EG up to the MAR and Western Group (WG). However, despite the high connectivity of the most plausible scenarios, a low percentage of successfully settled larvae is denoted. This low settlement rate can pose a significant constraint to effective connectivity between populations (Gaines et al., 2005). Notwithstanding the high level of connectivity, different populations face situations of lack of self-recruitment. Mostly in the October scenarios considering swimming behaviour, and less in the passive scenarios. Results show that seasonality is determinant for populations connectivity and self-recruitment, as a consequence of the hydrodynamic patterns. During October scenarios, stronger currents induce particle dispersion instead of retaining. Hydrodynamic patterns also induce a higher particle exchange from East to West in the October release, with larvae from the Eastern Group settling in the MAR populations; and from West to East in the March release.

Connectivity results indicate that the populations in MAR, namely Gigante, Cavala, Ferradura and Voador seamounts are important source locations, presenting connectivity across the Azores region, including the WG, MAR, the CG and the EG. Likewise, MAR populations are also retaining areas for *Chaceon affinis* larvae, receiving larvae from all the populations in the study.

Model results show how the larval behaviour (either a passive or swimming behaviour) and the longer PLD impact their dispersal patterns, and consequently population connectivity. The swimming behaviour simulated for DSRC larvae contributes to the higher larval travel distance (median values from <25km to 250 km; maximum values from higher than 1000km), and more variable dispersion patterns.

The general results of this biophysical model application suggest that populations of *Chaceon affinis* in the Azores may be connected and patchily distributed, however, the low percentage of larvae exchange between populations, and the lack of self-recruitment, indicates that despite existing connectivity between populations, they might be isolated. Since this is a species of potential economic interest (Hilário and Cunha, 2013; Pinho et al., 2001), caution should be made in the maintenance of these populations, and assuring their reserves' before any potential fisheries exploitation.

Q.4 How the MPA are effective in the protection of these selected deep-sea species, regarding their connectivity patterns?

Connectivity patterns can be used to study the effectiveness of the MPA, as a biodiversity conservation instrument, and to explore alternative MPA configurations (Ospina-Alvarez et al., 2020), for the assessment of populations vulnerability (Kenchington et al., 2019; Ross et al., 2019), and to inform deep-sea fisheries management (Lausche et al., 2021). These case-study results were used for a qualitative assessment of the present Azores Marine Park, regarding the protection of these target populations in the Azores.

Connectivity model results for both cases show that the MPA of Condor and Princesa Alice revealed to be important locations, by retaining larvae from different locations in the archipelago. Condor is an important source location exchanging larvae with all the populations in the study from the WG and the MAR. And Princesa Alice is an important sink location retaining larvae from Cavala, Gigante and Condor seamounts also from South of Faial. The studied sponge aggregation at Princesa Alice is localized neighbouring but outside the limits of the PMA. Therefore, the extension of the Princesa Alice MPA, covering this location could be beneficial regarding this sink population. The João de Castro MPA is revealed to be an important linking point between the more isolated populations from the Eastern Group and the central part of the archipelago. Therefore these 3 MPA in the CG are beneficial to these species' connectivity. Moreover expanding Princesa Alice MPA will be beneficial.

Populations along the MAR support connectivity along the archipelago. Passive sponge larvae, and both passive and swimming larvae from *C. affinis*, settle in different locations along the MAR. Therefore, MAR populations serve as a linking point between the Western populations and the CG and Eastern populations which may be poorly connected due to hydrodynamic currents in the archipelago.

Therefore, besides the marine protected areas of the MenezGwen, and the most recent Luso MPA, the Azores archipelago would benefit from more protection regulations along the MAR. New protection areas are proposed along the MAR: in Gigante, in Cavala and Ferradura seamounts, and in Voador seamount. The Cavala and Ferradura complex, and Gigante, promote the connectivity between populations of the Western and Central Group. Furthermore, the Gigante population also connects with the populations along the MAR towards the North, including locations South of the Kurtchatof Fracture Zone. On the other hand, Voador Seamount will preserve the connectivity along the MAR, and South of the Azores EEZ.

Regarding the Eastern part of the archipelago, the establishment of a new protected area in Mar da Prata will preserve the connectivity in the plateau south of São Miguel island, and both

Mar da Prata and Formigas populations, which can be isolated from the remaining populations of the archipelago, due to their distance, but also restricted by the hydrodynamic patterns. The vulnerability of Formigas populations, which faces several scenarios with no connectivity or the absence of self-recruitment also reinforces the need to maintain the MPA of Formigas.

Likewise, larvae dispersal results also show that the island's slopes are important recruitment areas, crucial zones for preserving the deep-sea biodiversity of the Azores, reinforcing their need for protection, which also would benefit from further protection besides the Azores Marine Park protection areas already implemented.

Regarding the *C. afffinis* species, this particle tracking model approach can be valuable for further studies in distribution and population dynamics, considering other scenarios, and more detailed biological information. Model results can be used to support decision-making regarding fisheries assessment studies for this DSRC species in the Azores, the establishment of protected areas and guaranteeing the protection of this species before the development of any fishery activity (Santos et al. 2019).

The results of this case study, considering the connectivity and larval dispersal results provide valuable information for the assessment of the existing MPA (Balbar and Metaxas, 2019; Botsford et al., 2009; Howell et al., 2016; Lausche et al., 2021; Ross et al., 2017). Nevertheless, a multidisciplinary approach must always be used together with ecological and biological studies, and if possible including population genetics (Swearer et al. 2019, Busch et al. 2021). Different habitats can have different species-specific effects on movement (Kool et al. 2013), further study should also consider the deep-seabed and neighbourhood characteristics, as well as local landscape aspects, providing a better understanding of larval dispersal (Combes et al. 2021).

Q.5 What are the spatial and temporal biogeochemical properties at these specific sponge grounds of the species *Pheronema carpenteri* in the Azores?

The use of modelling tools, specifically 3-D biogeochemical models, helps to bridge the knowledge gap in the study of deep-sea habitats (Samuelsen et al., 2022; Wang et al., 2020).

The 3-D biogeochemical model implemented for the Azores region (Chapter 3), was used to study the environmental conditions at specific *Pheronema carpenteri* sponge grounds) in the

Azores, and to characterize this deep-sea ecosystem. Found between 600 and 1000 meters in depth, these sponge aggregations are located in regions with low nutrient and temperature gradients and low velocities. Nutrient concentrations at these deep-sea sponges' locations vary from 0.214 to 0.262 (SD 0.0011) mgN/l for nitrate, 0.19 to 0.32 (SD 0.027) mgSi/l for dissolved silica, and 0.027 to 0.037 (SD 0.0019) mgP/l for inorganic phosphorous. The temperature varies from 9.22 to 11.84◦C (2.62 maximum range). The seasonal variation is less than 2ºC in each specific sponge location. South of Pico, a dense sponge ground is distinguished from the others by the lowest variance in temperature values (0.18°C). These sponge populations are located in zones with minimum oxygen concentrations with values ranging from 6.24 to 6.84 mgO2/l, and low current velocities (from 0 to 0.06m/s). These results are in concordance with published studies stating that these deep-sea sponges inhabit environments with low nutrient gradients and low current velocities (Howell et al., 2016; Rice et al., 1990; White, 2003).

Further considerations and future work

As a major outcome, this thesis provides fundamental knowledge of the processes driving larval dispersion in the deep sea. Characterization of the biogeochemical environment at the deep-sea sponge grounds in the Azores. It further demonstrated model capabilities to study different biological traits, serving as a baseline to assess deep-sea connectivity and to support management actions and marine spatial plan studies.

This biogeochemical model parameterized for the Azores can now provide data for different ecological and environmental studies. Coupled with the particle tracking model, it can be used to study future climate change scenarios, habitat suitability modelling and species distribution modelling. Furthermore, this modelling approach can provide valuable information for the implementation of protection plans and the establishment and prioritization of future management plans.

In future work, my major objectives are to compute the hydrodynamic and biogeochemical models up to the present date; also to improve the parameterization to optimize the solution and surpass the problems identified during the development of this dissertation. The MOHID water quality model reveals robustness and versatility leaving room for further improvements.

References

Abecasis, R.C., Longnecker, N., Schmidt, L., Clifton, J., 2013. Marine conservation in remote small island settings: Factors influencing marine protected area establishment in the Azores. Mar. Policy 40, 1–9. https://doi.org/10.1016/j.marpol.2012.12.032

Adams, D.K., Arellano, S.M., Govenar, B., 2012. Larval dispersal, vent life in the water column. Oceanography 25, 255–268. https://doi.org/10.5670/oceanog.2012.24

Allen, J.I., Somerfield, P.J., 2009. A multivariate approach to model skill assessment. J. Mar. Syst. 76, 83–94. https://doi.org/10.1016/j.jmarsys.2008.05.009

Alves, M.L.G.R., De Verdière, A.C., 1999. Instability dynamics of a subtropical jet and applications to the Azores front current system: Eddy-driven mean flow. J. Phys. Oceanogr. 29, 837–864. https://doi.org/10.1175/1520-0485(1999)029<0837:IDOASJ>2.0.CO;2

Amorim, P., Perán, A.D., Pham, C.K., Juliano, M., 2017. Overview of the Ocean Climatology and Its Variability in the Azores Region of the North Atlantic Including Environmental Characteristics at the Seabed 4, 1–16. https://doi.org/10.3389/fmars.2017.00056

Antonio Baeza, J., Holstein, D., Umaña-Castro, R., Mejía-Ortíz, L.M., 2019. Population genetics and biophysical modeling inform metapopulation connectivity of the Caribbean king crab Maguimithrax spinosissimus. Mar. Ecol. Prog. Ser. 610, 83–97. https://doi.org/10.3354/meps12842

Anugerahanti, P., Kerimoglu, O., Smith, S.L., 2021. Enhancing Ocean Biogeochemical Models With Phytoplankton Variable Composition. Front. Mar. Sci. 8, 1–20. https://doi.org/10.3389/fmars.2021.675428

Arhonditsis, G.B., Adams-Vanharn, B.A., Nielsen, L., Stow, C.A., Reckhow, K.H., 2006. Evaluation of the current state of mechanistic aquatic biogeochemical modeling: Citation analysis and future perspectives. Environ. Sci. Technol. 40, 6547–6554. https://doi.org/10.1021/es061030q

Arteaga, L., Pahlow, M., Oschlies, A., 2016. Modeled Chl:C ratio and derived estimates of phytoplankton carbon biomass and its contribution to total particulate organic carbon in the global surface ocean. Global Biogeochem. Cycles 30, 1791–1810. https://doi.org/10.1002/2016GB005458

Aumont, O., 2005. PISCES biogeochemical model. Report 1–36.

Aumont, O., Ethé, C., Tagliabue, A., Bopp, L., Gehlen, M., 2015. PISCES-v2: An ocean biogeochemical model for carbon and ecosystem studies. Geosci. Model Dev. 8, 2465–2513.

https://doi.org/10.5194/gmd-8-2465-2015

Ayata, S.D., Lévy, M., Aumont, O., Sciandra, A., Sainte-Marie, J., Tagliabue, A., Bernard, O., 2013. Phytoplankton growth formulation in marine ecosystem models: Should we take into account photo-acclimation and variable stoichiometry in oligotrophic areas? J. Mar. Syst. 125, 29–40. https://doi.org/10.1016/j.jmarsys.2012.12.010

Baird, M.E., Emsley, S.M., Mcglade, J.M., 2001. Modelling the interacting effects of nutrient uptake, light capture and temperature on phytoplankton growth. J. Plankton Res. 23, 829–840. https://doi.org/10.1093/plankt/23.8.829

Balbar, A.C., Metaxas, A., 2019. The current application of ecological connectivity in the design of marine protected areas. Glob. Ecol. Conserv. 17, e00569. https://doi.org/10.1016/j.gecco.2019.e00569

Barcelos e Ramos, E.J., Schulz, K.G., Voss, M., Narciso, Á., Müller, M.N., Reis, F. V., Cachão, M., Azevedo, E.B., 2017. Nutrient-specific responses of a phytoplankton community: A case study of the North Atlantic Gyre, Azores. J. Plankton Res. 39, 744–761. https://doi.org/10.1093/plankt/fbx025

Barthel, D., Tendal, O.S., Thiel, H., 1996. A Wandering Population of the Hexactinellid Sponge *Pheronema carpenteri* on the Continental Slope off Morocco, Northwest Africa. Mar. Ecol. 17, 603–616. https://doi.org/10.1111/j.1439-0485.1996.tb00420.x

Barton, E.D., 2001. Canary And Portugal Currents. Encycl. Ocean Sci. 380–389. https://doi.org/10.1006/rwos.2001.0360

Bashmachnikov, I., Nascimento, Â., Neves, F., Menezes, T., Koldunov, N. V, 2015. Distribution of intermediate water masses in the. Ocean Model. 11, 803–827. https://doi.org/10.5194/os-11-803-2015

Beazley, L., Kenchington, E., Murillo, F.J., Brickman, D., Wang, Z., Davies, A.J., Roberts, E.M., Rapp, H.T., 2021. Climate change winner in the deep sea? predicting the impacts of climate change on the distribution of the glass sponge vazella pourtalesii. Mar. Ecol. Prog. Ser. 657, 1–23. https://doi.org/10.3354/meps13566

Behrenfeld, M.J., Halsey, K.H., Milligan, A.J., 2008. Evolved physiological responses of phytoplankton to their integrated growth environment. Philos. Trans. R. Soc. B Biol. Sci. 363, 2687–2703. https://doi.org/10.1098/rstb.2008.0019

Bell, M.J., Barciela, R., Hines, A., Martin, M., Sellar, A., Storkey, D., 2004. FOAM. Met Office, Exeter.

Berline, L., Brankart, J.M., Brasseur, P., Ourmières, Y., Verron, J., 2007. Improving the physics of a coupled physical-biogeochemical model of the North Atlantic through data assimilation: Impact on the ecosystem. J. Mar. Syst. 64, 153–172.

https://doi.org/10.1016/j.jmarsys.2006.03.007

Bett, B.J., Rice, A.L., 1992. The influence of hexactinellid sponge (*Pheronema carpenteri*) spicules on the patchy distribution of macrobenthos in the porcupine seabight (Bathyal ne atlantic). Ophelia 36, 217–226. https://doi.org/10.1080/00785326.1992.10430372

Bianchi, D., Dunne, J.P., Sarmiento, J.L., Galbraith, E.D., 2012. Data-based estimates of suboxia , denitrification , and N 2 O production in the ocean and their sensitivities to dissolved O 2 26, 1–13. https://doi.org/10.1029/2011GB004209

Biscoito, M., Freitas, M., Pajuelo, J.G., Triay-Portella, R., Santana, J.I., Costa, A.L., Delgado, J., González, J.A., 2015. Sex-structure, depth distribution, intermoult period and reproductive pattern of the deep-sea red crab *Chaceon affinis* (Brachyura, Geryonidae) in two populations in the north-eastern Atlantic. Deep. Res. Part I Oceanogr. Res. Pap. 95, 99–114. https://doi.org/10.1016/j.dsr.2014.10.010

Black, K.S., Peppe, O.C., Gust, G., 2003. Erodibility of pelagic carbonate ooze in the northeast Atlantic. J. Exp. Mar. Bio. Ecol. 285–286, 143–163. https://doi.org/10.1016/S0022-0981(02)00524-5

Bode, M., Leis, J.M., Mason, L.B., Williamson, D.H., Harrison, H.B., Choukroun, S., Jones, G.P., 2019. Successful validation of a larval dispersal model using genetic parentage data. PLoS Biol. 17, 1–13. https://doi.org/10.1371/journal.pbio.3000380

Bonfardeci, A., Caruso, A., Bartolini, A., Bassinot, F., Blanc-Valleron, M.M., 2018. Distribution and ecology of the Globigerinoides ruber — Globigerinoides elongatus morphotypes in the Azores region during the late Pleistocene-Holocene. Palaeogeogr. Palaeoclimatol. Palaeoecol. 491, 92–111. https://doi.org/10.1016/j.palaeo.2017.11.052

Botsford, L.W., White, J.W., Coffroth, M.A., Paris, C.B., Planes, S., Shearer, T.L., Thorrold, S.R., Jones, G.P., 2009. Connectivity and resilience of coral reef metapopulations in marine protected areas: Matching empirical efforts to predictive needs. Coral Reefs 28, 327–337. https://doi.org/10.1007/s00338-009-0466-z

Boury-Esnault, N., Efremova, S., BÉzac, C., Vacelet, J., 1999. Reproduction of a hexactinellid sponge: First description of gastrulation by cellular delamination in the porifera. Invertebr. Reprod. Dev. 35, 187–201. https://doi.org/10.1080/07924259.1999.9652385

Bower, A.S., Le Cann, B., Rossby, T., Zenk, W., Gould, J., Speer, K., Richardson, P.L., Prater, M.D., Zhang, H.M., 2002. Directly measured mid-depth circulation in the northeastern North Atlantic Ocean. Nature 419, 603–607. https://doi.org/10.1038/nature01078

Bowie, G.L., Mills, W.B., Porcella, D.B., Campbell, C.L., Pagenkopf, J.R., Rupp, G.L., Johnson, K.M., Chan, P.W.H., Gherini, S.A., 1985. Rates , Constants , and Kinetics Formulations in S urface Water Quali , t y Modeling (Second Edition), Epa/600/3-85/040.

Bracco, A., Liu, G., Galaska, M.P., Quattrini, A.M., Herrera, S., 2019. Integrating physical circulation models and genetic approaches to investigate population connectivity in deep-sea corals. J. Mar. Syst. 198, 103189. https://doi.org/10.1016/j.jmarsys.2019.103189

Bracher, A., Bouman, H.A., Brewin, R.J.W., Bricaud, A., Brotas, V., Ciotti, A.M., Clementson, L., Devred, E., Di Cicco, A., Dutkiewicz, S., Hardman-Mountford, N.J., Hickman, A.E., Hieronymi, M., Hirata, T., Losa, S.N., Mouw, C.B., Organelli, E., Raitsos, D.E., Uitz, J., Vogt, M., Wolanin, A., 2017. Obtaining phytoplankton diversity from ocean color: A scientific roadmap for future development. Front. Mar. Sci. 4, 1–15. https://doi.org/10.3389/fmars.2017.00055

Braga-Henriques, A., Porteiro, F.M., Ribeiro, P.A., De Matos, V., Sampaio, Í., Ocaña, O., Santos, R.S., 2013. Diversity, distribution and spatial structure of the cold-water coral fauna of the Azores (NE Atlantic). Biogeosciences 10, 4009–4036. https://doi.org/10.5194/bg-10-4009-2013

Brzezinski, M.A., 1985. The Si : C : N ratio of marine diatoms: interspecific variability and the effect of 5 some environmental variables. J. Phycol. https://doi.org/10.1111/j.0022-3646.1985.00347.x

Buchanan, P.J., Matear, R.J., Chase, Z., Phipps, S.J., Bindoff, N.L., 2018. Dynamic Biological Functioning Important for Simulating and Stabilizing Ocean Biogeochemistry. Global Biogeochem. Cycles 32, 565–593. https://doi.org/10.1002/2017GB005753

Buitenhuis, E.T., Rivkin, R.B., Séailley, S., Le Quéré, C., 2010. Biogeochemical fluxes through microzooplankton. Global Biogeochem. Cycles 24. https://doi.org/10.1029/2009GB003601

Burchard, H., Bolding, K., Villarreal, M., 1999. GOTM – a general ocean turbulence model. Theory, applications and test cases.

Burchard, H., Bolding, K., Villarreal, M.R., 1999. GOTM, a general ocean turbulence model. Theory, implementation and test cases. Eur. Com. Rep. EUR 18745 103 pp.

Busch, K., Taboada, S., Riesgo, A., Koutsouveli, V., Ríos, P., Cristobo, J., Franke, A., Getzlaff, K., Schmidt, C., Biastoch, A., Hentschel, U., 2021. Population connectivity of fan-shaped sponge holobionts in the deep Cantabrian Sea. Deep. Res. Part I Oceanogr. Res. Pap. 167, 103427. https://doi.org/10.1016/j.dsr.2020.103427

Cáceres, C., Taboada, F.G., Höfer, J., Anadón, R., 2013. Phytoplankton Growth and Microzooplankton Grazing in the Subtropical Northeast Atlantic. PLoS One 8. https://doi.org/10.1371/journal.pone.0069159

Calbet, A., Atienza, D., Henriksen, C.I., Saiz, E., Adey, T.R., 2009. Zooplankton grazing in the Atlantic Ocean: A latitudinal study. Deep. Res. Part II Top. Stud. Oceanogr. 56, 954–963. https://doi.org/10.1016/j.dsr2.2008.10.009

Caldeira, R.M.A., Reis, J.C., 2017. The Azores confluence zone. Front. Mar. Sci. 4, 1–14.

https://doi.org/10.3389/fmars.2017.00037

Campuzano, F.J., Juliano, M., Fernandes, R., Pinto, L., Neves, R., 2013. Downscalling From the Deep Ocean To the Estuarine Intertidal Areas: an Operational Framework for the Portuguese Exclusive Economic Zone. 6th SCACR – Int. Short Course/Conference Appl. Coast. Res. Fig. 1–9.

Capotondi, A., Jacox, M., Bowler, C., Kavanaugh, M., Lehodey, P., Barrie, D., Brodie, S., Chaffron, S., Cheng, W., Dias, D.F., Eveillard, D., Guidi, L., Iudicone, D., Lovenduski, N.S., Nye, J.A., Ortiz, I., Pirhalla, D., Pozo Buil, M., Saba, V., Sheridan, S., Siedlecki, S., Subramanian, A., de Vargas, C., Di Lorenzo, E., Doney, S.C., Hermann, A.J., Joyce, T., Merrifield, M., Miller, A.J., Not, F., Pesant, S., 2019. Observational Needs Supporting Marine Ecosystems Modeling and Forecasting: From the Global Ocean to Regional and Coastal Systems. Front. Mar. Sci. 6, 1–30. https://doi.org/10.3389/fmars.2019.00623

Carmo, V., Santos, M., Menezes, G.M., Loureiro, C.M., Lambardi, P., Martins, A., 2013a. Variability of zooplankton communities at Condor seamount and surrounding areas, Azores (NE Atlantic). Deep. Res. Part II Top. Stud. Oceanogr. 98, 63–74. https://doi.org/10.1016/j.dsr2.2013.08.007

Carmo, V., Santos, M., Menezes, G.M., Loureiro, C.M., Lambardi, P., Martins, A., 2013b. Variability of zooplankton communities at Condor seamount and suCarmo, V., Santos, M., Menezes, G.M., Loureiro, C.M., Lambardi, P., Martins, A., 2013. Variability of zooplankton communities at Condor seamount and surrounding areas, Azores (NE Atlantic). D. Deep. Res. Part II Top. Stud. Oceanogr. 98, 63–74. https://doi.org/10.1016/j.dsr2.2013.08.007

Cascão, I., Domokos, R., Lammers, M.O., Marques, V., Domínguez, R., Santos, R.S., Silva, M.A., 2017. Persistent enhancement of micronekton backscatter at the summits of seamounts in the Azores. Front. Mar. Sci. 4, 1–15. https://doi.org/10.3389/FMARS.2017.00025

Chai, F., Dugdale, R.C., Barber, R.T., Peng, T.H., Wilkerson, F.P., 2002. One-dimensional ecosystem model of the equatorial Pacific upwelling system. Part II: Sensitivity analysis and comparison with JGOFS EqPac data. Deep. Res. Part II Top. Stud. Oceanogr. 49, 2747–2768. https://doi.org/10.1016/S0967-0645(02)00056-5

Chaput, R., Sochala, P., Miron, P., Kourafalou, V.H., Iskandarani, M., 2022. Quantitative uncertainty estimation in biophysical models of fish larval connectivity in the Florida Keys. ICES J. Mar. Sci. 1–24. https://doi.org/10.1093/icesjms/fsac021

Chen, B., Laws, E.A., Liu, H., Huang, B., 2014. Estimating microzooplankton grazing half-saturation constants from dilution experiments with nonlinear feeding kinetics. Limnol. Oceanogr. 59, 639–644. https://doi.org/10.4319/lo.2014.59.3.0639

Chenillat, F., Rivière, P., Ohman, M.D., 2021. On the sensitivity of plankton ecosystem models to the formulation of zooplankton grazing. PLoS One 16.

https://doi.org/10.1371/journal.pone.0252033

Clark, M.R., Rowden, A.A., Schlacher, T., Williams, A., Consalvey, M., Stocks, K.I., Rogers, A.D., Hara, T.D.O., White, M., Shank, T.M., Hall-spencer, J.M., 2010. The Ecology of Seamounts : Structure , Function , and Human Impacts. Ann. Rev. Mar. Sci. 2, 253–278. https://doi.org/10.1146/annurev-marine-120308-081109

Colaço, A., Creemers, M., Mienis, F., Beazley, L., Hanz, U., Bouchard-Marmen, M., Kenchington, E., Pham, C., 2020. Deliverable D4.5 (SponGES) - Deep-sea Sponge Grounds Ecosystems of the North Atlantic: an integrated approach towards their preservation and sustainable exploitation.

Collins, C.D., 1980. Formulation and Validation of a Mathematical Model of Phytoplankton Growth. Ecology 61. https://doi.org/Https://doi.org/10.2307/1937430

Comas-Rodríguez, I., Hernández-Guerra, A., Fraile-Nuez, E., Martínez-Marrero, A., Benítez-Barrios, V.M., Pérez-Hernández, M.D., Vélez-Belchí, P., 2011. The Azores Current System from a meridional section at 24.5°W. J. Geophys. Res. Ocean. 116, 1–9. https://doi.org/10.1029/2011JC007129

Combes, M., Vaz, S., Grehan, A., Morato, T., Arnaud-Haond, S., Dominguez-Carrió, C., Fox, A., González-Irusta, J.M., Johnson, D., Callery, O., Davies, A., Fauconnet, L., Kenchington, E., Orejas, C., Roberts, J.M., Taranto, G., Menot, L., 2021. Systematic Conservation Planning at an Ocean Basin Scale: Identifying a Viable Network of Deep-Sea Protected Areas in the North Atlantic and the Mediterranean. Front. Mar. Sci. 8, 1–27. https://doi.org/10.3389/fmars.2021.611358

Connolly, S.R., Baird, A.H., 2010. Estimating dispersal potential for marine larvae: Dynamic models applied to scleractinian corals. Ecology 91, 3572–3583. https://doi.org/10.1890/10-0143.1

Cornec, M., Claustre, H., Mignot, A., Guidi, L., Lacour, L., Poteau, A., D’Ortenzio, F., Gentili, B., Schmechtig, C., 2021. Deep Chlorophyll Maxima in the Global Ocean: Occurrences, Drivers and Characteristics. Global Biogeochem. Cycles 35, 1–30. https://doi.org/10.1029/2020GB006759

Costa, P., Gómez, B., Venâncio, A., Pérez, E., Pérez-Muñuzuri, V., 2012. Using the Regional Ocean Modelling System (ROMS) to improve the sea surface temperature predictions of the MERCATOR Ocean System. Sci. Mar. 76, 165–175. https://doi.org/10.3989/scimar.03614.19E

Cowen, R.K., Sponaugle, S., 2009. Larval dispersal and marine population connectivity. Ann. Rev. Mar. Sci. 1, 443–466. https://doi.org/10.1146/annurev.marine.010908.163757

Creemers, M.F., Pham, C., Defise, A., Goulard, J., Smith, V., Silva, A.P., Colaço, A., 2019. Sponges On The Rocks: Exploring A New Deep-Sea Sponge Ground Of The Azores (Portugal). Deep.

Life Vol 12 Vol 12 7-8.

Criales, M.M., Chérubin, L., Gandy, R., Garavelli, L., Ghannami, M.A., Crowley, C., 2019. Blue crab larval dispersal highlights population connectivity and implications for fishery management. Mar. Ecol. Prog. Ser. 625, 53–70. https://doi.org/10.3354/meps13049

Cullen, J.J., Franks, P.J.S., Karl, D.M., Longhurst, A., 2002. Physical influences on marine ecosystem dynamics, The Sea: Biological-Physical Interactions in the Ocean.

Cunha, M., Génio, L., Pradillon, F., Clavel Henry, M., Beaulieu, S., Birch, J., Campuzano, F., Carretón, M., De Leo, F., Gula, J., Laming, S., Lindsay, D., Matos, F., Metaxas, A., Meyer-Kaiser, K., Mills, S., Queiroga, H., Rodrigues, C., Sarrazin, J., Watanabe, H., Young, R., Young, C., 2020. Foresight Workshop on Advances in Ocean Biological Observations: a sustained system for deep-ocean meroplankton. Res. Ideas Outcomes 6. https://doi.org/10.3897/rio.6.e54284

Da Silva Cortinhas, M.C., Ortega, I., de Souza Alves Teodoro, S., Proietti, M., Masello, A., Kersanach, R., Barutot, R., Ramos Vieira, R.R., Firpo, C., Mauna, C., Cestari Dumont, L.F., 2022. Defining deep-sea fishery stocks through multiple methods: The case of the red crab *Chaceon notialis* Manning & Holthuis, 1989 (Crustacea, Decapoda, Geryonidae) in the Southwestern Atlantic. Deep. Res. Part I Oceanogr. Res. Pap. 179, 103659. https://doi.org/10.1016/j.dsr.2021.103659

Daewel, U., Schrum, C., MacDonald, J.I., 2019. Towards end-to-end (E2E) modelling in a consistent NPZD-F modelling framework (ECOSMO E2E-v1.0): Application to the North Sea and Baltic Sea. Geosci. Model Dev. 12, 1765–1789. https://doi.org/10.5194/gmd-12-1765-2019

de Boyer Monte ́Gut, C., Madec, G., Fischer, A.S., Lazar, A., Iudicone, D., 2004. Mixed layer depth over the global ocean : An examination of profile data and a profile-based climatology 109, 1–20. https://doi.org/10.1029/2004JC002378

de Pablo, H., Sobrinho, J., Garcia, M., Campuzano, F., Juliano, M., Neves, R., 2019. Validation of the 3D-MOHID hydrodynamic model for the Tagus coastal area. Water (Switzerland) 11. https://doi.org/10.3390/w11081713

de Voogd, N.., Alvarez, B., Boury-Esnault, N., Carballo, J.L., Cárdenas, P., Díaz, M.-C., Dohrmann, M., Downey, R., Hajdu, E., Hooper, J.N.A., Kelly, M., Klautau, M., Manconi, R., Morrow, C.C. Pisera, A.B., Ríos, P., Rützler, K., Schönberg, C., Vacelet, J., van Soest, R.W.M., 2022. World Porifera Database. *Pheronema carpenteri* (Thomson, 1869) [WWW Document]. World Porifera Database. *Pheronema carpenteri* (Thomson, 1869).

DeMaster, D.J., 2001. Marine Silica Cycle, in: Steele, J.H. (Ed.), Encyclopedia of Ocean Sciences. Academic Press, Oxford, pp. 1659–1667. https://doi.org/https://doi.org/10.1006/rwos.2001.0278

Deutsch, C., Frenzel, H., McWilliams, J.C., Renault, L., Kessouri, F., Howard, E., Liang, J.H., Bianchi, D., Yang, S., 2021. Biogeochemical variability in the California Current System. Prog. Oceanogr. 196, 102565. https://doi.org/10.1016/j.pocean.2021.102565

Dolan, J.R., 2018. Microbial Ecology of the Oceans, Journal of Plankton Research. https://doi.org/10.1093/plankt/fby022

Doney, S.C., Doney, S.C., Lima, I., Lima, I., Lindsay, K., Lindsay, K., Moore, J.K., Moore, J.K., Dutkiewicz, S., Dutkiewicz, S., 2001. Marine Biogeochemical Modeling: Society 14, 93–107.

Dorandeu, J., Le Traon, P.Y., 1999. Effects of global mean atmospheric pressure variations on mean sea level changes from TOPEX/Poseidon. J. Atmos. Ocean. Technol. 16, 1279–1283. https://doi.org/10.1175/1520-0426(1999)016<1279:EOGMAP>2.0.CO;2

Edwards, K.P., Barciela, R., Butenschön, M., 2012. Validation of the NEMO-ERSEM operational ecosystem model for the North West European continental shelf. Ocean Sci. 8, 983–1000. https://doi.org/10.5194/os-8-983-2012

Emery, W.J., 2001. Water Types and Water Masses Descriptive Tools : The TS Curve 3179–3187. https://doi.org/10.1006/rwos.2001.0108

EMODnet Bathymetry Consortium, 2018. No Title. https://doi.org/doi.org/10.12770/18ff0d48-b203-4a65-94a9-5fd8b0ec35f6

Eppley, R.W., Thomas, W.H., 1969. Comparison of Half-Saturation Constants for Growth and Nitrate Uptake of Marine Phytoplankton. J. Phycol. 5, 375–379. https://doi.org/10.1111/j.1529-8817.1969.tb02628.x

Espinoza-Morriberon, D., Echevin, V., Tam, J., Ledesma, J., Oliveros-Ramos, R., Ramos, J., Romero, C.Y., 2016. Biogeochemical validation of an interannual simulation of the ROMS-PISCES coupled model in the Southeast Pacific. Rev. Peru. Biol. 23, 159–168. https://doi.org/10.15381/rpb.v23i2.12427

FAO, 2008. International guidelines: Management of deep-sea fisheries in the high seas, Environmental Policy and Law. Rome.

Fasham, M.J.R., Ducklow, H.W., McKelvie, S.M., 1990. A nitrogen-based model of plankton dynamics in the oceanic mixed layer. J. Mar. Res. 48, 591–639. https://doi.org/10.1357/002224090784984678

Fasham, M.J.R., Platt, T., Irwin, B., Jones, K., 1985. Factors affecting the spatial pattern of the deep chlorophyll maximum in the region of the Azores front. Prog. Oceanogr. 14, 129–165. https://doi.org/10.1016/0079-6611(85)90009-6

Fennel, K., Gehlen, M., Brasseur, P., Brown, C.W., Ciavatta, S., Cossarini, G., Crise, A., Edwards, C.A., Ford, D., Friedrichs, M.A.M., Gregoire, M., Jones, E., Kim, H.C., Lamouroux, J., Murtugudde, R., Perruche, C., 2019. Advancing marine biogeochemical and ecosystem reanalyses and forecasts as tools for monitoring and managing ecosystem health. Front. Mar. Sci. 6, 1–9. https://doi.org/10.3389/fmars.2019.00089

Fennel, K., Hetland, R., Feng, Y., Dimarco, S., 2011. A coupled physical-biological model of the Northern Gulf of Mexico shelf: Model description, validation and analysis of phytoplankton variability. Biogeosciences 8, 1881–1899. https://doi.org/10.5194/bg-8-1881-2011

Fennel, K., Wilkin, J., Levin, J., Moisan, J., O'Reilly, J., Haidvogel, D., 2006. Nitrogen cycling in the Middle Atlantic Bight: Results from a three-dimensional model and implications for the North Atlantic nitrogen budget. Global Biogeochem. Cycles 20, 1–14. https://doi.org/10.1029/2005GB002456

Fennel, W., 2009. Parameterizations of truncated food web models from the perspective of an end-to-end model approach. J. Mar. Syst. 76, 171–185. https://doi.org/10.1016/j.jmarsys.2008.05.005

Fernandez-Vergaz, V., Lopez Abellan, L.J., Balguerias, E., 2000. Morphometric, functional and sexual maturity of the deep-sea red crab *Chaceon affinis* inhabiting Canary Island waters: Chronology of maturation. Mar. Ecol. Prog. Ser. 204, 169–178. https://doi.org/10.3354/meps204169

Fogarty, M.J., Botsford, L.W., 2007. Population connectivity and spatial management of marine fisheries. Oceanography 20, 112–123. https://doi.org/10.5670/oceanog.2007.34

Foster, N.L., Paris, C.B., Kool, J.T., Baums, I.B., Stevens, J.R., Sanchez, J.A., Bastidas, C., Agudelo, C., Bush, P., Day, O., Ferrari, R., Gonzalez, P., Gore, S., Guppy, R., McCartney, M.A., McCoy, C., Mendes, J., Srinivasan, A., Steiner, S., Vermeij, M.J.A., Weil, E., Mumby, P.J., 2012. Connectivity of Caribbean coral populations: Complementary insights from empirical and modelled gene flow. Mol. Ecol. 21, 1143–1157. https://doi.org/10.1111/j.1365-294X.2012.05455.x

Franz, G., Delpey, T.M., Brito, D., Neves, R., Leitão, P., Pinto, L., 2017. Modelling of sediment transport and morphological evolution under the combined action of waves and currents. Ocean Sci. 13, 673–690. https://doi.org/10.5194/os-13-673-2017

Friedlander, A., Afonso, P., Morato, T., Carreiro-Silva, M., Fontes, J., Abecasis, D., Ballesteros, E., Botelho, A., Diaz, D., Das, D., Dominguez-Carrió, C., Caselle, J., Estep, A., Goodell, W., Milla, D., Ocaña, O., Pham, C., Pipa, T., Rose, P., Salinas de León, P., Schmiing, M., Silva, C., Taranto, G., Tempera, F., Thompson, C., Verdura, J., Sala, E., Gonçalves, E., 2019. Blue Azores - The best kept secret in the Atlantic. Sci. Rep. to Reg. Gov. Azores 1–107.

Gaines, S.D., 2001. Dependence of sustainability on the configuration of marine reserves and larval dispersal distance 144–150.

Gaines, S.D., Gaylord, B., Gerber, L.R., Hastings, P.A., Kinlan, B.P., 2005. The ecological consequences of dispersal in the sea. Oceanography 20, 90–99.

Gaines, S.D., White, C., Carr, M.H., Palumbi, S.R., 2010. Designing marine reserve networks for both conservation and fi sheries management 107, 18286–18293. https://doi.org/10.1073/pnas.0906473107

Garcia, H.E., Boyer, T.P., Baranova, O.K., Locarnini, R.A., Mishonov, A.V., Grodsky, A., Paver, C.R., Weathers, K.W., Smolyar, I.V., Reagan, J.R., Seidov, D., Zweng, M.M., 2018. World Ocean Atlas 2018: Product Documentation. A. Mishonov, Technical Editor. 1, 1–20.

Garcia, H.E., Locarnini, R., Boyer, T.P., Antonov, J.I., Baranova, O.K., Zweng, M.M., Reagan, J.R., Johnson, D.R., 2013. World Ocean Atlas 2013 Volume 4 : Nutrients (phosphate , nitrate , silicate). NOAA Atlas NESDIS 76 4, 396.

Gary, S.F., Fox, A.D., Biastoch, A., Roberts, J.M., Cunningham, S.A., 2020. Larval behaviour, dispersal and population connectivity in the deep sea. Sci. Rep. 10, 1–12. https://doi.org/10.1038/s41598-020-67503-7

Giacomello, E., Menezes, G., 2012. CONDOR Observatory for long-term study and monitoring of Azorean seamount ecosystems. Final Project Report. 261 PP + 9 ANNEXES.

Gnanadesikan, A., Dunne, J.P., John, J., 2011. What ocean biogeochemical models can tell us about bottom-up control of ecosystem variability. ICES J. Mar. Sci. 68, 1030–1044. https://doi.org/10.1093/icesjms/fsr068

Gomes-Pereira, J.N., Carmo, V., Catarino, D., Jakobsen, J., Alvarez, H., Aguilar, R., Hart, J., Giacomello, E., Menezes, G., Stefanni, S., Colaço, A., Morato, T., Santos, R.S., Tempera, F., Porteiro, F., 2017. Cold-water corals and large hydrozoans provide essential fish habitat for Lappanella fasciata and Benthocometes robustus. Deep. Res. Part II Top. Stud. Oceanogr. 145, 33–48. https://doi.org/10.1016/j.dsr2.2017.09.015

Gómez-Zambrano, H.J., López-Ríos, V.I., Toro-Botero, F.M., 2017. New methodology for calibration of hydrodynamic models in curved open-channel flow. Rev. Fac. Ing. 2017, 82–91. https://doi.org/10.17533/udea.redin.n83a11

Graves, K.P., Bridges, A.E.H., Dabrowski, T., Furey, T., Lyons, K., Howell, K.L., 2022. Deep-Sea Research Part I Oceanographic variability drives the distribution but not the density of the aggregation forming deep-sea sponge *Pheronema carpenteri.* Deep. Res. Part I 103917. https://doi.org/10.1016/j.dsr.2022.103917

Gregg, W.W., Ginoux, P., Schopf, P.S., Casey, N.W., 2003. Phytoplankton and iron: Validation of a global three-dimensional ocean biogeochemical model. Deep. Res. Part II Top. Stud. Oceanogr. 50, 3143–3169. https://doi.org/10.1016/j.dsr2.2003.07.013

Guerao, G., Abelló, P., Castejón, M.R., 1996. Morphology of the larval stages of the deep-sea crab geryon longipes (Brachyura: Geryonidae). J. Nat. Hist. 30, 505–521.

https://doi.org/10.1080/00222939600770271

Guillas, K.C., Kahn, A.S., Grant, N., Archer, S.K., Dunham, A., Leys, S.P., 2019. Settlement of juvenile glass sponges and other invertebrate cryptofauna on the Hecate Strait glass sponge reefs. Invertebr. Biol. 138, 1–11. https://doi.org/10.1111/ivb.12266

Guillou, N., Neill, S.P., Robins, P.E., 2018. Characterising the tidal stream power resource around France using a high-resolution harmonic database. Renew. Energy 123, 706–718. https://doi.org/10.1016/j.renene.2017.12.033

Gutknecht, E., Reffray, G., Gehlen, M., Triyulianti, I., Berlianty, D., Gaspar, P., 2016. Evaluation of an operational ocean model configuration at 1/12° spatial resolution for the Indonesian seas (NEMO2.3/INDO12) - Part 2: Biogeochemistry. Geosci. Model Dev. 9, 1523–1543. https://doi.org/10.5194/gmd-9-1523-2016

Hahn-Woernle, L., Dijkstra, H.A., van der Woerd, H.J., 2016. Vertical mixing derived from surface chlorophyll-a concentrations of the north atlantic ocean. J. Atmos. Ocean. Technol. 33, 2165–2183. https://doi.org/10.1175/JTECH-D-16-0053.1

Haney, J.D., Jackson, G.A., 1996. Modeling phytoplankton growth rates. J. Plankton Res. 18, 63–85. https://doi.org/10.1093/plankt/18.1.63

Hashioka, T., Vogt, M., Yamanaka, Y., Le Quéré, C., Buitenhuis, E.T., Aita, M.N., Alvain, S., Bopp, L., Hirata, T., Lima, I., Sailley, S., Doney, S.C., 2013. Phytoplankton competition during the spring bloom in four plankton functional type models. Biogeosciences 10, 6833–6850. https://doi.org/10.5194/bg-10-6833-2013

Henriksen, H.J., Troldborg, L., Nyegaard, P., Sonnenborg, T.O., Refsgaard, J.C., Madsen, B., 2003. Methodology for construction, calibration and validation of a national hydrological model for Denmark. J. Hydrol. 280, 52–71. https://doi.org/10.1016/S0022-1694(03)00186-0

Henry, L.A., Roberts, J.M., 2014. Applying the OSPAR habitat definition of deep-sea sponge aggregations to verify suspected records of the habitat in UK waters. JNCC Report, JNCC Report No. 508.

Heymans, J.J., Skogen, M., Schrum, C., Solidoro, C., (2018) Enhancing Europe's capability in marine ecosystem modelling for societal benefit. Larkin, K.E., Coopman, J., Muñiz Piniella, A., Kellett, P., Simon, C., Rundt, C., Viegas, C., Heymans, J.J., 2018. Enhancing Europe ' s Capability in Marine Ecosystem Modelling for Societal Benefit.

Hilário, A., Cunha, M.R., 2013. Notes on a mating event of the deep-sea crab Chaecon affinis in the Gorringe Bank (NE Atlantic). Deep. Res. Part II Top. Stud. Oceanogr. 92, 58–62. https://doi.org/10.1016/j.dsr2.2013.01.021

Hilário, A., Metaxas, A., Gaudron, S.M., Howell, K.L., Mercier, A., Mestre, N.C., Ross, R.E., Thurnherr, A.M., Young, C., 2015. Estimating dispersal distance in the deep sea: Challenges and applications to marine reserves. Front. Mar. Sci. 2, 1–14. https://doi.org/10.3389/fmars.2015.00006

Hinrichsen, H.H., Dickey-Collas, M., Huret, M., Peck, M.A., Vikebø, F.B., 2011. Evaluating the suitability of coupled biophysical models for fishery management. ICES J. Mar. Sci. 68, 1478–1487. https://doi.org/10.1093/icesjms/fsr056

Hirose, K., Kamiya, H., 2003. Vertical nutrient distributions in the western North Pacific ocean: Simple model for estimating nutrient upwelling, export flux and consumption rates. J. Oceanogr. 59, 149–161. https://doi.org/10.1023/A:1025535003841

Hjelmervik, K., 2012. Demonstration of Comparison Methods for Ocean Model Validation. Open Ocean Eng. J. 5, 1–14. https://doi.org/10.2174/1874835x01205010001

Hodin, J., Ferner, M.C., Ng, G., Gaylord, B., 2018. Turbulence exposure recapitulates desperate behavior in late-stage sand dollar larvae. BMC Zool. 3, 1–13. https://doi.org/10.1186/s40850-018-0034-5

Holgate, S.J., Matthews, A., Woodworth, P.L., Rickards, L.J., Tamisiea, M.E., Bradshaw, E., Foden, P.R., Gordon, K.M., Jevrejeva, S., Pugh, J., 2013. New Data Systems and Products at the Permanent Service for Mean Sea Level 493–504. https://doi.org/10.2112/JCOASTRES-D-12-00175.1

Holstein, D.M., Paris, C.B., Mumby, P.J., 2014. Consistency and inconsistency in multispecies population network dynamics of coral reef ecosystems. Mar. Ecol. Prog. Ser. 499, 1–18. https://doi.org/10.3354/meps10647

Howell, K.L., Piechaud, N., Downie, A.L., Kenny, A., 2016. The distribution of deep-sea sponge aggregations in the North Atlantic and implications for their effective spatial management. Deep. Res. Part I Oceanogr. Res. Pap. 115, 309–320. https://doi.org/10.1016/j.dsr.2016.07.005

ICES. 2019. Azores ecoregion – Ecosystem overview, ICES, 2019. Azores ecoregion – Ecosystem overview. Rep. ICES Advis. Comm. ICES Advic, 1–18. https://doi.org/Https://doi.org/10.17895/ices.advice.5753

Ilyina, T., Six, K.D., Segschneider, J., Maier-Reimer, E., Li, H., Núñez-Riboni, I., 2013. Global ocean biogeochemistry model HAMOCC: Model architecture and performance as component of the MPI-Earth system model in different CMIP5 experimental realizations. J. Adv. Model. Earth Syst. 5, 287–315. https://doi.org/10.1029/2012MS000178

IMAR, 2018. Blue Azores Program: Expedition 2018 on board the NRP Gago Coutinho.

Instituto Superior Técnico, 2003. Mohid Description: Description of the 3D water modeling system Mohid (2003).

IOC-UNESCO, 2022. Implementing Operational Ocean Monitoring and Forecasting Systems, GOOS-275. ed.

IST, 2003. Water System model Hydrodynamic Module, MOHID.

Itoh, S., Yasuda, I., Saito, H., Tsuda, A., Komatsu, K., 2015. Mixed layer depth and chlorophyll a: Profiling float observations in the Kuroshio-Oyashio Extension region. J. Mar. Syst. 151, 1–14. https://doi.org/10.1016/j.jmarsys.2015.06.004

Janjic, Z.I., 2003. A nonhydrostatic model based on a new approach. Meteorol. Atmos. Phys. 82, 271–285. https://doi.org/10.1007/s00703-001-0587-6

Jones, B.T., Solow, A., Ji, R., 2016. Resource allocation for lagrangian tracking. J. Atmos. Ocean. Technol. 33, 1225–1235. https://doi.org/10.1175/JTECH-D-15-0115.1

Juliano, M.F., Alves, M., 2006. the South Atlantic Subtropical Front / Current of St . Helena. Proc. 8 ICSHMO, Foz do Iguaçu, Brazil, April 24-28, 2006, INPE 1283–1288.

Juliano, M.F., Alves, M.L.G.R., 2007. The atlantic subtropical front/current systems of Azores and St. Helena. J. Phys. Oceanogr. 37, 2573–2598. https://doi.org/10.1175/2007JPO3150.1

Juliano, M.M.F., Neves, R., Rodrigues, P.P.G.W., Junior, J.L., Fernandes, R., 2012. Aplicação da Plataforma MOHID para simulação computacional de deriva oceânica de petróleo na bacia de Campos - RJ 161–172.

Julien, P., 2019. Global_Analysis_Forecast_Bio_001_028. E.U. Copernicus Mar. Serv. Inf. 18.

Jung, H.C., Moon, B.K., Lee, H., Choi, J.H., Kim, H.K., Park, J.Y., Byun, Y.H., Lim, Y.J., Lee, J., 2020. Development and Assessment of NEMO(v3.6)-TOPAZ(v2), a Coupled Global Ocean Biogeochemistry Model. Asia-Pacific J. Atmos. Sci. 56, 411–428. https://doi.org/10.1007/s13143-019-00147-4

Kane, A., Moulin, C., Thiria, S., Bopp, L., Berrada, M., Tagliabue, A., Crépon, M., Aumont, O., Badran, F., 2011. Improving the parameters of a global ocean biogeochemical model via variational assimilation of in situ data at five time series stations. J. Geophys. Res. Ocean. 116, 1–14. https://doi.org/10.1029/2009JC006005

Karpowicz, M., Ejsmont-Karabin, J., Kozłowska, J., Feniova, I., Dzialowski, A.R., 2020. Zooplankton community responses to oxygen stress. Water (Switzerland) 12, 1–20. https://doi.org/10.3390/w12030706

Katavouta, A., Thompson, K.R., 2016. Downscaling ocean conditions with application to the Gulf of Maine, Scotian Shelf and adjacent deep ocean. Ocean Model. 104, 54–72. https://doi.org/10.1016/j.ocemod.2016.05.007

Kelly, P., Sulkin, S.D., Van Heukelem, W.F., 1982. A dispersal model for larvae of the deep sea red crab Geryon quinquedens based upon behavioral regulation of vertical migration in the hatching stage. Mar. Biol. 72, 35–43. https://doi.org/10.1007/BF00393945

Kenchington, E., Wang, Z., Lirette, C., Murillo, F.J., Guijarro, J., Yashayaev, I., Maldonado, M., 2019. Connectivity modelling of areas closed to protect vulnerable marine ecosystems in the northwest Atlantic. Deep. Res. Part I Oceanogr. Res. Pap. 143, 85–103. https://doi.org/10.1016/j.dsr.2018.11.007

Kessouri, F., McLaughlin, K., Sutula, M., Bianchi, D., Ho, M., McWilliams, J.C., Renault, L., Molemaker, J., Deutsch, C., Leinweber, A., 2021. Configuration and Validation of an Oceanic Physical and Biogeochemical Model to Investigate Coastal Eutrophication in the Southern California Bight. J. Adv. Model. Earth Syst. 13, 1–34. https://doi.org/10.1029/2020MS002296

Kishi, M.J., Kashiwai, M., Ware, D.M., Megrey, B.A., Eslinger, D.L., Werner, F.E., Noguchi-Aita, M., Azumaya, T., Fujii, M., Hashimoto, S., Huang, D., Iizumi, H., Ishida, Y., Kang, S., Kantakov, G.A., Kim, H. cheol, Komatsu, K., Navrotsky, V. V., Smith, S.L., Tadokoro, K., Tsuda, A., Yamamura, O., Yamanaka, Y., Yokouchi, K., Yoshie, N., Zhang, J., Zuenko, Y.I., Zvalinsky, V.I., 2007. NEMURO-a lower trophic level model for the North Pacific marine ecosystem. Ecol. Modell. 202, 12–25. https://doi.org/10.1016/j.ecolmodel.2006.08.021

Klein, B., Siedler, G., 1989. On the origin of the Azores Current. J. Geophys. Res. 94, 6159. https://doi.org/10.1029/jc094ic05p06159

Koné, V., Machu, E., Penven, P., Andersen, V., Garçon, V., Fréon, P., Demarcq, H., 2005. Modeling the primary and secondary productions of the southern Benguela upwelling system: A comparative study through two biogeochemical models. Global Biogeochem. Cycles 19. https://doi.org/10.1029/2004GB002427

Kool, J.T., Moilanen, A., Treml, E.A., 2013. Population connectivity: Recent advances and new perspectives. Landsc. Ecol. 28, 165–185. https://doi.org/10.1007/s10980-012-9819-z

Kough, A.S., 2014. Population connectivity and larval dispersal of caribbean spiny lobster. Diss. Abstr. Int. Vol. 76, no. 01, suppl. B, 191 p. 2014. 1–191.

Kough, A.S., Paris, C.B., Butler IV, M.J., 2013. Larval Connectivity and the International Management of Fisheries. PLoS One 8. https://doi.org/10.1371/journal.pone.0064970

Kwiatkowski, L., Yool, A., Allen, J.I., Anderson, T.R., Barciela, R., Buitenhuis, E.T., Butenschön, M., Enright, C., Halloran, P.R., Le Quéré, C., De Mora, L., Racault, M.F., Sinha, B., Totterdell, I.J., Cox, P.M., 2014. IMarNet: An ocean biogeochemistry model intercomparison project within a common physical ocean modelling framework. Biogeosciences 11, 7291–7304. https://doi.org/10.5194/bg-11-7291-2014

Lafon, V., Martins, A., Figueiredo, M., Rodrigues, M., Bashmachnikov, I., Mendonça, A., Macedo, L., Goulart, N., 2004. Sea surface temperature distribution in the Azores region. Part I:

AVHRR imagery and in situ data processing.

Lampitt, R.S., Salter, I., de Cuevas, B.A., Hartman, S., Larkin, K.E., Pebody, C.A., 2010. Long-term variability of downward particle flux in the deep northeast Atlantic: Causes and trends. Deep. Res. Part II Top. Stud. Oceanogr. 57, 1346–1361. https://doi.org/10.1016/j.dsr2.2010.01.011

Lan Smith, S., Pahlow, M., Merico, A., Wirtz, K.W., 2011. Optimality-based modeling of planktonic organisms. Limnol. Oceanogr. 56, 2080–2094. https://doi.org/10.4319/lo.2011.56.6.2080

Lancelot, C., Spitz, Y., Gypens, N., Ruddick, K., Becquevort, S., Rousseau, V., Lacroix, G., Billen, G., *2005. Modelling diatom and Phaeocystis blooms and nutrient cycles in the Southern Bight of the North Sea: The MIRO model. Mar. Ecol. Prog. Ser. 289, 63–78. https://doi.org/10.3354/meps289063*

*Landeria, J.M., Tamura, H., 2018. Morphology of the first zoea of Chaceon affinis (A. Milne-*Edwards & Bouvier, 1894) and occurrence of *Chaceon sp*. larvae (Decapoda: Brachyura: Gerynonidae) in the Canary Islands waters, Northeastern Atlantic. Zootaxa 4413, 579–585. https://doi.org/10.11646/zootaxa.4413.3.11

Lausche, B., Laur, A., Collins, M., 2021. Marine Connectivity Conservation ' Rules of Thumb ' For MPA and MPA Network Design 15.

Lavelle, W., Mohn, C., 2010. Motion , Commotion , and Biophysical Connections at Deep Ocean Seamounts. Oceanography 23.

Lázaro, C., Juliano, M.F., Fernandes, M.J., 2013. Semi-automatic determination of the Azores Current axis using satellite altimetry: Application to the study of the current variability during 1995-2006. Adv. Sp. Res. 51, 2155–2170. https://doi.org/10.1016/j.asr.2012.12.021

Legaloudec, O., Desportes, C., Levier, B., 2015. For Global Sea Physical Analysis and Forecasting Product GLOBAL _ ANALYSIS _ FORECAST _ PHYS _ 001 _ 002 1–100.

Leis, J.M., 2020. Perspectives on Larval Behaviour in Biophysical Modelling of Larval Dispersal in Marine, Demersal Fishes. Oceans 2, 1–25. https://doi.org/10.3390/oceans2010001

Leitão, J.C., Leitão, P., Braunchweig, F., Fernandes, R., Neves, R., Montero, P., 2003. Emergency activities support by an operational forecast system 'e The Prestige accident \n. 4th Semin. Mar. Environ.

Leitão, P.C., Mateus, M., Braunschweig, F., Fernandes, L., Neves, R., 2008. Modelling coastal systems: the MOHID water numerical lab. Perspect. Integr. Coast. Zo. Manag. South Am. 77–88. https://doi.org/10.13140/2.1.1482.4008

Lellouche, J.M., Greiner, E., Le Galloudec, O., Garric, G., Regnier, C., Drevillon, M., Benkiran, M., Testut, C.E., Bourdalle-Badie, R., Gasparin, F., Hernandez, O., Levier, B., Drillet, Y., Remy, E., Le Traon, P.Y., 2018. Recent updates to the Copernicus Marine Service global ocean monitoring and forecasting real-time 1g 12° high-resolution system. Ocean Sci. 14, 1093–1126. https://doi.org/10.5194/os-14-1093-2018

Lenz, J., Harris, R., Wiebe, P., Skjoldal, H.-R., Huntley, M.E. (Ed. ., 2000. ICES Zooplankton Methodology Manual, ICES Zooplankton Methodology Manual. https://doi.org/10.1016/b978-0-12-327645-2.x5000-2

Leys, S.P., Lauzon, N.R.J., 1998. Hexactinellid sponge ecology: Growth rates and seasonality in deep water sponges. J. Exp. Mar. Bio. Ecol. 230, 111–129. https://doi.org/10.1016/S0022-0981(98)00088-4

Lima, M.J., Sala, I., Caldeira, R.M.A., 2020. Physical Connectivity Between the NE Atlantic Seamounts. Front. Mar. Sci. 7, 1–17. https://doi.org/10.3389/fmars.2020.00238

Lin, P., Li, C.W., 2002. A σ-coordinate three-dimensional numerical model for surface wave propagation. Int. J. Numer. Methods Fluids 38, 1045–1068. https://doi.org/10.1002/fld.258

Lindemann, C., St. John, M.A., 2014. A seasonal diary of phytoplankton in the North Atlantic. Front. Mar. Sci. 1, 1–6. https://doi.org/10.3389/fmars.2014.00037

Litchman, E., de Tezanos Pinto, P., Edwards, K.F., Klausmeier, C.A., Kremer, C.T., Thomas, M.K., 2015. Global biogeochemical impacts of phytoplankton: A trait-based perspective. J. Ecol. 103, 1384–1396. https://doi.org/10.1111/1365-2745.12438

Litchman, E., Klausmeier, C.A., Schofield, O.M., Falkowski, P.G., 2007. The role of functional traits and trade-offs in structuring phytoplankton communities: Scaling from cellular to ecosystem level. Ecol. Lett. 10, 1170–1181. https://doi.org/10.1111/j.1461-0248.2007.01117.x

Longmore, C., Trueman, C.N., Neat, F., Jorde, P.E., Knutsen, H., Stefanni, S., Catarino, D., Milton, J.A., Mariani, S., 2014. Ocean-scale connectivity and life cycle reconstruction in a deep-sea fish. Can. J. Fish. Aquat. Sci. 71, 1312–1323. https://doi.org/10.1139/cjfas-2013-0343

Lopes, D., 2005. Zootaxa, Hexactinosida (Porifera, Hexactinellida) 56, 43–56.

López Abellán, L.J., Balguerías, E., Fernández-Vergaz, V., 2002. Life history characteristics of the deep-sea crab *Chaceon affinis* population off Tenerife (Canary Islands). Fish. Res. 58, 231–239. https://doi.org/10.1016/S0165-7836(01)00384-8

Losa, S., Dutkiewicz, S., Losch, M., Oelker, J., Soppa, M., Trimborn, S., Xi, H., Bracher, A., 2019. On modeling the Southern Ocean Phytoplankton Functional Types. Biogeosciences Discuss. 1–37. https://doi.org/10.5194/bg-2019-289

Losa, S.N., Soppa, M.A., Dinter, T., Wolanin, A., Brewin, R.J.W., Bricaud, A., Oelker, J., Peeken, I., Gentili, B., Rozanov, V., Bracher, A., 2017. Synergistic exploitation of hyper- and multi-spectral precursor sentinel measurements to determine phytoplankton functional types

(SynSenPFT). Front. Mar. Sci. 4, 1–22. https://doi.org/10.3389/fmars.2017.00203

Lyard, F.H., Allain, D.J., Cancet, M., Carrère, L., Picot, N., 2021. FES2014 global ocean tides atlas: design and performances Florent. Ocean Sci. 17, 615–649. https://doi.org/https://doi.org/10.5194/os-17-615-2021

Macedo, M.F., Duarte, P., Ferreira, J.G., Alves, M., Costa, V., 2000. Analysis of the deep chlorophyll maximum across the Azores Front. Hydrobiologia 441, 155–172. https://doi.org/10.1023/A:1017519330995

Maldonado, M., 2006. The ecology of the sponge larva. Can. J. Zool. 84, 175–194. https://doi.org/10.1139/z05-177

Maldonado, M., Aguilar, R., Bannister, R.J., James, J., Conway, K.W., Dayton, P.K., Cristina, D., Gutt, J., Kelly, M., Kenchington, E.L.R., Leys, S.P., Shirley, A., Tendal, O.S., Rapp, H.T., Klaus, R., Young, C.M., 2016. Marine Animal Forests, Marine Animal Forests. https://doi.org/10.1007/978-3-319-17001-5

Maldonado, M., Aguilar, R., Bannister, R.J., James, J., Conway, K.W., Dayton, P.K., Cristina, D., Gutt, J., Kelly, M., Kenchington, E.L.R., Leys, S.P., Shirley, A., Tendal, O.S., Rapp, H.T., Klaus, R., Young, C.M., 2015. Sponge Grounds as Key Marine Habitats: A Synthetic Review of Types, Structure, Functional Roles, and Conservation Concerns, in: Rossi, S., Bramanti, L., Gori, A., Orejas Saco del Valle, C. (Eds.), Marine Animal Forests. Springer International Publishing. https://doi.org/https://doi.org/10.1007/978-3-319-17001-5_24-1

Maldonado, M., Carmona, M.C., Velásquez, Z., Puig, A., Cruzado, A., López, A., Young, C.M., 2005. Siliceous sponges as a silicon sink: An overlooked aspect of benthopelagic coupling in the marine silicon cycle. Limnol. Oceanogr. 50, 799–809. https://doi.org/10.4319/lo.2005.50.3.0799

Maldonado, M., López-Acosta, M., Sitjà, C., García-Puig, M., Galobart, C., Ercilla, G., Leynaert, A., 2019. Sponge skeletons as an important sink of silicon in the global oceans. Nat. Geosci. 12, 815–822. https://doi.org/10.1038/s41561-019-0430-7

Maldonado, M., Young, C.M., 1999. Effects of the duration of larval life on postlarval stages of the demosponge Sigmadocia caerulea. J. Exp. Mar. Bio. Ecol. 232, 9–21. https://doi.org/10.1016/S0022-0981(98)00076-8

Marañón, E., 2005. Phytoplankton growth rates in the Atlantic subtropical gyres. Limnol. Oceanogr. 50, 299–310. https://doi.org/10.4319/lo.2005.50.1.0299

Marañón, E., Behrenfeld, M.J., González, N., Mouriño, B., Zubkov, M. V., 2003. High variability of primary production in oligotrophic waters of the Atlantic Ocean: Uncoupling from phytoplankton biomass and size structure. Mar. Ecol. Prog. Ser. 257, 1–11. https://doi.org/10.3354/meps257001

Maranõn, E., Holligan, P.M., Varela, M., Mourin, B., Bale, A.J., 2000. Basin-scale variability of phytoplankton biomass, production and growth in the Atlantic Ocean. Deep. Res. Part I Oceanogr. Res. Pap. 47, 825–857.

Marañón, E., Pérez, V., Fernández, E., Anadón, R., Bode, A., González, N., Huskin, I., Isla, A., Morán, X.A.G., Mouriño, B., Quevedo, M., Robinson, C., Serret, P., Teira, E., Varela, M.M., Woodward, E.M.S., Zubkov, M. V., 2007. Planktonic carbon budget in the eastern subtropical North Atlantic. Aquat. Microb. Ecol. 48, 261–275. https://doi.org/10.3354/ame048261

Mariani, S., Uriz, M.J., Turon, X., Alcoverro, T., 2006. Dispersal strategies in sponge larvae: Integrating the life history of larvae and the hydrologic component. Oecologia 149, 174–184. https://doi.org/10.1007/s00442-006-0429-9

Marrero-Díaz, Á., Rodríguez-Santana, Á., Machín, F., Pelegrí, J.L., 2006. Analytic salinity-temperature relations for the upper-thermocline waters of the eastern North Atlantic subtropical gyre. Sci. Mar. 70, 167–175. https://doi.org/10.3989/scimar.2006.70n2167

Martínez-Rivera, S., Stevens, B.G., 2020. Embryonic development and fecundity of the red deep-sea crab *Chaceon quinquedens* (Smith, 1879) (Decapoda: Brachyura: Geryonidae) in the Mid-Atlantic Bight determined by image analysis. J. Crustac. Biol. 40, 230–236. https://doi.org/10.1093/jcbiol/ruaa017

Martinez, E., Antoine, D., D'Ortenzio, F., De Boyer Montégut, C., 2011. Phytoplankton spring and fall blooms in the North Atlantic in the 1980s and 2000s. J. Geophys. Res. Ocean. 116, 1–11. https://doi.org/10.1029/2010JC006836

Martins, F.. R.N. e P.C.L., 1998. A three-dimensional hydrodynamic model with generic vertical coordinate. Proc. Hydroinformatics 1403–1410.

Matear, R.J., Hirst, A.C., 2003. Long-term changes in dissolved oxygen concentrations in the ocean caused by protracted global warming. Global Biogeochem. Cycles 17, 1125. https://doi.org/10.1029/2002GB001997

Mateus, M., 2006. A process-oriented biogeochemical model for marine ecosystems: development, numerical study, and application 246.

Mattern, J.P., Song, H., Edwards, C.A., Moore, A.M., Fiechter, J., 2017. Data assimilation of physical and chlorophyll a observations in the California Current System using two biogeochemical models. Ocean Model. 109, 55–71. https://doi.org/10.1016/j.ocemod.2016.12.002

McKinley, G.A., Ritzer, A.L., Lovenduski, N.S., 2018. Mechanisms of northern North Atlantic biomass variability. Biogeosciences 15, 6049–6066. https://doi.org/10.5194/bg-15-6049-2018

Ménesguen, A., Cugier, P., Loyer, S., Vanhoutte-Brunier, A., Hoch, T., Guillaud, J.F., Gohin, F.,

2007. Two- or three-layered box-models versus fine 3D models for coastal ecological modelling? A comparative study in the English Channel (Western Europe). J. Mar. Syst. 64, 47–65. https://doi.org/10.1016/j.jmarsys.2006.03.017

Metaxas, A., Saunders, M., 2009. Quantifying the “Bio-” Components in Biophysical Models of Larval Transport in Marine Benthic Invertebrates: Advances and Pitfalls. Biol. Bull. 216, 257–272. https://doi.org/10.1086/bblv216n3p257

Mitra, A., Castellani, C., Gentleman, W.C., Jónasdóttir, S.H., Flynn, K.J., Bode, A., Halsband, C., Kuhn, P., Licandro, P., Agersted, M.D., Calbet, A., Lindeque, P.K., Koppelmann, R., Møller, E.F., Gislason, A., Nielsen, T.G., St. John, M., 2014. Bridging the gap between marine biogeochemical and fisheries sciences; configuring the zooplankton link. Prog. Oceanogr. 129, 176–199. https://doi.org/10.1016/j.pocean.2014.04.025

Moll, A., Radach, G., 2003. Review of three-dimensional ecological modelling related to the North Sea shelf system. Prog. Oceanogr. 57, 175–217. https://doi.org/10.1016/s0079-6611(03)00067-3

Moore, J.K., Doney, S.C., Kleypas, J.A., Glover, D.M., Fung, I.Y., 2001. An intermediate complexity marine ecosystem model for the global domain. Deep. Res. Part II Top. Stud. Oceanogr. 49, 403–462. https://doi.org/10.1016/S0967-0645(01)00108-4

Morato, T., Afonso, P., Menezes, G.M., Santos, R.S., Silva, M.A., 2020. Editorial: The Azores Marine Ecosystem: An Open Window Into North Atlantic Open Ocean and Deep-Sea Environments. Front. Mar. Sci. 7, 1–3. https://doi.org/10.3389/fmars.2020.601798

Morato, T., Colaço, M.A., Juliano, M., 2016a. Azores case study. MIDAS Newsl. Summer 201.

Morato, T., Dominguez-Carrió, C., Mohn, C., Ocaña Vicente, O., Ramos, M., Rodrigues, L., Sampaio, Í., Taranto, G.H., Fauconnet, L., Tojeira, I., Gonçalves, J., E., Carreiro-Silva, M., 2021. Dense cold-water coral garden of Paragorgia johnsoni suggests the importance of the Mid-Atlantic Ridge for deep-sea biodiversity. Ecol. Evol. 11, 16426–16433.

Morato, T., Lemey, E., Menezes, G., Pham, C., Brito, J., Soszynski, A., Pitcher, T., Heymans, J., 2016b. Food-web and ecosystem structure of the open-ocean and deep-sea environments of the azores, NE Atlantic. Front. Mar. Sci. 3, 1–13. https://doi.org/10.3389/fmars.2016.00245

Morato, Te., Machete, M., Kitchingman, A., Tempera, F., Lai, S., Menezes, G., Pitcher, T.J., Santos, R.S., 2008. Abundance and distribution of seamounts in the Azores. Mar. Ecol. Prog. Ser. 357, 17–21. https://doi.org/10.3354/meps07268

Mouw, C.B., Barnett, A., McKinley, G.A., Gloege, L., Pilcher, D., 2016. Global ocean particulate organic carbon flux merged with satellite parameters. Earth Syst. Sci. Data 8, 531–541. https://doi.org/10.5194/essd-8-531-2016

Mulder, C., Hendriks, A.J., 2014. Half-saturation constants in functional responses. Glob. Ecol. Conserv. 2, 161–169. https://doi.org/10.1016/j.gecco.2014.09.006

Mullineaux, L.S., Jr, D.J.M., Mills, S.W., Kosnyrev, V.K., Thurnherr, A.M., Ledwell, J.R., Lavelle, J.W., 2013. Deep-Sea Research II Active positioning of vent larvae at a mid-ocean ridge. Deep. Res. Part II 92, 46–57. https://doi.org/10.1016/j.dsr2.2013.03.032

Narciso, Á., Gallo, F., Valente, A., Cachão, M., Cros, L., Azevedo, E.B., e Ramos, J.B., 2016. Seasonal and interannual variations in coccolithophore abundance off Terceira Island, Azores (Central North Atlantic). Cont. Shelf Res. 117, 43–56. https://doi.org/10.1016/j.csr.2016.01.019

National Centers for Environmental Prediction, National Weather Service, NOAA, U.S.D. of C., 2015. NCEP GFS 0.25 Degree Global Forecast Grids Historical Archive. https://doi.org/https://doi.org/10.5065/D65D8PWK

Neves, R.J.J., Coelho, H., Taborda, R., 2003. Ocean Margin Systems, Ocean Margin Systems. https://doi.org/10.1007/978-3-662-05127-6

North, E.W., Gallego, A., Petitgas, P., Ådlandsvik, B., Bartsch, J., Brickman, D., Browman, H.I., Edwards, K., Fiksen, Ø., Hermann, A.J., others, 2009. Manual of recommended practices for modelling physical-biological interactions during fish early life.

Oddo, P., Pinardi, N., 2008. Lateral open boundary conditions for nested limited area models: A scale selective approach. Ocean Model. 20, 134–156. https://doi.org/10.1016/j.ocemod.2007.08.001

OECD, 2016. Marine Protected Areas Marine Protected Areas- Economics, Management and Effective Policy Mixes- Policy highlights.

OSPAR, 2010. Background Document for Deep-sea sponge aggregations Biodiversity Series 88.

Ospina-Alvarez, A., Juan, S., Alós, J., Basterretxea, G., Alonso-Fernández, A., Follana-Berná, G., Palmer, M., Catalán, I., 2020. MPA network design based on graph theory and emergent properties of larval dispersal. Mar. Ecol. Prog. Ser. 650, 309–326.

Palma, C., Lillebø, A.I., Borges, C., Souto, M., Pereira, E., Duarte, A.C., Abreu, M.P. de, 2012. Water column characterisation on the Azores platform and at the sea mounts south of the archipelago. Mar. Pollut. Bull. 64, 1884–1894. https://doi.org/10.1016/j.marpolbul.2012.06.015

Palmer, J.R., Totterdell, I.J., 2001. Production and export in a global ocean ecosystem model. Deep. Res. 1, 1169–1198. https://doi.org/10.1080/00222937608682395

Paris, C.B., Helgers, J., van Sebille, E., Srinivasan, A., 2013. Connectivity Modeling System: A probabilistic modeling tool for the multi-scale tracking of biotic and abiotic variability in the ocean. Environ. Model. Softw. 42, 47–54. https://doi.org/10.1016/j.envsoft.2012.12.006

Pata, P.R., Yñiguez, A.T., Deauna, J.D.L., De Guzman, A.B., Jimenez, C.R., Rosario, R.T.B. Del, Villanoy, C.L., 2021. Insights into the environmental conditions contributing to variability in the larval recruitment of the tropical sardine Sardinella lemuru. Ecol. Modell. 451. https://doi.org/10.1016/j.ecolmodel.2021.109570

Peña, M.A., Masson, D., Callendar, W., 2016. Annual plankton dynamics in a coupled physical–biological model of the Strait of Georgia, British Columbia. Prog. Oceanogr. 146, 58–74. https://doi.org/10.1016/j.pocean.2016.06.002

Peran, A.D., Pham, C.K., Amorim, P., Cardigos, F., Tempera, F., Morato, T., 2016. Seafloor characteristics in the azores region (North Atlantic). Front. Mar. Sci. 3, 2014–2017. https://doi.org/10.3389/fmars.2016.00204

Perruche C, Hameau A, Paul J, Régnier C, Drévillon M, 2016. Quality information document for Global Biogeochemical Analysis and Forecast Product GLOBAL_ANALYSIS_FORECAST_BIO_001_014 CHANGE RECORD Issue Date Description of Change Author Validated By 1–38.

Pham, C.K., Vandeperre, F., Menezes, G., Porteiro, F., Isidro, E., Morato, T., 2015. The importance of deep-sea vulnerable marine ecosystems for demersal fish in the Azores. Deep. Res. Part I Oceanogr. Res. Pap. 96, 80–88. https://doi.org/10.1016/j.dsr.2014.11.004

Phelps, J.J.C., 2015. Modelling Hydrodynamic Transport and Larval Dispersal in North-East Atlantic Shelf Seas.

Pinho M., Santos R., Melo O., Isidro E., Medeiros-Leal W., Gonçalves J., 2020. Estimates of biomass and potential yield for the deep-water red crab, *Chaceon affinis* and the toothed rock crab, *Cancer bellianus* (Decapoda: Brachyura) off the Azores (Mid-North Atlantic). Arquipel. Life Mar. Sci. 37, 21–36.

Pinho, M.R., Gonçalves, J.M., Martins, H.R., Menezes, G.M., 2001. Some aspects of the biology of the deep-water crab, *Chaceon affinis* (Milne-Edwards and Bouvier, 1894) off the Azores. Fish. Res. 51, 283–295. https://doi.org/10.1016/S0165-7836(01)00252-1

Pinto, L., Campuzano, F., Juliano, M., Fernandes, R., Neves, R., 2014. Implementation and validation of an operational model for the Portuguese exclusive economic zone. 3ª Jornadas Eng. Hidrográfica.

PSMSL, 2018. Tide Gauge data [WWW Document]. Tide Gauge data. URL http://www.psmsl.org/data/obtaining/ (accessed 3.1.18).

Purser, A., Marcon, Y., 2016. Managing Impacts of Deep Sea Resource Exploitation Research Highlights.

Ragueneau, O., Tréguer, P., Leynaert, A., Anderson, R.F., Brzezinski, M.A., DeMaster, D.J., Dugdale, R.C., Dymond, J., Fischer, G., François, R., Heinze, C., Maier-Reimer, E., Martin-

Jézéquel, V., Nelson, D.M., Quéguiner, B., 2000. A review of the Si cycle in the modern ocean: Recent progress and missing gaps in the application of biogenic opal as a paleoproductivity proxy. Glob. Planet. Change 26, 317–365. https://doi.org/10.1016/S0921-8181(00)00052-7

Raick, C., Delhez, E.J.M., Soetaert, K., Grégoire, M., 2005. Study of the seasonal cycle of the biogeochemical processes in the Ligurian Sea using a 1D interdisciplinary model. J. Mar. Syst. 55, 177–203. https://doi.org/10.1016/j.jmarsys.2004.09.005

Ramiro-Sánchez, B., González-Irusta, J.M., Henry, L.-A., Cleland, J., Yeo, I., Xavier, J.R., Carreiro-Silva, M., Sampaio, Í., Spearman, J., Victorero, L., Messing, C.G., Kazanidis, G., Roberts, J.M., Murton, B., 2019. Characterization and Mapping of a Deep-Sea Sponge Ground on the Tropic Seamount (Northeast Tropical Atlantic): Implications for Spatial Management in the High Seas. Front. Mar. Sci. 6, 1–19. https://doi.org/10.3389/fmars.2019.00278

Reboreda, R., 2013. Modelling the biogeochemical dynamics of the iberian upwelling system.

Rice, A.L., Thurston, M.H., New, A.L., 1990. Dense aggregations of a hexactinellid sponge, P*heronema carpenteri,* in the Porcupine Seabight (northeast Atlantic Ocean), and possible causes. Prog. Oceanogr. 179–196.

Riflet, G., Juliano, M., Fernandes, L., Leitão, Paulo Chambel Neves, R., 2008. Operational Ocean forecasting of the Portuguese waters. Mercat. Ocean Q. Newsl. 30.

Roberts, C.M., Andelman, S., Branch, G., Bustamante, R.H., Castilla, J.C., Dugan, J., Halpern, B.S., Lafferty, K.D., Leslie, H., Lubchenco, J., McArdle, D., Possingham, H.P., Ruckelshaus, M., Warner, R.R., 2003. Ecological criteria for evaluating candidate sites for marine reserves. Ecol. Appl. 13, 199–214. https://doi.org/10.1890/1051-0761(2003)013[0199:ecfecs]2.0.co;2

Roberts, E., Bowers, D., Meyer, H., Samuelsen, A., Rapp, H., Cárdenas, P., 2021. Water masses constrain the distribution of deep-sea sponges in the North Atlantic Ocean and Nordic Seas. Mar. Ecol. Prog. Ser. 659, 75–96. https://doi.org/10.3354/meps13570

Robson, B.J., 2014. State of the art in modelling of phosphorus in aquatic systems: Review, criticisms and commentary. Environ. Model. Softw. 61, 339–359. https://doi.org/10.1016/j.envsoft.2014.01.012

Rocha, C., Edwards, C.A., Roughan, M., Cetina-Heredia, P., Kerry, C., 2019. A high-resolution biogeochemical model (ROMS 3.4+bio-Fennel) of the East Australian current system. Geosci. Model Dev. 12, 441–456. https://doi.org/10.5194/gmd-12-441-2019

Rodríguez-Basalo, A., Prado, E., Sánchez, F., Ríos, P., Gómez-Ballesteros, M., Cristobo, J., 2021. High Resolution Spatial Distribution for the Hexactinellid Sponges Asconema setubalense and *Pheronema carpenteri* in the Central Cantabrian Sea. Front. Mar. Sci. 8, 1–15. https://doi.org/10.3389/fmars.2021.612761

Roemmich, D., Alford, M.H., Claustre, H., Johnson, K.S., King, B., Moum, J., Oke, P.R., Owens, W.B., Pouliquen, S., Purkey, S., Scanderbeg, M., Suga, T., Wijffels, S.E., Zilberman, N., Bakker, D., Baringer, M.O., Belbeoch, M., Bittig, H.C., Boss, E., Calil, P., Carse, F., Carval, T., Chai, F., Conchubhair, D.O., D'Ortenzio, F., Dall'Olmo, G., Desbruyères, D., Fennel, K., Fer, I., Ferrari, R., Forget, G., Freeland, H., Fujiki, T., Gehlen, M., Greenan, B., Hallberg, R., Hibiya, T., Hosoda, S., Jayne, S., Jochum, M., Johnson, G.C., Kang, K.R., Kolodziejczyk, N., Koertzinger, A., Le Traon, P.Y., Lenn, Y.D., Maze, G., Mork, K.A., Morris, T., Nagai, T., Nash, J., Garabato, A.N., Olsen, A., Pattabhi, R.R., Prakash, S., Riser, S., Schmechtig, C., Shroyer, E., Sterl, A., Sutton, P., Talley, L., Tanhua, T., Thierry, V., Thomalla, S., Toole, J., Troisi, A., Trull, T., Turton, J.D., Velez-Belchi, P.J., Walczowski, W., Wang, H., Wanninkhof, R., Waterhouse, A., Watson, A., Wilson, C., Wong, A.P., Xu, J., Yasuda, I., 2019. On the future of Argo: A global, full-depth, multi-disciplinary array. Front. Mar. Sci. 6. https://doi.org/10.3389/fmars.2019.00439

Roman, M.R., Boicourt, W.C., 1999. Dispersion and recruitment of crab larvae in the Chesapeake Bay plume: Physical and biological controls. Estuaries 22, 563–574. https://doi.org/10.2307/1353044

Ross, R.E., Howell, K.L., 2013. Use of predictive habitat modelling to assess the distribution and extent of the current protection of "listed" deep-sea habitats. Divers. Distrib. 19, 433–445. https://doi.org/10.1111/ddi.12010

Ross, R.E., Nimmo-Smith, W.A.M., Howell, K.L., 2017. Towards 'ecological coherence': Assessing larval dispersal within a network of existing Marine Protected Areas. Deep. Res. Part I Oceanogr. Res. Pap. 126, 128–138. https://doi.org/10.1016/j.dsr.2017.06.004

Ross, R.E., Nimmo-Smith, W.A.M., Howell, K.L., 2016. Increasing the depth of current understanding: Sensitivity testing of deep-sea larval dispersal models for ecologists. PLoS One 11, 1–25. https://doi.org/10.1371/journal.pone.0161220

Ross, R.E., Nimmo-Smith, W.A.M., Torres, R., Howell, K.L., 2020. Comparing Deep-Sea Larval Dispersal Models: A Cautionary Tale for Ecology and Conservation. Front. Mar. Sci. 7, 1–15. https://doi.org/10.3389/fmars.2020.00431

Ross, R.E., Wort, E.J.G., Howell, K.L., 2019. Combining Distribution and Dispersal Models to Identify a Particularly Vulnerable Marine Ecosystem. Front. Mar. Sci. 6, 1–12. https://doi.org/10.3389/fmars.2019.00574

Sala, I., Caldeira, R.M.A., Estrada-allis, S.N., Froufe, E., Couvelard, X., 2013. Lagrangian transport pathways in the northeast Atlantic and their environmental impact 3, 40–60. https://doi.org/10.1215/21573689-2152611

Sala, I., Harrison, C.S., Caldeira, R.M.A., 2016. The role of the Azores Archipelago in capturing and retaining incoming particles. J. Mar. Syst. 154, 146–156. https://doi.org/10.1016/j.jmarsys.2015.10.001

Salon, S., Cossarini, G., Bolzon, G., Feudale, L., Lazzari, P., Teruzzi, A., Solidoro, C., Crise, A., 2019. Novel metrics based on biogeochemical argo data to improve the model uncertainty evaluation of the cmems mediterranean marine ecosystem forecasts. Ocean Sci. 15, 997–1022. https://doi.org/10.5194/os-15-997-2019

Samuelsen, A., Schrum, C., Yumruktepe, V.Ç., Daewel, U., Roberts, E.M., 2022. Environmental Change at Deep-Sea Sponge Habitats Over the Last Half Century: A Model Hindcast Study for the Age of Anthropogenic Climate Change. Front. Mar. Sci. 9, 1–17. https://doi.org/10.3389/fmars.2022.737164

Santos, M., Moita, M.T., Bashmachnikov, I., Menezes, G.M., Carmo, V., Loureiro, C.M., Mendonça, A., Silva, A.F., Martins, A., 2013. Phytoplankton variability and oceanographic conditions at Condor seamount, Azores (NE Atlantic). Deep. Res. Part II Top. Stud. Oceanogr. 98, 52–62. https://doi.org/10.1016/j.dsr2.2013.05.037

Santos, R., Medeiros-Leal, W., Pinho, M., 2020. Stock assessment prioritization in the Azores: procedures, current challenges and recommendations. Arquipelago. Life Mar. Sci. 37, 20–45.

Santos, R., Pinho, M., Melo, O., Gonçalves, J., Leocádio, A., Menezes, G., Isidro, E., 2019. Biological and ecological aspects of the deep-water red crab populations inhabiting isolated seamounts to the west of the Azores (Mid-Atlantic Ridge). Fish. Oceanogr. 28, 723–734. https://doi.org/10.1111/fog.12454

Sarmiento, J.L., Slater, R.D., Fasham, M.J.R., Ducklow, W., H., Toggweiler, J.. R., Evans, G.. T., 1993. Seasonal three-dimensional ecossystem Model. Global Biogeochem. Cycles 7, 417–450.

Sathyendranath, S., Brewin, R.J.W., Brockmann, C., Brotas, V., Calton, B., Chuprin, A., Cipollini, P., Couto, A.B., Dingle, J., Doerffer, R., Donlon, C., Dowell, M., Farman, A., Grant, M., Groom, S., Horseman, A., Jackson, T., Krasemann, H., Lavender, S., Martinez-Vicente, V., Mazeran, C., Mélin, F., Moore, T.S., Müller, D., Regner, P., Roy, S., Steele, C.J., Steinmetz, F., Swinton, J., Taberner, M., Thompson, A., Valente, A., Zühlke, M., Brando, V.E., Feng, H., Feldman, G., Franz, B.A., Frouin, R., Gould, R.W., Hooker, S.B., Kahru, M., Kratzer, S., Mitchell, B.G., Muller-Karger, F.E., Sosik, H.M., Voss, K.J., Werdell, J., Platt, T., 2019. An ocean-colour time series for use in climate studies: The experience of the ocean-colour climate change initiative (OC-CCI). Sensors (Switzerland) 19. https://doi.org/10.3390/s19194285

Sathyendranath, S., Jackson, T., Brockmann, C., Brotas, V., Calton, B., Chuprin, A., Clements, O., Cipollini, P., Danne, O., Dingle, J., Donlon, C., Grant, M., Groom, S., Krasemann, H., Lavender, S., Mazeran, C., Mélin, F., Müller, D., Steinmetz, F., Valente, A., Zühlke, M., Feldman, G., Franz, B., Frouin, R., Werdell, J., Platt, T., 2021. ESA Ocean Colour Climate Change Initiative (Ocean_Colour_cci): Version 5.0 Data. [WWW Document]. NERC EDS Cent. Environ. Data Anal. [dataset]. https://doi.org/https://catalogue.ceda.ac.uk/uuid/fa199424852d49f4ba85afddd850eae6

Selkoe, K.A., Toonen, R.J., 2011. Marine connectivity: A new look at pelagic larval duration and genetic metrics of dispersal. Mar. Ecol. Prog. Ser. 436, 291–305. https://doi.org/10.3354/meps09238

Shank, T.M., 2010. Mountauns in the Sea- seamounts Deep-ocean Laboratories of Faunal Connectivity, evolution, and endemism. Oceanography 23.

Sharada, M.K., Yajnik, K.S., Swathi, P.S., 2005. Evaluation of six relations of the kinetics of uptake by phytoplankton in multi-nutrient environment using JGOFS experimental results. Deep. Res. Part II Top. Stud. Oceanogr. 52, 1892–1909. https://doi.org/10.1016/j.dsr2.2005.06.006

Shen, M., Duan, H., Cao, Z., Xue, K., Loiselle, S., Yesou, H., 2017. Determination of the downwelling diffuse attenuation coefficient of lakewater with the sentinel-3A OLCI. Remote Sens. 9. https://doi.org/10.3390/rs9121246

Siddorn, J.R., Allen, J.I., Blackford, J.C., Gilbert, F.J., Holt, J.T., Holt, M.W., Osborne, J.P., Proctor, R., Mills, D.K., 2007. Modelling the hydrodynamics and ecosystem of the North-West European continental shelf for operational oceanography 65, 417–429. https://doi.org/10.1016/j.jmarsys.2006.01.018

Siegel, D.A., Buesseler, K.O., Behrenfeld, M.J., Benitez-Nelson, C.R., Boss, E., Brzezinski, M.A., Burd, A., Carlson, C.A., D'Asaro, E.A., Doney, S.C., Perry, M.J., Stanley, R.H.R., Steinberg, D.K., 2016. Prediction of the export and fate of global ocean net primary production: The exports science plan. Front. Mar. Sci. 3, 1–10. https://doi.org/10.3389/fmars.2016.00022

Silva, A., Brotas, V., Valente, A., Sá, C., Diniz, T., Patarra, R.F., álvaro, N. V., Neto, A.I., 2013. Coccolithophore species as indicators of surface oceanographic conditions in the vicinity of Azores islands. Estuar. Coast. Shelf Sci. 118, 50–59. https://doi.org/10.1016/j.ecss.2012.12.010

Simons, R.D., Siegel, D.A., Brown, K.S., 2013. Model sensitivity and robustness in the estimation of larval transport: A study of particle tracking parameters. J. Mar. Syst. 119–120, 19–29. https://doi.org/10.1016/j.jmarsys.2013.03.004

Sommer, U., Charalampous, E., Genitsaris, S., Moustaka-Gouni, M., 2017. Benefits, costs and taxonomic distribution of marine phytoplankton body size. J. Plankton Res. 39, 494–508. https://doi.org/10.1093/plankt/fbw071

Somoza, L., Medialdea, T., González, F.J., Calado, A., Afonso, A., Albuquerque, M., Asensio-Ramos, M., Bettencourt, R., Blasco, I., Candón, J.A., Carreiro-Silva, M., Cid, C., De Ignacio, C., López-Pamo, E., Machancoses, S., Ramos, B., Ribeiro, L.P., Rincón-Tomás, B., Santofimia, E., Souto, M., Tojeira, I., Viegas, C., Madureira, P., 2020. Multidisciplinary Scientific Cruise to the Northern Mid-Atlantic Ridge and Azores Archipelago. Front. Mar. Sci. 7, 1–9. https://doi.org/10.3389/fmars.2020.568035

Stark, J., Donlon, C., Martin, M., McCulloch, M., 2007. OSTIA : An operational, high resolution, real time, global sea surface temperature analysis systemOceans 07 IEEE Aberdeen, conference proceedings. Marine challenges: coastline to deep sea. Aberdeen, Scotland.IEEE.

Stevens, B.G., Guida, V., 2016. Depth and temperature distribution, morphometrics, and sex ratios of red deepsea crab (*Chaceon quinquedens*) at 4 sampling sites in the mid-atlantic bight. Fish. Bull. 114, 343–359. https://doi.org/10.7755/FB.114.3.7

Stramma, L., Siedler, G., 1988. Seasonal changes in the North Atlantic subtropical gyre. J. Geophys. Res. 93, 8111. https://doi.org/10.1029/jc093ic07p08111

Stratoudakis, Y., Hilario, A., Ribeiro, C., Abecasis, D., Gonçalves, E.J., Andrade, F., Carreira, G.P., Gonçalves, J.M.S., Freitas, L., Menezes, L., Batista, M.I., Henriques, M., Oliveira, P.B., Oliveira, P., Afonso, P., 2019. Environmental representativity in marine protected area networks over large and partly unexplored seascapes. Glob. Ecol. Conserv. 17. https://doi.org/10.1016/j.gecco.2019.e00545

Sulkin, S., van Heukelem, W., 1980. Ecological and Evolutionary Significance of Nutritional Flexibility in Planktotrophic Larvae of the Deep Sea Red Crab Geryon quinquedens and the Stone Crab (Menippe mercenaria). Mar. Ecol. Prog. Ser. 2, 91–95. https://doi.org/10.3354/meps002091

Sunda, W.G., Hardison, D.R., 2010. Evolutionary tradeoffs among nutrient acquisition, cell size, and grazing defense in marine phytoplankton promote ecosystem stability. Mar. Ecol. Prog. Ser. 401, 63–76. https://doi.org/10.3354/meps08390

Sverdrup, H.U., 1953. On conditions for the vernal blooming of phytoplankton. ICES J. Mar. Sci. 18, 287–295. https://doi.org/10.1093/icesjms/18.3.287

Swearer, S.E., Treml, E.A., Shima, J.S., 2019. A review of biophysical models of marine larval dispersal. Oceanogr. Mar. Biol. 57, 325–356. https://doi.org/10.1201/9780429026379-7

Taylorl, A.H., Geider, R.J., Gilbertl, F.J.H., 1997. Seasonal and latitudinal dependencies of phytoplankton carbon-to-chlorophyll a ratios: results of a modelling study. Mar. Ecol. Prog. Ser. 152, 51–66.

Teira, E., Mouriño, B., Marañón, E., Pérez, V., Pazó, M.J., Serret, P., De Armas, D., Escánez, J., Woodward, E.M.S., Fernández, E., 2005. Variability of chlorophyll and primary production in the Eastern North Atlantic Subtropical Gyre: Potential factors affecting phytoplankton activity. Deep. Res. Part I Oceanogr. Res. Pap. 52, 569–588. https://doi.org/10.1016/j.dsr.2004.11.007

Tempera, F., Atchoi, E., Amorim, P., Gomes-pereira, J., 2013. Adding new Macaronesian habitat types from the Azores. https://doi.org/10.13140/RG.2.1.3479.8808

Thomson, R.E., Fine, I. V., 2003. Estimating mixed layer depth from oceanic profile data. J. Atmos.

Ocean. Technol. 20, 319–329. https://doi.org/10.1175/1520-0426(2003)020<0319:EMLDFO>2.0.CO;2

Tirok, K., Scharler, U.M., 2013. Dynamics of pelagic and benthic microalgae during drought conditions in a shallow estuarine lake (Lake St. Lucia). Estuar. Coast. Shelf Sci. 118, 86–96. https://doi.org/10.1016/j.ecss.2012.12.023

Tomlinson, M.C., Stumpf, R.P., Vogel, R.L., 2019. Approximation of diffuse attenuation, Kd, for MODIS high-resolution bands. Remote Sens. Lett. 10, 178–185. https://doi.org/10.1080/2150704X.2018.1536301

Toublanc, F., Ayoub, N.K., Lyard, F., Marsaleix, P., Allain, D.J., 2018. Tidal downscaling from the open ocean to the coast: a new approach applied to the Bay of Biscay. Ocean Model. 124, 16–32. https://doi.org/10.1016/j.ocemod.2018.02.001

Trancoso, A.R., Braunschweig, F., Chambel Leitão, P., Obermann, M., Neves, R., 2009. An advanced modelling tool for simulating complex river systems. Sci. Total Environ. 407, 3004–3016. https://doi.org/10.1016/j.scitotenv.2009.01.015

Treml, E.A., Roberts, J.J., Chao, Y., Halpin, P.N., Possingham, H.P., Riginos, C., 2012. Reproductive output and duration of the pelagic larval stage determine seascape-wide connectivity of marine populations. Integr. Comp. Biol. 52, 525–537. https://doi.org/10.1093/icb/ics101

Triay-Portella, R., Pajuelo, J.G., González, J.A., 2017. Spatio- temporal variation in biomass of the deep- sea red crab *Chaceon affinis* in Gran Canaria Island (Canary Islands, Eastern- Central Atlantic). Mar. Ecol. 38. https://doi.org/https://doi.org/10.1111/maec.12462 wileyonlinelibrary.com/journal/maec

Tuset, V.M., Espinosa, D.I., García-Mederos, A., Santana, J.I., González, J.A., 2011. Egg development and fecundity estimation in deep-sea red crab, *Chaceon affinis* (Geryonidae), off the Canary Islands (NE Atlantic). Fish. Res. 109, 373–378. https://doi.org/10.1016/j.fishres.2011.02.021

Valente, A. dos S.F.G., 2013. Climatic patterns and physical controls of chlorophyll-a in the northeast Atlantic. Univ. Azores. University of the Azores. https://doi.org/http://hdl.handle.net/10400.3/3077

Vallino, J.J., 2000. Improving marine ecosystem models: Use of data assimilation and mesocosm experiments. J. Mar. Res. 58, 117–164. https://doi.org/10.1357/002224000321511223

van Sebille, E., Griffies, S.M., Abernathey, R., Adams, T.P., Berloff, P., Biastoch, A., Blanke, B., Chassignet, E.P., Cheng, Y., Cotter, C.J., Deleersnijder, E., Döös, K., Drake, H.F., Drijfhout, S., Gary, S.F., Heemink, A.W., Kjellsson, J., Koszalka, I.M., Lange, M., Lique, C., MacGilchrist, G.A., Marsh, R., Mayorga Adame, C.G., McAdam, R., Nencioli, F., Paris, C.B., Piggott, M.D., Polton, J.A., Rühs, S., Shah, S.H.A.M., Thomas, M.D., Wang, J., Wolfram, P.J., Zanna, L., Zika, J.D., 2018. Lagrangian ocean analysis: Fundamentals and practices. Ocean Model. 121, 49–

75. https://doi.org/10.1016/j.ocemod.2017.11.008

Vasile, R., Hartmann, K., Hobday, A.J., Oliver, E., Tracey, S., 2017. Evaluation of hydrodynamic ocean models as a first step in larval dispersal modelling 1–42.

Vic, C., Gula, J., Roullet, G., Pradillon, F., 2018. Dispersion of deep-sea hydrothermal vent effluents and larvae by submesoscale and tidal currents. Deep. Res. Part I Oceanogr. Res. Pap. 133, 1–18. https://doi.org/10.1016/j.dsr.2018.01.001

Vichi, M., Masina, S., Navarra, A., 2007a. A generalized model of pelagic biogeochemistry for the global ocean ecosystem. Part II: Numerical simulations. J. Mar. Syst. 64, 110–134. https://doi.org/10.1016/j.jmarsys.2006.03.014

Vichi, M., Pinardi, N., Masina, S., 2007b. A generalized model of pelagic biogeochemistry for the global ocean ecosystem. Part I: Theory. J. Mar. Syst. https://doi.org/10.1016/j.jmarsys.2006.03.006

Viegas, C.N., Nunes, S., Fernandes, R., Neves, R., 2009. Streams contribution on bathing water quality after rainfall events in Costa do Estoril - A tool to implement an alert system for bathing water quality. J. Coast. Res. 2009, 1691–1695.

Vieira, R.P., Bett, B.J., Jones, D.O.B., Durden, J.M., Morris, K.J., Cunha, M.R., Trueman, C.N., Ruhl, H.A., 2020. Deep-sea sponge aggregations (*Pheronema carpenteri*) in the Porcupine Seabight (NE Atlantic) potentially degraded by demersal fishing. Prog. Oceanogr. 183, 102189. https://doi.org/10.1016/j.pocean.2019.102189

Wang, S., Kenchington, E., Wang, Z., Davies, A.J., 2021. Life in the Fast Lane: Modeling the Fate of Glass Sponge Larvae in the Gulf Stream. Front. Mar. Sci. 8, 1–24. https://doi.org/10.3389/fmars.2021.701218

Wang, S., Kenchington, E.L., Wang, Z., Yashayaev, I., Davies, A.J., 2020. 3-D ocean particle tracking modeling reveals extensive vertical movement and downstream interdependence of closed areas in the northwest Atlantic. Sci. Rep. 10, 1–18. https://doi.org/10.1038/s41598-020-76617-x

Ward, B.A., Friedrichs, M.A.M., Anderson, T.R., Oschlies, A., 2010. Parameter optimisation techniques and the problem of underdetermination in marine biogeochemical models. J. Mar. Syst. https://doi.org/10.1016/j.jmarsys.2009.12.005

Ward, B.A., Schartau, M., Oschlies, A., Martin, A.P., Follows, M.J., Anderson, T.R., 2013. When is a biogeochemical model too complex? Objective model reduction and selection for North Atlantic time-series sites. Prog. Oceanogr. 116, 49–65. https://doi.org/10.1016/j.pocean.2013.06.002

Weber, T.S., Deutsch, C., 2010. Ocean nutrient ratios governed by plankton biogeography. Nature 467, 550–554. https://doi.org/10.1038/nature09403

Weinberg, J.R., Dahlgren, T.G., Trowbridge, N., Halanych, K.M., 2003. Genetic differences within and between species of deep-sea crabs (Chaceon) from the North Atlantic Ocean. Biol. Bull. 204, 318–326. https://doi.org/10.2307/1543602

Werdell, P.J., Bailey, S.W., 2005. An improved in-situ bio-optical data set for ocean color algorithm development and satellite data product validation. Remote Sens. Environ. 98, 122–140. https://doi.org/10.1016/j.rse.2005.07.001

Werner, F.E., Cowen, R.K., Paris, C.B., 2007. Coupled Biological and Physical Models. Oceanography 20, 54–69.

White, M., 2003. Comparison of near seabed currents at two locations in the Porcupine Sea Bight - Implications for benthic fauna. J. Mar. Biol. Assoc. United Kingdom 83, 683–686. https://doi.org/10.1017/S0025315403007641h

Wong, A.P.S., Wijffels, S.E., Riser, S.C., Pouliquen, S., Hosoda, S., Roemmich, D., Gilson, J., Johnson, G.C., Martini, K., Murphy, D.J., Scanderbeg, M., Bhaskar, T.V.S.U., Buck, J.J.H., Merceur, F., Carval, T., Maze, G., Cabanes, C., André, X., Belbéoch, M., Ignaszewski, M., Baringer, M.O.N., Schmid, C., Lyman, J.M., Mctaggart, K.E., Purkey, S.G., Zilberman, N., Alkire, M.B., Swift, D., Owens, W.B., Jayne, S.R., Hersh, C., Robbins, P., West-mack, D., Bahr, F., Yoshida, S., Sutton, P.J.H., Cancouët, R., Coatanoan, C., Dobbler, D., Juan, A.G., Gourrion, J., Kolodziejczyk, N., Bernard, V., Bourlès, B., Loch, S.G., Mowat, M., Turton, J., Rao, E.P.R., 2020. Argo Data 1999 – 2019 : Two Million Temperature-Salinity Profiles and Subsurface Velocity Observations From a Global Array of Profiling Floats Edited by : 7, 1–23. https://doi.org/10.3389/fmars.2020.00700

Wood, S., Paris, C.B., Ridgwell, A., Hendy, E.J., 2014. Modelling dispersal and connectivity of broadcast spawning corals at the global scale. Glob. Ecol. Biogeogr. 23, 1–11. https://doi.org/10.1111/geb.12101

Xavier, J.R., Rees, D.J., Pereira, R., Colaço, A., Pham, C.K., Carvalho, F.C., 2021. Diversity, Distribution and Phylogenetic Relationships of Deep-Sea Lithistids (Porifera, Heteroscleromorpha) of the Azores Archipelago. Front. Mar. Sci. 8. https://doi.org/10.3389/fmars.2021.600087

Xavier, J.R., Tojeira, I., Van Soest, R.W.M., 2015. On a hexactinellid sponge aggregation at the Great Meteor seamount (North-east Atlantic). J. Mar. Biol. Assoc. United Kingdom 95, 1389–1394. https://doi.org/10.1017/S0025315415000685

Xi, H., Losa, S.N., Mangin, A., Soppa, M.A., Garnesson, P., Demaria, J., Liu, Y., d'Andon, O.H.F., Bracher, A., 2020. Global retrieval of phytoplankton functional types based on empirical orthogonal functions using CMEMS GlobColour merged products and further extension to OLCI data. Remote Sens. Environ. 240, 111704. https://doi.org/10.1016/j.rse.2020.111704

Xu, Q., Lin, H., Liu, Y., Lv, X., Cheng, Y., 2008. Data assimilation in a coupled physical-biological model for the Bohai Sea and the Northern Yellow Sea. Mar. Freshw. Res. 59, 529–539. https://doi.org/10.1071/MF07144

Yamanaka, Y., Yoshie, N., Fujii, M., Aita, M.N., Kishi, M.J., 2004. An ecosystem model coupled with nitrogen-silicon-carbon cycles applied to station A7 in the northwestern Pacific. J. Oceanogr. 60, 227–241. https://doi.org/10.1023/B:JOCE.0000038329.91976.7d

Yearsley, J.M., Sigwart, J.D., 2011. Larval transport modeling of deep-sea invertebrates can aid the search for undiscovered populations. PLoS One 6. https://doi.org/10.1371/journal.pone.0023063

Yool, A., Popova, E.E., Anderson, T.R., 2013. MEDUSA-2.0: An intermediate complexity biogeochemical model of the marine carbon cycle for climate change and ocean acidification studies. Geosci. Model Dev. 6, 1767–1811. https://doi.org/10.5194/gmd-6-1767-2013

Yool, A., Tyrrell, T., 2003. Role of diatoms in regulating the ocean's silicon cycle. Global Biogeochem. Cycles 17. https://doi.org/10.1029/2002gb002018

Young, C.M., He, R., Emlet, R.B., Li, Y., Qian, H., Arellano, S.M., Van Gaest, A., Bennett, K.C., Wolf, M., Smart, T.I., Rice, M.E., 2012. Dispersal of deep-sea larvae from the intra-American seas: Simulations of trajectories using ocean models. Integr. Comp. Biol. 52, 483–496. https://doi.org/10.1093/icb/ics090

Zhang, R.H., Tian, F., Wang, X., 2018. A New Hybrid Coupled Model of Atmosphere, Ocean Physics, and Ocean Biogeochemistry to Represent Biogeophysical Feedback Effects in the Tropical Pacific. J. Adv. Model. Earth Syst. 10, 1901–1923. https://doi.org/10.1029/2017MS001250

List of Figures

List of Tables

Annex I

Monthly Percentile 90 for Phytoplankton at surface 2017

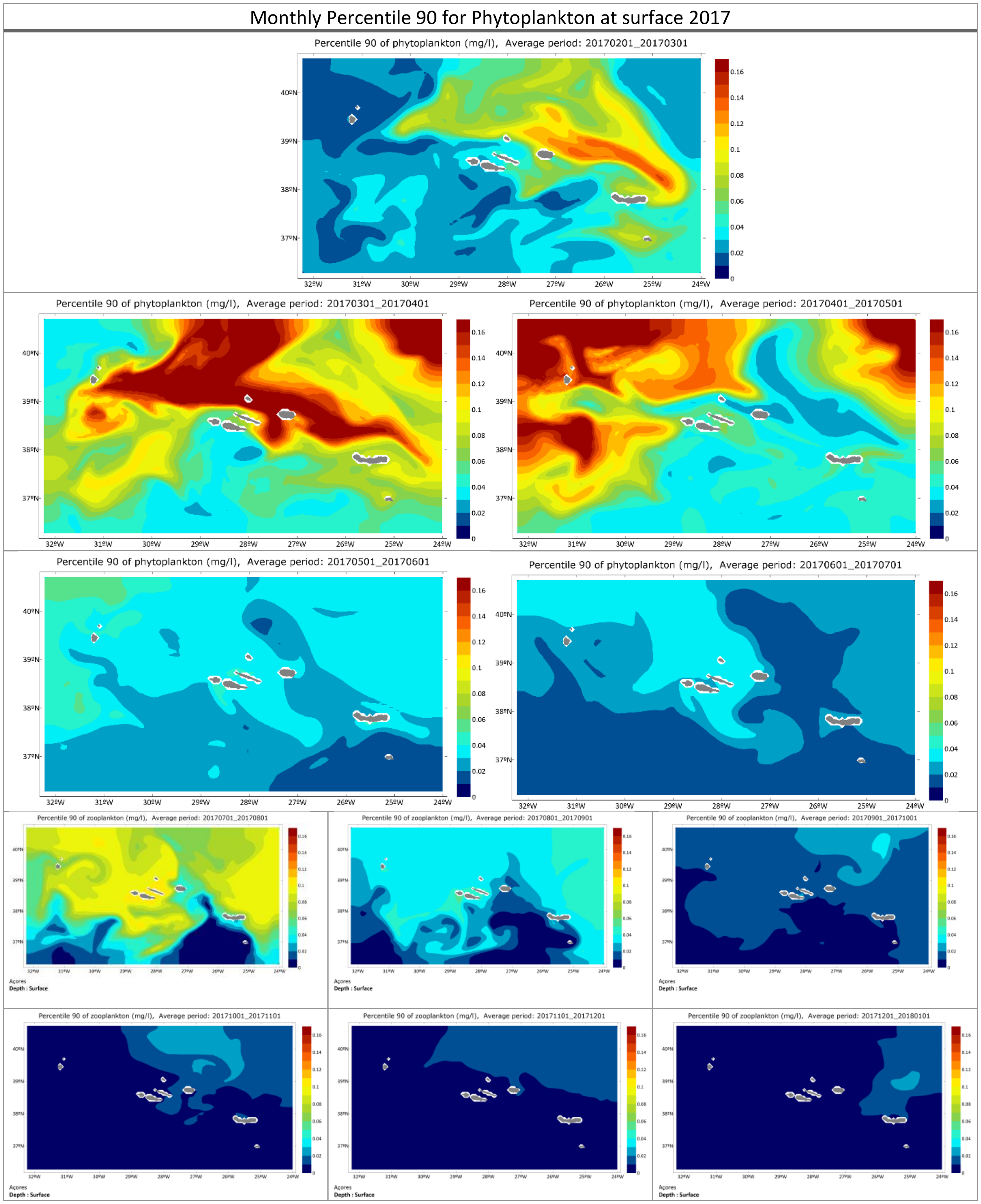

Figure A. 1- Monthly Percentile 90 for phytoplankton model results at surface from February 2017 to December 2018

Zooplankton at surface 2017

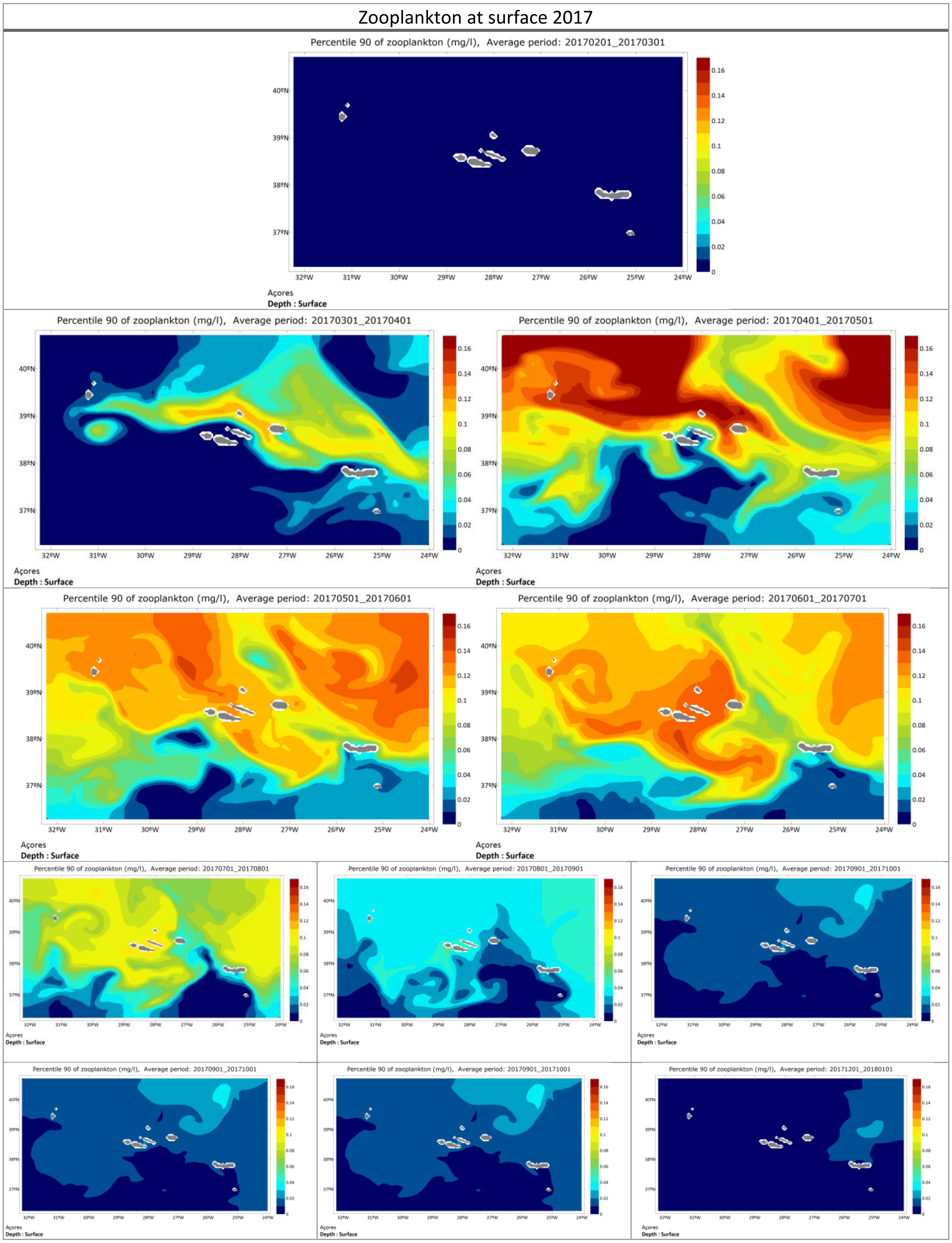

Percentile 90 of zooplankton (mg/l), Average period: 20170201_20170301

Percentile 90 of zooplankton (mg/l), Average period: 20170301_20170401

Percentile 90 of zooplankton (mg/l), Average period: 20170401_20170501

Percentile 90 of zooplankton (mg/l), Average period: 20170501_20170601

Percentile 90 of zooplankton (mg/l), Average period: 20170601_20170701

Percentile 90 of zooplankton (mg/l), Average period: 20170701_20170801

Percentile 90 of zooplankton (mg/l), Average period: 20170801_20170901

Percentile 90 of zooplankton (mg/l), Average period: 20170901_20171001

Percentile 90 of zooplankton (mg/l), Average period: 20170901_20171001

Percentile 90 of zooplankton (mg/l), Average period: 20170901_20171001

Percentile 90 of zooplankton (mg/l), Average period: 20171201_20180101

Figure A. 2- Monthly Percentile 90 for zooplankton model results at surface from February 2017 to December 2017

Nitrate at surface 2017

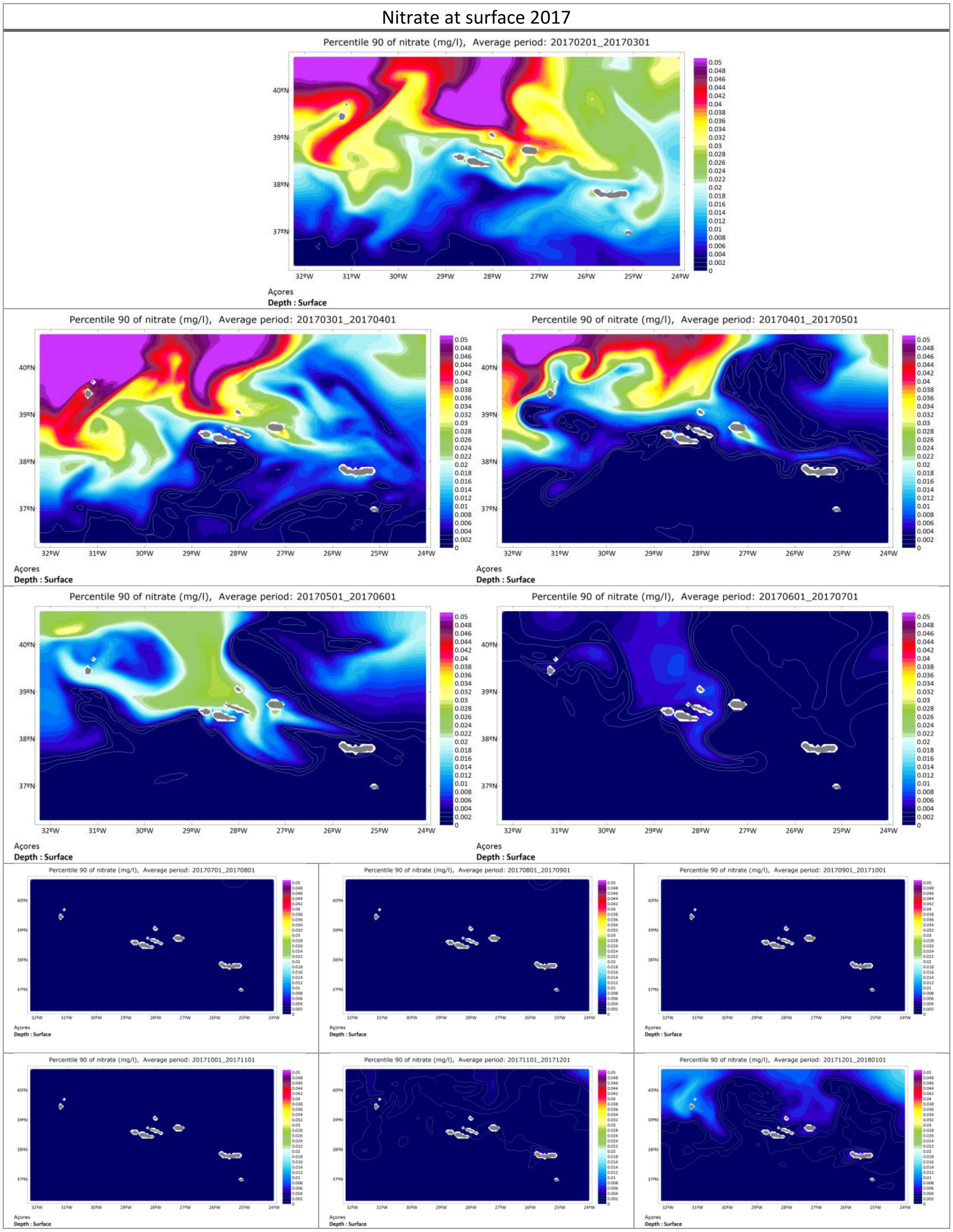

Percentile 90 of nitrate (mg/l), Average period: 20170201_20170301

Percentile 90 of nitrate (mg/l), Average period: 20170301_20170401

Percentile 90 of nitrate (mg/l), Average period: 20170401_20170501

Percentile 90 of nitrate (mg/l), Average period: 20170501_20170601

Percentile 90 of nitrate (mg/l), Average period: 20170601_20170701

Percentile 90 of nitrate (mg/l), Average period: 20170701_20170801

Percentile 90 of nitrate (mg/l), Average period: 20170801_20170901

Percentile 90 of nitrate (mg/l), Average period: 20170901_20171001

Percentile 90 of nitrate (mg/l), Average period: 20171001_20171101

Percentile 90 of nitrate (mg/l), Average period: 20171101_20171201

Percentile 90 of nitrate (mg/l), Average period: 20171201_20180101

Figure A. 3- Monthly Percentile 90 for nitrate model results at surface from February 2017 to December 2017

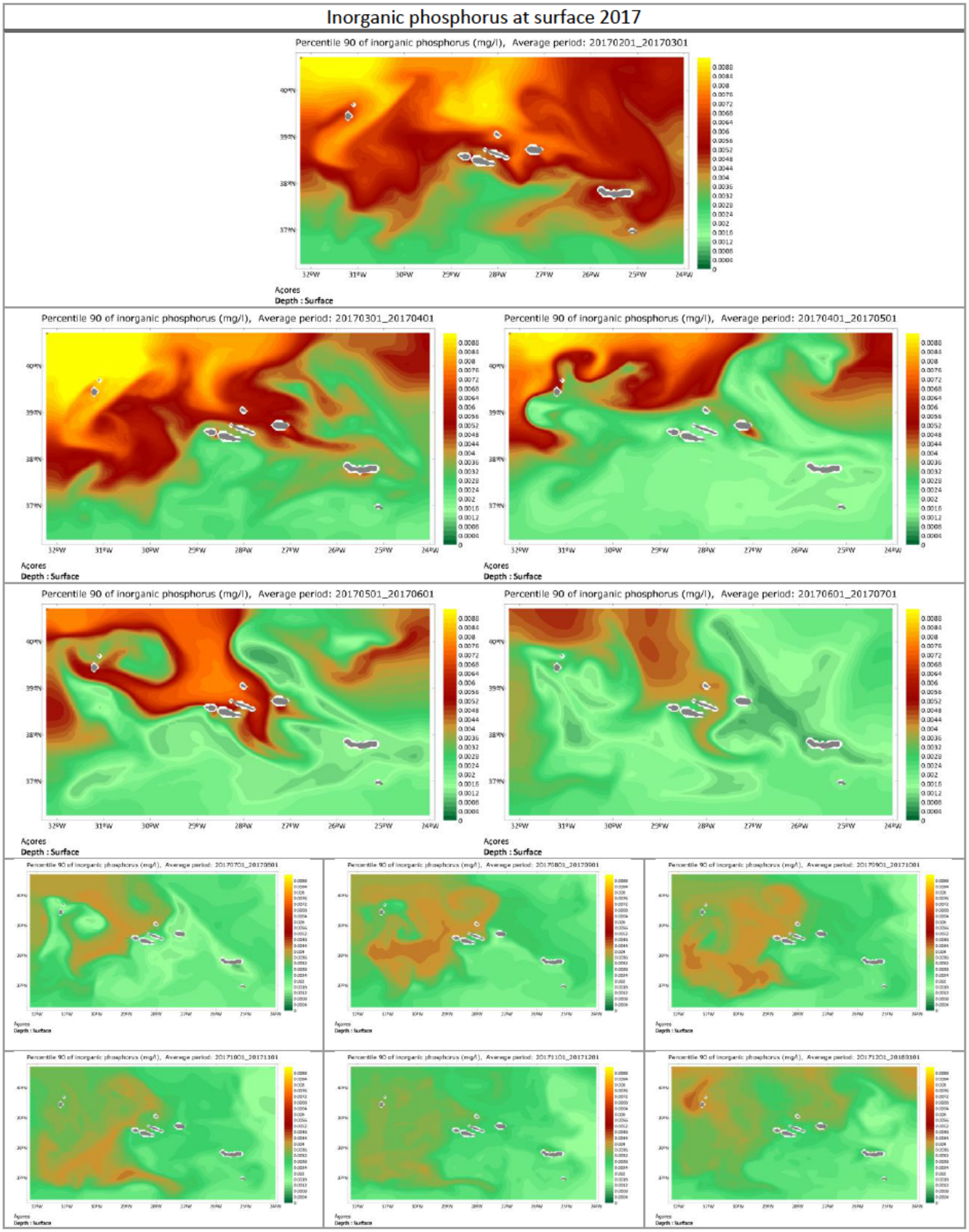

Inorganic phosphorus at surface 2017

Percentile 90 of inorganic phosphorus (mg/l), Average period: 20170201_20170301

Percentile 90 of inorganic phosphorus (mg/l), Average period: 20170301_20170401

Percentile 90 of inorganic phosphorus (mg/l), Average period: 20170401_20170501

Percentile 90 of inorganic phosphorus (mg/l), Average period: 20170501_20170601

Percentile 90 of inorganic phosphorus (mg/l), Average period: 20170601_20170701

Percentile 90 of inorganic phosphorus (mg/l), Average period: 20170701_20170801

Percentile 90 of inorganic phosphorus (mg/l), Average period: 20170801_20170901

Percentile 90 of inorganic phosphorus (mg/l), Average period: 20170901_20171001

Percentile 90 of inorganic phosphorus (mg/l), Average period: 20171001_20171101

Percentile 90 of inorganic phosphorus (mg/l), Average period: 20171101_20171201

Percentile 90 of inorganic phosphorus (mg/l), Average period: 20171201_20180101

Figure A. 4- Monthly Percentile 90 for inorganic phosphorus model results at surface from February 2017 to December 2017

Dissolved silica at surface 2017

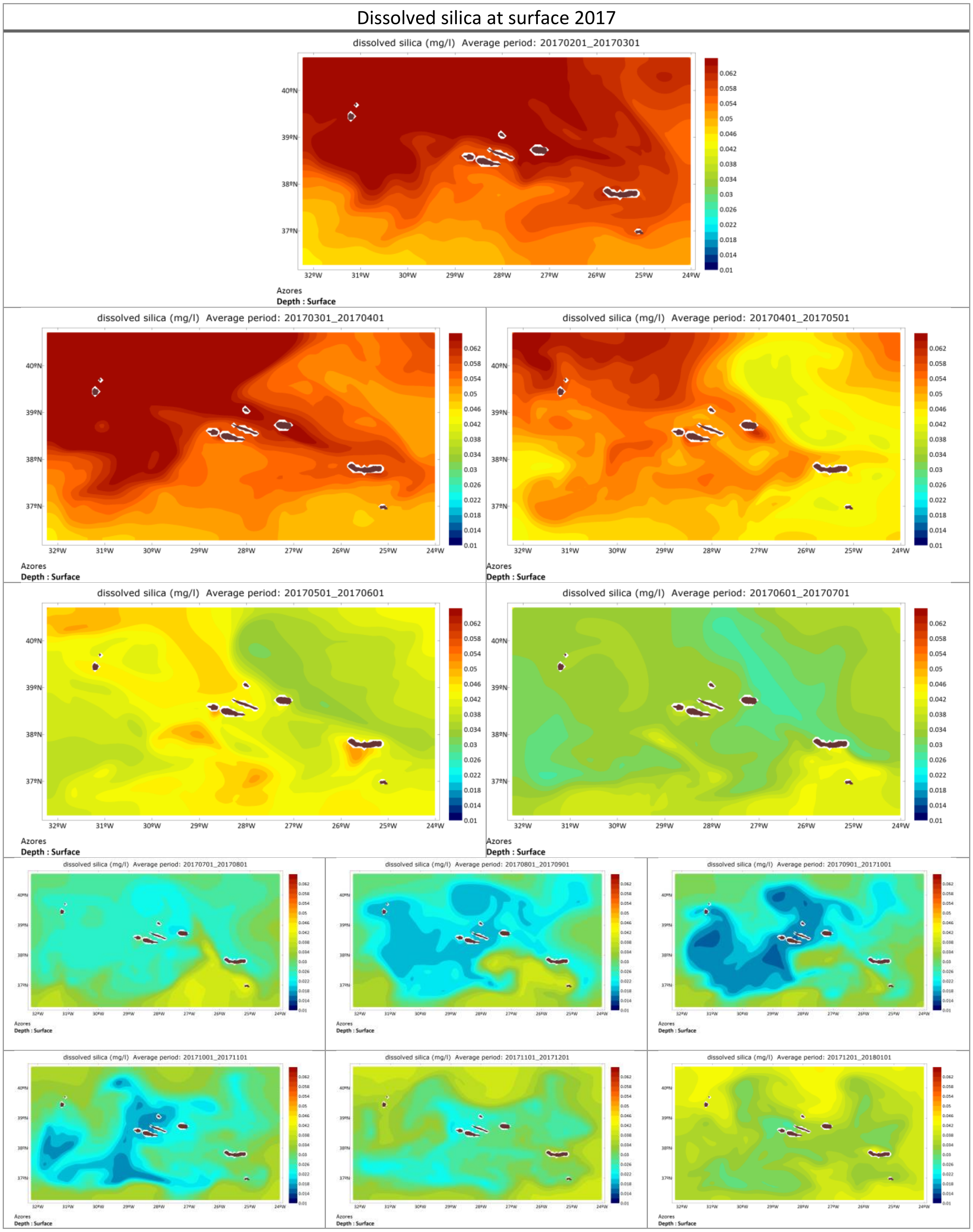

Figure A. 5- Monthly average for dissolved silica at the surface from February to December 2017

Monthly average Dissolved oxygen 2018 at 500meters depth

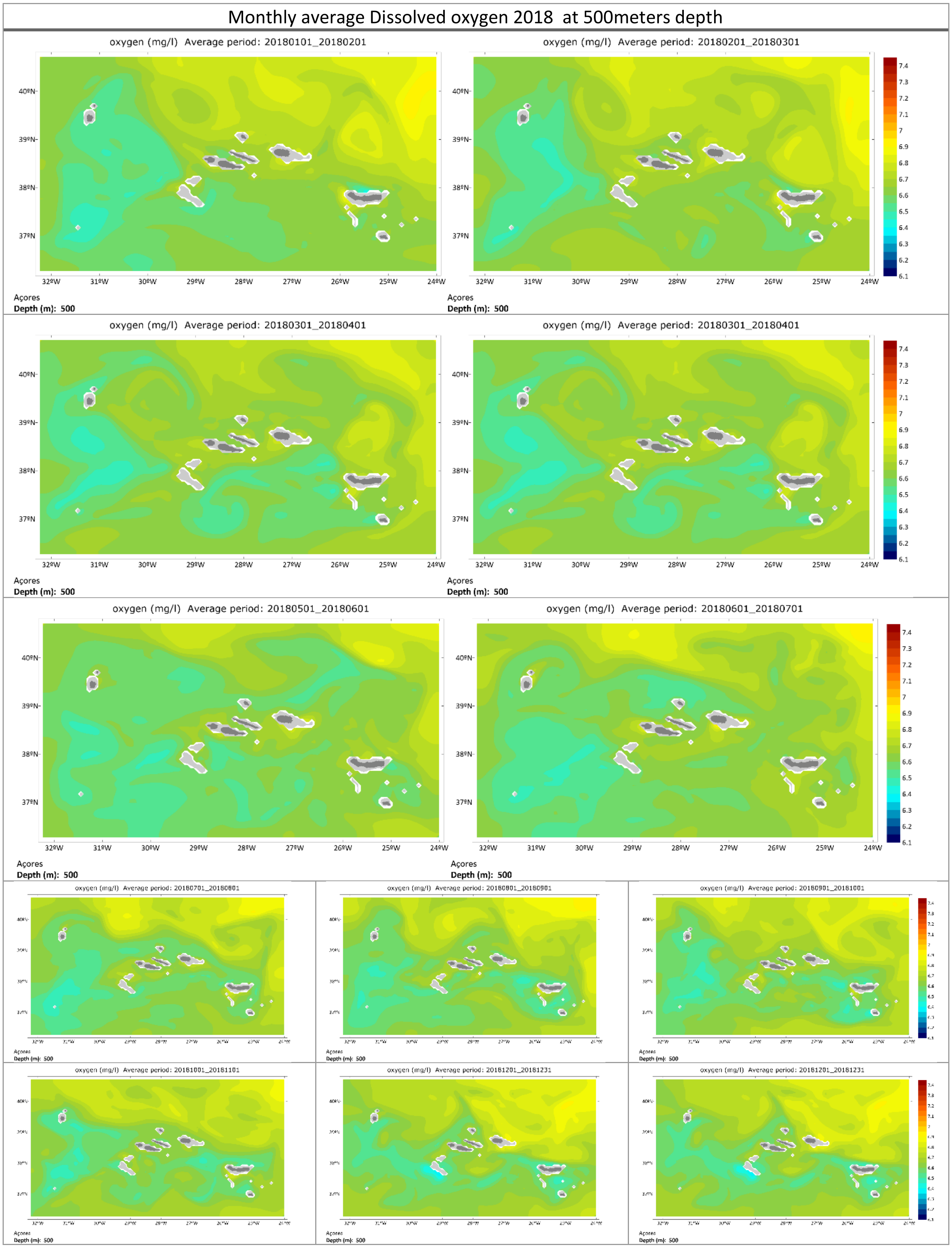

Figure A. 6- Monthly average for dissolved silica at the surface from January to December 2017

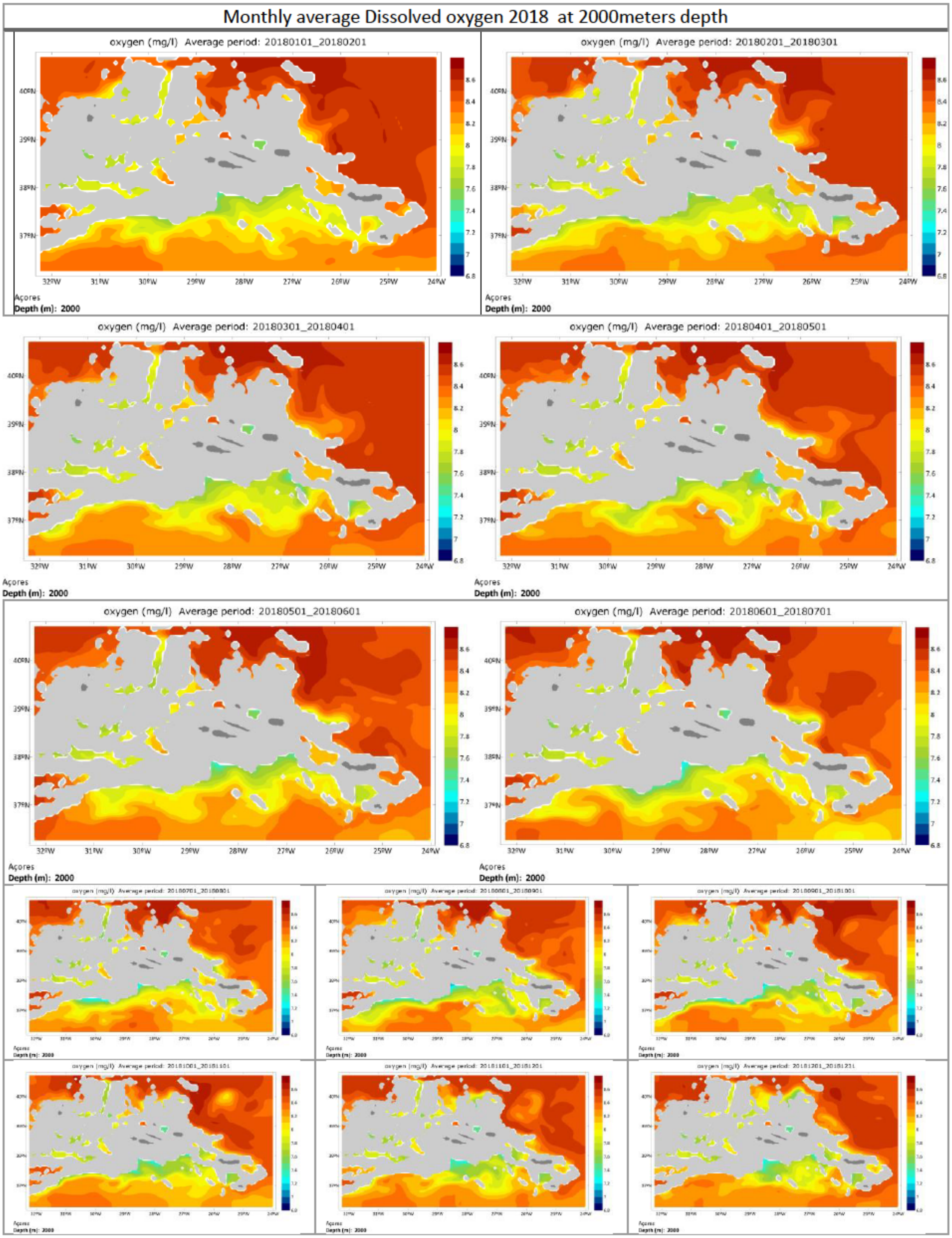

Figure A. 7- Monthly average for dissolved oxygen model results at 2000 meters depth from January to December 2018

Meridional and zonal sections of model results: monthly average

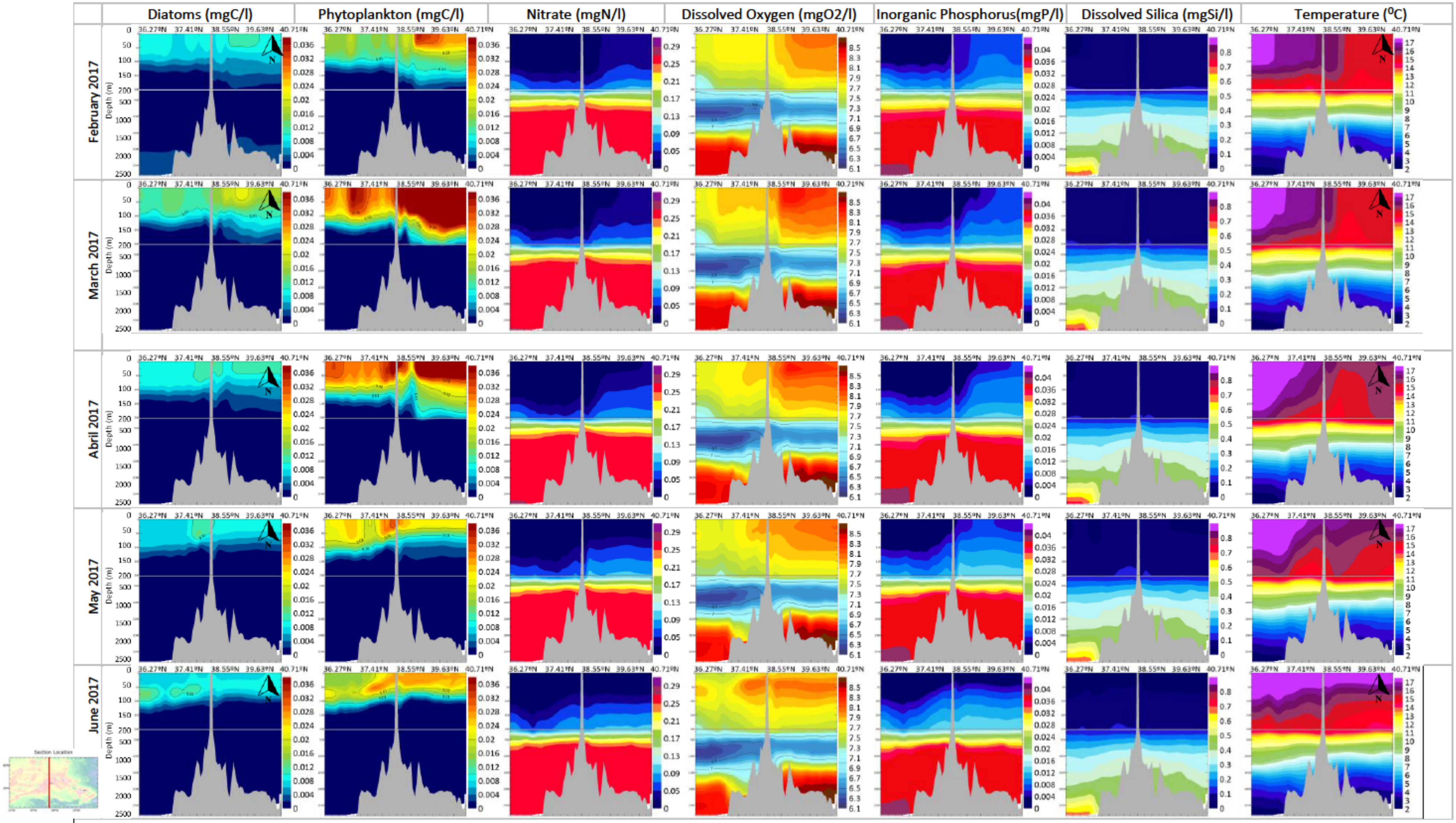

Figure B. 1 - *Monthly average of model results from February 2017 to June 2017, for diatoms (mgC/l), small phytoplankton (mgC/l), nitrate (mgN/l), dissolved oxygen (mgO2/l), inorganic phosphorus (mgP/l), dissolved Silica (mgSi/l), and temperature (ºC) along water column (from surface 3000meters depth), along the meridional section at -28.5ºW, from 36.27ºN to 40.71ºN. Depth profiles present a higher resolution until 250 meters depth, and less resolution from 250 meters until 3000 meters depth.*

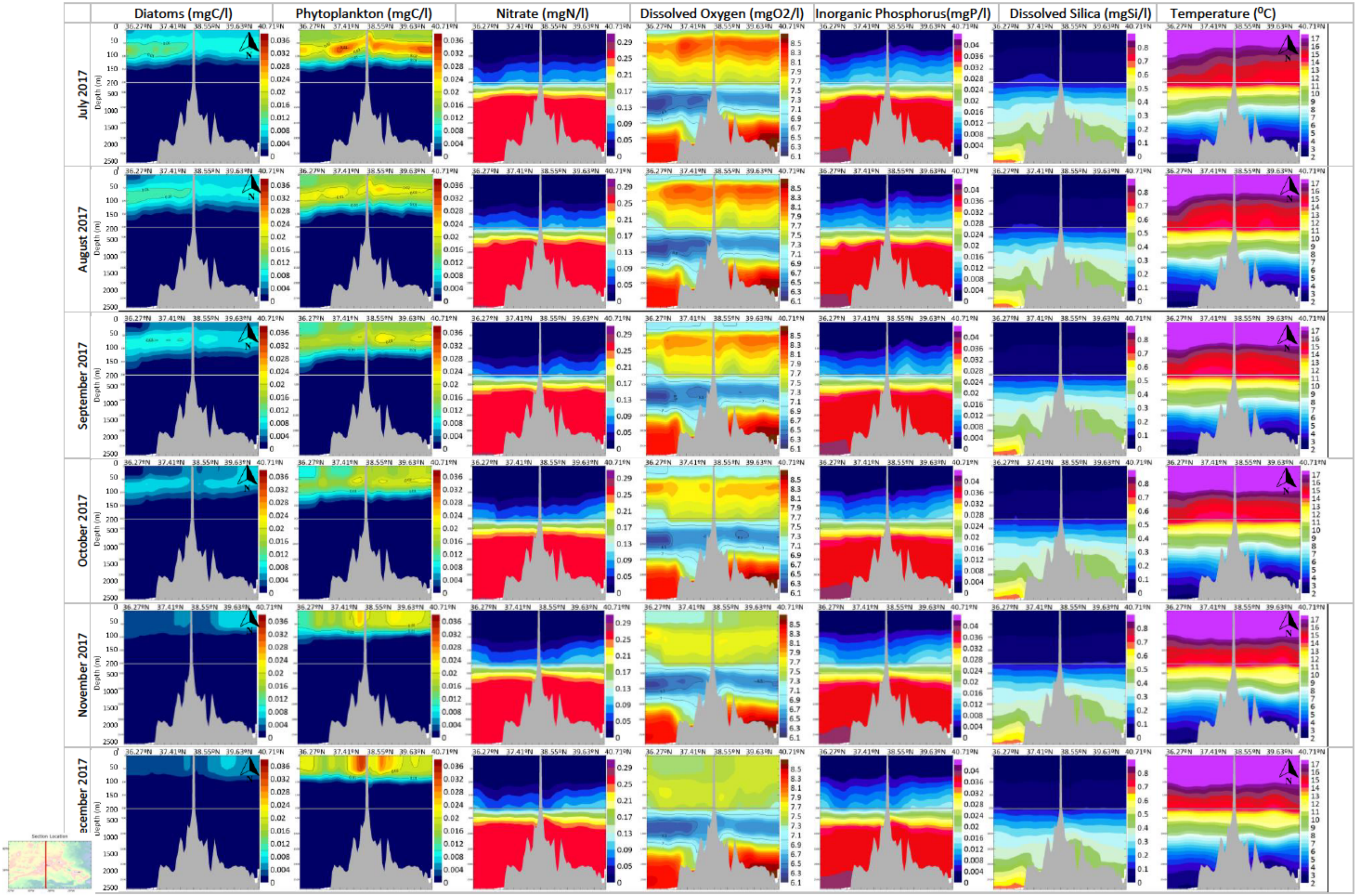

Figure B. 2- *Monthly average of model results from July 2017 to December 2017, for diatoms (mgC/l), small phytoplankton (mgC/l), nitrate (mgN/l), dissolved oxygen (mgO2/l), inorganic phosphorus (mgP/l), dissolved Silica (mgSi/l), and temperature (⁰C) along water column (from surface 3000meters depth), along the meridional section at -28.5⁰W, from 36.27⁰N to 40.71⁰N. Depth profiles present a higher resolution until 250 meters depth, and less resolution from 250 meters until 3000 meters depth*

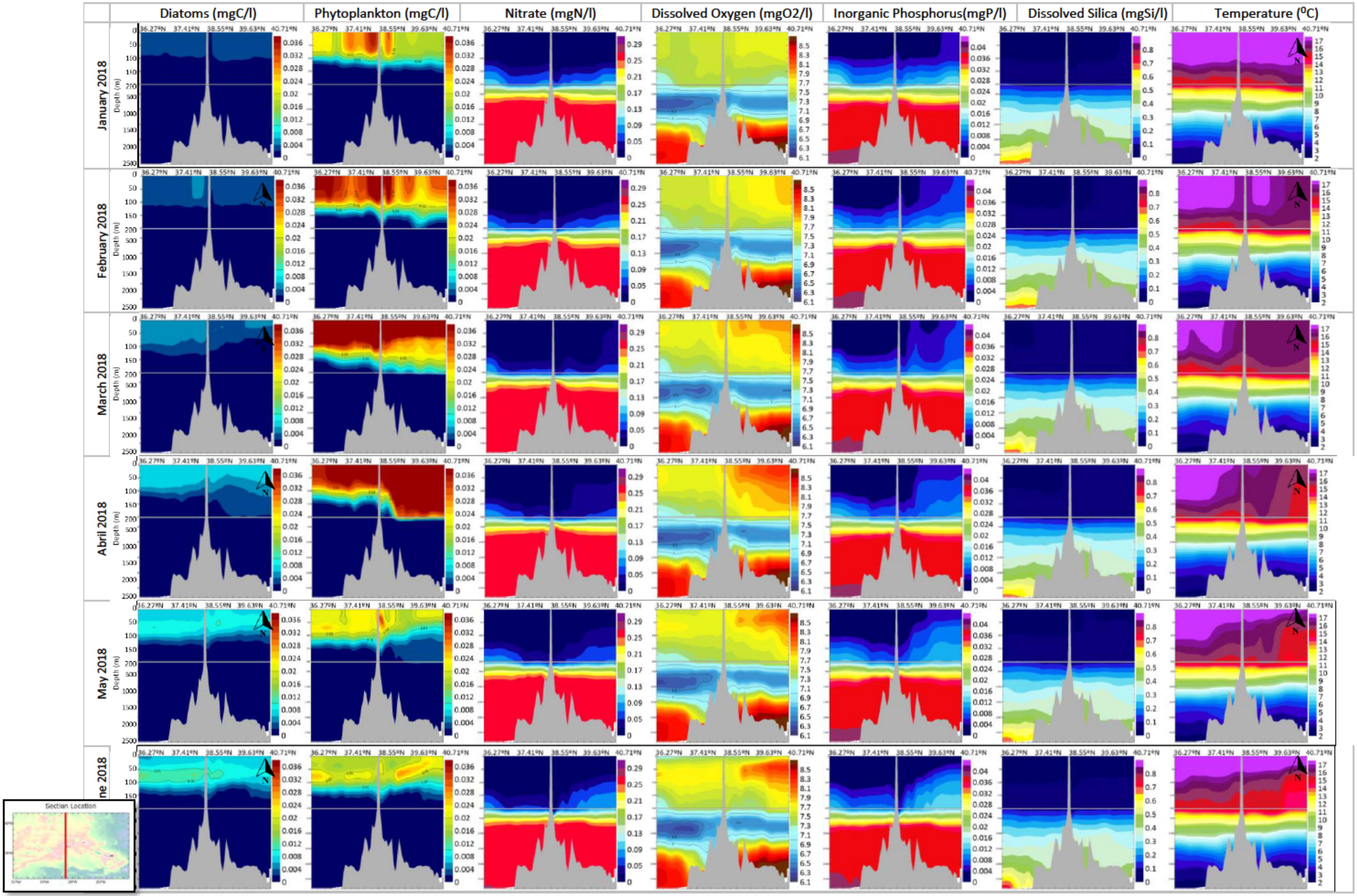

Figure B. 3- *Monthly average of model results from January 2018 to June 2018, for diatoms (mgC/l), small phytoplankton (mgC/l), nitrate (mgN/l), dissolved oxygen (mgO2/l), inorganic phosphorus (mgP/l), dissolved Silica (mgSi/l), and temperature (ºC) along water column (from surface 3000meters depth), along the meridional section at -28.5ºW, from 36.27ºN to 40.71N.º Depth profiles present a higher resolution until 250 meters depth, and less resolution from 250 meters until 3000 meters depth*

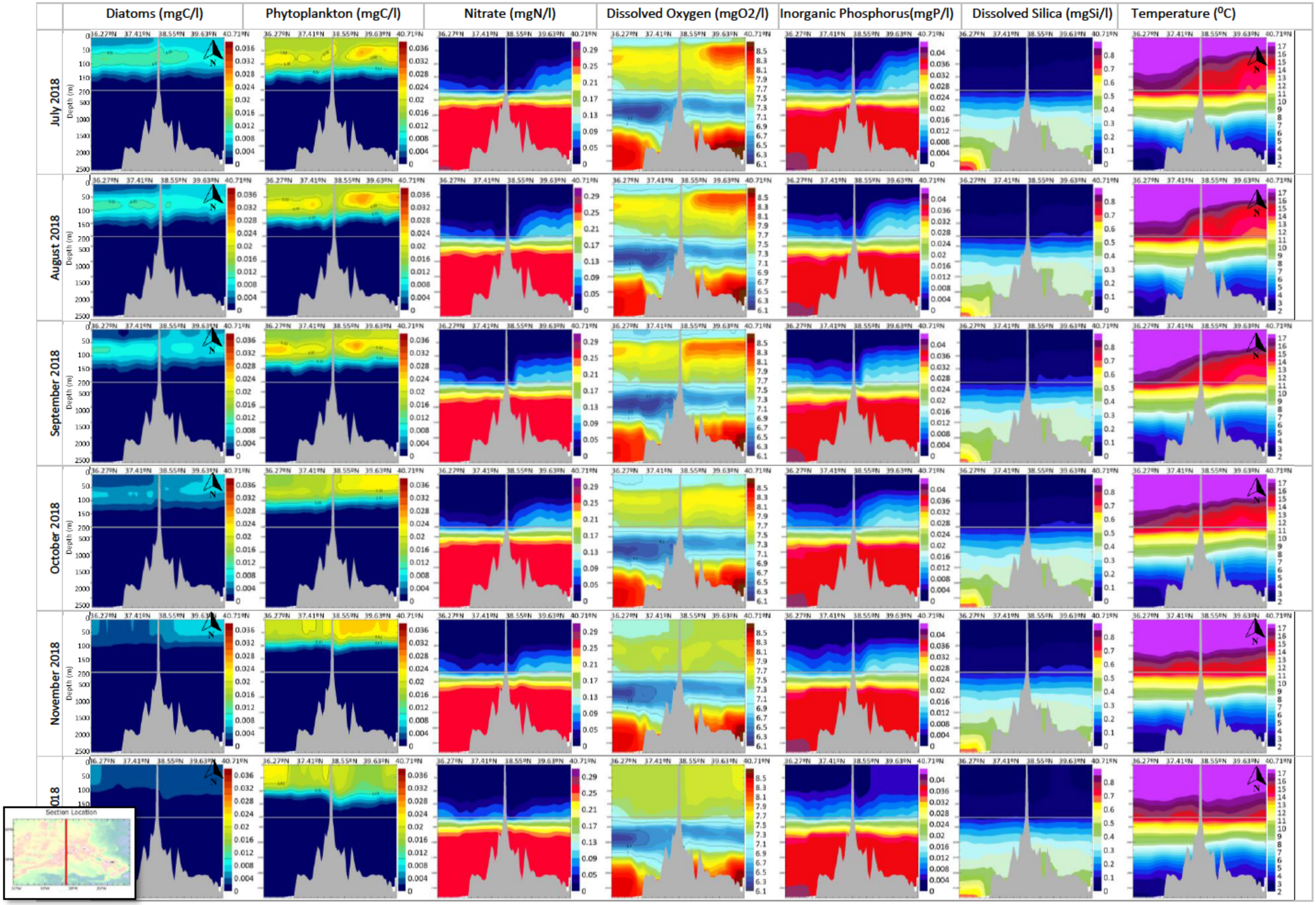

Figure B. 4- *Monthly average of model results from June 2018 to December 2018, for diatoms (mgC/l), small phytoplankton (mgC/l), nitrate (mgN/l), dissolved oxygen (mgO2/l), inorganic phosphorus (mgP/l), dissolved Silica (mgSi/l), and temperature (ºC) along water column (from surface 3000meters depth), along the meridional section at -28.5ºW, from 36.27ºN to 40.71ºN. Depth profiles present a higher resolution until 250 meters depth, and less resolution from 250 meters until 3000 meters depth*

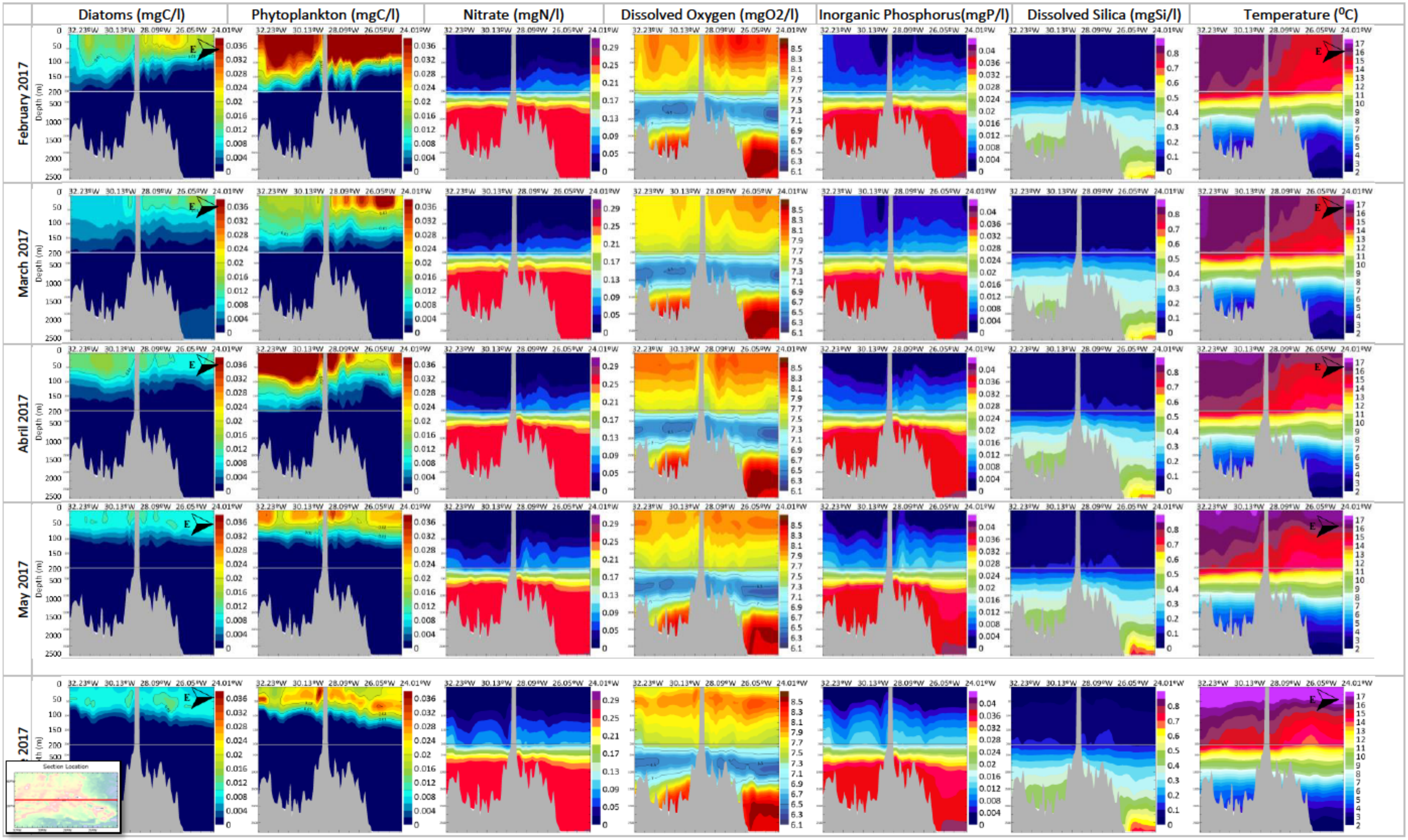

Figure B. 5- Monthly average of model results from February 2017 to June 2017, for diatoms (mgC/l), small phytoplankton (mgC/l), nitrate (mgN/l), dissolved oxygen (mgO2/l), inorganic phosphorus (mgP/l), dissolved Silica (mgSi/l), and temperature (⁰C) along the water column (from surface up to 3000meters depth), along the zonal section at 38.5⁰N, from -32.26⁰W to -23.32⁰W Depth profiles present a higher resolution until 250 meters depth, and less resolution from 250 meters until 3000 meters

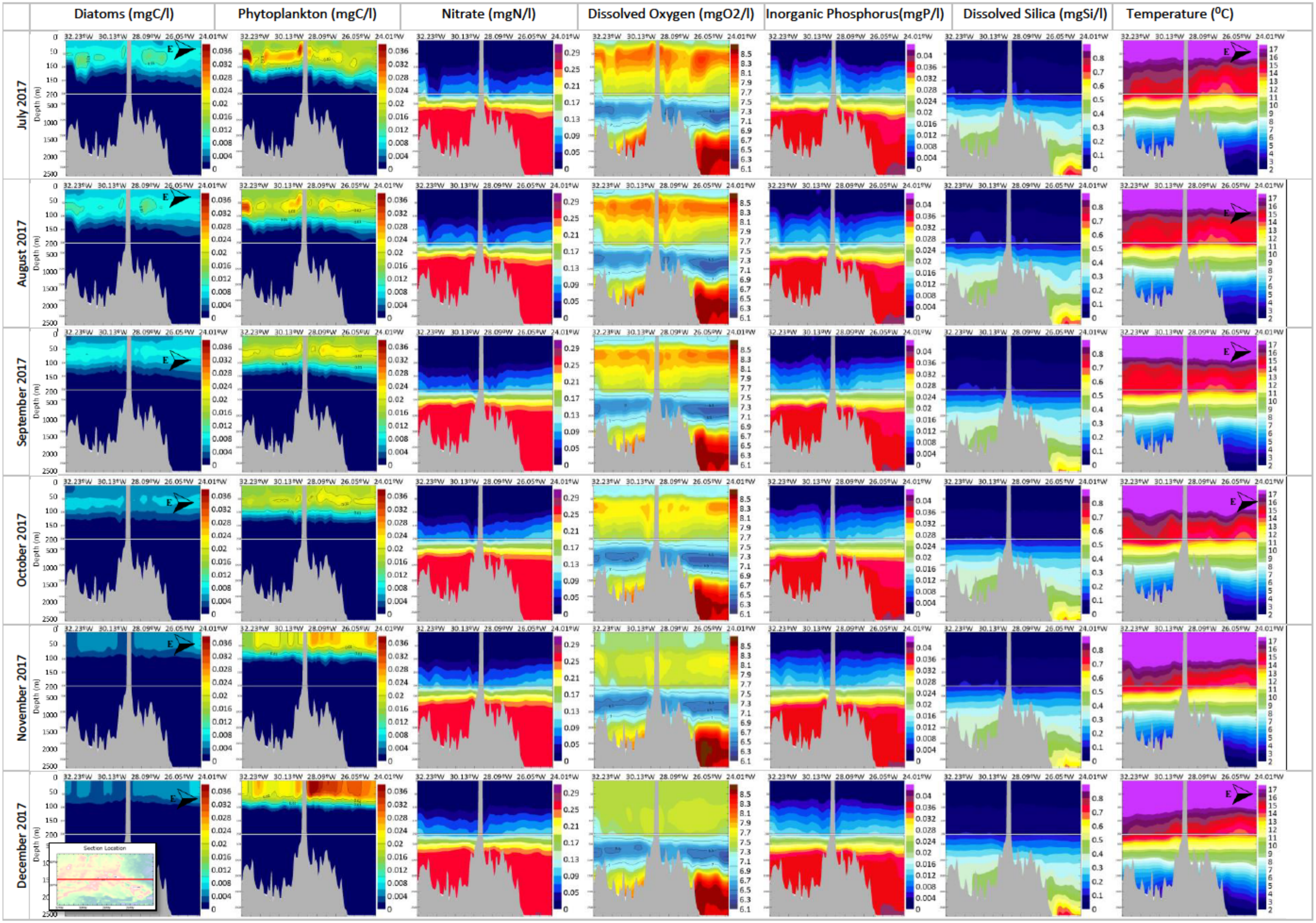

Figure B. 6- Monthly average of model results from July2017 to December 2017, for diatoms (mgC/l), small phytoplankton (mgC/l), nitrate (mgN/l), dissolved oxygen (mgO2/l), inorganic phosphorus (mgP/l), dissolved Silica (mgSi/l), and temperature (^{0}C) along the water column (from surface up to 3000meters depth), along the zonal section at 38.5^{0}N, from -32.26^{0}W to -23.32^{0}W Depth profiles present a higher resolution until 250 meters depth, and less resolution from 250 meters until 3000 meters.

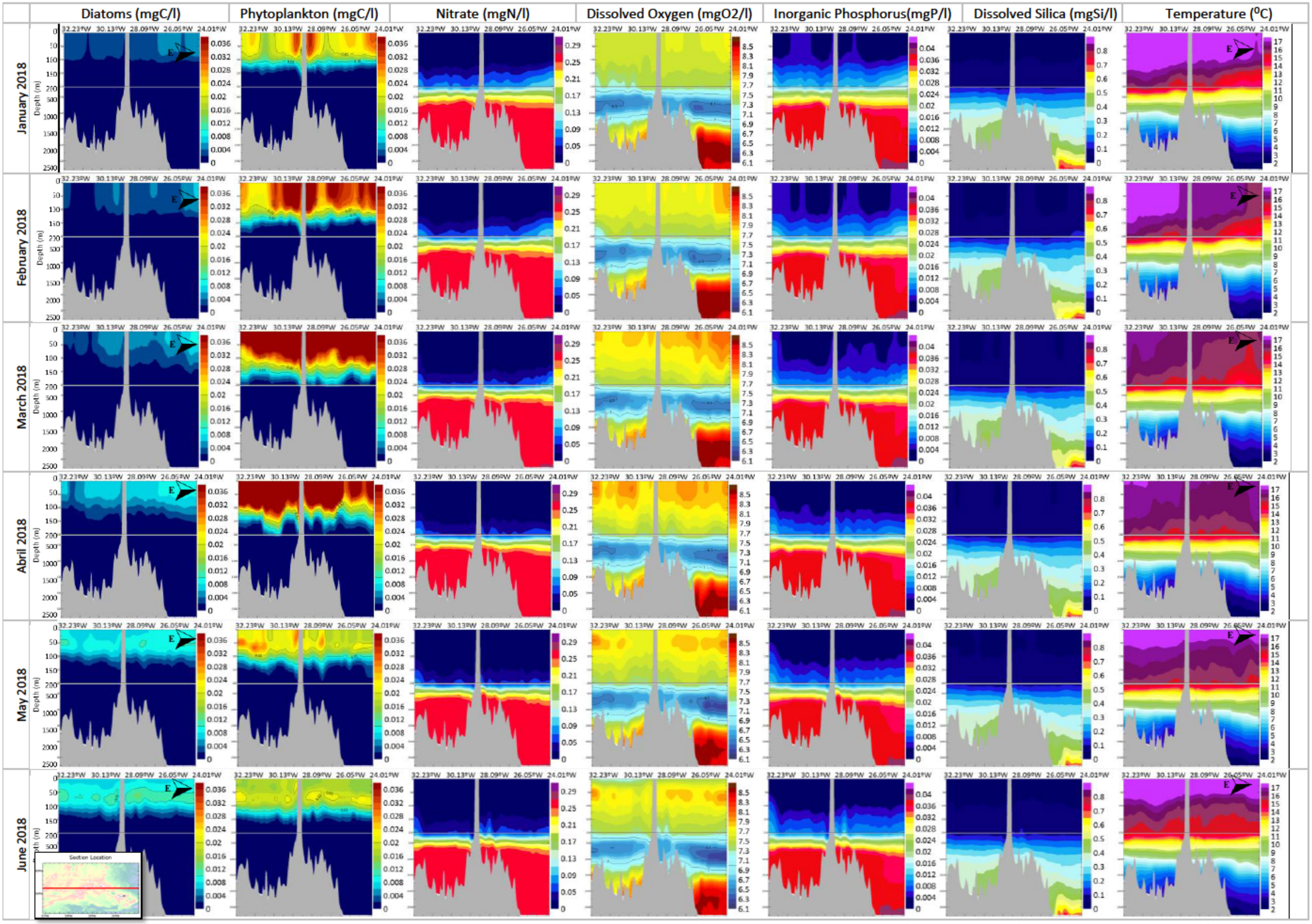

Figure B. 7- *Monthly average of model results from January 2018 to June 2018, for diatoms (mgC/l), small phytoplankton (mgC/l), nitrate (mgN/l), dissolved oxygen (mgO2/l), inorganic phosphorus (mgP/l), dissolved Silica (mgSi/l), and temperature (⁰C) along the water column (from surface up to 3000meters depth), along the zonal section at 38.5⁰N, from -32.26⁰W to -23.32⁰W Depth profiles present a higher resolution until 250 meters depth, and less resolution from 250 meters until 3000 meters depth*

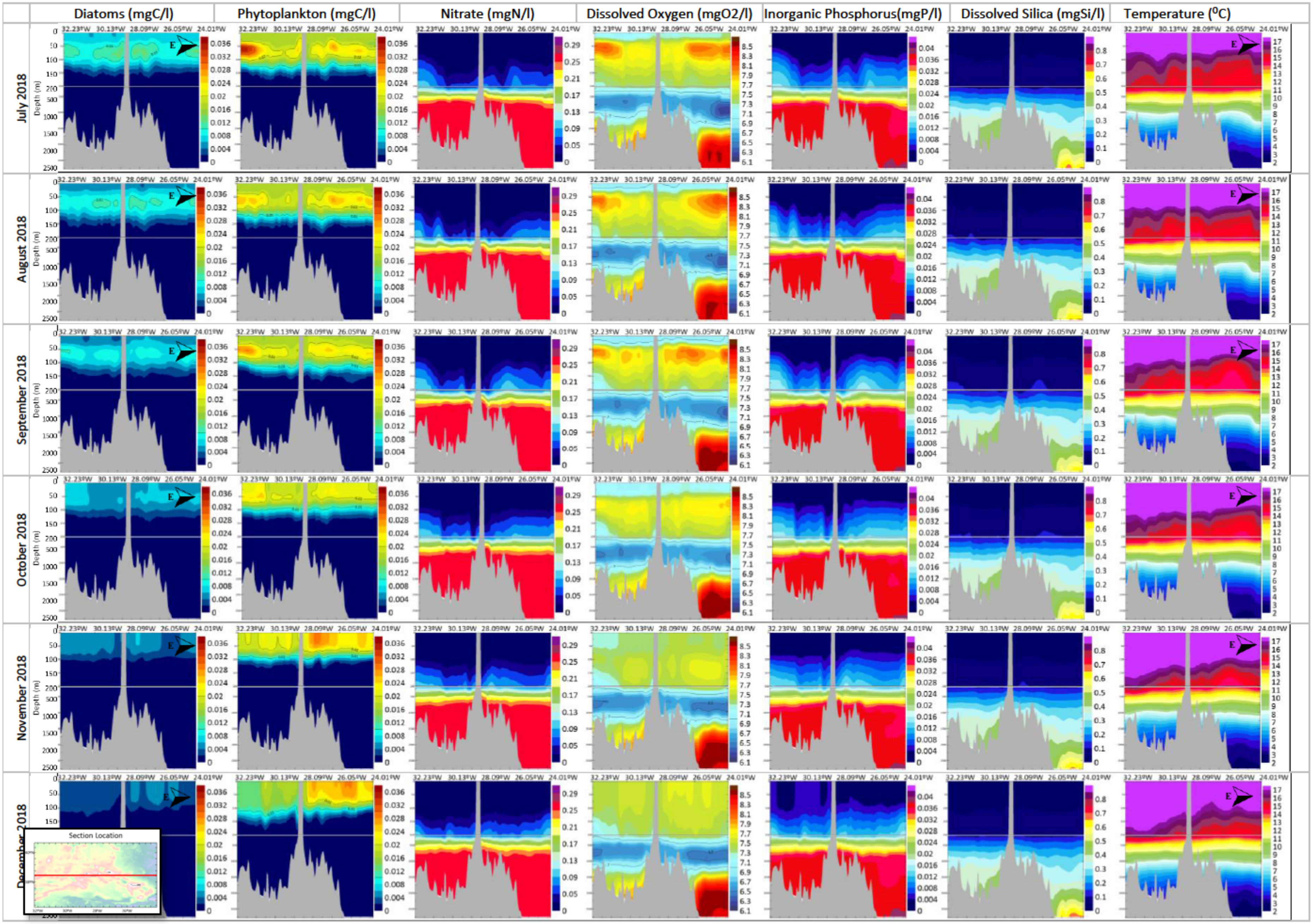

Figure B. 8- *Monthly average of model results from July 2018 to December 2018, for diatoms (mgC/l), small phytoplankton (mgC/l), nitrate (mgN/l), dissolved oxygen (mgO2/l), inorganic phosphorus (mgP/l), dissolved Silica (mgSi/l), and temperature (ºC) along the water column (from surface up to 3000meters depth), along the zonal section at 38.5ºN, from -32.26ºW to -23.32ºW Depth profiles present a higher resolution until 250 meters depth, and less resolution from 250 meters until 3000 meters depth*

Annex II

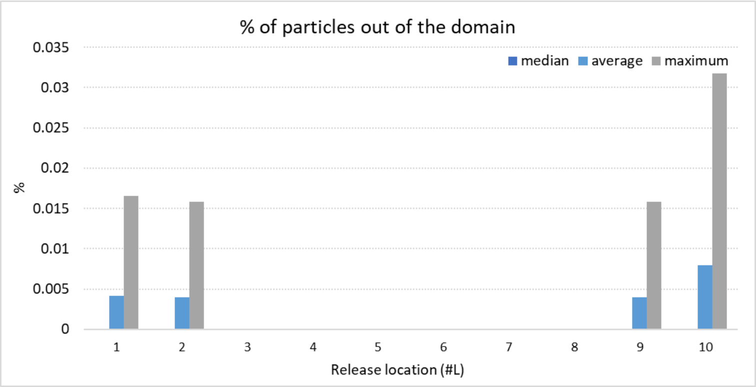

Figure C1- Median, average and maximum percentage of particles advected out of the domain, from all the locations, considering all the scenarios for *P. carpenteri* case study

Tabela A 1- Connectivity tables detailing the percentage of *P. carpenteri* released particles from each location (rows) that settled in each recruitment area (columns). For the scenario: Annual PLD15

	1	2	3	4	5	6	7	8	9	10
1	0.5713%									
2	0.0397%	0.0000%		0.0001%	0.0000%					
3			5.6448%							
4				5.6540%	0.4207%					
5				0.0093%	1.7308%					
6			0.0145%	0.0545%	0.1381%	1.0909%	0.6496%			
7						0.0005%	2.4358%			
8								4.7421%		
9									1.6738%	
10									0.0003%	0.7600%

Tabela A 2- Connectivity tables detailing the percentage of *P. carpenteri* released particles from each location (rows) that settled in each recruitment area (columns). For the scenario: Annual PLD30;

location	1	2	3	4	5	6	7	8	9	10
1	0.1367%	0.0768%		0.0086%	0.0037%					
2	0.2493%	0.0000%	0.0002%	0.0311%	0.0069%					
3			3.9452%			0.0004%	0.0001%			
4		0.0001%	0.0004%	3.4696%	1.1518%	0.0093%	0.0000%			
5	0.0002%	0.0201%	0.0001%	0.1699%	0.9759%	0.0002%	0.0002%	0.1040%		
6		0.0037%	0.2970%	0.1073%	0.1316%	0.8052%	0.7177%			
7			0.0001%	0.0008%	0.0001%	0.0118%	1.6633%	0.0001%		
8					0.0010%	0.0000%	0.0009%	2.3386%		
9									1.1073%	0.0062%
10									0.0636%	0.5057%

Tabela A 3- Connectivity tables detailing the percentage of *P. carpenteri* released particles from each location (rows) that settled in each recruitment area (columns). For the scenario: March PLD15 2017;

location	1	2	3	4	5	6	7	8	9	10
1	0.0012%									
2		0.0000%								
3			4.8707%							
4				4.1795%	0.0591%					
5					1.5391%					
6						0.3511%	4.9544%			
7							1.4782%			
8								1.9522%		
9									2.7241%	
10										1.5824%

Tabela A 4- Connectivity tables detailing the percentage of *P. carpenteri* released particles from each location (rows) that settled in each recruitment area (columns). For the scenario: March PLD30 2017;

location	1	2	3	4	5	6	7	8	9	10
1	0.0053%									
2	0.0638%	0.0000%								
3			2.8944%							
4			0.0006%	0.9000%	0.1879%	0.0328%				
5				0.0023%	0.1001%		0.0006%	0.9065%		
6						0.8093%	2.2109%			
7						0.0152%	1.0674%			
8								0.1381%		
9									3.2022%	
10										2.1869%

Tabela A 5- Connectivity tables detailing the percentage of particles released in each location (rows) that settled in each recruitment area (columns). For the scenario October PLD15 2017;

location	1	2	3	4	5	6	7	8	9	10
1	0.0901%									
2		0.0000%								
3			7 8418%							
4				0.2903%	2.7546%					
5					3.0864%					
6			0 0936%	0.0006%	0.0012%	0.0778%				
7							3 0126%			
8								3.3895%		
9										
10									0.0006%	2.2975%

Tabela A 6- Connectivity tables detailing the percentage of *P. carpenteri* released particles from each location (rows) that settled in each recruitment area (columns). For the scenario: October PLD30 2017;

location	1	2	3	4	5	6	7	8	9	10
1	0.1563%									
2		0.0000%								
3			17.1366%							
4				0.6033%	7.2004%					
5				0.0012%	6.9037%					
6			0.2885%	0.0023%	0.0047%	0.2025%				
7							6.4267%			
8								6.8931%		
9										
10										5.5665%